

PERFORMANCE-BASED EVALUATION OF UNBOUND AGGREGATES AFFECTING
MECHANISTIC RESPONSE AND PERFORMANCE OF FLEXIBLE PAVEMENTS

BY

YUANJIE XIAO

DISSERTATION

Submitted in partial fulfillment of the requirements
for the degree of Doctor of Philosophy in Civil Engineering
in the Graduate College of the
University of Illinois at Urbana-Champaign, 2014

Urbana, Illinois

Doctoral Committee:

Professor Erol Tutumluer, Chair and Director of Research
Professor W. James Wilde, Minnesota State University, Mankato
Professor Imad L. Al-Qadi
Professor Emeritus Marshall R. Thompson
Professor Jeffery R. Roesler

ABSTRACT

Unbound aggregates are widely used in road construction to replace unsuitable soil, prepare pavement working platform or construct pavement foundation layers. Their primary function in flexible pavements is to distribute wheel loads and provide adequate protection of the subgrade. However, the empirical strength based quality evaluations and current “recipe-based” specifications have little direct consideration of the actual performance of materials used in unbound aggregate layers. Based on a comprehensive set of laboratory repeated load triaxial test results archived for a variety of unbound aggregate materials, research efforts in this dissertation are aimed at linking aggregate physical and mechanical properties to pavement response and performance, identifying correlations among resilient modulus (M_R), plastic deformation and shear strength behavior under repeated loading, and developing viable models to predict engineering behavior and field performance. This thesis is organized into three sections. First, statistical and generic algorithm (GA) based models are developed to estimate M_R and shear strength properties for performance prediction using aggregate properties. The M_R sensitivities are assessed using both Monte Carlo type simulation and First-order Reliability Method (FORM) with the interactions between aggregate properties properly taken into account. Both gradation and aggregate shape properties are identified as influential factors affecting M_R . The effects of unbound aggregate quality on mechanistic response and performance (M_R , shear strength and rutting) and layer characteristics on pavement life expectancies are investigated. Secondly, aggregate gradation effects on strength and modulus characteristics of unbound aggregates are analyzed from laboratory test results to develop improved material specifications. The most significant correlations are found between a gravel-to-sand ratio (proposed based on ASTM D2487-11) and aggregate shear strength properties. A certain value of gravel-to-sand ratio is

proposed to optimize aggregate gradations for improved unbound layer performances primarily influenced by shear strength. To further confirm the optimal range of the gravel-to-sand ratio and verify existing packing theory based analytical gradation framework, a validated image-aided Discrete Element Method (DEM) modeling approach is also employed to realistically study optimum contact and packing arrangements of the aggregate skeleton from various gradations and morphological levels for better aggregate interlock. Guidelines are recommended for engineering the aggregate shape and gradation properties to achieve such desired improved engineering performances of unbound aggregate layers. Finally, this research described employs the shakedown concept to interpret laboratory single-stage repeated load triaxial permanent deformation test results performed at varying dynamic stress states and aggregate physical conditions. A stable permanent strain rate is highlighted to give a viable criterion for ranking the rutting potential of unbound aggregate layers under realistic field stress states and also relating to shear strength via the Mohr-Coulomb failure criteria. A unified approach to rutting prediction that is applicable to a much wider range of stress states and physical conditions is also developed based on shear strength properties and validated using actual rutting measurements from field full-scale accelerated pavement testing (APT) sections. The methodology and results in this dissertation provide insights that could potentially be used to develop a performance based material characterization and design framework for unbound aggregates.

ACKNOWLEDGEMENTS

This PhD journey would never reach its destination without the generous help from many individuals who I cannot all name here. Despite much more challenges and setbacks than I originally expected were encountered during this course, it is indeed a truly memorable and unique experience of my life. I consider myself extremely blessed and lucky to have those who made me feel that I was not alone. First and foremost, mere words cannot express enough my special, heartfelt gratitude to my enthusiastic advisor, Professor Dr. Erol Tutumluer, who kindly offered me the challenging but immensely rewarding opportunity to join his research group and always provided me with as much unwavering support and thoughtful advice on both academic and personal matters as I needed. In addition to teaching me the professional knowledge, he was also the most important and inspiring figure who helped me eventually get through the lowest point ever in my life, when I was struck by a life-changing incident in 2012. Without his continuing support and encouragement, I could never have gone this far. The way he advises and inspires students also exemplifies a dedicated scholar, great mentor, encouraging friend, and role model for me to admire and follow during the rest of my life.

I am also grateful to other members of my doctoral committee, Dr. W. James Wilde, Dr. Imad L. Al-Qadi, Dr. Marshall R. Thompson, and Dr. Jeffery R. Roesler for their support and most constructive and helpful comments. Their marvelous expertise in pavement technologies contributed to the completion of this dissertation. Collaborating with Dr. W. James Wilde on the research project sponsored by the Minnesota Department of Transportation (MnDOT) was a great learning experience for me. The courses I have taken and the research experiences I have attained at the University of Illinois at Urbana-Champaign are extremely helpful in further cultivating my professional knowledge and skills.

During the course of this research study, both financial support and technical assistance were received from the Minnesota Department of Transportation Office of Materials and Road Research via two sponsored research projects (Contract #H09PS07 and #89260). My sincere thanks go to the members of the Technical Advisory Panels (TAPs) for both projects. The constant support from Mr. John A. Siekmeier, Mr. Terry Beaudry, Dr. Shongtao Dai, and others at MnDOT is gratefully acknowledged.

I also want to thank all of the previous and existing members of the Transportation Geotechnics Research Group for our friendship and collaboration on different research projects. Special thanks are due to Dr. Hai Huang for not only introducing me to the University of Illinois Aggregate Image Analyzer (UIAIA) and discrete element modeling but also continuing to help me in different aspects. Yu Qian and Huseyin Boler are appreciated for sharing their knowledge that I needed for the discrete element modeling. In addition, Huseyin has been a good officemate to work together in many late nights and weekends. Such appreciation and sincere thanks also extend to other friends and classmates I have known over the years, especially Dr. Qiao Dong who encouraged me to pursue my PhD study in the U.S. and has been a cheerful brother to me.

Finally, I am forever indebted to my parents, grandma, and sister for their unconditional love and understanding, endless encouragement and patience, as well as enormous sacrifices they have made during my absence. They are the heroes behind the scene that make my dreams come true.

Last but not the least; I will always be grateful to Jingli who has spiritually accompanied me all the way through many bitter and sweet moments I have experienced in the past few years. I also thank Karen Zhu for the time we spent together, the recollection of which remains memorable and inspiring in the depth of my heart and lingers hauntingly in my dreams.

Table of Contents

List of Figures.....	x
List of Tables	xvii
Chapter 1 Introduction.....	1
1.1 Background.....	1
1.1.1 Unbound Aggregate Layer Functionality	1
1.1.2 Unbound Aggregate Layer As A Pavement Structural Component	2
1.2 Problem Statement.....	4
1.3 Research Objective and Scope.....	7
1.4 Contributions to Advancing Knowledge	8
1.5 Thesis Organization	9
Chapter 2 Literature Review	12
2.1 Aggregate Properties Affecting Unbound Aggregate Layer Behavior.....	12
2.1.1 Particle Size Distribution and Fines Content	13
2.1.2 Particle Shape, Surface Texture and Angularity	14
2.1.3 Degree of Compaction	15
2.1.4 Moisture Content.....	16
2.2 Aggregate Specifications and Classification Systems	17
2.2.1 Physical Classification System	17
2.2.2 Performance-based Mechanical Classification System	18
2.2.3 Best Value Granular Material Concept.....	19
2.3 Gradation Analysis and Packing Theories.....	20
2.3.1 Review of Gradation Quantification Methods	22
2.3.2 Analytical Gradation Analysis Framework.....	25
2.3.3 Imaging based Determination of Particle Morphology.....	31
2.3.4 Discrete Element Method (DEM) based Aggregate Packing Simulation.....	33
2.4 Resilient Response of Unbound Aggregate Layers	37
2.4.1 Laboratory Characterization Methods	37
2.4.2 Review of Current Resilient Modulus Models	40
2.5 Shear Strength of Unbound Aggregate Layers	42
2.5.1 Laboratory Characterization Methods	42
2.5.2 Review of Current Shear Strength Models	43
2.6 Permanent Deformation of Unbound Aggregate Layers	45
2.6.1 Laboratory Characterization Methods	47
2.6.2 Review of Current Permanent Deformation Models	48
2.6.3 “Shakedown” Theory for Analyzing Permanent Deformation Behavior	56
2.6.4 Stress Path Loading Effects	59
2.6.5 Importance of Shear Strength in Controlling Rutting Accumulation	62
2.7 Numerical Simulation of Unbound Aggregate Materials	65
2.7.1 Continuum-based Finite Element (FE) Modeling.....	65
2.7.2 Discrete Element Method (DEM) Modeling	67
2.8 Summary.....	69

Chapter 3	Research Approach and Databases	70
3.1	University of Illinois Aggregate Modulus and Strength Databases	70
3.1.1	NCHRP 4-23 Research Project Database	70
3.1.2	Federal Aviation Administration (FAA) Granular Base/Subbase Material Study Database	71
3.1.3	Illinois Center for Transportation R27-1 Research Project Database	73
3.1.4	Geogrid Aggregate Base Reinforcement Database	74
3.2	MnDOT Laboratory Aggregate Databases	77
3.2.1	Materials Tested	78
3.2.2	Experimental Program	79
3.3	FAA NAPTF Field Trafficking Study Database	80
3.3.1	NAPTF Pavement Sections	80
3.3.2	APT Loading System	81
3.4	University of Illinois Field Study Database	83
3.4.1	Full-scale Pavement Sections	83
3.4.2	Accelerated Loading Facility and Test Program	87
3.4.3	Key Observations from Field Rutting Measurements	88
3.5	Summary	91
Chapter 4	Resilient Modulus Behavior Estimated from Aggregate Source Properties and Its Effects on Flexible Pavement Performance	92
4.1	Resilient Modulus Model for Unbound Aggregates	92
4.2	Importance of Aggregate Shape Properties	95
4.3	Regression based Resilient Modulus Model Development	102
4.3.1	Regression Analysis Methodology	102
4.3.2	Selection and Diagnostics of Predictor Variables	103
4.3.3	First-order Model	104
4.3.4	Examine and Test for Normality and Constant Variance	109
4.3.5	Model Validation Using 15% Data	110
4.3.6	Final Model Development with Combined Data Sets	113
4.4	Monte Carlo Simulation of Resilient Modulus	114
4.4.1	Development of M_R Predictive Model	115
4.4.2	Simulation Results	116
4.5	Reliability-Based Evaluation of Aggregate Source Properties Affecting Resilient Modulus Behavior	120
4.5.1	Limit State Function Used	120
4.5.2	Variables and Distributions	122
4.5.3	First-Order Reliability Method (FORM) Analysis	123
4.5.4	Sensitivity of Variables to the Reliability Index	126
4.6	Mechanistic-Empirical Evaluation of Aggregate Quality Affecting Flexible Pavement Performance	128
4.6.1	Representative Aggregate Quality Levels	129
4.6.2	Sensitivity Analysis Matrix	133
4.6.3	GT-PAVE Structural Finite Element Modeling	135
4.6.4	Effect of Aggregate Quality on Fatigue Life Performance	138

4.6.5	Effect of Aggregate Quality on Rutting Life Performance	141
4.6.6	Statistical and Sensitivity Analyses	142
4.7	Summary	144
Chapter 5	Experimental Investigation of Aggregate Packing Affecting Shear	
	Strength of Unbound Aggregates	148
5.1	Different Gradation Designs Studied in the MnDOT Aggregate Database.....	148
5.2	Analyses of Experimental Results	154
5.2.1	Determination of Key Gradation Parameters	154
5.2.2	Modulus-Strength Relationship	155
5.2.3	Critical Gradation Parameter(s) Governing Shear Strength Behavior	157
5.3	Discussions	159
5.3.1	Interpretation of the Gravel-to-Sand Ratio	159
5.3.2	Analyses of Other Aggregate Databases Collected	163
5.4	Engineering Application of the Gravel-to-Sand Ratio Concept	167
5.5	Summary	172
Chapter 6	Discrete Element Modeling of Gradation Effects Influencing Contact	
	and Packing Characteristics of Aggregate Skeleton.....	174
6.1	Calibration of the DEM Model Parameters with Rapid Shear Tests	175
6.1.1	Description of Laboratory Rapid Shear Tests	175
6.1.2	Discrete Element Modeling of Rapid Shear Tests	176
6.1.3	Calibration of the DEM Model with Rapid Shear Tests	181
6.2	DEM Approach for Studying Underlying Mechanisms of Aggregate Packing ...	186
6.2.1	Roles of Particles in an Aggregate Structure	187
6.2.2	DEM Simulations for Determining Breaking-Sieve-Size.....	189
6.3	Gradation Effects Influencing Contact and Packing Characteristics of	
	Aggregate Skeleton	199
6.3.1	Determination of Gradation Design Alternatives	200
6.3.2	Analysis Results of the Analytical Gradation Framework.....	201
6.3.3	DEM Packing Simulation Results.....	206
6.4	DEM Validation of the Gravel-to-Sand Ratio Concept.....	209
6.5	Summary	220
Chapter 7	Unified Approach to Unbound Aggregate Permanent Deformation	
	Modeling Based on Shear Strength.....	223
7.1	Evaluating MEPDG Rutting Model for Unbound Aggregates.....	223
7.1.1	Applicability for Dynamic Stress States Induced by Moving Wheel Loading	226
7.1.2	Applicability for Different Aggregate Physical Properties	233
7.1.3	Correlation between Resilient Modulus and Permanent Deformation for	
	Unbound Aggregate under Repeated Loading	242
7.1.4	Enhancement of the Current MEPDG Permanent Deformation Model for	
	Unbound Materials.....	255
7.2	Modeling Degradation Stiffness for Permanent Deformation Prediction	261

7.2.1	Degradation Stiffness Model	263
7.2.2	Parameter Estimation for the Degradation Stiffness Model	265
7.3	Shakedown based Interpretation of Permanent Deformation Test Results	268
7.3.1	Modeling the Primary and the Secondary Regions of Permanent Deformation Curves	269
7.3.2	Effects of Aggregate Physical Properties.....	272
7.3.3	Effects of Constant Confining Pressure (CCP) Stress States.....	276
7.3.4	Effects of Varying Confining Pressure (VCP) Stress States.....	280
7.4	Development of Phenominological Stable Permanent Strain Rate Model	286
7.4.1	Mohr-Coulomb Representation of Stable Permanent Strain Rate Envelope	286
7.4.2	p-q Diagram Representation of Stable Permanent Strain Rate Envelope	291
7.5	Unified Rutting Prediction Model Development.....	293
7.5.1	Model Development for Different Aggregate Physical Properties	293
7.5.2	Model Development for Different Dynamic Stress States.....	300
7.6	Summary.....	307
Chapter 8	Field Validation of Unified Rutting Prediction Model for Unbound Granular Materials Using Accelerated Pavement Tests	310
8.1	Permanent Deformation Predictions of the NAPTF Test Sections.....	310
8.1.1	Modeling Responses of NAPTF Test Sections.....	310
8.1.2	Permanent Deformation Predicted by the Unified Rutting Model	311
8.2	Permanent Deformation Predictions of ICT Full Scale Test Sections.....	316
8.2.1	Modeling Responses of ICT Full Scale Test Sections.....	316
8.2.2	Permanent Deformation Predicted by the MEPDG Model.....	325
8.3	Shear Stress Ratio Analysis for Interpreting Field Rutting Performance	333
8.4	Summary	338
Chapter 9	Conclusions, Findings, and Recommendations	340
9.1	Conclusions.....	340
9.2	Detailed Research Findings	341
9.3	Recommendations for Future Research	346
References	348	

List of Figures

FIGURE 1.1 NON-STANDARD MATERIAL GROUPS AND THEIR LIKELY PROBLEMS (COOK AND GOURLEY, 2002)	3
FIGURE 1.2 FLOWCHART OF ANALYSIS APPROACH.....	8
FIGURE 2.1 PHYSICAL (LEFT) VERSUS MECHANICAL (RIGHT) CLASSIFICATION FOR VARIOUS UNBOUND GRANULAR MATERIALS (PAUTE ET AL., 1994)	18
FIGURE 2.2 BEST VALUE GRANULAR MATERIAL MNPAVE DESIGN IMPLEMENTATION (XIAO AND TUTUMLUER, 2012)	20
FIGURE 2.3 PACKING THEORY BASED GRADATION MODEL PROPOSED BY YIDETI ET AL. (2013): (A) SKELETON OF UNBOUND GRANULAR MATERIAL AND (B) VOLUMETRIC COMPOSITION OF SKELETON	26
FIGURE 2.4 ILLUSTRATION OF THE UNIVERSITY OF ILLINOIS AGGREGATE IMAGE ANALYZER (UIAIA): (A) THE FIRST GENERATION, (B) THE SECOND ENHANCED GENERATION, (C) IMAGES CAPTURED FROM THREE ORTHOGONAL VIEWS OF A PARTICLE, AND (D) KEY MORPHOLOGICAL DESCRIPTORS AND THEIR ALGORITHMS (RAO, 2001; PAN, 2006; MOAVENI ET AL., 2013).....	32
FIGURE 2.5 FOUR DISTINCT GRAIN SIZE DISTRIBUTION CURVES FOR DEM SIMULATION (EVANS, 2009).....	34
FIGURE 2.6 DEM SIMULATION RESULTS BY HUANG (2010): (A) CHARACTERISTIC MAXIMUM DENSITY GRADATION CURVES STUDIED, (B) DEM CYLINDRICAL SAMPLE FOR AIR VOIDS DETERMINATION, AND (C) EFFECT OF MINIMUM PARTICLE SIZE ON MEAN AIR VOIDS CONTENT.....	36
FIGURE 2.7 STRESS STATES AND ROTATION OF PRINCIPAL STRESSES EXPERIENCED BY THE AGGREGATE LAYER BENEATH A ROLLING WHEEL LOAD (TUTUMLUER, 2013)	38
FIGURE 2.8 CONCEPT OF STRESS PATH LOADING SHOWING SLOPE AND LENGTH (KIM, 2005).....	39
FIGURE 2.9 SCHEMATIC REPRESENTATION OF DIFFERENT PERMANENT DEFORMATION BEHAVIOR	49
FIGURE 2.10 SCHEMATIC REPRESENTATION OF STRESS PATH LOADING (TUTUMLUER, 2013)	61
FIGURE 2.11 REPRESENTATION OF MOHR-COULOMB FAILURE ENVELOPE IN (A) Σ -T DIAGRAM AND (B) P-Q DIAGRAM	64
FIGURE 2.12 DEM SIMULATION FOR (A) CBR AND (B) DCP TESTS (HILL ET AL., 2012).....	68
FIGURE 3.1 MNDOT SPECIFIED GRADATION BANDS FOR DIFFERENT AGGREGATE CLASSES.....	78
FIGURE 3.2 CROSS SECTIONS OF NAPTF PAVEMENT TEST SECTIONS (KIM, 2005)	82
FIGURE 3.3 SCHEMATIC LAYOUT OF FULL-SCALE PAVEMENT TEST SECTIONS: (A) AERIAL VIEW AND (B) PLAN VIEW AND CROSS-SECTIONAL PROFILES (MISHRA AND TUTUMLUER, 2013).....	85
FIGURE 3.4 GRADATION CURVES OF MATERIALS USED IN FULL-SCALE TEST SECTIONS.....	86
FIGURE 3.5 MAXIMUM RUT DEPTH MEASURED UNDER NEAR-OPTIMUM CONDITIONS FOR (A) SECTION 1, (B) SECTION 2, AND (C) SECTION 3 OF CELLS 1, 2, 4, AND 5	89
FIGURE 3.6 MAXIMUM RUT DEPTH MEASURED UNDER FLOODED CONDITIONS FOR (A) SECTION 1, (B) SECTION 2, AND (C) SECTION 3 OF CELLS 1, 2, 4, AND 5	90
FIGURE 4.1 EFFECTS OF (A) AGGREGATE ANGULARITY AND (B) SURFACE TEXTURE ON RESILIENT MODULUS ANALYZED FROM GEOGRID REINFORCEMENT APPLICATIONS	97

FIGURE 4.2 COMPARISON OF RAPID SHEAR TEST RESULTS FOR (A) UNCRUSHED GRAVEL (ROUNDED AND SMOOTH SURFACED PARTICLES) AND (B) CRUSHED LIMESTONE (ANGULAR AND ROUGH SURFACED PARTICLES) WITH 4% NON-PLASTIC FINES AT OPTIMUM MOISTURE CONTENT (DATA SOURCE: TUTUMLUER ET AL., 2009)	100
FIGURE 4.3 COMPARISON OF RAPID SHEAR TEST RESULTS FOR (A) UNCRUSHED GRAVEL (ROUNDED AND SMOOTH SURFACED PARTICLES) AND (B) CRUSHED LIMESTONE (ANGULAR AND ROUGH SURFACED PARTICLES) WITH 4% PLASTIC FINES AT OPTIMUM MOISTURE CONTENT (DATA SOURCE: TUTUMLUER ET AL., 2009)	101
FIGURE 4.4 MEASURED VS. PREDICTED VALUES FOR LOGK ₁	111
FIGURE 4.5 MEASURED VS. PREDICTED VALUES FOR K ₂	112
FIGURE 4.6 MEASURED VS. PREDICTED VALUES FOR K ₃	112
FIGURE 4.7 SENSITIVITY CHARTS FOR M _R : (A) STRESS LEVELS IN AGGREGATE BASE AND (B) STRESS LEVELS IN GRANULAR SUBBASE.....	119
FIGURE 4.8 FORM APPROXIMATIONS (HAUKAAS AND KIUREGHIAN, 1999)	124
FIGURE 4.9 RELATIVE CONTRIBUTIONS OF VARIOUS VARIABLES TO RESILIENT MODULUS (M _R)	125
FIGURE 4.10 THE RELATIVE CONTRIBUTION OF EACH VARIABLE TO RESILIENT MODULUS (M _R)	126
FIGURE 4.11 COMPUTED RESILIENT MODULI FOR DIFFERENT UNBOUND (A) AGGREGATE BASE AND (B) GRANULAR SUBBASE MATERIALS (1 PSI = 6.89 kPA).....	131
FIGURE 4.12 GRADATIONS OF REPRESENTATIVE AGGREGATE BASE AND GRANULAR SUBBASE MATERIALS.....	133
FIGURE 4.13 ILLUSTRATIONS OF GT-PAVE (NOT TO SCALE): (A) FINITE ELEMENT MESH OF PAVEMENT STRUCTURE, AND (B) PREDICTED MODULUS DISTRIBUTIONS IN THE BASE AND SUBBASE.....	136
FIGURE 4.14 EQUIVALENT M _R VALUES LINKED TO AGGREGATE QUALITY FOR (A) 4-IN., (B) 6-IN., (C) 8-IN. ASPHALT SURFACE THICKNESSES, AND (D) CURRENT DEFAULT MNPAVE FALL DESIGN MODULI	137
FIGURE 4.15 FATIGUE LIFE PREDICTIONS FOR DIFFERENT BASE-SUBBASE QUALITIES: (A) BELTRAMI COUNTY, AND (B) OLMSTED COUNTY (M-L STANDS FOR MEDIUM QUALITY BASE AND LOW QUALITY SUBBASE)	139
FIGURE 4.16 EFFECTS OF UNBOUND GRANULAR MATERIAL QUALITY ON FATIGUE LIFE FOR BELTRAMI COUNTY: (A) 0.6 MILLION ESALS, (B) 1.5 MILLION ESALS, AND (C) 6 MILLION ESALS (H-L STANDS FOR HIGH QUALITY BASE AND LOW QUALITY SUBBASE) ..	140
FIGURE 4.17 RUTTING LIFE PREDICTIONS FOR DIFFERENT BASE-SUBBASE QUALITIES IN (A) BELTRAMI AND (B) OLMSTED COUNTIES (M-L STANDS FOR MEDIUM QUALITY BASE AND LOW QUALITY SUBBASE)	141
FIGURE 4.18 EFFECTS OF UNBOUND GRANULAR MATERIAL QUALITY ON RUTTING LIFE FOR BELTRAMI COUNTY: (A) 0.6 MILLION ESALS, (B) 1.5 MILLION ESALS, AND (C) 6 MILLION ESALS (H-L STANDS FOR HIGH QUALITY BASE AND LOW QUALITY SUBBASE) ..	143
FIGURE 5.1 GRADATIONS OF TRADITIONAL BASE/SUBBASE MATERIALS IN MNDOT DATABASE: (A) SELECT GRANULAR; (B) GRANITE; (C) PIT-RUN GRAVEL; AND (D) LIMESTONE.....	151
FIGURE 5.2 GRADATIONS OF NON-TRADITIONAL WASTE BASE/SUBBASE MATERIALS IN MNDOT DATABASE: (A) TACONITE TAILINGS; (B) RECLAIMED CONCRETE (CLASS 7C); (C) RECLAIMED BITUMINOUS (CLASS 7B); AND (D) FULL-DEPTH RECLAMATION (FDR)	152

FIGURE 5.3 RESILIENT MODULUS-SHEAR STRENGTH RELATIONSHIPS FOR “STANDARD” (A) AGGREGATE BASE AND (B) GRANULAR SUBBASE MATERIALS AT NEAR OPTIMUM MOISTURE CONDITIONS	157
FIGURE 5.4 PEAK DEVIATOR STRESS AT FAILURE (σ_{DF}) VS GRAVEL-TO-SAND (G/S) RATIO FOR VARIOUS AGGREGATES: (A) 4-PSI, (B) 5-PSI, (C) 8-PSI, AND (D) 10-PSI CONFINING PRESSURE (σ_3).....	158
FIGURE 5.5 DIFFERENT PACKING STATES OF GRAVEL-SAND-FINES MIXTURE WITH DIFFERENT GRAVEL/SAND RATIOS (G/S) (SMALL BLACK DOTS REPRESENT FINES FRACTION): (A) LARGE G/S, (B) OPTIMUM G/S, (C) SMALL G/S.....	160
FIGURE 5.6 MAXIMUM DRY DENSITY (Σ_{DMAX}) AND OPTIMUM MOISTURE CONTENT (Ω_{OPT}) VS GRAVEL-TO-SAND RATIO (G/S) AT (A) 4-PSI AND (B) 8-PSI CONFINING PRESSURE (σ_3).....	162
FIGURE 5.7 THE GRAVEL-TO-SAND RATIO EFFECTS OBSERVED IN OTHER DATABASES COLLECTED FROM (A) GARG AND THOMPSON (1997) AND (B) TIAN ET AL. (1998)	164
FIGURE 5.8 THE GRAVEL-TO-SAND RATIO EFFECTS OBSERVED IN OTHER DATABASES COLLECTED FROM TUTUMLUER ET AL. (2009)	166
FIGURE 5.9 MNDOT GRADATION SPECIFICATIONS (A) FOR UNBOUND PERMEABLE AGGREGATE BASES (PAB); (B) GRADATION CHART WITH CONTOURS OF THE GRAVEL TO SAND (G/S) RATIO GRADATION PARAMETER FOR MNDOT UNBOUND PAB GRADATION BAND	168
FIGURE 5.10 FOUR BOUNDARY GRADATION CURVES CONSISTING OF MNDOT UNBOUND PAB GRADATION BAND AND THE PROPOSED OPTIMAL GRADATION	171
FIGURE 6.1 GRADATION CURVE OF AGGREGATE SPECIMENS (A) AND AGGREGATE BLENDING EFFECT ON MAXIMUM DEVIATOR STRESS Σ_d (B) AND PERMANENT STRAIN E_p (C) (DATA SOURCE: TUTUMLUER AND PAN, 2008).....	179
FIGURE 6.2 ILLUSTRATION OF TRIAXIAL COMPRESSION DEM SIMULATION: (A) ARRANGEMENT OF MEMBRANE ELEMENTS, (B) AGGREGATE SPECIMEN MODELED, AND (C) SPECIMEN PREPARATION PROCESS	181
FIGURE 6.3 TRIAXIAL COMPRESSION DEM TEST RESULTS FOR THREE SPECIMENS REPRESENTING HIGH, MEDIUM, AND LOW MAXIMUM DEVIATOR STRESS LEVELS.....	185
FIGURE 6.4 VARIATION OF PEAK FRICTION ANGLE (ϕ_p) WITH (A) ANGULARITY INDEX AI AND (B) SURFACE TEXTURE ST	185
FIGURE 6.5 (A) CONTACT FORCES FOR TWO-DIMENSIONAL NUMERICAL SIMULATION UNDER ANISOTROPIC LOADING (DOBRY ET AL., 1989) AND (B) SCHEMATIC REPRESENTATION OF LOAD TRANSFER IN THE BASE LAYER (TUTUMLUER, 1995).....	187
FIGURE 6.6 GRADATION BANDS SPECIFIED BY MNDOT FOR DIFFERENT AGGREGATE CLASSES	190
FIGURE 6.7 DEM SIMULATED MNDOT CL-6 GRADATION ALTERNATIVES: (A) CL-6 LOWER BOUND AND (B) CL-6 UPPER BOUND	190
FIGURE 6.8 ILLUSTRATION OF DEM PARTICLE GENERATION PROCESS FOR (A) GRADATION #1, (B) GRADATION #2, AND (C) GRADATION #3 OF CL-6 UPPER BOUND AND (D) PARTICLE COMPACTION PROCESS	194
FIGURE 6.9 RELATIVE IMPORTANCE OF EACH CONTROL SIEVE IN PRIMARY STRUCTURE POROSITY AND COORDINATION NUMBER FROM SPHERICAL PACKING THEORY BASED ANALYTICAL FRAMEWORK: (A) 19 MM, (B) 9.5 MM, (C) 4.75 MM, AND (D) 2 MM.....	204

FIGURE 6.10 RELATIVE IMPORTANCE OF EACH CONTROL SIEVE IN PRIMARY STRUCTURE POROSITY AND COORDINATION NUMBER FROM DEM PACKING SIMULATION (HIGH ANGULARITY): (A) 19 MM AND (B) 9.5 MM.....	208
FIGURE 6.11 DEM SIMULATED GRADATION CURVES WITH VARYING G/S RATIOS.....	209
FIGURE 6.12 FINAL COMPACTED AGGREGATE SAMPLES IN DEM SIMULATION FOR DIFFERENT G/S RATIO VALUES: (A) 1.0 AND (B) 1.6 (LEFT: LOW AI; RIGHT: HIGH AI).....	211
FIGURE 6.13 FINAL COMPACTED AGGREGATE SAMPLES IN DEM SIMULATION FOR DIFFERENT G/S RATIO VALUES: (A) 2.0 AND (B) 2.5 (LEFT: LOW AI; RIGHT: HIGH AI).....	212
FIGURE 6.14 DEM CALCULATED (A) COORDINATION NUMBER AND (B) POROSITY VERSUS G/S RATIO FOR HIGH AND LOW ANGULARITY LEVELS	213
FIGURE 6.15 COMPARISON OF INTERNAL CONTACT FORCE DISTRIBUTIONS FOR THREE DIFFERENT G/S RATIOS.....	214
FIGURE 6.16 ILLUSTRATION OF DEM CALCULATED INTERNAL CONTACT FORCE VECTORS FOR G/S=1.0 WITH HIGH ANGULARITY LEVEL: (A) X-Z PLANE VIEW, (B) Y-Z PLANE VIEW, (C) X-Y PLANE VIEW, AND (D) THREE DIMENSIONAL (3D) VIEW	216
FIGURE 6.17 ILLUSTRATION OF DEM CALCULATED INTERNAL CONTACT FORCE VECTORS FOR G/S=1.6 WITH HIGH ANGULARITY LEVEL: (A) X-Z PLANE VIEW, (B) Y-Z PLANE VIEW, (C) X-Y PLANE VIEW, AND (D) THREE DIMENSIONAL (3D) VIEW	217
FIGURE 6.18 ILLUSTRATION OF DEM CALCULATED INTERNAL CONTACT FORCE VECTORS FOR G/S=2.5 WITH HIGH ANGULARITY LEVEL: (A) X-Z PLANE VIEW, (B) Y-Z PLANE VIEW, (C) X-Y PLANE VIEW, AND (D) THREE DIMENSIONAL (3D) VIEW	218
FIGURE 6.19 3D VIEW OF DEM CALCULATED INTERNAL CONTACT FORCE VECTORS FOR HIGH ANGULARITY LEVEL: (A) G/S=1.0 AND (B) G/S=1.6	219
FIGURE 6.20 3D VIEW OF DEM CALCULATED INTERNAL CONTACT FORCE VECTORS FOR HIGH ANGULARITY LEVEL: G/S=2.5.....	220
FIGURE 7.1 RELATIONSHIP BETWEEN LABORATORY MEASURED AND PREDICTED VALUES OF (A) $\log(E_0/E_R)$, (B) $\log B$ AND (C) $\log P$ BY THE TSENG & LYTTON MODEL FORM AND (D) BY THE MEPDG MODEL FOR P209 MATERIAL	232
FIGURE 7.2 RELATIONSHIP BETWEEN LABORATORY MEASURED AND PREDICTED VALUES OF (A) $\log(E_0/E_R)$, (B) $\log B$ AND (C) $\log P$ BY THE TSENG & LYTTON MODEL FORM AND (D) BY THE MEPDG MODEL FOR P154 MATERIAL	233
FIGURE 7.3 RELATIONSHIP BETWEEN LABORATORY MEASURED AND PREDICTED VALUES OF (A) $\log(E_0/E_R)$, (B) $\log B$ AND (C) $\log P$ BY THE TSENG & LYTTON MODEL FORM (LEFT) AND BY THE MEPDG MODEL (RIGHT) FOR CRUSHED DOLOMITE.....	237
FIGURE 7.4 RELATIONSHIP BETWEEN LABORATORY MEASURED AND PREDICTED VALUES OF (A) $\log(E_0/E_R)$, (B) $\log B$ AND (C) $\log P$ BY THE TSENG & LYTTON MODEL FORM (LEFT) AND BY THE MEPDG MODEL (RIGHT) FOR CRUSHED LIMESTONE	239
FIGURE 7.5 RELATIONSHIP BETWEEN LABORATORY MEASURED AND PREDICTED VALUES OF (A) $\log(E_0/E_R)$, (B) $\log B$ AND (C) $\log P$ BY THE TSENG & LYTTON MODEL FORM (LEFT) AND BY THE MEPDG MODEL (RIGHT) FOR UNCRUSHED GRAVEL.....	241
FIGURE 7.6 RELATIONSHIP BETWEEN PLASTIC STRAIN AND VERTICAL RESILIENT MODULUS FOR P209 MATERIAL OBSERVED DURING CCP TEST WITH STRESS SLOPE $M=3$: (A) $\Sigma_{3s}=3$ PSI, (B) $\Sigma_{3s}=5$ PSI, (C) $\Sigma_{3s}=8$ PSI, AND (D) $\Sigma_{3s}=10$ PSI.....	246
FIGURE 7.7 RELATIONSHIP BETWEEN PLASTIC STRAIN AND VERTICAL RESILIENT MODULUS FOR P209 MATERIAL OBSERVED DURING VCP TEST WITH STRESS SLOPE $M=1.5$: (A) $\Sigma_{3s}=3$ PSI, (B) $\Sigma_{3s}=5$ PSI, (C) $\Sigma_{3s}=8$ PSI, AND (D) $\Sigma_{3s}=10$ PSI	247

FIGURE 7.8 RELATIONSHIP BETWEEN PLASTIC STRAIN AND VERTICAL RESILIENT MODULUS FOR P209 MATERIAL OBSERVED DURING VCP TEST WITH STRESS SLOPE $M=0$: (A) $\Sigma_{3s}=3$ PSI, (B) $\Sigma_{3s}=5$ PSI, AND (C) $\Sigma_{3s}=8$ PSI	247
FIGURE 7.9 RELATIONSHIP BETWEEN PLASTIC STRAIN AND VERTICAL RESILIENT MODULUS FOR P154 MATERIAL OBSERVED DURING CCP TEST WITH STRESS SLOPE $M=3$: (A) $\Sigma_{3s}=3$ PSI, (B) $\Sigma_{3s}=5$ PSI, AND (C) $\Sigma_{3s}=8$ PSI	248
FIGURE 7.10 RELATIONSHIP BETWEEN PLASTIC STRAIN AND VERTICAL RESILIENT MODULUS FOR P154 MATERIAL OBSERVED DURING VCP TEST WITH STRESS SLOPE $M=1.5$: (A) $\Sigma_{3s}=3$ PSI, (B) $\Sigma_{3s}=5$ PSI, (C) $\Sigma_{3s}=8$ PSI, AND (D) $\Sigma_{3s}=10$ PSI	248
FIGURE 7.11 RELATIONSHIP BETWEEN PLASTIC STRAIN AND VERTICAL RESILIENT MODULUS FOR P154 MATERIAL OBSERVED DURING VCP TEST WITH STRESS SLOPE $M=0$: (A) $\Sigma_{3s}=3$ PSI, (B) $\Sigma_{3s}=5$ PSI, AND (C) $\Sigma_{3s}=8$ PSI	249
FIGURE 7.12 RELATIONSHIP BETWEEN PLASTIC STRAIN AND VERTICAL RESILIENT MODULUS FOR CRUSHED DOLOMITE WITH VARYING FINES CONTENT (LEFT: NON-PLASTIC; RIGHT: PLASTIC)	252
FIGURE 7.13 RELATIONSHIP BETWEEN PLASTIC STRAIN AND VERTICAL RESILIENT MODULUS FOR CRUSHED LIMESTONE WITH VARYING FINES CONTENT (LEFT: NON-PLASTIC; RIGHT: PLASTIC)	253
FIGURE 7.14 RELATIONSHIP BETWEEN PLASTIC STRAIN AND VERTICAL RESILIENT MODULUS FOR UNCRUSHED GRAVEL WITH VARYING FINES CONTENT (LEFT: NON-PLASTIC; RIGHT: PLASTIC)	254
FIGURE 7.15 CHARACTERISTIC RESPONSE OF UNBOUND MATERIAL: (A) STRESS-STRAIN RELATIONSHIP (KHOGALI AND MOHAMED, 2004) AND (B) THE CONCEPT OF DEGRADATION STIFFNESS (ACHMUS ET AL., 2009)	264
FIGURE 7.16 VARIATION OF DEGRADED SECANT MODULUS WITH LOAD CYCLES FOR FAA P154 MATERIAL DURING CCP TESTS: (A) 3-PSI CONFINING STRESS AND (B) 5-PSI AND 8-PSI CONFINING STRESSES.....	266
FIGURE 7.17 CUMULATIVE PERMANENT AXIAL STRAIN ($E_p, N=1,000$) VARYING WITH PERMANENT AXIAL STRAIN RATE FOR (A) CRUSHED LIMESTONE, (B) CRUSHED DOLOMITE AND (C) UNCRUSHED GRAVEL.....	274
FIGURE 7.18 PERMANENT AXIAL STRAIN RATE VARYING WITH FINES CONTENT FOR (A) CRUSHED LIMESTONE, (B) CRUSHED DOLOMITE AND (C) UNCRUSHED GRAVEL.....	275
FIGURE 7.19 LABORATORY REPEATED LOAD TRIAXIAL PERMANENT DEFORMATION TESTS FOR FAA NAPTF AGGREGATE MATERIALS: (A) STRESS PATH LOADING SCHEME AND IDENTIFIED SHAKEDOWN RANGES FOR (B) P209 AND (C) P154 MATERIALS	277
FIGURE 7.20 PERMANENT DEFORMATION CHARACTERIZATION OF P209 AND P154 AGGREGATE MATERIALS DURING CCP TESTS: (A) AXIAL PERMANENT STRAIN RATE VS. AXIAL PERMANENT STRAIN AND (B) STABILIZED PERMANENT STRAIN RATE VS. MAXIMUM AXIAL STRESS	279
FIGURE 7.21 SHAKEDOWN RANGES IDENTIFIED FOR P209 AND P154 MATERIALS UNDER VCP STRESS STATES: (A) LOADING SLOPE $M=1.5$ AND (B) $M=0$	281
FIGURE 7.22 PERMANENT AXIAL STRAIN RATE VERSUS AXIAL STRESS AT DIFFERENT VCP STRESS STATES FOR P209 AND P154 MATERIALS: (A) $M=1.5$ AND (B) $M=0$	282
FIGURE 7.23 RELATIONSHIP BETWEEN STABLE PERMANENT AXIAL STRAIN RATE ($\dot{\epsilon}$) AND VCP STRESS PATH LOADING PARAMETERS FOR P209 AND P154 MATERIALS: (A) $M=3$, (B) $M=1.5$ AND (C) $M=0$	285

FIGURE 7.24 REGRESSION COEFFICIENT C IN EQUATION 7.10 VERSUS LOADING SLOPE M FOR (A) P209 AND (B) P154 MATERIALS	286
FIGURE 7.25 PREDICTED VS. OBSERVED STABLE PERMANENT STRAIN RATE FOR (A) P209 AND (B) P154.....	287
FIGURE 7.26 MOHR CIRCLES (A) REPRESENTING STABLE PERMANENT STRAIN RATE FOR P154 AND (B) RUTTING RESISTANCE ENVELOPES FOR P209 AND P154 AGGREGATE MATERIALS	289
FIGURE 7.27 STABLE PERMANENT PLASTIC STRAIN RATE DESIGN CHART USING SHEAR STRESS RATIO AND MINOR PRINCIPAL STRESS (Σ_3) FOR (A) P209 AND (B) P154 AGGREGATE MATERIALS	290
FIGURE 7.28 PREDICTED VS. OBSERVED STABLE PERMANENT STRAIN RATE FOR (A) P209 AND (B) P154 UNDER VCP STRESS STATES	292
FIGURE 7.29 SCHEMATIC REPRESENTATION OF SHEAR STRESS RATIO IN P-Q DIAGRAM FOR STRESS PATH LOADING CONDITION	292
FIGURE 7.30 MEASURED CUMULATIVE PERMANENT AXIAL STRAIN VS. PREDICTED CUMULATIVE PERMANENT AXIAL STRAIN FOR (A) UNCRUSHED GRAVEL, (B) CRUSHED DOLOMITE AND (C) CRUSHED LIMESTONE	296
FIGURE 7.31 MEASURED CUMULATIVE PERMANENT AXIAL STRAIN VS. PREDICTED CUMULATIVE PERMANENT AXIAL STRAIN BY THE UNIFIED MODEL	299
FIGURE 7.32 MEASURED CUMULATIVE PERMANENT AXIAL STRAIN VS. PREDICTED CUMULATIVE PERMANENT AXIAL STRAIN BY DIFFERENT MODELS FOR P209 MATERIAL AT A LOADING SLOPE OF (A) M=3 AND (B) M=1.5.....	302
FIGURE 7.33 SCHEMATIC REPRESENTATION OF MODEL PARAMETERS IN EQUATION 8.19 (PÉREZ AND GALLEG0, 2010)	304
FIGURE 7.34 MEASURED PERMANENT AXIAL STRAIN VS. PREDICTED VALUES BY THE UNIFIED MODEL FOR FAA P209 AND P154 MATERIALS AT DIFFERENT LOADING SLOPES: (A) M=3, (B) M=1.5, AND (C) M=0.....	306
FIGURE 8.1 COMPARISON OF FIELD-MEASURED AND MODEL-PREDICTED LAYER RUT DEPTH FOR P209 LAYERS	315
FIGURE 8.2 COMPARISON OF FIELD-MEASURED AND MODEL-PREDICTED LAYER RUT DEPTH FOR P154 LAYERS	316
FIGURE 8.3 PAVEMENT (A) LAYER THICKNESSES CONSIDERED AND (B) THE GT-PAVE FE MESH.....	318
FIGURE 8.4 COMPARISONS OF MEASURED AND PREDICTED SUBGRADE VERTICAL STRESS VALUES FOR TEST SECTION 2 AND 3 IN CELL 1	323
FIGURE 8.5 VERTICAL RESILIENT STRAIN PROFILE ALONG THE CENTER OF THE WHEEL LOAD FOR: (A) CELL 1, (B) CELL 2, (C) CELL 3, (D) CELL 4, AND (E) CELL 5.....	324
FIGURE 8.6 MEASURED VS. PREDICTED MAXIMUM RUT DEPTH FOR TEST SECTIONS USED FOR CALIBRATION: (A) CELL 1, (B) CELL 2, (C) CELL 3, (D) CELL 4, AND (E) CELL 5.....	328
FIGURE 8.7 TRANSVERSE RUT PROFILE FOR TEST SECTIONS OF CELL 3: (A) SECTION 1 (USED FOR CALIBRATION), (B) SECTION 2, AND (C) SECTION 3	329
FIGURE 8.8 MEASURED VS. PREDICTED MAXIMUM RUT DEPTH FOR TEST SECTIONS USED IN VALIDATION: (A) CELL 1, (B) CELL 2, AND (C) CELL 3	331
FIGURE 8.9 MEASURED VS. PREDICTED MAXIMUM RUT DEPTH FOR TEST SECTIONS USED IN VALIDATION: (A) CELL 4 AND (B) CELL 5.....	332

FIGURE 8.10 SCHEMATIC ILLUSTRATIONS OF THE LOCATIONS FOR CALCULATING STRESS
PATH FOR MOVING WHEEL AT DIFFERENT PAVEMENT DEPTHS 335

FIGURE 8.11 STRESS PATH INDUCED BY MOVING WHEEL AT DIFFERENT PAVEMENT DEPTHS
FOR ICT FULL-SCALE TEST SECTIONS 337

List of Tables

TABLE 2.1 SUMMARY OF CURRENT RESILIENT MODULUS MODELS	40
TABLE 2.2 SUMMARY OF CURRENT PERMANENT DEFORMATION MODELS	51
TABLE 3.1 AGGREGATE MATERIAL TYPES, SOURCES AND MOISTURE-DENSITY PROPERTIES USED IN GEOGRID-REINFORCED APPLICATIONS	75
TABLE 3.2 AVERAGE AGGREGATE SHAPE AND SURFACE TEXTURE INDICES FOR AGGREGATE SAMPLES USED IN GEOGRID REINFORCEMENT APPLICATIONS	76
TABLE 3.3 AVERAGE AGGREGATE SHAPE AND SURFACE TEXTURE INDICES (MISHRA, 2012).....	77
TABLE 3.4 SUMMARY OF AGGREGATE MATERIAL PROPERTIES FOR FIELD TEST SECTIONS (MISHRA AND TUTUMLUER, 2013)	84
TABLE 3.5 GRAIN-SIZE DISTRIBUTION CURVE CHARACTERISTICS OF FULL-SCALE PAVEMENT TEST SECTION	86
TABLE 3.6 IN-PLACE MOISTURE-DENSITY VALUES FOR COMPACTED AGGREGATE LAYERS (MISHRA, 2012).....	87
TABLE 4.1 SUMMARY OF MULTIPLE LINEAR REGRESSION (MLR) ANALYSIS RESULTS FOR IDENTIFYING PROPERTIES USED TO PREDICT LOGK ₁ OF M _R CONSTITUTIVE EQUATION	107
TABLE 4.2 SUMMARY OF MLR ANALYSIS RESULTS FOR IDENTIFYING PROPERTIES USED TO PREDICT K ₂ PARAMETER OF M _R CONSTITUTIVE EQUATION	108
TABLE 4.3 SUMMARY OF MLR ANALYSIS RESULTS FOR IDENTIFYING PROPERTIES USED TO PREDICT K ₃ PARAMETER OF M _R CONSTITUTIVE EQUATION	109
TABLE 4.4 COMPARISONS BETWEEN MSPR AND MSE VALUES FOR THE THREE K PARAMETERS.....	111
TABLE 4.5 REPRESENTATIVE STRESS LEVELS IN TYPICAL MNDOT PAVEMENT LAYERS	116
TABLE 4.6 INPUT PARAMETERS AND DISTRIBUTIONS	117
TABLE 4.7 MONTE CARLO SIMULATION RESULTS FOR M _R (UNIT: KSI)	118
TABLE 4.8 REPRESENTATIVE STRESS LEVEL AND DESIGN MODULUS FOR AGGREGATE BASE LAYER IN A TYPICAL CONVENTIONAL PAVEMENT STRUCTURE.....	120
TABLE 4.9 ABBREVIATIONS AND BRIEF DESCRIPTIONS OF SIGNIFICANT VARIABLES INFLUENCING RESILIENT MODULUS BEHAVIOR	121
TABLE 4.10 BASIC STATISTICS OF AGGREGATE SOURCE PROPERTIES USED.....	122
TABLE 4.11 CORRELATION COEFFICIENTS OF VARIABLES	123
TABLE 4.12 IMPORTANCE VECTOR OF VARIABLES OBTAINED FROM FERUM PROGRAM	125
TABLE 4.13 SENSITIVITY OF VARIABLES STUDIED WITH THE RELIABILITY INDEX.....	127
TABLE 4.14 CHARACTERIZATION OF REPRESENTATIVE AGGREGATE BASE AND GRANULAR SUBBASE MATERIALS.....	132
TABLE 4.15 INPUT VALUES FOR ALL THE VARIABLES USED IN THE SENSITIVITY ANALYSIS.....	134
TABLE 5.1 DETAILS OF THE AGGREGATE MATERIALS COMPILED IN THE MNDOT DATABASE ...	153
TABLE 5.2 EMPIRICAL MODELS FOR ESTIMATING PERMEABILITY OF UNBOUND GRANULAR MATERIALS	170
TABLE 6.1 AGGREGATE TYPES AND TEST RESULTS (DATA SOURCE: TUTUMLUER AND PAN, 2008).....	180
TABLE 6.2 CALIBRATED DEM MODEL PARAMETERS	184
TABLE 6.3 TRIAXIAL COMPRESSION DEM SIMULATION RESULTS.....	184

TABLE 6.4 MNDOT SPECIFIED CLASS 6 (CL-6) GRADATION CONTROL SPECIFICATIONS AND DEM SIMULATED GRADATION ALTERNATIVES	191
TABLE 6.5 TWO PARTICLE SHAPE LIBRARIES REPRESENTING HIGH AND LOW ANGULARITY LEVELS USED IN DEM SIMULATIONS.....	193
TABLE 6.6 DEM PACKING SIMULATION RESULTS (HIGH ANGULARITY) FOR CL-6 UPPER BOUND	197
TABLE 6.7 DEM PACKING SIMULATION RESULTS FOR CL-6 LOWER BOUND.....	198
TABLE 6.8 MNDOT SPECIFIED GRADATION CONTROL SIEVES FOR UNBOUND PAB	200
TABLE 6.9 ANALYTICAL GRADATION ANALYSIS RESULTS FOR MNDOT SPECIFIED PAB GRADATION BAND	202
TABLE 6.10 RECOMMENDED UNBOUND PAB GRADATION BASED ON PACKING CHARACTERISTICS.....	205
TABLE 6.11 PACKING CHARACTERISTICS OBTAINED FROM DEM SIMULATION FOR UNBOUND PAB	207
TABLE 6.12 PACKING CHARACTERISTICS OBTAINED FROM DEM SIMULATION FOR DIFFERENT G/S RATIOS.....	213
TABLE 7.1 PERMANENT STRAIN MODEL PARAMETERS FOR STRESS PATH LOADING RLT TESTS OF FAA P209 MATERIAL.....	228
TABLE 7.2 PERMANENT STRAIN MODEL PARAMETERS FOR STRESS PATH LOADING RLT TESTS OF FAA P154 MATERIAL.....	230
TABLE 7.3 PERMANENT STRAIN MODEL PARAMETERS FOR ICT CRUSHED DOLOMITE MATERIALS OF DIFFERENT PHYSICAL PROPERTIES	236
TABLE 7.4 PERMANENT STRAIN MODEL PARAMETERS FOR ICT CRUSHED LIMESTONE MATERIALS OF DIFFERENT PHYSICAL PROPERTIES	238
TABLE 7.5 PERMANENT STRAIN MODEL PARAMETERS FOR ICT UNCRUSHED GRAVEL MATERIALS OF DIFFERENT PHYSICAL PROPERTIES	240
TABLE 7.6 ENHANCED RUTTING PREDICTION MODEL FOR P209 MATERIALS.....	257
TABLE 7.7 ENHANCED RUTTING PREDICTION MODEL FOR P154 MATERIALS.....	258
TABLE 7.8 ENHANCED RUTTING PREDICTION MODEL FOR CRUSHED DOLOMITE MATERIALS.....	260
TABLE 7.9 ENHANCED RUTTING PREDICTION MODEL FOR CRUSHED LIMESTONE MATERIALS ...	260
TABLE 7.10 ENHANCED RUTTING PREDICTION MODEL FOR UNCRUSHED GRAVEL MATERIALS	261
TABLE 7.11 MODEL COEFFICIENTS FOR DEGRADED SECANT MODULUS OF FAA P154 MATERIAL (M=3)	267
TABLE 7.12 SUMMARY OF PERMANENT STRAIN MODEL COEFFICIENTS WITH GOODNESS OF FIT FOR ICT UNCRUSHED GRAVEL MATERIALS OF DIFFERENT PHYSICAL PROPERTIES	297
TABLE 7.13 SUMMARY OF PERMANENT STRAIN MODEL COEFFICIENTS WITH GOODNESS OF FIT FOR ALL THREE DIFFERENT ICT AGGREGATE MATERIALS OF VARYING PHYSICAL PROPERTIES	299
TABLE 8.1 RESILIENT MODULUS MODEL PARAMETERS FOR AGGREGATE SUBBASE MATERIALS USED.....	320
TABLE 8.2 RESILIENT MODULUS MODEL PARAMETERS FOR SUBGRADE SOILS	321
TABLE 8.3 CALIBRATED PARAMETERS FOR RUTTING PREDICTION FROM SECTION 1 OF EACH TEST CELL (BASED ON FIELD RUTTING MEASUREMENTS).....	327

Chapter 1 Introduction

1.1 Background

1.1.1 Unbound Aggregate Layer Functionality

A large quantity of annually produced aggregate materials (crushed stone, sand, and gravel) is used in the construction of pavement foundation layers known as unbound aggregate base and subbase. In flexible pavements, the primary function of base/subbase layers is to distribute the repeated wheel load over weaker subgrade soils. Permanent deformation (or rutting) is the predominant distress type and failure criterion for such layers. Whereas, in rigid pavements, those unbound layers are built mainly for providing uniform support, adequate drainage, and long-term durability for Portland cement concrete (PCC) slabs. As demands for heavier and greater number of loads are increasingly being placed on highway and airport pavements, unbound aggregate layers need to not only be accurately characterized for structural behavior but also be adequately designed for cost-effectiveness.

Unbound aggregate base/subbase layers transfer wheel loads through the aggregate skeleton. The layer responses and performance are greatly affected by material properties and composition of such aggregate skeleton, not to mention the changing environmental conditions. The aggregate type and quality, in addition to traffic load related factors, should influence the thickness requirements of unbound aggregate layers in pavement applications. Note that “quality” in this dissertation study refers exclusively to structural support (or bearing capacity) and permeability, not to other aspects of quality such as freeze-thaw or wet-dry durability, and so on. Those aggregate properties affecting quality in regards to structural component may include aggregate shape, texture and angularity, gradation, fines content (percentage passing No.200 or

0.075-mm sieve), plasticity index (PI), moisture and density conditions related to compaction, and their interactions.

1.1.2 Unbound Aggregate Layer As A Pavement Structural Component

The quality of the unbound aggregate layer materials can have a significant impact on the performance of the pavement. The low stiffness of the unbound aggregate layer and the resulting excessive rutting in pavement are often attributed to the quality of the material used for road construction. Currently, unbound aggregate layers are often constructed using aggregate materials that are preferably dense-graded crushed stone. Pavement engineers commonly use aggregate quality to describe the suitability of an aggregate for use in road construction, while highway agencies commonly use density and proof rolling to determine the quality of base/subbase layers. However, different approaches may exist for classifying aggregate materials and rating the quality of an aggregate for structural layer function. Furthermore, different aggregate sources can be classified as meeting the same specification as long as the material meets the gradation requirements even though they may have varying physical properties affecting performance. Effects of physical shape, texture and angularity of aggregate particles, in addition to gradation, on the strength, stability and performance of unbound pavement layers are often not considered by current practice. The reason might be due to the lack of accurate and repeatable measurements of the coarse aggregate morphology in the past.

Traditionally, “recipe-based” physical classification systems judge the performance of an aggregate by using a variety of aggregate tests and specifications developed by ASTM, AASHTO, and state and local agencies. As listed in Figure 1.1, only the intrinsic physical properties of the material that are related to basic geologic origin, mineralogy, and other properties such as hardness and durability are considered by such physical classification systems;

more importantly, these testing techniques, material specifications and design procedures are several decades old and/or intended for “standard” materials with proven field performance. This results in one major disadvantage, i.e., the lack of direct and robust linkages between intrinsic physical properties and field performance requirements. Therefore, unsuitable materials can be accepted in some cases or rejected in other cases (Cook and Gourley, 2002). Under such physical classification framework, naturally occurring or locally available materials could also be excluded for use due to any combination of grading, plasticity, particle hardness, strength, etc. lying outside the specification requirements. This becomes a major concern in developing countries where naturally occurring or locally available materials need to be used extensively for cost-effective low volume road construction. In summary, confident decisions regarding the use of a specific aggregate material in unbound pavement layers may not be guaranteed.

		Non-Standard Material Groups																						
		Strong Rock		Weak Rock							Natural Granular Materials					Pedogenic Materials								
		Foliated Metamorphic Rocks	Basic Igneous Rocks	Recent Coral Deposits	Marls and weak Limestones	Weak Volcanic Breccias/Agglomerates	Weak Conglomerates	Weak Sandstones	Weak Volcanic Tufts	Fractured/Weathered Limestones	Shales/Mudstones	Weathered Strong Rocks	Alluvial Sands	Alluvial Clayey Sand Deposits	Aeolian Sand Deposits	Colluvial Deposits	Alluvial Gravel Deposits	Volcanic Pyroclastics	Residual Clayey Sand Deposits	Residual Gravel Deposits	Laterite Deposits	Calcrete Deposits	Silcrete Deposits	
Primary Specification Criteria	High PI Fines																							
	Low Particle Strength																							
	Poor Grading																							
	Poor Durability																							
	Poor Particle Shape																							
Additional Impacting Criteria	High Mica Content																							
	High Water Absorbtion																							
	High Variability																							
	In-service Deterioration																							
	Low PI Fines																							


 Potential Problem Characteristics

Figure 1.1 Non-standard Material Groups and Their Likely Problems (Cook and Gourley, 2002)

Unbound aggregates are becoming increasingly scarce and expensive in many parts of the U.S. and around the world as gravel mines and rock quarries are being lost to other land uses. As pavement design procedures transition from using empirical strength based evaluations, such as the California Bearing Ratio (CBR), the Hveem R-value and Soil Factor and modulus of subgrade reaction (k-value), to the use of resilient modulus (M_R) based mechanistic-empirical (M-E) structural analysis and design procedures, an awareness of optimizing aggregate type, quality and layer thicknesses from mechanistic-based pavement design according to site-specific performance requirements would be useful for selecting aggregate, reducing waste, better utilizing construction dollars, and eventually achieving best values. To promote sustainability, more adaptable design methods and performance-based material specifications also need to be developed to accommodate aggregates with a wider range of physical characteristics, especially locally available marginal quality aggregates. This requires the development of mechanistic based aggregate classification systems that quantitatively address individual aggregate properties influencing quality for material selection.

1.2 Problem Statement

Unbound aggregate base and granular subbase layers commonly used in conventional flexible pavements serve as major structural components for distributing wheel loads and providing adequate protection of subgrade to ensure longevity or proper pavement performance. In essence, this functionality is achieved mainly through the aggregate skeleton in which individual aggregate particles in contact with each other to transmit the external load. From a mechanistic-empirical pavement design perspective, resilient modulus and permanent deformation characteristics, linked to aggregate quality and layer thickness, are the primary properties influencing mechanistic response and pavement performance. A stable and

adequately-designed unbound aggregate layer is expected to experience low-magnitude resilient and permanent deformations throughout the targeted service life. To achieve this goal, it still remains crucial to develop a sophisticated design and characterization methodology.

In the past few decades, significant efforts have been made to better understand individual aggregate properties as factors influencing mechanical and hydraulic response trends of unbound aggregate materials (Thompson and Smith, 1990; Garg and Thompson, 1997; Tian et al., 1998; Bilodeau et al., 2009; Tutumluer et al., 2009). When compared to aggregate type and mineralogy, not well understood are properties such as aggregate shape, texture and angularity to be evaluated together with fines content (percentage passing No.200 sieve or smaller than 0.075 mm size), plasticity index, and moisture and density conditions related to compaction. For example, particle size distribution or gradation is a key factor influencing not only the mechanical response behavior characterized by resilient modulus (M_R), shear strength and permanent deformation, but also the permeability, frost susceptibility, and erosion susceptibility (Bilodeau et al., 2007; Bilodeau et al., 2008).

To ensure adequate pavement performance, State highway agencies currently employ “recipe-based” specifications for unbound aggregates used in road base/subbase construction. These empirical gradation bands used in pavement applications specify different aggregate classes and source rock quality, etc., which reportedly have no robust linkage with actual performance in the field (Mulvaney and Worel, 2002). Such requirements based on various grading envelopes (e.g., well-graded, uniformly-graded, etc.) and limits of maximum particle size may not only be conflicting in regards to pavement layer stability and drainability but may also fail to distinguish different gradations within the specified bands, especially when aggregates from different sources are used (Tian et al., 1998; Tao et al., 2008). With “standard”

high-quality materials becoming increasingly scarce and expensive, such traditional gradation specifications may potentially reject many marginal materials that are often lowering cost and local availability. Recent research efforts demonstrated that marginal materials could become quite economical for use in low-volume roads and serve properly the design traffic levels and the operating environment (Bullen, 2003). Therefore, development of performance based gradation specifications can help maximize beneficial use of the locally available materials that is potentially a green and sustainable transportation infrastructure alternative.

Resilient modulus (M_R) is a key mechanistic pavement analysis input for designing conventional flexible pavements with unbound aggregate base and granular subbase layers. For satisfactory pavement design and performance, it is often challenging to determine unbound aggregate layer modulus inputs when only limited aggregate source property data are available. Laboratory testing for M_R requires expensive test equipment and time-consuming and detailed testing procedures. Therefore, using correlations to link M_R behavior with performance-related aggregate source properties would be more cost-effective in the current M-E pavement design applications.

Moreover, unbound pavement layers are subjected to both extension and compression type stress states under moving wheel loading. Such complex loading stress paths, stress levels, and continuous rotation of the principal stress planes lead to complicated nonlinear elastic and/or elasto-plastic behavior that are rarely incorporated into laboratory test procedures or mechanistic response prediction models. While many of the performance models in current pavement design procedures have reached a level of accuracy appropriate for design, permanent deformation models continue to inaccurately predict actual performance in the field, making permanent deformation still remain a highly studied topic. These challenges stem from complex mechanistic

behavior of the pavement systems as well as from the susceptibility of these models to variations in climatic and loading conditions. Although shear strength properties have been demonstrated to play an important role in field rutting development of unbound aggregate layers, shear strength is not routinely incorporated into most of the existing rutting prediction models. The absence of shear strength in these models could possibly limit their prediction abilities. As such, the significance of further investigation into the development of improved rutting prediction models is obvious.

1.3 Research Objective and Scope

The primary objective of this research study is to evaluate through experimental investigations and numerical simulations the effects of material properties on mechanical behavior of unbound aggregate layers, as characterized by resilient modulus, shear strength, and permanent deformation resistance, for the development/recommendation of performance-based specification guidelines. The scope includes three different methodologies employed to achieve the aforementioned objective: (i) laboratory data analysis to link physical and mechanical properties of unbound aggregate materials for pavement response and performance; (ii) an image-aided Discrete Element Method (DEM) modeling approach for engineering aggregate shape and gradation properties for improved shear strength (or rutting resistance behavior); and (iii) a unified approach to permanent deformation (or rutting) prediction of unbound aggregate layers based on shear strength. Based on all these methodologies successfully employed, a set of recommendations for improving material specifications for unbound aggregates used in conventional flexible pavement foundation will be presented. The corresponding research approaches (see Figure 1.2) and their significant contributions to advancing the state-of-the-art in knowledge are described next.

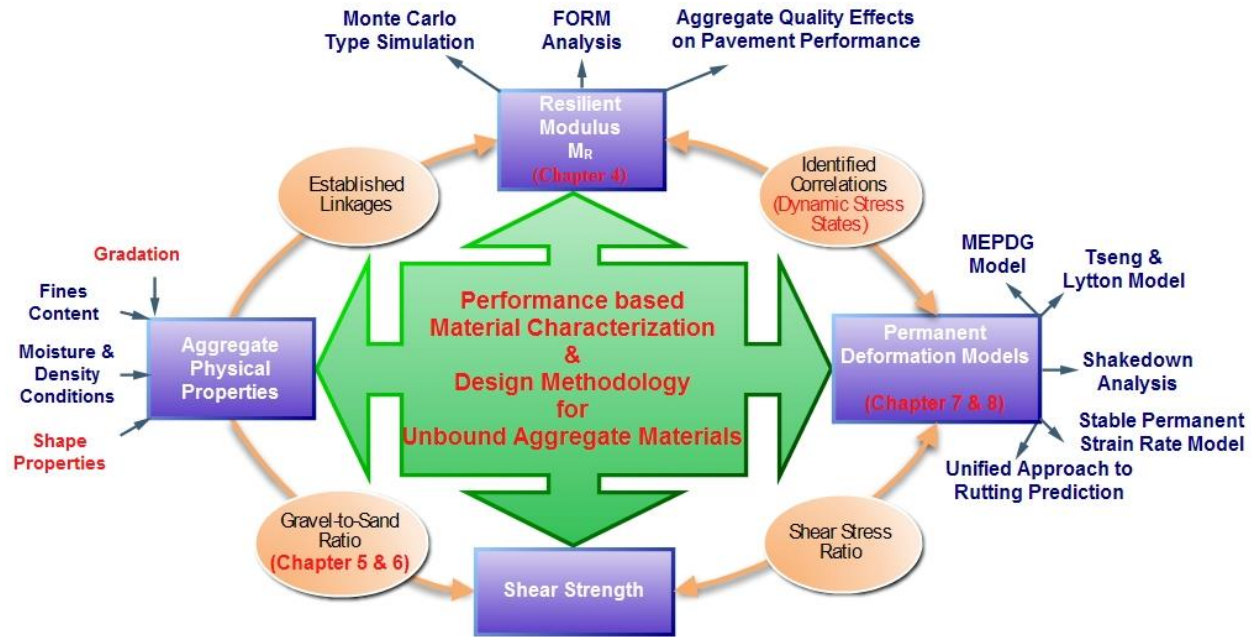


Figure 1.2 Flowchart of Analysis Approach

1.4 Contributions to Advancing Knowledge

To address the inefficiency of current material specifications and design methodologies for unbound aggregate layers in conventional flexible pavements, this research study is aimed at synthesizing all the laboratory and field data recently available with our Transportation Geotechnics research group at UIUC and developing a performance-related material specification methodology for unbound aggregate materials. Although scoped for conventional flexible pavements, such specifications could potentially help design cost effective base types and thicknesses suitable for rigid pavements as well. The major contributions of this dissertation study are aligned with the following research tasks:

- (1) A large laboratory and field performance database on unbound aggregate layers is synthesized and analyzed to demonstrate the potential of the performance-based material specification methodology for achieving pavement longevity and cost-effectiveness;
- (2) Guidelines are established to prepare improved aggregate material classifications by not only considering gradation but also including aggregate shape properties and drainage characteristics, with the aid of laboratory data analysis and particle imaging-aided DEM modeling approach; and
- (3) Relative importance of each aggregate physical property in controlling resilient modulus, shear strength, and permanent deformation behavior of unbound aggregates is identified, along with other design features and site conditions, based on mechanistic-empirical pavement analysis.

1.5 Thesis Organization

Background information and literature review on laboratory characterization and numerical modeling of unbound aggregate behavior is presented in Chapter 2. Major factors influencing resilient modulus, shear strength, and rutting resistance are reviewed with respect to load related factors and secondary factors due to material physical properties. Various resilient modulus and permanent strain models used to characterize the resilient and permanent deformation behavior of granular materials are also reviewed for major input variables, such as the number of load applications and applied stress states.

In Chapter 3, the laboratory testing and field performance databases of unbound aggregate materials collected for this dissertation study including the descriptions of testing procedures and trafficking information of pavement test sections are introduced. The different types of granular materials extensively used in the laboratory studies and field pavement test

sections are also described in detail. The full-scale tests conducted in related studies are presented.

Chapter 4 mainly focuses on developing regression based models for the M_R data as a function of the various performance-related aggregate properties. The study further details M_R sensitivities using both Monte Carlo type simulation and First-order Reliability Method (FORM). The interactions between these aggregate properties are properly taken into account during sensitivity analyses. Mechanistic design input ranges are also identified and the effects of unbound aggregate quality and layer characteristics (i.e., material quality affecting modulus input and layer thickness) on pavement life expectancies are investigated in Chapter 4.

In Chapter 5, improved linkages between quantitative gradation parameters and critical mechanical behavior of aggregate base/granular subbase materials are first established from a comprehensive statewide aggregate database, followed by further validation from other related aggregate databases and potential engineering applications. Commonly used gradation quantification methods are employed to identify key gradation parameters governing the shear strength behavior of the studied aggregate materials.

Chapter 6 deals with applying a validated image-aided DEM modeling approach to engineer aggregate shape and gradation for desired end-use performance of unbound aggregate layers. The required DEM model parameters are first calibrated from laboratory triaxial compression tests of unbound aggregate materials. The calibrated DEM model is then employed to realistically study optimum contact and packing arrangements from various gradations for improved aggregate interlock. Existing analytical gradation analysis techniques that are developed from packing theory are further verified in Chapter 6 for their applicability through

DEM based packing simulations. Insightful guidelines are recommended for further classifying currently used gradation bands based on analytical and DEM based gradation analysis results.

Chapter 7 details the development of a unified approach to permanent deformation (or rutting) prediction of unbound aggregate layers based on shear strength properties by using laboratory repeated triaxial test results.

Chapter 8 presents the validation of this unified approach by using actual rutting measurements from field full-scale accelerated pavement testing (APT) sections. The current MEPDG rutting model for unbound aggregates is also evaluated for their accuracy in predicting field rut depth development. The importance of shear strength in controlling rutting development is confirmed.

In Chapter 9, research findings are summarized and recommendations are made for selecting unbound granular base and subbase materials for use in conventional flexible pavements. Suggestions are also made for future research needs to conduct follow-on research based on the findings presented in this dissertation.

Chapter 2 Literature Review

This chapter first highlights the important aggregate physical properties governing granular layer modulus, strength, and permanent deformation characteristics. Commonly used laboratory tests and constitutive models to characterize the elastic (or resilient) and plastic (permanent) deformation trends of unbound aggregate materials are discussed next with a review of typical pavement stress states and initial loading conditions due to repeated traffic loading. Accordingly, different mechanisms contributing to the failure of pavement systems with unbound aggregate layers are reviewed to emphasize the importance of aggregate material quality governing pavement performance. Both empirical and mechanistic-empirical methods developed for designing unbound aggregate pavement systems are summarized with a historical perspective by listing their advantages and limitations. Numerical simulation techniques for modeling mechanical behavior of unbound aggregate materials, including finite element and discrete element methods, are also reviewed in this chapter.

2.1 Aggregate Properties Affecting Unbound Aggregate Layer Behavior

The geologic characteristics of aggregates are not very critical for pavement application purposes. Rather, physical characteristics of the rocks governing load distribution and particle interlocking aspects differentiate “good quality” and “poor quality” aggregates. Moreover, chemical properties of the aggregates governing their durability and soundness are also critical to ensuring long-lasting pavement structures. The recent NCHRP Project 4-23, “Performance-Related Tests of Aggregates for Use in Unbound Pavement Layers (Report 453),” summarized the most important tests that relate to the performance of aggregates in unbound pavement layers (Saeed et al., 2001). Among the tests highlighted, the screening tests (sieve analysis, Atterberg

limits, moisture–density relationship, flat and elongated particles, uncompacted voids), durability test (magnesium sulfate soundness), shear strength tests (triaxial tests conducted on wet and dry samples and California bearing ratio or CBR test), stiffness test (resilient modulus conducted on wet and dry samples), toughness and abrasion resistance tests (micro-Deval), frost susceptibility test (tube suction) are the most relevant for unbound aggregate pavement layers. Extensive review of technical literature was conducted to identify the most important physical properties affecting aggregate strength, modulus and deformation behavior in unbound pavement layers. A summary of the findings on important physical properties from the literature review is presented below.

2.1.1 Particle Size Distribution and Fines Content

One of the primary variables in any laboratory testing of aggregate materials is the grain size distribution. Gradation itself is a key factor influencing not only the mechanical response behavior characterized by resilient modulus, shear strength and permanent deformation, but also permeability, frost susceptibility, and erosion susceptibility. (Bilodeau, 2007; Bilodeau, 2008). Aggregate gradation is also critical to achieving good packing and thus stability in an aggregate mix. Differences in aggregate gradations can often lead to significantly different performances for the same aggregate type. This is due to the different packing order and void distributions that play a crucial role in load carrying through particle to particle contact in an aggregate matrix.

Using a directional modulus approach by changing the pulsing direction in repeated load triaxial tests, Tutumluer and Seyhan (2000) determined an optimum fines content (percentage of material passing No. 200 sieve or smaller than 0.075 mm) of 7% for a dense graded crushed limestone aggregate base material. Well graded aggregates have been found to have higher resilient modulus values up to the point where the fines content of the mixture displaces the

coarse particles and the properties of the fines dominate (Jorenby and Hicks, 1986; Kamal et al., 1993; Lekarp et al., 2000). Thom and Brown (1988) found that the effect of grading varied with the compaction level. Brown and Chan (1996) successfully reduced rutting in granular base layers by selection of an optimum aggregate material grading which maximized compacted density.

Bilodeau et al. (2009) identified, from a laboratory study conducted on unbound granular materials with six gradations and three aggregate sources commonly used in Canada, one fines-related volumetric parameter (termed fine fraction porosity) that described satisfactorily not only the mechanical performance but also the environmental stress sensitivity of materials tested. Also identified from their study were the optimized gradation zones that ensured adequate overall performance of those three aggregate sources.

2.1.2 Particle Shape, Surface Texture and Angularity

The gradation, shape, and hardness have a great influence on the mechanical behavior and the strength properties of aggregate particles in contact. Angularity, a measure of crushed faces of an aggregate particle is important because it determines the level of internal shear resistance that can be developed in the particulate medium. Coarse aggregate angularity provides rutting resistance in flexible pavements as a result of improved shear strength of the unbound aggregate base. The maximum size of aggregates, the size distribution, and the shape of the particles determine the packing density that can be derived with an aggregate sample, assuming sufficient compaction is provided.

Rounded river gravel with smooth surfaces was found to be twice as susceptible to rutting compared to crushed stones (Barksdale et al., 1989). Aggregates made with uncrushed or partially crushed particles have a lower resilient modulus than those with angular crushed

particles. This effect has been attributed to the higher number of contact points in crushed aggregates which distribute loads better and create more friction between particles (Lekarp et al., 2000). Saeed et al. (2001) showed that aggregate particle angularity and surface texture mostly affected shear strength and stiffness.

Using the UIAIA system, Uthus et al. (2007) studied the aggregate morphological property changes due to rounding of aggregate particles in a Ball Mill drum. For cubical aggregates, the changes in both angularity and surface texture seemed to have a significant effect on both the elastic and plastic aggregate shakedown threshold limits. Tutumluer and Pan (2008) reported that aggregate blends comprising angular, rough particles consistently showed lower permanent deformation accumulations when studied using the UIAIA system. The angularity property was found to contribute mainly to the strength and stability of aggregate structure through confinement, whereas the surface texture property tended to mitigate the dilation effects through increasing friction between individual aggregate particles.

2.1.3 Degree of Compaction

Compaction methods applied on aggregate samples affect considerably the moisture-density relationship for determining maximum dry density and optimum moisture content. Commonly, impact type Proctor compaction effort is applied on aggregate samples using the methods specified in the AASHTO T99 Standard and AASHTO T180 Modified Proctor test procedures (also ASTM D698 and D1557) although other laboratory compaction procedures, such as the vibratory and gyratory compaction techniques, are known to be more realistic for simulating field applied stress conditions under vibratory rollers. Density is used in pavement construction as a quality control measure to help determine the compaction level of the constructed layers. Generally, increasing the density of a granular material makes the aggregate

layer stiffer and reduces the magnitude of the resilient and permanent deformation response to both static and dynamic loads (Seyhan and Tutumluer, 2002). While some have found the research on density to be ambiguous in regards to the resilient behavior of soils causing little change in the resilient modulus (Knutson and Thompson, 1977; Elliott and Thornton, 1988; Lekarp et al., 2000) others have found that there is a general increase in the resilient modulus with increasing density (Rowshanzamir, 1995; Tutumluer and Seyhan, 1998).

The impact of density seems to be larger on the permanent deformation behavior of aggregates. Decreased density, as measured by degree of compaction, substantially increases permanent deformation. Barksdale (1972) found that decreasing the degree of compaction from 100% to 95% of maximum dry density increased permanent axial strain by 185% (on average). Increasing density from the standard Proctor to the modified Proctor maximum density decreased permanent deformation 80% for crushed limestone and 22% for gravel (Allen, 1973). The degree of compaction (DOC) was reported as the most important factor controlling permanent deformation development by Van Niekerk (2002).

2.1.4 Moisture Content

Moisture has been widely accepted to adversely affect the performance of unbound aggregate layers in pavement structures, and can affect aggregates in three different ways: (i) make them stronger with capillary suction, (ii) make them weaker by reducing suction forces and causing lubrication between the soil particles, and (iii) reduce the effective stress between particle contact points due to increasing pore water pressure thus decreasing the strength of the soil. Degree of saturation is a factor that reflects the combined effect of density and moisture content. The resilient modulus is strongly correlated with degree of saturation (Thompson and Robnett, 1979). Based on the comprehensive subgrade soil resilient modulus testing study,

Thompson and LaGrow (1988) proposed using the “moisture adjustment” factors to adjust resilient modulus values for moisture contents in excess of optimum. For example, resilient modulus of a silt loam soil may decrease approximately 1500 psi for 1% increase in moisture content (Thompson and Robnett, 1979).

Wetting up from a shallow ground water table reduces suction and may cause a constructed unbound pavement layer to deform permanently. Moisture sensitivity will vary depending on specified gradations and the amount and plasticity index (PI) of the fines, i.e., percent passing No. 200 sieve (P200). Tutumluer et al. (2009) compared relative impacts of molding (as-compacted) moisture content and plasticity of fines on the permanent deformation behavior of both crushed (dolomite) and uncrushed (gravel) aggregate materials with P200 = 12%. A drastic reduction in aggregate performance can be clearly seen when plastic fines are combined with increased molding moisture. Accordingly, the specification limits for compaction moisture content must be based on accumulated permanent deformation.

2.2 Aggregate Specifications and Classification Systems

2.2.1 Physical Classification System

Pavement engineers commonly use aggregate quality to describe the suitability of an aggregate for use in road construction; however, a number of ways rather than one single formalized procedure exist for classifying aggregate materials and rating the quality of an aggregate. These “recipe-based” physical and mechanical classification systems are currently used for judging the performance of an aggregate. By using a variety of aggregate tests and specifications developed by ASTM, AASHTO, and certain state and local agency procedures, the former system considers the intrinsic physical properties of the material that are related to basic geologic origin, mineralogy, and other properties such as hardness and durability. One

major disadvantage associated with such physical classification systems is that it could possibly accept unsuitable materials in some cases and reject desired materials in other cases (Cook and Gourley, 2002). Under such physical classification framework, naturally occurring materials could be excluded for use due to any combination of grading, plasticity, particle hardness, strength, etc. lying outside the specification-demanded requirements. As illustrated in Figure 2.1, soft limestones could be categorized as unacceptable materials for use in pavement foundation applications due to their high Los Angeles coefficient and wet micro-Deval coefficient both of which are indicators of aggregate toughness and abrasion characteristics; however, they could actually be acceptable if examined by mechanistic properties such as characteristic secant modulus E and characteristic permanent strain ϵ_p .

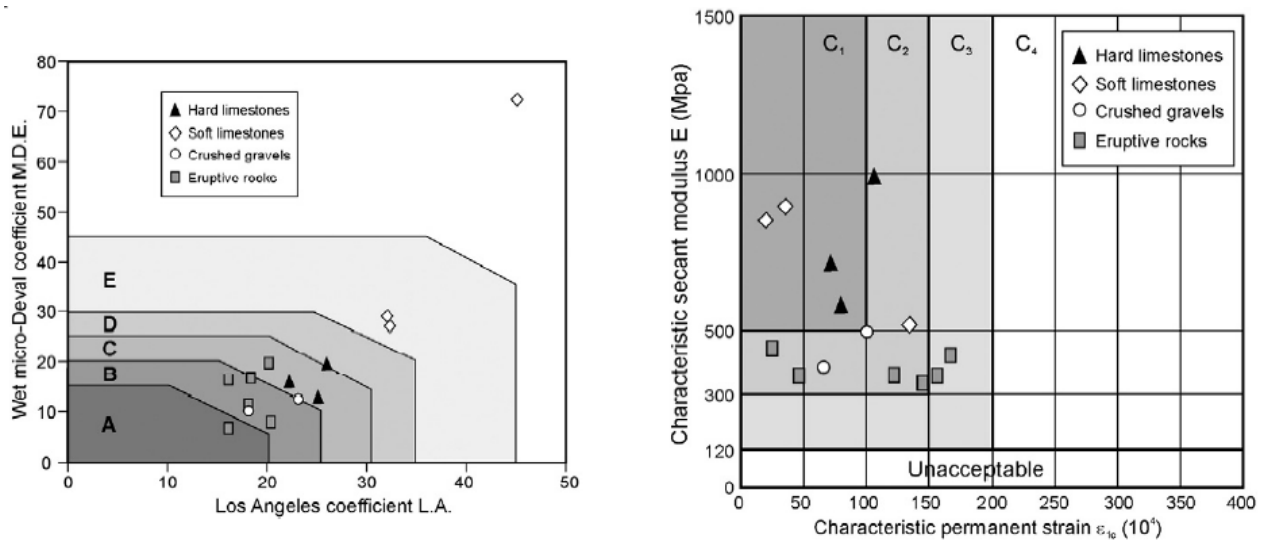


Figure 2.1 Physical (Left) Versus Mechanical (Right) Classification for Various Unbound Granular Materials (Paute et al., 1994)

2.2.2 Performance-based Mechanical Classification System

Separate from the physical classification presented above, the mechanistic classification discerns different qualities of unbound aggregates from mechanical properties that are required

as input to the constitutive relationships incorporated into mechanistic-empirical pavement design procedures, such as the characteristic secant modulus E and characteristic permanent strain ϵ_p shown in Figure 2.1. It is expected that such mechanistic classification systems, in combination with certain levels of local experiences, should have direct relevance or even robust linkage to the actual performance of materials used in pavement layers. To better assess performance and rank different sources of aggregate materials, coupling mechanistic characteristics including moduli, strength, and permanent strains under representative ranges of operating traffic and environmental conditions is of essential importance from the Mechanistic-Empirical Pavement Design perspective. Without utilizing performance-based material specifications to be developed, optimized material use with reduced waste, and eventually better utilized construction dollars cannot be achieved extensively.

2.2.3 Best Value Granular Material Concept

More attention is nowadays paid to better or sustainable utilization of best value granular materials, thus reducing the cost and energy associated with material hauling. Figure 2.2 presents the concept of best value granular materials illustrated as an implementation challenge of a recent research study findings (Xiao and Tutumluer, 2012). Three components were proposed for incorporation into the M-E pavement analysis and design to implement the best value granular material aggregate selection, utilization and mechanistic based design concepts: (i) GIS-based aggregate source management component, (ii) aggregate property selection component for design, and (iii) aggregate source selection/utilization component. Specifically, aggregate material source locations should be identified with certain aggregate properties to be linked to mechanistic pavement analysis property inputs. The quality aspects of those utilized aggregates

should then be assessed for both cost effectiveness and unbound aggregate layer design thickness requirements for a sustainable pavement performance.

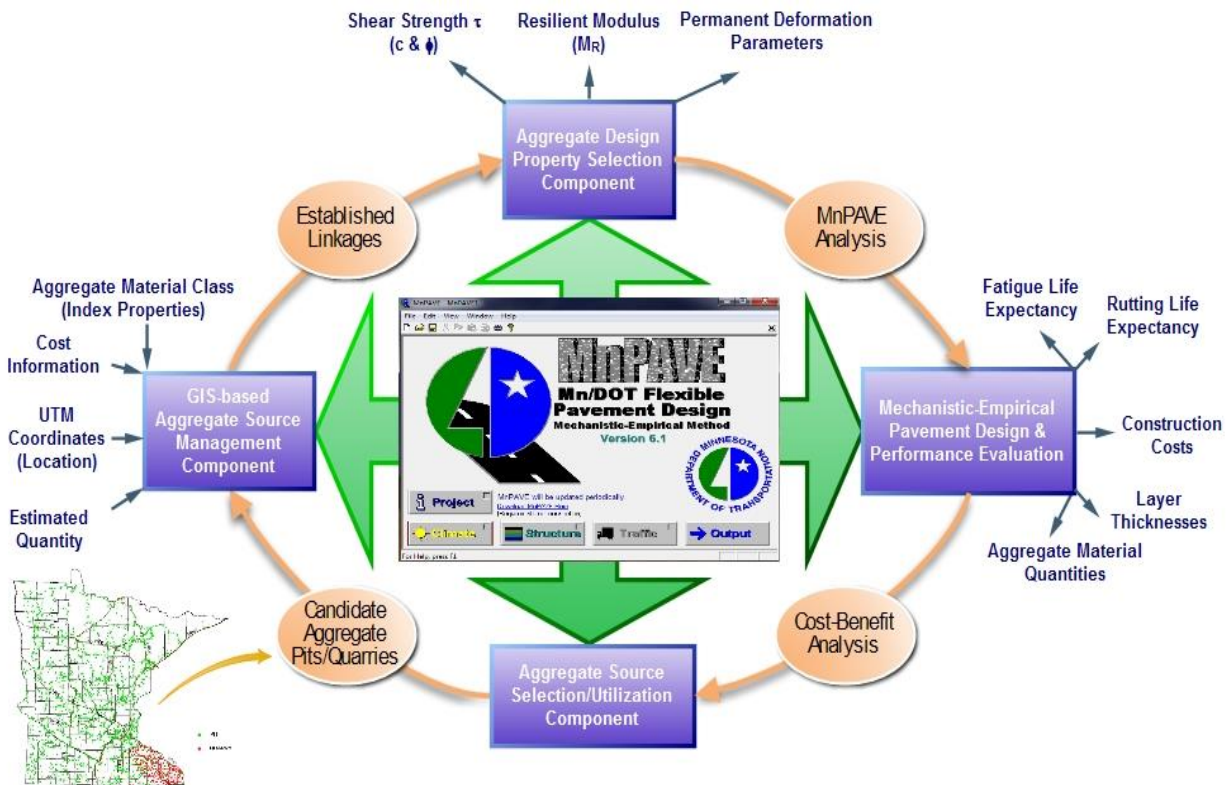


Figure 2.2 Best Value Granular Material MnPAVE Design Implementation (Xiao and Tutumluer, 2012)

2.3 Gradation Analysis and Packing Theories

To ensure adequate pavement performance, state highway agencies currently employ “recipe-based” specifications for unbound aggregates used in road base/subbase construction. These empirical gradation bands used in pavement applications specify different aggregate classes and source rock quality, etc., which reportedly have no robust linkage with actual performance in the field (Mulvaney and Worel, 2002). Such requirements based on various grading envelopes (e.g., well-graded, uniformly-graded, etc.) and limits of maximum particle

size may not only be conflicting in regards to pavement layer stability and drainability but may also fail to distinguish different gradations within the specified bands, especially when aggregates from different sources are used (Tian et al., 1998; Tao et al., 2008). With “standard” high-quality materials becoming increasingly scarce and expensive, such traditional gradation specifications may potentially reject many marginal materials that are often lowering cost and locally available. Recent research demonstrated that marginal materials could become quite economical for use in low-volume roads and serve properly the design traffic levels and the operating environment (Bullen, 2003). Therefore, development of performance based gradation specifications can help maximize beneficial use of the locally available materials that is potentially a green and sustainable transportation infrastructure alternative.

Establishing robust linkages between gradation and satisfactory unbound aggregate mechanical behavior is essential for the development of performance based gradation specifications. The qualitative gradation descriptions (e.g., upper, median, and lower limits), as documented in previous laboratory experiments investigating gradation influences, are certainly not applicable for this purpose (Thompson and Smith, 1990; Tian et al., 1998; Molenaar and van Niekerk, 2002; Cunningham, 2009). With the advent of analytical gradation models and aggregate packing theories, recent research efforts have focused on quantifying gradation curves as numbers on a continuous scale to better relate them to mechanistic behavior trends (Kim et al., 2007; Bilodeau et al., 2009). These analytical gradation measures can quantify the change in performance of a given aggregate material within specified gradation bands leading to optimized gradation zones for desirable mechanical and hydraulic performance based on site-specific traffic and environmental conditions, respectively.

2.3.1 Review of Gradation Quantification Methods

Among the various mathematical functions proposed to describe aggregate particle size distribution, the Talbot equation was quite possibly one of the earliest to describe a maximum density curve for a given maximum aggregate size (Talbot and Richart, 1923). By regressing percent passing data (p_i) against sieve sizes (D_i) as per Equation 2.1, a given gradation curve can be represented as a “point” with coordinates (n, D_{\max}) in a similar Cartesian plane where shape factor n is on x-axis and D_{\max} is on y-axis. Using this representation, Sánchez-Leal (2007) proposed a gradation-chart approach to promote “free design” in which a calculated Gravel-to-Sand ratio was used in lieu of the traditional gradation bands to ensure that required Hot Mix Asphalt (HMA) performance was met by available aggregate sources. According to Sánchez-Leal (2007), an increasing Gravel-to-Sand ratio markedly resulted in diminished workability, greater rutting resistance, and increased permeability.

$$p_i = \left(\frac{D_i}{D_{\max}} \right)^n \quad (2.1)$$

where p_i is the percentage of material by weight passing the i th sieve size; D_i is the opening size of this particular i th sieve; D_{\max} is the maximum size of aggregate; and n is called the shape factor of the gradation curve.

It is worth mentioning that the above gradation-chart approach was developed from gradation curves explained by the Talbot equation with R^2 values greater than 0.97, and that extending such an approach to gradation curves with R^2 values less than 0.97 still remains unexplored. For gradations other than well-graded ones (e.g., open-graded) that may not be well explained by the Talbot equation, the Rosin-Rammler distribution function described by Djamarani and Clark (1997) can outperform others, as it is reported to be particularly suitable for describing the particle size distribution of powders of various nature and sizes generated by

grinding, milling, and crushing operations. As given in Equation 2.2, two parameters, the mean particle size D_m and the measure of the spread of particle size distribution n , are used to represent the Rosin-Rammler function.

$$p_i = 1 - \exp \left[- \left(\frac{D_i}{D_m} \right)^n \right] \quad (2.2)$$

where p_i is the percentage of material by weight passing the i th sieve size; D_i is the i th sieve opening size; D_m is the mean size of aggregate; and n is called the spread factor.

The Unified Soil Classification System (USCS), as per ASTM D 2487-11 (2001), quantifies the gradation of a soil with less than 12% of fines using two parameters, i.e., coefficient of uniformity, C_u (D_{60}/D_{10}), and coefficient of curvature, C_c ($D_{30}^2/D_{60}D_{10}$). Soils are considered very poorly graded when $C_u < 3$; whereas gravels and sands are deemed well-graded when C_u is larger than 4 and 6, respectively. Note that C_c for well-graded soils or aggregates often ranges between 1 and 3. The definitions for “gravel” and “sand” are not unique, with USCS defining “gravel” as particles passing 75-mm (3-in.) sieve and retained on 4.75-mm (No. 4) sieve and “sand” as particles passing 4.75-mm (No. 4) sieve and retained on 75- μ m (No. 200) sieve. Thus, an aggregate would be classified as gravel or sand (coarse aggregate or fine aggregate) depending on whichever proportion present is larger.

The influence of gravel (or coarse aggregate) content on the shear strength of cohesionless soil-gravel/sand-gravel mixtures has been the topic of investigation by many geotechnical researchers. According to Vallejo (2002), the frictional resistance between the gravel particles controlled the shear strength of the soil/sand-gravel mixtures when the percentage by weight of gravel was on average greater than 70%; whereas the gravel particles with a concentration by weight less than average 49% basically had no control over the shear strength of the mixtures.

This scientific observation could imply that the relative contents of gravel and sand particles in aggregate base/granular subbase materials may possibly be an inherent factor controlling mixture performance mechanically and/or hydraulically, as supported by findings of Sánchez-Leal (2007) from hot mix asphalt (HMA) studies.

In terms of characterizing aggregate packing in stone-based infrastructure materials, such as HMA, the Bailey method is one of the pioneers. It analyzes the combined aggregate blend using three parameters: the coarse aggregate ratio (CA), the coarse portion of fine aggregate ratio (FA_c), and the fine portion of the fine aggregate ratio (FA_f), which are all calculated from the following designated sieves: half sieve, primary control sieve (PCS), secondary control sieve (SCS), and tertiary control sieve (TCS) (Vavrik et al., 2002). Although the Bailey method has been widely used in HMA gradation design and performance evaluation, its application and validity for aggregate base/granular subbase gradation design has not been fully explored yet. Equation 2.3 summarizes the essential equations associated with the Bailey method.

$$\begin{aligned}
 \text{Half sieve} &= 0.5 * \text{NMPS} ; \\
 \text{PCS} &= 0.22 * \text{NMPS} ; \text{ SCS}=0.22 * \text{PCS} ; \text{ TCS}=0.22 * \text{SCS} ; \\
 \text{CA ratio} &= \frac{\% \text{Passing Half sieve} - \% \text{Passing PCS}}{100\% - \% \text{Passing Half sieve}} ; \\
 \text{FA}_c &= \frac{\% \text{Passing SCS}}{\% \text{Passing PCS}} ; \\
 \text{FA}_f &= \frac{\% \text{Passing TCS}}{\% \text{Passing SCS}} .
 \end{aligned} \tag{2.3}$$

where NMPS is the Nominal Maximum Particle Size, a Superpave® asphalt mix design terminology defined as one sieve larger than the first sieve that retains more than 10%.

2.3.2 Analytical Gradation Analysis Framework

2.3.2.1 Concept of Gravel-to-Sand Ratio

Xiao et al. (2012) employed commonly used gradation quantification methods, including the Talbot equation, the Rosin-Rammler distribution function, the Unified Classification System parameters, the conventional Gravel-to-Sand ratio, as well as the Bailey method, to identify key gradation parameters governing the shear strength behavior of the studied aggregate materials. While other gradation parameters seemed to be less significant, the Gravel-to-Sand (G/S) ratio was found to control the shear strength behavior of both “standard” and reclaimed materials. Depending on the relative concentrations of gravel and sand sized fractions, different packing states with varying stability and porosity can be achieved.

2.3.2.2 Concept of Primary Structure (PS) and Secondary Structure (SS)

Yideti et al. (2013) developed a gradation model based on packing theory to evaluate the effect of the aggregate size distribution on the strength and permanent deformation performance of unbound granular materials. As illustrated in Figure 2.3, two basic components of the skeleton of the unbound aggregate materials, i.e., Primary Structure (PS) and Secondary Structure (SS), are identified by this framework along with their volumetric composition. The procedure to identify the load carrying part of the aggregate skeleton (PS) was developed and packing parameters controlling the stability of the loading carrying material were identified. It is shown that strength values of granular materials are controlled to a great extent by the packing characteristics of their load carrying skeleton (Yideti et al., 2013).

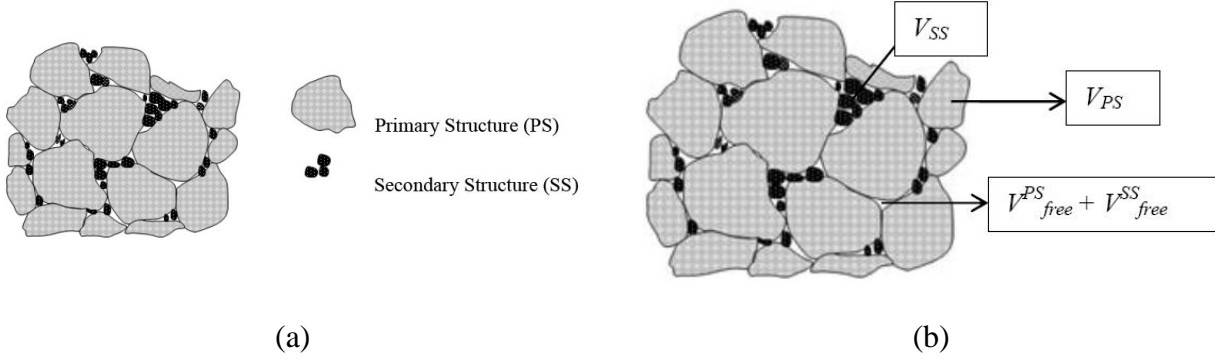


Figure 2.3 Packing Theory based Gradation Model Proposed by Yideti et al. (2013): (a) Skeleton of Unbound Granular Material and (b) Volumetric Composition of Skeleton

Determination of Primary Structure

According to the gradation analysis framework proposed by Lira et al. (2013), the upper and lower limits for the average particle size between two contiguous sieve sizes can be formulated as in Equation 2.4, which determines the interaction between particles retained on two contiguous sieve sizes.

$$0.311\overline{D}_n + 0.689\overline{D}_{n+1} \leq D_{avg} \leq 0.703\overline{D}_n + 0.297\overline{D}_{n+1} \quad (2.4)$$

where \overline{D}_n is the mean size of particles for the sieve size D_n with material retained at D_{min} (opening of the sieve) and smaller than D_{max} (opening of the previous sieve). It is defined as in Equation 2.5.

$$\overline{D}_n = B(D_{min} + D_{max}) \quad (2.5)$$

where B is a dimensionless parameter representing the mean value for a distribution between 0 and 1. The parameter B can be calculated using probability distributions.

Lira et al. (2013) determined the interaction between two consecutive sieve sizes (i.e., stone-on-stone contact) by assuming that all particles are considered as spherical, and that the material within a sieve presents a uniform distribution of sizes (i.e., B=0.5). The gradation

analysis via Equation 2.4 is done in a systematic way until the last sieve size and a list of interaction ranges are obtained. Note that the interaction range might include several sieve sizes; and in some cases, these consecutive ranges can be interrupted by a non-interactive case, giving several possible ranges for the Primary Structure. To select which one of these ranges is the strongest one, the total concentration of material at each range is accounted. Then, the range of sieve sizes that has the highest concentration will be the Primary Structure. According to the fundamentals of the model, the PS range must have a minimum concentration of 45% to carry load, but these values are not always achieved. According to the literature (Lira et al., 2013), the smallest material to be part of the Primary Structure is the one passing the 2.36 mm sieve and retained at the 1.18 mm sieve (AASHTO T27, ASTM C136) or retained at 2 mm (ISO 565, DIN 4188, BS 410).

Porosity of the Primary Structure

The porosity of the PS is calculated as the fraction of volume of voids over the total volume, as shown in Equation 2.6.

$$\eta_{PS} = \frac{V_T - V_a^{other} - V_a^{PS}}{V_T - V_a^{other}} \quad (2.6)$$

where V_T is the total mix volume, V_a^{other} is the volume of aggregates that are of a size larger than the PS and just float in the whole aggregate matrix, and V_a^{PS} is the volume of aggregates belonging to the Primary Structure.

In the analysis by Lira et al. (2013), only the influence of the whole structure formed by the stones was considered, which is characterized by porosity of the assemblage, contact points, and air void size as a key parameter to understand the stability of the structure. Contact points are

the number of points where a particle touches its neighbor and is related to the shear and rutting resistance of unbound granular materials. Coordination number (m) is the average of contact points per particle and can be calculated using the relationship derived based on packing theory. Lira et al. (2013) presented the relation (as in Equation 2.7) found from plotting coordination number (m) against porosity (η) for four theoretical packing arrangements for spheres, i.e., Simple cubic, Orthorhombic, Tetragonal-Sphenoidal, and Rhombohedral.

$$m = 2.827 \cdot \eta^{-1.069} \quad (2.7)$$

Disruption Factor

To determine the influence of the Secondary Structure on the stability of the Primary Structure as defined previously, Lira et al. (2013) proposed the Disruption Factor (DF) as a rational measure. The DF is calculated as in Equation 2.8.

$$DF = \frac{V_{dp}}{V_v^{PS}} = \frac{W_{dp}/G_{sb}}{No.Voids^{PS} \cdot V_{1Void}} = \frac{W_{dp}/G_{sb}}{\frac{V_a^{PS}}{\frac{4}{3}\pi r^3} \cdot V_{1Void}} \quad (2.8)$$

where V_{dp} is the volume of the potentially disruptive portion of the Secondary Structure which includes particles bigger than the PS average void size according to packing (obtained from the PS porosity) and smaller than the smallest PS particle size, W_{dp} is the weight of the potentially disruptive particles, G_{sb} is the specific gravity of the aggregates, $No.Voids^{PS}$ is the number of voids in the PS, V_{1Void} is the volume of each void in the PS, V_a^{PS} is the volume of aggregate in the PS, and r is one half of the weighted average size of PS.

Rutting performance of unbound aggregate layers is related to the capacity of the aggregate skeleton formed to resist shear. In addition to a strong aggregate skeleton (i.e., the PS), an adequate amount of Secondary Structure, especially the potentially disruptive particles, will benefit the whole aggregate matrix in the load carrying capacity. The amount of Secondary Structure will also determine the microstructural behavior of an aggregate matrix and its response to failure. The gradation analysis framework presented above, as developed by Lira et al. (2013) allows identifying the load carrying aggregate size range. The PS gives information about the way the aggregates are arranged within the mix, the air void distribution, its capacity to resist shearing and its durability. The porosity and disruption factor allows us to characterize the Primary Structure to subsequently relate it to performance of unbound aggregate layers. Relating such gradation analysis framework parameters to field rutting performance of several asphalt mixtures, they found that those mixtures with a more balanced combination between coarse and fine material (around 60/40) showed a low rut depth. Interestingly, this 60/40 combination coincides with the optimal value of around 1.5 proposed from the Gravel-to-Sand ratio concept (Xiao et al., 2012).

2.3.2.3 Concept of Gradation Weighing Factor (f_v)

Shen and Yu (2011) defined a gradation weighing factor f_v (Equation 2.9) as the percentage of voids change by volume due to the addition of unit aggregate, which is an indication of the resulting volumetric impact when smaller aggregates are added into the structure. The newly added aggregates typically have two effects, either enlarge the structures by creating more voids, or fill the voids created by the original aggregates without changing the total volume of the structure. It is also possible that part of the added aggregate particles serve as creating voids while others serve as filling the voids.

$$f_v = \frac{V_{v2} - V_{v1}}{V_{a2}} = \frac{V_2 p_2 - V_1 p_1}{V_{a2}} \quad (2.9)$$

In the gradation and packing analysis, the actual f_v values can be determined for each sieve size when added into the aggregate structure consisting of upper sieve size aggregates. The development of the f_v parameter provides a straightforward method to estimate the porosity or VMA of an aggregate structure. This method is an iteration process starting from an aggregate structure with uniform size (typically NMAS) of aggregates. When smaller size aggregates are added in, the resulting porosity of the new structure can be determined as in Equation 2.10. Repeating the same procedure, smaller size aggregates will be added into the mixed aggregate structure, and the corresponding f_v values will be determined. Once all f_v values for each sieve size are determined, the following Equation 2.11 will be used to predict the void in mineral aggregates (VMA) of the mix. It provides a linkage between the aggregate gradation properties and the resulting porosity. It can be used to estimate the f_v values or the porosity values when the other information is available. Shen and Yu (2011) assumed that the f_v values are not sensitive as long as they have the same nominal maximum aggregate size (NMAS) and belongs to the same gradation type (coarse-graded, medium-graded, or fine-graded), which was later verified by the DEM simulation.

$$p_2 = \frac{V_{v2}}{V_2} = \frac{f_v V_{a2} + V_{v1}}{V_1 + (1 + f_v) V_{a2}} \quad (2.10)$$

$$p = \frac{\sum_{i=1}^n f_{vi} V_{ai}}{\sum_{i=1}^n (1 + f_{vi}) V_{ai}} \quad (2.11)$$

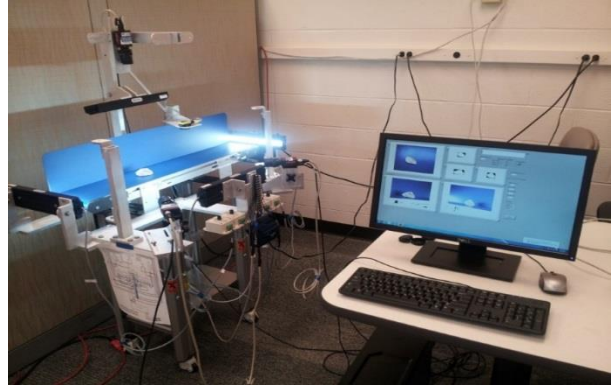
where V_{v2} is the total air void volume at state II, V_2 is the total volume at state II, p_2 is aggregate porosity at state II, f_{vi} is the f_v value for i th sieve size of the gradation, V_{ai} is the percentage by volume of aggregate retained in the i th sieve size, and p is the porosity or VMA of the aggregate structure.

2.3.3 Imaging based Determination of Particle Morphology

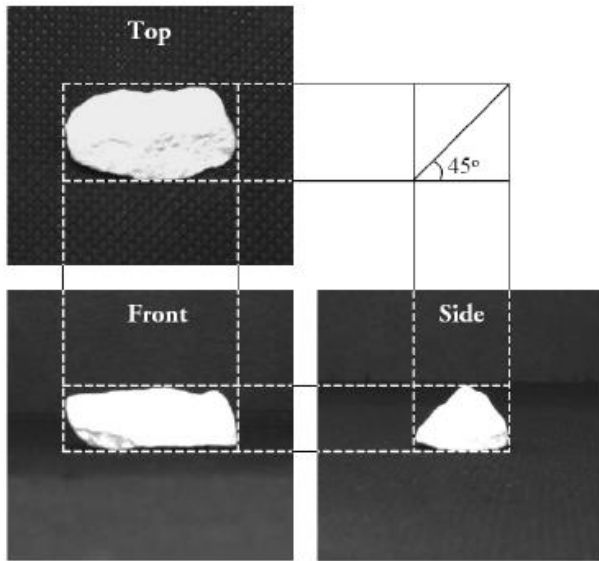
Past research efforts have correlated the size and shape properties of aggregates to mechanical response of pavement structural layers and pavement performance. This necessitates the objective and accurate quantification of particle size and morphology. The NCHRP 4-30A project, “Test Methods for Characterizing Aggregate Shape, Texture, and Angularity (Report 555)” recommended the University of Illinois Aggregate Image Analyzer (UIAIA) as a viable imaging system for analyzing aggregate morphology and quantifying aggregate morphological effects to influence strength and permanent deformation behavior of unbound aggregate materials (Masad et al., 2007). The UIAIA uses 3 cameras to collect individual aggregate particle images from three orthogonal directions and in essence captures an “actual” 3D view of each aggregate particle, as illustrated in Figure 2.4(a). The captured images are then processed using software developed specifically for this application and the needed size and shape properties are determined (Rao, 2001; Pan, 2006). Coarse aggregate particle shape indices defined by the UIAIA system include the Flat and Elongated Ratio (F&E Ratio), Angularity Index (AI), and Surface Texture (ST) Index. These three indices were developed to represent the three key morphological descriptors of coarse aggregate materials as the shape or form, angularity, and surface texture.



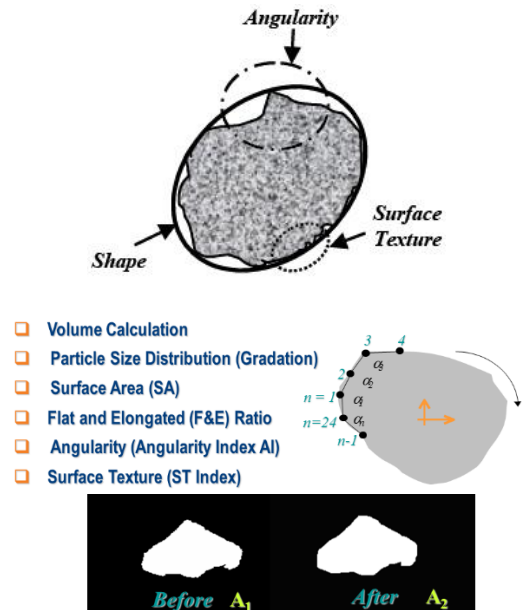
(a)



(b)



(c)



(d)

Figure 2.4 Illustration of the University of Illinois Aggregate Image Analyzer (UIAIA): (a) the First Generation, (b) the Second Enhanced Generation, (c) Images Captured from Three Orthogonal Views of a Particle, and (d) Key Morphological Descriptors and their Algorithms (Rao, 2001; Pan, 2006; Moaveni et al., 2013)

A second-generation, enhanced UIAIA (E-UIAIA), was designed and manufactured recently at the University of Illinois with many improvements, as pictured in Figure 2.4(b). Equipped with three high-resolution (1292×964 pixels), charge-coupled device, progressive-scan

digital color cameras, the new version of UIAIA is able to capture digital color images of aggregate particles. Therefore, different types of mineral aggregates with a wide variety of colors can be scanned with this system. The best contrast and sharpest-possible aggregate images can also be achieved by optimizing light intensity and minimizing shadows of the four LED illumination lights with dimmer controls (Moaveni et al., 2013).

2.3.4 Discrete Element Method (DEM) based Aggregate Packing Simulation

In reality, the granular assembly consists of discrete grains that have different shapes and sizes; therefore, the suggestion to treat the assembly as a continuum is not correct. Further, no well formulated equations have been developed to quantify the effects of the surface roughness and grain shape. Accounting for the influences of unbound aggregate physical properties (e.g., gradation and geometry) and their interactions through experimental methods requires a very comprehensive, time-consuming, and labor-extensive set of experiments, yet still may not provide insight for understanding the mechanical behavior of unbound aggregates in relation to aggregate selection and optimizing the internal structure to improve performance. It is imperative that the contribution of the aggregate properties to unbound layer performance is better understood, and that methods are developed to analyze this contribution during aggregate selection. Current specifications often delineate maximum and minimum percentages of material that pass certain critical sieve sizes (e.g., 1-in., No. 4, and No. 200); however, in many cases, these specifications for grain size distribution are often empirical and ad-hoc in nature, simply require the use of well-graded materials (as per Unified Soil Classification System). By adjusting the percentages of particles at different sizes, aggregate gradations can be optimized at the microstructure level for large enough void space and adequate structural performance.

Evans et al. (2009) simulated biaxial compression tests on 2D particulate assemblies of four grain size distributions (GSD) and interpreted material responses in terms of stress-strain-strength behavior at both the macroscale and particle-level properties at the microscale. They found that a coarser well-graded specimen had a higher shear strength than a finer well-graded specimen, and that more uniformly graded specimen is softer at low strains, requires a higher strain to peak, and is significantly more dilatant than the well-graded assemblies. As shown in Figure 2.5, four distinct GSDs were used for their simulations, i.e., fine, baseline, coarse, and linear. Note that the fine, baseline, and coarse distributions were selected to represent upper, middle, and lower bound distributions of commonly used unbound aggregate base course materials. To avoid unaffordable simulation time which is the function of both sample size (a function of the maximum particle size) and the minimum particle size, the particle size bins were mapped into smaller margins to have analogous grain size distributions to desired grain size distributions and yield a more practical number of particles (around 5×10^4) in DEM simulation.

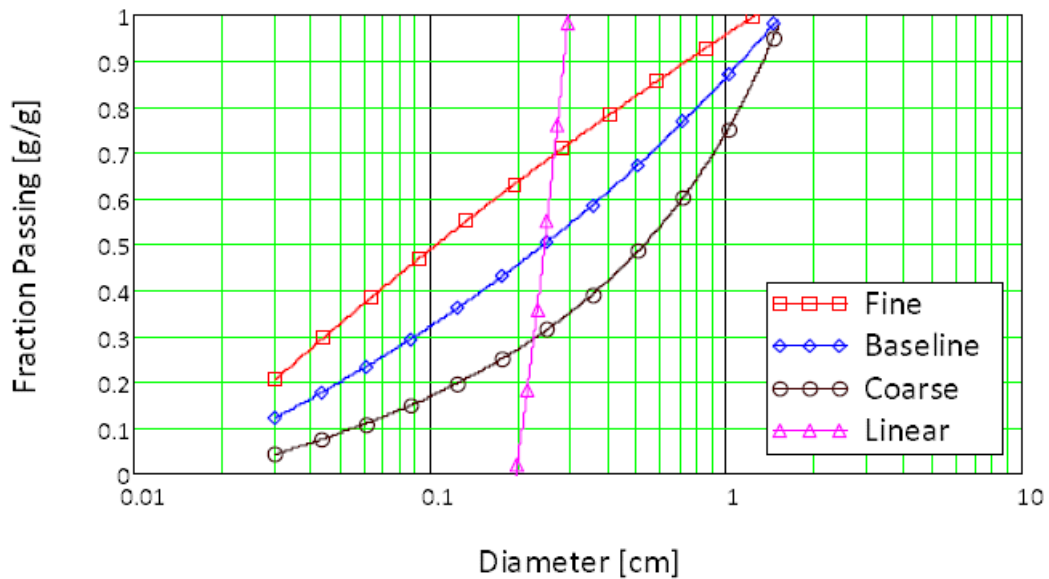
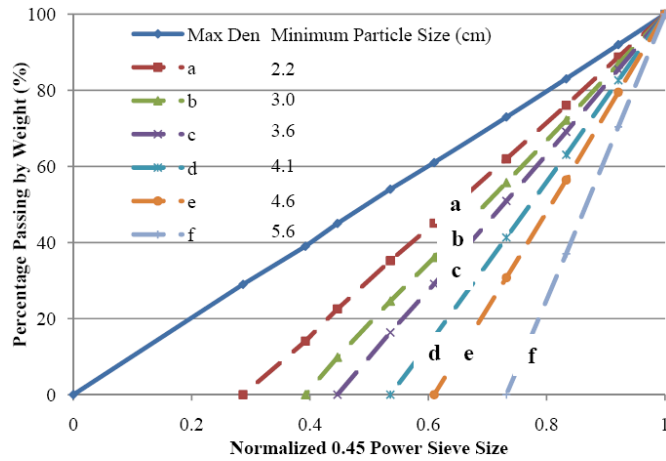


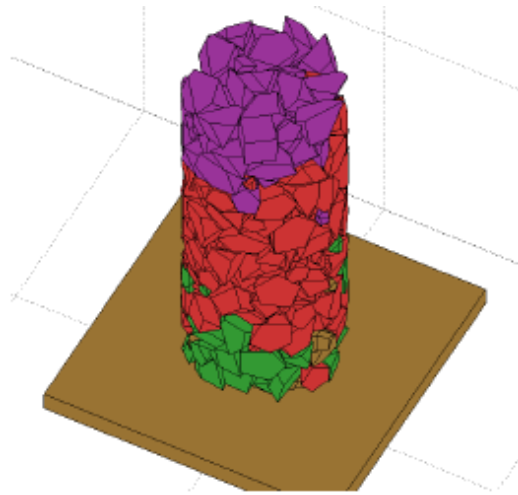
Figure 2.5 Four Distinct Grain Size Distribution Curves for DEM Simulation (Evans, 2009)

With the realistic particle shape representation (polyhedron), Huang (2010) investigated the effect of gradation on ballast volumetric properties using the validated digital image aided DEM ballast model. As shown in Figure 2.6(a), different gradation lines with varying minimum particle sizes (termed as “characteristic gradation curves”) that were derived from the Talbot Equation (see Equation 2.1) were studied for their effects on aggregate assembly volumetric properties and the structural layer support characteristics. Figure 2.6(b) shows the ballast gradation samples generated to conduct air void test DEM simulations. Figure 2.6(c) illustrates the effect of minimum particle size on mean air voids content. Clearly, there exists a threshold minimum particle size at which the densest packing can be achieved. Huang (2010) also found out that AREMA ballast gradation specifications could be possibly engineered based on DEM simulation results in an effort to improve the structural support and resistance to settlement.

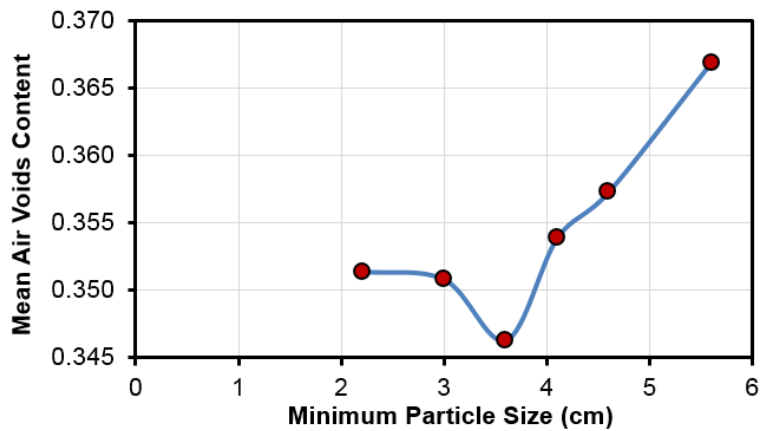
Cao and Lin (2010) built a 2D packing model in which a random distribution and compacted contact of different size aggregates were assumed. The mathematical solution to this model was achieved by using the geometric theory of space topology.



(a)



(b)



(c)

Figure 2.6 DEM Simulation Results by Huang (2010): (a) Characteristic Maximum Density Gradation Curves Studied, (b) DEM Cylindrical Sample for Air Voids Determination, and (c) Effect of Minimum Particle Size on Mean Air Voids Content

2.4 Resilient Response of Unbound Aggregate Layers

This section and the one immediately following present an overview of unbound aggregate material characteristics and structural layer behavior as the primary structural component in pavement systems. A thorough review of different aggregate test procedures and characterization methods commonly used to model granular pavement layer resilient responses and permanent deformation behavior is imperative to facilitate better designs of pavement systems, and ultimately ensure adequate performance under repeated moving wheel loading.

2.4.1 Laboratory Characterization Methods

Ideally, pavement layer response under traffic loading should be purely elastic, and thus no accumulation of permanent deformation should occur during its service life. Accordingly, mechanistic-based pavement design approaches have traditionally focused on the elastic or resilient response of unbound aggregate layers to predict the critical pavement responses under traffic loading. The most important input property for characterizing repeated load behavior of unbound aggregate layer in pavement analysis has been the “resilient modulus”. Defined as a secant modulus representing hysteretic stress-strain behavior of materials, the resilient modulus (M_R) is a critical material property needed for mechanistic-empirical (M-E) pavement design methods (Puppala, 2008).

As reviewed by Tutumluer (2013) in the recent NCHRP Synthesis 445 report, entitled “Practices for Unbound Aggregate Pavement Layers”, pavement stresses are mainly composed of two parts, initial in-situ stresses and stresses due to moving wheel loads. The initial in-situ stresses, static in nature, are the overburden and compaction-induced residual stresses. The initial stresses are typically lower at shallow depths than at greater depths. Compaction-induced residual stresses that are compressive in nature can often exist in the unbound aggregate layers

and contribute to the static stress states (Uzan, 1985; Barksdale et al., 1997). On the other hand, traffic loading due to moving wheel loads induces much higher dynamic stresses than the static ones. In summary, a pavement element constantly experiences a combination of varying magnitudes of static and dynamic stresses depending on the depth in the pavement layer and the radial offset from the wheel load. The principal stress rotation and the constantly rotating fields of stresses under moving wheel loads have been observed from field measurements. In the case of aggregate bases, the cyclic component of load imposes a change (increment) of stress state which is not co-axial with the stress state under the static (overburden) load. This is illustrated in Figure 2.7. The major principal stress due to overburden is always aligned in the vertical direction regardless of the location of a moving wheel. The incremental stresses imposed by a wheel load, however, are not co-axial with this system, and as a result, the total principal stresses rotate as the wheel load passes. Principal stress rotation may cause increased rates of shear and volumetric strains during cyclic loading relative to equivalent stress paths without stress rotation (Kim and Tutumluer, 2005).

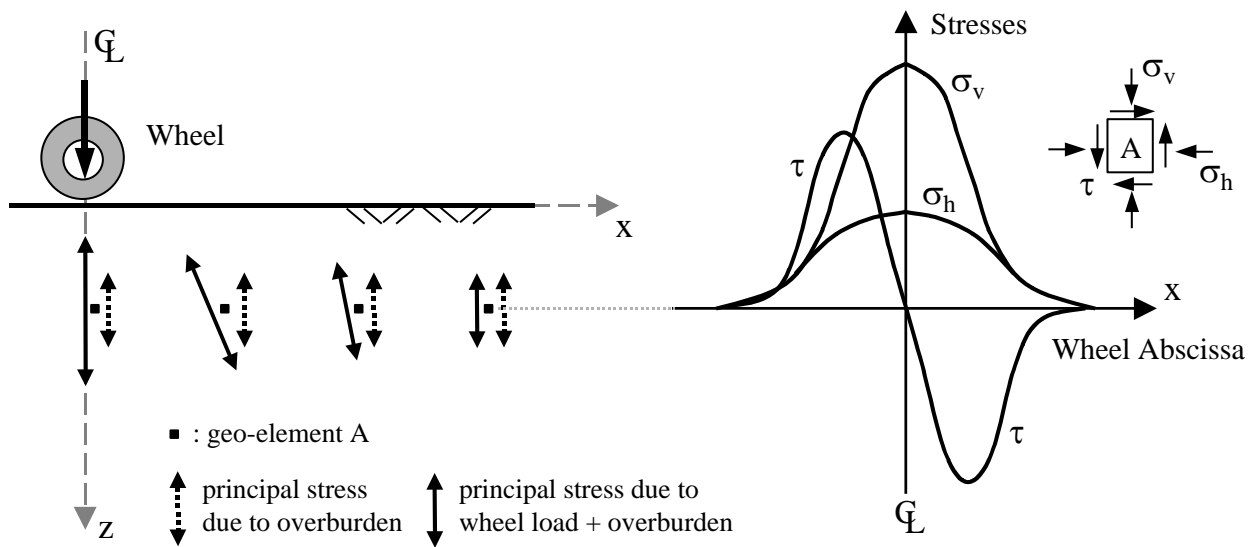


Figure 2.7 Stress States and Rotation of Principal Stresses Experienced by the Aggregate Layer beneath a Rolling Wheel Load (Tutumluer, 2013)

Figure 2.8 illustrates the concept of stress path loading related to stress path slope (m) and stress path length (L) on a q - p diagram (Kim, 2005). Static overburden stresses correspond to q_{\min} and p_{\min} , whereas dynamic traffic load reaches up to q_{\max} and p_{\max} following a constant stress path slope (m). Analyses of test data often require defining geomaterial behavior in terms of these principal stresses considering a mean normal stress component (p) influencing volume change, and the deviator stress component (q) affecting shear behavior for shape change and distortion (Kim and Tutumluer, 2005). In general, the stress path slope ($m = \Delta q / \Delta p$) for the standard CCP tests takes a constant value of 3.0. For variable confining pressure (VCP) tests, the stress slope varies generally from -1.5 to 3. VCP tests offer the capability to apply a wide combination of stress paths by pulsing both cell pressure, σ_3 , and vertical deviator stress, σ_d . Various stress paths cause different loading effects on pavement elements, which are not yet fully studied and understood to explain permanent deformation accumulation.

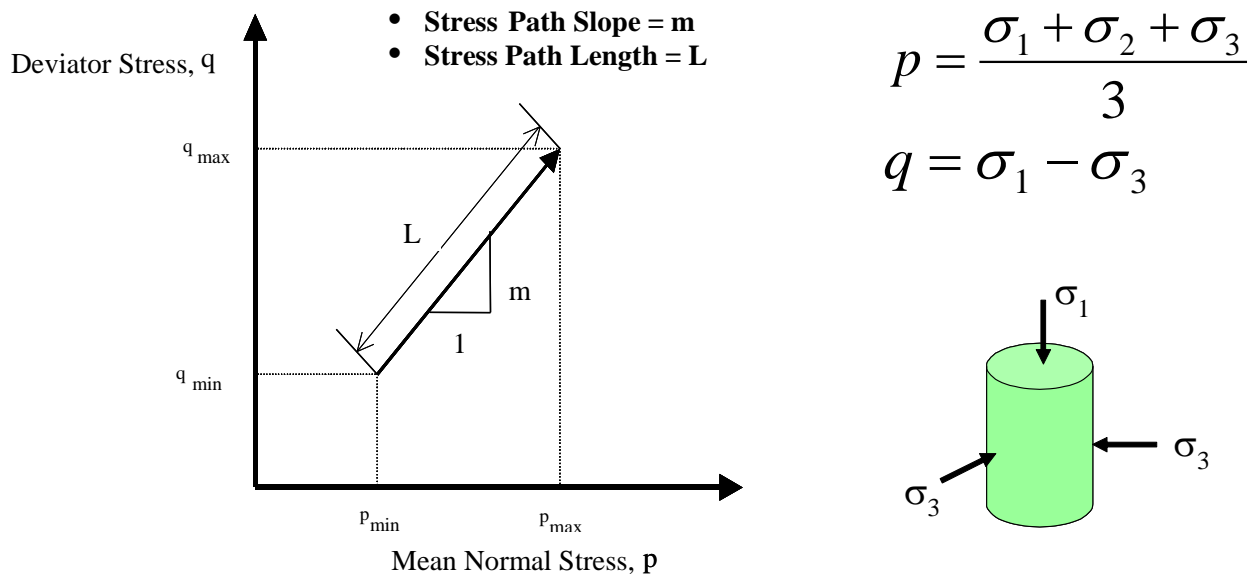


Figure 2.8 Concept of Stress Path Loading Showing Slope and Length (Kim, 2005)

2.4.2 Review of Current Resilient Modulus Models

Resilient moduli of granular materials increase with increasing stress states (stress-hardening), especially with confining pressure and/or bulk stress, and slightly with deviator stress (Lekarp et al., 2000). Resilient behavior of unbound aggregate materials can be reasonably characterized by using stress dependent models which express the modulus as nonlinear functions of stress states. Such a characterization model must include in the formulation the two triaxial stress conditions, i.e., the confining pressure σ_3 and the deviator stress σ_d or, the applied mean pressure p and the deviator stress q , to account for the effects of both confinement and shear loading. The model parameters are traditionally obtained from the multiple regression analyses of the repeated load triaxial test data. Currently available models are summarized in Table 2.1.

Table 2.1 Summary of Current Resilient Modulus Models

Model Name	Model Form	
Confining Pressure Model (Seed et al., 1967)	$M_R = K_1(\sigma_3)^{K_2}$	(2.12)
K- θ Model (Hicks and Monismith, 1971)	$M_R = K(\theta)^n$	(2.13)
Bulk-Shear Modulus Model (Boyce, 1980)	$K = \frac{K_i p^{(1-n)}}{1 - \beta \left(\frac{q}{p}\right)^2}; \quad G = G_i p^{(1-n)}$ $\varepsilon_v = \left(\frac{1}{K_i}\right) p^n \left[1 - \beta \left(\frac{q}{p}\right)^2\right]; \quad \varepsilon_q = \left(\frac{1}{3} G_i\right) p^n \left(\frac{p}{q}\right)$	(2.14)

Table 2.1 (cont.)

Model Name	Model Form	
Shackel's Model (Shackel, 1973)	$M_R = K_1 \left[\frac{(\tau_{\text{oct}})^{K_2}}{(\sigma_{\text{oct}})^{K_3}} \right]$	(2.15)
Uzan Model (Uzan, 1985)	$M_R = K_1 (\theta)^{K_2} (\sigma_d)^{K_3}$	(2.16)
Lade and Nelson Model (Lade and Nelson, 1987)	$E = M p_a \left[\left(\frac{I_1}{p_a} \right)^2 + R \frac{J_2}{p_a} \right]^\lambda$	(2.17)
Universal Octahedral Shear Stress Model (Witczak and Uzan, 1988)	$M_R = K_1 p_a \left(\frac{I_1}{p_a} \right)^{K_2} \left(\frac{\tau_{\text{oct}}}{p_a} \right)^{K_3}$	(2.18)
Itani Model (Itani, 1990)	$M_R = K_1 p_a \left(\frac{\sigma_\theta}{p_a} \right)^{K_2} \sigma_d^{K_3} \sigma_3^{K_4}$	(2.19)
Crockford et al. Model (Crockford et al., 1990)	$M_R = \beta_0 \left(\theta + 3\Psi \frac{V_w}{V_t} \right)^{\beta_1} \tau_{\text{oct}}^{\beta_2} \left(\frac{\gamma}{\gamma_w} \right)^{\beta_4}$	(2.20)
UT-Austin Model (Pezo, 1993)	$M_R = \frac{\sigma_D}{\varepsilon_t} = \frac{\sigma_d}{a \sigma_d^b \sigma_3^c} = \frac{1}{a} (\sigma_d^{1-b} \sigma_3^{-c}) = K_1 (\sigma_d)^{K_2} (\sigma_3)^{K_3}$	(2.21)
Lytton Model (Lytton, 1995)	$M_R = K_1 p_a \left(\frac{I_1 - 3\theta f h_m}{p_a} \right)^{K_2} \left(\frac{\tau_{\text{oct}}}{p_a} \right)^{K_3}$	(2.22)
MEPDG Model (NCHRP 1-37A, 2004)	$M_R = K_1 p_a \left(\frac{\theta}{p_a} \right)^{K_2} \left(\frac{\tau_{\text{oct}}}{p_a} + 1 \right)^{K_3}$	(2.23)

where θ is bulk stress = $(\sigma_1+2\sigma_3)$ or $(\sigma_d+3\sigma_3)$, σ_d is deviator stress = $(\sigma_1-\sigma_3)$, p_a is atmospheric pressure, K_i is an initial value of bulk modulus, G_i is an initial value of shear modulus and n is a constant less than 1.0, β is $(1-n)\frac{K_i}{6G_i}$, p is mean stress, q is deviator stress, ϵ_v and ϵ_q are the

volumetric and shear strains, respectively, I_1 is the first stress invariant and I_2 is the second invariant, τ_{oct} is octahedral shear stress = $1/3\{(\sigma_1-\sigma_2)^2 + (\sigma_1-\sigma_3)^2 + (\sigma_2-\sigma_3)^2\}^{1/2} = \frac{\sqrt{2}}{3}(\sigma_1 - \sigma_3)$,

β_0 , β_1 , β_2 , and β_3 are material constants, Ψ is suction stress, $\frac{V_w}{V_t}$ is volumetric water content,

$\frac{\gamma}{\gamma_w}$ is unit weight of material normalized by the unit weight of water, and n and K_i are material

regression constants obtained from triaxial test data.

2.5 Shear Strength of Unbound Aggregate Layers

2.5.1 Laboratory Characterization Methods

Strength is defined as the maximum level of stress that material can sustain before it fails or excessively deforms. Strength properties of a granular material can be best determined from static triaxial testing with monotonically increasing loading. Usually three triaxial tests are conducted over a range of confining pressure levels representative of probable in-service conditions. Confining pressures used typically vary from 3 to 40 psi. Axial strain rates used in triaxial testing are typically 1% to 2% strain per minute. Triaxial test data are then interpreted to determine the cohesion (c) and angle of internal friction (ϕ) of the material tested. The parameters c and ϕ define the shear strength of the material, which is given by the Mohr-Coulomb equation:

$$\tau_{\max} = c + \sigma_n \tan \phi \quad (2.24)$$

where τ_{\max} is shear strength, c is cohesion, σ_n is the normal stress on specimen failure plane, and ϕ is the angle of internal friction.

Considering vehicles usually move across a pavement very quickly, triaxial shear tests have been performed at University of Illinois at a rapid shearing rate which is more representative of usual loading conditions than the conventional slow triaxial shear test. Three different samples are tested at confining pressures of 5, 10, and 15 psi to determine the shear strength properties, friction angle and cohesion, of the aggregate materials. Compared to the conventional triaxial shear tests, a very high loading rate of 1.5 in./sec. is applied in rapid shear tests, causing 12.5% deformation in a 12-in. high specimen instantly. The rapid shear test initiated at the University of Illinois has been listed by the recent NCHRP Project 4-23 as a fairly simple and precise test method for accurate quantification of aggregate shear strength. It has also been reported to better simulate any possible failure condition of an in-service pavement layer under the dynamic application of a moving wheel load as compared to conventional triaxial shear tests (Thompson and Smith, 1990; Garg and Thompson, 1997).

2.5.2 Review of Current Shear Strength Models

The aforementioned linear Mohr-Coulomb criterion by Terzaghi has been used extensively to characterize the failure of soils; however, the use of this simple form to some types of soils and stabilized soils has led to a number of anomalies, as pointed out in previous studies. Results of many studies have shown that failure envelope of certain types of soils, especially cement treated soils, are curved; therefore, it is impossible to report a particular internal friction angle to characterize the strength over the wide range of confining pressures. Several failure criteria such as, Griffith crack theory, modified Griffith crack theory, Hoek and

Brown, and Johnston (1985) have been presented to improve the strength description of geomaterials. It must be noted that application of each failure criteria is limited to type of material and stress conditions.

The stress pulse caused by moving vehicle loading consists of normal and shear stress components (Wang, 2011). Depending on the relative locations with respect to the loading, various multi-axial stress states can be found to exist in pavement layers. Such multi-axial stress states need to be considered rather than the one-dimensional tensile or shear stress only. The failure potential of unbound materials under the complex 3-D stress states can be better evaluated using the experimental methods that can simulate such multi-axial stress states, such as the triaxial test or hollow cylinder test. Several failure theories can consider multi-axial stress states, including maximum shear stress criterion (Tresca criterion), maximum octahedral shear stress (maximum distortional energy criterion or von Mises criterion), Mohr-Coulomb criterion, and Drucker-Prager criterion. The widely used Mohr-Coulomb criterion is expressed in terms of maximum and minimum principal stresses, and hence does not incorporate the effects of intermediate principal stresses.

In addition to being plotted as a series of Mohr's circles, the stress state is often plotted alternatively as points in a p-q diagram. The Mohr-Coulomb failure criterion states that a material would fail (either by fracture or by the onset of yielding) when a Mohr's circle reaches its failure envelope. This can then be interpreted in such a way that a stress ratio can be defined to measure the closeness of a multi-axial stress state to the critical failure envelope. In this study, the shear stress ratio defined based on each of the two failure criteria is used to evaluate the failure potential, as shown in Equations 2.25 and 2.26.

$$\text{Stress Ratio} = \frac{q}{q_{failure}} = \frac{q}{a + p \tan \alpha} = \frac{\sigma_1 - \sigma_3}{2c \cdot \cos \phi + (\sigma_1 + \sigma_3) \sin \phi} \quad (2.25)$$

$$\text{Stress Ratio} = \frac{q}{q_{failure}} = \frac{q}{A + pB} = \frac{\sqrt{3J_2} (3 - \sin \phi)}{2I_1 \cdot \sin \phi + 6c \cdot \cos \phi} \quad (2.26)$$

where p is the mean normal stress at failure with $p = \frac{1}{3}I_1 = \frac{1}{3}(\sigma_1 + \sigma_2 + \sigma_3)$; q is the shear

stress at failure with $q = \sqrt{3J_2} = \frac{1}{6}[(\sigma_1 - \sigma_2)^2 + (\sigma_2 - \sigma_3)^2 + (\sigma_1 - \sigma_3)^2]$; I_1 is the first

stress invariant; and J_2 is the second stress invariant of deviatoric stress.

2.6 Permanent Deformation of Unbound Aggregate Layers

Rutting or accumulation of permanent deformation is the primary distress mechanism of unbound aggregate base/subbase layers in pavements. Accordingly, rutting resistance is a major performance measure for designing these pavement foundation layers. Field experiences, such as those from the AASHO road test, Minnesota Road Research test facility (Mn/ROAD), and the National Airport Pavement Test Facility (NAPTF) among many others, have clearly shown that granular base/subbase permanent deformation may contribute significantly to the overall flexible pavement surface ruts (Christopher et al., 2006; Dai et al., 2007; Kim and Tutumluer, 2006).

To ensure satisfactory pavement performance and longevity, unbound aggregate layers should be properly designed to possess adequate rutting resistance, especially for unsurfaced or thinly surfaced pavements where nonlinear and inelastic behavior induced by dynamic wheel load stresses become quite crucial. Despite being a highly researched topic in the past few decades, realistic characterization and accurate prediction of rutting accumulation still remain challenging with great complexity arising from both traffic and environmental loading aspects. Better understanding of long-term rutting mechanism as well as more accurate and reliable

rutting models become urgent needs in the design of new pavements, especially those built with locally available marginal quality and/or recycled materials possessing greater performance uncertainty than traditional “standard” materials with proven field performance (Xiao et al., 2012).

Both experimental and field results indicated that permanent deformation response depends strongly on stress level and material state conditions (e.g., water content and density). Aggregate type, quality, and physical properties are long realized as individual factors to greatly influence the unbound pavement layer rutting performance, yet the underlying mechanisms of their interactions with in-situ stress states controlling field rutting development have not been fully explored. Mishra and Tutumluer (2012) studied a factorial combination of aggregate type, particle shape and surface texture, type and amount of fines, and moisture and density in relation to required compaction conditions for their effects on mechanistic pavement response and rutting performance through both laboratory repeated load triaxial (RLT) and field accelerated pavement testing (APT). They found that improved behavior in terms of both permanent deformation and resilient modulus could be achieved by maintaining a stable aggregate matrix (e.g., optimal fines contents); meanwhile, the stability of the aggregate matrix also depends on the interactions among individual aggregate physical properties such as moisture and plastic (cohesive) fines content, defined in this thesis study as the amount of material passing sieve No. 200 or 0.075 mm. Gabr and Cameron (2013) studied permanent strain behavior of recycled concrete aggregate for unbound pavement construction and related the accumulated permanent strain to moisture content and maximum dry density corresponded to the optimum, weighted plasticity index, and maximum shear stress ratio.

2.6.1 Laboratory Characterization Methods

Empirical tests such as California Bearing ratio (CBR) cannot truly assess rutting performance; instead, rutting resistance should be assessed from tests that realistically mimic actual traffic loading encountered in the field (i.e., moving wheel loading). Although repeated load triaxial (RLT) test procedures, such as the AASHTO T307-99, have been established for determining resilient modulus of granular materials, there is currently no standard test procedure in the U.S. for evaluating permanent deformation or field rutting potential of unbound aggregate materials. The need to include permanent deformation aspects along with the resilient properties, when characterizing unbound granular materials, has recently been confirmed (Puppala, 1999). High modulus materials could still undergo severe plastic strain or permanent deformation, indicating that relying on resilient properties alone may not prevent excessive deformation or failure. Further, stress path RLT testing procedures are in fact needed to properly account for moving wheel loading and its effects on permanent deformation in pavement granular layers.

Tutumluer et al. (2001, 2005, 2007) considered in laboratory testing the dynamic nature of moving wheel loads. They found that greater rutting damage could occur especially in the loose base/subbase under the extension-compression-extension type rotating stress states induced by a moving wheel pass. This kind of laboratory testing result is consistent with the previous field findings by Hornyk et al. (2000) that permanent deformations observed under moving wheel load conditions can be up to three times higher than those obtained from plate loading tests. Gräbe and Clayton (2003, 2009, 2013) also concluded that principal stress rotation (PSR) caused by moving wheel loads has a significant and deleterious impact on both resilient moduli and permanent deformation of some types of road and track foundation materials, i.e., reduced resilient moduli and increased rate of permanent strain. Research using a hollow cylinder triaxial apparatus (Chan 1990) has shown that permanent strains increase significantly when a rotation of

the principal stresses is applied (for the same principal stress amplitude). Countries of the European Union recently approved a joint norm for permanent deformation testing of aggregate materials (prEN13286-7). The main objective of this new test procedure is to apply repeated loadings, based on both field and laboratory stress states, on test specimens to analyze the permanent deformation behavior of unbound granular materials. There are two ways to test aggregate specimens by following either a single stage or a multi-stage loading test procedure.

2.6.2 Review of Current Permanent Deformation Models

Cumulative permanent deformation has historically been categorized for a wide range of materials, such as metals, polymers, and some composites, into three stages: primary, secondary, and tertiary, as indicated on the representative RLT data set in Figure 2.9. The primary stage is characterized by a decreasing rate of accumulated permanent deformation and a relatively small permanent deformation magnitude, which results from abrasion at the aggregate particle contacts. In the secondary stage, permanent strain accumulates (or creeps) in a relatively linear fashion with a constant (or stable) rate due to the rearrangement of the particle grains. The tertiary stage occurs as the specimen fails (or flows) and is characterized by an increasing rate of accumulated permanent deformation that is attributed to the fracture of particle grains. In general, the permanent deformation is typically expected to increase rapidly during the early stage after initial pavement construction and being exposed to traffic, and then tend to stabilize (or continue to increase at a very small rate). The rate of accumulation depends not only on the state variables such as void ratio and stress, but also on the cyclic preloading history, i.e., the fabric of the grain skeleton (arrangement of the contacts, orientation of the contact normal, coordination number, fluctuation of stress).

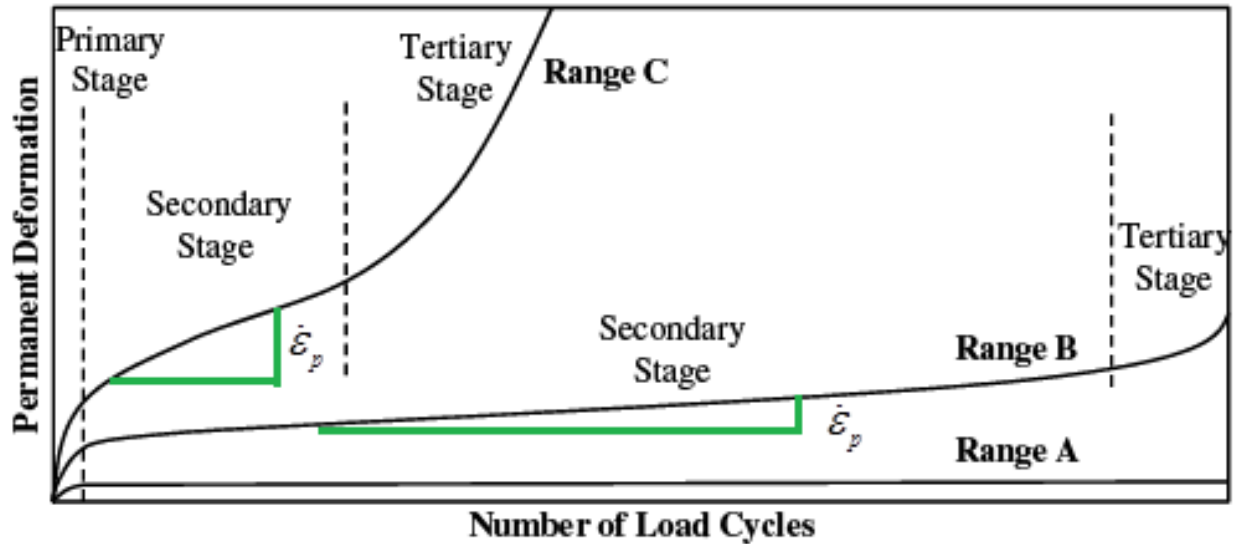


Figure 2.9 Schematic Representation of Different Permanent Deformation Behavior

Existing permanent deformation models for unbound pavement materials are mostly developed based on RLT tests for characterizing permanent deformation behavior at one or more of the three stages. They are of two main types, i.e., analytical or empirical relationships describing the variation of permanent strains with the number of load applications and the applied stresses, as well as increment models developed from plasticity theory for use in finite element based calculations. Well-known examples of the first type are summarized in Table 2.2. They provide relatively simple and intuitively understandable constitutive relationships to predict the amount of permanent deformation (or strain) at any number of loading applications.

For example, the classical power law model simply correlates the cumulative permanent strain with the number of load cycles; consequently, regression coefficients (a and b) obtained from fitting laboratory RLT test results change with varying material properties, loading conditions, and environmental conditions such as moisture content. To give good predictions of laboratory RLT tests, the effects of both stresses and number of load applications are coupled in

some relationships, such as the one proposed by Gidel et al. (2001). Like the classical power law model, the majority of those empirical relationships is limited in characterizing the material behavior under all the stages of permanent deformation because the model parameters derived from the linear (secondary) portion of the cumulative permanent strain against the number of load applications curve ignore the tertiary zone of the deformation. To overcome this limitation, the three-state model in which a power law model, a linear model, and an exponential model is proposed to present the primary, secondary, and tertiary stages of the permanent deformation, respectively. However, the model coefficients still vary significantly with different material types because no fundamental material property is included in the model. Relationships that predict permanent strain from resilient properties (strain and modulus), such as the Tseng and Lytton model (1989), were reported to give erroneous predictions with permanent deformation decreasing as the resilient strain steadied. The current Mechanistic-Empirical Pavement Design Guide (MEPDG) rutting model for unbound granular materials, modified by Witczak et al. (2004) from the original Tseng and Lytton model, was also found to yield poor predictions, as is demonstrated later in this study. The relationship by Choi et al. (2012) was simplified from a rigorous mechanical model based on visco-plasticity for asphalt mixtures.

Contrary to the empirical relationships, the plasticity theory based models are formulated in an incremental form and can be readily applied to the finite element modeling of pavement structures under realistic loading conditions (e.g., multiple wheel load interactions). However, they are sophisticated in nature and almost impractical to implement in routine pavement design, as applying thousands of repeated load cycles is still computationally expensive if not impossible. Model calibration is another challenging aspect requiring more advanced laboratory tests that highway agencies rarely perform on a routine basis.

Table 2.2 Summary of Current Permanent Deformation Models

Model Name	Model Form	
Barksdale Model (Barksdale, 1972)	$\varepsilon_p = a + b \log(N)$	(2.27)
Phenomenological Model (Monismith et al., 1975)	$\varepsilon_p = AN^b$	(2.28)
Strain Rate Model (El-Mitiny, 1980; Khedr, 1985)	$\frac{\varepsilon_p}{N} = aN^{-b}$	(2.29)
Tseng and Lytton Model (Tseng and Lytton, 1989)	$\varepsilon_a = \varepsilon_0 e^{-\left(\frac{\rho}{N}\right)^\beta}$	(2.30)
Wolff Model (Wolff, 1992)	$\varepsilon_p = (mN + a)(1 - e^{-bN})$	(2.31)
Rutting Rate Model (Thompson and Naumann, 1993)	$RR = \frac{RD}{N} = aN^b$	(2.32)
Van Niekerk and Hurrman Model (van Niekerk and Hurrman, 1995)	$\varepsilon_p = a_1 \left(\frac{\sigma_1}{\sigma_{1,f}} \right)^{a_2} \left(\frac{N}{1000} \right)^{b_1} \left(\frac{\sigma_1}{\sigma_{1,f}} \right)^{b_2}$	(2.33)
Paute Model (Paute et al., 1996)	$\varepsilon_p = a \left(1 - \left(\frac{N}{100} \right)^{-b} \right)$	(2.34)
Hurrman Model (Hurrman, 1997)	$\varepsilon_p = A \left(\frac{N}{1000} \right)^B + C \left(\exp \left(D \cdot \frac{N}{1000} \right) - 1 \right)$	(2.35)
Ullidtz Model (Ullidtz, 1997)	$\varepsilon_p = a \left(\frac{\sigma_d}{p_0} \right)^b N^c$	(2.36)

Table 2.2 (cont.)

Model Name	Model Form	
Lekarp and Dawson Model (Lekarp and Dawson, 1998)	$\frac{\varepsilon_p(N_{ref})}{\left(\frac{L}{p_0}\right)} = a \left(\frac{q}{p}\right)_{max}^b$	(2.37)
Theyse Model (1997)	$PD = e^c N^s \left(e^{B\sigma_c} - 1\right)$	(2.38)
Wu et al. Model (2011)	$\varepsilon_p(N) = \varepsilon_v \cdot a \cdot \left[\frac{(N+1)^{1-b} - 1}{1-b} \right]$	(2.39)

Where ε_p is the axial permanent strain; ε_a is the axial permanent strain; $\varepsilon_p(N_{ref})$ is the permanent axial strain at a given reference number of cycles N_{ref} ; N is the number of load applications; ε_0 , β , and ρ are material parameters that are different for each sample (determined based on the water content, resilient modulus, and stress states for base aggregate and subgrade soils through multiple regression analyses); RR is Rutting rate; RD is Rut depth; σ_1 is the major principal stress, $\sigma_{1,f}$ is the major principal stress at failure; a_1 , a_2 , b_1 , and b_2 are model parameter estimates; σ_d is the axial deviator stress, p_0 is the normalizing reference stress (often $p_0 = 1$ psi or 1 kPa); L is the length of stress path, p is the mean normal stress $\left(p = \frac{(\sigma_1 + \sigma_2 + \sigma_3)}{3}\right)$; q is the deviatoric stress $(q = \sigma_1 - \sigma_3)$; $(q/p)_{max}$ is the maximum stress ratio.

2.6.2.1 Permanent Deformation in Unbound Materials

Permanent deformation in unbound granular materials (UGMs) is influenced by a number of factors such as number of load cycles, stress level, stress history, and moisture content and aggregate gradation. Several attempts have been made to develop analytical or M-E rut predictive models for unbound pavement materials. Each model has its own pros and cons. For instance, the Tseng and Lytton (1981) model is a function of resilient strain and the number of load repetitions. This model has been implemented for estimating the permanent deformation in base, subbase, and subgrade layers in MEPDG (ARA, 2004). The permanent deformation model for granular base materials accepted in the current MEPDG was modified from Tseng and Lytton's model. A large amount of calibration work has been performed in the NCHRP Project 1-37a against the permanent deformation data collected from the Long Term Pavement Performance (LTPP) Program. The final calibrated form of permanent deformation model for granular materials is as follows.

$$\begin{aligned}
 PD &= \beta_{s1} k_{s1} \varepsilon_v h_{soil} \left(\frac{\varepsilon_0}{\varepsilon_r} \right) \cdot e^{-\left(\frac{\rho}{N}\right)^\beta} = k_{cal} \cdot \varepsilon_v h_{soil} \left(\frac{\varepsilon_0}{\varepsilon_r} \right) \cdot e^{-\left(\frac{\rho}{N}\right)^\beta} \\
 \left(\frac{\varepsilon_0}{\varepsilon_r} \right) &= \frac{0.15 \cdot e^{(\rho)^\beta} + 20 \cdot e^{\left(\frac{\rho}{10^9}\right)^\beta}}{2} \\
 \log \beta &= -0.61119 - 0.017638 \cdot \omega_c \\
 \rho &= 10^9 \left(\frac{-4.89285}{1 - (10^9)^\beta} \right)^{\frac{1}{\beta}}
 \end{aligned} \tag{2.40}$$

where PD is the permanent deformation or plastic deformation accumulated in the layer; N is the number of axle load applications, ε_v is the average vertical strain in the layer, k_{s1} is the global calibration coefficients (1.673 for granular materials and 1.35 for fine-grained materials), β_{s1} is

the local calibration constant for the rutting in the unbound layers (by default 1.0), and k_{cal} is the combined calibration constant. Note that water content is the only parameter needed in the above equations, because it was calibrated by the best fit of all the data collected regardless of aggregate type, density, or stress level.

Note that the MEPDG uses one permanent deformation model with different sets of calibration factors for pavement unbound layers, including aggregate base, subbase, and soil subgrade (NCHRP, 2002). For an unbound pavement layer or sublayer, the permanent deformation of the layer or sublayer can be calculated by the following model:

$$\delta_p = \sum_{i=1}^n \beta_{cal} \left(\frac{\varepsilon_0}{\varepsilon_r} \right) e^{-\left(\frac{\rho}{N}\right)^\beta} \varepsilon_v h_i \quad (2.41)$$

where δ_p = permanent deformation; ε_r = resilient strain imposed in laboratory test (typically triaxial tests); ε_v = average vertical resilient strain in the layer; $\varepsilon_0, \beta, \rho$ = material parameters; N = number of load applications; n = the number of sublayers; and h_i = the i -th sublayer thickness.

A layer strain model (Barksdale, 1972) can be utilized to compute the permanent deformation in each unbound pavement layer from a corresponding permanent deformation model using a set of respective material properties. Once the permanent strain within each pavement layer is calculated, the total rut depth of the pavement surface can then be obtained by summing up the contributions of permanent deformation from each layer. This approach can also be extended for cases with thick pavement layers by further dividing the layers into sublayers. The procedure is mathematically given as follows:

$$\delta_p = \int_0^{\infty} \varepsilon_p(z) dz = \sum_{i=1}^n \varepsilon_{p,i} \Delta z_i \quad (2.42)$$

where $\varepsilon_{p,i}$ and Δz_i denotes permanent strain and the thickness of the i-th sublayer, respectively; n is the total number of sublayers, and δ_p is the rut depth.

2.6.2.2 Permanent Deformation in the Subgrade

The model by Tseng and Lytton (1989) has been used to estimate the development of permanent deformation in the subgrade and it is performed in two steps: first, the top 2 m of the subgrade layer is divided into 10 sublayers, each with a thickness of 20 cm and the permanent strains within these sublayers are then computed from the model. Second, for the remaining part of the subgrade, the influence of the induced resilient strain is assumed to decrease exponentially with depth, $a \cdot e^{-kz'}$, where a and k are constants and z' is the depth from the surface of the subgrade (Erlingsson, 2012). Thus, the contribution of the permanent deformation from the lower part of the subgrade can be computed by integrating $a \cdot e^{-kz'}$ over the depth:

$$\delta_{r_{sg}} = \int_{z'=0}^{z'_{end}} \varepsilon_r(z') dz' = \left(\frac{a}{k} \right) (1 - e^{-k \cdot z'_{end}}) \quad (2.43)$$

where the constant a and k can be computed by using vertical strain values at two locations (at the surface of the subgrade and 150 mm below the surface of the subgrade) and they are given by:

$$a = \varepsilon_{v1} \text{ and } k = \frac{1}{z'_2} \ln \left(\frac{\varepsilon_{v1}}{\varepsilon_{v2}} \right) \quad (2.44)$$

This gives the contribution to the rut from the subgrade for one repetition. For other repetitions, a similar approach is used

$$\delta_{sg} = \left(\frac{\varepsilon_{v1}}{k} \right) (1 - e^{-k \cdot z'_{end}}) \varepsilon_0 e^{-\left(\frac{\rho}{N} \right)^\beta} \quad (2.45)$$

where δ_{sg} is the permanent deformation in the lower part of the subgrade, ϵ_{v1} and ϵ_{v2} are the vertical strain at the surface of the subgrade and 150 mm below the surface of the subgrade, respectively, and z' is the computation depth measured from the surface of the subgrade.

2.6.3 “Shakedown” Theory for Analyzing Permanent Deformation Behavior

New concepts have been developed to determine the long-term mechanical behavior of unbound granular materials under repeated loadings. Researchers (Sharp and Booker 1984; Yu 2005) also related the magnitude of the accumulated plastic strain to the shear stress level and concluded that the range of behaviors, obtained at various stress ratios in RLT tests, can be described using the shakedown concept. The “shakedown” theory pioneered by Sharp and Booker (1984) has been increasingly used to rank unbound granular materials on the basis of their structural responses under repeated loading. In particular, three possible categories of material response, as illustrated in Figure 2.9, can be distinguished by the criterion proposed by Werkmeister (2004), i.e., plastic shakedown (Range A), plastic creep (Range B), and incremental collapse (Range C).

This classification assumes the existence of certain limiting values that define the stress states at which the permanent strain magnitudes and accumulation rates differ. The so-called “plastic shakedown limit” defines the plastic shakedown-plastic creep boundary, whereas the “plastic creep limit” defines the plastic creep-incremental collapse boundary. According to the European Standard (2004), the stress level corresponding to a permanent strain value of 4.5×10^{-5} accumulated from 3,000 to 5,000 load applications is practically defined as the plastic shakedown limit, and the stress level corresponding to an accumulated permanent strain of 4×10^{-4} practically defines the plastic creep limit. For an adequately designed pavement section,

incremental collapse (Range C) type permanent deformation is expected to rarely occur; instead, either plastic shakedown or plastic creep behavior prevails throughout the intended service life.

From the laboratory RLT permanent deformation curves of unbound granular materials tested, it is possible to evaluate for any confining pressure the axial stresses generating permanent strains close to the shakedown limits. Then, all possible combinations of confining and axial stresses (σ_1 , σ_3) that cause the investigated shakedown limit conditions can be identified, followed by plotting those stress combinations on a plane axial stress (σ_1) versus stress ratio (σ_1/σ_3) to evidence the boundary envelopes between the three possible permanent deformation responses. To determine the relatively linear slope of the secondary stage of the permanent deformation curve, the RLT test data is fit to the analytical models in Table 2.2, such as plotting the accumulated permanent strain versus the number of load applications (N) on a log-log scale. Noticeable is the model proposed by Perez and Gallego (2010) that fits the permanent strain data by using a combination of power law and exponential models. Five fitting coefficients are obtained with one of them representing the linear slope of the secondary stage. It has been proved that this model offers not only an excellent description of the material behavior in Range B (plastic creep) and Range C (incremental collapse) but also unbiased predictions, as contrary to the classic power law model and the Francken model which tend to underestimate and overestimate the measured permanent strain, respectively (Perez et al., 2010).

Rushing and Little (2013) reported that the rate of increase in permanent strain (i.e., the slope of the secondary flow region) determined from triaxial static creep testing provided the strongest correlation to Asphalt Pavement Analyzer (APA) simulated traffic rutting and thus produced a reasonable indication of asphalt mixture rutting resistance. As pointed out by Wichtmann (2005), it is also possible to add into the rutting accumulation model a scalar variable

for a phenomenological description of the important stress history (or cyclic preloading) effects, which is expected to weight the number of load applications with corresponding permanent strain amplitude.

Besides laboratory RLT tests, the shakedown theory has recently been found valid for field APT test sections and real roads. Raad and Minassian (2005) determined the relative influence of granular base characteristics on upper bound shakedown limit of pavement structures through a matrix of numerical runs. Tao et al. (2010) explained different shakedown responses of traditional and recycled pavement base materials obtained from both laboratory RLT and full-scale APT tests based on the dissipated energy concept. It was implied that permanent deformation characteristics of pavement materials provided a better measure for evaluating recycled and marginal materials against traditional unbound aggregates. Chen et al. (2013) examined the shakedown behavior of geogrid-reinforced unbound granular materials based on multi-stage RLT test results. In the project sponsored by Nordic countries, the field performance including rutting of eight 10-20 year old LTPP roads were monitored to validate pavement performance models for use in the design of new roads (NordFoU, 2010). Important findings from this project include that the shape of the rutting growth on real roads is the same as the shape of the deformations seen in the triaxial testing, indicating the validity of the shakedown theory for real roads. The trend of permanent deformation accumulation of the reported NAPTF full-scale testing granular base/subbase layers, as stress history built up and/or stress levels increased, became more of a linear type (Kim, 2005), similar to experimental findings by El abd et al. (2004).

2.6.4 Stress Path Loading Effects

In-situ pavement stresses in unbound granular layers are mainly composed of two parts, i.e., initial static stresses and dynamic stresses due to moving wheel loads. The initial stresses, static in nature, are the overburden and compaction-induced residual stresses. The initial stresses are typically lower at shallow depths than at greater depths. Compaction-induced residual stresses that are compressive in nature can often exist in the unbound aggregate layers and contribute to the static stress states (Uzan, 1985; Barksdale et al., 1997). On the other hand, traffic loading due to moving wheel loads induces much higher dynamic stresses than the static ones. Therefore, a pavement element constantly experiences a combination of varying magnitudes of static and dynamic stresses depending on the depth in the pavement layer and the radial offset from the wheel load. The principal stress rotation and the constantly rotating fields of stresses under moving wheel loads have been observed from field measurements. In the case of aggregate bases, the cyclic component of load imposes a change (increment) of stress state which is not co-axial with the stress state under the static (overburden) load (Kim, 2005). The major principal stress due to overburden is always aligned in the vertical direction regardless of the location of a moving wheel. The incremental stresses imposed by a wheel load, however, are not co-axial with this system, and as a result, the total principal stresses rotate as the wheel load passes. Principal stress rotation may cause different resilient behavior and increased rates of shear and volumetric strains during cyclic loading relative to equivalent stress paths without stress rotation (Kim and Tutumluer, 2005; Grabe and Clayton, 2013).

Among different test procedures proposed to mimic such moving wheel load effects is the stress path loading concept, which is represented by the stress path slope (m) and stress path length (L) as illustrated on a deviator stress q vs. mean normal pressure p diagram in Figure 2.10. Static overburden stresses correspond to q_{\min} and p_{\min} , whereas dynamic traffic load reaches up

to q_{\max} and p_{\max} following a constant stress path slope m . Note that the initial overburden stress state in the field often corresponds to the K_0 (horizontal stress divided by the vertical) conditions, i.e., $q_{\min}/p_{\min}=3(1-K_0)/(1+2k_0)$. According to plasticity theory of soil mechanics, the mean normal pressure p influences volume change behavior, while the deviator stress component q affects shear behavior for shape change and distortion. In general, the stress path slope (m) for the standard constant confining pressure (CCP) tests, such as AASHTO T307-99, takes a constant value of 3.0. In the variable confining pressure tests performed by Kim and Tutumluer (2005), both vertical and horizontal stresses are pulsed at different magnitudes to more realistically simulate conditions due to moving wheel loads with the stress slope varied from -1.5 to 3. Permanent deformation models were developed accordingly for such CCP and VCP stress states (Kim, 2005). A common misunderstanding regarding CCP and VCP tests is that they deliver similar irrecoverable and resilient strains if the average stress is the same. Rondon et al. (2009) systematically compared cyclic triaxial behavior of unbound granular material under CCP and VCP conditions. They concluded that both types of test deliver similar permanent axial or volumetric strains only for some special stress paths, while the CCP test may underestimate the permanent axial strain for some other stress paths as compared to the corresponding VCP tests.

Note that when dynamic loading is applied in both vertical and radial directions (i.e., VCP tests), the following Equation 2.46 derived from axisymmetric stress-strain relations can be solved simultaneously for the isotropic aggregate properties: resilient modulus M_R and Poisson's ratio ν (Seyhan and Tutumluer, 2002). Previous studies demonstrate that the loading path only has minor influence on the shear strength of unbound aggregates, despite of the significant effect on the deformation behavior (Xu et al., 2012). Therefore, strength parameters obtained from conventional triaxial tests with constant confining pressures would be sufficient for pavement

analysis, as far as only shear strength is concerned. However, a realistic assessment of permanent deformation or rutting accumulation requires a better understanding of the stress-strain behavior along representative loading paths by laboratory testing, as well as developing suitable numerical models capable of simulating the observed stress-path-dependent behavior.

$$\begin{aligned}\varepsilon_1 &= \frac{1}{M_R} [\sigma_{1d} - 2\nu\sigma_{3d}] \\ \varepsilon_3 &= \frac{1}{M_R} [\sigma_{3d}(1-\nu) - \nu\sigma_{1d}]\end{aligned}\tag{2.46}$$

where ε_1 and ε_3 are resilient strains recorded in the vertical and radial directions, respectively; and σ_{1d} and σ_{3d} are the dynamic stresses pulsed during VCP tests in the vertical and radial directions, respectively.

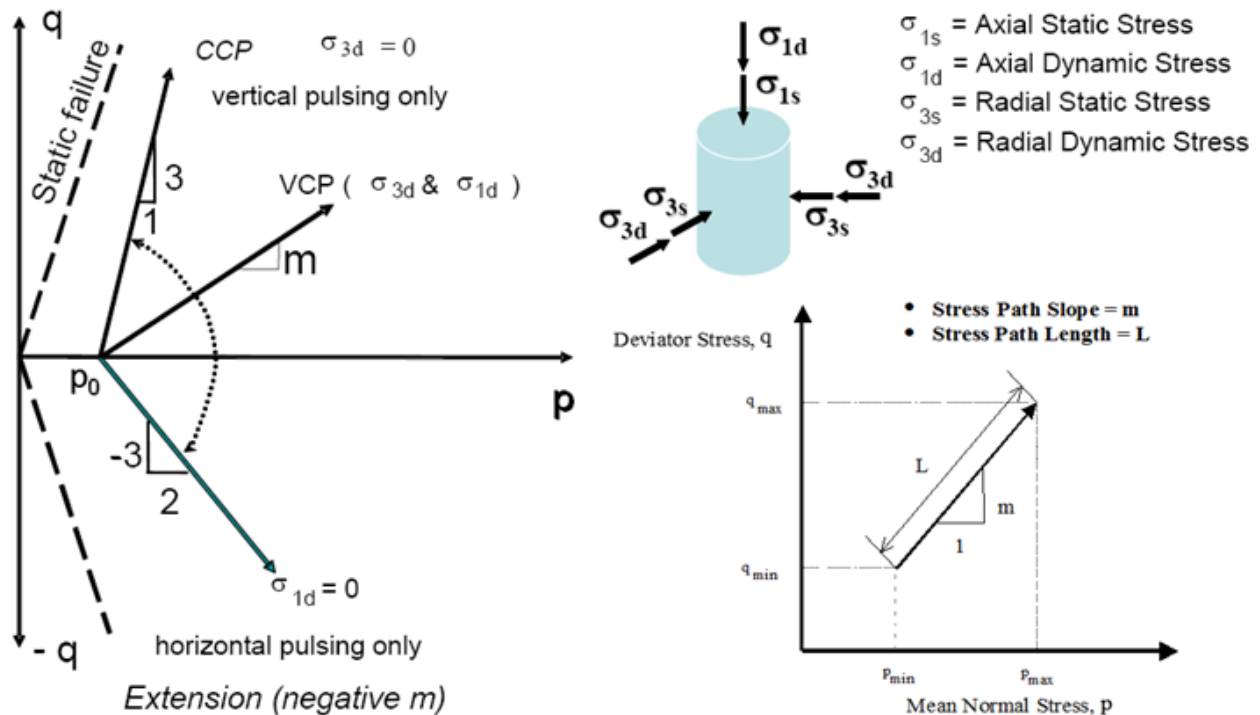


Figure 2.10 Schematic Representation of Stress Path Loading (Tutumluer, 2013)

2.6.5 Importance of Shear Strength in Controlling Rutting Accumulation

Known trends of the traditional low quality unbound granular materials indicate that lower shear strength of the material is generally associated with a higher permanent deformation potential in the field; on the other hand, a properly compacted good quality aggregate base/subbase can adequately prevent settlement and any lateral movement in the layer through high shearing resistance and dissipating effectively wheel load stresses (Garg and Thompson, 1997). The NCHRP 4-23 study identified shear strength as one of the most significant mechanistic properties influencing pavement performance (Saeed et al., 2001). A research project on VTT in Finland also reported that the shear stress level in the road structure is the predominant reason for permanent deformations in unbound granular material (Korkiala-Tanttu, 2008). Further, shear strength property rather than “resilient modulus” has been always shown to better correlate with unbound aggregate permanent deformation behavior for predicting field rutting performance (Thompson, 1998; Tao et al., 2010; Xiao et al., 2012). Despite its long-realized role in controlling field rutting development, shear strength is still absent from the majority of the rutting prediction models, such as the one used in the MEPDG or AASHTO’s Pavement ME software.

As presented previously, multi-axial stress state is commonly experienced in unbound granular layers that are known to be incapable of taking tensile stresses. The stress state with the greatest failure potential depends on a combination of normal and shear stresses and does not necessarily occur at the location of maximum shear stress. The closeness of the stress state to the failure envelope can be described by the shear stress ratio (SSR), which in essence is the actual shear stress divided by the maximum (failure) shear stress at the same normal stress. At any applied stress state, a SSR value is believed to give a certain fraction of the shear strength of the material that is acting on the failure plane due to the applied total stresses. The lower the SSR is

kept, the less likely the material would fail in a bearing capacity or shear type failure. A SSR value below 100 percent literally means that the material does not fail upon shearing. As illustrated in Figure 2.11 and formulated in Equation 2.47, two similar SSR definitions are commonly used in practice to evaluate the rutting potential and corresponding shear strength requirements of base/subbase layers: applied shear stress to shear strength (τ_f/τ_{max}) in the σ - τ Diagram; and alternatively, applied deviator stress (q) to maximum deviator stress at failure ($q/q_{failure}$) in the p - q diagram. Note that both definitions are based on the Mohr-Coulomb failure criteria for unbound granular materials.

$$\begin{aligned}
 SSR &= \frac{\tau_f}{\tau_{max}} = \frac{\sqrt{(\sigma_d/2)^2 - (\sigma_f - (\sigma_3 + \sigma_d/2))^2}}{c + \sigma_f \tan \phi} \\
 \sigma_f &= \frac{2\sigma_3 + 2\tan^2 \phi \sigma_3 + \sigma_d + \tan^2 \phi \sigma_d - \sqrt{\tan^2 \phi \sigma_d^2 + \tan^4 \phi \sigma_d^2}}{2(1 + \tan^2 \phi)} \quad (2.47) \\
 q_{ratio} &= \frac{q}{q_{failure}} = \frac{\sigma_d \tan \phi (3 - \sin \phi)}{6c \sin \phi + 2 \sin \phi \tan \phi (3\sigma_3 + \sigma_d)} \quad (\text{triaxial compression})
 \end{aligned}$$

where τ_f and τ_{max} denote the shear stress acting on the potential failure plane and the maximum allowable shear stress at failure, respectively; σ_d and q represent the deviator stress in the triaxial stress space, i.e., the difference between axial and radial stresses; σ_1 and σ_3 are major and minor principal stresses, respectively; and c and ϕ are shear strength parameters representing internal cohesion and friction angle, respectively.

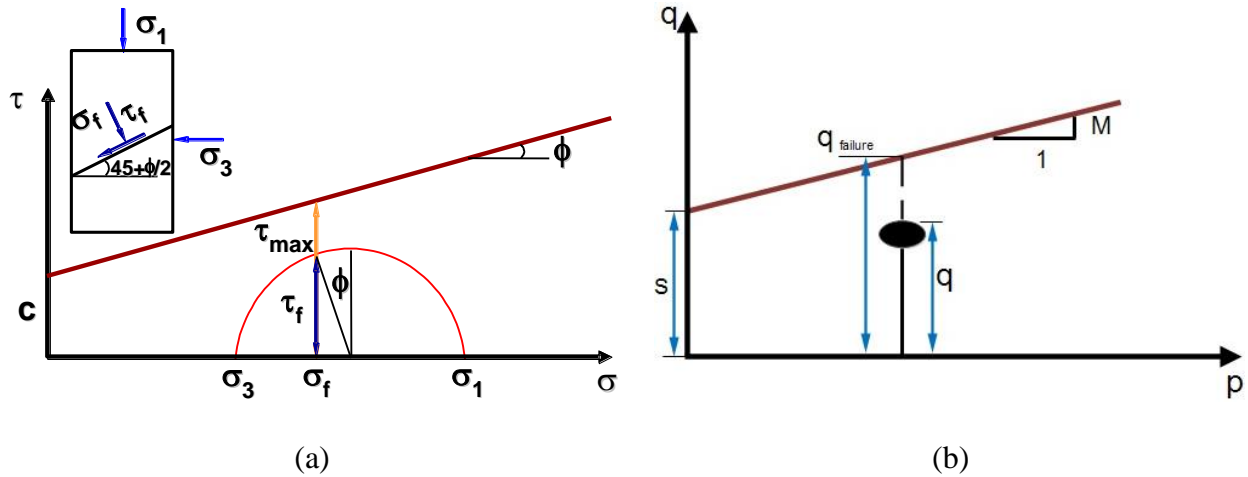


Figure 2.11 Representation of Mohr-Coulomb Failure Envelope in (a) σ - τ Diagram and (b) p - q Diagram

Seyhan and Tutumluer (2002) reported the strong linkage between the SSR (τ_f/τ_{max}) and the anisotropic modular ratios established as aggregate performance indicators during their study on the loading related dependency of granular material properties. They concluded that the SSR is not only an indicator of unbound aggregate performance under varying stress states, but also determines the maximum allowable working stress to control the permanent deformation of an unbound aggregate layer. The decreasing anisotropic moduli ratios typically indicate a stress-softening behavior caused by increasing applied stress states or SSR values, and “good” quality aggregates typically have low SSR values in the range of 0.2 to 0.5 (Seyhan and Tutumluer, 2002). Recently, Hashem and Zapata (2013) proved the shear stress/strength ratio to be a better predictor than the resilient modulus when enhancing the MPEDG rutting model for unbound materials. According to classical linear Mohr-Coulomb theory, shear strength can be characterized by cohesion intercept c and friction angle ϕ from monotonic triaxial compression tests conducted at different confinement levels, which are much less time consuming and easier to conduct than complex and tedious laboratory permanent deformation tests.

Instead of implementing more complex plasticity theory based models, the shear stress ratios as formulated in Equation 2.47 are explored subsequently in this study for their potential use in predicting the rutting accumulation of unbound aggregates under the application of moving wheel loads, provided that the shear properties of granular materials are available, i.e., the angle of internal friction ϕ and the cohesion c . If no strength properties are measured from RLT tests, the empirical equations similar to the one developed by Huurman and Molenaar (2006) can be used to predict the strength parameters of unbound granular materials from gradation, compaction quality index, and other common material properties.

2.7 Numerical Simulation of Unbound Aggregate Materials

Constitutive relationships often need to be developed to properly describe permanent deformation accumulation in unbound granular materials with number of load applications. In this section, a summary is given of the different models proposed by many researchers to predict permanent strain as a function of load and material property related factors.

2.7.1 Continuum-based Finite Element (FE) Modeling

Granular pavement foundation material is a nonlinear elasto-plastic material and shows nonlinear behavior starting from small strains. Traditional continuum-based finite element models have been developed to mimic such nonlinear response of granular materials to variations in confining pressure, grain size, density, and microscopic properties, etc., as observed from much experimental work.

Developed at Georgia Institute of Technology in 1996, the nonlinear finite element program GT-PAVE uses isoparametric eight-node quadrilateral elements to analyze a flexible pavement as an axisymmetric solid consisting of either linear or nonlinear elastic layers with an optional cross-anisotropic characterization of the granular layers (Tutumluer, 1996). For the

analyses of conventional flexible pavements, predicted responses by the axisymmetric GT-PAVE FE program have been validated in several instances in the past with measured data from instrumented full-scale pavement sections as well as verified with similar computed responses by the commercial ABAQUSTM FE program (Tutumluer, 1996; Kim, 2007).

Gudehus and Nubel (2004) emphasized on the fact that the angularity of the grains will control to some extent the polar friction which will affect the rotational resistance of the grains, as supported by Oda and Iwashita (1999). Vardoulakis and Sulem (1995) emphasized that the surface roughness affects the inter-particle slipping in granular materials. Therefore, the angle of internal friction and dilation angle are highly affected. Huang et al. (2002) attempted to bring the surface roughness and shape of the grains into a hypo-plastic numerical model to study their effect on the strain localization in granular materials. Despite the fact that they have put solid theoretical efforts in their work, these theories lack linkages between the theoretical parameters and physical quantities.

Alsaleh et al. (2006) employed Cosserat continuum as the foundation of the mathematical formulations of the numerical model in their paper. The Cosserat theory can successfully separate grains rotation from their translation by adding three additional degrees of freedom to any point in the 3-D continuum. Primarily, the Cosserat continuum requires two internal length scales: the length of contact between particles and the arm of rotation (Alsaleh et al., 2004). The length or the size of the contact surface will influence the couple stress value and the arm of rotation will influence the curvature of the rotation. It is believed that these quantities highly depend on the size and the shape of the particles as well as the density and the confining pressure applied at those particles. Since it is not easy to quantify it, most of the published research considers the mean particle size to present those two length scales. Looking at particles at the

micro scale, one might consider the particle size distribution, the surface roughness distribution, and the shape indices distribution to account for the internal length scales (Alshibli and Alsaleh, 2004). However, the present constitutive relations do not allow incorporating such parameters explicitly. Alsaleh et al. (2006) proposed to incorporate the effects of such parameters via their heterogeneous distributions at the finite-element level and the method seems to work properly. Based on a parametric study performed on large number of particles with different shapes, Alsaleh (2004) assumed that the surface roughness is assumed to contribute to the arm of rotation curvature and the angular moment of inertia; whereas the shape indices will affect the length of the contact surface, the angular moment of inertia, and the arm of rotation as well.

2.7.2 Discrete Element Method (DEM) Modeling

The discrete element method (DEM) modeling approach has recently been demonstrated to have the potential of being used effectively to identify differences in current aggregate specifications in terms of drainage and structural support and provide insight into optimizing foundation layer aggregate gradation for improved pavement performance. Hill et al. (2012) presented a framework for a unified approach for modeling several laboratory tests used for the characterization of unbound materials for pavement applications, including the California bearing ratio (CBR) test, the dynamic cone penetrometer (DCP) test, and the resilient modulus test (see Figure 2.12). Although some limitations still exist, this proposed methodology is shown to be promising for developing mechanistic-based correlation between test results.

Buechler et al. (2012) investigated the relationships between soil properties and the mechanical responses for both plate (simulated LWD) and drum-roller loading. It was shown that purely cohesionless granular soils exhibited substantially different stress and strain fields

compared to cohesive soils. The ability of DEM to accurately model macro-scale features from variable microstructure and interactions was demonstrated.

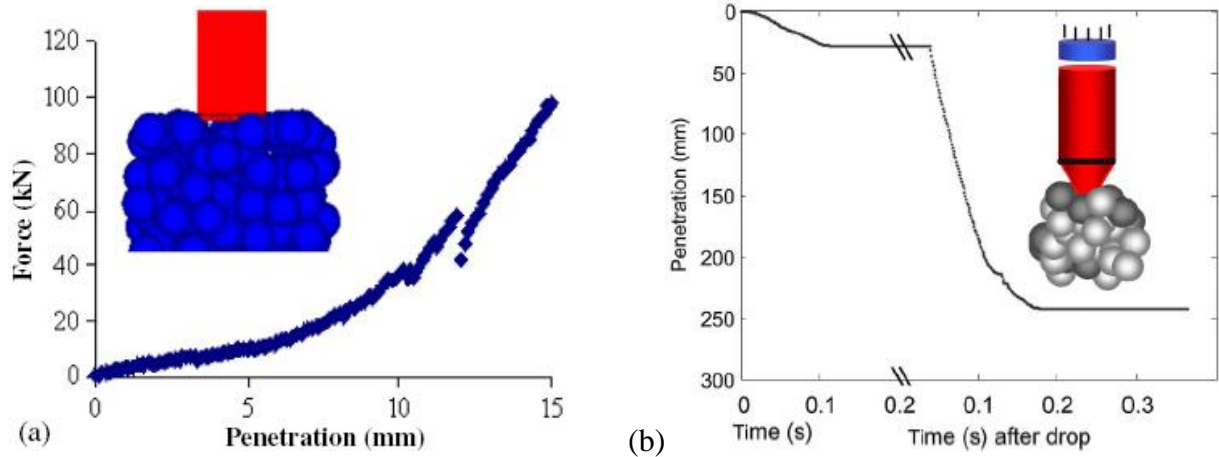


Figure 2.12 DEM Simulation for (a) CBR and (b) DCP Tests (Hill et al., 2012)

The potential of using DEM simulations for representing granular material behavior during shear via the triaxial compression and other lab tests has been demonstrated by extensive studies. Lin and Ng (1997) used 3D discrete elements to model drained triaxial tests with cubic periodic cells and ellipsoidal particles with a focus on the effect of particle shapes on shear strength development. Liu performed 2D DEM simulations of direct shear box test on dense and loose samples of circular particles. The realistic particle shape modeling, which was absent in previous studies, is however considered to be critical for enhancing the quality of numerical simulation results.

BLOKS3D, used later in this study, is a DEM program that is capable of modeling 3-dimensional polyhedral particles as granular assemblies (Zhao et al., 2006; Tutumluer et al., 2009). Ghaboussi and Barbosa (1989) established the fundamental principles and developed the original code for BLOKS3D program. Nezami (2004) and Zhao (2006) later on modified this

program significantly and established new contact detection algorithms, which considerably improved the speed of DEM simulations. These contact detection algorithms were named as the fast common plane (Hashash et al., 2007) and the shortest link methods (Zhao et al., 2006). Moreover, Huang (2010) developed a method to create particle shape libraries for BLOKS3D program using aggregate particle images with their morphological properties F&E ratio, AI, and STI quantified using the UIAIA. These particle libraries can be combined in DEM simulations to achieve target average AI and F&E ratio morphological properties within a granular ballast assembly.

2.8 Summary

This chapter reviewed important aggregate physical properties governing granular layer strength, modulus and permanent deformation characteristics. Commonly used laboratory tests and constitutive models to characterize the elastic (or resilient) and plastic (permanent) deformation trends of unbound aggregate materials were discussed next with a review of typical pavement stress states and initial loading conditions related to aggregate repeated load behavior. Both empirical and mechanistic methods developed for classifying aggregate materials were summarized with historical perspective by listing their advantages and limitations.

Chapter 3 Research Approach and Databases

This chapter presents all the databases (both laboratory and field) from which field pavement performance and laboratory tested mechanistic analysis inputs (i.e., strength, permanent deformation, and M_R data along with corresponding aggregate index properties) were collected for unbound aggregate pavement base/subbase materials. The primary data source for this study is the existing laboratory and/or in situ test data for Minnesota's aggregates that were obtained from related research studies performed for/by Minnesota Department of Transportation (MnDOT) (Xiao and Tutumluer, 2012). In addition, as part of a comprehensive literature search, strength, permanent deformation and resilient modulus (M_R) data were also collected from many relevant research studies completed for the last two decades at the University of Illinois Advanced Transportation Research and Engineering Laboratory (ATREL).

3.1 University of Illinois Aggregate Modulus and Strength Databases

3.1.1 NCHRP 4-23 Research Project Database

As part of the NCHRP 4-23 Phase II laboratory testing program, UI-FastCell testing was undertaken to determine directional dependency (anisotropy) of M_R at various stress states and then to correlate anisotropic modular ratios to the quality and strength properties of the aggregate (Seyhan and Tutumluer, 2002). Twelve aggregates with varying material types and properties were selected for MR testing using the UI-FastCell. In the selection process, consideration was given to both good and poor performing granular base/subbase materials obtained from seven different states. A realistic range of aggregate qualities and properties, such as average and top sizes, gradations (both uniform and well-graded samples), particle shapes (rounded gravel to angular crushed stone), and fines contents, i.e., materials less than 0.075 mm (No. 200 sieve)

size, were represented. The top aggregate sizes vary from 25-mm (1-in.) to 51-mm (2-in.). There is a considerable variation in the fines content values ranging from less than 1% to 17.9%. The variations among the aggregate types and properties were considered essential for studying the effects of material properties on the anisotropic resilient behavior under the application of vertical and radial pulse loadings.

The maximum dry densities and the optimum moisture contents are for modified Proctor tests (AASHTO T-180). The static strength properties were obtained from standard triaxial tests (ASTM D 2850) conducted at confining pressures of 35, 69, and 104 kPa (5, 10, 15 psi) on samples compacted at optimum moisture states. Cylindrical specimens, 150 mm in diameter by 150 mm high (approximately 6-in. in diameter by 6-in. high), were prepared to fit in the confinement chamber of the UI-FastCell for the repeated load triaxial testing. A total of 46 specimens, four samples for each aggregate were prepared using a pneumatic vibratory compactor. For each material, samples were prepared at two moisture contents: (i) optimum moisture content corresponding to maximum dry density and (ii) wet of optimum moisture content near saturation. The achieved dry densities at optimum moisture contents match closely with the maximum Proctor densities. For the wet of optimum tests, minimum moisture contents that provided at least 90% saturation were typically achieved.

3.1.2 Federal Aviation Administration (FAA) Granular Base/Subbase Material Study Database

Two crushed aggregate materials, specified herein as the P209 granular base and P154 subbase materials, were tested for permanent deformation trends in the laboratory to study effects of moving wheel loads and the degree of compaction. The P209 material was a crushed limestone and the P154 material consisted of manufactured screenings specified by FAA's Advisory Circular 150/5370-10B. The P209 aggregate material was classified as A-1-a according

to AASHTO procedure and as GP-GM (poorly graded gravel with silt) according to ASTM procedure; whereas the P154 aggregate material was classified as A-1-b according to AASHTO procedure and as SW-SM (well graded sand with silt) according to ASTM procedure. The National Airfield Pavement Testing Facility (NAPTF) P209 had a maximum size of 50-mm (2-in) and 6.7 % fines content, whereas the NAPTF P154 had a maximum size of 12.5-mm (0.5-in) and 10% fines content. The P209 has much less amount of fines fraction than the P154. The mean particle sizes for the NAPTF P209 and P154 were 8-mm and 1.7-mm, respectively.

The dry densities and moisture contents for the NAPTF P209 and P154 aggregates were determined following the procedure of the modified Proctor (AASHTO T180) test. The standard AASHTO T307-99 modulus test procedures were followed for NAPTF P209 and P154, respectively. Rapid shear tests were conducted at 35, 69, and 104 kPa (5, 10, and 15 psi) confining pressures. The NAPTF P209 aggregate had a friction angle of 61.7° with a cohesion intercept of 132 kPa and the NAPTF P154 material had a friction angle of 44° with a cohesion intercept of 182 kPa. Material properties, stress path RLT permanent deformation test programs, and corresponding laboratory test results for this study were detailed elsewhere (Kim, 2005).

Both constant confining pressure (CCP) and variable confining pressure (VCP) tests were performed using an advanced repeated load triaxial testing device named UI-FastCell to clearly account for the effects of variable stress states, including stress ratio, stress magnitude, and stress path loading slope (representing rotating principal stress directions) on permanent deformation accumulation for the FAA P209 and P154 aggregate materials. As reviewed previously in Chapter 2, in the CCP tests, vertical wheel load stresses were repeatedly applied on laboratory specimens to adequately simulate the conditions realized directly under the wheel. In contrary to the CCP tests, the variable confining pressure (VCP) tests were performed by subjecting the

specimens to various constant stress path loadings realized under actual traffic. Specifically, two dynamic stresses of prescribed magnitudes were pulsed simultaneously in both horizontal and vertical directions, in addition to the applied constant hydrostatic confining stress. Different combinations of the stress path slope (m) and its length (L) were therefore applied to simulate the various dynamic loading conditions experienced under the moving wheels.

3.1.3 Illinois Center for Transportation R27-1 Research Project Database

The research focus of this study was on the characteristics and performances of dense graded structural layers for constructing aggregate working platforms over soft subgrades. A comprehensive experimental test matrix was developed for the three most commonly used aggregate types in Illinois: uncrushed gravel (denoted as G), limestone (L), and dolomite (Do). The primary objective was to establish ranges for major aggregate properties that primarily influence strength, modulus, and deformation behavior of unbound aggregate layers in any pavement system. These major physical properties studied include: fines content, Plasticity Index (PI) of fines, particle shape (flatness and elongation), angularity and surface texture, and moisture content and dry density (compaction) properties. The detailed laboratory test matrix, mechanistic property test programs, material properties, and complete test results can be found elsewhere (Tutumluer et al., 2009).

In brief, for studying the effect of fines on aggregate behavior, laboratory specimens with four different target fines contents, i.e., 0%, 4%, 8% and 12% material passing No. 200 sieve, were fabricated and tested. To study the effect of type of fines on aggregate behavior, two different types of fines were used: one was non-plastic in nature such as mineral filler type (PI=0), and the other was plastic such as cohesive fine-grained soil type (PI in the range of 10-12). The effect of moisture content on aggregate performance was also studied by testing the

blended aggregate specimens at three different moisture contents: optimum moisture content (w_{opt}), 90 percent of w_{opt} , and 110 percent of w_{opt} , whereas the w_{opt} was established through the standard Proctor (AASHTO T-99) test for each aggregate gradation. Therefore, the laboratory test matrix was a 4x2x3 factorial (4 different fines contents, 2 different types of fines, 3 different moisture contents) for each one of the three different aggregate types (Tutumluer et al., 2009).

Resilient modulus and permanent deformation tests were performed on specimens according to AASHTO T307-99, i.e., the specimens were first conditioned for 1,000 load cycles to characterize their permanent deformation behavior at an applied stress state of 15-psi deviator stress and 15-psi confining pressure. Then, resilient modulus tests were conducted at the 15 AASHTO T307 stress states. Three different samples were tested at confining pressures of 5, 10, and 15 psi to determine the shear strength properties, friction angle and cohesion, of the aggregate materials from rapid shear tests. Note that the permanent deformation test data analyzed subsequently in this Chapter were recorded from the condition stage. Rapid shear triaxial strength tests were also conducted on the aggregate samples to determine shear strength properties. Detailed laboratory test results can be found elsewhere (Tutumluer et al., 2009; Mishra, 2012).

3.1.4 Geogrid Aggregate Base Reinforcement Database

3.1.4.1 Materials Tested

Recently, under the partnership with a lead geogrid producer, a total of six aggregate samples were received at the University of Illinois Advanced Transportation Research and Engineering Laboratory (ATREL) for imaging based shape analysis using the University of Illinois Aggregate Image Analyzer (UIAIA). The objective of the whole laboratory test program was to evaluate the relationship between aggregate physical properties (i.e., angularity index and

surface texture) and laboratory based resilient modulus, shear strength and permanent deformation characteristics. Those aggregate samples ranging from uncrushed to crushed ones were collected from various field construction sites and tested in the laboratory for physical and mechanical property characterization. Table 3.1 summarizes the aggregate types, sources and moisture-density properties used in the test program.

Table 3.1 Aggregate Material Types, Sources and Moisture-Density Properties Used in Geogrid-Reinforced Applications

Sample Number	Classification	Source	Maximum Dry Density (pcf)	Optimum Moisture Content (%)
1	Crushed Limestone	Kentucky	141.8	6.5
2	DGA1	Kentucky	146.0	7.0
3	Salvage Base	North Dakota	136.3	7.8
4	Crushed Miscellaneous	California	127.4	9.3
5	-	USACOE	148.9	4.3
6	Crushed Gravel	Utah	136.9	6.8

Notes: (1) 1 pcf = 16.02 kg/m³; (2) AASHTO T-99 procedure was followed for compaction.

3.1.4.2 Experimental Program

For the aggregate samples used in geogrid reinforced applications, the resilient modulus and repeated load triaxial tests were performed on cylindrical samples first air-dried and then moisture-conditioned in the laboratory to achieve the optimum moisture content. Samples were prepared using moderate compaction energy (20-blow modified Proctor hammer) to achieve a 150-mm diameter by 300-mm tall cylindrical test specimen at the targeted density level. Two 5-

gallon buckets of each aggregate sample were received during the year of 2010. Each bucket received was spread onto plastic tarps on the floor and allowed to air-dry overnight. Once air-dried, the material was split and quartered, thus four specimens of representative composition were produced for subsequent testing.

All the aggregate samples were scanned for particle morphological/shape indices which include the flat and elongated (F&E) ratio, angularity index (AI), and surface texture (ST) index. An enhanced, second generation University of Illinois Aggregate Image Analyzer (UIAIA) with color image thresholding scheme was used to determine morphological indices, such as angularity index, AI (Rao et al., 2002) and surface texture index, ST (Rao et al., 2003) of the aggregate samples used in the test program. The UIAIA uses 3 orthogonally positioned cameras to capture 3 dimensional shape properties. The AI and ST indices are determined based on the particle image outlines obtained from each of the top, side and front views. Table 3.2 and Table 3.3 list the average aggregate shape indices quantified for aggregate samples used in geogrid reinforcement applications and the ICT studies, respectively.

Table 3.2 Average Aggregate Shape and Surface Texture Indices for Aggregate Samples Used in Geogrid Reinforcement Applications

Sample Number	Angularity Index (AI)	Surface Texture Index (ST)	Flat & Elongated Ratio (by Weight)
1	380	1.3	2.7
2	460	2.2	2.7
3	328	0.9	2.1
4	434	1.5	2.1
5	462	2.5	2.4
6	372	0.5	2.1

Table 3.3 Average Aggregate Shape and Surface Texture Indices (Mishra, 2012)

Aggregate Type	Angularity Index (AI)		Surface Texture Index (ST)		Flat & Elongated Ratio (by Weight)
	Measured Value	Typical Range*	Measured Value	Typical Range	Measured Value
Crushed Limestone	481	400 - 500	1.8	1.2-1.8	2.5
Crushed Dolomite	428	N/A**	1.3	N/A	3.3
Uncrushed Gravel	330	250 - 350	1.0	0.5-1.2	1.9

Notes: * Typical values identified from 39 different coarse aggregate materials in a pool fund study; ** N/A = data not available.

3.2 MnDOT Laboratory Aggregate Databases

In this research study, the results of a variety of aggregate index property and resilient modulus tests conducted by the MnDOT Office of Materials and/or its contracting agencies on different Minnesota project materials were collected and evaluated (Gupta et al., 2007; Xiao and Tutumluer, 2012). Two resultant databases, one for the MEPDG M_R constitutive model parameters k_1 , k_2 and k_3 and the other one for corresponding aggregate source properties, were created and used in the subsequent statistical correlation studies. Each of these two databases contains a total of 376 effective aggregate specimens after eliminating samples with incomplete information such as missing gradation or index properties. The majority of the tested materials are “standard” or traditional unbound aggregate base and subbase materials of Classes ranging from 3, 4, 5 to 6 according to the MnDOT classification, and no reclaimed/salvaged materials were included in the resilient modulus database provided by MnDOT. The MnDOT specified

gradation bands for each individual aggregate classes are shown in Figure 3.1. Note that no crushed/fractured particles are allowed for Class 3 or 4. Class 5 requires at least 10% crushed particles, whereas Class 6 requires at least 15% crushed particles.

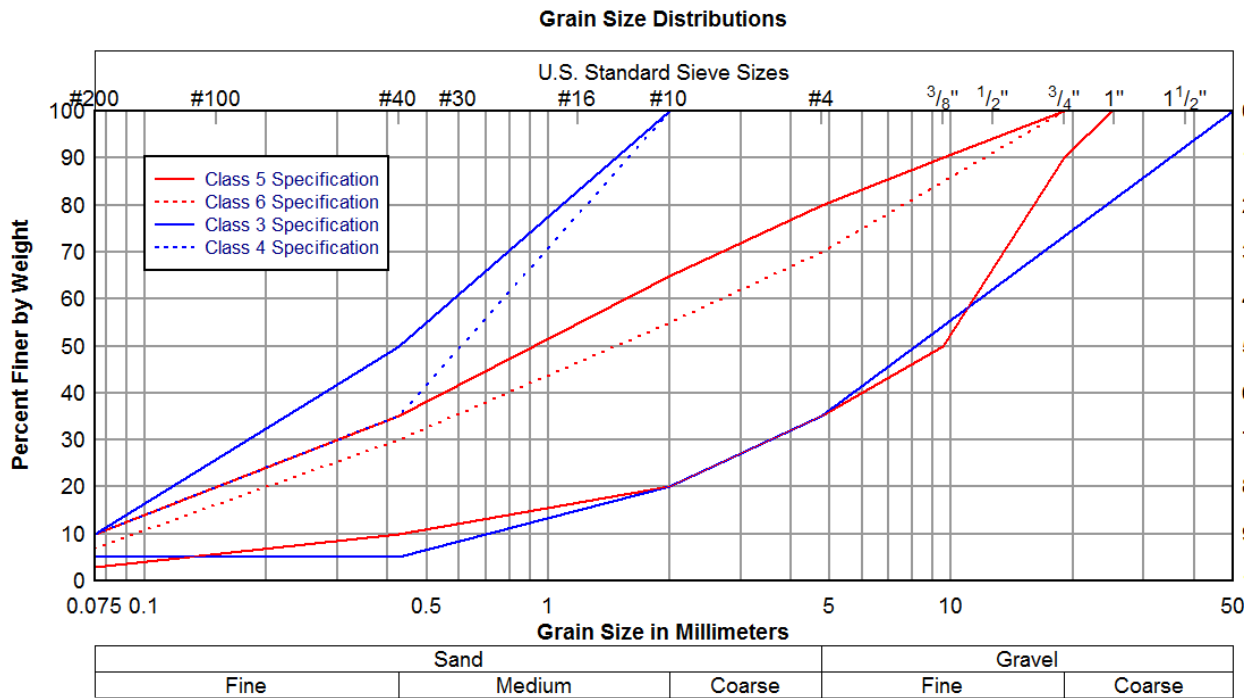


Figure 3.1 MnDOT Specified Gradation Bands for Different Aggregate Classes

3.2.1 Materials Tested

The database provided by MnDOT includes various types of aggregates ranging from “standard” gravel (pit-run), limestone, granite and select granular materials to “non-standard” taconite tailings (a waste mining material), reclaimed asphalt pavement (RAP) and reclaimed concrete aggregates (RCA) blended with virgin aggregates at different blending ratios, and materials recovered from full-depth reclamation (FDR) sites. All the materials were collected from road construction sites in Minnesota for testing at the MnDOT Office of Materials and

Road Research laboratories and/or MnDOT's contracting agencies/universities using consistent quality control procedures. Collected from this database, the results of a variety of aggregate index property and resilient modulus tests conducted were evaluated. Two resultant databases, one for the MEPDG M_R constitutive model parameters k_1 , k_2 and k_3 and the other one for corresponding aggregate source properties, were created and used in the subsequent statistical correlation studies. Each of these two databases contains a total of 376 effective aggregate specimens after eliminating samples with incomplete information such as missing gradation or index properties. The majority of the tested materials are "standard" or traditional unbound aggregate base and subbase materials of Classes ranging from 3, 4, 5 to 6 according to the MnDOT classification, and no reclaimed/salvaged materials were included in the resilient modulus database provided by MnDOT due to the scope of this study.

3.2.2 Experimental Program

Resilient modulus test data include the following load-time history information recorded for each load sequence: confining pressures, deviator stresses, and resilient strain and resilient deformation values. The laboratory M_R tests were conducted according to the NCHRP 1-28A protocol (Dai and Zollars, 2002). The load sequences start with 1,000 cycles of 207 kPa (30 psi) deviator stress at 103.5 kPa (15 psi) confining pressure for conditioning the specimen before M_R data collection and continue with cycles repeated 100 times for 30 loading sequences with different combinations of confining pressures and deviator stresses. The M_R is then calculated from recoverable axial strain and cyclic axial stress values from the last five cycles of each sequence. The moisture content of the specimens was within $\pm 0.5\%$ from the target moisture content. The vibratory hammer or gyratory compactor was used for compacting specimens to the target dry densities. Not all the tests were carried out at the optimum moisture content. Detailed

information about laboratory measured aggregate index properties includes AASHTO classification, MnDOT classification, material type, optimum moisture content, maximum dry density, actual sample moisture content, actual sample density, compaction method, gradation (i.e., percentages of materials passing specified sieves), silt content, clay content, liquid limit, plastic limit, and plasticity index.

Considering the well-recognized significant effects that coarse aggregate morphology, i.e., flat and elongation ratio, angularity, and surface texture, have on the strength and resilient and permanent strain behavior of unbound aggregate materials (Pan et al., 2005; Pan et al., 2006; Tutumluer and Pan, 2008), twelve representative MnDOT aggregate resilient modulus (M_R) test samples were shipped to the University of Illinois Advanced Transportation Research and Engineering Laboratory (ATREL) for imaging based shape analysis using the University of Illinois Aggregate Image Analyzer (UIAIA). Identified and recommended by the NCHRP 4-30A project among the most promising aggregate imaging systems to provide an automated means to determine coarse aggregate size and shape properties, the UIAIA system can take images of an individual aggregate particle from three orthogonal views, which has been very effective in reconstructing three-dimensional (3-D) particle shape and computing accurately the volume and size and shape indices (Tutumluer et al., 2000; Rao, 2001).

3.3 FAA NAPTF Field Trafficking Study Database

3.3.1 NAPTF Pavement Sections

Widely used in pavement research, accelerated load testing is a middle solution between real field pavement sections and simple laboratory tests. Its advantages over real trafficking lie in the fact that the loading is applied in a shorter period, and that the environmental conditions are controllable. The National Airport Pavement Test Facility (NAPTF) at the Federal Aviation

Administration (FAA) was constructed to test full-scale instrumented pavement sections to investigate pavement performance subjected to complex gear loading of next generation aircraft. The NAPTF pavement test strip was 274.3-m long and 18.3-m wide. The first built group of test sections, named as Construction Cycle 1 (CC1) included nine test pavements composed of six flexible and three rigid pavements. These were built on three different subgrade materials, i.e., low (L), medium (M), and high (H) strength and two base sections, i.e., conventional (C) and stabilized (S) bases. The structural thickness requirements of CC1 cross sections are shown in Figure 3.2.

A series of laboratory and field tests were conducted to characterize the pavement geomaterials before, during, and after pavement construction. Repeated load triaxial tests were also conducted in the laboratory to determine resilient modulus, shear strength, and permanent deformation properties of subgrade soil and base/subbase aggregates and to develop proper material characterization models based on the laboratory test data. The subgrade and site preparation and construction of the pavement test sections are skipped in this study for brevity. The measured pavement critical responses and rutting depths were intended to be used for validating/calibrating the developed mechanistic rutting models for unbound layers in flexible pavements.

3.3.2 APT Loading System

The National Airport Pavement Test Machine (NAPTM) was used to load the NAPTF test sections. The NAPTM can carry up to 34-ton per wheel on two loading gears with 6-wheel per gear. Typical aircraft gear configurations, i.e., single, dual single, dual tandem, dual tridem, can be accommodated with the capability to change wheel load, wheel spacing, and wheel speed. This NAPTF pavement testing was conducted within two phases: response testing and trafficking

testing. The response testing was performed to determine the effects of static, monotonic and slow rolling gear configuration (0.55 km/hour). The trafficking tests were conducted at 8 km/hour to investigate gear configuration and wander effects by monitoring pavement responses and performances as a function of number of load repetitions.

To measure the structural responses in the CC1 test sections, several sensors were installed within the pavement sections. The NAPTF structural response instrumentations were Multi-Depth Deflectometers (MDD), Pressure Cells (PC), and Asphalt Strain Gauges (ASG). Details about the locations of the sensors such as MDDs and pressure cells were presented elsewhere (Kim, 2005; Kim, 2007).

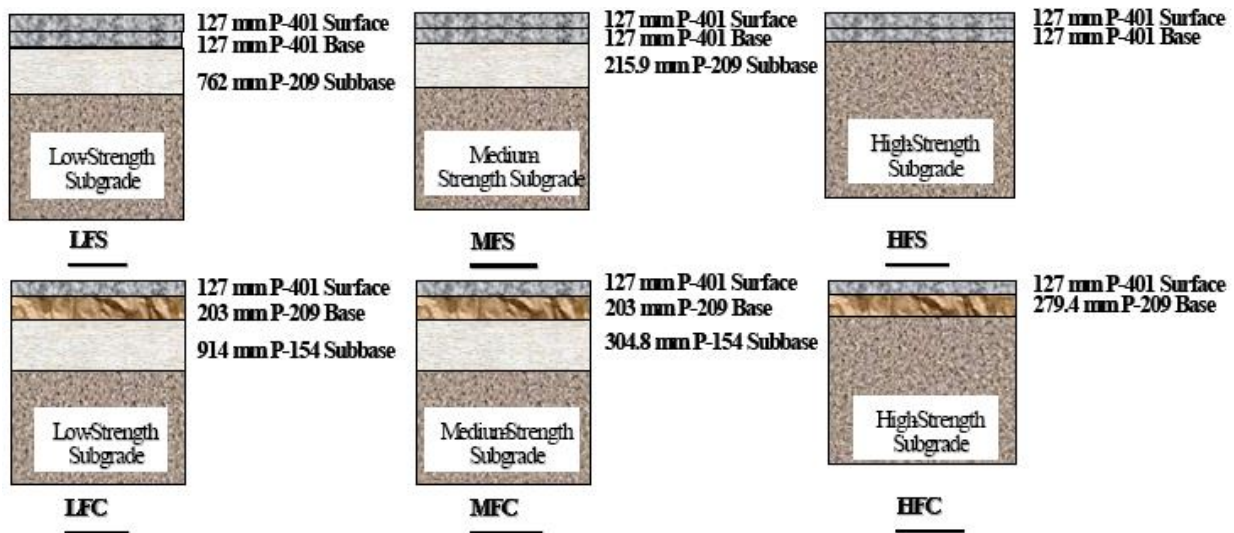


Figure 3.2 Cross Sections of NAPTF Pavement Test Sections (Kim, 2005)

3.4 University of Illinois Field Study Database

3.4.1 Full-scale Pavement Sections

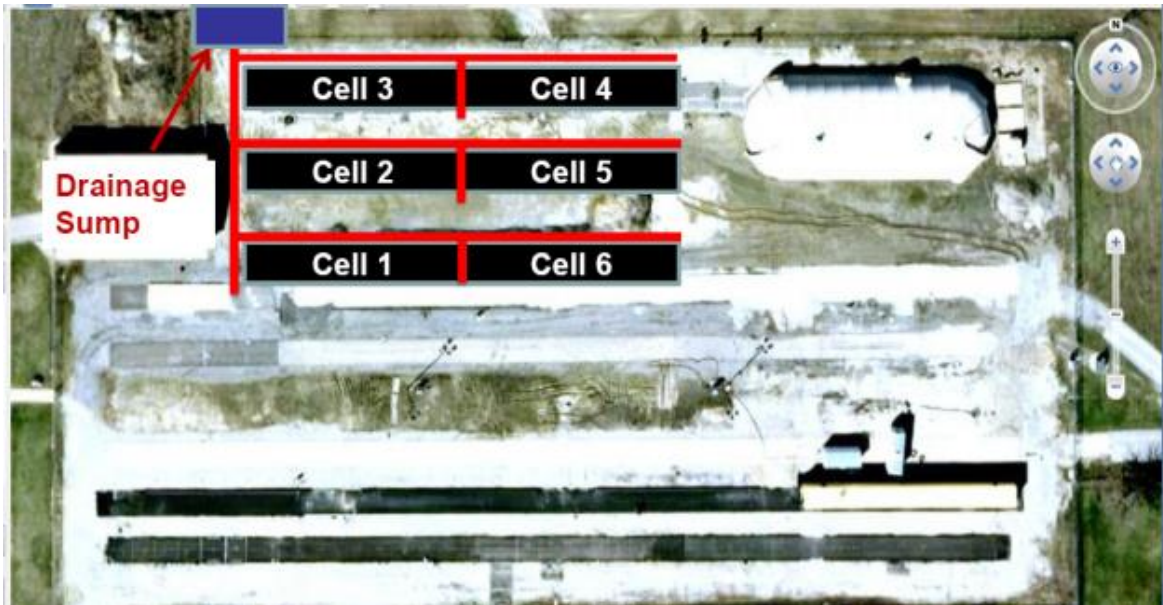
Full-scale pavement working platform test sections were constructed using different aggregate materials and loaded to failure using an Accelerated Transportation Loading Assembly (ATLAS) at the University of Illinois ATREL facility for the ICT R27-81 research project (Mishra and Tutumluer, 2013). The main purpose was to evaluate the effect of subgrade strength on unsurfaced pavement performance and mechanisms contributing to rut accumulation. Figure 3.3(a) shows the layout of the six test “cells” (numbered 1 through 6) constructed along three longitudinal test strips using the four aggregate types listed in Table 3.4 (Mishra and Tutumluer, 2013). Figure 3.3(b) presents the plan view (on top) and cross-sectional details of a representative test cell constructed over a subgrade of IBV = 3% (same configuration for Cells 1 through 4). The particle size distribution curve for each full-scale test section material was averaged from ordinary sieve analysis results of two replicate samples. Gradation charts for those test section materials are plotted in Figure 3.4, along with the determination of D_{10} , D_{60} , and C_u as tabulated in Table 3.5.

Cells 1 through 4 were constructed with the four selected aggregate materials over a weak subgrade of IBV = 3%, whereas Cell 5 was constructed using material 2 (same as Cell 2) over a stronger subgrade of IBV = 6%. Cell 6 was constructed over a subgrade of IBV = 1% by first placing a 12-in. thick layer of porous granular embankment (PGE) which was subsequently capped by a 6-in. thick layer of IDOT CA-6 dense-graded aggregate (material 2 used for capping). As it can be seen from Figure 3.3, each individual test cell (except Cell 5) was constructed 39.6-m (130-ft) long and comprised of three test “sections” with aggregate layers of thicknesses 356 mm (14 in.), 305 mm (12 in.) and 203 mm (8 in.), respectively. Cell 5 was

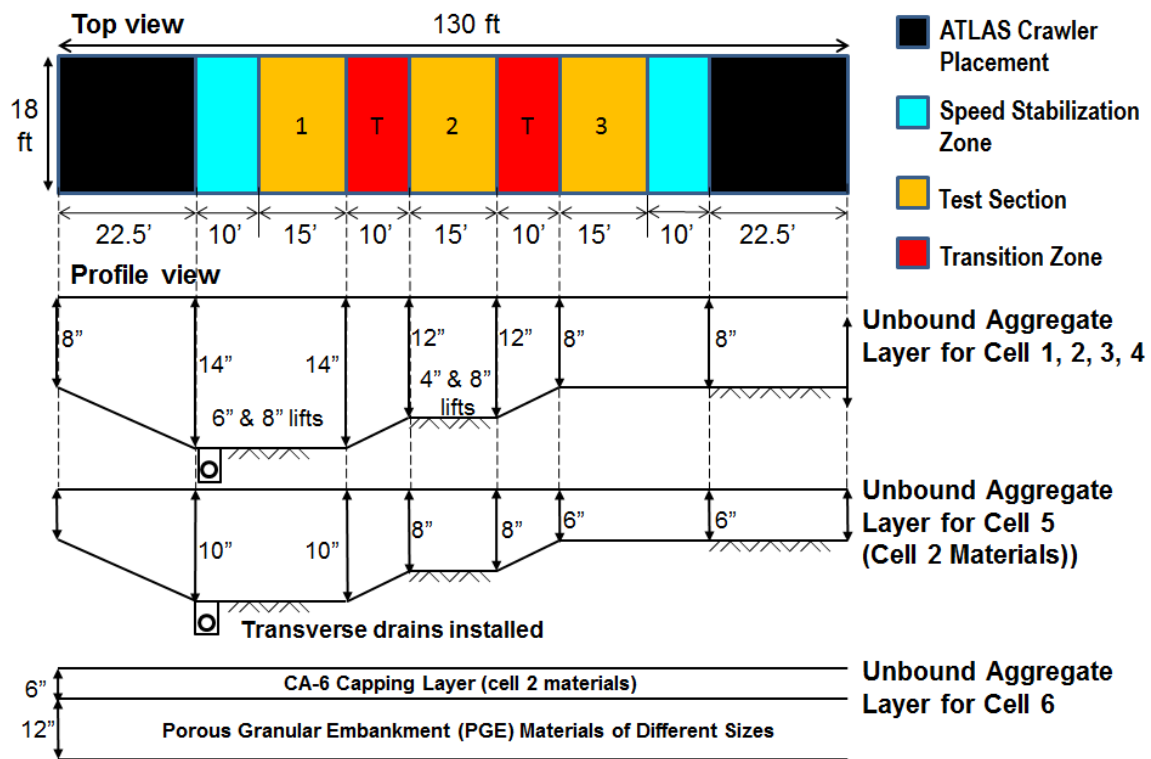
constructed over a subgrade of CBR = 6% and therefore the aggregate layer thicknesses for the three sections were 254 mm, 203 mm and 152 mm (10, 8 and 6 in.), respectively. Note that the three sections for Cell 6 were constructed to similar thicknesses, using different PGE materials. More details about those test sections can be found elsewhere (Mishra and Tutumluer, 2013). The “as-constructed” moisture contents and dry densities of compacted aggregate layers were determined from nuclear gauge testing, are summarized in Table 3.6. To evaluate the effects of aggregate material type and quality on the dissipation of traffic-imposed stresses with depth, earth pressure cells were installed at the aggregate-subgrade interface along the North wheel path of individual test cells for monitoring the subgrade vertical compressive stresses.

Table 3.4 Summary of Aggregate Material Properties for Field Test Sections (Mishra and Tutumluer, 2013)

Test Cell No.	Subgrade CBR (%)	Material Type	Aggregate Layer Thickness (in.)	P200 (%)	Plasticity Index (PI)
1	3	Uncrushed Gravel, High Fines, Non-plastic	8, 12, 14	12.3	0.0
2	3	Crushed Limestone, Low Fines, Moderately Plastic	8, 12, 14	5.15	5.7
3	3	Crushed Dolomite, High Fines, Non-plastic	8, 12, 14	12.75	0.0
4	3	Crushed Limestone, High Fines, Non-plastic	8, 12, 14	9.95	0.2
5	6	Crushed Limestone, Low Fines, Moderately Plastic	6, 8, 10	5.15	5.7
6	1	Porous Granular Embankment (PGE) Topped with CA-6	12-in. PGE overlain by 6-in. CA-6	-	-



(a)



(b)

Figure 3.3 Schematic Layout of Full-scale Pavement Test Sections: (a) Aerial View and (b) Plan View and Cross-sectional Profiles (Mishra and Tutumluer, 2013)

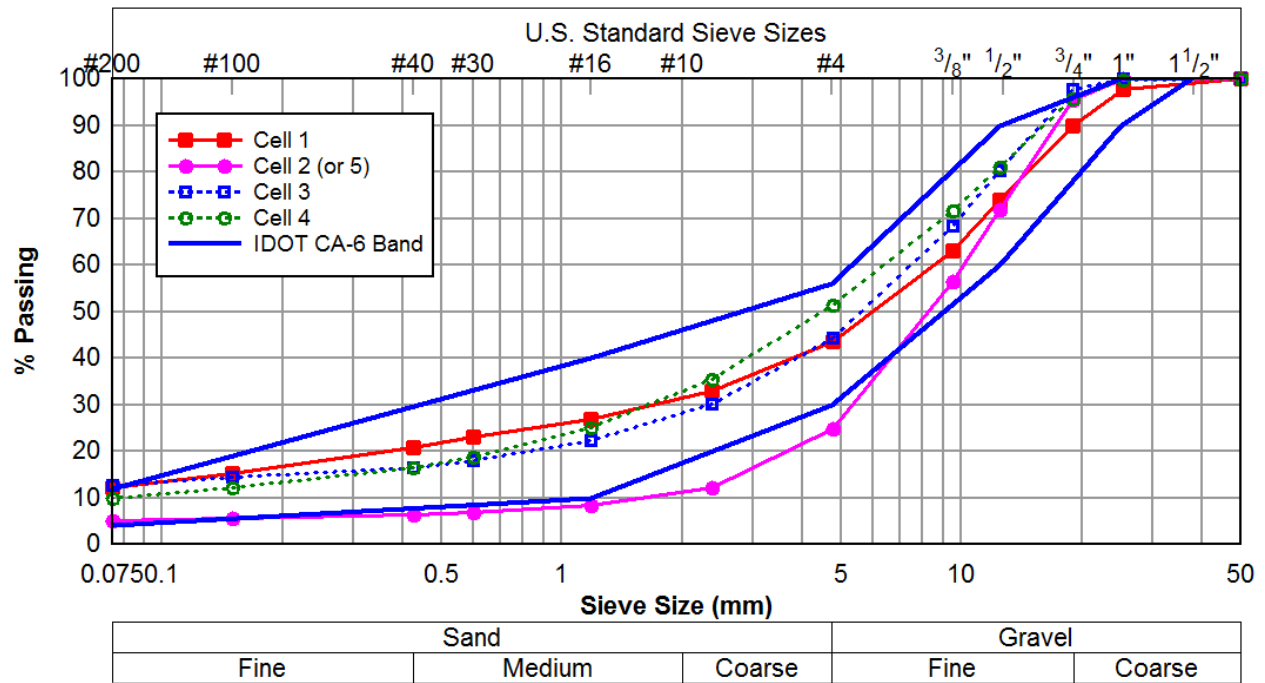


Figure 3.4 Gradation Curves of Materials Used in Full-scale Test Sections

Table 3.5 Grain-size Distribution Curve Characteristics of Full-scale Pavement Test Section

Test Cell No.	D ₁₀ (mm)	D ₆₀ (mm)	C _u	P ₂₀₀ (%)
1	0.05	9.62	197.1	12.27
2 (or 5)	1.36	10.17	7.5	5.14
3	0.01	7.80	671.6	12.76
4	0.20	6.21	31.4	9.97

Table 3.6 In-place Moisture-Density Values for Compacted Aggregate Layers (Mishra, 2012)

Cell No.	Section 1		Section 2		Section 3	
	Moisture Content (%)	Dry Density (pcf)	Moisture Content (%)	Dry Density (pcf)	Moisture Content (%)	Dry Density (pcf)
1	7.6	129.7	7.3	129.3	6.9	131.2
2	3.6	119.9	3.5	122.9	3	125.5
3	6.1	129.8	6.1	126.3	5.8	129.7
4	3.6	127.4	4.2	129.8	4.1	132.4
5	3.6	124.7	4	129.2	3.6	124.4

3.4.2 Accelerated Loading Facility and Test Program

After construction, the pavement sections were loaded to failure by applying a 44.5-kN (10-kip) wheel load through a super-single tire (455/55R22.5) at a tire pressure of 758 kPa (110 psi). Uni-directional loading was applied to simulate vehicular field loading conditions. The pavement test sections were loaded at two offset locations, one in the north side and the other in the south side. The one in the north side represents optimum moisture condition, whereas the one in the south side represents flooded condition.

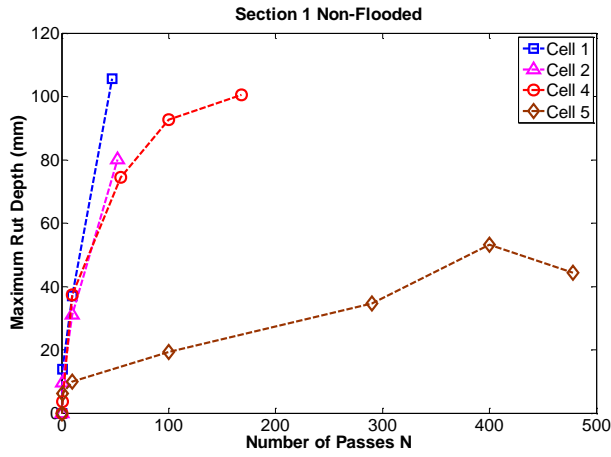
The development of rutting with load application for each test section was monitored through surface profile measurements using a digital calliper. Average surface profile for each test section was calculated using two measurements separated by a distance of 152 cm (5 ft), located 152-cm (5-ft) away from the section boundaries on either side. Note that rut depth in the research study was defined as the deflection of any point on the pavement surface from its original profile. Trafficking of the test sections was continued up to a total rut depth of

approximately 102 mm (4 in.) in most cases, while some sections could be tested to rut depths more than 102 mm (Mishra and Tutumluer, 2013).

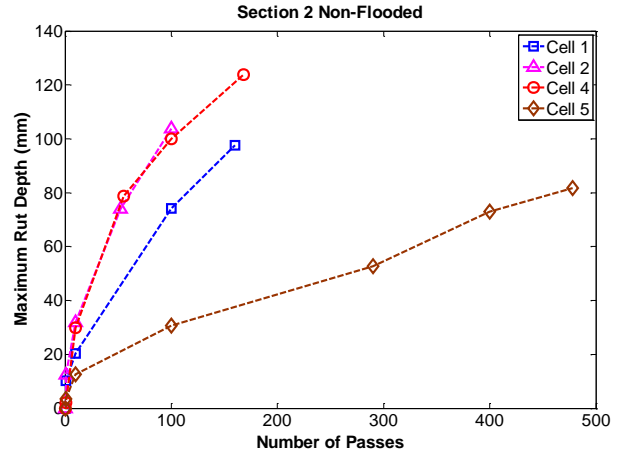
3.4.3 Key Observations from Field Rutting Measurements

Figure 3.5 shows the maximum rut depth recorded with load cycles for test sections at the optimum moisture condition, whereas Figure 3.6 shows the results at the flooded condition. As observed in all the test cells, flooding of the test sections led to weakening of the subgrade, which failed by undergoing excessive deformation.

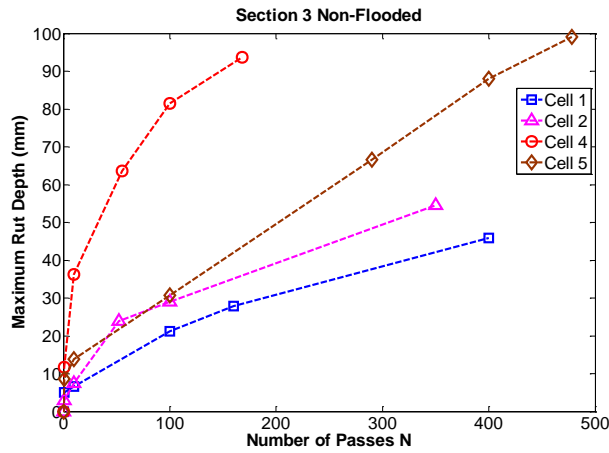
The uncrushed gravel in Cell 1 showed excessive shear movement within the aggregate layer, whereas the crushed aggregate sections in Cells 3, 4, and 5 failed primarily due to subgrade rutting. The crushed limestone material with low fines used in Cell 2 showed unstable matrix behavior under standard compaction conditions, leading to internal shear failure of Section 1 (14 in.) in Cell 2. Other two sections did not show significant shear movement within the aggregate layer, making excessive subgrade deformation the primary mechanism that contributed to failure of pavement sections under such conditions (Mishra and Tutumluer, 2013).



(a)

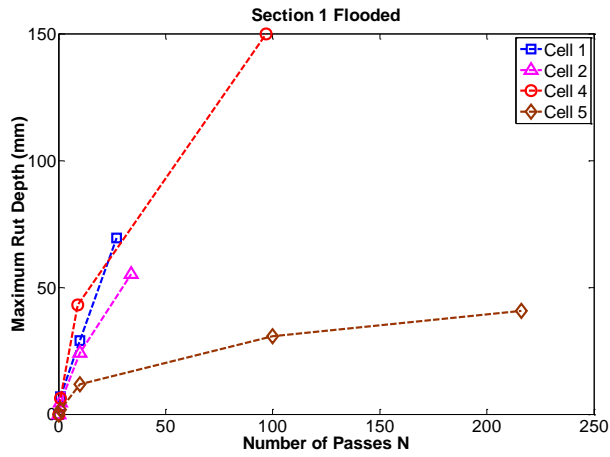


(b)

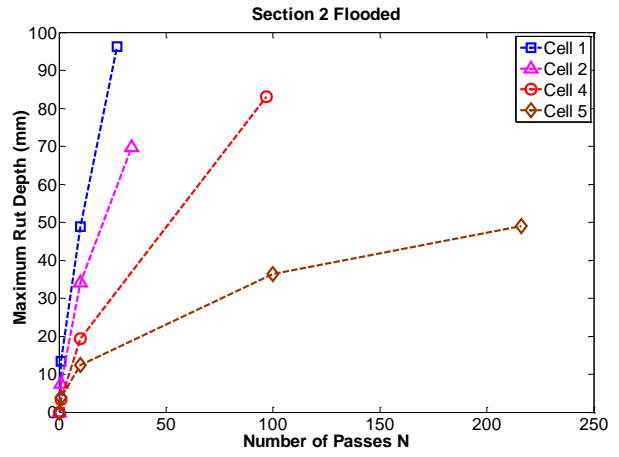


(c)

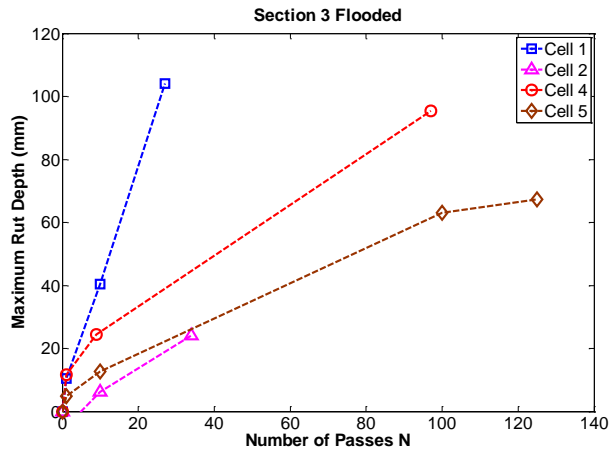
Figure 3.5 Maximum Rut Depth Measured under Near-Optimum Conditions for (a) Section 1, (b) Section 2, and (c) Section 3 of Cells 1, 2, 4, and 5



(a)



(b)



(c)

Figure 3.6 Maximum Rut Depth Measured under Flooded Conditions for (a) Section 1, (b) Section 2, and (c) Section 3 of Cells 1, 2, 4, and 5

3.5 Summary

This chapter reviewed all the laboratory and field databases from which laboratory tested mechanistic design inputs (i.e., shear strength, permanent deformation, and M_R data along with corresponding aggregate index properties) and field pavement performance were collected for unbound aggregate pavement base/subbase applications. The primary data source for this study is the existing laboratory test data for Minnesota's aggregates that were obtained from related research studies performed for/by MnDOT and for geogrid reinforcement aggregate materials, as well as the in-situ test data obtained from the FAA NAPTF test sections. In addition, as part of a comprehensive literature search, strength, permanent deformation and resilient modulus (M_R) data were also collected from many relevant research studies completed for over the last two decades at the University of Illinois. The recently completed full-scale pavement working platform test sections that were constructed at the University of Illinois ATREL facility for the ICT R27-81 research project is also used to verify the developed rutting prediction model.

Chapter 4 Resilient Modulus Behavior Estimated from Aggregate Source Properties and Its Effects on Flexible Pavement Performance

This chapter first presents the establishment of regression based correlations between performance-related aggregate source properties and aggregate M_R data, archived through modulus testing at the laboratories of Minnesota Department of Transportation (MnDOT) and University of Illinois, for identifying modulus ranges of unbound aggregate materials for mechanistic based pavement design applications. The performance-related aggregate source properties investigated in this study include percent fines content, gradation of particles, and imaging-based shape, angularity and surface texture of the aggregates, which have been long realized to significantly affect unbound aggregate mechanical behavior. Subsequently, the Monte Carlo type simulations and the First-order Reliability Method (FORM) are presented to assess the sensitivities of M_R at given stress states to various aggregate source properties studied.

4.1 Resilient Modulus Model for Unbound Aggregates

The evaluation of typical mechanistic analysis inputs is an important first step towards implementing new mechanistic-based pavement design procedures. Resilient modulus (M_R), a rational measure of the elastic response of unbound aggregate materials subjected to dynamic, repeated traffic loading, is a key mechanistic pavement analysis and design input. It is defined as the ratio of the maximum cyclic stress to the recoverable resilient strain in one repeated dynamic loading cycle. The stress-dependent nature of the resilient modulus has been well-observed from both laboratory and field testing. As reviewed in Chapter 2, various constitutive models have been developed to express the modulus as a function of applied stress states (e.g., bulk stress, deviator stress, or the combination of them) (Thompson et al., 1998). Among these, the Uzan

model (1985) first related M_R to both confinement and shear stress effects. An advanced version of this model by Witczak and Uzan (1988) is well known as the Universal model to give high prediction accuracy by considering the confinement and shear stress effects under traffic loading for three-dimensional stress states. Owing to these advantages, the Witczak-Uzan Universal model has been recently adopted in the new NCHRP 1-37A developed Mechanistic-empirical Pavement Design Guide (MEPDG) with a hierarchical methodology to input M_R of unbound aggregate base/granular subbase layers for the Level 1 flexible pavement analysis (www.trb.org/mepdg). This MEPDG model includes a bulk stress term and an octahedral shear stress component through which the confinement and shear stress effects are accounted for (see Equation 4.1). Other forms of M_R constitutive models are also available in the literature with the capability to incorporate simultaneously the moisture- and stress-dependent characteristics of the resilient modulus of unbound aggregates, such as the one proposed by Lytton (1995). However, determining the matric suction and the soil water characteristic curve (SWCC) of the unbound aggregates was not included in the laboratory testing scope of the aggregate databases collected in this study. Therefore, the MEPDG M_R model as in Equation 4.1 is selected for use in this study.

$$M_R = K_1 \cdot P_a \cdot \left(\frac{\theta}{P_a} \right)^{K_2} \cdot \left(\frac{\tau_{oct}}{P_a} + 1 \right)^{K_3} \quad (4.1)$$

where,

M_R = Resilient modulus;

θ = Bulk stress = $\sigma_1 + \sigma_2 + \sigma_3$;

σ_1 = Major principal stress;

σ_2 = Intermediate principal stress = σ_3 for M_R test on cylindrical specimen;

σ_3 = Minor principal stress or confining pressure in the triaxial tests;

σ_d = Deviator stress = $\sigma_1 - \sigma_2 = \sigma_1 - \sigma_3$;

τ_{oct} = Octahedral shear stress,

$$\begin{aligned} &= \frac{1}{3} \sqrt{(\sigma_1 - \sigma_2)^2 + (\sigma_1 - \sigma_3)^2 + (\sigma_2 - \sigma_3)^2} \\ &= \frac{\sqrt{2}}{3} (\sigma_1 - \sigma_3) \text{ for cylindrical specimen in triaxial tests;} \end{aligned}$$

P_a = Normalizing stress (atmospheric pressure = 100 kPa = 14.7 psi);

K_1, K_2, K_3 = Model parameters obtained from regression analysis.

Laboratory testing for determining M_R constitutive model parameters, which is the most accurate approach, requires expensive triaxial test equipment and time-consuming and detailed testing procedures such as the AASHTO T309 and NCHRP project 1-28A procedures. Therefore, using correlations to link M_R constitutive model parameters with performance-related aggregate source properties would be more cost-effective in less advanced hierarchical level, such as MEPDG Level 2 or 3, pavement design applications.

Commonly used material properties for such purposes include dry unit weight, moisture content, plasticity index, liquid limit, and percentage by weight of materials passing No. 200 sieve (or fines content defined in this dissertation study). However, not very accurate correlations as indicated by low R^2 values were often reported from using these index properties, some of which not only exhibit great variability but also are not directly related to the pavement performance. Therefore, repeatable and performance-related properties need to be employed to develop accurate correlations for estimating M_R constitutive model parameters.

4.2 Importance of Aggregate Shape Properties

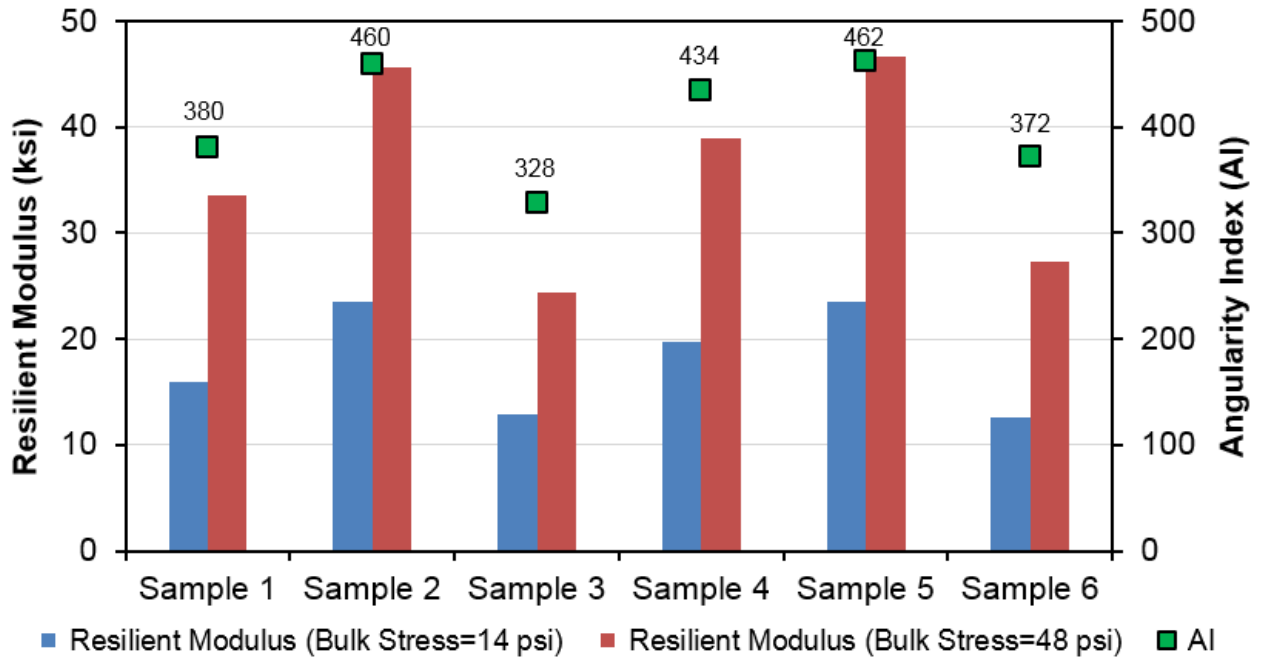
The quality of the unbound aggregate base material can have a significant impact on the performance of the pavement. Despite being demonstrated by previous studies to be very influential (Tutumluer et al., 2006), effects of physical shape, texture and angularity of coarse aggregate particles on the strength, stability and performance of the pavement base/subbase layer are often not considered by current practice. The reason might be due to the lack of accurate and repeatable measurements of the coarse aggregate morphology in the past.

The objective of this section is to illustrate importance of the aggregate morphology affecting engineering properties and performance of unbound granular materials. Test results from the two aforementioned University of Illinois databases were analyzed and presented herein for this purpose. The laboratory tests conducted include resilient modulus, permanent deformation, and the triaxial compression test, referred to as the rapid shear test in AASHTO T-307. The readily available and recently enhanced image analysis device, University of Illinois Aggregate Image Analyzer (UIAIA), with its color image thresholding was used to quantify imaging based morphological indices, i.e., flat and elongated (F&E) ratio, angularity index (AI) and surface texture (ST) index, of the coarse aggregates. Previous studies have shown that there is a correlation between imaging-based particle shape indices and resilient behavior, strength and stability of aggregates (Pan et al., 2006; Tutumluer and Pan, 2008). The research approach, testing procedure, and results were presented in Chapter 3.

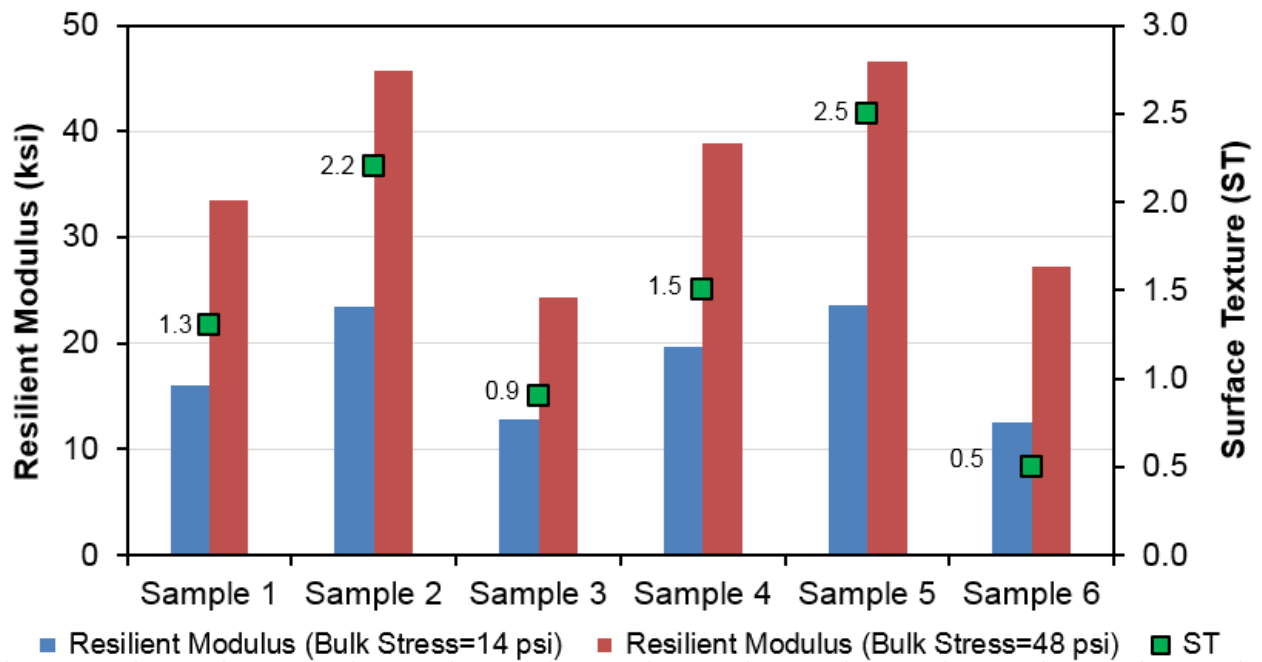
For the aggregate samples received from geogrid reinforcement applications and tested at the University of Illinois, the morphological index results of the aggregate samples are presented in Figure 4.1. The aggregate samples No. 2 and 5 have angularity index values that are greater than 400 and surface texture index values greater than 2.0. These values indicate that the samples

No. 2 and 5 consist of sub-angular and rough surfaced aggregate particles. The aggregate sample No. 4 also have angularity index values greater than 400 and surface texture index values below 2.0. These values indicate that the sample No. 4 consists of sub-angular and rough surfaced aggregate particles. The aggregate sample No. 3 also has angularity index value that is close to 325 and surface texture index values below 1.7. These values indicate that the sample No. 3 consists of rounded and smooth surfaced aggregate particles. The applied stress states on a laboratory resilient modulus test specimen are always the primary factors governing the resilient behavior of that unbound material. For this reason, the resilient modulus values estimated at two bulk stress levels of 14 psi and 48 psi are presented together with morphological index results of the aggregate samples in Figure 4.1.

The results graphed in Figure 4.1 showed a good correlation between aggregate shape properties and resilient modulus existed. Aggregates with high angularity index (AI) and surface texture (ST) properties, quantified from imaging using the newly enhanced University of Illinois Aggregate Image Analyzer, were found to have greater resilient moduli in comparison to aggregates with low AI and ST values (i.e., rounded particles with smooth surface texture). Furthermore, the effects of the AI and ST indices on the coarse aggregate resilient moduli are more significant when specimens are subjected to higher bulk stress-levels. This is due to the increase in confinement and aggregate particle contact under higher stresses. At lower stress conditions, particle contacts and related confinement effects are less dominant thus making resilient modulus correlations with the AI and ST morphological indices relatively less significant.



(a)



(b)

Figure 4.1 Effects of (a) Aggregate Angularity and (b) Surface Texture on Resilient Modulus Analyzed from Geogrid Reinforcement Applications

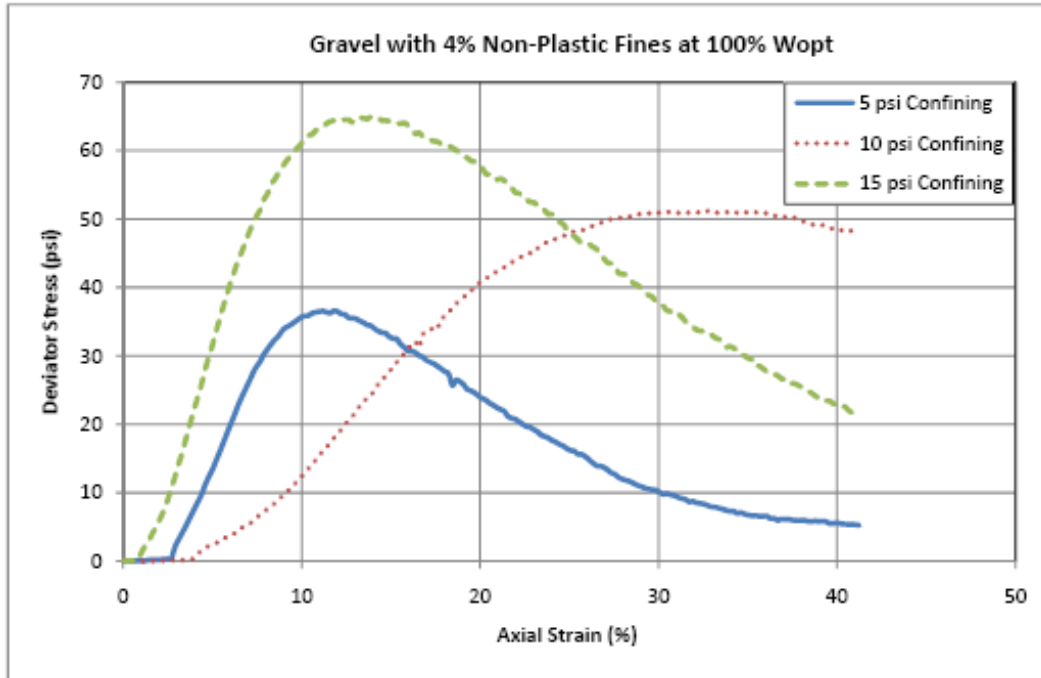
For the three different types of aggregates tested by Tutumluer et al. (2009), crushed limestone aggregates are regarded to consist of angular and rough surfaced particles, whereas the uncrushed gravel aggregates are deemed to consist of rounded and smooth surfaced particles, according to the imaging based quantification of aggregate morphological indices (see Table 3.2). To show the differences between both types of aggregates in shear strength behavior as caused by aggregate morphology, the rapid shear test results obtained with a target fines content of 4% (based on dry sieving) at the optimum moisture content were graphed in Figure 4.2 and Figure 4.3. An interesting behavior can readily be seen when looking at the results of the rapid shear test.

As explained by Mishra (2012), the achieved fines contents based on wet sieving for limestone and gravel aggregate samples, corresponding to the 4% target fines content, are in fact 8.1% and 6.8%, respectively. Such difference was attributed to the significant amount of fines that remained on the surfaces of larger particles during dry sieving and contributed toward the total fines content determined by washed sieve analysis (Mishra, 2012). The reason why the 4% target fines content is selected for comparison is that the resulting achieved fines contents are approximately around 7%, an optimum fines content value determined by Seyhan and Tutumluer (2002) using the directional dependency (i.e., anisotropy) of aggregate stiffness as the criterion. To minimize the interfering effects of other aggregate physical properties such as moisture content, both moisture and density conditions selected for comparison are at the optimum.

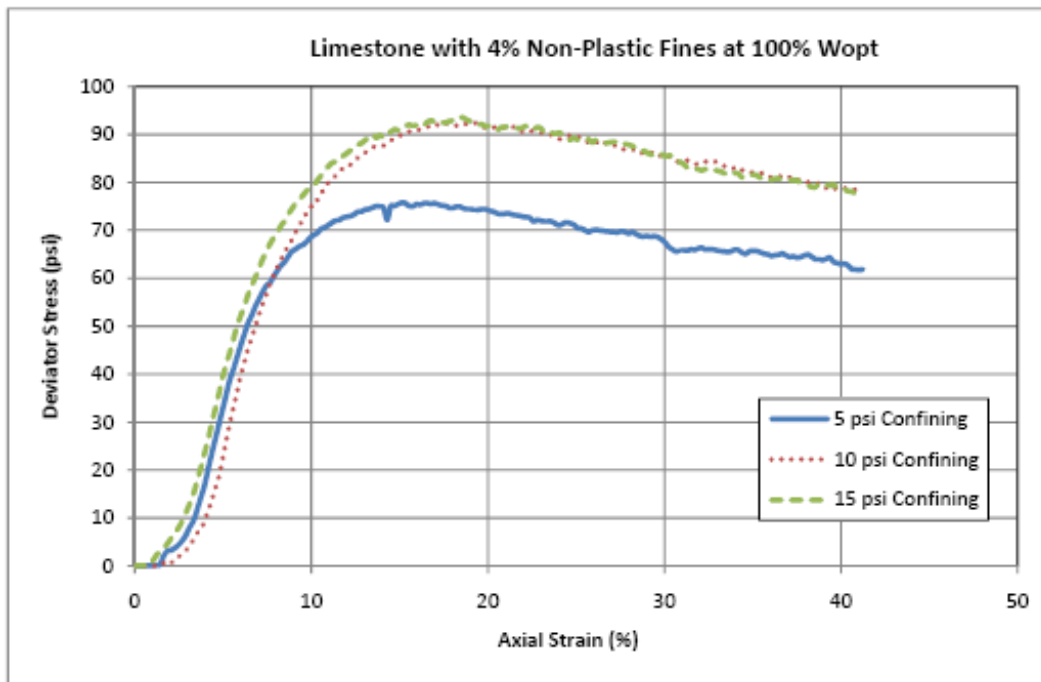
Figure 4.2 graphically depicts the results of this test for both aggregate types with non-plastic fines, and clearly demonstrates the influence of the AI and ST indices on shear failure behavior of the aggregates. Crushed limestone aggregate samples consisting of relatively angular and rough surfaced particles show stable shear displacement after each sample reaches its peak

strength, whereas uncrushed gravel aggregate samples which consist of relatively rounded and smooth surfaced particles exhibit well-defined peak shear strength values although the dilative aspects would be expected to be much less for rounded and smooth surfaced aggregate particles. Moreover, the peak strength values at different confinement levels are much higher for crushed limestone aggregate samples consisting of relatively angular and rough surfaced particles. Note that other aggregate properties affecting the shear strength test results, such as the gradation properties, especially passing No. 200 sieve, and achieved specimen compaction densities and moisture contents, are intentionally selected to be at the optimum during this comparison. This further highlights the importance of aggregate morphology.

Similar trends are also observed in Figure 4.3 for aggregate samples with plastic fines. However, the existence of plastic fines in both types of aggregates not only reduces the peak strength values but also cause unstable post-peak shear displacement. Interestingly, rounded aggregates exhibited a well-defined peak shear strength behavior, which could be influenced by their gradation properties and achieved specimen densities. The findings in this study also demonstrated that unbound aggregate resilient modulus properties should not be used alone to characterize aggregate base course performance mainly governed by rutting potential in the field. Laboratory permanent deformation tests should be conducted for evaluating rutting performances of unbound base/subbase courses.

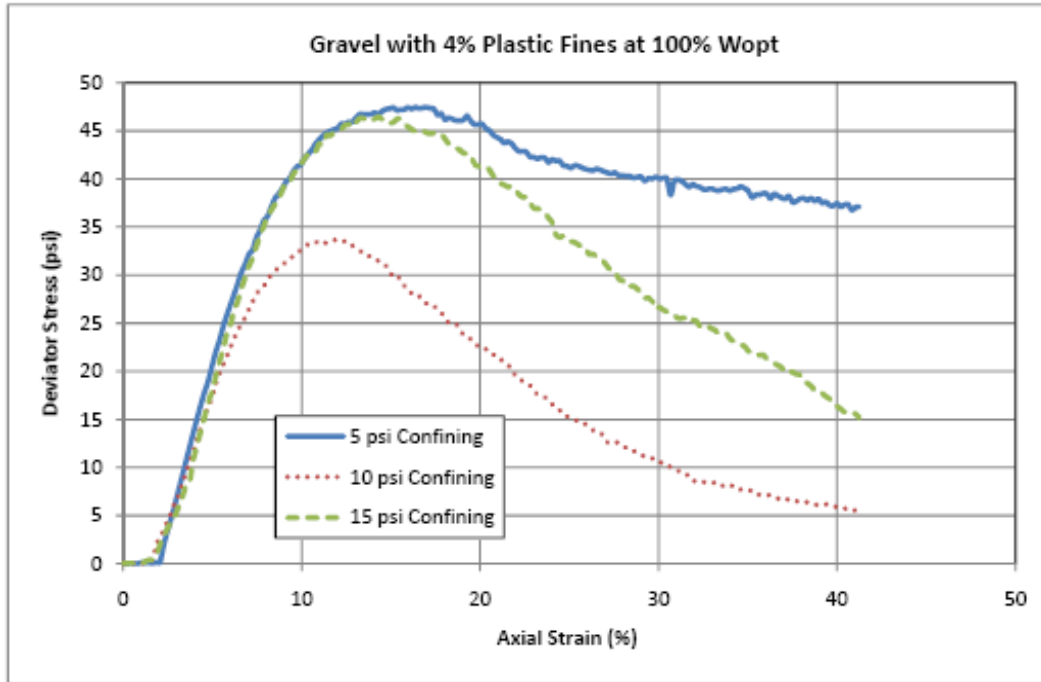


(a)

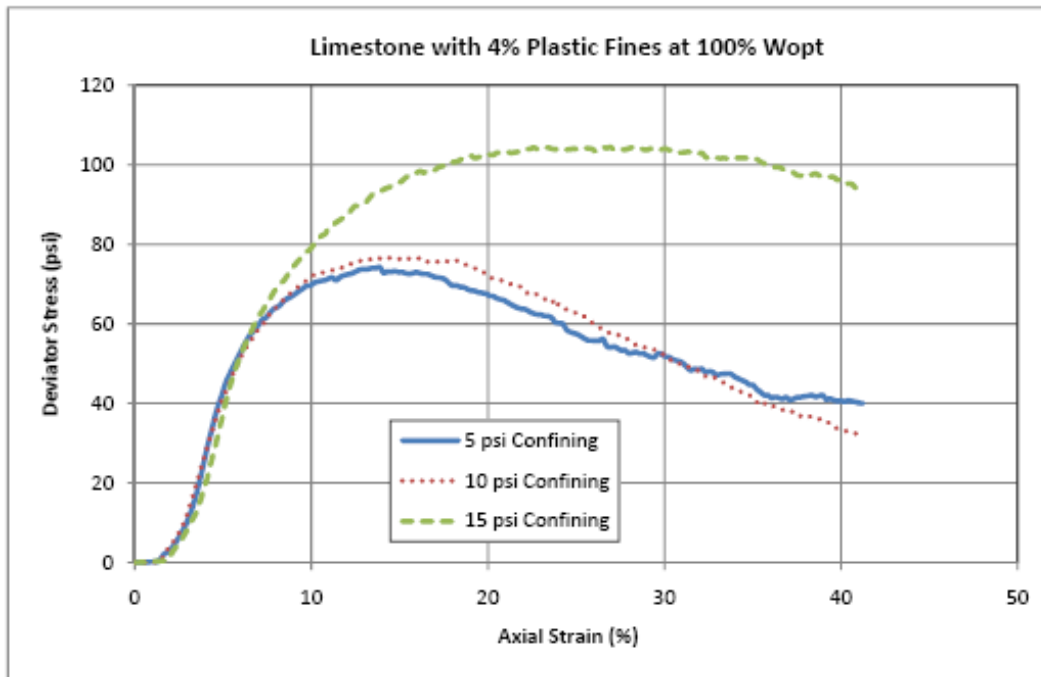


(b)

Figure 4.2 Comparison of Rapid Shear Test Results for (a) Uncrushed Gravel (Rounded and Smooth Surfaced Particles) and (b) Crushed Limestone (Angular and Rough Surfaced Particles) with 4% Non-plastic Fines at Optimum Moisture Content (Data source: Tutumluer et al., 2009)



(a)



(b)

Figure 4.3 Comparison of Rapid Shear Test Results for (a) Uncrushed Gravel (Rounded and Smooth Surfaced Particles) and (b) Crushed Limestone (Angular and Rough Surfaced Particles) with 4% Plastic Fines at Optimum Moisture Content (Data source: Tutumluer et al., 2009)

In addition, based on comprehensive statistical analysis such as ANOVA, Xiao and Tutumluer (2012) also identified that among the three imaging shape indices examined (F&E ratio, AI and ST), surface texture ST is statistically the most significant influencing M_R model parameter K_1 predictions, whereas AI is the most significant for M_R model parameters K_2 and K_3 predictions. This finding was further validated with larger sample sizes (Mishra et al., 2010). The addition of aggregate shape properties into regression analysis can significantly improve the model prediction as is to be concluded from the following sections.

4.3 Regression based Resilient Modulus Model Development

This section presents the establishment of the regression models for the three model parameters (i.e., K_1 , K_2 , and K_3 as in Equation 4.1) using the first model-building data set first without using shape properties and then with shape properties. The steps included in the regression analysis methodology are described next.

4.3.1 Regression Analysis Methodology

The flowchart description of the multiple linear regression analysis approach consists of the following consecutive steps: (i) determination of the pool of possible predictor variables to be regressed against response variables (i.e., k parameters); (ii) identification of the functional forms in which the predictor variables should enter the regression model and important interactions that should be included in the model; (iii) reduction of predictor variables and identification of “good” subsets of potentially useful predictor variables to be included in the final regression model; (iv) selection of the ultimate regression models; and (v) validation of the built regression models. The mean squared prediction error, denoted by MSPR in Eq. 4.2 below, is used as a means of measuring the actual prediction ability of the selected regression model;

hence, the calculated MSPR which is fairly close to MSE (mean squared error) is an indication of the appropriateness of the selected model.

$$MSPR = \frac{\sum_{i=1}^{n^*} (Y_i - \hat{Y}_i)^2}{n^*} \quad (4.2)$$

where Y_i = the value of the response variable in the i th validation case;

\hat{Y}_i = the predicted value for the i th validation case based on the model-building data set;

n^* = the number of cases in the validation data sets.

4.3.2 Selection and Diagnostics of Predictor Variables

To identify which aggregate index properties significantly affect the resilient modulus, ANOVA analysis via SAS® statistical software was conducted for both MnDOT and ICT R27-1 project databases. As introduced before, for the MnDOT database, the data set without shape properties has 376 observations, whereas the one with shape properties has 135 observations. In this application, each of those quantitative aggregate index properties to be studied is first grouped into different categories according to the magnitudes of their values. ANOVA then compares the means of the response variables, i.e., three k parameters here, for those newly-created categories. A predetermined level of significance, denoted as α , is compared against the resultant level of significance of the categories, namely the p value, through which a statistical difference between the mean values of those categories can be identified as significant or not. The null and alternative hypotheses used for ANOVA in this case are expressed as follows:

$$H_0: \mu_1 = \mu_2 = \dots = \mu_n;$$

H_a : At least one of the category means differs from the rest;

where μ_i is the mean value for the i th category of each aggregate index property. If the resultant p value is less than the α value (usually 0.05), then conclude H_a , indicating the aggregate index property analyzed is important for the response variable; otherwise, this property is considered insignificant.

In addition to the ANOVA analysis, scatter plots matrix and Pearson's correlation coefficients matrix are also powerful alternatives to identify important predictor variables for M_R prediction models/equations. The principles of using scatter plots and Pearson's correlation coefficients for preliminary diagnostics for nonlinear relationships and strong interactions among those basic parameters are as follows: (1) predictor variables that are highly correlated, as indicated by the high R values (usually above 0.8) in Pearson's correlation matrix, are not combined due to strong multi-collinearity; (2) predictor variables that have the highest R values with dependent variables are selected first; and (3) it is desirable to select such predictor variables that are highly correlated with the dependent variable and, meanwhile, are less inter-correlated with other predictor variables.

4.3.3 First-order Model

As no obvious nonlinear trends were observed in the scatter plots, a tentative first-order multiple linear regression model was examined first. All of the candidate variables were included in the model development. Due to the large number of predictor variables and their inter-correlated nature, it was necessary to use different model selection criteria to select the most significant variables and thereby reduce the number of variables. In this process, a list of models was first obtained using RSQUARE selection criteria available in SAS. The RSQUARE criterion ranks the subsets of candidate variables according to the coefficient of multiple determination R^2 , with a higher value of R^2 indicating a better model. Besides R^2 , other indicators, such as adjusted

R^2 , Mallows's C_p , PRESS (Prediction sum of squares) and VIF (Variance Inflation Factor) were also examined while selecting a model. Since ordinary R^2 value always increases as more predictor variables are added to the regression model regardless of their relative significances to the response variable; the adjusted R^2 takes into account the number of parameters in the regression model through the degrees of freedom and thus can indeed decrease as the number of parameters increases. Therefore, a model which produces least predictor variables, highest adjusted R^2 , smallest C_p value near the total number of parameters, smallest PRESS value, and VIF value much less than 10, besides having highest R^2 value, was selected. The final selected models for three response variables (i.e., K_1 , K_2 , and K_3 as in Equation 4.1), as shown in Table 4.1 through Table 4.3, were generated by the stepwise regression method. Note that logarithmic transformation is demonstrated to be effective for K_1 .

It can be seen from Table 4.1 through Table 4.3 that the VIF values for all regression coefficients are much less than the critical value of 10. As a rule of thumb, a maximum VIF value in excess of 10 is frequently indicative of serious multi-collinearity problems, whereas a VIF value close to 1 is taken as an indication that the predictor variable of interest is not linearly related to others. Therefore, it appears that multi-collinearity is not a serious issue in this case. The p values of all regression coefficients are much less than the significance level of 0.05 (reject null hypothesis), indicating all predictor variables included are statistically significant, though the adjusted R^2 values for three models are relatively low. The reason may be that all the aggregate samples studied came from different sources and locations and were tested for M_R in different laboratories by different personnel, which may amplify the measurement variance and obscure the real statistical regression correlations. The magnitudes of standard errors of estimated regression coefficients are also reasonably low.

To better test the significance of one regression model and/or the significance of some specific regression coefficients, the corresponding hypothesis tests are conducted for the general multiple linear regression model as follows:

$$Y = \beta_0 + \sum_{i=1}^{p-1} \beta_i X_i + \varepsilon_i$$

The overall F test of whether or not there is a regression relation between the response variable Y and the set of X variables:

$$H_0: \beta_1 = \beta_2 = \dots = \beta_{p-1} = 0$$

$$H_a: \text{not all } \beta_k \text{ (} k=1, \dots, p-1 \text{) equal zero}$$

The partial F test of whether a particular regression coefficient β_k equals zero: $H_0: \beta_k = 0$
 $H_a: \beta_k \neq 0$

If the p-value of the corresponding hypothesis test is greater than the predetermined α value (e.g., 0.05), then the null hypothesis H_0 is concluded; otherwise, the alternative hypothesis H_a is concluded. It is clearly listed in Table 4.1 through Table 4.3 that, not only all the three multiple linear regression models are significant because of the small p values (<0.0001), but all the individual predictor variables are also significant in the corresponding models as indicated by the individual p values, which are much less than the predetermined level of significance (i.e., $\alpha=0.05$).

Table 4.1 Summary of Multiple Linear Regression (MLR) Analysis Results for Identifying Properties Used to Predict $\log K_1$ of M_R Constitutive Equation

Model Parameters	Case 1 (376 observations)			Case 2 (115 observations)		
	Parameter Estimate	Pr> t	VIF	Parameter Estimate	Pr> t	VIF
Intercept	1.379	<.0001	0	4.323	<.0001	0
ω_{opt}	-0.041	<.0001	1.51	-0.026	0.0031	1.74
γ_d	-0.005	0.0044	1.86			
ω/ω_{opt}	-0.294	<.0001	1.12	-0.555	<.0001	1.63
FSAND	0.001	0.0441	1.85			
FE_Ratio				-0.052	<.0001	2.49
ST				-0.060	<.0001	1.68
$P_{1''}$				-0.025	0.0001	1.33
$P_{\#100}$				-0.064	<.0001	3.71
R^2	0.14			0.58		
Adj. R^2	0.13			0.56		
Root MSE	0.16			0.12		
$P_r > F$	<.0001 (F=15.09)			<.0001 (F=25.36)		

Table 4.2 Summary of MLR Analysis Results for Identifying Properties Used to Predict K_2 Parameter of M_R Constitutive Equation

Model Parameters	Case 1 (376 observations)			Case 2 (115 observations)		
	Parameter Estimate	$P_r> t $	VIF	Parameter Estimate	$P_r> t $	VIF
Intercept	1.606	<.0001	0	1.785	<.0001	0
ω	-0.012	0.0311	1.25			
γ_d	0.006	0.0021	2.27			
$(\gamma_{dmax})^2/P_{\#40}$	-0.0002	<.0001	1.86	-0.001	<.0001	6.09
C_u	-0.004	<.0001	3.97			
C_c	-0.427	0.0102	5.71			
$P_{3/4}$	-0.011	<.0001	2.39			
AI				-0.001	0.0297	4.35
$P_{\#200}/\log C_u$				-0.073	<.0001	4.40
GRAVEL				0.008	<.0001	5.42
R^2	0.32			0.50		
Adj. R^2	0.31			0.48		
Root MSE	0.16			0.12		
$P_r>F$	<.0001 (F=28.64)			<.0001 (F=27.29)		

Table 4.3 Summary of MLR Analysis Results for Identifying Properties Used to Predict K_3 Parameter of M_R Constitutive Equation

Model Parameters	Case 1 (376 observations)			Case 2 (115 observations)		
	Parameter Estimate	$P_{r> t }$	Variance Inflation	Parameter Estimate	$P_{r> t }$	Variance Inflation
Intercept	-9.867	<.0001	0	-8.602	0.0002	0
ω/ω_{opt}				0.528	0.0314	1.45
$(\gamma_{dmax})^2/P_{\#40}$	0.001	<.0001	4.46	0.001	<.0001	1.63
C_u	0.007	<.0001	3.25			
$P_{2''}$	0.067	0.0023	1.52			
$P_{1.5''}$				0.131	<.0001	2.20
$P_{1''}$				-0.062	0.0015	1.71
$P_{3/4''}$	0.015	0.0604	3.33			
$P_{\#40}$	0.009	0.0001	4.59			
R^2	0.394			0.53		
Adj. R^2	0.386			0.52		
Root MSE	0.42			0.32		
$P_{r>F}$	<.0001 (F=48.12)			<.0001 (F=31.34)		

4.3.4 Examine and Test for Normality and Constant Variance

Several graphic diagnostics were executed for examining whether the model assumptions have been violated: 1) linearity of regression functions, 2) constant error variance; and 3) normality of error terms (Xiao and Tutumluer, 2012). From a residual plot against the predicted values, whether a linear regression function is appropriate for the data being analyzed can be

studied. Both the Residual and Studentized Residual (RStudent) plots against predicted values for K_1 show that the residuals approximately fall within a horizontal band centered around 0 with some outlying observations; therefore, no systematic tendencies towards positive and negative are displayed indicating a linear regression model is somewhat appropriate. The plots of Residual by regressors also reveal that no clear increasing or decreasing tendencies between residual and regressors exist, thus the non-constancy of error variance is not an issue in this case. The normality of error terms can be roughly studied from the histogram of residuals, namely Percent against Residual and the plot of Residual against Quantile. The facts that the histogram is more or less close to the normal distribution, and that the plot of Residual against Quantile almost falls on a straight line support the assumption of normality of error terms. The diagnostics analysis for model parameters K_2 and K_3 are similar to that for K_1 . It is concluded that all the inherent statistical assumptions embedded in the multiple linear regression analyses are satisfied here.

4.3.5 Model Validation Using 15% Data

To validate regression models developed with shape properties, the following data sets were used, i.e., 20 randomly-selected cases (around 15%) out of the 135 model-building cases. The validation results in terms of MSPR values for the remaining 20 cases are presented in Table 4.4 below. As listed, the MSE and MSPR values are very close for these three regression models, which is indicative of the satisfactory model prediction ability. Furthermore, the measured values versus the predicted values for three K parameters are plotted in Figures 5.1 to 5.3. Accordingly, the developed models would have fairly good prediction abilities when used in the MEPDG level 2 or level 3 design analyses as long as no extrapolations were made during the use of these regression models.

Table 4.4 Comparisons between MSPR and MSE Values for the Three k Parameters

Validation Dataset	Dependent Variables	MSE	MSPR
20 cases from MnDOT (with Shape Properties)	K ₁	0.01479	0.013205
	K ₂	0.01530	0.017817
	K ₃	0.10537	0.10791

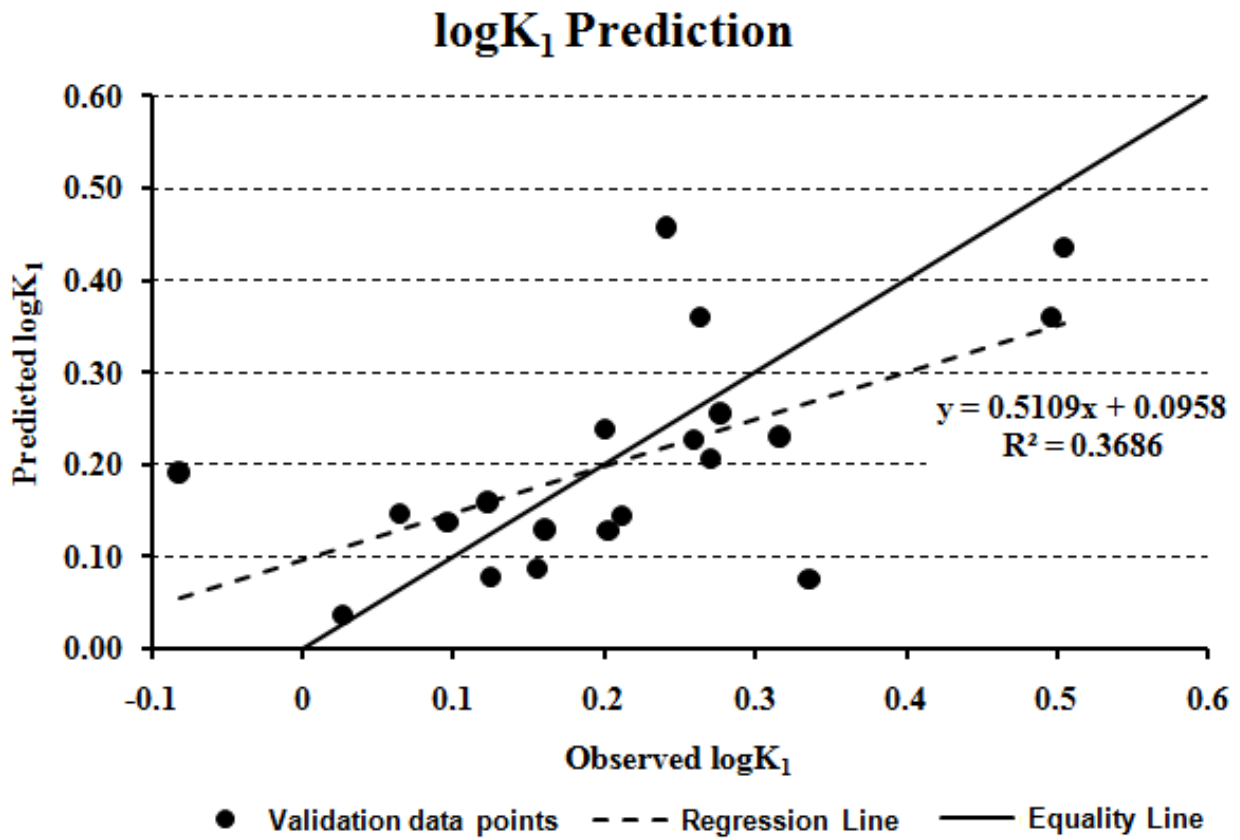


Figure 4.4 Measured vs. Predicted Values for logK₁

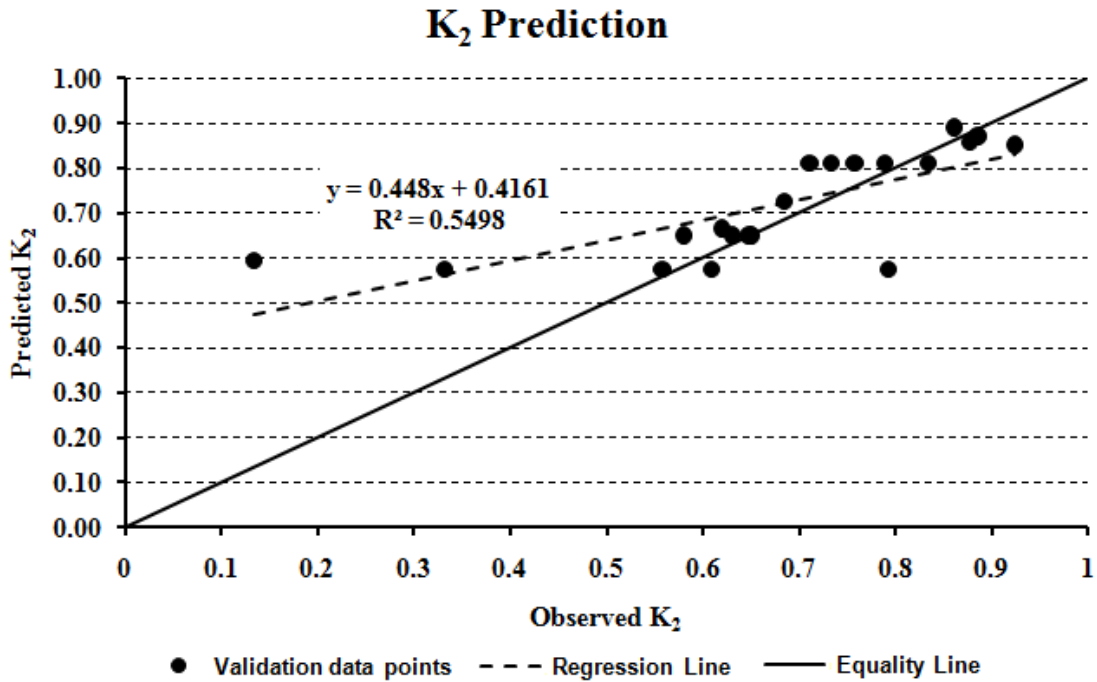


Figure 4.5 Measured vs. Predicted Values for K₂

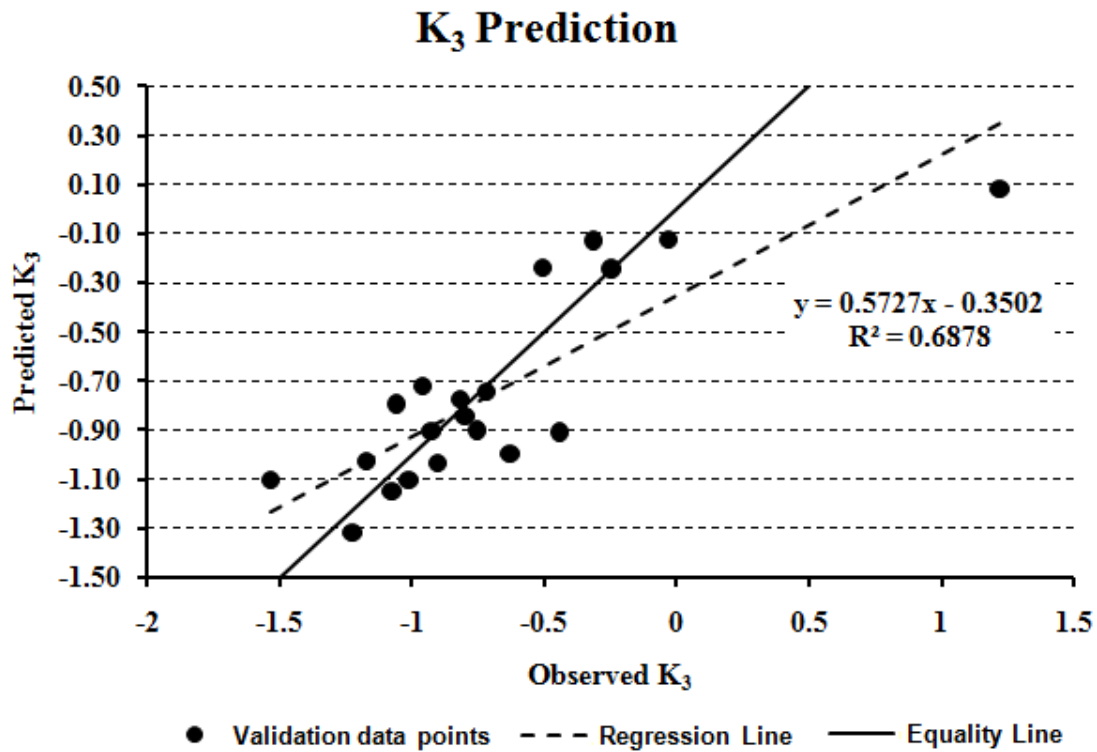


Figure 4.6 Measured vs. Predicted Values for K₃

4.3.6 Final Model Development with Combined Data Sets

As the regression models developed using the model-building data set (85% random observations) have been validated using the cross validation data set, it is then customary practice to re-develop the models by combining both the model-building and validation data sets as one single data set. The rebuilt regression models using the combined data set are presented in Equation 4.3. The residuals of model K_1 pass all the tests for normality; however, the residuals of model K_2 and K_3 both fail to pass some of the tests for normality (Xiao and Tutumluer, 2012). The histograms of all the residuals are approximately close to normal distribution. Failing some of the tests for normality would not seriously violate the normality assumption of error terms; indeed, it still indicates that the residuals still approximate normal distribution to a reasonable extent. It is noteworthy that the regression models rebuilt from the combined data set should be used for M_R prediction in further analysis. The subsequent sensitivity analysis is also based on the rebuilt regression models. The developed regression models with shape indices for K parameters are given by Equation 4.3 as follows:

$$\left\{ \begin{array}{l}
 M_R = K_1 P_a \left(\frac{\theta}{P_a} \right)^{K_2} \left(\frac{\tau_{oct}}{P_a} + 1 \right)^{K_3} \\
 K_1 = 10^{\left(0.132 - 0.016 FE_Ratio - 0.05 ST - 0.026 \omega_{opt} - 0.628 \frac{\omega}{\omega_{opt}} + 0.0004 \frac{\gamma_{max}^2}{P_{40}} + 1.197 C_c \right)} \\
 \left(R^2 = 0.5523; \text{Adj. } R^2 = 0.5313; p < 0.0001; \text{MSE} = 0.01478 \right) \\
 K_2 = 1.573 + 0.007 \gamma_d - 0.0009 \frac{\gamma_{max}^2}{P_{40}} - 0.013 P_{10} - 0.046 P_{200} \\
 \left(R^2 = 0.5062; \text{Adj. } R^2 = 0.4910; p < 0.0001; \text{MSE} = 0.01543 \right) \\
 K_3 = -15.914 + 0.041 FE_Ratio + 0.004 AI + 0.015 \gamma_d + 0.488 \frac{\omega}{\omega_{opt}} - 0.0008 \frac{\gamma_{max}^2}{P_{40}} \\
 + 0.246 \frac{P_{200}}{\log C_u} + 0.145 P_{2''} - 0.057 P_{1''} \\
 \left(R^2 = 0.6633; \text{Adj. } R^2 = 0.6419; p < 0.0001; \text{MSE} = 0.08328 \right)
 \end{array} \right. \quad (4.3)$$

The validation results in terms of MSPR values for the remaining 15% data indicated that the MSE and MSPR values are very close for these three regression models, which is indicative of the satisfactory predictive capability of these models. Therefore, the developed models are believed to have fairly good predictive capabilities to be used in MEPDG level 2 or level 3 design analysis, as long as no extrapolations are made during the use of those regression models. Not only are all the three multiple linear regression models significant because of the small p values (<0.0001), but all the individual predictor variables are also significant in the corresponding models, as indicated by the individual p values which are much less than the predetermined level of significance (i.e., $\alpha=0.05$). The variance inflation factor (VIF) value for each individual predictor variable is less than the critical value of 10. According to the rule of thumb, it appears that multi-collinearity is not a serious issue in this case. The magnitudes of standard errors of estimated regression coefficients are also reasonably low. No serious violations of the linearity, constancy and normality assumptions have been found in these three regression models developed with shape properties.

4.4 Monte Carlo Simulation of Resilient Modulus

To investigate sensitivities of resilient moduli of aggregate base/granular subbase materials to various input parameters (i.e., aggregate source properties) and their inherent variability, advanced risk modeling by Monte Carlo type simulation was performed via @RISK. The Monte Carlo type simulation models each input parameter as a stochastic variable with a distribution function assigned such that the distribution of the output values can be predicted. As contrary to conventional local sensitivity analysis techniques that change one variable at a time while keeping others at the reference levels, it is capable of varying all the variables simultaneously, which is advantageous to examine the global sensitivity.

4.4.1 Development of M_R Predictive Model

After the developed regression models for Case 2 (with aggregate shape indices) were validated using the cross-validation dataset, basic procedures of a customary practice were followed to re-develop the models by combining both the model-building and validation datasets as one single model development dataset. The resultant regression models for the K parameters were then entered into the MEPDG M_R constitutive model (see Equation 4.1), leading to the following analytical model that expresses M_R as a function of the applied stress states and aggregate source properties. To calculate M_R values, the stress terms included in the model given below, i.e., bulk stress θ and octahedral shear stress τ_{oct} , must be specified. Based on the MnPAVE program default layer modulus inputs and the 18-kip dual-tire axle loads (ESALs) applied, Table 4.5 lists the representative stress levels calculated in MnDOT aggregate base, granular subbase, and subgrade layers, respectively.

$$M_R = 10^{\left(0.132 - 0.016 FE_Ratio - 0.05 ST - 0.026 \omega_{opt} - 0.628 \frac{\omega}{\omega_{opt}} + 0.0004 \frac{\gamma_{max}^2}{P_{40}} + 1.197 C_c\right)} P_a \times \left(\frac{\theta}{P_a}\right)^{\left(1.573 + 0.007 \gamma_d - 0.0009 \frac{\gamma_{max}^2}{P_{40}} - 0.013 P_{10} - 0.046 P_{200}\right)} \times \left(\frac{\tau_{oct}}{P_a} + 1\right)^{\left(-15.914 + 0.041 FE_Ratio + 0.004 AI + 0.015 \gamma_d + 0.488 \frac{\omega}{\omega_{opt}} - 0.0008 \frac{\gamma_{max}^2}{P_{40}} + 0.246 \frac{P_{200}}{\log C_u} + 0.145 P_2 - 0.057 P_1\right)} \quad (4.4)$$

where: $\theta = \sigma_1 + 2\sigma_3$; $\sigma_d = \sigma_1 - \sigma_3$; $\tau_{oct} = \frac{1}{3} \sqrt{(\sigma_1 - \sigma_2)^2 + (\sigma_1 - \sigma_3)^2 + (\sigma_2 - \sigma_3)^2}$

Atmospheric (normalizing) pressure $p_a = 101.35$ -kPa (14.7-psi)

$\log k_1$ model: $R^2 = 0.55$, $Adj.R^2 = 0.53$, $P < .0001$, $SSE = 1.89$

k_2 model: $R^2 = 0.51$, $Adj.R^2 = 0.49$, $P < .0001$, $SSE = 2.01$

k_3 model: $R^2 = 0.66$, $Adj.R^2 = 0.64$, $P < .0001$, $SSE = 10.49$

Table 4.5 Representative Stress Levels in Typical MnDOT Pavement Layers

MnDOT Layer Material	Layer Thickness		Representative Stress Levels		MnPAVE <i>Fall</i> Design Moduli	
	in.	cm	psi	kPa	ksi	MPa
HMA: PG 58-34	6	15.2	-	-	-	-
Aggregate Base: Class 6	6	15.2	$\sigma_1=9.0$ $\sigma_3=1.0$	$\sigma_1=62.1$ $\sigma_3=6.9$	24	164
Granular Subbase: Select Granular	18	45.7	$\sigma_1=5.0$ $\sigma_3=1.0$	$\sigma_1=34.5$ $\sigma_3=6.9$	11.7	81
Subgrade: Engineered Soil	12	30.5	$\sigma_1=4.5$ $\sigma_3=1.0$	$\sigma_1=31.0$ $\sigma_3=6.9$	-	-

4.4.2 Simulation Results

The Monte Carlo simulation was performed which allows for the analysis to be performed in Excel spreadsheets. The Latin Hypercube sampling and 100,000 iterations were adopted. The Monte Carlo simulation properly captured the distribution function for each input parameter. The initial distributions assigned to each of the input parameters, as detailed in Table 4.6, were fitted from the databases collected. Summary statistics for the resulting distribution of calculated M_R are presented in Table 4.7. As shown in Table 4.7, the MnPAVE fall-season design moduli listed in Table 4.5 for aggregate base and granular subbase have the reliability of at least 95% and 85% in the specified pavement structure, respectively. The mean M_R values under both typical base and subbase stress levels are above the minimum MnPAVE requirement of 5 ksi, and the listed statistics are also within reasonable limits.

Table 4.6 Input Parameters and Distributions

Input Parameters	Mean	Std. Dev.	Min.	Max.	Distribution
ω_{opt} (%)	8.7	1.8	6.2	12.2	Log-logistic
ω/ω_{opt}	0.83	0.16	0.33	1.21	Weibull
γ_d (pcf)	128	5	119	141	Beta general
γ_{dmax} (pcf)	128	6	122	140	Log-logistic
$(\gamma_{dmax})^2/P_{\#40}$	897	311	404	1573	Log-logistic
$P_{2''}$ (%)	99.4	1.6	95	100	Weibull
$P_{1''}$ (%)	98.7	2.2	91	100	Weibull
$P_{\#10}$ (%)	48.6	20.0	17	71	Beta general
$P_{\#200}$ (%)	6.3	2.4	2.9	12.4	Johnson SB
C_c	0.56	0.11	0.36	0.70	Johnson SB
$P_{\#200}/\log C_u$	4.97	1.51	3.48	8.35	Beta general
FE_Ratio	4.1	2.4	1.8	10.6	Johnson SB
AI	425	61	307	499	Inverse Gauss
ST	2.5	2.3	0.6	1.6	Pareto

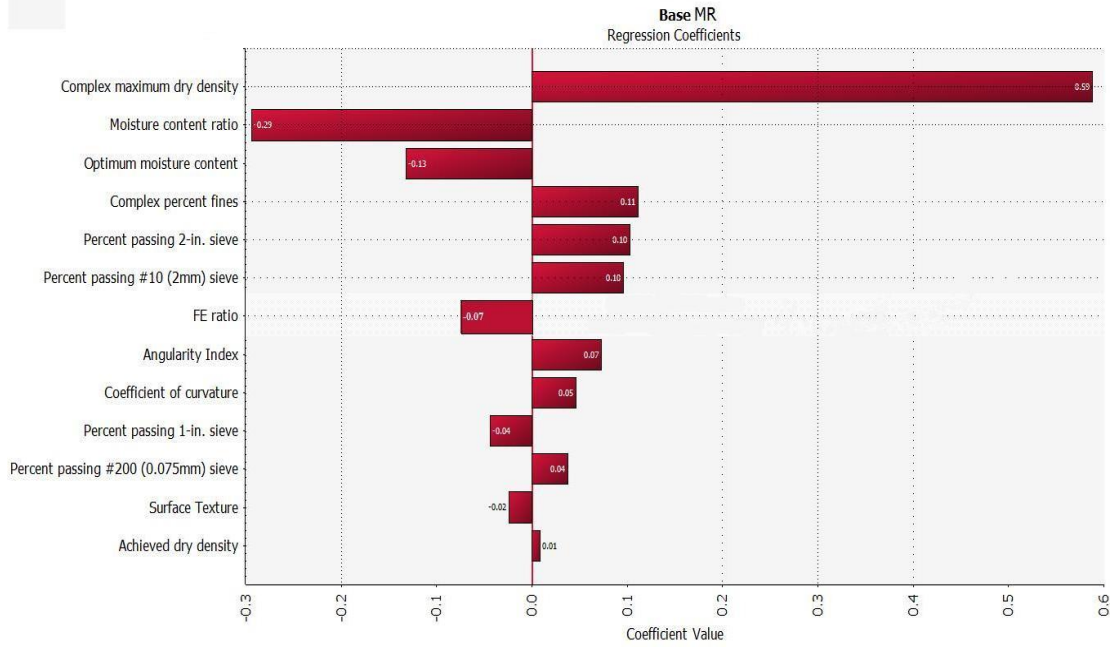
Note: Min. =Minimum, Max.=Maximum, and Std. Dev.=Standard Deviation.

Table 4.7 Monte Carlo Simulation Results for M_R (Unit: ksi)

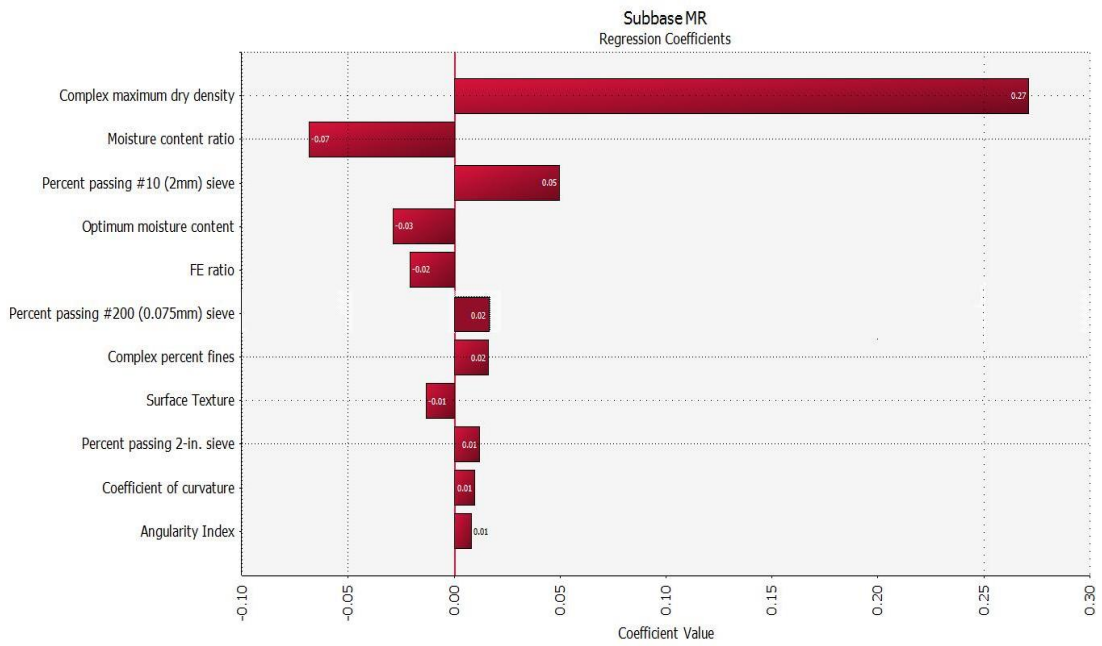
Statistics	M_R at Base Stress Level	M_R at Subbase Stress Level
Minimum	0	0
Maximum	898.8*	4225.3*
Mean	7.8	8.1
Std Dev	6.0	19.2
Median	6.9	6.1
95% Percentile	15.6	18.5
75% Percentile	9.4	9.3
25% Percentile	5.0	4.0
MnPAVE M_R reliability	>95%	85%

Note: * Unreliable extreme outliers; 1 ksi=6.9 MPa.

Figure 4.7 shows the sensitivity charts for aggregate base and granular subbase M_R from which the relative influences of aggregate source properties on M_R can be compared. At the representative aggregate base stress levels, the term γ_{\max}^2 / P_{40} positively affects M_R the most, while the moisture content ratio and the optimum moisture content are the primary negative factors. The same trends are also observed at granular subbase stress levels. As one would expect, larger F&E ratio and less angularity result in lower M_R levels. However, the M_R is found to increase with increased percent passing No.200 sieve (fines). The reason for that is probably the maximum percent fines found around 12% in the database; i.e., the coarse aggregate particle contact is not seriously severed by excessive fines. In general, the sensitivities of M_R to aggregate source properties are in accordance with expectations, indicating that the developed correlations are reasonable.



(a)



(b)

Figure 4.7 Sensitivity Charts for MR: (a) Stress Levels in Aggregate Base and (b) Stress Levels in Granular Subbase

4.5 Reliability-Based Evaluation of Aggregate Source Properties Affecting Resilient Modulus Behavior

4.5.1 Limit State Function Used

The failure mode of this problem is defined as when the measured resilient modulus is below the designed value of resilient modulus. Therefore, the limit state function is expressed as follows:

$$g(\mathbf{X}) = M_R - M_{R_design} \quad (4.5)$$

A typical conventional pavement structure used in Minnesota was selected to calculate the representative stress levels in aggregate base layer. The stress results were tabulated in Table 4.8, as well the standard design modulus specified by Minnesota Department of Transportation for Class 6 aggregate base materials. The resilient modulus constitutive equation used in this study is the model just developed and presented previously. The reason to use this model is that the database for this model was generated from real laboratory tests done on aggregate materials collected from different construction projects through Minnesota. This model also included all significant variables affecting resilient modulus behavior. Table 4.9 gives the abbreviations of variables used in this study.

Table 4.8 Representative Stress Level and Design Modulus for Aggregate Base Layer in a Typical Conventional Pavement Structure

Layer Material	Layer Thickness	Representative Stress Levels	Design Modulus
Units	(in.)	(psi)	(ksi)
Aggregate Base: Class 6	6	$\sigma_1=9.0$ $\sigma_3=1.0$	24

Table 4.9 Abbreviations and Brief Descriptions of Significant Variables Influencing Resilient Modulus Behavior

Abbreviation	Brief description
<i>FE ratio</i>	Flat and Elongated ratio
<i>ST</i>	Surface Texture index
ω_{opt}	Optimum Moisture Content
ω / ω_{opt}	Moisture content ratio
γ_{max}^2 / P_{40}	Complex maximum dry density
C_c	Coefficient of Curvature
γ_d	Achieved dry density
P_{10}	Percent passing #10 (2mm) size sieve
P_{200}	Percent passing #200 (0.075mm) size sieve
<i>AI</i>	Angularity Index
$P_{200} / \log C_u$	Complex percent fines

It is worth mentioning that the effects of variables $P_{1''}$ and $P_{2''}$ (percent passing 1'' and 2'' sieves, respectively) were not included because most of the samples do not have sizes larger than 1'' in diameter and the values of these two variables in most of the observed datasets thus remained constant (100 percent passing). Gradation was quantified by parameters $P_{\#10}$, $P_{\#200}$, C_c , and $P_{\#200} / \log C_u$. Moisture and density were quantified by parameters γ_{max}^2 / P_{40} , γ_d , ω_{opt} , and ω / ω_{opt} . Aggregate particle shape or morphology was quantified as Flat and Elongated (F&E) ratio, Angularity Index (AI), and Surface Texture (ST) index measured by the University of Illinois Aggregate Image Analyzer (UIAIA).

4.5.2 Variables and Distributions

Totally 135 M_R observations from MnDOT database supplemented with aggregate shape properties measured from 9 MnDOT samples via University of Illinois Aggregate Image Analyzer (UIAIA) were employed in this study. The initial distribution assigned to each of the random variables, as detailed in Table 4.10, were obtained by distribution fitting tool in MATLAB® from the databases collected. Corresponding distribution parameters were also calculated and presented in Table 4.10. The correlation matrix, as shown in Table 4.11, was established from the 135 datasets and adjusted according to definitions and characteristics of variables wherever necessary. Reasonable Assumptions were reasonably made for shape properties (FE ratio, ST and AI) that they are not correlated to other variables except density (γ_{\max}^2 / P_{40} and γ_d), and that FE ratio is not correlated to AI or ST.

Table 4.10 Basic Statistics of Aggregate Source Properties Used

Property	Variable	Distribution	Mean	Standard Deviation
<i>FE ratio</i>	X_1	Lognormal	4.110	2.446
<i>ST</i>	X_2	Exponential	2.504	2.300
ω_{opt}	X_3	Gumbel	8.653	1.761
ω / ω_{opt}	X_4	Weibull	0.828	0.156
γ_{\max}^2 / P_{40}	X_5	Weibull	898.897	309.842
C_c	X_6	Uniform	0.529	0.097
γ_d	X_7	Lognormal	128.390	4.880
P_{10}	X_8	Uniform	44.000	15.820
P_{200}	X_9	Lognormal	6.351	2.689
<i>AI</i>	X_{10}	Normal	424.809	60.895
$P_{200} / \log C_u$	X_{11}	Lognormal	4.958	1.386

Table 4.11 Correlation Coefficients of Variables

	<i>FE ratio</i>	<i>ST</i>	ω_{opt}	ω / ω_{opt}	γ_{max}^2 / P_{40}	C_c	γ_d	P_{10}	P_{200}	<i>AI</i>	$P_{200} / \log C_u$
<i>FE ratio</i>	1	0	0	0	-0.3	0	-0.1	0	0	0	0
<i>ST</i>		1	0	0	0.1	0	0.2	0	0	0.5	0
ω_{opt}			1	-0.3	-0.3	0.5	-0.4	0.5	0	0	0.3
ω / ω_{opt}				1	0	0	0	0	0	0	-0.1
γ_{max}^2 / P_{40}					1	-0.5	0.5	-0.5	0	0.4	-0.4
C_c						1	-0.5	0.5	-0.2	0	0.4
γ_d			Symmetric				1	-0.4	0	0.4	-0.4
P_{10}								1	0	0	0.4
P_{200}									1	0	0.5
<i>AI</i>										1	0
$P_{200} / \log C_u$											1

4.5.3 First-Order Reliability Method (FORM) Analysis

Statistical analysis was performed using a First Order Reliability Method (FORM). The FORM algorithm approximates the integral of the joint probability distribution function of the basic variables X over the portion of the sample space that corresponds to failure of a component (Madsen et al., 1986). The function which defines this region is the limit-state function, ($g(\mathbf{X}) = 0$). FORM uses an one-to-one transformation of the random variables into a standardized normal space as shown below:

$$X = (X_1, X_2, \dots, X_n) \rightarrow U = (U_1, U_2, \dots, U_n) \quad (4.6)$$

where U_1, U_2, \dots, U_n are uncorrelated random variables with standard normal distributions. Next, the limit-state surface in the X -space is mapped on the corresponding limit-state surface in the U -space. The probability content of the failure set in the U -space is obtained by a search for the minimum distance β (also called the reliability index) from the origin to a point u^* on the failure space (see Figure 4.8). The point u^* is also known as the design point, or the most likely failure point. While various software/programs are available to perform these calculations, the FERUM program developed by Haukaas and Kiureghian (1999) at the University of California, Berkeley is used in this study.

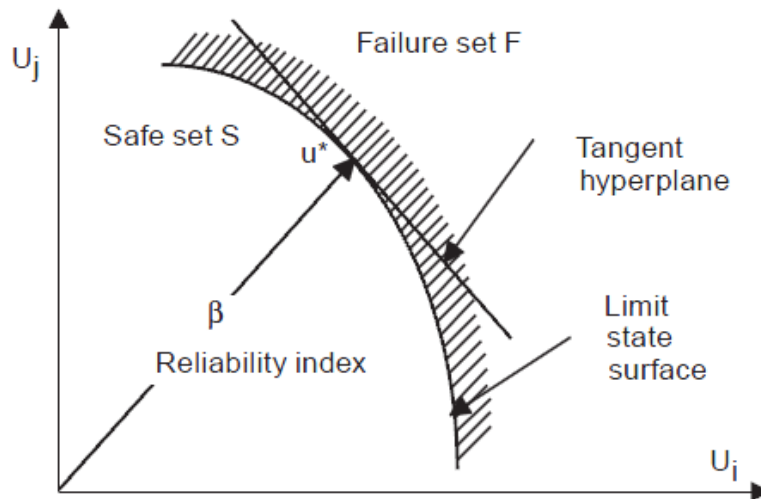


Figure 4.8 FORM Approximations (Haukaas and Kiureghian, 1999)

Table 4.12 and Figure 4.9 show the calculated importance vector from FERUM. Negative sign of Importance Vector γ means that the variable in the original space is capacity type and as the increase of the value of this variable, resilient modulus will increase. Positive sign of Importance Vector γ means that the variable in the original space is demand type and as the increase of the value of this variable, resilient modulus will decrease. $P_{200} / \log C_u, AI, P_{200}, P_{10},$

γ_d , C_c , and γ_{\max}^2 / P_{40} were found to be capacity type and ω / ω_{opt} , ω_{opt} , ST , and $FE Ratio$ were found to be demand type.

Table 4.12 Importance Vector of Variables Obtained from FERUM Program

Source Properties	Importance Vector γ
$FE\ ratio$	0.0689
ST	0.292
ω_{opt}	0.1954
ω / ω_{opt}	0.4277
γ_{\max}^2 / P_{40}	-0.5771
C_c	-0.5463
γ_d	-0.0122
P_{10}	-0.145
P_{200}	-0.058
AI	-0.0999
$P_{200} / \log C_u$	-0.1514

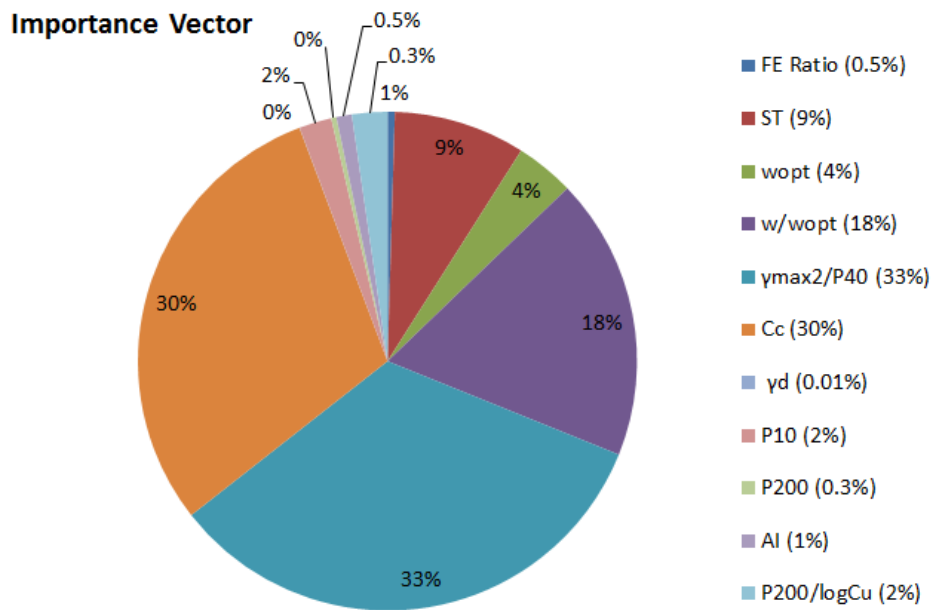


Figure 4.9 Relative Contributions of Various Variables to Resilient Modulus (M_R)

4.5.4 Sensitivity of Variables to the Reliability Index

The relative contribution of each variable can be examined by comparing the magnitude of γ^2 . Figure 4.10 shows that γ_{\max}^2 / P_{40} has the most important contribution to resilient modulus behavior, followed by C_c , ω / ω_{opt} , ST , ω_{opt} , $P_{200} / \log C_u$, and P_{10} . The contributions of $FE Ratio$, γ_d , P_{200} , and AI were found to be insignificant as compared to others.

A sensitivity analysis was used to quantify the effect of the variability of the parameters of those different random variables included in the analysis. This was done by taking the partial derivative of the reliability index β , with respect to the parameters considered. The results as summarized in Table 4.13 showed that the resilient modulus behavior is most sensitive to the variability in C_c and ω / ω_{opt} .

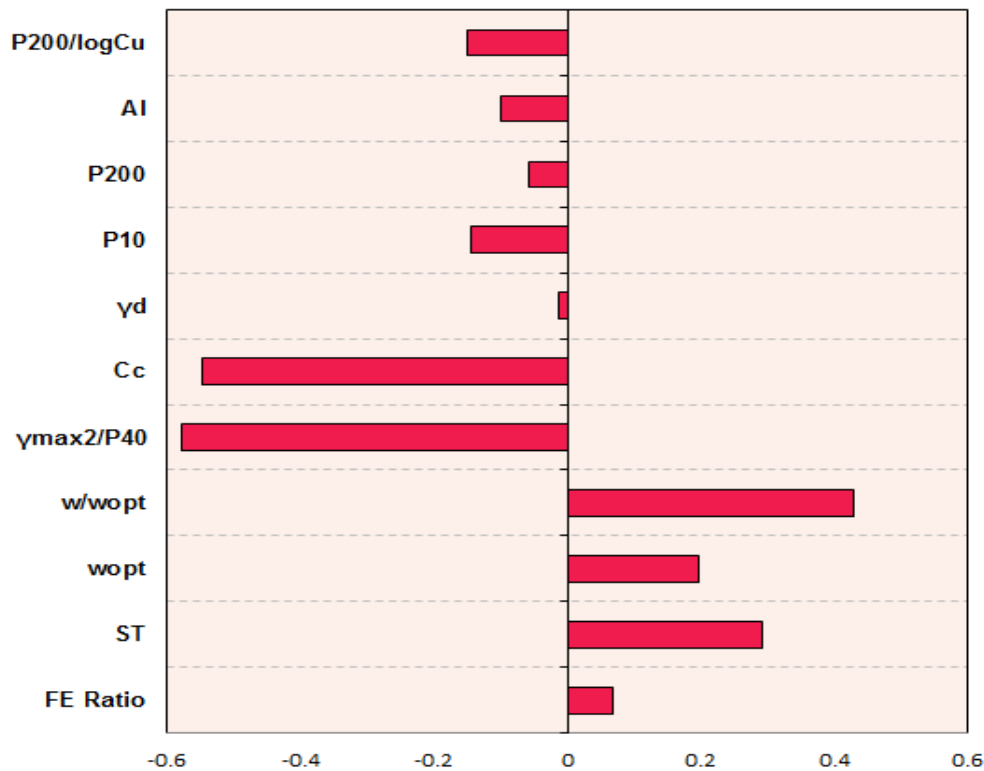


Figure 4.10 The Relative Contribution of Each Variable to Resilient Modulus (M_R)

Table 4.13 Sensitivity of Variables Studied with the Reliability Index

Variable	Sensitivity with respect to Mean	Sensitivity with respect to Standard Deviation
$FE\ ratio$	-0.063	0.038
ST	-0.277	0.160
ω_{opt}	-0.144	-0.030
ω / ω_{opt}	-3.261	3.095
γ_{max}^2 / P_{40}	0.002	0.001
C_c	6.636	5.376
γ_d	0.003	0
P_{10}	0.009	0.003
P_{200}	0.034	-0.010
AI	0.002	0.001
$P_{200} / \log C_u$	0.141	0.031

4.6 Mechanistic-Empirical Evaluation of Aggregate Quality Affecting Flexible Pavement Performance

The main objective of this section was to investigate effects of unbound aggregate layer characteristics (i.e., material quality affecting modulus input and layer thickness) on conventional flexible pavement performances predicted from a layer elastic program, MnPAVE. It is expected that the findings will help verify the current understanding of pavement performance and assist design engineers in selecting better and more appropriate strategies including the optimized use of locally available aggregate materials in pavements in order to achieve cost-effective and satisfactory pavement performance.

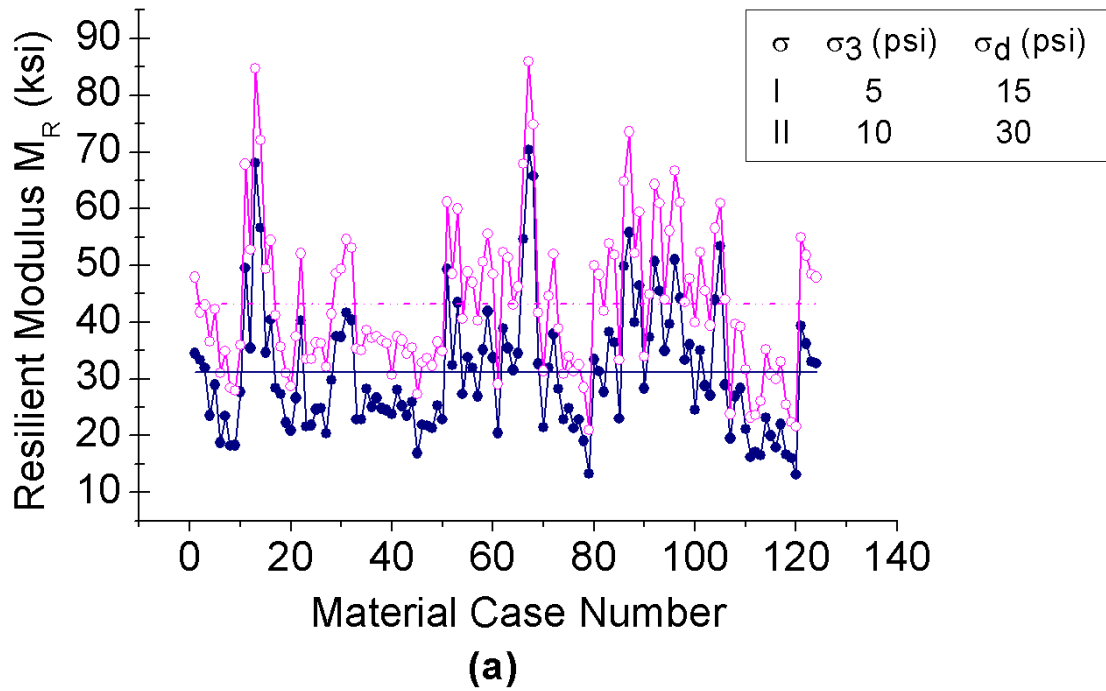
A comprehensive mechanistic analysis matrix was carefully designed with various scenarios considering pavement structure and climatic effects. Two mechanistic aggregate inputs, i.e., resilient modulus and peak deviator stress at failure, were used to uniquely characterize the approximately 376 different Minnesota aggregates considered for quality ranges in the sensitivity analyses. The MEPDG stress-dependent M_R models were used to identify k_1 - k_2 - k_3 model parameters associated with high, medium and low M_R levels of representative aggregate materials, i.e., MnDOT Class 5 and 6 materials for aggregate base and Class 3 and 4 materials for granular subbase from MnDOT laboratory-tested M_R database. Using the MEPDG stress dependent models, the GT-PAVE nonlinear finite element (FE) program predicted modulus distributions in the base and subbase layers. Averaging the moduli along the load axis throughout each layer depth established equivalent single M_R values in base and subbase for subsequent input into MnPAVE program so that fatigue and rutting life expectancies could be studied.

4.6.1 Representative Aggregate Quality Levels

According to the literature review, classifying unbound aggregates into different quality levels by mechanistic means requires the simultaneous examination of resilient modulus and permanent deformation behavior; the second linked to shear strength properties. Provided that the MEPDG M_R model is selected to characterize the nonlinear stress-dependent behavior of unbound aggregate materials, the corresponding M_R model parameters k_1 - k_2 - k_3 then can be assigned based on material quality. If one combination of parameters k_1 - k_2 - k_3 results in the greatest calculated M_R value for any predetermined stress level, then the aggregate material from which this combination was determined would most probably have the highest quality level in terms of resilient behavior; however, in order to avoid potential exceptions, permanent deformation behavior and shear strength properties should also be checked to confirm these levels identified according to M_R values. As compared to the cohesion “ c ” and friction angle “ ϕ ” which may not be consistent when individually compared, the peak deviator stresses at failure can be used to consistently compare shear strength characteristics of different aggregate samples. Note that the three representative aggregate materials with high, medium, and low modulus results were selected from a pool of 124 Class 5 and 6 aggregate base materials and 64 Class 3 and 4 granular subbase materials. As illustrated in Figure 4.11(a) and (b), two typical stress levels were chosen associated with field unbound aggregate base and granular subbase conditions, respectively, and the averaged M_R values are also shown for each stress level.

The selected M_R model parameters k_1 - k_2 - k_3 for the three modulus/quality levels are listed in Table 4.14 for the MEPDG and Uzan (1985) characterization models. The particle size distributions of those selected aggregate materials and the MnDOT gradation specifications for different material classes are shown in Figure 4.12. Note that similar aggregate gradations shown in Figure 4.12 may have in fact significant differences in mechanical properties as

depicted from Table 4.14. Further, the peak deviator stresses at failure for those selected unbound base and subbase materials, also listed in Table 4.14, confirm the representative quality levels assigned from resilient moduli. In other words, higher peak deviator stresses at failure are associated with higher calculated M_R values to adequately represent high, medium, and low quality levels.



● Stress State I ○ Stress State II
— Average I - - - Average II

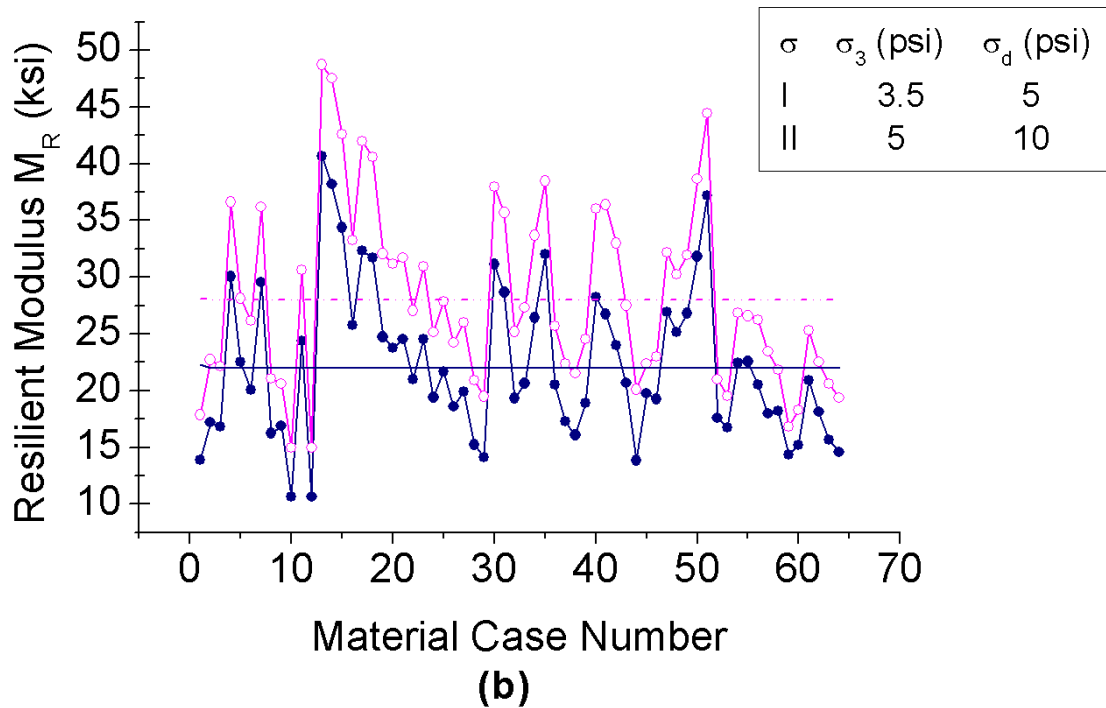


Figure 4.11 Computed Resilient Moduli for Different Unbound (a) Aggregate Base and (b) Granular Subbase Materials (1 psi = 6.89 kPa)

Table 4.14 Characterization of Representative Aggregate Base and Granular Subbase Materials

Material Properties		Quality Level					
		Aggregate Base			Granular Subbase		
		High	Medium	Low	High	Medium	Low
MEPDG Model Parameters*	K ₁	4.716	1.817	0.620	3.195	1.621	0.724
	K ₂	1.042	0.924	1.022	0.711	0.624	0.795
	K ₃	-1.855	-0.959	-0.895	-1.226	-0.593	-0.289
	R ²	0.740	0.830	0.972	0.606	0.943	0.993
Uzan Model Parameters**	K ₄ (psi)	8360.71	4537.26	1259.31	12526.46	6898.65	1707.14
	K ₅	1.223	0.943	1.022	0.778	0.628	0.782
	K ₆	-0.846	-0.455	-0.432	-0.535	-0.271	-0.140
	R ²	0.76	0.89	0.93	0.72	0.91	0.99
Peak Deviator Stress (psi) @ 4-psi Confining Pressure		115	81	56	61	47	37
Achieved Dry Density (pcf)		135.3	130.2	130.6	119.3	125.4	129.0
Max. Dry Density*** (pcf)		133.0	127.4	131.1	124.3	126.2	127.7

Notes: *MEPDG Model: $M_R = K_1 P_a \left(\frac{\theta}{P_a} \right)^{K_2} \left(\frac{\tau_{oct}}{P_a} + 1 \right)^{K_3}$;

** Uzan Model: $M_R = K_4 \left(\frac{\theta}{P_0} \right)^{K_5} \left(\frac{\sigma_d}{P_0} \right)^{K_6}$

*** AASHTO T180; (1 psi = 6.89 kPa, 1 pcf = 0.157 kN/m³)

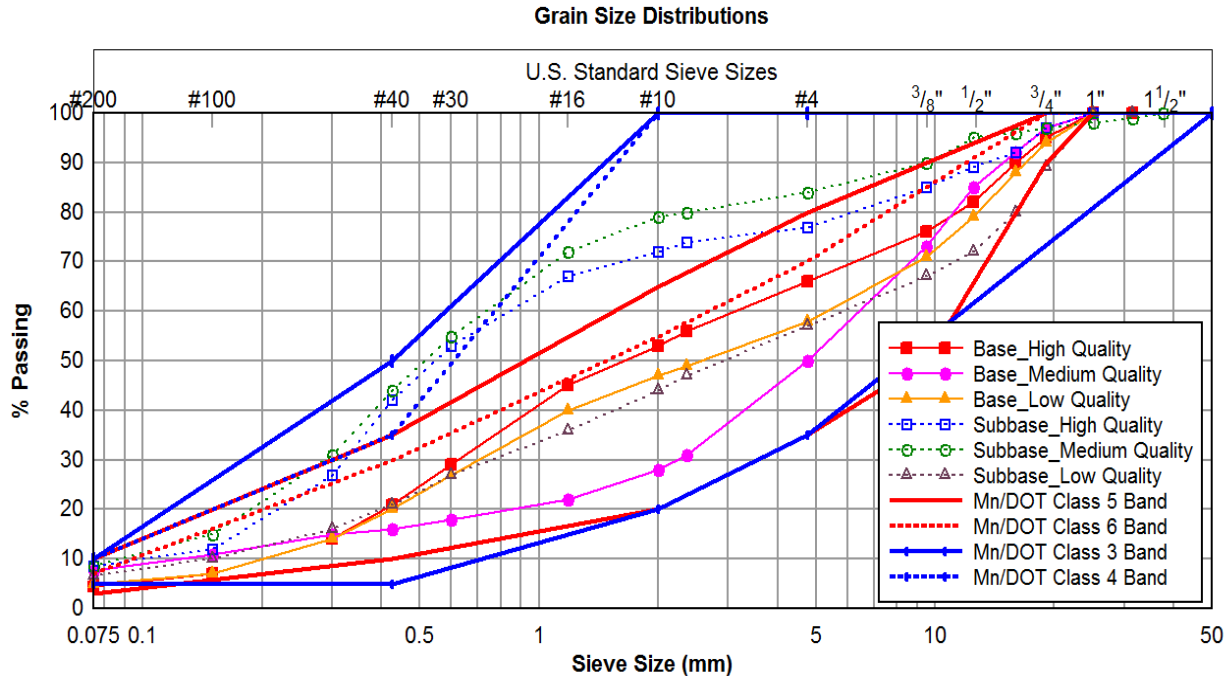


Figure 4.12 Gradations of Representative Aggregate Base and Granular Subbase Materials

4.6.2 Sensitivity Analysis Matrix

To better evaluate the effects of various design features and site factors on predicted pavement performance, a full factorial sensitivity matrix was designed for MnPAVE analysis and design. The variables considered in the full factorial are listed in Table 4.15. Since the environmental conditions may have a significant effect on the performance of conventional flexible pavements, two representative climate zones in Minnesota, i.e., Beltrami County in north and Olmsted County in south, were selected. Different pavement sections were also analyzed to represent a wide spectrum of structural designs. Since the main goal was to investigate effects of unbound aggregate quality and layer thicknesses on pavement performance, the unrealistic pavement design alternatives, which might be found in the developed sensitivity analysis matrix, were not specifically excluded from the mechanistic analyses. Both aggregate base and granular subbase layers were modeled as nonlinear isotropic materials using the MEPDG resilient

modulus models. The asphalt concrete surface layer using PG58-34 binder and the subgrade, however, were simplified as linear elastic materials. It is worth noting that the elastic modulus of asphalt concrete layer was taken from the default value in MnPAVE program; and that the elastic modulus of natural subgrade was taken as 50 percent of that of engineered subgrade. A total number of 2,592 pavement section combinations were analyzed.

Table 4.15 Input Values for All the Variables Used in the Sensitivity Analysis

Input Category	Input Variables		Number of Variables
Climate Zones	Beltrami and Olmsted		2
Design Traffic Volume (20-year ESALs in Millions)	0.2, 0.6, 1.5, 3, and 6		5
Asphalt Concrete (AC) Layer	Type of Asphalt Binder	PG58-34	1
	Layer Thickness (in.)	4, 6, and 8	3
Aggregate Base Layer	Quality Levels	Low, Medium, and High quality Class 5/6	3
	Layer Thickness (in.)	3, 6, 9, and 12	4
Granular Subbase Layer	Quality Levels	Low, Medium, and High quality Class 3/4	3
	Layer Thickness (in.)	6, 12, and 18	3
Engineered Subgrade Layer	Elastic Modulus (ksi)	2, 4, 7, and 10	4
	Layer Thickness (in.)	12, and 36	2

Notes: 1 ksi = 6.89 MPa; 1 in. = 25.4 mm.

4.6.3 GT-PAVE Structural Finite Element Modeling

The Uzan base/subbase models were employed in GT-PAVE finite element (FE) program (described in Chapter 2) for the characterization of the unbound aggregate base and granular subbase layers. The GT-PAVE FE mesh designed consisted of 780 isoparametric eight-node quadrilateral elements used to analyze each pavement section consistently with the same mesh in the sensitivity matrix. The FE mesh used and the typical distributions of predicted stress dependent moduli in both aggregate base and granular subbase layers are illustrated in Figure 4.13(a) for one pavement section studied out of 2,592 analyses.

The single wheel load of 9 kip (40 kN) was applied as a uniform pressure of 80 psi (552 kPa) over a circular area of radius 6 in. (152 mm). The Poisson's ratios for asphalt concrete, unbound aggregate base/granular subbase, and engineered/natural subgrade were taken as 0.3, 0.4, and 0.45, respectively. The MnPAVE default elastic modulus of 490 ksi (3,380 MPa) in the Fall season was used for the PG58-34 asphalt concrete. The equivalent single M_R values for the aggregate base/granular subbase to be used in subsequent linear elastic MnPAVE analyses were obtained by averaging moduli throughout each layer depth from the elements located at the load axis. The results of such equivalent M_R values linked to high, medium and low aggregate quality levels are presented in Figure 4.14. Note that the equivalent M_R value associated with each quality level was averaged from all the pavement sections studied in the sensitivity matrix. It is worth noting that in some cases the granular subbase material had much larger moduli than the aggregate base (see Figure 4.14).

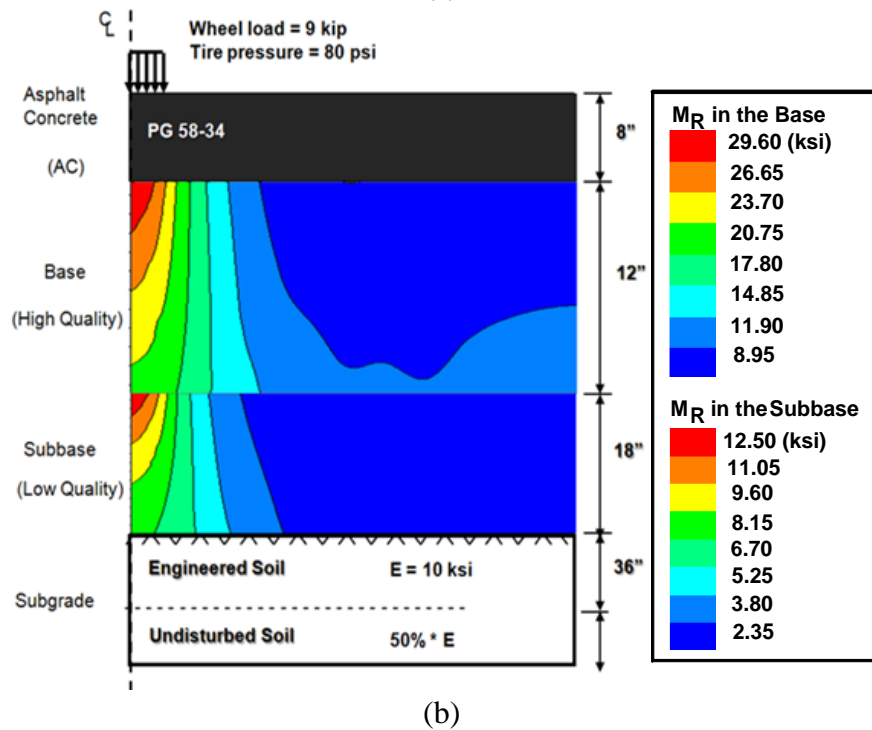
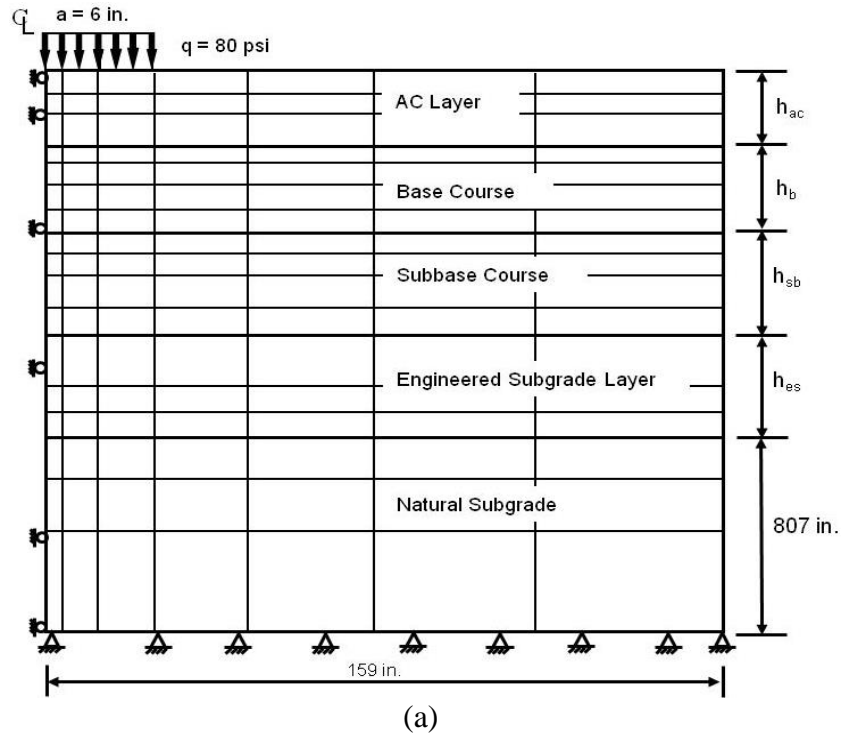


Figure 4.13 Illustrations of GT-PAVE (Not to Scale): (a) Finite Element Mesh of Pavement Structure, and (b) Predicted Modulus Distributions in the Base and Subbase

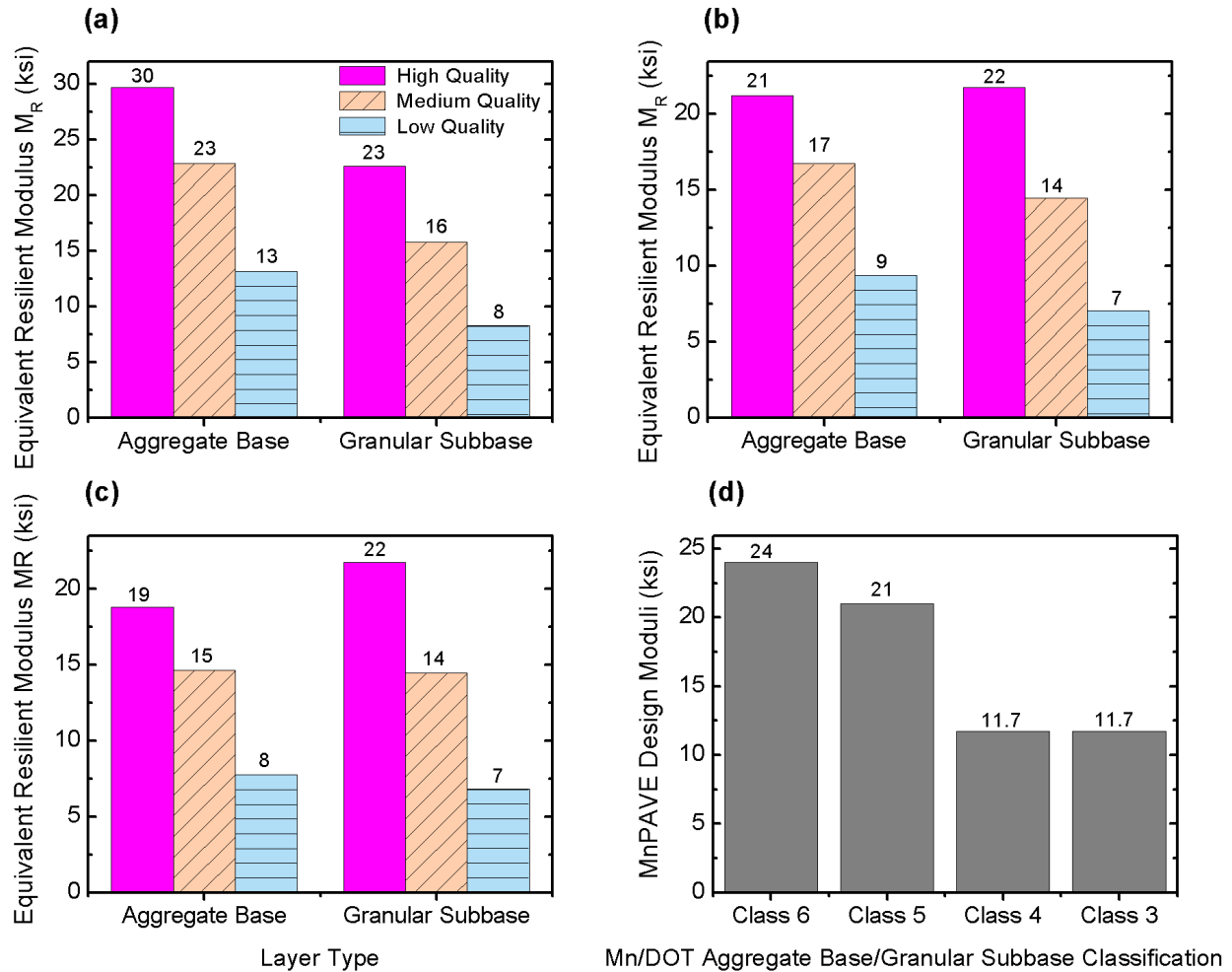


Figure 4.14 Equivalent M_R Values Linked to Aggregate Quality for (a) 4-in., (b) 6-in., (c) 8-in. Asphalt Surface Thicknesses, and (d) Current Default MnPAVE Fall Design Moduli

The nonlinear FE program GT-PAVE predictions were a key step for establishing the single equivalent M_R values for the high (H), Medium (M) and low (L) modulus levels of aggregate base and granular subbase as shown in Figure 4.14. Those equivalent M_R values, assumed to closely represent the related H, M, and L material quality standards, were subsequently input during MnPAVE analyses to calculate fatigue and rutting life expectancies. The MnPAVE program was run for all 51,840 combinations with each run generating an Excel spreadsheet file including the damage details. The major damage indicators are fatigue life,

rutting life, fatigue damage ratio, and rutting damage ratio, though other distress indicators including International Roughness Index (IRI), alligator cracks (% of length), and rutting ≥ 0.5 in. (% of length) can also be predicted using empirical regression equations. In this section, pavement performance is mainly referred to rutting life and fatigue life, and the effects of various variables on rutting life and fatigue life were identified using the results from the cases studied.

4.6.4 Effect of Aggregate Quality on Fatigue Life Performance

Figure 4.15 shows pavement fatigue lives predicted according to the five design traffic levels studied for each base/subbase quality combinations in Beltrami and Olmsted Counties. The standard pavement structure consisted of 4-in. (102-mm) asphalt concrete surfacing over 12-in. (305-mm) of base and 12-in. (305-mm) of subbase over a 12-in. (305-mm) engineered subgrade ($E = 2$ ksi or 14 MPa) considered in Beltrami and Olmsted Counties. For low traffic designs, less than 0.6 million equivalent single axle loads (ESALs), base and subbase quality is less important for achieving 20-year fatigue and rutting performance lives, even in the case of 4-in. (102-mm) thick asphalt concrete surfacing (see Figure 4.15). For low-volume roads, using locally available and somewhat marginal materials may therefore be quite cost-effective. However, for traffic designs greater than 1.5 million ESALs, aggregate material quality becomes quite critical for the fatigue performance.

With regard to the two climate zones studied, a move from Beltrami County in the north to Olmsted County in south Minnesota brings the following seasonal changes into pavement analysis and design: (i) lower winter temperatures, (ii) lower summer temperatures, and (iii) longer winter and shorter summer durations. The main effect of this change is expected to be on asphalt pavement surface temperatures and accordingly on fatigue performances, which was also supported by the similar results for the case of Olmsted County (see Figure 4.15b).

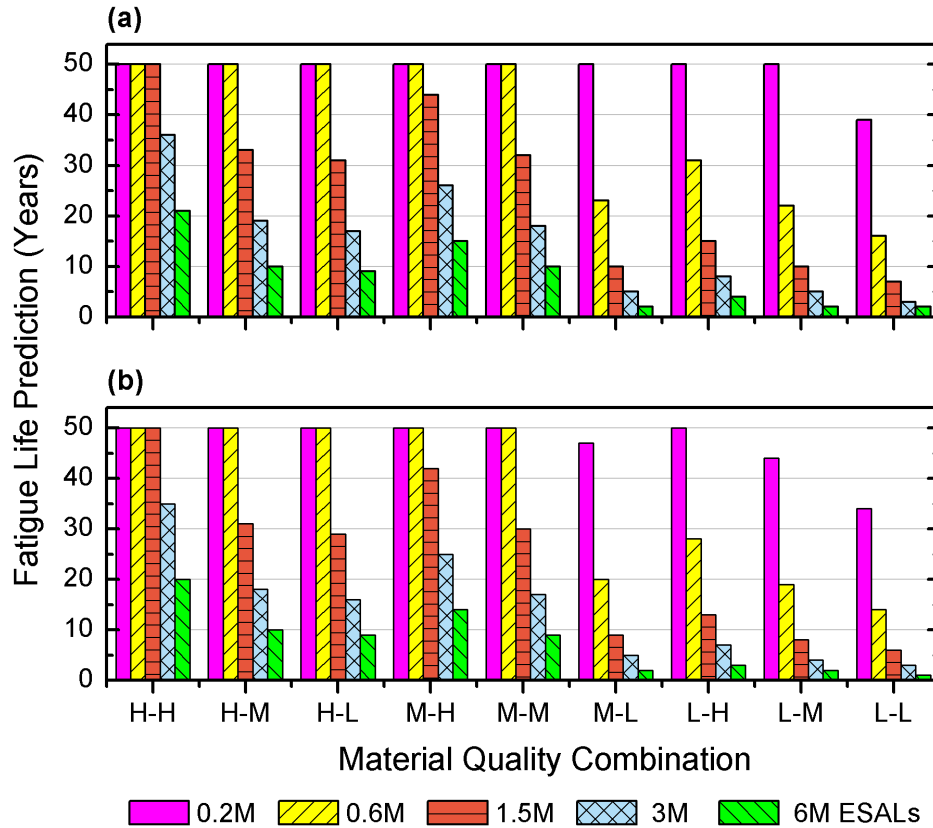


Figure 4.15 Fatigue Life Predictions For Different Base-Subbase Qualities: (a) Beltrami County, and (b) Olmsted County (M-L Stands for Medium Quality Base and Low Quality Subbase)

The effect of unbound aggregate quality on pavement fatigue life prediction is further illustrated in Figure 6 for the case of Beltrami County. Figure 6 shows the percentages of pavement sections (y-axis) having service lives greater than a certain target performance life (x-axis). Important conclusions can be drawn from Figure 6 in terms of overall fatigue life, using high (H) quality base and low (L) quality subbase material combinations does not make any significant difference from the use of low quality (L) base and high (H) quality subbase material combinations; however, a large decrease in fatigue life can be seen when the qualities of base and subbase materials both are changed from high (H) to low (L). Further, the quality of base layer has been found to directly impact fatigue life expectancy. With low quality materials used

in the base, increasing base layer thickness does not seem to improve fatigue life as there is not enough support under the asphalt concrete surfacing to minimize bending under wheel loading.

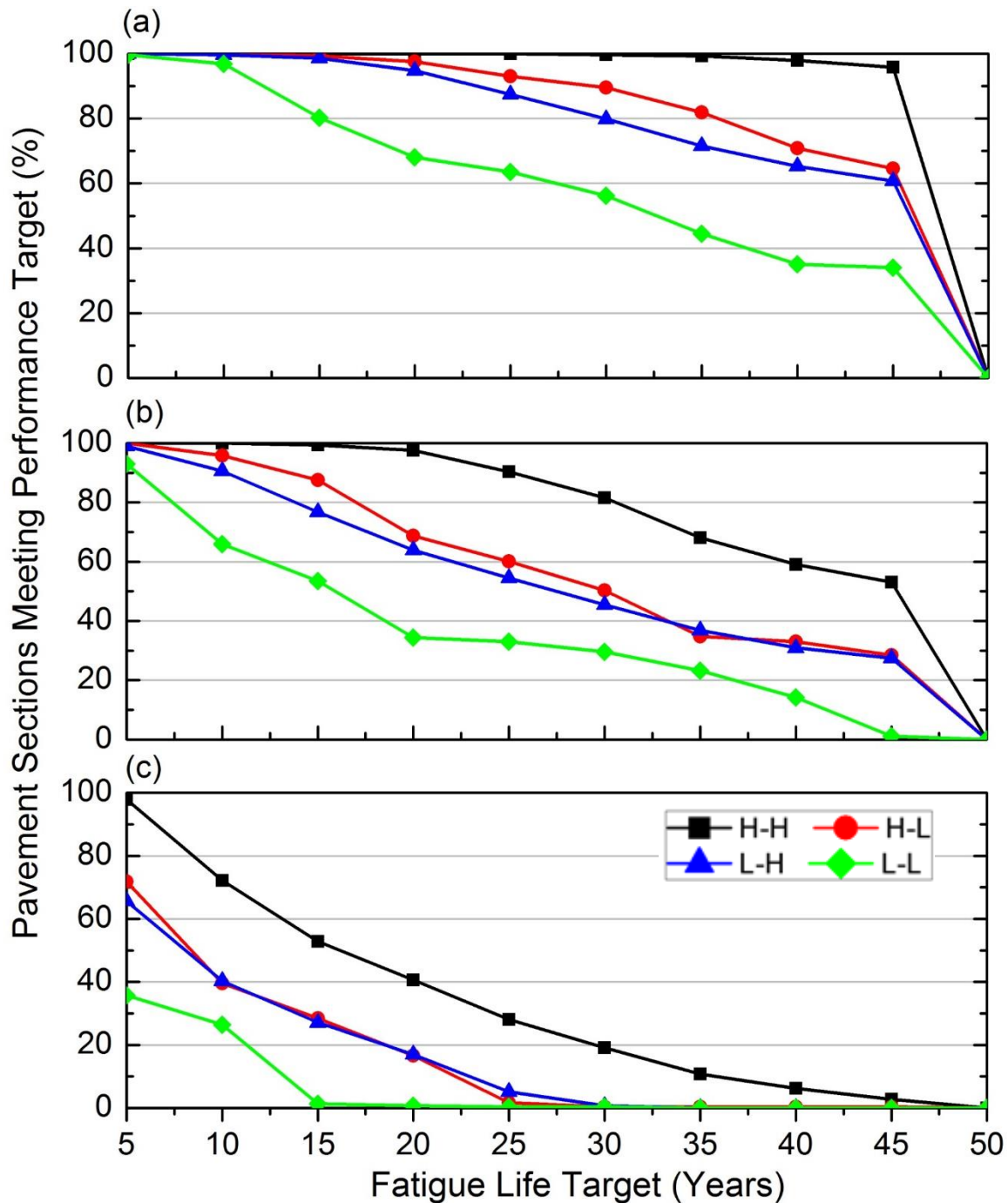


Figure 4.16 Effects of Unbound Granular Material Quality on Fatigue Life for Beltrami County: (a) 0.6 Million ESALs, (b) 1.5 Million ESALs, and (c) 6 Million ESALs (H-L Stands for High Quality Base and Low Quality Subbase)

4.6.5 Effect of Aggregate Quality on Rutting Life Performance

The effect of unbound aggregate quality on pavement rutting life prediction is illustrated in Figure 4.17 for both Beltrami and Olmsted Counties. The standard pavement structure again consisted of 4-in. (102-mm) asphalt concrete surfacing over 12-in. (305-mm) of base and 12-in. (305-mm) of subbase over a 12-in. (305-mm) engineered subgrade ($E=2$ ksi or 14 MPa) considered in Beltrami and Olmsted Counties. For this pavement structure with the thinnest asphalt concrete thickness (4 in. or 102 mm), pavement rutting life decreases as the quality standards of base and subbase layers decrease from the high (H) to low (L), indicating stiff granular layers are required to maintain structural integrity and protect subgrade.

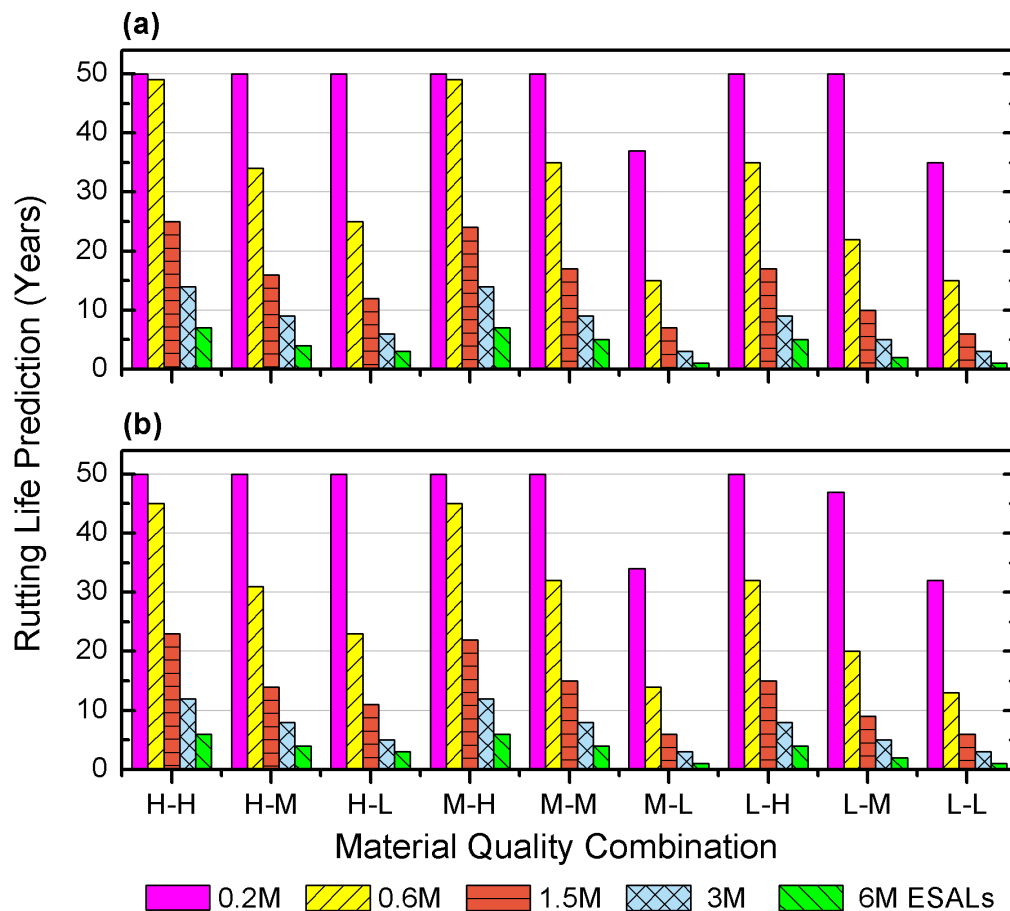


Figure 4.17 Rutting Life Predictions for Different Base-Subbase Qualities in (a) Beltrami and (b) Olmsted Counties (M-L Stands for Medium Quality Base and Low Quality Subbase)

It can be seen from Figure 4.18 that, if the aggregate base quality decreases from high (H) to low (L), its effect on rutting performance is almost negligible for any traffic designs from 0.6 million to 6.0 million ESALs. Whereas, if a similar high (H) to low (L) quality drop is observed in the subbase, the rutting life is shortened more rapidly. Such a difference in the subbase behavior has been proven to be statistically significant when all the sensitivity results were analyzed. Accordingly, a high quality, stiff subbase exhibits a bridging effect to better protect the subgrade and offset some of the detrimental effects of low base stiffness, and as a result, the quality of base materials becomes less important. Note that this is the same concept as utilized in the South-African “Inverted Pavement” designs, which often use a cement-stabilized subbase over soft soils to effectively protect the subgrade while providing a very stiff underlying layer for the base course above, which enables compaction of aggregate base materials in excess of 100% Proctor densities.

The comparison between Beltrami and Olmsted County results revealed a less significant effect of climate on rutting performance, which might be attributed to a constant seasonal pore suction resistance factor of 1.0 used in these MnPAVE analyses.

4.6.6 Statistical and Sensitivity Analyses

The effects of different base and subbase material quality combinations on fatigue and rutting life predictions were statistically confirmed in the form of the notched box plots which compare two median values differing at the 95% confidence level and also from one-way Analysis of Variance (ANOVA). According to the statistical analysis results, the granular subbase material quality makes a significant difference/impact on both predicted fatigue and rutting lives even for low quality aggregate base; however, aggregate base quality is primarily related to pavement fatigue performance.

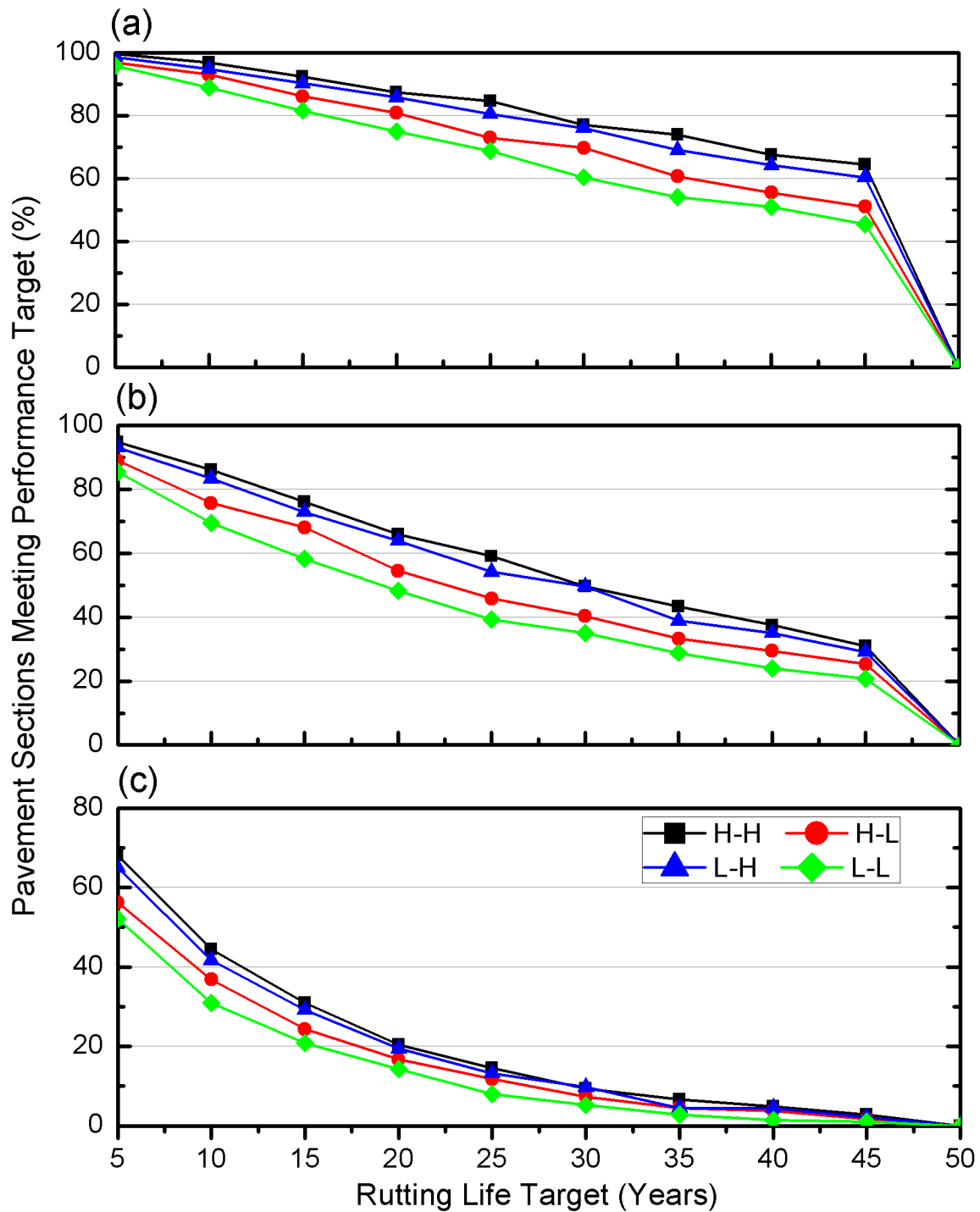


Figure 4.18 Effects of Unbound Granular Material Quality on Rutting Life for Beltrami County: (a) 0.6 Million ESALs, (b) 1.5 Million ESALs, and (c) 6 Million ESALs (H-L Stands for High Quality Base and Low Quality Subbase)

From the sensitivity analyses the following general observations can also be made. Both fatigue and rutting life performances improve as asphalt concrete (AC) thickness increases, with higher fatigue performance and less rutting performance improvements expected for AC thickness increasing from 6 in. to 8 in. (152 mm to 203 mm) than from 4 in. to 6 in. (102 mm to 152 mm). Increasing aggregate base thickness may also result in longer fatigue life and significantly improved subgrade rutting life performance. For the same AC thickness, the rutting life performance increases considerably with increasing aggregate base thickness; and for the same AC and aggregate base thicknesses, the rutting life performance increases with increasing subgrade stiffness. Interestingly, increasing granular subbase thickness seems to significantly improve both rutting and fatigue performances. As compared to fatigue performance, rutting performance can benefit much more from an increase in granular subbase thickness. As expected, a stronger engineered subgrade contributes significantly to improved rutting performance.

4.7 Summary

This chapter presented the establishment of regression based correlations between aggregate source properties and aggregate M_R data archived through modulus testing at the laboratories of MnDOT and University of Illinois for identifying mechanistic design moduli ranges of locally available materials in MEPDG Level 2 type pavement design applications. The effects of both stress sensitivity and seasonal variations were captured using the MEPDG M_R model with three model parameters, i.e., k_1 , k_2 , and k_3 . Aggregate shape properties measured from the University of Illinois Aggregate Image Analyzer (UIAIA) and quantified through shape indices were also included in the study to improve developed correlations. The results showed a good correlation between aggregate shape properties and resilient modulus existed. Aggregates with high angularity index (AI) and surface texture (ST) properties were found to have greater

resilient moduli in comparison to aggregates with low AI and ST values (i.e., rounded particles with smooth surface texture). Interestingly, rounded aggregates exhibited a well-defined peak shear strength behavior, which could be influenced by their gradation properties and achieved specimen densities. The findings in this study also demonstrated that unbound aggregate resilient modulus properties should not be used alone to characterize aggregate base course performance mainly governed by rutting potential in the field. Laboratory permanent deformation tests should be conducted for evaluating rutting performances of unbound base/subbase courses.

Monte Carlo type simulations and the FORM analysis were performed to assess the sensitivities of M_R at given stress states to aggregate source properties. The detrimental effect of excessive moisture within pavement layers was also confirmed from the Monte Carlo simulation. The currently used aggregate base/granular subbase design moduli in MnPAVE Minnesota DOT mechanistic analysis and design program for the standard fall season were compared with the simulated M_R distributions, and the design reliability of at least 85% was achieved for the selected conventional flexible pavement structure with aggregate base and granular subbase.

FORM analysis was performed using FERUM program based on the developed model for estimating M_R . The importance vector and the sensitivity of reliability index with respect to distribution parameters of different variables were investigated. It was concluded that the complex maximum dry density (γ_{\max}^2 / P_{40}), coefficient of curvature (C_c), and relative moisture content ratio (ω / ω_{opt}) have the most important contributions to the resilient modulus behavior, and that the resilient modulus behavior is most sensitive to the variability in the distribution of coefficient of curvature (C_c) and relative moisture content ratio (ω / ω_{opt}). Future work is needed to refine the distributions of those aggregate source property variables provided that more data are available; moreover, the significant negative correlations existing between several variables

caused problems when running FERUM program, leading to the slight modification of those correlation coefficients. This issue will also need to be looked into in more detail.

A methodology used to investigate effects of unbound aggregate quality on conventional flexible pavement performance was also demonstrated. A comprehensive matrix of conventional flexible pavement layer thicknesses and mechanistic design moduli was carefully designed. The type and quality of unbound aggregate materials were represented by the resilient modulus (M_R). Three representative sets of the MEPDG stress-dependent M_R model parameters, k_1 , k_2 , and k_3 , were selected for the aggregate base and granular subbase layers from the MnDOT laboratory-tested M_R database. The nonlinear finite element (FE) program GT-PAVE was then used to determine the single equivalent M_R values for the aggregate base and granular subbase by averaging layer moduli distributions computed for the elements in the nonlinear GT-PAVE FE analyses. Those equivalent M_R values, assumed to closely represent the related H, M, and L material quality standards, were subsequently input during MnPAVE analyses to calculate fatigue and rutting life expectancies for the comprehensive matrix of pavement structures considered.

For low-volume roads, using locally available and somewhat marginal materials may be quite cost-effective provided that the 20-year design traffic level would not exceed 1.5 million ESALs. For traffic designs greater than 1.5 million ESALs, aggregate material quality becomes quite critical for the fatigue and rutting performance. To consider structurally sound and cost-effective design alternatives, base and subbase aggregate quality standards should be linked to mechanistic-empirical evaluation of satisfactory pavement performance. For example, a high quality, stiff granular subbase was found to exhibit a bridging effect that better protected the subgrade and offset some detrimental effects of low aggregate base stiffness on rutting

performance. As a result, the use of marginal quality locally available materials as aggregate base materials could be justified in some cases. The conclusions, which are subject to further validation using field performance data prior to implementation, pertain to aggregate base and granular subbase materials used in Minnesota and the local climatic conditions.

Chapter 5 Experimental Investigation of Aggregate Packing Affecting Shear Strength of Unbound Aggregates

Establishing robust linkages between gradation and satisfactory unbound aggregate mechanical behavior is essential for the development of performance based gradation specifications. The analytical gradation measures can quantify the change in performance of a given aggregate material within specified gradation bands leading to optimized gradation zones for desirable mechanical and hydraulic performance based on site-specific traffic and environmental conditions, respectively. This chapter presents an aggregate gradation mechanism based on the proportionality between gravel and sand size particles (as per ASTM D2487-11) to demonstrate how mechanical behavior, i.e., shear strength and resilient modulus (M_R) characteristics, of aggregate base/granular subbase materials can be quantified and related to grain size distributions. A secondary goal is to also demonstrate that there is no unique relationship between modulus and shear strength properties as obtained from analyzing a comprehensive aggregate database established from a variety of sources in Minnesota, and further, the actual field rutting performance of an unbound aggregate base/granular subbase is primarily linked to the shear strength but not the modulus characteristics.

5.1 Different Gradation Designs Studied in the MnDOT Aggregate Database

The database provided by MnDOT (as presented in Chapter 3) includes various types of aggregates ranging from “standard” gravel (pit-run), limestone, granite and select granular materials to “non-standard” taconite tailings (a waste mining material), reclaimed asphalt pavement (RAP) and reclaimed concrete aggregates (RCA) blended with virgin aggregates at different blending ratios, and materials recovered from full-depth reclamation (FDR) sites. All

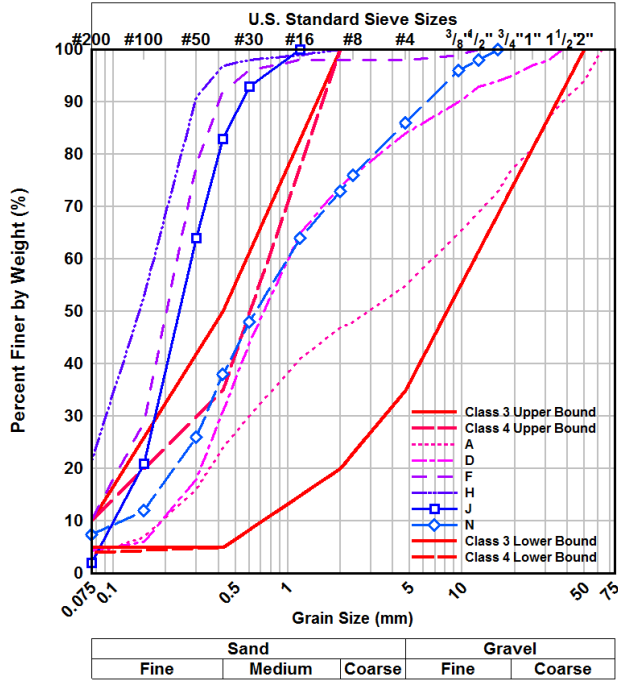
the materials were collected from road construction sites in Minnesota for testing at the MnDOT Office of Materials and Road Research laboratories and/or MnDOT's contracting agencies/universities using consistent quality control procedures.

Figure 5.1 and Figure 5.2 present the grain size distributions of these materials in relation to corresponding aggregate base/granular subbase gradation bands. Grouping them according to rock type and mineralogy is to minimize the confounding effects that aggregate shape properties (form, texture and angularity), which have been demonstrated to be quite influential (Xiao et al., 2011), have on analyses of gradation. It appears that quarried limestone and granite materials have much less variability in gradation than the others. Proctor compaction tests were performed on the aggregate materials following the AASHTO T99 standard energy with index properties and optimum moisture contents and maximum dry densities determined accordingly. Table 5.1 summarizes other sample details at optimum moisture conditions sorted from the database for subsequent correlation analyses, such as MnDOT specification designations and Nominal Maximum Particle Size (NMPS). The different aggregate top sizes available in the database make it possible to compare the laboratory measured performances of different top-sized gradations.

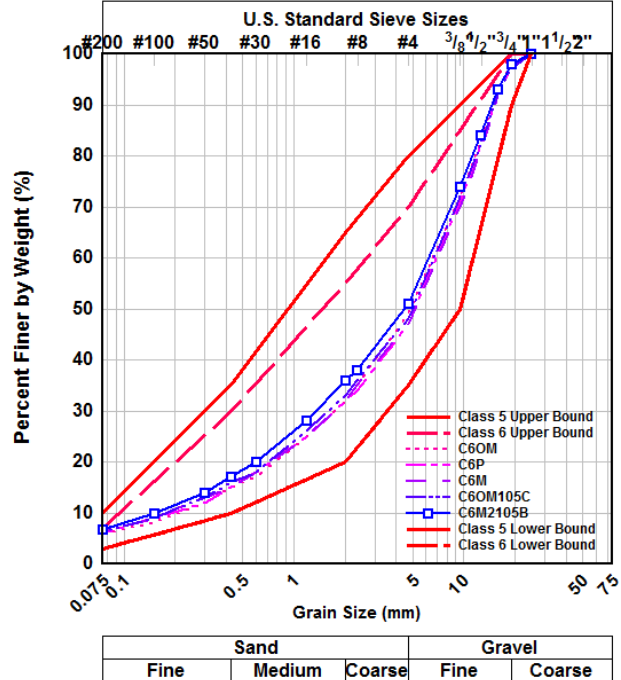
Resilient modulus (M_R) tests were conducted on compacted specimens following the NCHRP 1-28A protocol. After completion of M_R tests, specimens were typically loaded to failure at constant confining pressures (σ_3) ranging from 4 to 10 psi (see Table 5.1) using a constant loading rate of 0.03 in./s (0.76 mm/s) to obtain the peak deviator stress (σ_{df}) values. Note that such shear strength tests performed after the completion of the repeated-load resilient modulus sequences were conditioned and thus included the effect of stress history as compared to unconditioned ones. The resilient modulus results of this database were analyzed in Chapter 4

to establish correlations between aggregate source properties and the MEPDG M_R constitutive model parameters for use in Level 2 pavement design applications. Hence, this chapter focuses on the shear strength results to provide much more definite evaluation of base/subbase material quality and performance potential as compared to M_R .

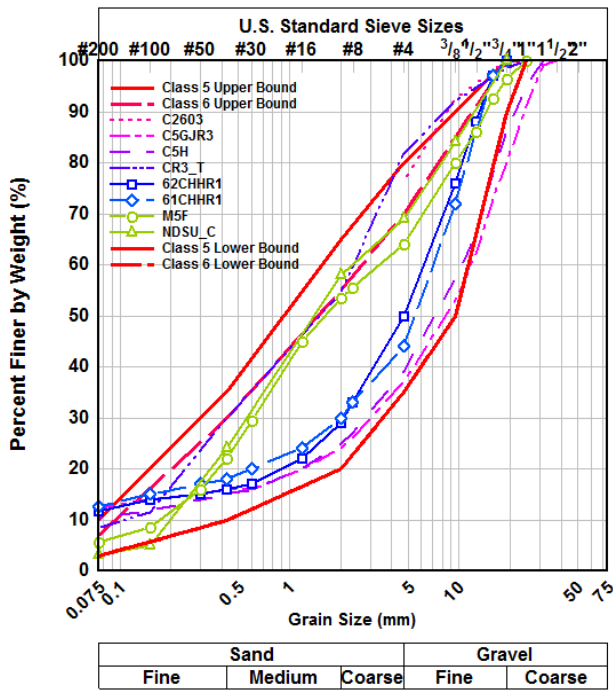
Considering the fact that permanent deformations were not recorded from the conditioning stages of M_R tests and saved in the database, the permanent deformation trends linked to field rutting performances were then indirectly evaluated for these aggregate materials from the peak deviator stresses at failure (σ_{df}) measured at a given confining pressure. The σ_{df} data presented herein are therefore used as an indicator of the aggregate material's shear strength. Tutumluer and Pan (2008) observed good correlations between maximum σ_d at failure (at $\sigma_3=34.5$ kPa or 5 psi) and permanent strains at the 10,000th load repetition for twenty-one unbound aggregate blends in a study of aggregate shape effects. Although the Mohr-Coulomb shear strength parameters, cohesion "c" and friction angle " ϕ ," could be determined for some of the samples, to be consistent, they are not used in the following correlation analyses.



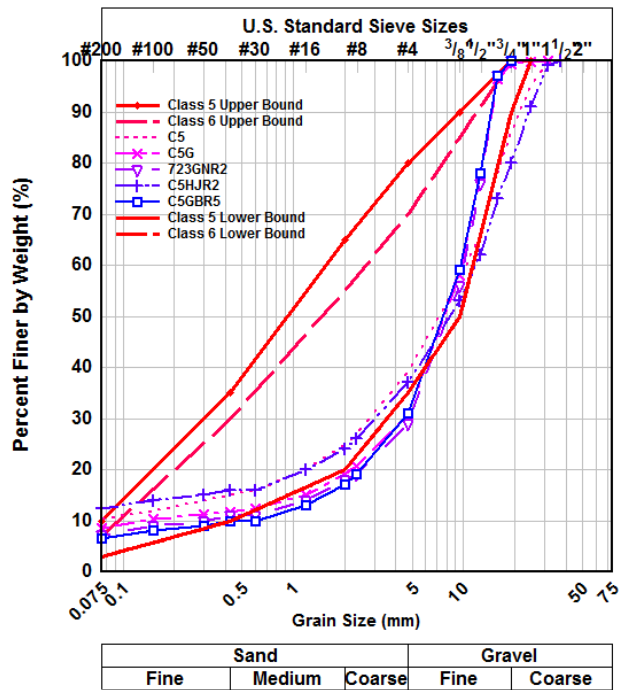
(a)



(b)

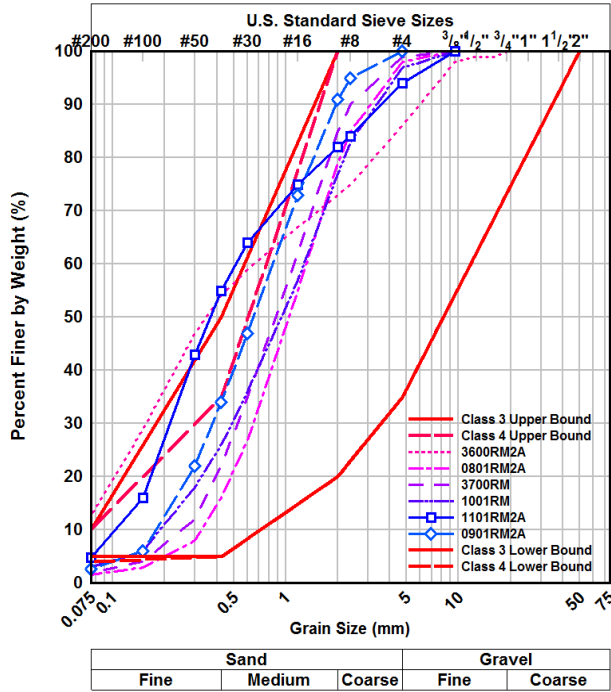


(c)

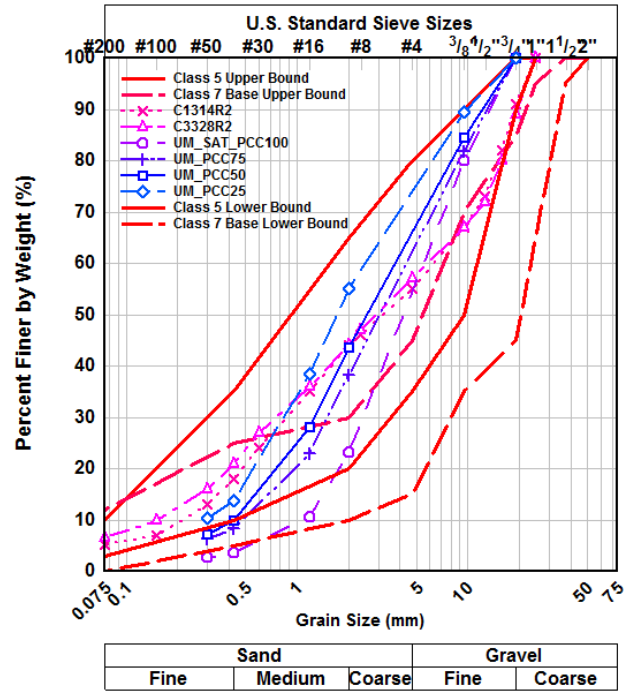


(d)

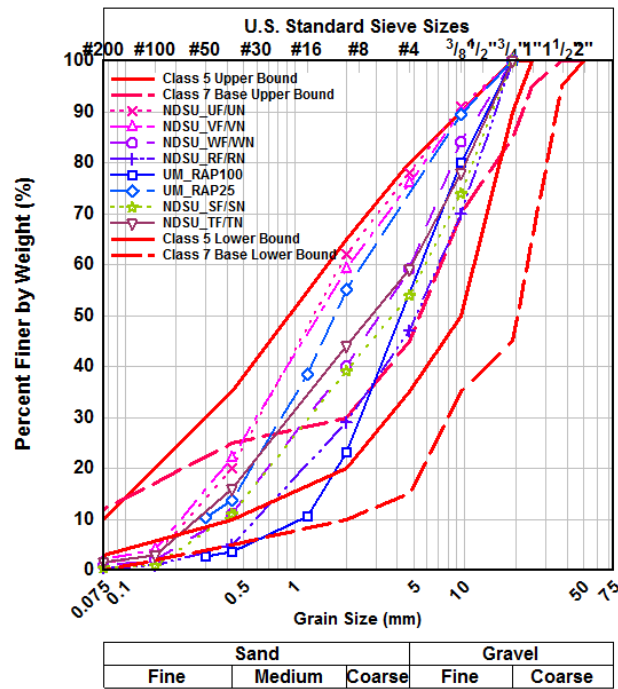
Figure 5.1 Gradations of Traditional Base/Subbase Materials in MnDOT Database: (a) Select Granular; (b) Granite; (c) Pit-run Gravel; and (d) Limestone



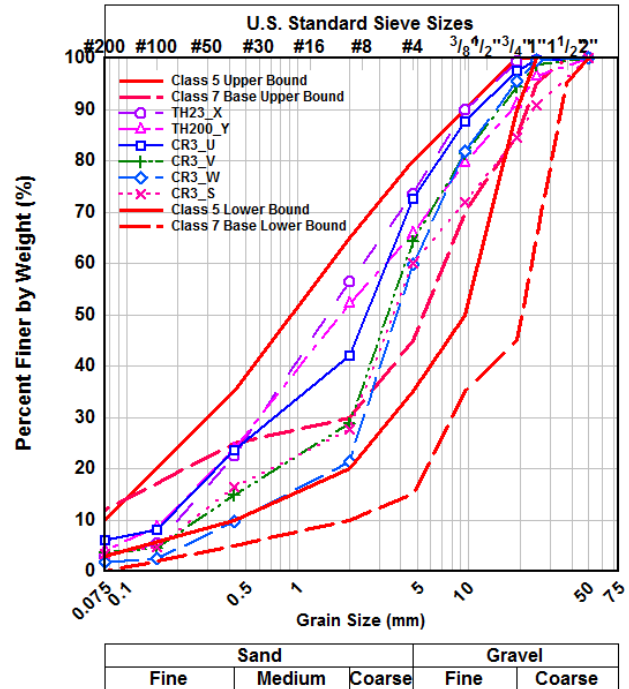
(a)



(b)



(c)



(d)

Figure 5.2 Gradations of Non-traditional Waste Base/Subbase Materials in MnDOT Database: (a) Taconite Tailings; (b) Reclaimed Concrete (Class 7C); (c) Reclaimed Bituminous (Class 7B); and (d) Full-depth Reclamation (FDR)

Table 5.1 Details of the Aggregate Materials Compiled in the MnDOT Database

Material Type		MnDOT Specification	σ_3 for σ_{df} (psi)	NMPS (mm)	Major Gradation Type
“Standard”	Select Granular	Class 3/4	4, 8	0.425, 0.6, 9.5, 37.5	Fine-graded
	Granite	Class 6	4	16	Coarse-graded
	Gravel	Class 5	4, 5, 8, 10	9.5, 16, 19, 25, 31.5	Both
	Limestone	Class 5	4	16, 25, 31.5	Coarse-graded
“Non-standard”	Taconite Tailings	Class 3/4	4	2, 4.75, 9.5	Fine-graded
	Reclaimed Bituminous	Class 7B	4, 5, 8, 10	9.5, 19	Fine-graded
	Reclaimed Concrete	Class 7C	5, 10	19	Fine-graded
	FDR	Class 7	5, 10	19, 25	Fine-graded

Notes: (1) No crushed/fractured particles are allowed for Class 3/4; (2) Class 5 requires at least 10% crushed particles; (3) Class 6 requires at least 15% crushed particles; (4) σ_3 and σ_{df} denote confining pressure and peak deviator stress at failure, respectively; and (5) 1 psi = 6.89 kPa, 1 inch = 25.4 mm.

5.2 Analyses of Experimental Results

5.2.1 Determination of Key Gradation Parameters

To develop correlations between gradation parameters and the resilient modulus and peak deviator stress responses of base/subbase materials, the first step was to establish datasets containing all the independent and dependent variables. It was necessary to eliminate any differences among samples related to compaction moisture and density conditions. This was accomplished by choosing samples with only molded moisture contents within $\pm 0.5\%$ of the targeted optimum, as per the NCHRP 1-28A protocol, for subsequent investigation. This way, samples compared were closely kept at optimum conditions with only gradations varying. It is worth mentioning that all the results presented in this paper were in fact based on the $\pm 1\%$ moisture content criterion, such a trial relaxation of $\pm 0.5\%$ criterion to $\pm 1\%$ increased the sample population but did not change the results and the trends observed in statistical analyses, and, the data included in the analyses were referred to as “near optimum conditions.” Unlike the moisture contents, the achieved dry densities were not found to influence results significantly in this study. The average relative compaction level (achieved dry density over the maximum dry density) was 98.9% with a standard deviation of 3.5% for all the samples tested.

The previously reviewed gradation quantification methods were employed one by one to calculate gradation parameters for all the samples selected; thus, the independent variables considered were: 1) maximum particle size D_{\max} and shape factor n from the Talbot equation; 2) mean aggregate size D_m and spread factor n from the Rosin-Rammler distribution function; 3) uniformity coefficient C_u , curvature coefficient C_c , the fines percentage $\%F$, and the diameter values corresponding to 60, 50, 30, and 10% passing in weights d_{60} , d_{50} , d_{30} , and d_{10} from the USCS, respectively; 4) the Gravel-to-Sand (G/S) ratio; and 5) three aggregate ratios of the Bailey

method aggregate (CA, FA_c, and FA_f). It is worth emphasizing here that the G/S ratios for MnDOT database gradations studied were calculated using Equation 5.1 that was derived from the two parameters of the Talbot equation (D_{\max} and n) fitted from the percent passing data, according to the “Gravel” and “Sand” definitions of the USCS. This way, percentages passing all sieve sizes, but not just No. 4 (4.75-mm) and No. 200 (75- μ m), were used.

$$\frac{G}{S} = \frac{P_{75mm} - P_{4.75mm}}{P_{4.75mm} - P_{0.075mm}} = \frac{1 - \left(\frac{4.75}{D_{\max}}\right)^n}{\left(\frac{4.75}{D_{\max}}\right)^n - \left(\frac{0.075}{D_{\max}}\right)^n} = \frac{(D_{\max})^n - 4.75^n}{4.75^n - 0.075^n} \quad (5.1)$$

5.2.2 Modulus-Strength Relationship

To determine representative aggregate base/granular subbase stress levels, MnPAVE layered structural analyses were performed on typical MnDOT pavement sections, given in Table 4.5, subjected to the 18-kip dual-tire axle loads (ESALs). MnPAVE program default values were assumed for parameters not specified in Table 4.5, which presents the representative stress states computed at mid-depth in the aggregate base and granular subbase, respectively. The representative stress states were needed for calculating base/subbase M_R values using the modulus characterization models reported from laboratory testing of these aggregate materials.

Relationships between modulus and shear strength properties were investigated for different MnDOT aggregate classes. Due to the limited number of datasets selected, the primary objective, however, was to verify if any consistent trends existed between modulus and strength (e.g., high shear strength for high modulus, and vice versa) for each MnDOT aggregate class, as assumed in a previous study on aggregate quality effects (Lindly et al., 1995). Modulus-strength trends for “standard” or conventional aggregate base and granular subbase materials at near

optimum moisture conditions are illustrated in Figure 5.3. The resilient modulus values of base and subbase materials were calculated at the representative stress levels computed at mid-depth base and subbase (as tabulated in Table 4.5), respectively.

As shown in Figure 5.3, for standard high-quality crushed stones, such as granite, high resilient moduli generally correspond to high shear strength properties; while this trend is surprisingly reversed for weak subbase materials such as select granular. Overall, there seems to be no clear and significant modulus-strength relationship for all aggregate materials studied, which is probably due to the fact that the shear strength test is destructive in nature; whereas the M_R test, by contrast, is nondestructive in nature. By testing materials close to maximum dry density and optimum moisture conditions, Thompson and Smith (1990) pointed out that permanent deformation under repeated loading, instead of resilient modulus, was a better and more definite property for ranking granular base performance potential. Bilodeau et al. (2009) tested materials at three water contents (+2% higher than the absorption, near saturation, and drained water contents) and also found that the permanent strain behavior of all source aggregates were related to grain-size properties of the smaller fractions; while the resilient behavior (at saturated water content) depended highly on the grain-size distribution of the gravel (or coarse) fraction for crushed rocks or on the gradation uniformity for partially crushed gneiss. These findings may partly explain the results shown in Figure 5.3, although further in-depth analysis is needed on suction stress which reportedly has different relative effects on resilience and strength. Contrary to the conventional wisdom that the load-carrying capacity of base/subbase materials increases with larger aggregate top sizes, it was observed for the data graphed in Figure 5.3 (although not explicitly shown) that gradations with larger top sizes did not necessarily perform better than those with smaller top sizes in terms of both resilient modulus

and shear strength characteristics, i.e., the top size appears to have no definite effect on resilient modulus and shear strength, as reported by Lindly et al. (1995).

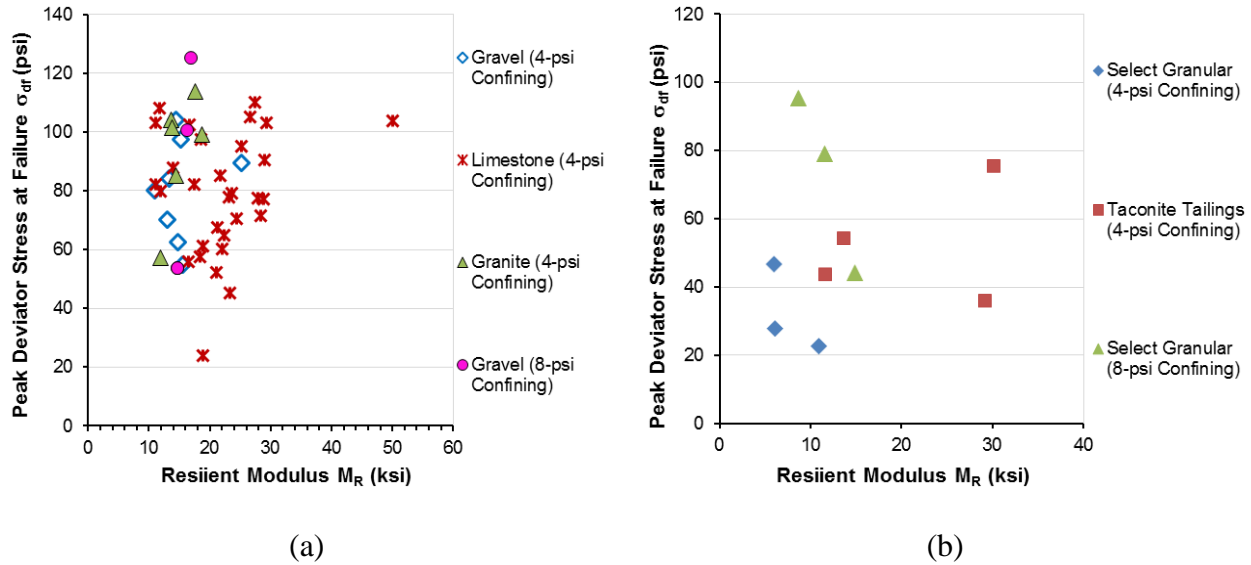


Figure 5.3 Resilient Modulus-Shear Strength Relationships for “Standard” (a) Aggregate Base and (b) Granular Subbase Materials at Near Optimum Moisture Conditions

Based on similar findings, a limiting shear stress ratio (applied shear stress over shear strength) was recommended for implementation in the MnPAVE flexible pavement analysis and design program so that potential rutting performances of aggregate base and especially granular subbase courses in Minnesota could be taken into account. Such an approach would avoid any catastrophic shear failure in base/subbase layer, such as the one reported by Mulvaney and Worel (2002) in Mn/ROAD forensic case studies.

5.2.3 Critical Gradation Parameter(s) Governing Shear Strength Behavior

To identify the most important gradation parameter(s) governing the shear strength behavior of base/subbase materials, a bivariate analysis, useful for identifying bivariate unusual points and bivariate collinearities, was employed to investigate relationships between the

dependent variable (σ_{df} at given confining pressure) and explanatory variables (gradation parameters). The coefficients of determination (R^2 and adjusted R^2) were the criteria for evaluating the strength of association between each pair of these parameters. The statistical normality of each parameter was also verified with the Shapiro-Wilk test.

Among those calculated gradation parameters, the Gravel-to-Sand (G/S) ratio, in spite of its relative simplicity, was found to exhibit the best correlation with σ_{df} for all the materials studied at various confining pressures, as shown in Figure 5.4. For instance, aggregate ratios of the Bailey method, which were thought to be very promising for governing influential factors, were found to be statistically insignificant except for the fine aggregate coarse ratio (FA_c).

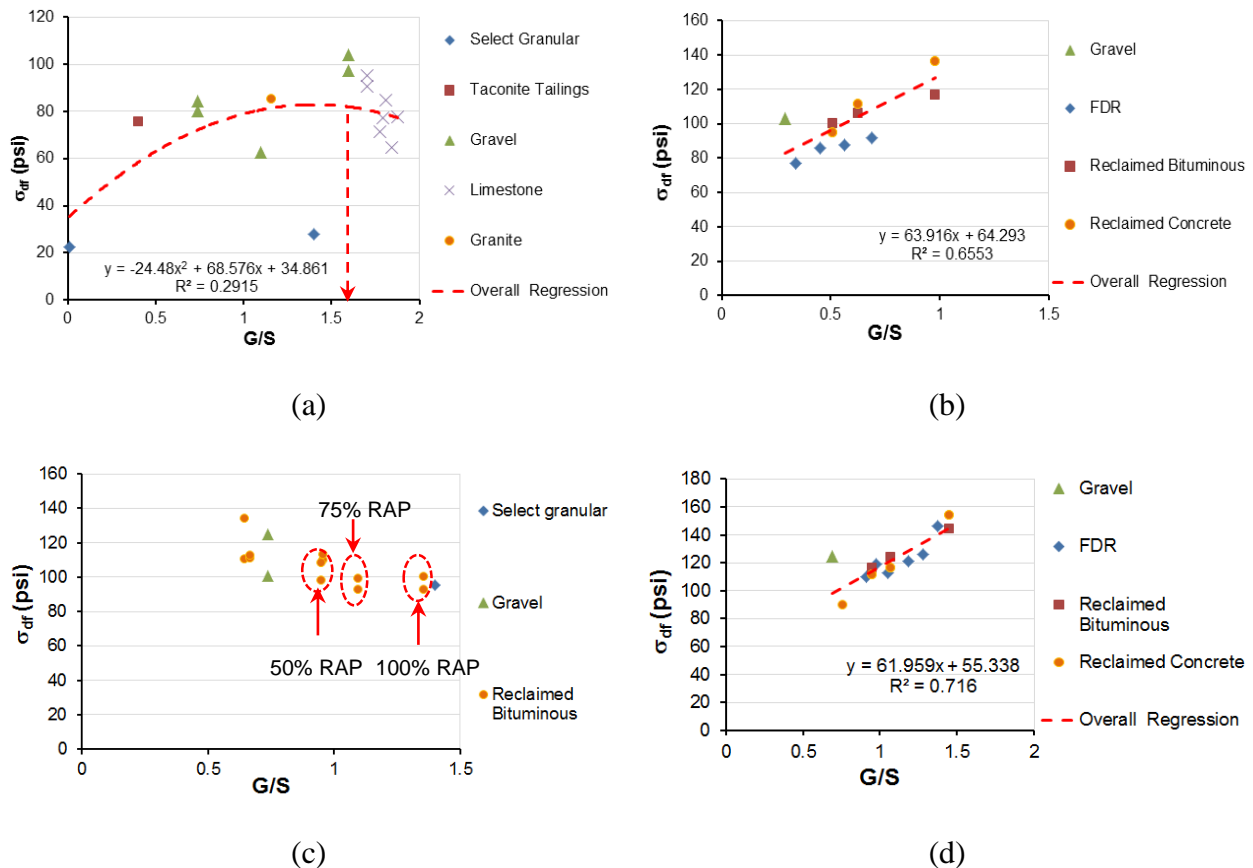


Figure 5.4 Peak Deviator Stress at Failure (σ_{df}) vs Gravel-to-Sand (G/S) Ratio for Various aggregates: (a) 4-psi, (b) 5-psi, (c) 8-psi, and (d) 10-psi Confining Pressure (σ_3)

As shown in Figure 5.4(a), the Gravel-to-Sand (G/S) ratio appears to have an optimal value somewhere between 1.5 and 2 at which maximum σ_{df} was computed for different gradations. Limestone samples exhibited decreased peak deviator stress at failure with increased G/S ratio (larger than a possible optimal G/S ratio). The examination of Figure 5.4(b) and (d) tends to confirm the inference made from Figure 5.4(a), as σ_{df} values increase with larger G/S ratios regardless of aggregate types and gradations when G/S ratio is less than 1.5. The trend in Figure 5.4(c) however is less obvious. As reported by Kim and Labuz (2005), specimens with increased RAP percentages exhibited higher permanent deformation. Almost the same σ_{df} level for those three different RAP percentages in Figure 5.4(c) may be attributed to the increasing G/S ratios (less than 1.5 still), which could to a certain extent offset the detrimental effect of increasing RAP percentages (further study is needed to make this inference conclusive). In other words, it appears that when G/S ratios gradually approach about 1.5, shear strength behavior is improved.

5.3 Discussions

5.3.1 Interpretation of the Gravel-to-Sand Ratio

The profound effect of the Gravel-to-Sand (G/S) ratio on the peak deviator stress at failure (or shear strength behavior) can also be interpreted from the particle packing and porosity characteristics acquired by different relative concentrations of gravel and sand size particles. Aggregate base/granular subbase materials, in essence, are mixtures of the gravel fractions, sand fractions and fines. Coarse aggregate grains can be deemed to enclose a void space in which finer sand particles fill; whereas the fines (passing No. 200 sieve or smaller than 0.075 mm) basically fill the void space created by the sand particles (see Figure 5.5).

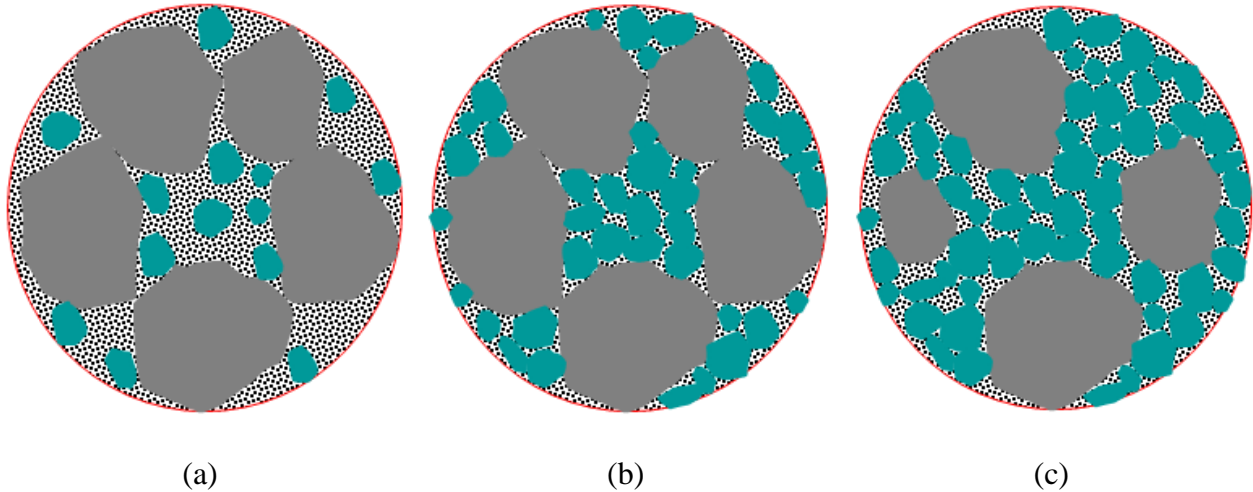


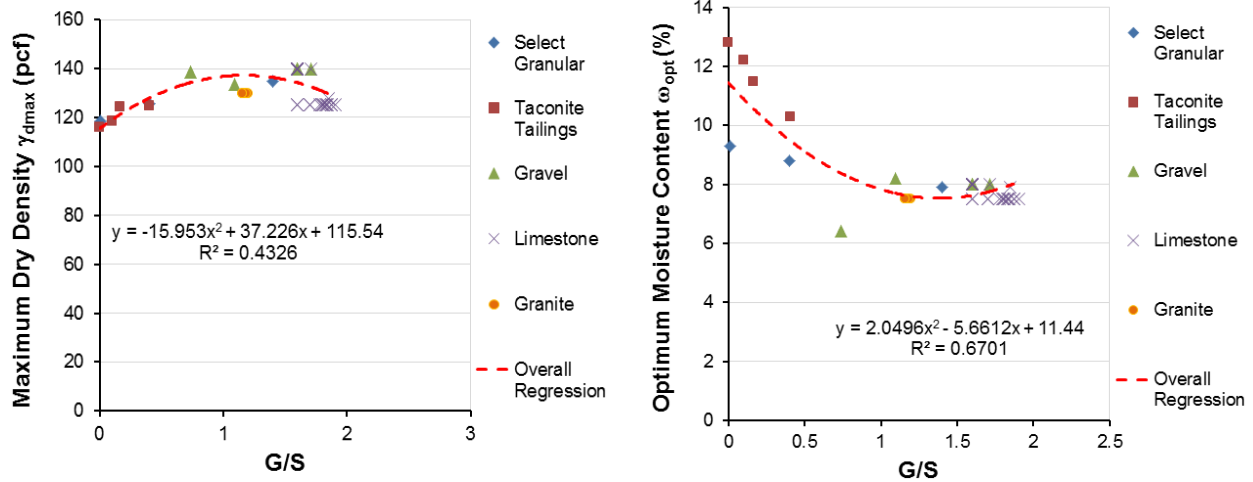
Figure 5.5 Different Packing States of Gravel-Sand-Fines Mixture with Different Gravel/Sand Ratios (G/S) (small black dots represent fines fraction): (a) Large G/S, (b) Optimum G/S, and (c) Small G/S

Figure 5.5(a) indicates the packing state resulting in the largest G/S ratio as almost no sand grains to occupy a portion of the voids between the coarse aggregate particles. Mixtures at this state develop shear or permanent deformation resistance primarily by friction resistance between gravel size particles and may not be very stable depending on the grading of the gravel-size particle distribution. G/S ratio decreases when more sand fractions exist until an optimal packing configuration is reached at the ideal state shown in Figure 5.5(b). This ideal state means the voids between the gravel size particles are completely occupied by the bulk volume of the sand grains, developing the condition of minimum porosity. The minimum porosity of the mixture can be theoretically interpreted as the boundary between a gravel-controlled and a sand-controlled mixture. The phase diagram analysis of Figure 5.5(b) can also derive that the minimum porosity of the mixture is the product of the porosity of each individual fraction (i.e., $n_{min}=n_G*n_s*n_f$) with the same specific gravity assumed for all fractions. After that, if sand fractions keep increasing (or G/S ratio decreases), then packing conditions will dictate gravel (or

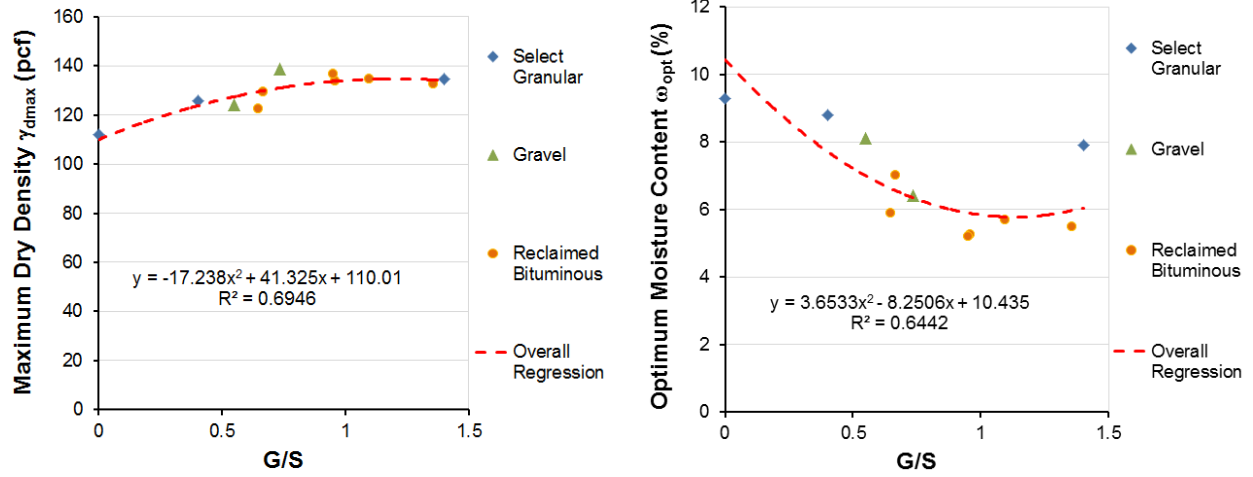
coarse) particles to “float” in the sand-fine matrix and have trivial control over shear strength behavior of the mixture (see Figure 5.5c).

To validate such inferences made above, the trends between the maximum dry density (γ_{dmax}) and optimum moisture content (ω_{opt}) and the Gravel-to-Sand (G/S) ratio are plotted in Figure 5.6 for those materials studied. Intuitively, the maximum dry density and optimum moisture content obtained under a given compactive effort can serve as indicators of the porosity of the mixture, with lower maximum dry density and higher optimum moisture content representing greater porosity. The porosity is then related to the shear strength developed, and the maximum shear strength of the mixture tends to occur at an optimum range of low porosity values.

As shown in Figure 5.6, maximum dry density approaches a maxima and optimum moisture content reaches a minima when the G/S ratio is around 1.5, indicating the minimum possible porosity achieved by mixtures with G/S of around 1.5. The relative importance of the suction stress is also reduced as the G/S ratio increases and the optimum moisture content decreases. Since mixtures with G/S ratios of around 1.5 at the moment is at the possibly densest packing state, it explains well why peak deviator stress at failure has a maxima at this point, as presented previously. Note that the minimum porosity of a mixture is a function of porosities of both coarse aggregate particles and fine aggregate particles. Therefore, the approximate value of 1.5 found here may change when different material sources (e.g., with different bulk specific gravity) with different gradations are used. Nevertheless, such optimal proportions of gravel and sand fractions may exist when the mixture reaches its minimum porosity, gets packed to the densest state, and thus yields the highest shear strength.



(a)



(b)

Figure 5.6 Maximum Dry Density (σ_{dmax}) and Optimum Moisture Content (ω_{opt}) vs Gravel-to-Sand Ratio (G/S) at (a) 4-psi and (b) 8-psi Confining Pressure (σ_3)

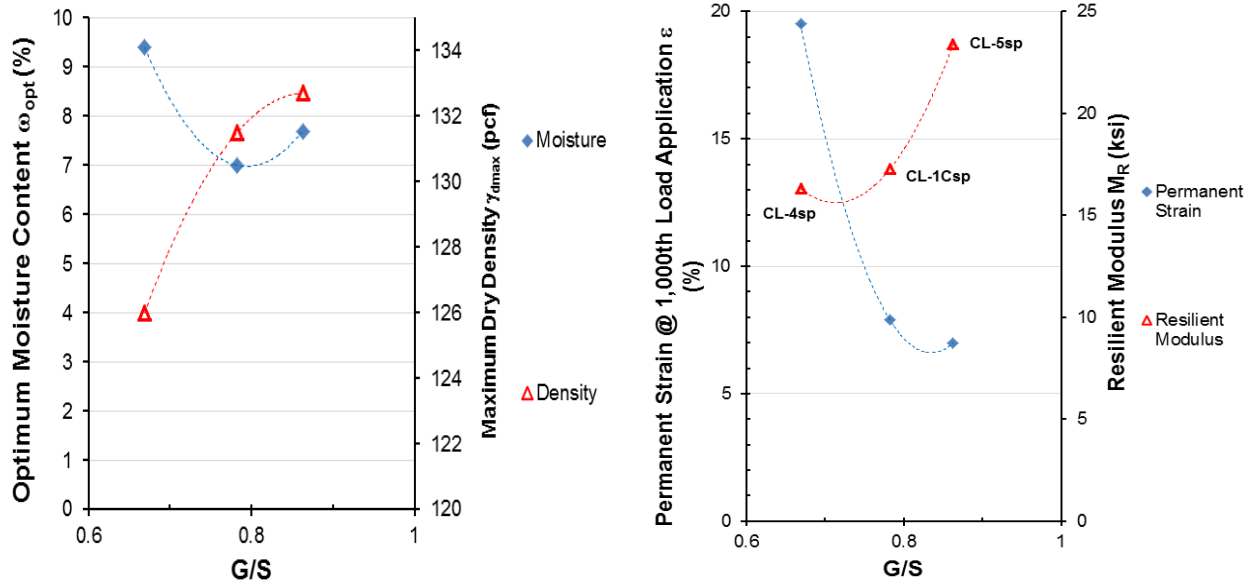
The G/S ratio may also help better understand effects of unsaturated hydraulic conductivity on the suction behavior of base/subbase materials, especially those with broad particle size distributions. The G/S ratio reflects the relative concentrations of larger gravel (or coarse aggregate) and smaller sand particles which according to Gupta et al. (2005) control the saturated hydraulic conductivity and the water retention characteristics, respectively. Future

research in this area could potentially explain how moisture suction may become more controlling with smaller G/S ratios.

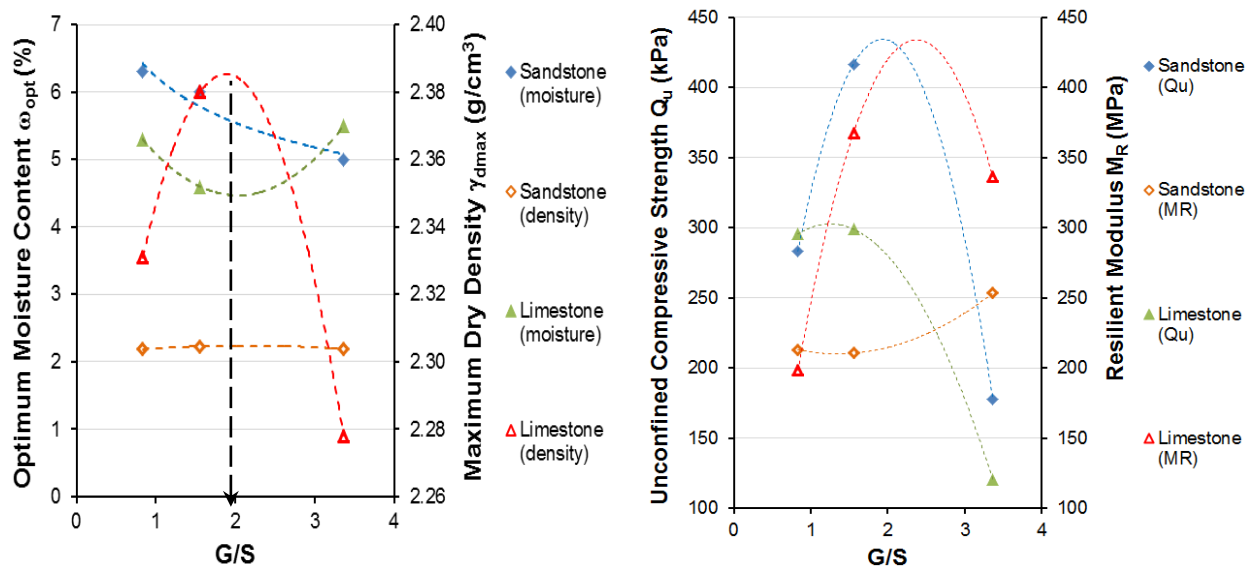
5.3.2 Analyses of Other Aggregate Databases Collected

To support the observed gradation effects and G/S ratio trends summarized so far, similar analysis results from other aggregate databases collected from the literature are also presented in this section. The first data source was collected from the comprehensive laboratory testing program performed by Garg and Thompson (1997) in which six base and subbase materials (CL-1Fsp, CL-1Csp, CL-3sp, CL-4sp, CL-5sp, and CL-6sp) collected from the Mn/ROAD flexible pavement test sections were characterized for shear strength, resilient modulus, and rutting potential from rapid shear and repeated load triaxial tests. Since samples were tested in that study at varying moisture and density levels, to be consistent, only results of three samples (CL-1Csp, CL-4sp, and CL-5sp) tested at reported maximum dry density and optimum moisture content values (AASHTO T99) are presented here. In Figure 5.7(a), the calculated G/S ratios are plotted against the maximum dry density, optimum moisture content, resilient modulus calculated at 100-psi bulk stress, and permanent strain calculated at the 1,000th load application from the reported values of “A” and “b” ($\epsilon_p\% = A * N^b$), respectively. It clearly shows that as the G/S ratio increases, the optimum moisture content decreases and maximum dry density increases, indicating the densification trend towards the minimum porosity. Note that higher permanent strain (at the 1,000th load application) represents increased rutting potential and lower shear strength. The decreased permanent strain or increased shear strength is also observed for increasing G/S ratio, which agrees with the previous findings. Although aggregate class CL-5sp required 10-15% crushed/fractured particles and no crushed/fractured particles were allowed in CL-1Csp or CL-4sp, a permanent strain decrease of up to 64% from CL-5sp to CL-4sp

demonstrates the significant role of G/S ratio for improving shear strength. Interestingly, resilient modulus increases with decreased permanent strain or increased shear strength.



(a)



(b)

Figure 5.7 The Gravel-to-Sand Ratio Effects Observed in Other Databases Collected from (a) Garg and Thompson (1997) and (b) Tian et al. (1998)

The second data source collected was from the study of Tian et al. (1998) aimed at investigating resilient modulus and shear strength characteristics of two good quality aggregates commonly used in Oklahoma as base/subbase materials at three different gradations (finer, median, and coarser limits). As shown in Figure 5.7(b), the calculated G/S ratios (from actual gradation curves) are plotted against the unconfined compressive strength (Q_u), maximum dry density (AASHTO T180), and optimum moisture content, respectively. The resilient modulus values were obtained at 689-kPa (100-psi) bulk stress. As indicated in Figure 5.7(b), both aggregates have an optimal G/S ratio of around 2 where mixture porosity reaches its minimum and the shear strength reaches its maximum values. The greater optimal G/S ratio found here may be possibly attributed to higher compaction energy used (AASHTO T180 rather than T99). In addition, the modulus-strength relationship does not show any consistent or unique trends similar to the previous MnDOT aggregate database findings.

Tutumluer et al. (2009) recently characterized strength, stiffness, and deformation behavior of three aggregate materials (limestone, dolomite, and uncrushed pit-run gravel) with controlled gradations for subgrade replacement and subbase applications through a comprehensive laboratory test matrix. This comprehensive database was also analyzed for verification purpose. To be consistent, only samples that had nonplastic fines at optimum moisture conditions were studied here for the G/S ratio effects. The results are shown in Figure 5.8. Note that the peak deviator stress values were recorded at 15-psi confining pressure, and M_R values were calculated at 345-kPa (50-psi) bulk stress. The increasing maximum dry density (AASHTO T99) and decreasing optimum moisture content trends are consistent and indicate that the minimum porosity levels for the uncrushed gravel, crushed limestone, and crushed dolomite materials approximately take place at the G/S ratios of 1.6, 1.68, and 1.56, respectively.

Considering the specific gravity variations of those three materials, the three very close G/S ratios can actually be regarded as the same. Note that investigation of the gradation effect was in fact not the primary objective of this research study, so the gradations were well controlled and engineered by only varying percent fines. Although the peak deviator stress values do not consistently increase with increasing G/S ratios (or decreasing porosity), overall, the peak deviator stress values at the maximum G/S ratios for all three different aggregate materials are still approximately the maximum ones. Once again, no definite relationship exists between modulus and shear strength trends, which may require further investigation into effects of moisture-related suction stress for various fines percentages.

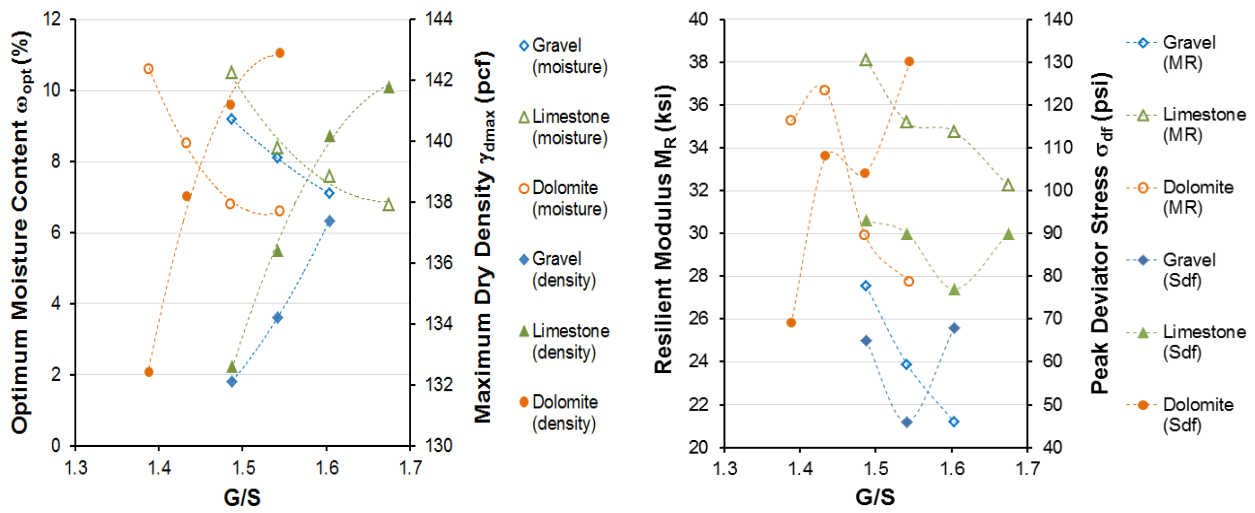


Figure 5.8 The Gravel-to-Sand Ratio Effects Observed in Other Databases Collected from Tutumluer et al. (2009)

5.4 Engineering Application of the Gravel-to-Sand Ratio Concept

Using open-graded aggregate base has been demonstrated to be one of the effective strategies for improving drainage efficiency and thus pavement longevity. For instance, two main types of permeable base materials are widely used in Minnesota, i.e., stabilized and unbound. Figure 5.9(a) illustrates the MnDOT gradation specifications for both unbound and stabilized permeable aggregate base (PAB) materials (Arika et al., 2009). It can be seen that the gradation of the stabilized material becomes much coarser due to the addition of a stabilizer (asphalt or cement) than unbound materials that need high contents of finer-size aggregates to achieve stability through aggregate interlock. Typical permeability values are 1000~3000 ft/day (0.35~1.06 cm/s) for unbound granular ones and 6800 ft/day (2.40 cm/s) for stabilized bases. In addition to maintaining adequate permeability, these layers are also required to remain stable during construction as well as future rehabilitation activities over the design service life.

The aggregate gradation mechanism based on the proportionality between gravel and sand size particles (as per ASTM D2487-11) was presented previously to demonstrate how mechanical behavior, i.e., shear strength and resilient modulus (M_R) characteristics, of aggregate base/granular subbase materials can be quantified and related to grain size distributions (Xiao et al., 2012). By using the concept of the G/S ratio gradation parameter, the current MnDOT specified gradation band for unbound permeable aggregate bases is analyzed herein for the optimal gradation that is qualified as drainable aggregate base but also potentially yields optimized strength and deformation characteristics.

The selection process is illustrated in Figure 5.9(b). First of all, by regressing percent passing data (p_i) against sieve sizes (D_i) as per Equation 5.1, a gradation curve within the MnDOT unbound PAB gradation band can be represented as a “point” with coordinates (n, D_{max})

in a similar Cartesian plane where shape factor n is on x-axis and D_{max} is on y-axis. The four vertices of the rectangular shown in Figure 5.9(b) represent the four boundary gradation curves illustrated in Figure 5.9(a). Note that candidate gradation curves are represented by points falling on the G/S ratio contour of 1.6 (see Figure 5.9(b)) which was found to be optimal in the aforementioned study. Among those points falling on the G/S ratio contour of 1.6, the point with maximum D_{max} is preferred herein due to the potential to accommodate the use of larger-size recycled concrete aggregates (RCA) and reduce crushing costs. It turns out that the point (0.52, 25.7) is the one representing the optimal gradation curve to be proposed.

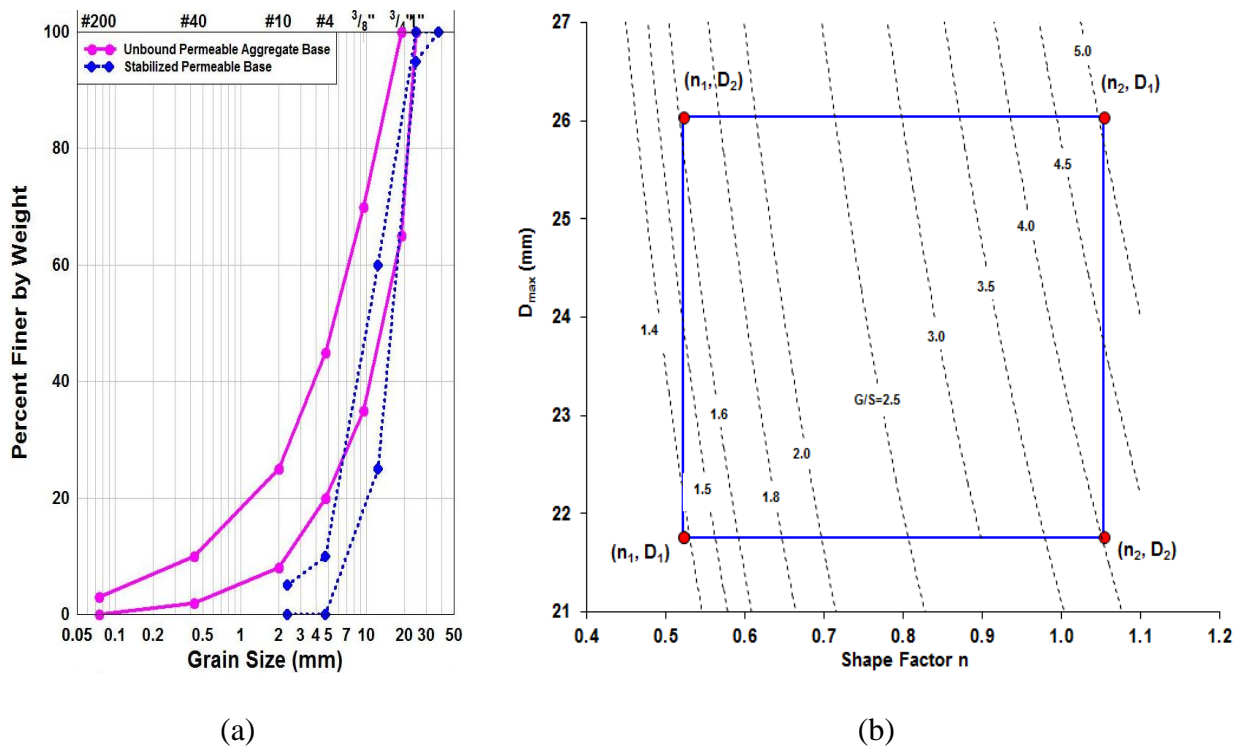


Figure 5.9 MnDOT Gradation Specifications (a) for Unbound Permeable Aggregate Bases (PAB); (b) Gradation Chart with Contours of the Gravel to Sand (G/S) Ratio Gradation Parameter for MnDOT Unbound PAB Gradation Band

Prior to conducting any laboratory permeability tests, empirical relationships listed in Table 5.2 between hydraulic conductivity and grain size can be used to give a first-hand estimation of the order of magnitude of permeability. For example, Hazen (1930) proposed a widely used relationship between saturated hydraulic conductivity and soil particle diameter. The hydraulically based Kozeny-Carman equation is another frequently referenced relationship that relates hydraulic conductivity to the square of a representative grain size, porosity, and physical properties of the fluid. The Hazen equation (1930) and Kozeny-Carman equation (Carman, 1956) are formulated in Equations 5.8 and 5.9. It seems that the parameter d_{10} plays a significant role in permeability (K_{sat}) calculation and thus needs to be properly maximized, as it is included in most of the empirical relations. The following optimization problem as formulated in Equation 5.2 was solved using Excel Solver. The resulting final optimal gradation is shown in Figure 5.10.

$$\begin{aligned}
 & \max D_{10} \\
 & \text{subject to :} \\
 & \left\{ \begin{array}{l} 10\% = (D_{10} / D_{max})^n \\ 21.76 \leq D_{max} \leq 26.04 \\ 0.52 \leq n \leq 1.05 \\ \frac{(D_{max})^n - 4.75^n}{4.75^n - 0.075^n} = 1.6 \end{array} \right. \quad (5.2)
 \end{aligned}$$

A drainable aggregate base with such a proposed optimal gradation was already constructed to support a new PCC pavement on MnROAD test Facility 2013 Test Section 13 reconstruction (an interstate test section) that needed to include a significant amount of recycled Portland cement concrete (PCC). The field performance of such a drainable aggregate base in terms of structural stability and drainability will be studied in the future upon the completion of the MnROAD test programs. It is also worth mentioning that the proposed gradation happens to be very similar to one of the permeable unbound aggregate gradations used by Ohio DOT and

designated as C307-IA (Liang, 2007). The C307-IA gradation is found to have a saturated permeability of 0.803 cm/s and an average resilient modulus of 72 ksi (500 MPa) according to AASHTO test protocol (Liang, 2007).

Table 5.2 Empirical Models for Estimating Permeability of Unbound Granular Materials

Model	Formula	
Moulton (1980)	$K_{sat} \text{ (cm/s)} = \frac{6.214 \times 10^5 D_{10}^{1.478} n^{6.654}}{2834.6 \times p_{200}^{0.597}}$	(5.3)
MEPDG EICM	$K_{sat} \text{ (cm/s)} = 10^{-6} \times 10^{\left(5.3D_{10} + 0.049D_{60} + 0.0092\frac{D_{60}}{D_{10}} - 0.1P_{200} + 1.5\right)}$	(5.4)
Hazen (1930)	$K_{sat} \text{ (cm/s)} = C_H \times D_{10}^2$	(5.5)
Kozeny-Carman (Carman, 1956)	$K_{sat} \text{ (cm/s)} = 1.99 \times 10^4 \times \left(\frac{1}{SF}\right)^2 \times \left(100\% \div \sum \left(\frac{f_i}{D_{(av)i}}\right)\right)^2 \times \left(\frac{e^3}{1+e}\right)$	(5.6)
Amer-Award (1974)	$K_{sat} \text{ (cm/s)} = 35 \times \left(\frac{e^3}{1+e}\right) \times C_u^{0.6} \times D_{10}^{2.32}$	(5.7)
Chapuis (2004)	$K_{sat} \text{ (cm/s)} = 2.462 \times \left(D_{10}^2 \times \frac{e^3}{1+e}\right)^{0.7825}$	(5.8)
Vardanega- Waters (2011)	$K_{sat} \text{ (cm/s)} = A(R_p)^b = A\left(\frac{2}{3} \times \frac{AV}{100} \times D_{eff}\right)^b$	(5.9)

where CH is a coefficient varying from 1 to 1.5; SF is a shape factor varying from 6 to 8 depending on the angularity of individual soil particles; fi is percent fraction of particles between two consecutive sieve sizes; D_{(av)i} is average particle size between consecutive sieves; e is void

ratio; C_u is coefficient of uniformity (needed to be less than 2.5 for the Hazen model); D_{10} (varying from 0.1 to 3 mm as limited by the model applicability) and D_{60} are sieve sizes corresponding to 10 and 60 percent passing, respectively; R_p is representative pore size in mm; AV is percent air voids; D_{eff} is effective particle size in mm; and K_{sat} is the saturated hydraulic conductivity.

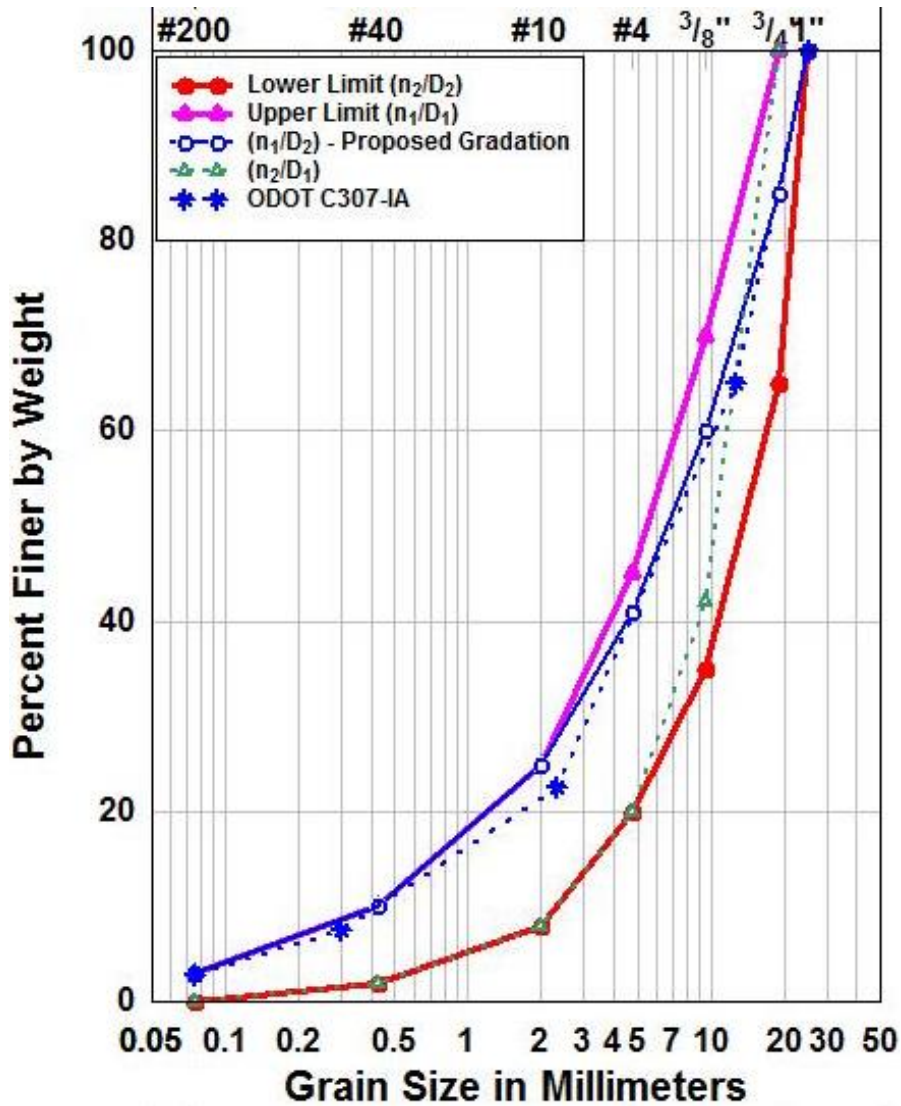


Figure 5.10 Four Boundary Gradation Curves Consisting of MnDOT Unbound PAB Gradation Band and the Proposed Optimal Gradation

5.5 Summary

A comprehensive statewide aggregate database, including both standard virgin and nontraditional aggregate materials collected from various sources in Minnesota, was used to investigate the influence of gradation parameters of these primarily aggregate base/granular subbase materials on the shear strength and resilient modulus characteristics. Commonly used gradation quantification methods, including the Talbot equation, the Rosin-Rammler distribution function, the Unified Classification System parameters, the conventional Gravel-to-Sand ratio, as well as the Bailey method, were employed to identify key gradation parameters governing the shear strength behavior of the studied aggregate materials. While other gradation parameters seemed to be less significant, the Gravel-to-Sand (G/S) ratio was found to control the shear strength behavior of both “standard” and reclaimed materials. For the MnDOT database samples studied, the highest shear strength was reached around an optimal G/S ratio of 1.5 where void spaces enclosed by the coarse aggregate fraction were probably filled completely by the sand size particles and fines. Further, there was inconclusive evidence of an apparent modulus-strength relationship which suggested incorporating a limiting working shear stress to strength ratio to avoid catastrophic shear failure in base and especially subbase courses.

Previous studies on soil/sand-gravel mixtures indicated that for large gravel (or coarse aggregate) concentrations, the friction resistance between gravel particles controls the shear strength behavior of mixtures; while at low gravel concentrations, the friction resistance of sand/soil grains controls the shear strength behavior. By applying this observation to this study, interpretation regarding the role of G/S was made, which well explained the validity of the optimal G/S ratio of 1.5 in this case. Additional aggregate databases collected from literature also confirmed the existence of such an optimal G/S ratio and the significant influence of the G/S

ratio gradation parameter. In light of these findings, current gradation specification bands, which may reject non-standard base/subbase materials for use in cost-effective road constructions, can be further revised and transferred into performance-based specifications in which the G/S ratio, together with other important factors, can be used to utilize available aggregate sources to match the site-specific design traffic levels and operating environmental conditions, for the sake of promoting sustainability. It is postulated here that within the current MnDOT specified gradation bands, those with the same G/S value of around 1.5 may exhibit similar shear strength behavior regardless of their maximum particle size, provided that other properties such as fines content, moisture and density conditions (AASHTO T99), and aggregate shape are not dramatically different from each other.

To better understand the underlying mechanism of the G/S ratio from a microscopic level, Chapter 6 is to present the research work conducted using an image-aided Discrete Element Modeling (DEM) approach well-validated in railroad ballast studies (Tutumluer et al., 2009; Yohannes et al., 2009). The goal is to simulate aggregate shear strength tests with the capability to recreate the three-dimensional aggregate shapes as individual discrete elements (“polyhedrons/blocks”) based on the scanned images from the University of Illinois Aggregate Image Analyzer (UIAIA). This way, optimum contact and packing arrangements from various gradations will be realistically studied for improved aggregate interlock. More aggregate material types and gradations will definitely be helpful in terms of better quantifying effects of G/S ratio on mechanical behavior of aggregate base/granular subbase materials.

Chapter 6 Discrete Element Modeling of Gradation Effects Influencing Contact and Packing Characteristics of Aggregate Skeleton

The primary objective of this chapter is to employ a validated DEM model for evaluating the effects of gradation properties on both packing characteristics and load-carrying abilities of unbound aggregate materials. To achieve this goal, DEM model parameters are first determined from calibrating an image-aided DEM program BLOKS3D developed at the University of Illinois (Zhao et al., 2006) against laboratory rapid shear strength (triaxial compression) test results. Once calibrated and validated, such a DEM program could be potentially utilized to investigate effects of multi-scale aggregate gradation and morphological properties on structural performances of unbound aggregate pavement layers. The relationships among the microscopic internal structure, micro-mechanical parameters, and macroscopic responses could also be identified from DEM based numerical simulations.

The DEM packing simulations using different gradations and particle shape are performed to investigate the validity of using the 4.75-mm sieve (or No. 4 sieve) as the breaking-sieve-size for typical Minnesota dense-graded aggregates. Based on the concept of the Gravel-to-Sand ratio (G/S) introduced in Chapter 5, the load-carrying coarse fraction is separated from the void-filling fine fraction. Finally, based on the DEM approach, current unbound permeable aggregate base (PAB) material gradations specified by Minnesota DOT are further engineered by optimizing the particle contact and packing characteristics in order to minimize the overall rutting potential (based on shear strength behavior) yet still accommodate desired drainage requirements. The optimal gradation proposed in Chapter 5 for unbound permeable aggregate

base (UPAB) materials according to the Gravel-to-Sand ratio concept is also verified in this chapter.

6.1 Calibration of the DEM Model Parameters with Rapid Shear Tests

6.1.1 Description of Laboratory Rapid Shear Tests

The coarse aggregate materials used in the laboratory study consisted of the most commonly used crushed aggregate types in the paving industry, i.e., limestone, gravel, sandstone, granite, and slag. The six unblended aggregate samples are listed in Table 6.1, along with their relevant physical properties and rapid shear and permanent deformation test results. The angularity index (AI) and surface texture (ST) index of the aggregate samples were quantified from three orthogonally acquired two-dimensional (2D) images of individual particles using the UIAIA (Tutumluer et al., 2000; Pan et al., 2006). None of these coarse aggregate samples has flat and elongated particles exceeding 10% by weight of greater than 5 to 1 (>5:1) longest to shortest dimensions. To minimize the influences of maximum aggregate sizes and/or gradations, all the specimens were prepared according to the same gradation with the same top aggregate size of 38 mm (see Figure 6.1a). Additionally, each crushed aggregate type was blended with uncrushed gravel at 0, 50, 67, 83, and 100% by volume fractions to generate a total of 21 aggregate blends for studying the effect of blending two different types of aggregates on the strength and rutting behavior, respectively (Tutumluer and Pan, 2008). Figure 6.1(b) illustrates that the blending with different crushed materials improved both shear strength and rutting resistance behavior of the uncrushed gravel. This is due to the fact that blending in this case results in more desirable aggregate shape properties than the uncrushed gravel.

The 21 aggregate blends were tested in dry (0% moisture content) condition with no fines included in gradation. Each specimen was prepared 152 mm in diameter and 305 mm in

height. The same void ratio of 67.5% (or porosity of 41%) was achieved for all triaxial rapid shear aggregate specimens by controlling the total volume of the aggregate particles contained in the specimen. The rapid shear test performed is a deformation controlled test with an axial strain of 12.5% (corresponding to 38 mm) obtained in 1 second at the confining pressure of 34.5 kPa. Such a loading rate is reported to be highly effective in characterizing the bearing capacity failure of the unbound aggregate base/subbase layer under moving traffic loading (Garg and Thompson, 1998). In this study, the maximum deviator stress at failure $(\sigma_d)_f = (\sigma_1 - \sigma_3)_f$ measured from only one rapid shear test at 34.5-kPa confining pressure is used as an indicator of the shear strength of each aggregate blend (see Table 6.1), instead of the friction angle and the cohesion intercept.

6.1.2 Discrete Element Modeling of Rapid Shear Tests

6.1.2.1 Particle Sizes and Shapes

The sample gradation (see Figure 6.1a) has a minimum aggregate size of 6.3 mm and a maximum aggregate size of 38 mm, which requires approximately 1,800 polyhedral particles in the DEM simulation with a time step of around 2.73×10^{-7} s, given the specified specimen dimensions. A set of particle shapes was selected from the pre-established DEM particle shape library to match the measured shape indices for each aggregate blend (see Table 6.1), respectively. More details about the DEM particle shape library can be found elsewhere (Huang, 2010). During particle generation, particle geometries were randomly chosen from the selected set of particle shapes.

6.1.2.2 Simulation of a Flexible Membrane and Rigid Platens

To model flexible membrane, the approach documented by Lee et al. (2012) was used. Specifically, a total of 240 rigid rectangular cuboid discrete elements are positioned in a

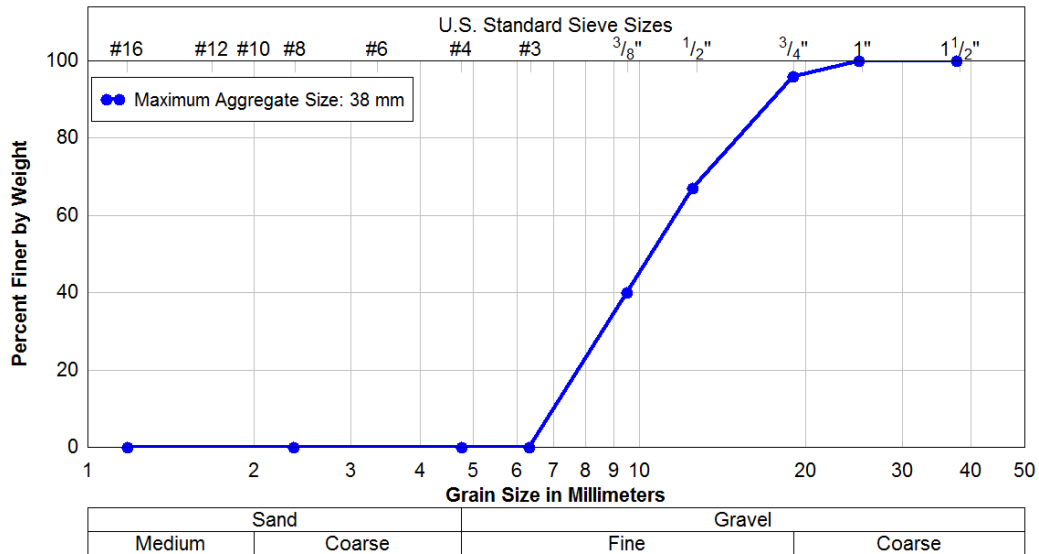
cylindrical arrangement to form a hollow space of 152.4-mm (6-in.) inner diameter and 304.8-mm (12-in.) height, respectively. The particles are positioned inside the hollow cylinder. As shown in Figure 6.2(a), the height of the cylinder is divided into 10 layers each of which is 30.48 mm high, and the circumference of each layer is simulated with 24 membrane elements. Each membrane element has a thickness of 4 cm and a surface area of 10 cm by 5 cm, which allows some initial overlap between neighboring membrane elements. To mimic the specimen deformation in the experiments, each membrane element is only allowed to have translation movement in radial direction and is independent of that of neighboring ones, with all the other degrees of freedom restricted. The external radial concentrated force is applied at the center of each membrane element and continuously adjusted to result in a constant confining cell pressure. The top platen is simulated as a frictional rigid rectangular cuboid element with a thickness of 2 cm and a square cross sectional area of 30 cm by 30 cm. The shearing of the aggregate specimen is controlled through vertical displacement of the frictional rigid platen. No contact detection is performed between any two membrane elements or between platens and membrane elements. The friction angle between aggregate particles and membrane elements is set to zero throughout the simulations. The material properties of the platen are approximated to be the same as those of the aggregate particles.

6.1.2.3 Sample Preparation and Shearing Procedure

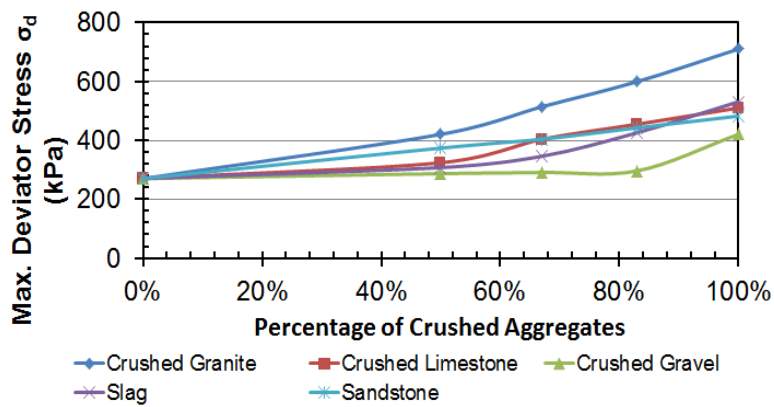
While detailed descriptions can be found elsewhere (Lee et al., 2012; Qian et al., 2013), the sample preparation process is illustrated in Figure 6.2 and briefly presented as follows: (i) generation of membrane elements and the top platen according to specified arrangement; (ii) particle generation with a target initial void ratio according to the prescribed gradation (different void ratios are achieved by changing either inter-particle friction angles or the gravitational

acceleration); and (iii) simultaneous application of (isotropic) confining pressure upon the top platen (in vertical/axial direction) and membrane elements (in radial direction). Once the sample preparation is complete, shearing of the aggregate specimen is performed by applying incremental vertical displacements on the top platen. Note that the particle-particle and platen-platen friction angles and the gravity constant are re-set to their desired values prior to shearing.

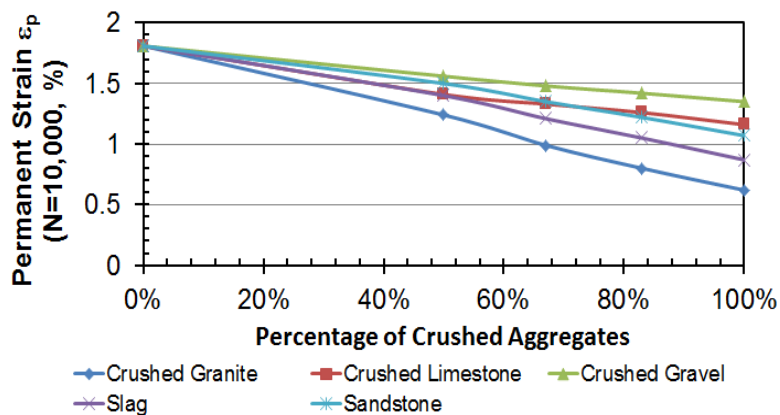
In the laboratory rapid shear test, the sample was sheared at a rate of 31 mm (1.25 in.) per second. To avoid a long run-time as well as computational instability problem caused by dynamic effect during continuous shearing, the incremental shearing scheme reported elsewhere is adopted to reproduce the shearing process (Lee et al., 2012; Qian et al., 2013). Note that rapid shear tests performed on railroad ballast materials were found not sensitive to strain rate and thus can be treated as a quasi-static problem according to Qian et al. (2013). The top platen is moved discretely by 0.01 mm (0.01% of axial strain) in each increment. Immediately after each incremental displacement, the platen is fixed in its new position and the simulation is continued to allow the particles and the membrane elements to re-equilibrate under this new boundary condition until the changes of both vertical and horizontal effective stresses are below a desired tolerance level. Once equilibrium is reached, vertical and horizontal effective stresses and volumetric strain are recorded. In this study, all simulations were carried up to 7% axial strain based on the experimental results.



(a)



(b)



(c)

Figure 6.1 Gradation Curve of Aggregate Specimens (a) and Aggregate Blending Effect on Maximum Deviator Stress σ_d (b) and Permanent Strain ϵ_p (c) (Data Source: Tutumluer and Pan, 2008)

Table 6.1 Aggregate Types and Test Results (Data Source: Tutumluer and Pan, 2008)

Aggregate Types *	Angular Index (AI)	Surface Texture Index (ST)	Specific Gravity (G _s)	Specimen Weight (grams)	Max. Deviator stress σ_d at Failure (kPa) **	Plastic strain ϵ_p at N=10,000 (%) ***
Uncrushed Gravel	252	0.9	2.583	8535	270.2	1.81
Crushed Granite	550	2.4	2.622	8664	710.2	0.61
Crushed Limestone	495	1.75	2.735	9037	510.2	1.15
Crushed Gravel	371	1.09	2.548	8419	420.6	1.35
Slag	516	2.2	2.435	8046	531.0	0.87
Sandstone	402	1.82	2.270	7501	482.6	1.07

Notes: * Void ratio=67.5% (porosity=41%);

** Confining pressure $\sigma_3=34.5$ kPa;

*** $\sigma_3=34.5$ kPa, bulk stress $\theta=172.4$ kPa.

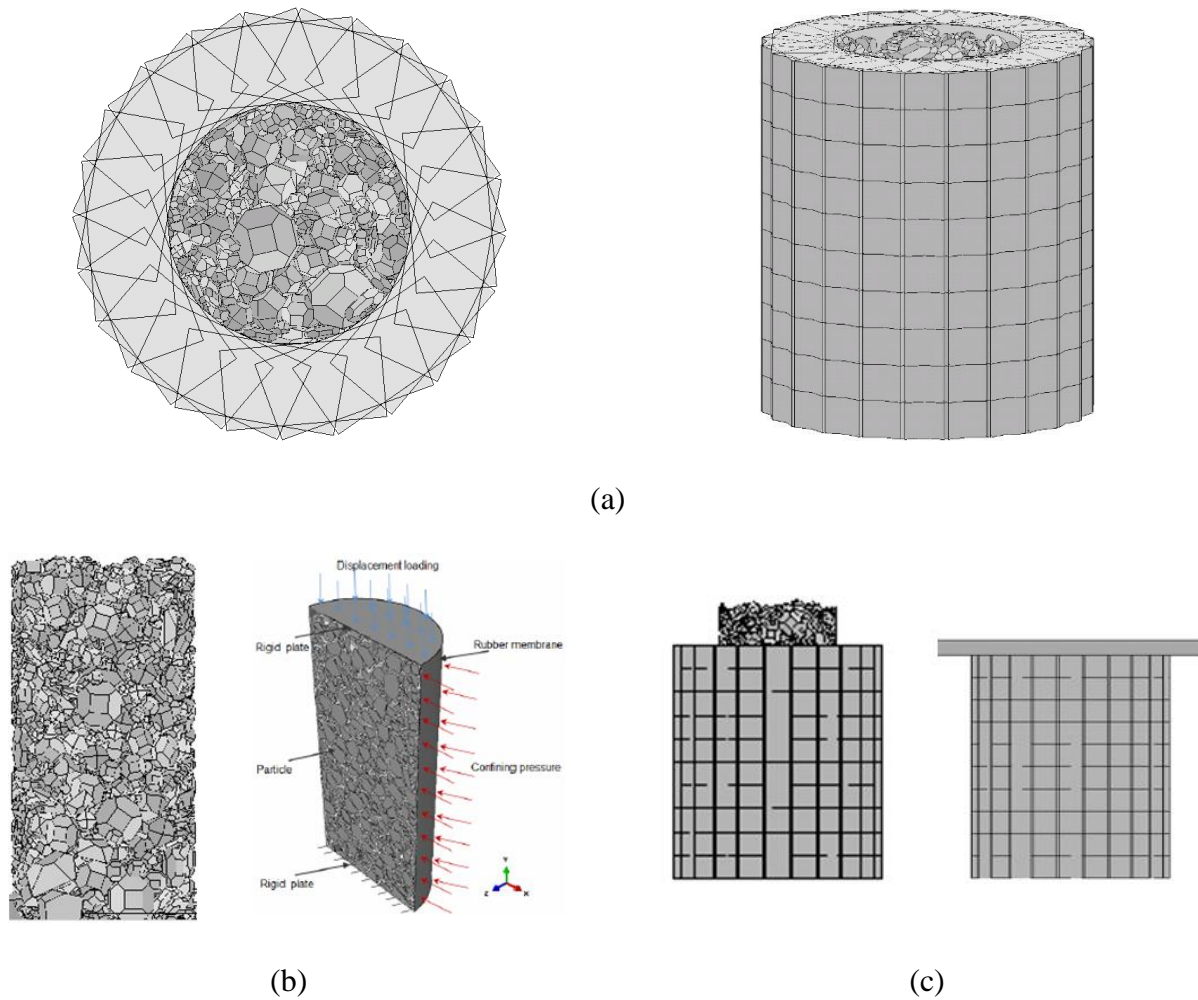


Figure 6.2 Illustration of Triaxial Compression DEM Simulation: (a) Arrangement of Membrane Elements, (b) Aggregate Specimen Modeled, and (c) Specimen Preparation Process

6.1.3 Calibration of the DEM Model with Rapid Shear Tests

The purpose of the calibration process is to select appropriate micro-parameters required in DEM simulations. Among required modeling parameters in the DEM simulation, particle shape and size are already chosen according to prescribed gradation, while inter-particle friction angle (ϕ'), normal contact stiffness (K_n), shear contact stiffness (K_s), and contact damping ratios remain to be selected. The global damping ratio is assumed as the default in this study (Lee et al., 2012). Those micro-mechanical parameters, which generally do not represent

real mechanical properties and are difficult to obtain experimentally, are often found by a trial and error procedure such that the simulation yields similar macroscopic (global) behavior as that of the aforementioned laboratory rapid shear tests. As compared to the normal and shear contact stiffness values, the inter-particle friction angle is reported to have a greater influence on the simulation results (Lee et al., 2012). To be specific, the normal and shear contact stiffness values are first kept constant; while the inter-particle friction angle that mainly depends on the particle surface roughness (i.e., the particle mineralogy) is varied within the typical range reported previously (Terzaghi et al., 1996). After selecting a proper inter-particle friction angle that results in simulated responses comparable to experimental data, the normal and shear contact stiffness values are then varied for calibration. For numerical stability, the shear contact stiffness value is chosen to be smaller than the normal contact stiffness value. For the very first trial, the stiffness values ($K_n=20$ MN/m and $K_s=10$ MN/m), successfully employed in prior studies (Huang, 2010; Qian et al., 2013) to simulate granite ballast behavior, were used. This procedure was repeated until the final stiffness values were selected. Since the critical time step for numerical stability is inversely proportional to the normal contact stiffness, the smallest normal contact stiffness value that matches experimental results fairly well was selected to allow for a larger simulation time step. It is worth noting that multiple simulations with different initial conditions (as resulted from randomly selecting DEM particle assembly from the pre-chosen particle library) were not performed in this study.

After a series of trials, the final parameters determined for the DEM simulations are listed in Table 6.2. The particle elastic modulus and Poisson's ratio are fixed at 97.9 MPa and 0.25, respectively. The contact damping ratio is set as 0.03. The DEM simulation results obtained using calibrated micro-mechanical parameters are tabulated in Table 6.3 where

satisfactory agreement is achieved. The DEM-predicted deviator stresses match closely with those from experiments, which means that the developed DEM model is capable of reproducing the typical mechanical behavior of unbound aggregate materials. The DEM simulations were carried out past each peak value of the deviator stress. Figure 6.3 shows the numerical results obtained with the micro-parameters reported in Table 6.2 at 34.5-kPa confining pressure level for uncrushed gravel, slag, and crushed granite specimens, as these three specimens represent three distinguishing deviator stress levels (i.e., high, medium, and low). It was revealed from DEM simulation results that the nonlinear stress-strain behavior of unbound aggregate materials (including dilatancy effects) was properly simulated by the DEM model.

According to the linear Mohr-Coulomb model, which is typically used to represent the shear strength of granular materials, the relationship between shear stress at failure (τ_f) and normal stress (σ_n) is described as a function of the cohesion (c) and angle of internal friction (ϕ), i.e., $\tau_f = c + \sigma_n \tan \phi$. Despite the argument by many researchers whether c represents the material's "true" cohesion or merely a parameter of a linear fit, i.e., apparent cohesion, of the linear Mohr-Coulomb model, c is assumed to be zero for aggregate specimens in this study which were sheared under dry conditions. As a result, the peak principal stress ratio (PSR) for a linear Mohr-Coulomb model is calculated for each DEM simulation to compute the peak friction angle (ϕ_p) as in Equation 6.1:

$$\phi_p = \sin^{-1} \left(\frac{(\sigma_1/\sigma_3)_p - 1}{(\sigma_1/\sigma_3)_p + 1} \right) \quad (6.1)$$

where ϕ_p is peak friction angle; and σ_1 and σ_3 are major and minor principal stresses, respectively.

Figure 6.4 shows the variation of ϕ_P with aggregate shape indices. Note that the peak friction angle ϕ_P increases with increased angularity index (AI) and surface texture (ST) index values, indicating improved shear resistance.

Table 6.2 Calibrated DEM Model Parameters

Aggregate Types	Uncrushed Gravel	Crushed Granite	Crushed Limestone	Crushed Gravel	Slag	Sandstone
Friction Coefficient f ($\tan\phi'$)	0.42	0.75	0.6	0.52	0.65	0.6
Normal Contact Stiffness K_n (MN/m)	10	40	20	20	20	20
Shear Contact Stiffness K_s (MN/m)	5	20	10	10	10	10

Table 6.3 Triaxial Compression DEM Simulation Results

Aggregate Types *	Void Ratio e (%)		Specimen Weight (g)		Max. Deviator Stress σ_d at Failure (kPa) *	
	Lab Measured	DEM Predictions	Lab Measured	DEM Predictions	Lab Measured	DEM Predictions
Uncrushed Gravel	67.5	67.5	8535	8535	270.2	262
Crushed Granite		66.9	8664	8693	710.2	705
Crushed Limestone		66.1	9037	9111	510.2	515
Crushed Gravel		67.0	8419	8442	420.6	415
Slag		67.8	8046	8030	531.0	542
Sandstone		66.3	7501	7554	482.6	490

Note: * $\sigma_3=34.5$ kPa.

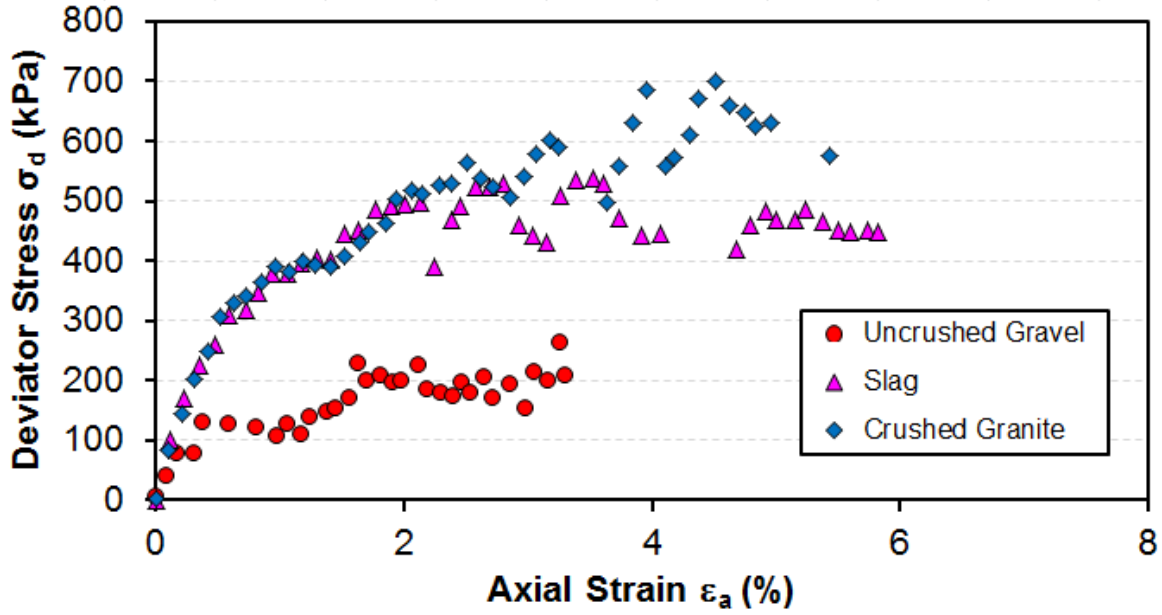


Figure 6.3 Triaxial Compression DEM Test Results for Three Specimens Representing High, Medium, and Low Maximum Deviator Stress Levels

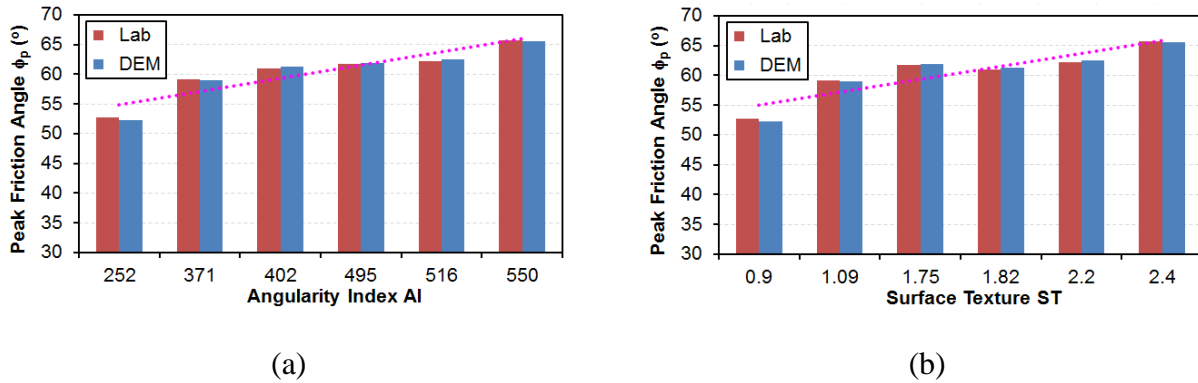


Figure 6.4 Variation of Peak Friction Angle (ϕ_p) with (a) Angularity Index AI and (b) Surface Texture ST

6.2 DEM Approach for Studying Underlying Mechanisms of Aggregate Packing

Unbound aggregates transfer external loads through forming the aggregate skeleton, which in turn is affected by aggregate gradation, surface texture, shape and stiffness. To ensure adequate particle contact for load transfer, proper gradation needs to be designed/selected for unbound aggregates possessing certain shape properties. However, limited analytical and numerical studies have been conducted in the past by considering only the packing and grain size distribution and the aggregate shape, angularity and surface texture were often neglected. There is currently no systematic procedure/guideline available for pavement engineers to engineer aggregate gradation and shape so that targeted performance can be achieved. In principle, the particle packing characteristics (e.g., contact points and porosity) are governed by the relative concentrations of aggregate particles of different sizes, as well as by the shape properties of individual aggregate particles. Those two governing factors interact with each other, thus necessitating the simultaneous consideration of both factors in developing technically sound gradation optimization framework.

The DEM model calibrated for six different aggregate materials has the potential to study the underlying mechanisms of aggregate packing and to engineer the gradations of aggregate base materials, especially permeable (open-graded) ones that require both permeability and long-term stability. By adjusting the percentages of aggregates at different sizes, aggregate gradation can be optimized at the microstructure level for large enough void space yet still adequate for structural performance (strength and stability).

6.2.1 Roles of Particles in an Aggregate Structure

The use of current gradation envelopes inherently assumes that aggregates of different sizes contribute differently to the load-carrying capacity of the aggregate assembly. The existence of a continuous network of coarse particles, i.e., the primary load transferring chain in the aggregate assembly, was long realized by previous studies (Dantu, 1957; Dobry et al., 1989). According to the experimental and numerical findings, the stresses in particulate media are not transferred in a uniform manner but are concentrated along continuous columns of particles. The particles in between the columns only provide lateral support but do not carry much load. The deformation pattern is directly related to load transfer by shear in the columns of particles. The orientation of the columns are primarily in the direction of the principal stresses and are also affected by the assembly of the grains and their shape (Tutumluer, 1995).

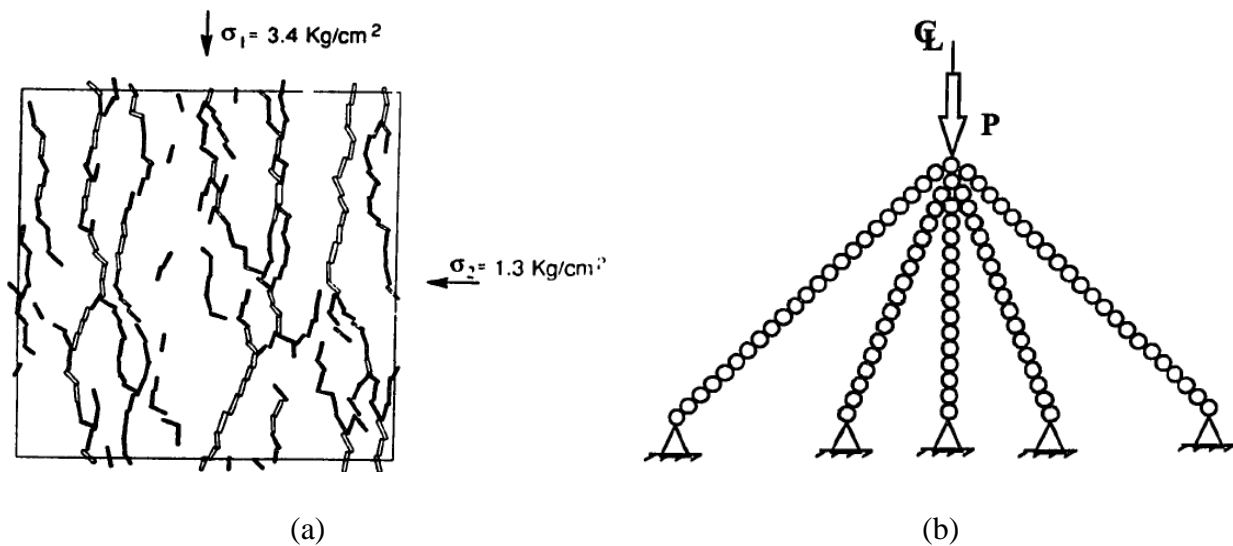


Figure 6.5 (a) Contact Forces for Two-dimensional Numerical Simulation under Anisotropic Loading (Dobry et al., 1989) and (b) Schematic Representation of Load Transfer in the Base Layer (Tutumluer, 1995)

Aggregate base/granular subbase materials, in essence, are mixtures of the gravel fractions, sand fractions and fines (as per ASTM D2487-11), as explained in Chapter 5. Coarse aggregate grains can be deemed to enclose a void space in which finer sand particles fill; whereas the fines (passing No. 200 sieve or smaller than 0.075 mm) basically fill the void space created by the sand particles (Xiao et al., 2012). Accordingly, Lira et al. (2013) define aggregate base/granular subbase materials as mixtures of the Primary Structure, the Secondary Structure, and other material, which was reviewed in detail in Chapter 2. According to this definition, the Primary Structure (PS) is a range of sizes in the gradation that due to its concentration forms the aggregate skeleton and thus provides the load bearing capacity for the mix (Lira et al., 2013). Within the PS, all the particles contact with each other, with more contacts existing in stronger skeletons. The Secondary Structure (SS) is formed by the particles with a smaller size than the PS. The SS fills in the voids between the PS particles and provides stability to the aggregate skeleton. Finally, there are other particles which are of a size larger than the PS and just float in the whole matrix. Relating gradation analysis framework parameters developed in their study to field rutting performances of several asphalt mixtures, they found that those mixtures with a more balanced combination between coarse and fine material (around 60/40) showed a low rut depth (Lira et al., 2013). Interestingly, this 60/40 combination coincides with the optimal value of around 1.5 proposed from the Gravel-to-Sand ratio concept (Xiao et al., 2012). This coincidence further indicates the necessity to explore the underlying mechanism of aggregate contact and packing characteristics affecting mechanical responses and performance of unbound aggregate materials.

6.2.2 DEM Simulations for Determining Breaking-Sieve-Size

Different criteria currently exist to define the breaking-sieve-size that separates the load-carrying coarse fraction and the void-filling fine fraction. For instance, according to the USCS definition, 4.75-mm (No. 4) sieve is the breaking-sieve-size for separating “gravel” and “sand” sizes. The gravel-to-sand ratio concept introduced in Chapter 5 was also based on this definition. Therefore, the validity of the 4.75-mm sieve as the breaking-sieve-size between coarse and fine fractions for typical Minnesota dense gradations needs to be examined. For this purpose, DEM simulations were performed using the polyhedral particles, and the results are presented in the following sections.

6.2.2.1 Determination of Gradation Design Alternatives

For the purposes of illustration and saving computational time, the DEM packing simulation targeted Minnesota DOT (MnDOT) specified Class 6 (CL-6) gradation band, which is coarser than other traditional MnDOT specified gradation bands (e.g., Class 5, Class 3, etc.), as shown in Figure 6.6. Table 6.4 lists the detailed lower and upper bounds of the MnDOT specified CL-6 gradation control sieve requirements. Since it is computationally expensive and almost impractical to model the whole distribution of the given gradations, the smallest particle size simulated in the DEM packing simulation was chosen as the one passing 4.75-mm sieve and retained at the 2-mm sieve. Different gradation design alternatives simulated in DEM were created by orderly changing the minimum particle sizes, as tabulated in Table 6.4. A visual representation of those gradations simulated in DEM is given in Figure 6.7 with the x-axis being the normalized 0.45 power sieve size. Note that the use of those gradation design alternatives in DEM is to mimic the process of sequentially adding finer aggregates into the aggregate structure.

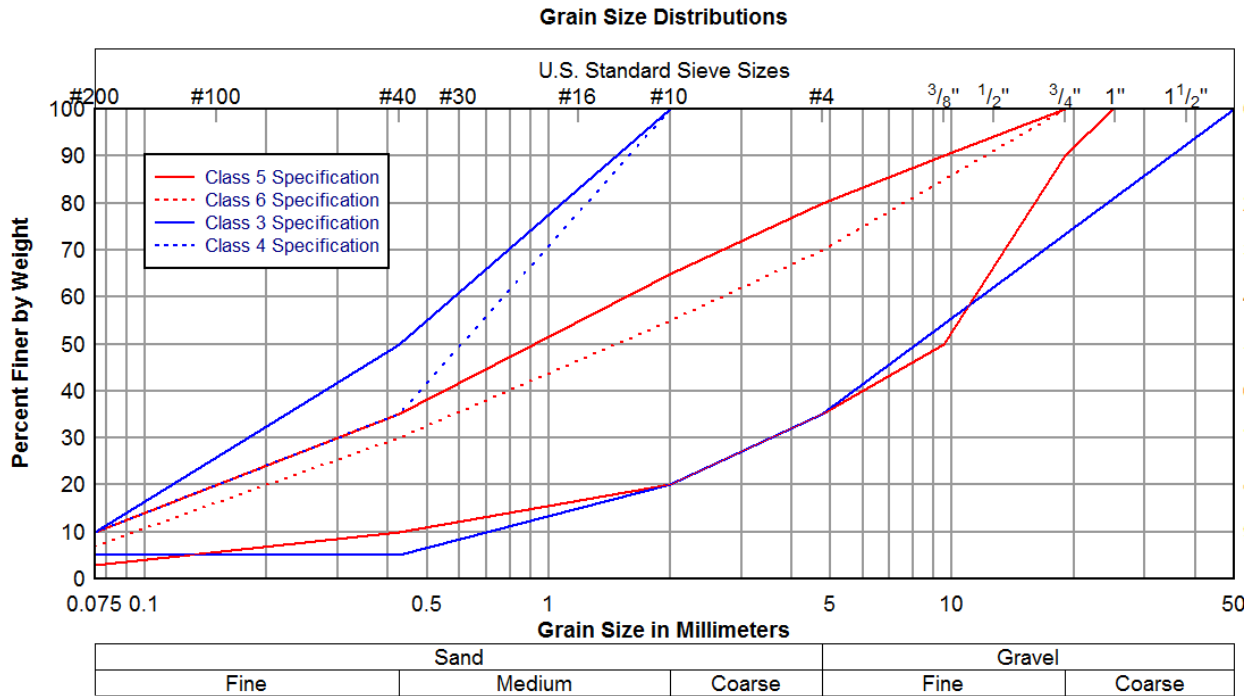


Figure 6.6 Gradation Bands Specified by MnDOT for Different Aggregate Classes

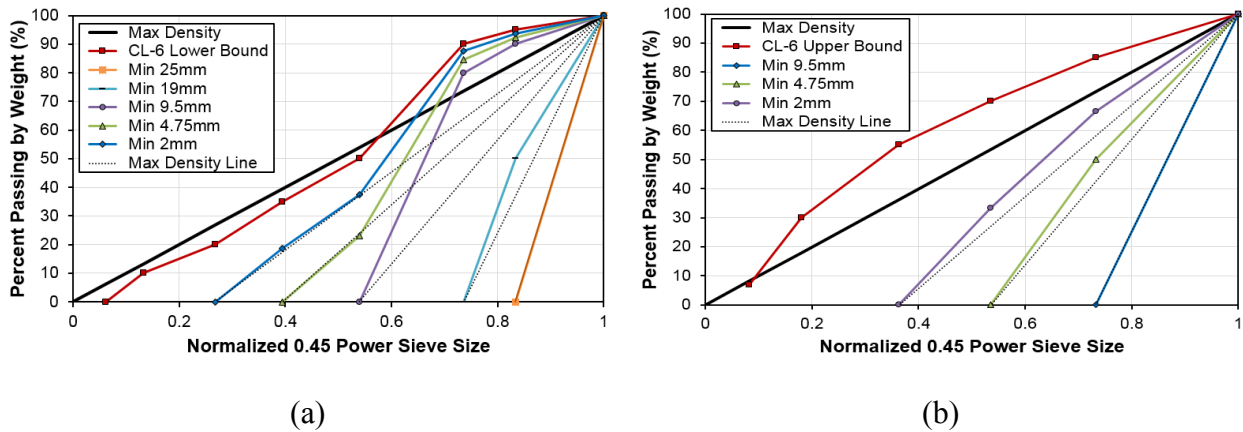


Figure 6.7 DEM Simulated MnDOT CL-6 Gradation Alternatives: (a) CL-6 Lower Bound and (b) CL-6 Upper Bound

Table 6.4 MnDOT Specified Class 6 (CL-6) Gradation Control Specifications and DEM Simulated Gradation Alternatives

Control Sieve		Upper Limit (% Passing)				Lower Limit (% Passing)					
mm	inches	Spec.*	Design Alternatives			Spec.*	Design Alternatives				
			#1	#2	#3		#1	#2	#3	#4	#5
37.5	1.5	100				100	100	100	100	100	100
25	1	100				95	0	50	90	92.3	93.8
19	3/4	100	100	100	100	90		0	80	84.6	87.5
9.5	3/8	85	0	50	66.7	50			0	23.1	37.5
4.75	#4	70		0	33.3	35				0	18.8
2	#10	55			0	20					0
0.425	#40	30				10					
0.075	No. 200	7				0					

Note: * denotes MnDOT specified control sieve specifications (spec.).

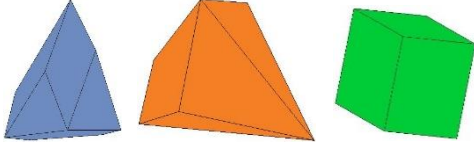
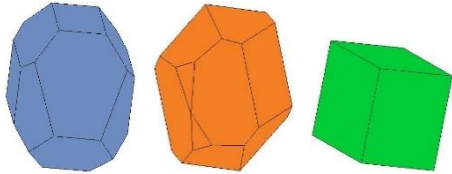
6.2.2.2 DEM Simulation Procedures

The main objective of this DEM simulation is to study and identify the breaking-sieve-size for CL-6 gradation band. The methodology involves the use of an image-aided aggregate particle generation and establishing a cubical domain to create aggregate packing model simulations based on the DEM. To achieve this main objective, this study was primarily focused on studying the upper and lower bounds of the MnDOT specified CL-6 gradation band and using 3-dimensional (3D) polyhedral discrete aggregate particles having low and high angularity categories quantified by image analysis.

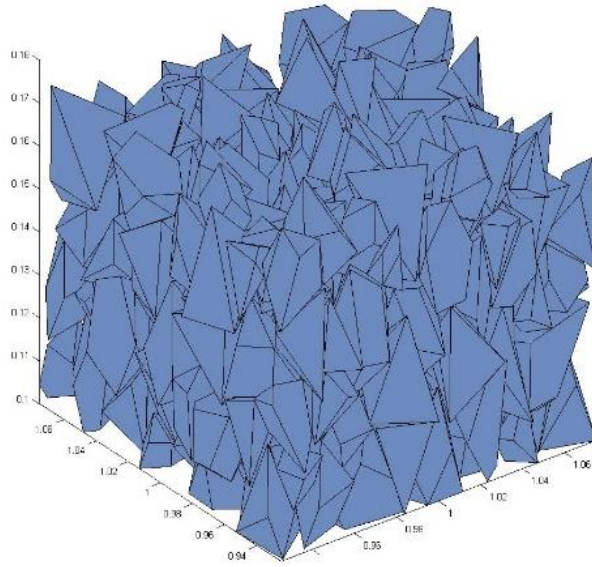
Based on the gradations given in Table 6.4, three DEM simulation gradations that included different fractions of the CL-6 upper bound were established. For CL-6 upper bound, Gradation #1 includes aggregates larger than 9.5 mm; Gradation #2 consists of aggregates larger than 4.75 mm; and Gradation #3 contains all aggregates larger than 2 mm. Particles smaller than 2 mm were assumed to behave as finer particles filling the voids of the aggregate skeleton and were not included in the DEM packing simulation. By analogy, five different gradations were created for CL-6 lower bound, as tabulated in Table 6.4.

In BLOKS3D, a rectangular container was first generated with a side dimension of 6 times the maximum particle size, i.e., 150 mm for CL-6 upper bound and 225 mm for CL-6 lower bound, respectively. Target gradations of different sized particles were then created from predefined particle shape libraries and used in the DEM simulations. As tabulated in Table 6.5, two particle shape libraries were used in the DEM simulations to represent high and low angularity levels. The flatness and elongation (F&E) ratio of aggregate particles for each shape library was fixed as 1:1 to specifically study the effect of different angularity levels. Each particle defined in libraries had equal chance of being picked up by the simulation program. Note that each library also contained cube-shaped particles limited to around 2.5% of all the particles in the simulation (Huang, 2010). The total weight (or volume) of aggregate particles for a specific size group of each DEM gradation were calculated according to the proportions of the given gradation.

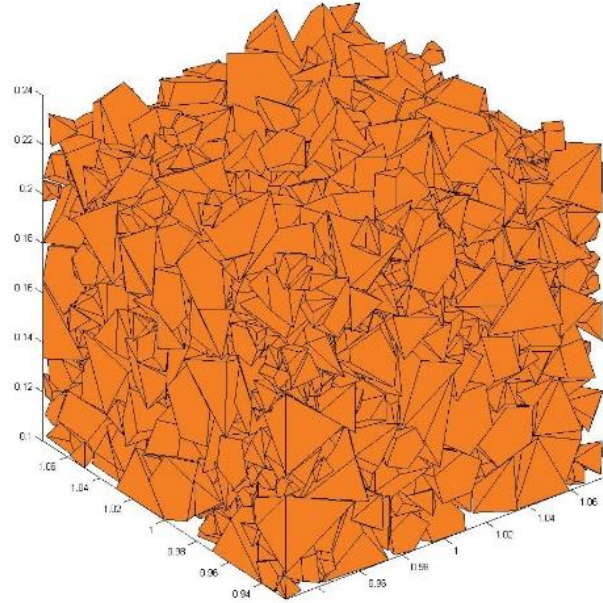
Table 6.5 Two Particle Shape Libraries Representing High and Low Angularity Levels Used in DEM Simulations

Particle Shape Library	Average Angularity Index (AI)	Flatness & Elongation (F&E) Ratio	Visual Representation
High Angularity	600	1:1	
Low Angularity	419	1:1	

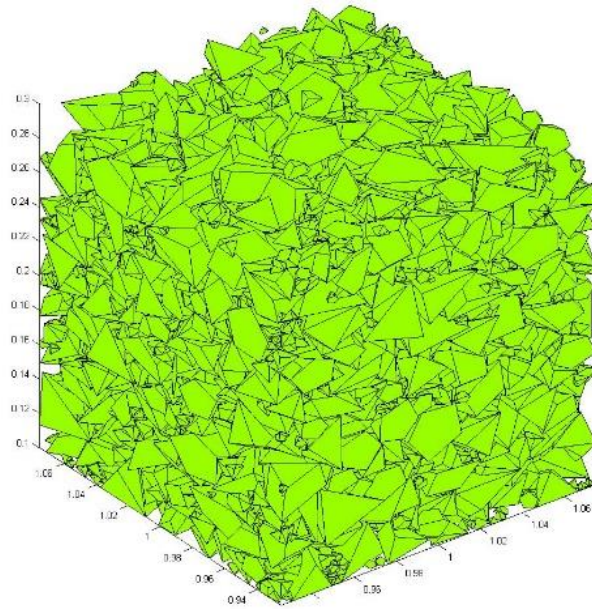
As illustrated in Figure 6.8, the aggregate gradation samples were generated and compacted in accordance to the following DEM procedure: (i) generate aggregate particles as discrete elements ($K_n=20 \text{ MN/m}$; $K_s=10 \text{ MN/m}$; $\theta=31^\circ$) and drop them, using a gravity constant of 9.8 m/s^2 , into the rectangular container also generated as a discrete element; (ii) switch the gravity constant between “+” and “-“ 9.8 m/s^2 a few times to obtain a uniformly packed assembly; (iii) compact samples using a force of 50 psi (344.7 kPa) for 10 seconds; (iv) delete particles if necessary so that the total aggregate weights for different DEM gradations are proportional according to the given gradation. Given the specific gravity of particles, the weight of the DEM aggregate sample and the sample air voids content can be calculated. The DEM simulations were repeated twice for each gradation alternative with the averages reported.



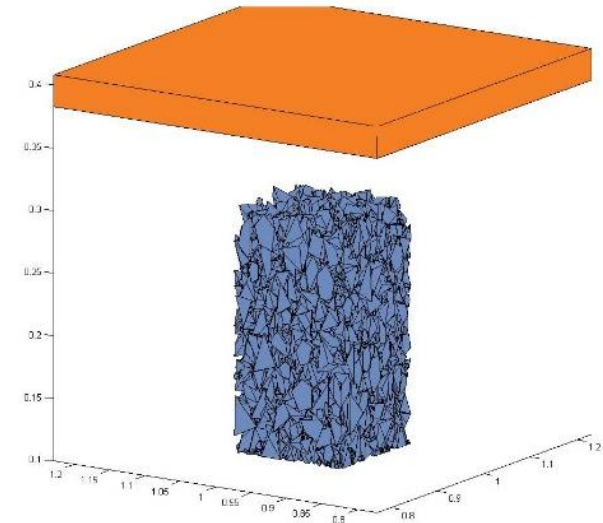
(a)



(b)



(c)



(d)

Figure 6.8 Illustration of DEM Particle Generation Process for (a) Gradation #1, (b) Gradation #2, and (c) Gradation #3 of CL-6 Upper Bound and (d) Particle Compaction Process

6.2.2.3 DEM Simulation Results

Table 6.6 and Table 6.7 list for CL-6 upper bound and lower bound the DEM simulated packing characteristics before and after compaction, respectively. By comparing the volume and porosity changes of different gradations simulated by DEM, the role of a specific particle size can be determined. To quantify the change of volume due to the addition of finer aggregates and to determine the roles of aggregate particles in a specific aggregate assembly, a parameter named relative volume change was used (Shen and Yu, 2011). It is defined as the ratio of the total volume increase (or decrease) to the solid volume of added finer aggregates (see Equation 6.2). A value greater than 1 indicates the added finer aggregates play a role of creating additional air voids in the aggregate assembly, whereas a value less than 1 indicates a role of filling the existing air voids. Therefore, the relative volume change for Gradation #2 is calculated from the difference between Gradations #1 and #2, and the relative volume change for Gradation #3 is calculated from the difference between Gradations #2 and #3.

Relative Volume Change :

$$\Delta V = \frac{V_{after}^T - V_{before}^T}{V_{added\ particles}^S} = \begin{cases} > 1, \text{ Creating additional voids} \\ < 1, \text{ Filling air voids} \end{cases} \quad (6.2)$$

where ΔV =relative volume change, V_{before}^T =total sample volume before adding finer aggregates, V_{after}^T =total sample volume after adding finer aggregates, and $V_{added\ particles}^S$ =solid volume of finer aggregates added.

As it can be seen from Table 6.6, adding aggregates within the size range of 4.75 to 2 mm into the coarser aggregate assembly decreases the value of relative volume change from above 1 to below 1. The same is true for CL6 lower bound (see Table 6.7). This means that aggregate particles passing 4.75 mm sieve play a role of filling the voids between larger particles instead of

creating additional voids. Therefore, #4 sieve (or 4.75-mm sieve) can be regarded as the breaking sieve size that separates the gravel-sized coarse fraction (aggregate skeleton) and sand-sized fine fraction for the CL-6 upper bound. This further confirms that the concept of gravel-to-sand ratio, presented in Chapter 5 with the 4.75 mm sieve used as the breaking sieve size, appears to be reasonable for typical Minnesota aggregate gradations studied.

Other packing characteristics such as the total number of contact points and coordination number (average stone-on-stone contact points per particle) are listed in Table 6.6 and Table 6.7 as well. Note that the coordination number was calculated as the ratio of total contact points between aggregate particles only to the total number of particles without counting the contact points between particles and compaction plate/rigid boundaries. The geometric stability of granular media under mechanical loading is commonly studied in terms of their mechanical coordination number, i.e., average number of load-bearing contacts per particle, at a given stage of loading (Antony and Kruyt, 2009). Antony and Kruyt (2009) also found that granular assemblies attain peak shear strength (and maximum fabric anisotropy of strong contacts) when a critical value of the mechanical coordination number is attained.

In general, compaction increases the coordination number value, an indication of improved structural stability and load-transferring ability of aggregate skeleton. Table 6.6 and Table 6.7 also reflect the fact that higher imaging based angularity levels generally result in greater number of particle contact points and thus greater coordination numbers. The decrease of the coordination number after adding aggregate particles within the range of 4.75 to 2 mm indicates that aggregate particles smaller than 4.75 mm have no apparent contribution to increasing load-carrying ability. It can be regarded as another indication of the validity of using 4.75 mm sieve as the breaking-sieve-size between coarse and fine fractions.

Table 6.6 DEM Packing Simulation Results (High Angularity) for CL-6 Upper Bound

Parameter		Gradation #1	Gradation #2	Gradation #3
High Angularity				
Particle Size Range (mm)		19 - 9.5	19 - 4.75	19 - 2
No. of Particles		296	1066	2415
Volume of Particles (mm ³)		967,144	1,963,852	2,918,135
Before Compaction	Total Volume (mm ³)	150*150*180	150*150*240	150*150*300
	Porosity	0.462	0.377	0.279
	No. of Contacts	1085	4030	8585
	Coordination Number	3.17	3.45	3.29
	Relative Volume Change	-	1.35	0.84
After Compaction	Total Volume (mm ³)	150*150*160	150*150*210	150*150*250
	Porosity	0.232	0.202	0.135
	No. of Contacts	1434	4986	9257
	Coordination Number	4.18	4.14	3.49
	Relative Volume Change	-	1.21	0.85
Low Angularity				
No. of Particles		295	963	2479
Volume of Particles (mm ³)		984,867	315,000	2,911,390
Before Compaction	Total Volume (mm ³)	150*150*180	150*150*240	150*150*300
	Porosity	0.453	0.379	0.353
	No. of Contacts	983	3340	8187
	Coordination Number	2.83	3.09	2.97
	Relative Volume Change	-	1.39	0.82
After Compaction	Total Volume (mm ³)	150*150*171	150*150*220	150*150*270
	Porosity	0.367	0.322	0.215
	No. of Contacts	1314	3774	9069
	Coordination Number	3.38	3.41	3.16
	Relative Volume Change	-	1.36	0.88

Table 6.7 DEM Packing Simulation Results for CL-6 Lower Bound

Parameter		Gradation #2	Gradation #3	Gradation #4	Gradation #5
Particle Size Range (mm)		37.5 - 19	37.5 - 9.5	37.5 - 4.75	37.5 - 2
High Angularity					
No. of Particles		40	584	960	1487
Volume of Particles (mm ³)		776,531	3,935,004	5,088,646	6,219,595
Before Compaction	Total Volume (mm ³)	226*226*152	226*226*234	226*226*260	226*226*300
	Porosity	0.708	0.425	0.377	0.308
	No. of Contacts	36	2039	3352	5187
	Coordination Number	0.55	3.10	3.13	3.09
	Relative Volume Change	-	1.33	1.15	0.72
After Compaction	Total Volume (mm ³)	226*226*140	226*226*210	226*226*240	226*226*258
	Porosity	0.620	0.300	0.288	0.229
	No. of Contacts	81	2576	3761	5269
	Coordination Number	2.0	3.72	3.43	3.12
	Relative Volume Change	-	1.13	1.33	0.81
Low Angularity					
No. of Particles		42	649	1017	1497
Volume of Particles (mm ³)		807,551	3,988,209	5,195,420	6,413,676
Before Compaction	Total Volume (mm ³)	226*226*141	226*226*236	226*226*266	226*226*300
	Porosity	0.614	0.426	0.387	0.325
	No. of Contacts	76	2105	3245	4816
	Coordination Number	1.40	2.86	2.76	2.75
	Relative Volume Change	-	1.53	1.27	0.84

Table 6.7 (cont.)

Parameter		Gradation #2	Gradation #3	Gradation #4	Gradation #5
Particle Size Range (mm)		37.5 - 19	37.5 - 9.5	37.5 - 4.75	37.5 - 2
Low Angularity					
No. of Particles		42	649	1017	1497
Volume of Particles (mm ³)		807,551	3,988,209	5,195,420	6,413,676
After Compaction	Total Volume (mm ³)	226*226*135	226*226*210	226*226*240	226*226*270
	Porosity	0.553	0.283	0.266	0.261
	No. of Contacts	66	2586	3759	4741
	Coordination Number	1.57	3.24	3.11	2.67
	Relative Volume Change	-	1.34	1.26	0.47

6.3 Gradation Effects Influencing Contact and Packing Characteristics of Aggregate Skeleton

For unbound aggregate layers, rutting or permanent deformation caused by repeated traffic loads is the most important single performance indicator. This occurs due to plastic flow in the base or subbase layer from the re-arrangement or crushing of the aggregate particles. Field observations have identified strong linkage between shear strength and rutting resistance. From the microscopic particle contact behavior perspective, unbound aggregate rutting or other stability criteria can be best addressed by improving the gradation design and material selection. By determining the load-carrying aggregate skeleton and its quality, the mechanism involving aggregate interactions is addressed. For this purpose, DEM packing simulation using different gradations was pursued to evaluate the gradation effects influencing the contact and packing characteristics of aggregate skeleton.

6.3.1 Determination of Gradation Design Alternatives

According to the gravel-to-sand ratio concept presented in Chapter 5, an optimum gradation was recommended for a drainable base that satisfies the current MnDOT gradation specification for unbound permeable aggregate base (PAB). In order to further validate this result, the DEM simulation targeted MnDOT specified gradation band for unbound PAB. Different gradations were created by adjusting the percent passing values of the control sieves tabulated in Table 6.8. Table 6.8 also lists the percent passing values used to create the individual gradation curves, which were then studied using both analytical gradation analysis framework (reviewed in Chapter 2) and DEM simulations for their effects on the contact and packing characteristics of aggregate skeleton.

Table 6.8 MnDOT Specified Gradation Control Sieves for Unbound PAB

Control Sieve		Upper Limit (% Passing)	Lower Limit (% Passing)	% Passing Values Considered
mm	inches			
25	1	100	100	100
19	3/4	100	65	65, 72, 79, 86, 93, 100
9.5	3/8	70	35	35, 40, 45, 50, 55, 60, 65, 70
4.75	#4	45	20	20, 25, 30, 35, 40, 45
2	#10	25	8	8, 16, 25
0.425	#40	10	2	2, 6, 10
0.075	No. 200	3	0	0, 1.5, 3

The individual grain size distributions studied are to realistically represent possible different new aggregate gradations that may be received from a pit/quarry source and all satisfy the MnDOT specified unbound PAB gradation requirements. Only the percent passing value for one control sieve was changed at a time, and the others were kept constant as the mid-range. In total, a full factorial of $6 \times 8 \times 6 \times 3 \times 3 \times 3 = 7776$ different individual gradation curves can be possibly generated with all falling within the MnDOT specified unbound PAB gradation band (see Table 6.8). However, the main objective of this gradation analysis is not to exhaust all the possible gradation curves but to identify the relative importance of each control sieve in governing aggregate packing characteristics. Therefore, special attention will be paid to the most important control sieves to achieve structural stability.

6.3.2 Analysis Results of the Analytical Gradation Framework

Different packing parameters have been proposed based on the analytical packing theory (spherical particles) based gradation framework to evaluate the unbound materials performance. The primary structure porosity (PS porosity) and PS coordination number were used to evaluate the resilient modulus property, whereas the disruption potential (DP) was used to evaluate the permanent deformation behavior (Yideti et al., 2013). Table 6.9 lists for each gradation curve the gradation analysis results using the aforementioned analytical framework, including the range of sizes that form Primary Structure (or aggregate skeleton), the Primary Structure Porosity, and the Coordination Number. As it can be seen, #4 sieve (or 4.75-mm sieve) is calculated as the breaking sieve size that separates the Primary Structure and Secondary Structure for the majority of those gradation curves.

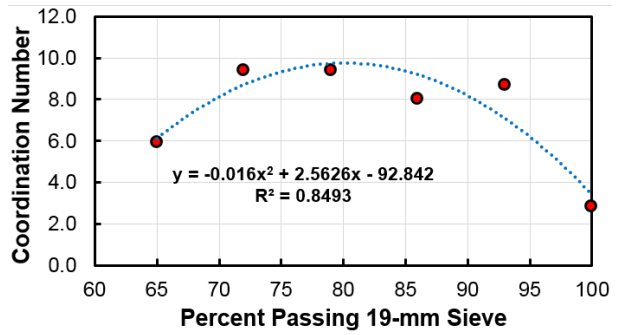
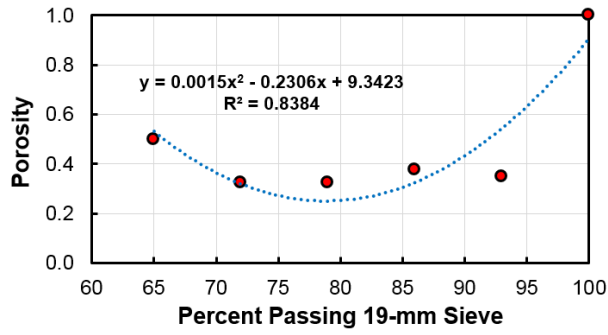
Table 6.9 Analytical Gradation Analysis Results for MnDOT Specified PAB Gradation Band

Control Sieve (mm)	% Passing	PS Range (mm)	% Material Retained			PS Porosity	Coordination Number m
			PS	SS	O		
19	100	-	0	100	0	1.00	2.8
	93	9.5 - 4.75	60.5	32.5	7	0.35	8.7
	86	9.5 - 4.75	53.5	32.5	14	0.38	8.0
	79	19 - 4.75	67.5	32.5	0	0.33	9.4
	72	19 - 4.75	67.5	32.5	0	0.33	9.4
	65	9.5 - 4.75	32.5	32.5	35	0.50	5.9
9.5	70	19 - 9.5	30	70	0	0.70	4.1
	65	19 - 4.75	67.5	32.5	0	0.33	9.4
	60	19 - 4.75	67.5	32.5	0	0.33	9.4
	55	19 - 4.75	67.5	32.5	0	0.33	9.4
	50	19 - 4.75	67.5	32.5	0	0.33	9.4
	45	19 - 9.5	55	45	0	0.45	6.6
	40	-	0	100	0	1.00	2.8
	35	-	0	100	0	1.00	2.8
4.75	45	19 - 9.5	47.5	52.5	0	0.53	5.6
	40	19 - 9.5	47.5	52.5	0	0.53	5.6
	35	19 - 4.75	65	35	0	0.35	8.7
	30	19 - 4.75	70	30	0	0.30	10.2
	25	19 - 4.75	75	25	0	0.25	12.4
	20	19 - 4.75	80	20	0	0.20	15.8
2	25	19 - 4.75	67.5	32.5	0	0.33	9.4
	16	19 - 4.75	67.5	32.5	0	0.33	9.4
	8	19 - 4.75	67.5	32.5	0	0.33	9.4
0.425	10	19 - 4.75	67.5	32.5	0	0.33	9.4
	6	19 - 4.75	67.5	32.5	0	0.33	9.4
	2	19 - 4.75	67.5	32.5	0	0.33	9.4
0.075	3	19 - 4.75	67.5	32.5	0	0.33	9.4
	1.5	19 - 4.75	67.5	32.5	0	0.33	9.4
	0	19 - 4.75	67.5	32.5	0	0.33	9.4

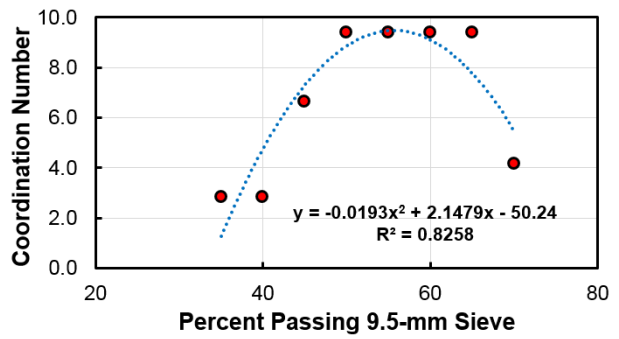
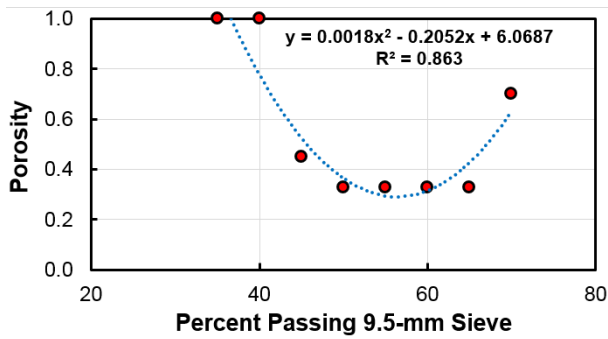
Notes: “-“ denotes that no obvious Primary Structure exists according to the analytical framework; PS=Primary Structure (or aggregate skeleton); SS=Secondary Structure; O=Other materials floating in the aggregate matrix; and the theory was developed by Yideti et al. (2013).

Figure 6.9 graphically plots the PS Porosity and Coordination Number results against different percent passing values at each control sieve. Note that these results plotted were computed by using the analytical gradation framework that was developed by Yideti et al. (2013) based on ideal arrangement of spherical particles. It can be seen from Figure 6.9(c) that increasing percent passing #4 sieve steadily decreases the coordination number, an indicator of the quality of the formed aggregate skeleton. As expected, particles smaller than 2 mm have no influence on the primary structure, as shown in Figure 6.9(d). This is due to the fact that the smallest particle size of the primary structure is limited to 2 mm (Yideti et al., 2013).

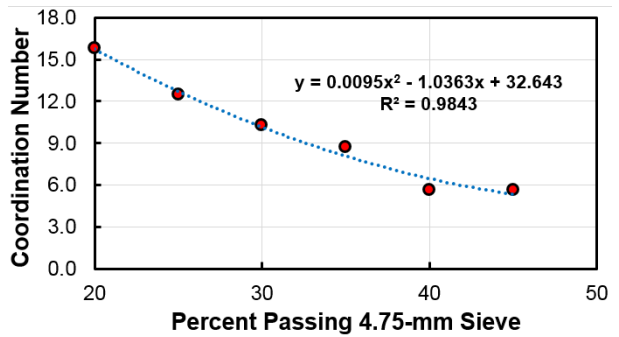
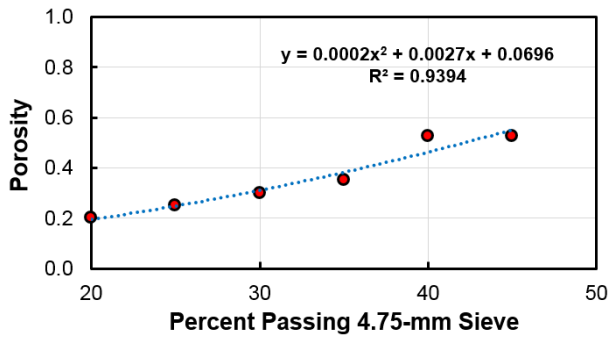
Based on the results presented in Figure 6.9, it is recommended that percent passing #4 sieve (or 4.75-mm sieve) be kept at lower bound (i.e., 20) in order to maximize the coordination number for structural stability of the Primary Structure. Meanwhile, percent passing 19-mm and 9.5-mm sieve could be kept around the corresponding mid-ranges, i.e., 80 and 60, respectively. Table 6.10 lists the optimum unbound PAB gradation in terms of maximum coordination number for structural stability and load transferring capacity of aggregate skeleton, which is obtained according to the aforementioned analytical gradation analysis results. Note that although percent passing 2-mm sieve has no effect on either porosity or coordination number in Figure 6.9, it was selected as 15 so that it falls within the range between 20 (percent passing 4.75-mm sieve) and 10 (percent passing 0.425-mm sieve). Except the percent passing values at two sieve sizes (i.e., 19 mm and 4.75 mm), it turns out to be reasonably close to the one recommended in Chapter 5 for use at MnROAD construction based on the gravel-to-sand ratio concept.



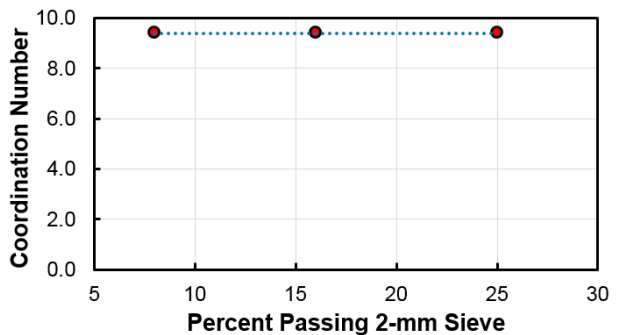
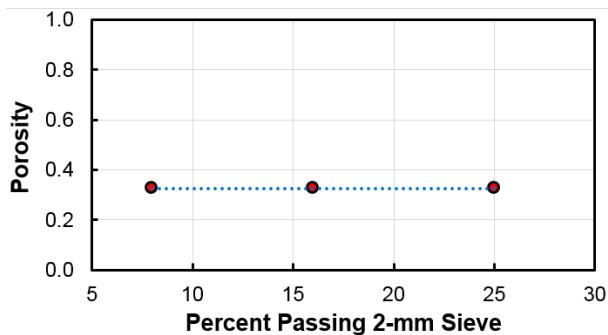
(a)



(b)



(c)



(d)

Figure 6.9 Relative Importance of Each Control Sieve in Primary Structure Porosity and Coordination Number from Spherical Packing Theory based Analytical Framework: (a) 19 mm, (b) 9.5 mm, (c) 4.75 mm, and (d) 2 mm

Table 6.10 Recommended Unbound PAB Gradation based on Packing Characteristics

Sieve Size (mm)	25	19	9.5	4.75	2	0.425	0.075
% Passing	Recommended by Packing Theory based Analytical Gradation Framework						
	100	80	60	20	15	10	3
	Recommended by Gravel-to-Sand Ratio Concept						
	100	92	61	41	24	10	3

Note: the percent passing values at two sieve sizes, i.e., 19 mm and 4.75 mm are different between the two methodologies.

The packing theory based analytical gradation framework was derived from the densest packing conditions of spherical particles (Yideti et al., 2013), whereas the optimal gravel-to-sand ratio of around 1.5 (for AASHTO T180 modified Proctor compaction) was observed from experimental results of a comprehensive aggregate database archived by MnDOT (Xiao et al., 2012). Therefore, the reasonably good match between the optimal gradations recommended by both approaches further indicates that there indeed exists an optimal ratio between the coarse (aggregate skeleton) and fine (void-filling) fractions in the aggregate assembly. Note that the methodology presented herein for MnDOT PAB gradation band can be readily extended to MnDOT traditional Class 5 and 6 bands as well.

6.3.3 DEM Packing Simulation Results

This section presents the verification results of the packing theory based framework using spherical particles against DEM packing simulation using polyhedral particles. DEM packing simulation was performed on a selection of gradations tabulated in Table 6.9 to verify the analysis results of the analytical gradation framework. The same DEM procedure as presented previously was followed. It is worth mentioning that the DEM code BLOKS3D employed herein currently cannot model individual particles as perfect spheres as assumed by the analytical gradation framework. The goal of the DEM simulation is to simulate the packing characteristics of different coarse aggregate structures, and to identify how the degree of aggregate contact and interlocking changes with varying percentages of material passing each individual sieve size. The effect of aggregate angularity was also considered directly by choosing different particle shape from pre-established shape library. The packing characteristic parameters obtained from the DEM simulation provide a promising approach to estimate the proper packing via stone-on-stone contacts in the aggregate skeleton without the need for experiments. Eventually, a direct linkage between aggregate gradation and mechanical performance of the aggregate assembly will be needed for optimizing the aggregate gradation design.

The minimum particle size simulated in the DEM is the one that retained on 4.75-mm sieve, according to the calculation results of the analytical gradation framework. The percent passing value for each of the two chosen control sieve sizes (i.e., 19 mm and 9.5 mm) was changed from upper bound, mid-range to lower bound at a time, and the others were kept constant as the mid-range, as shown in Table 6.11. The process of the DEM simulation involves three major steps. First, polyhedron particles are generated in the computer according to the target gradation. These particles are added to a square box (0.15*0.15*0.15 m) under a unidirectional gravitational force. Next, particles are compacted by the applied force to its stable

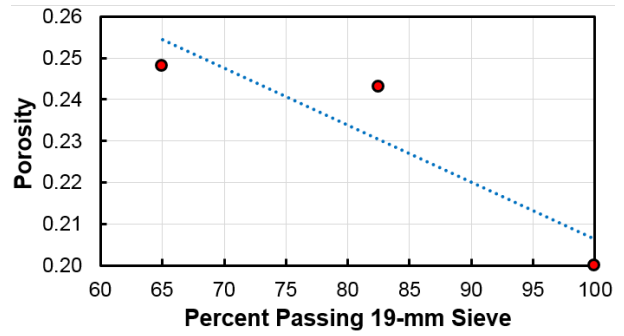
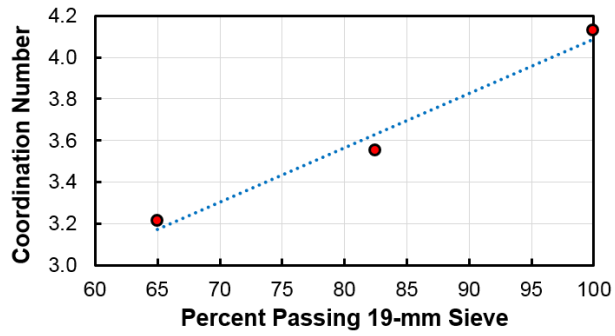
position. Finally, the volumetric properties and the mean contact force are calculated. Since the DEM aggregate samples of different gradations were compacted using the same amount of compaction energy, the resulting density and porosity levels could be different. In this study, the porosity was used as an indicator of the achieved density after compaction.

The DEM simulation results are shown in Figure 6.10 and tabulated in Table 6.11. The DEM simulated coordination number increases with increasing percentage of material passing 19-mm sieve, which is different than the trend predicted by the packing theory based analytical framework. The trend of the coordination number vs. percentage of material passing 9.5 mm sieve is, however, consistent with that predicted by the analytical framework. Therefore, to maximize the coordination number, the optimal unbound PAB gradation should be close to the upper bound at the 19-mm sieve and be close to the mid-range at the 9.5-mm sieve. The optimal gradation predicted by the gravel-to-sand ratio is found to be in agreement with the DEM simulation results.

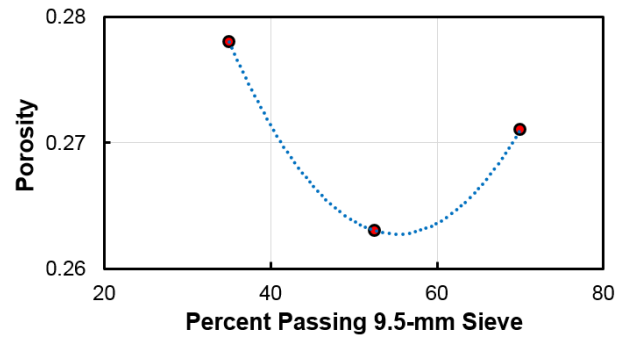
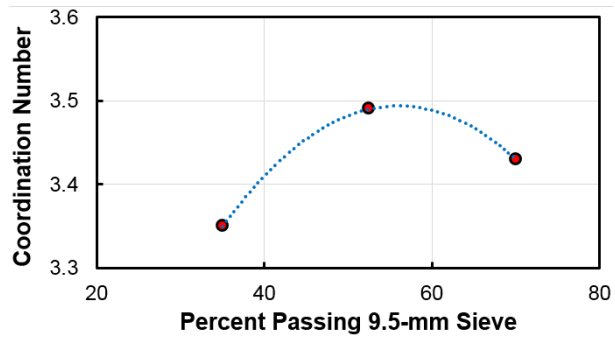
Table 6.11 Packing Characteristics Obtained from DEM Simulation for Unbound PAB

Control Sieve Size (mm)	% Passing*	Particle Volume (mm³)	No. of Particles	Porosity	No. of Contacts	Coordination Number
High Angularity						
19	100	1,554,455	629	0.200	2986	4.13
	82.5	1,471,804	326	0.243	1348	3.56
	65	1,462,115	253	0.248	1034	3.22
9.5	70	5,199,771	1496	0.271	5545	3.43
	52.5	5,737,862	1316	0.263	5034	3.49
	35	5,712,392	1128	0.278	4446	3.35

Note: * % Passing for each of the sieve sizes other than the control one is kept at the mid-range.



(a)



(b)

Figure 6.10 Relative Importance of Each Control Sieve in Primary Structure Porosity and Coordination Number from DEM Packing Simulation (High Angularity): (a) 19 mm and (b) 9.5 mm

6.4 DEM Validation of the Gravel-to-Sand Ratio Concept

In view of the slight difference in recommended optimal gradation between the Gravel-to-Sand ratio concept and the packing theory based analytical gradation framework, DEM simulations were first performed on five different gradations (see Figure 6.11) with the G/S ratio values of 1.0, 1.6, 2.0, and 2.5, respectively. Those different gradations were selected from the current MnDOT specified gradation band for unbound permeable aggregate base (UPAB). The main objective was to verify if the recommended UPAB gradation (in Chapter 5) for MnROAD 2013 construction cycle outperforms others in terms of both structural stability (as characterized by coordination number) and drainability (as characterized by porosity). Intermediate G/S ratio values of 1.2, 1.5, 1.7, 1.8, and 2.2 were also added subsequently into the DEM simulation.

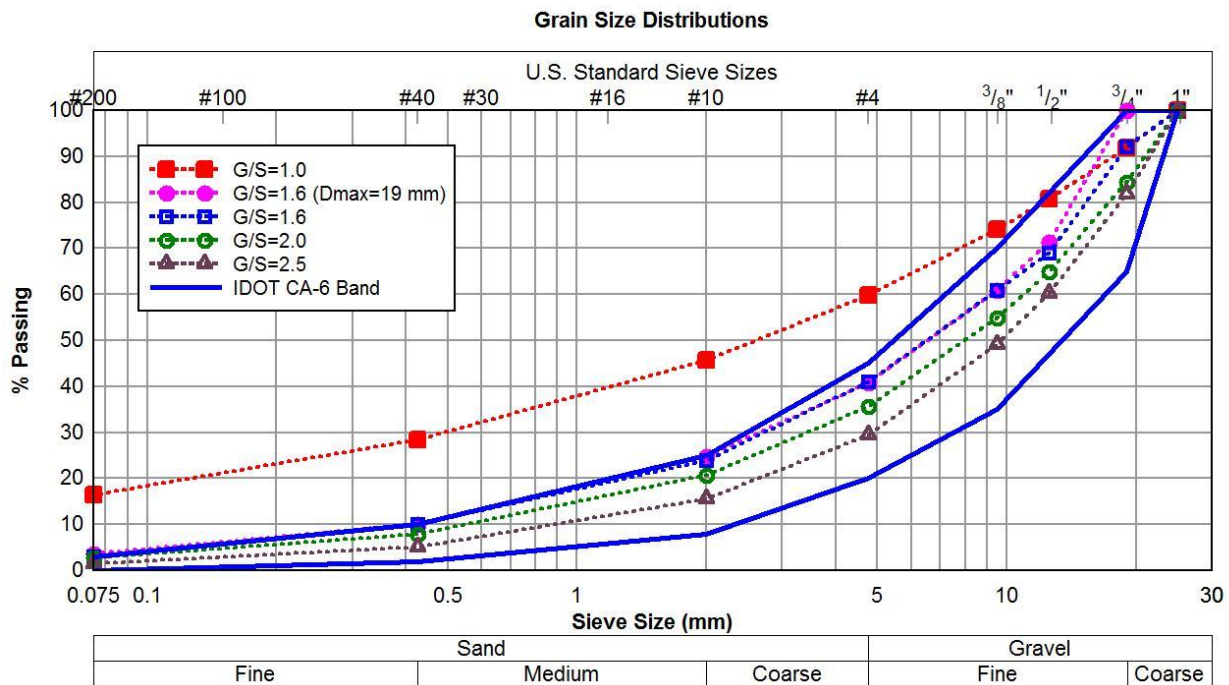
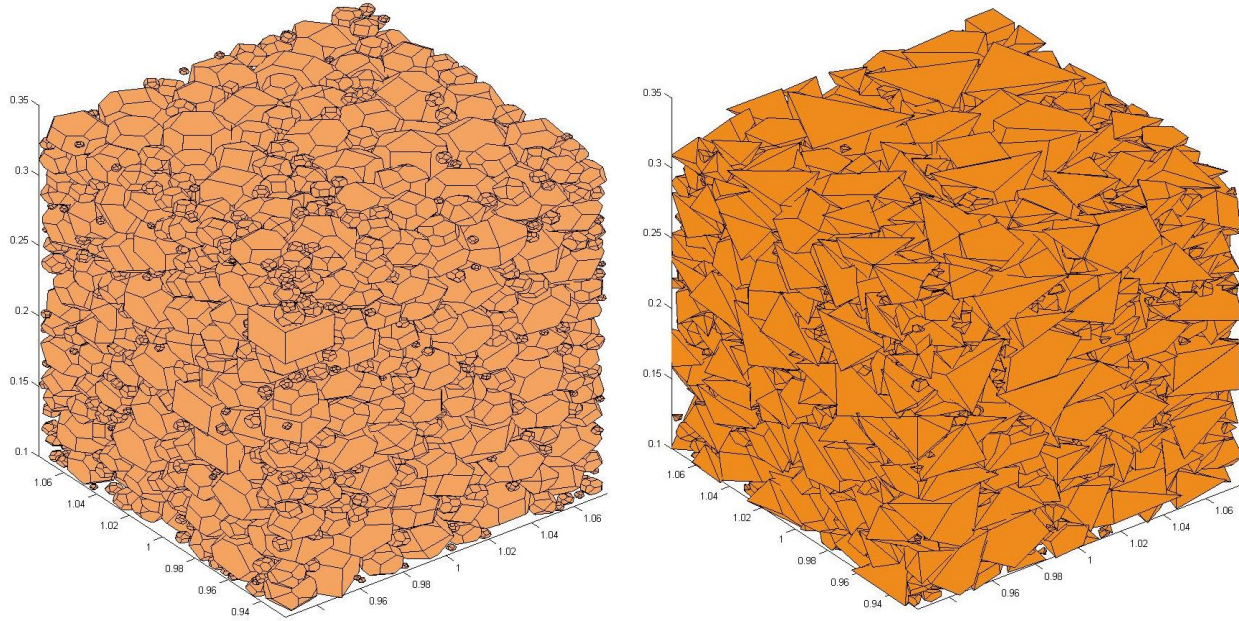


Figure 6.11 DEM Simulated Gradation Curves with Varying G/S Ratios

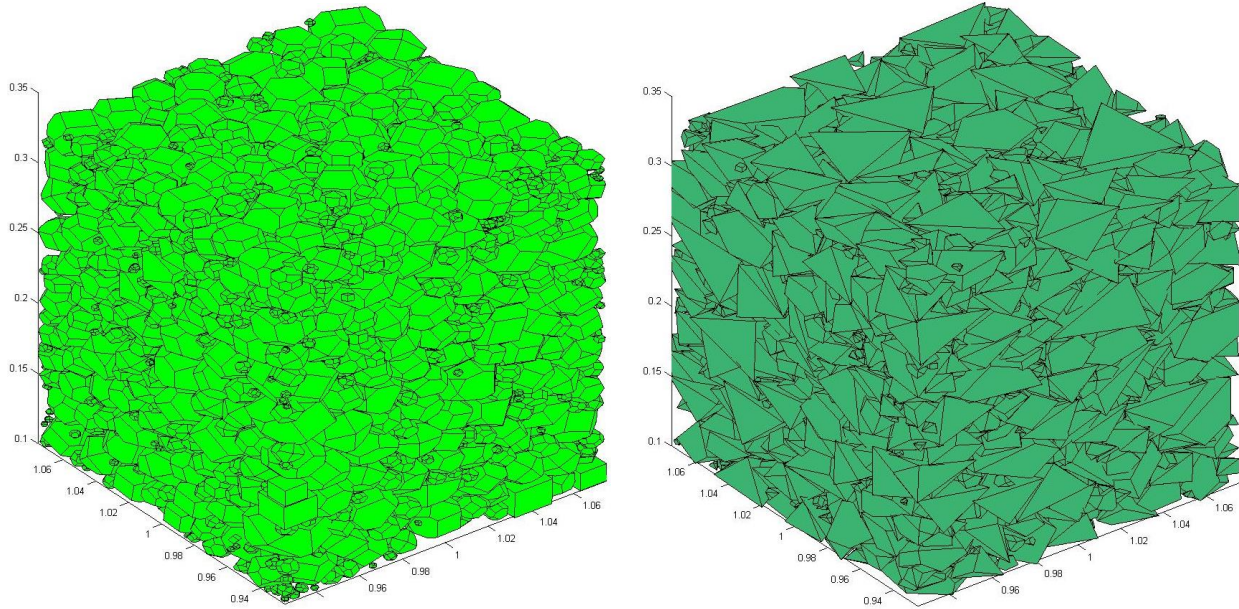
Note that the gradation with a G/S ratio of 1.0 lies outside of the MnDOT unbound PAB gradation band, because the minimum G/S ratio calculated for such gradation band is 1.4 (see

Figure 5.9(b)). The inclusion of the gradation with $D_{\max}=19$ mm and $G/S=1.6$ was to study the effect of the maximum aggregate size, while the maximum aggregate size for all other gradations was chosen as 25 mm. Two different aggregate angularity levels, i.e., high and low, were also considered to include the interaction effects of grain size and particle shape. Note that instead of simulating the entire particle size distribution, the minimum particle size simulated in DEM was 2 mm in order to avoid a long run time. The DEM procedure followed was presented previously.

Figure 6.12 and Figure 6.13 show the final compacted aggregate assemblies in the DEM simulations for different gradations with G/S ratio values of 1.0, 1.6, 2.0, and 2.5, respectively. Table 6.12 lists the contact and packing characteristic parameters obtained from the DEM simulations for both high and low angularity levels. As it can be seen, the G/S ratio of 1.6 results in the highest coordination number due to the densest packing (indicated by the lowest porosity). Therefore, the optimal G/S ratio of 1.6 observed in Chapter 5 from experimental results agrees well with the DEM simulation results using the 3D polyhedral particles with realistic aggregate shapes. The recommended optimal gradation for unbound PAB in Chapter 5 exhibits better contact and packing characteristics of aggregate skeleton as compared to others; hence, it is expected to yield better structural stability in the field while still satisfying the MnDOT unbound PAB gradation band requirements. It can also be observed from Figure 6.14 that the coordination number increases with increasing aggregate angularity level, whereas the porosity decreases with increasing aggregate angularity level. This indicates that more angular aggregates are expected to have better structural stability (e.g., shearing and rutting resistance) as represented by higher coordination number and lower porosity. Further DEM simulations of triaxial compression tests may prove this postulation made based on particle packing and contact characteristics.

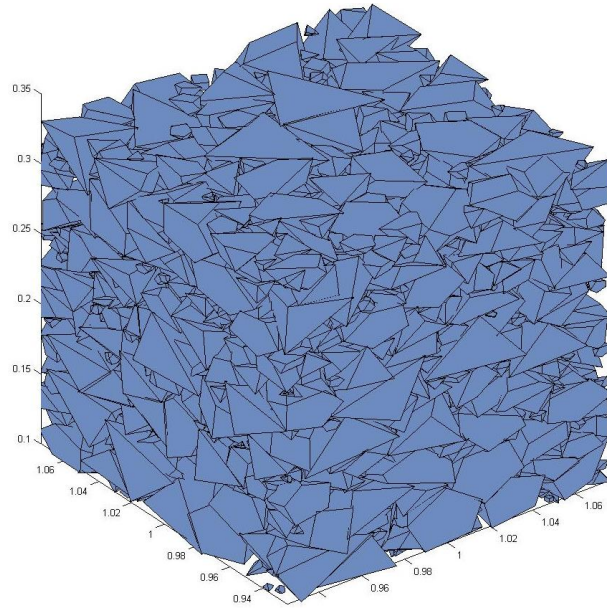
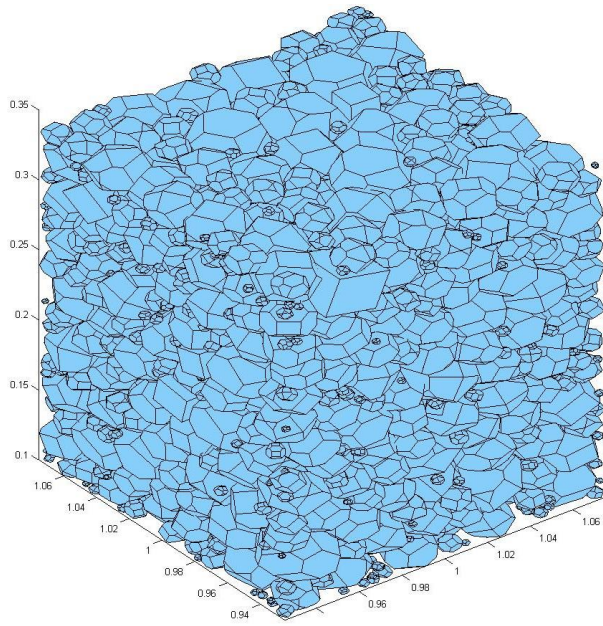


(a)

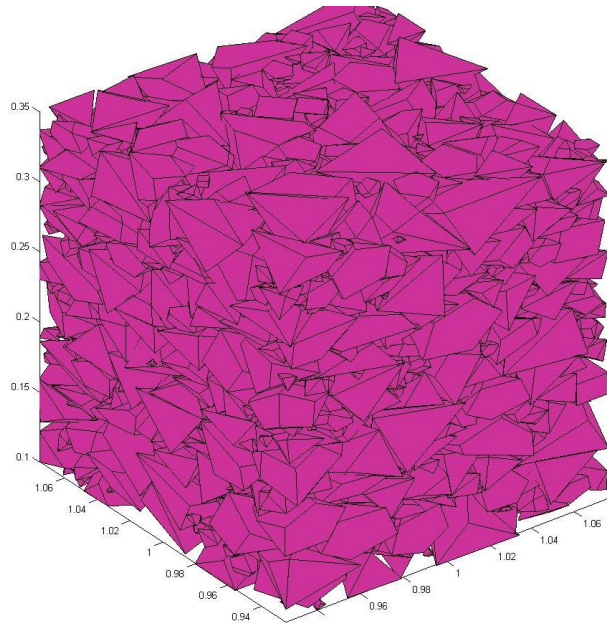
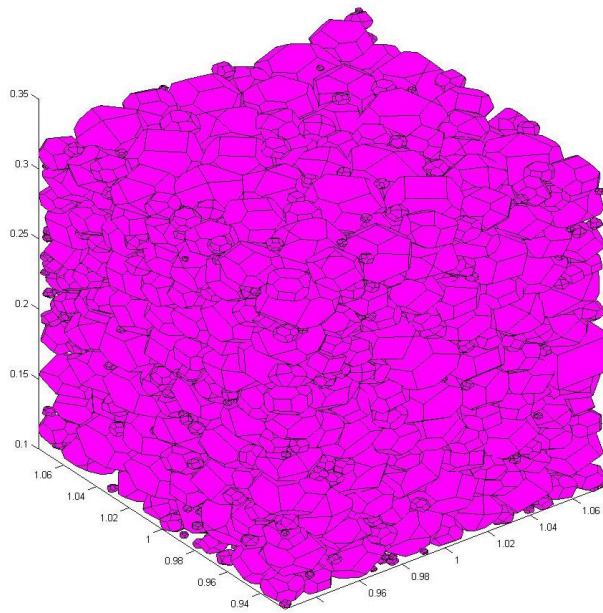


(b)

Figure 6.12 Final Compacted Aggregate Samples in DEM Simulation for Different G/S ratio Values: (a) 1.0 and (b) 1.6 (Left: Low AI; Right: High AI)



(c)



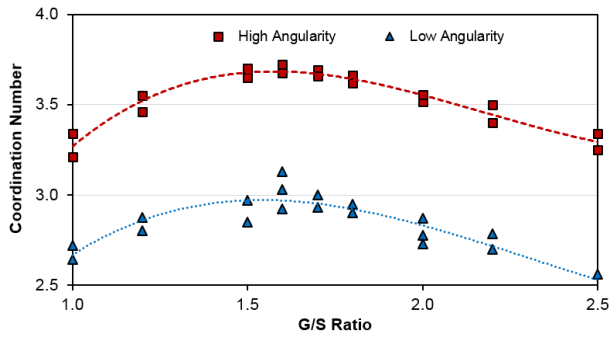
(d)

Figure 6.13 Final Compacted Aggregate Samples in DEM Simulation for Different G/S ratio Values: (a) 2.0 and (b) 2.5 (Left: Low AI; Right: High AI)

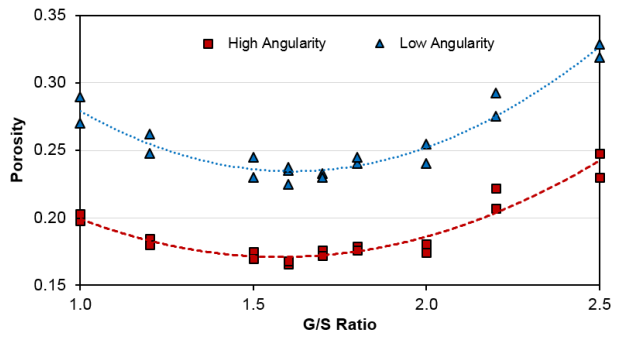
Table 6.12 Packing Characteristics Obtained from DEM Simulation for Different G/S Ratios

Angularity Level	G/S Ratio*	Particle Volume (mm ³)	No. of Particles	Porosity	No. of Contacts	Coordination Number
High	1.0	4,051,234	1499	0.198	5456	3.21
	1.6	4,219,308	1688	0.183	7483	3.67
	2.0	4,217,466	1274	0.181	5122	3.52
	2.5	4,221,270	1164	0.248	4422	3.34
Low	1.0	4,057,460	1399	0.248	4383	2.64
	1.6	3,971,062	1498	0.235	5161	2.98
	2.0	4,069,062	1189	0.241	4027	2.87
	2.5	4,046,569	1103	0.270	3961	2.80

Note: * maximum aggregate size $D_{max}=25$ mm.



(a)



(b)

Figure 6.14 DEM Calculated (a) Coordination Number and (b) Porosity versus G/S Ratio for High and Low Angularity Levels

Figure 6.15 shows the cumulative distribution of the internal contact forces for three different G/S ratio values. As it can be seen, the G/S ratio of 1.6 results in the least internal contact forces as compared to the other two, while the G/S ratio of 1.0 results in the highest internal contact forces. The difference of internal contact force distribution between G/S ratio values of 1.6 and 2.0 is not very significant, indicating the approximate optimal range of G/S ratio from 1.6 to 2.0. Figure 6.16 and Figure 6.17 give the visual representations of the internal contact force vectors for G/S ratio values of 1.0 and 1.6 from different views, respectively. It can be seen that the G/S ratio of 1.6 results in more uniformly distributed internal contact force vector. This indicates better structured aggregate skeleton with well-connected force chains can be expected from the optimal G/S ratio of 1.6.

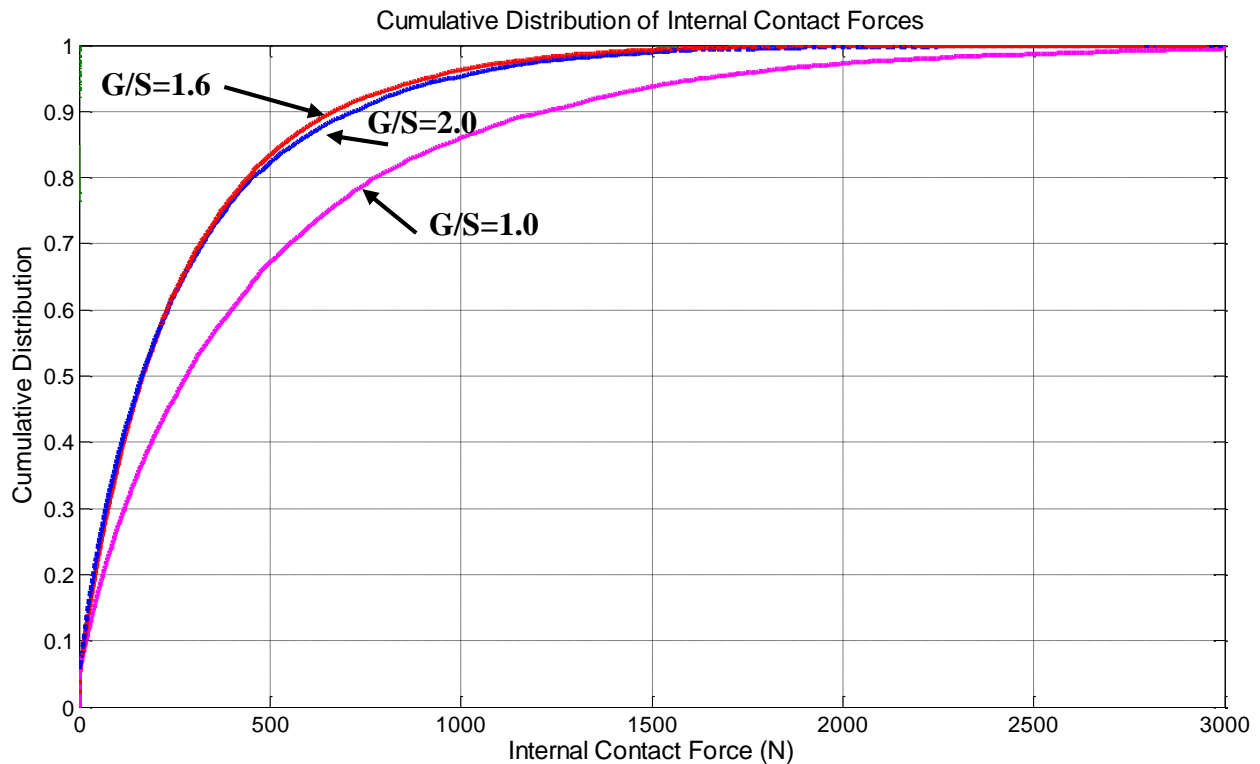


Figure 6.15 Comparison of Internal Contact Force Distributions for Three Different G/S Ratios

The close-up comparison of 3D contact force vectors is shown in Figure 6.19 for G/S values of 1.0 and 1.6 and in Figure 6.20 for G/S value of 2.5, respectively. The contact force vector plots were obtained at the same time step for aggregate samples with different G/S ratios that were tested in DEM under an applied normal force of 72 kN. The comparison between Figure 6.19 and Figure 6.20 clearly shows that aggregates with a G/S ratio of 1.6 somewhat indicate a clear, well-connected contact force chain network as compared to those with other G/S ratios. Also, aggregate samples having smooth surfaces have a relatively wider and scattered contact force bands than angular ones having rough surfaces. This could be attributed to the effects of aggregate angularity and surface texture.

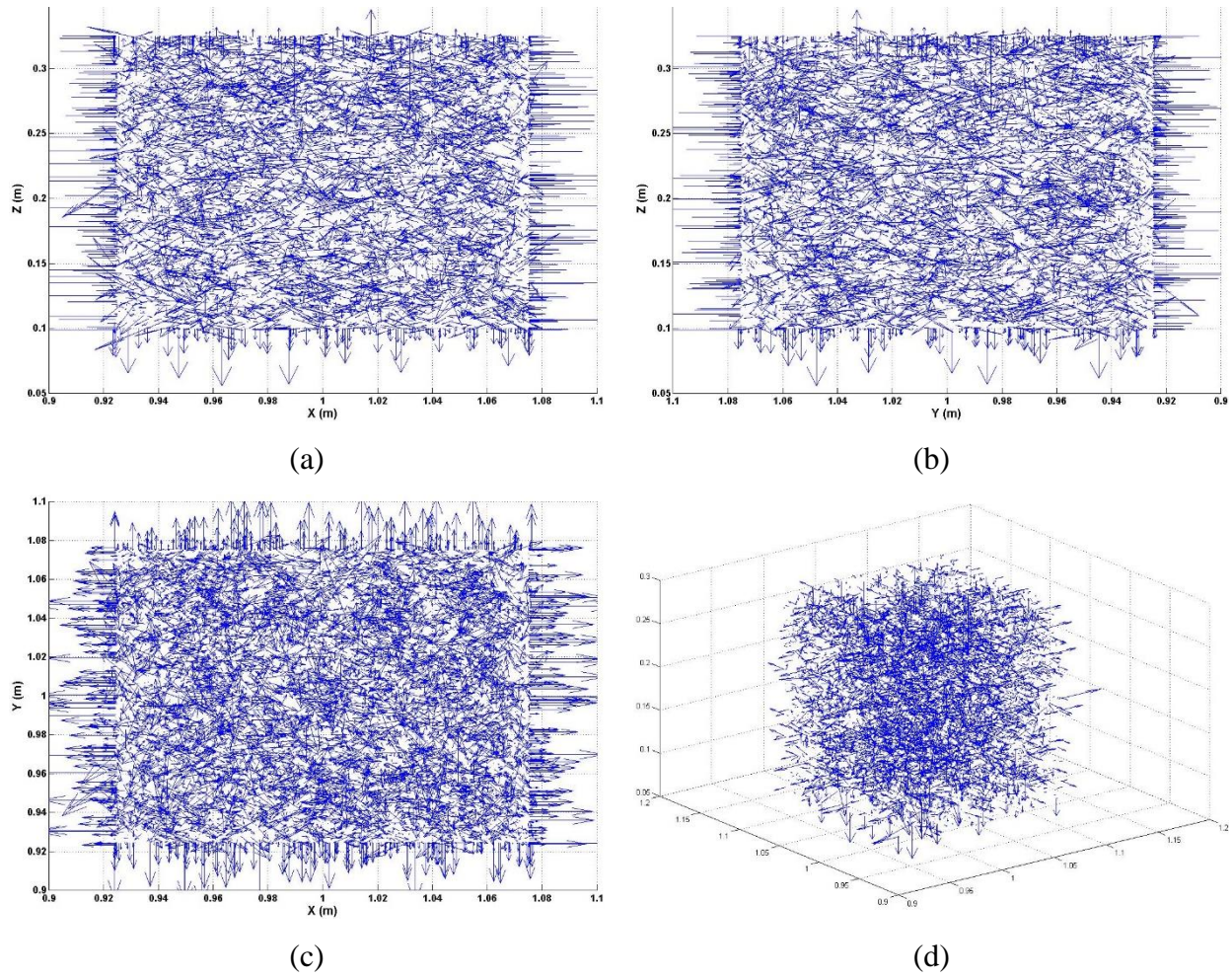
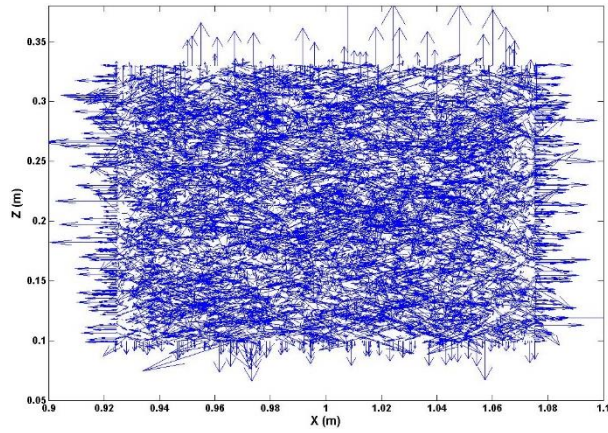
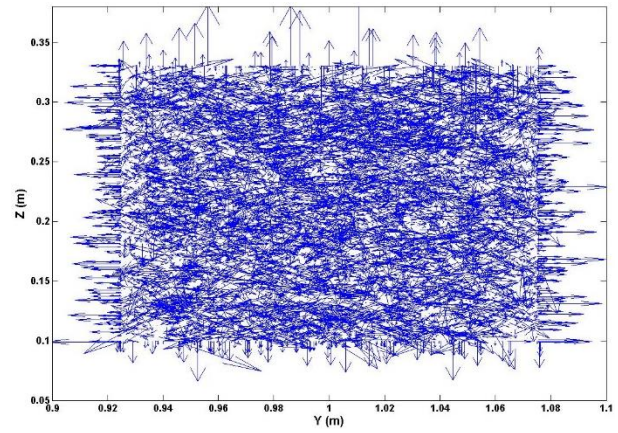


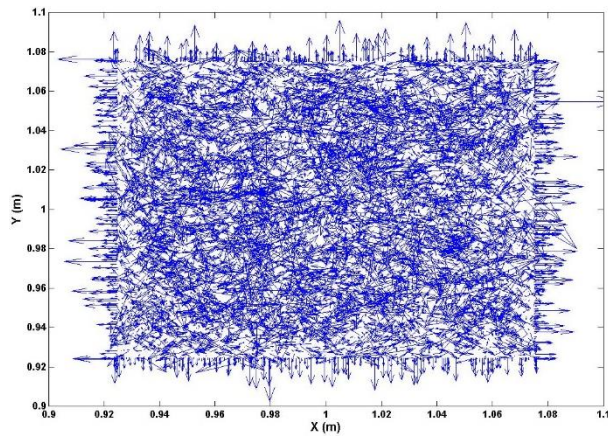
Figure 6.16 Illustration of DEM Calculated Internal Contact Force Vectors for $G/S=1.0$ with High Angularity Level: (a) X-Z Plane View, (b) Y-Z Plane View, (c) X-Y Plane View, and (d) Three Dimensional (3D) View



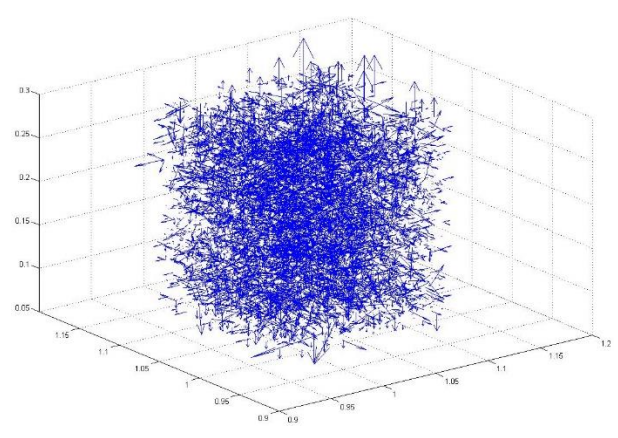
(a)



(b)

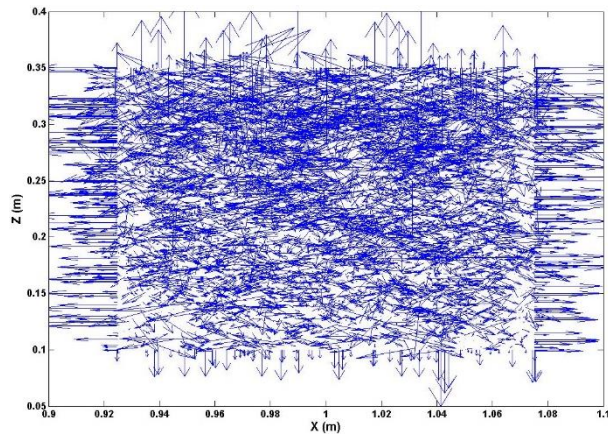


(c)

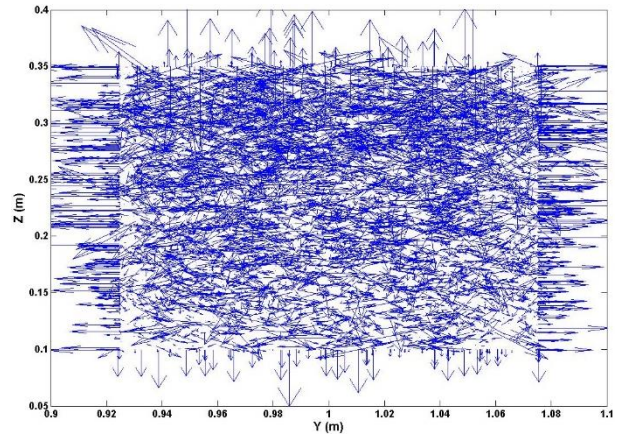


(d)

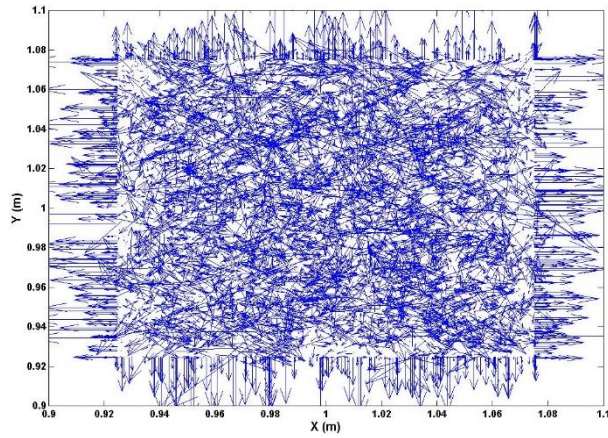
Figure 6.17 Illustration of DEM Calculated Internal Contact Force Vectors for $G/S=1.6$ with High Angularity Level: (a) X-Z Plane View, (b) Y-Z Plane View, (c) X-Y Plane View, and (d) Three Dimensional (3D) View



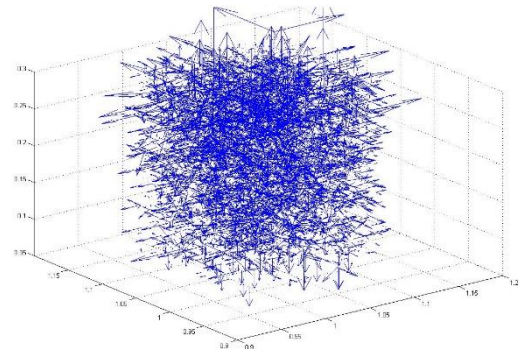
(a)



(b)

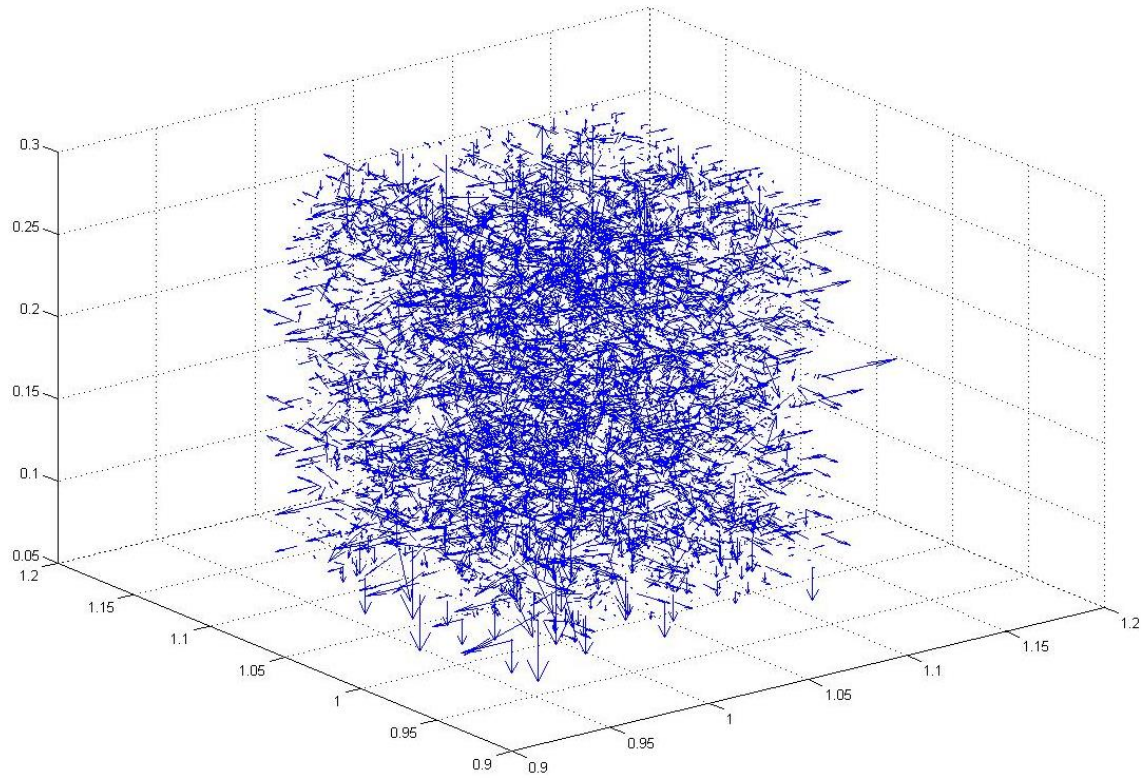


(c)

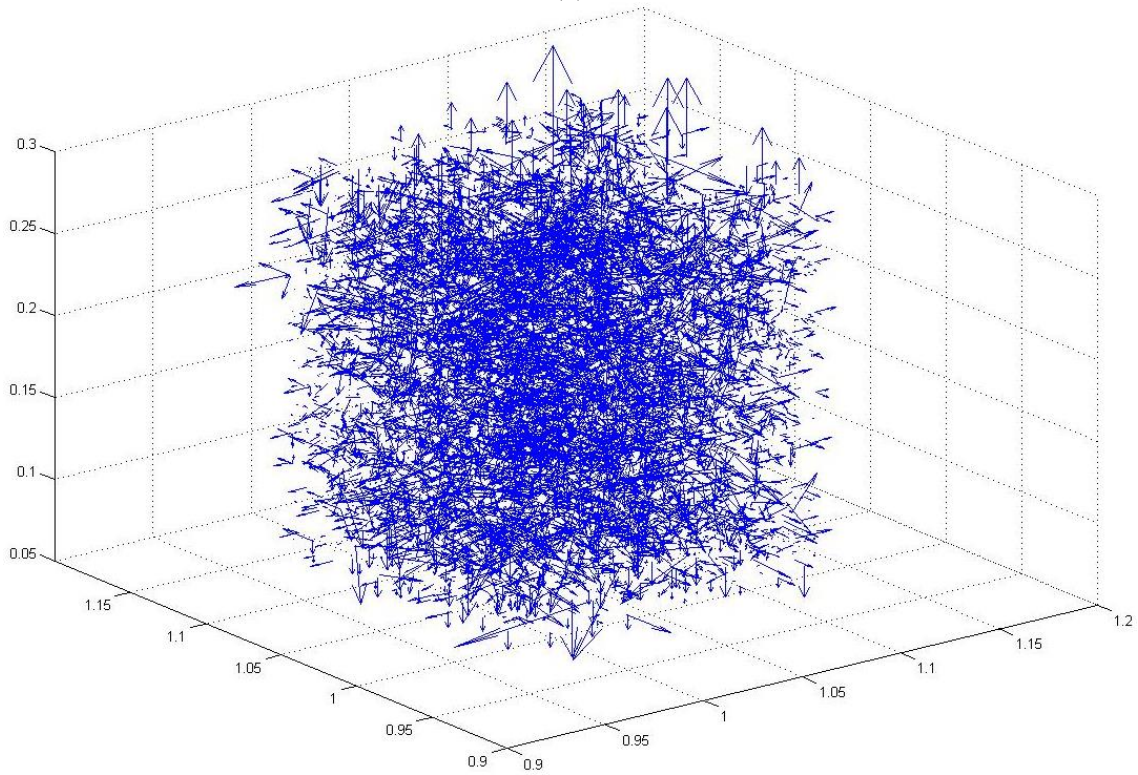


(d)

Figure 6.18 Illustration of DEM Calculated Internal Contact Force Vectors for $G/S=2.5$ with High Angularity Level: (a) X-Z Plane View, (b) Y-Z Plane View, (c) X-Y Plane View, and (d) Three Dimensional (3D) View



(a)



(b)

Figure 6.19 3D View of DEM Calculated Internal Contact Force Vectors for High Angularity Level: (a) $G/S=1.0$ and (b) $G/S=1.6$

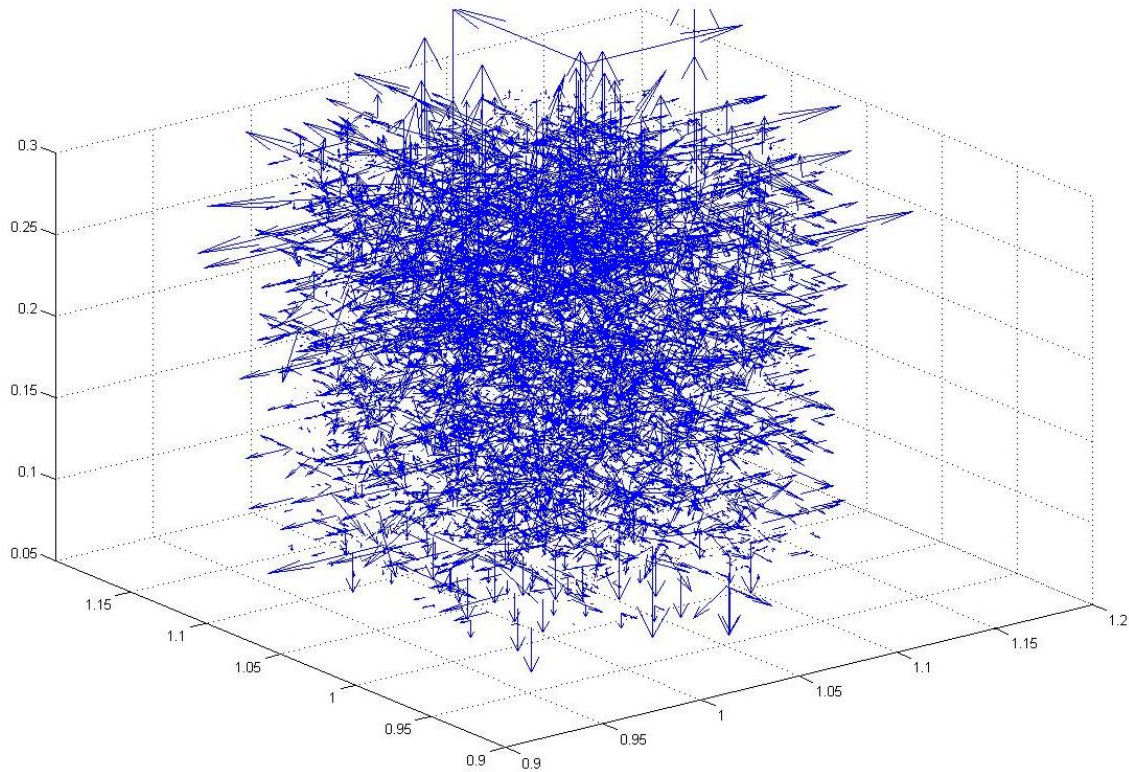


Figure 6.20 3D View of DEM Calculated Internal Contact Force Vectors for High Angularity Level: $G/S=2.5$

6.5 Summary

In this chapter, a validated DEM model was employed for evaluating the gradation effect on both packing characteristics and load-carrying performance of unbound aggregate materials. DEM model parameters were first determined from calibrating an image-aided DEM program BLOKS3D developed at the University of Illinois (Zhao et al., 2006) against laboratory rapid shear strength (triaxial compression) test results. The predicted deviator stresses matched closely with those from the experiments, indicating the capability of the developed DEM model to reproduce the typical shear strength results of unbound aggregate materials. For future efforts, the calibrated DEM model has the potential for optimizing the selection of size and shape properties of various types of unbound aggregates to achieve desired shear strength (or rutting

resistance) and hydraulic conductivity or drainage characteristics (function of aggregate shape and air void distribution) for open-graded permeable aggregate base.

The DEM packing simulations using different gradations and particle shape properties were performed to investigate the validity of using the 4.75-mm sieve (or No. 4 sieve) as the breaking-sieve-size for typical Minnesota dense-graded aggregates. The process involved the use of an image-aided aggregate particle generation and establishing a cubical domain to create aggregate packing model simulations based on the DEM. The focus was on studying the upper and lower bounds of the MnDOT specified CL-6 gradation band and using 3-dimensional (3D) polyhedral discrete aggregate particles with both low and high angularity categories quantified by image analysis. It was found from the DEM simulation results that #4 sieve (or 4.75-mm sieve) could be regarded as the breaking sieve size that separated the Primary Structure and Secondary Structure for the CL-6 gradation band. This further confirms that the concept of gravel-to-sand ratio presented in Chapter 5 that uses 4.75 mm sieve as the breaking sieve size appears to be working well for typical Minnesota aggregate gradations studied.

Based on the DEM approach, current unbound permeable aggregate base (PAB) material gradations specified by Minnesota DOT were further engineered by optimizing the particle contact and packing characteristics and minimizing the overall rutting potential (based on shear strength behavior) to still accommodate desired drainage requirements. The optimal gradation proposed in Chapter 5 for unbound permeable aggregate base (UPAB) materials according to the Gravel-to-Sand ratio concept was also verified. To maximize the coordination number, the optimal unbound PAB gradation should be close to the upper bound at the 19-mm sieve and be close to the mid-range at the 9.5-mm sieve. The optimal gradation predicted by the Gravel-to-Sand ratio was found to agree more closely with the DEM simulation results that took into

account the realistic 3D shape properties, as compared to that predicted by the packing theory based analytical gradation framework.

Finally, DEM simulations were performed on three different gradations with the G/S ratio values of 1.0, 1.6, and 2.0, respectively. The three different gradations were all chosen from the current MnDOT specified gradation band for unbound permeable aggregate base (UPAB). The main objective is to verify if the recommended UPAB gradation for MnROAD 2013 construction cycle outperforms others in terms of both structural stability (as characterized by coordination number) and drainability (as characterized by porosity). The G/S ratio of 1.6 resulted in the highest coordination number due to the achieved densest packing (indicated by the lowest porosity). Therefore, the optimal G/S ratio of 1.6 observed in Chapter 5 from experimental results agrees well with DEM simulation using 3D polyhedral particles with realistic aggregate shape properties.

Chapter 7 Unified Approach to Unbound Aggregate Permanent Deformation Modeling Based on Shear Strength

This chapter introduces viable criteria for ranking the long-term rutting potentials of unbound granular materials based on the shakedown theory and developing a unified approach for modeling permanent deformation behavior. This approach effectively takes into account various aggregate physical properties and field stress states due to moving wheel loads and thus can be applied with greater confidence to actual field conditions. This way, consequences of using different qualities of aggregates including local marginal and recycled materials can be effectively evaluated for a sustainable yet reliable utilization in pavement construction.

This chapter deals with utilizing two comprehensive aggregate mechanistic property databases recently compiled at the University of Illinois from a number of research studies spanning almost two decades. The first data source of unbound aggregate permanent deformation results of laboratory RLT tests was from the FAA's National Airport Pavement Test Facility (NAPTF) research study (Kim and Tutumluer, 2006). The second data source of unbound aggregate permanent deformation results of laboratory RLT tests is from an Illinois Center for Transportation (ICT) research project (Tutumluer et al., 2009). As presented in Chapter 3, resilient modulus, shear strength, and permanent deformation test data for several base/subbase aggregate materials used in highway and airport pavement foundation layers are included in this database.

7.1 Evaluating MEPDG Rutting Model for Unbound Aggregates

The AASHTOWare Pavement ME Design (formerly DARWin-ME) and the AASHTO Mechanistic-Empirical Pavement Design Guide Manual of Practice (MEPDG) provide a

methodology for the analysis and performance prediction of pavements (ARA, 2004). Although the rutting performance of flexible pavements is known to be closely related to properties of the subgrade and underlying layers (i.e., base and/or subbase), the rut depth predicted by this methodology has been found to show a low sensitivity to the properties of underlying layers. This methodology also does not always reflect the extent of the anticipated effect. Therefore, there is a need to evaluate the rutting prediction procedures contained in the Pavement ME Design and to identify or develop enhancements to ensure that the procedures appropriately account for the influence of subgrade and unbound layers on the rutting performance of flexible pavements (NCHRP 01-53, 2014).

As reviewed in Chapter 2, the original Tseng and Lytton model (1989) is formulated as in Equation 7.1 where the regression coefficients ε_0 , β , and ρ , regarded as material constants, are obtained from laboratory RLT tests by fitting permanent strains against the number of load applications. Relating permanent strain with resilient strain and the number of loading cycles, the model was developed based on repeated load triaxial tests for a large number of loading cycles at which the material response became stable. Empirical relationships were also developed by Tseng and Lytton (1989) to estimate those material constants from water content (w_c), bulk stress (θ) and resilient modulus (E_r).

$$\begin{aligned} \varepsilon_p(N) &= \varepsilon_0 e^{-(\rho/N)^\beta} \\ \log\left(\frac{\varepsilon_0}{\varepsilon_r}\right) &= 0.80978 - 0.06626\omega_c - 0.003077\sigma_\theta + 10^{-6}E_r \quad (R^2=0.60) \\ \log\beta &= -0.9190 + 0.03105\omega_c + 0.001806\sigma_\theta - 1.5 \times 10^{-6}E_r \quad (R^2=0.74) \\ \log\rho &= -1.78667 + 1.45062\omega_c - 3.784 \times 10^{-4}\sigma_\theta^2 - 2.074 \times 10^{-3}\omega_c^2\sigma_\theta - 1.05 \times 10^{-5}E_r \\ & \quad (R^2=0.66) \end{aligned} \tag{7.1}$$

The original Tseng and Lytton model was modified and calibrated by El-Basyouny et al. (2005) for implementation into the current MEPDG. As shown in Equation 7.2, it normalizes the predicted permanent strain to the resilient strain and thus requires knowledge of resilient modulus as well.

$$\frac{\varepsilon_p(N)}{\varepsilon_v} = \left(\frac{\varepsilon_0}{\varepsilon_r} \right) e^{-\left(\frac{\rho}{N}\right)^\beta}$$

$$\left(\frac{\varepsilon_0}{\varepsilon_r} \right) = \frac{\left(e^{(\rho)^\beta} \times a_1 \times E^{b_1} \right) + \left(e^{\left(\frac{\rho}{10^9}\right)^\beta} \times a_9 \times E^{b_9} \right)}{2} = \frac{\left(e^{(\rho)^\beta} \times 0.15 \right) + \left(e^{\left(\frac{\rho}{10^9}\right)^\beta} \times 20 \right)}{2}$$

$$\log \beta = -0.61119 - 0.017638 \omega_c \quad (7.2)$$

$$\rho = 10^9 \times \left(\frac{C_0}{[1 - (10^9)^\beta]} \right)^{\frac{1}{\beta}} = 10^9 \times \left(\frac{-4.89285}{[1 - (10^9)^\beta]} \right)^{\frac{1}{\beta}}$$

$$C_0 = \ln \left(\frac{a_1 \times E^{b_1}}{a_9 \times E^{b_9}} \right) = -4.89285$$

where ω_c is moisture content (%); σ_d and σ_θ are deviator stress (psi) and bulk stress (psi), respectively; ε_0 , β , and ρ are material constants; ε_r and E_r is resilient strain and resilient modulus (psi), respectively; and $a_1=0.15$, $b_1=0$, $a_9=20$, and $b_9=0$ are the fitting parameters finally selected by the Arizona State University (ASU) researchers after a considerable study to provide the best prediction for a wide range of unbound material types. Note that $b_1=0$ and $b_9=0$ lead to a constant C_0 value and the independency of parameter ρ on the resilient modulus E in Equation 7.2.

Both models correlate rutting in the unbound layers inversely with resilient modulus, resulting in the general misunderstanding that a high modulus is regarded to lead to high rutting resistance. It has recently been observed in the field that significant rutting can still be exhibited by unbound aggregate materials with high resilient modulus properties under service traffic loads

(Puppala et al., 2005). It is not necessarily valid to assume less permanent deformation for high resilient modulus properties. Furthermore, the “universal” constants of the MEPDG rutting model, as well as its general applicability to a wide range of materials, still remain debating and need to be validated further for it to become a truly universal model; otherwise, it cannot be expanded to unbound granular materials with confidence. For instance, Hashem and Zapata (2013) recently found that the use of $a_9=50$ yielded better prediction results as compared to $a_9=20$ adopted in the current MEPDG model. They also developed new prediction equation for β by replacing resilient modulus with shear stress/strength ratio. In a study of permanent deformation behavior of geogrid-reinforced flexible pavements using small scale accelerated pavement testing, Tang (2011) recalibrated the two constants b_1 and b_9 in the MEPDG rutting model (see Equation 2.26), instead of adopting nationally calibrated zero values, for subgrade soils using field APT subgrade rutting measurements. By doing so, the effects of stiffness of the unbound layer on the material constant ρ were properly accounted for.

7.1.1 Applicability for Dynamic Stress States Induced by Moving Wheel Loading

Under the application of moving wheel loads, unbound pavement layers are constantly subjected to dynamic stress states. That is, not only changes the magnitude of the load, but also the direction of the principal axes of the stresses rotates during the approaching and the departure of moving wheels. In this section, the original Tseng and Lytton model (1989) and nationally calibrated MEPDG rutting model for unbound granular materials are verified against laboratory triaxial test results obtained using both constant and varying confining pressure tests performed on two different types of base/subbase aggregates (i.e., FAA P209 and P154 materials). Permanent deformation data from laboratory RLT tests, as described previously, were first analyzed to obtain the accumulated permanent strain due to different loading along multiple

stress paths and different aggregate physical properties, respectively. Both permanent strain models were used to calculate the accumulated permanent strain after the corresponding number of load applications, respectively. The model parameters ϵ_0 , β , and ρ were solved for based on the least square error between the measured and calculated permanent strains.

Table 7.1 and Table 7.2 list such parameters obtained using this approach for FAA P209 and P154 materials, respectively. In both Tables, each CCP stress state applied is denoted by the constant radial confining stress σ_3 (psi) and the pulsed axial deviator stress σ_d (psi). For example, the stress state of 3-psi constant confining pressure and 9-psi axial deviator stress is denoted as “3/9”. On the other hand, each VCP stress state applied is denoted by the constant hydrostatic confining stress σ_s (psi), followed sequentially by the vertical deviator stress σ_{1d} (psi) and the horizontal deviator stress σ_{3d} (psi). For example, the stress state of 3-psi constant hydrostatic confining stress, 11-psi vertical deviator stress, and 3-psi horizontal deviator stress is denoted as “3/11/3”. High R^2 values close to 1 listed in both Tables indicate that the Tseng and Lytton model form can fit very well the permanent deformation curves obtained at each dynamic stress state.

Table 7.1 Permanent Strain Model Parameters for Stress Path Loading RLT Tests of FAA P209 Material

Material	Stress Path Slope m	Stress State (psi)	RLT Test Results		Model Parameters			
			ϵ_r (%)	M_R (ksi)	ϵ_0	ρ	β	R^2
FAA P209	3	03/09	-	-	0.13	0.61	0.10	0.962
		03/15	-	-	0.53	9.67	0.20	0.999
		03/21	-	-	0.59	1.59	0.19	0.999
		03/27	0.14	19.59	0.88	0.64	0.18	0.997
		05/15	0.08	18.73	0.42	40.00	0.28	0.999
		05/25	0.11	22.46	0.83	76.97	0.13	0.998
		05/35	0.14	25.53	0.94	3.12	0.17	0.998
		05/45	0.15	29.32	1.30	2.11	0.22	0.997
		08/24	0.09	26.92	0.66	7.51	0.18	0.999
		08/40	0.12	33.76	0.72	5.33	0.17	0.995
		08/56	0.15	36.76	0.86	3.20	0.18	0.999
		10/30	0.09	33.67	0.45	1.41	0.15	0.999
		10/50	0.14	35.30	0.87	5.26	0.14	0.998
		12/36	0.10	38.21	0.56	3.11	0.19	0.998
	12/60	0.13	43.09	0.79	24.12	0.12	0.998	
	1.5	3/11/3	0.11	8.72	0.45	27.69	0.21	0.998
		3/18/4	0.23	6.77	1.01	25.77	0.19	1.000
		3/24/6	0.23	8.85	0.94	15.17	0.21	0.998
		3/32/8	0.17	11.40	0.85	78.35	0.17	0.995
		5/18/4	0.05	30.38	0.51	17117.33	0.11	0.997
		5/29/7	0.16	13.80	0.65	15.04	0.22	0.997
		8/28/7	0.12	19.01	0.65	216.83	0.16	0.998
8/47/12		0.18	14.38	0.81	22.90	0.19	0.999	
10/35/9		0.16	15.63	0.84	107.43	0.16	0.999	

Table 7.1 (cont.)

Material	Stress Path Slope m	Stress State (psi)	RLT Test Results		Model Parameters			
			ϵ_r (%)	M_R (ksi)	ϵ_0	ρ	β	R^2
FAA P209	0	3/9/9	0.04	5.90	0.26	64.63	0.25	0.998
		3/16/16	0.07	7.00	0.40	111.56	0.19	0.999
		3/22/22	0.08	8.33	0.41	13.40	0.21	0.998
		3/28/28	0.08	9.38	0.46	36.17	0.19	0.997
		5/16/16	0.05	8.97	0.34	55.76	0.19	0.998
		5/26/26	0.07	9.35	0.56	38.85	0.17	0.999
		5/37/37	0.10	8.82	0.69	23.26	0.17	0.999
		5/47/47	0.09	11.84	0.72	251.46	0.14	0.999
		8/25/25	0.06	11.40	0.46	218.91	0.17	0.998
		10/32/32	0.06	15.01	0.35	50.52	0.19	0.998

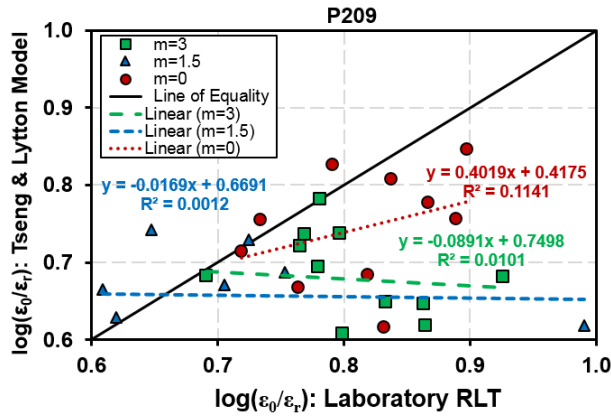
Note: “-“ denotes that information is not available.

Table 7.2 Permanent Strain Model Parameters for Stress Path Loading RLT Tests of FAA P154 Material

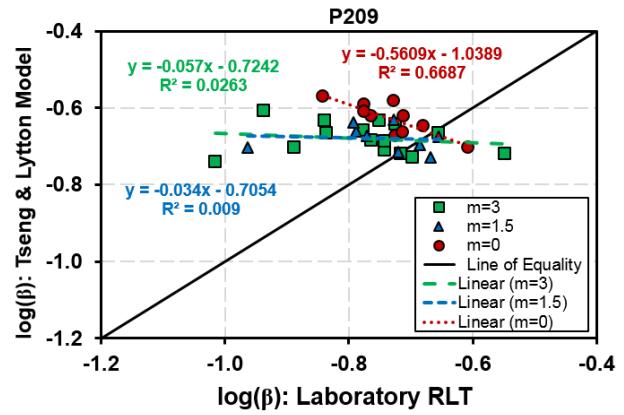
Material	Stress Path Slope m	Stress State (psi)	RLT Test Results		Model Parameters			
			ϵ_r (%)	M_R (ksi)	ϵ_0	ρ	β	R^2
FAA P154	3	03/09	0.06	12.63	0.28	21399.12	0.07	0.98
		03/15	0.10	13.03	0.40	4.26	0.15	0.99
		03/21	0.06	14.81	0.62	99.25	0.19	0.99
		03/27	0.14	15.48	0.56	1.13	0.21	0.98
		05/15	0.08	16.73	0.31	3.16	0.15	0.97
		05/35	0.16	20.33	0.53	3.72	0.13	0.98
		08/24	0.11	20.55	0.39	55.78	0.10	0.99
		08/40	0.17	21.37	0.48	3.44	0.14	0.99
	1.5	3/11/3	0.07	12.36	0.23	6023.60	0.09	0.97
		3/18/4	0.11	10.97	0.45	203.92	0.10	0.99
		3/24/6	0.12	15.29	0.57	0.44	0.15	0.98
		3/32/8	0.15	14.42	0.61	642.36	0.08	0.98
		5/18/4	0.09	16.23	0.41	2.50	0.17	0.99
		5/29/7	0.12	18.78	0.38	0.86	0.15	0.96
		5/41/10	0.14	21.59	0.41	0.31	0.13	0.96
	0	3/9/9	0.05	4.04	0.32	2004.22	0.09	0.98
		3/16/16	0.07	6.48	0.50	9074.76	0.07	0.99
		3/22/22	0.07	6.12	0.31	3.98	0.13	0.98
		3/28/28	0.10	6.30	0.56	22423.59	0.07	0.98
		5/16/16	0.06	7.26	0.20	10.75	0.14	0.99
		5/26/26	0.08	7.68	0.37	1417895.27	0.05	0.93
5/37/37		0.12	7.68	0.63	5974252.02	0.05	0.96	

The regressed parameters $\varepsilon_0/\varepsilon_r$, β , and ρ were then compared with those estimated from the original Tseng and Lytton's empirical relationships (see Equation 7.1) and with the universal constants of the MEPDG model (see Equation 7.2), respectively. Note that the original regression coefficients in Tseng and Lytton's empirical relationships (Equation 7.1) provided poor estimates for model parameters $\varepsilon_0/\varepsilon_r$, β , and ρ in terms of very low R^2 values; therefore, they were re-calculated by regressing fitted parameters $\varepsilon_0/\varepsilon_r$, β , and ρ against the same independent variables in the original relationships (Equation 7.1), i.e., moisture content, bulk stress and resilient modulus, respectively. The relationships between the measured and predicted values of $\varepsilon_0/\varepsilon_r$, β , and ρ are plotted in Figure 7.1 and Figure 7.2 for FAA P209 and P154 materials, respectively.

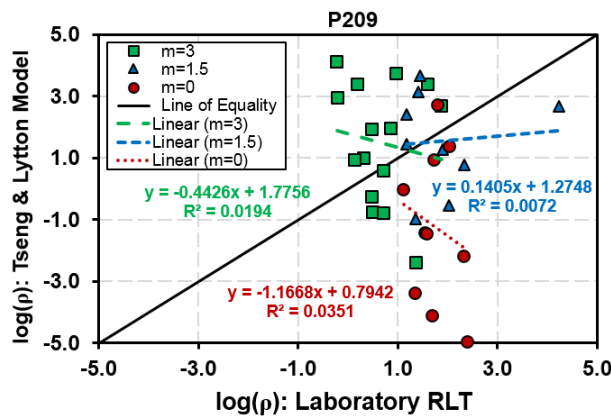
It can be seen from both Figure 7.1 and Figure 7.2 that low R^2 values were overall observed for all three stress path slopes by using the Tseng and Lytton's empirical relationships, even though the regression coefficients were recalculated. This indicates that the model parameters of Tseng and Lytton's permanent strain model vary significantly with applied stress states along different stress paths. As contrary to current practice, relying on resilient modulus and bulk stress alone may not be sufficient enough to provide accurate prediction of rutting accumulation, especially for in-situ moving wheel load conditions. Note that the current MEPDG permanent strain model, simplified from the original Tseng and Lytton's model, eliminates the dependence of model parameters on stresses and resilient moduli; instead, they are only dependent on moisture content. This explains why the same model parameters were obtained regardless of applied stress states. As shown in Figure 7.1 and Figure 7.2, such simplification apparently results in poor permanent deformation prediction that contradicts laboratory RLT test results.



(a)



(b)



(c)

MEPDG Model Predicted Values			
m	$\log(\epsilon_0/\epsilon_r)$	$\log(\beta)$	$\log(\rho)$
3	1.33	-0.69	3.44
1.5	1.33	-0.69	3.44
0	1.33	-0.69	3.44

(d)

Figure 7.1 Relationship between Laboratory Measured and Predicted Values of (a) $\log(\epsilon_0/\epsilon_r)$, (b) $\log\beta$ and (c) $\log\rho$ by the Tseng & Lytton Model Form and (d) by the MEPDG Model for P209 Material

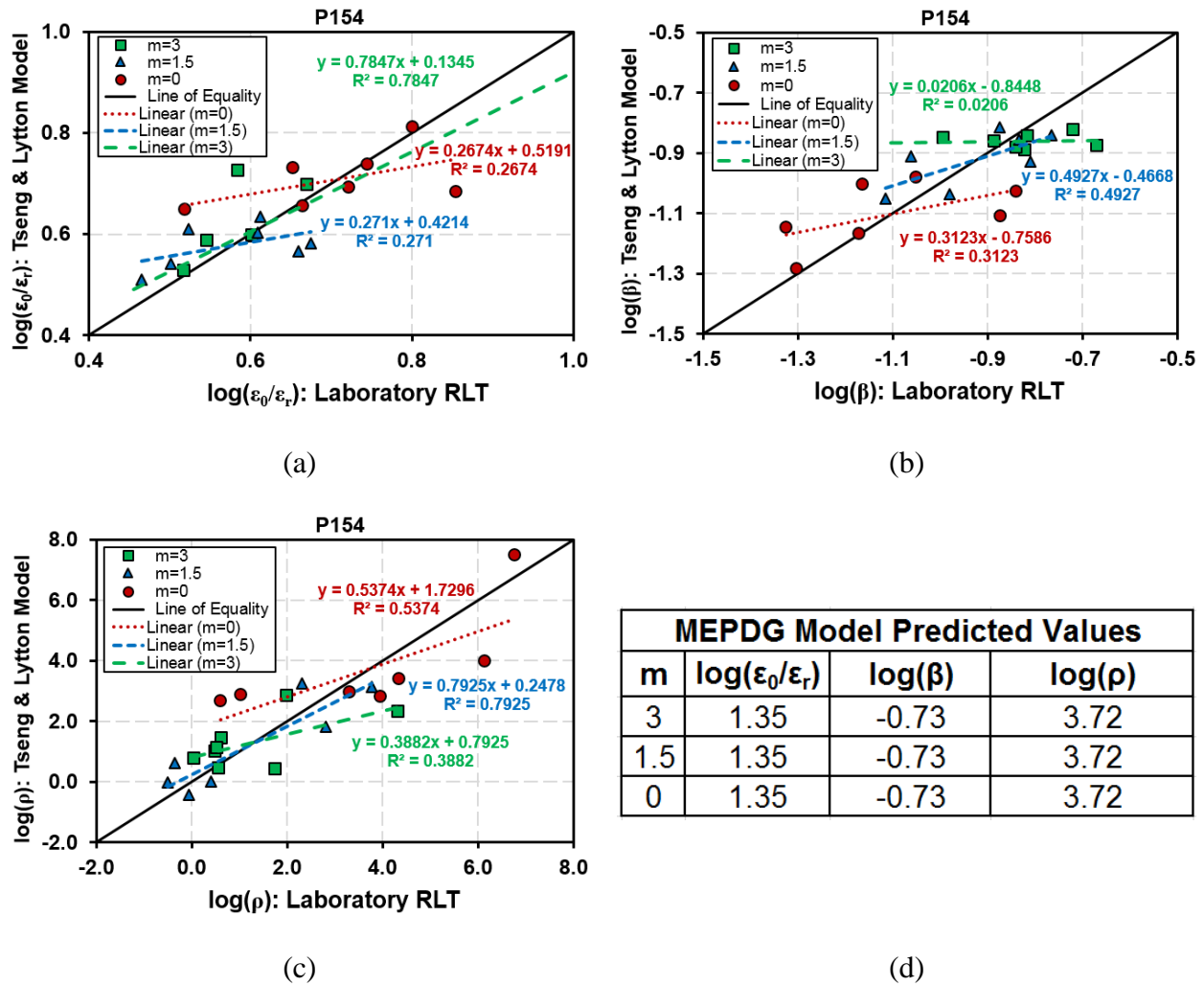


Figure 7.2 Relationship between Laboratory Measured and Predicted Values of (a) $\log(\epsilon_0/\epsilon_r)$, (b) $\log\beta$ and (c) $\log\rho$ by the Tseng & Lytton Model Form and (d) by the MEPDG Model for P154 Material

7.1.2 Applicability for Different Aggregate Physical Properties

The above section demonstrated that neither the Tseng and Lytton’s empirical relationships nor the MEPDG “universal” constants can accurately predict the rutting model parameters for different dynamic stress states. Therefore, both of them cannot be regarded as truly universal and be adapted with confidence for a specific material subject to a much wider range of dynamic stress states. In this section, efforts are paid to further verify the applicability

of the Tseng and Lytton's empirical relationships and the MEPDG "universal" constants to different aggregate materials that are of varying combinations of common aggregate physical properties but are subject to the same CCP stress state (15-psi axial deviator stress and 15-psi constant confining pressure).

Table 7.3 through Table 7.5 list the permanent strain model parameters of the original Tseng and Lytton model (Equation 7.1) for ICT crushed dolomite, crushed limestone, and uncrushed gravel at different fines content and moisture conditions, respectively. The Tseng and Lytton rutting model form can also accurately fit all the permanent deformation curves obtained at different aggregate physical conditions (i.e., moisture content, fines content, and plasticity index), as indicated by the high R^2 values very close to 1. Note that the achieved fines contents corresponding to the targeting 0%, 4%, 8%, and 12% fines were ensured at the order of 4%, 8%, 12%, and 16%, respectively, due to fines sticking to larger particles (Mishra, 2012). Also shown in Table 7.3 through Table 7.5 are the calculated resilient strain and resilient modulus values. It can be clearly seen that either resilient strain or resilient modulus exhibits a similar magnitude level among different physical conditions, implying that relying on resilient strain or resilient modulus alone may not differentiate permanent deformation behavior in this case.

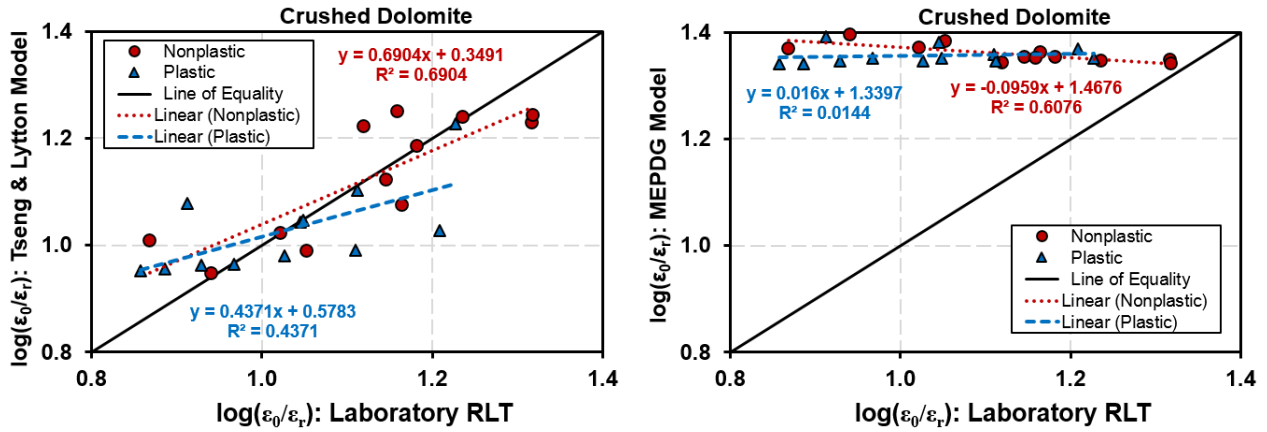
Figure 7.3 shows that the Tseng and Lytton's empirical relationships, on the other hand, predicted reasonably good values of material constants ϵ_0/ϵ_r , β , and ρ for ICT crushed dolomite materials tested at different physical conditions, as indicated by R^2 values (>0.54) comparable to those reported for the original empirical relationships. This could possibly imply that the difference in permanent deformation behavior caused by different aggregate physical properties under the same stress state can be reasonably captured by moisture content, bulk stress, and resilient moduli together. It is worth emphasizing that this finding is still subject to further

validation with greater number of load applications, as the permanent deformation results analyzed for ICT aggregates were collected from the conditioning stage with up to 1,000 load applications only. As expected, the laboratory measured values of ϵ_0/ϵ_r , β , and ρ are significantly different from those estimated from the universal constants of the MEPDG rutting model. Therefore, it may be inferred from this study that the use of the universal constants in the MEPDG rutting model, as well as its general applicability to a wide range of materials subject to varying dynamic stress states and/or physical conditions, still remain questionable and are at least not supported by laboratory permanent deformation results. The original Tseng and Lytton model, if well calibrated, appears to yield more reasonable rutting prediction than its simplified version, i.e., the MEPDG rutting model, yet it may still be regarded as ineffective in predicting rutting caused by different aggregate physical properties and more importantly by moving wheel loads.

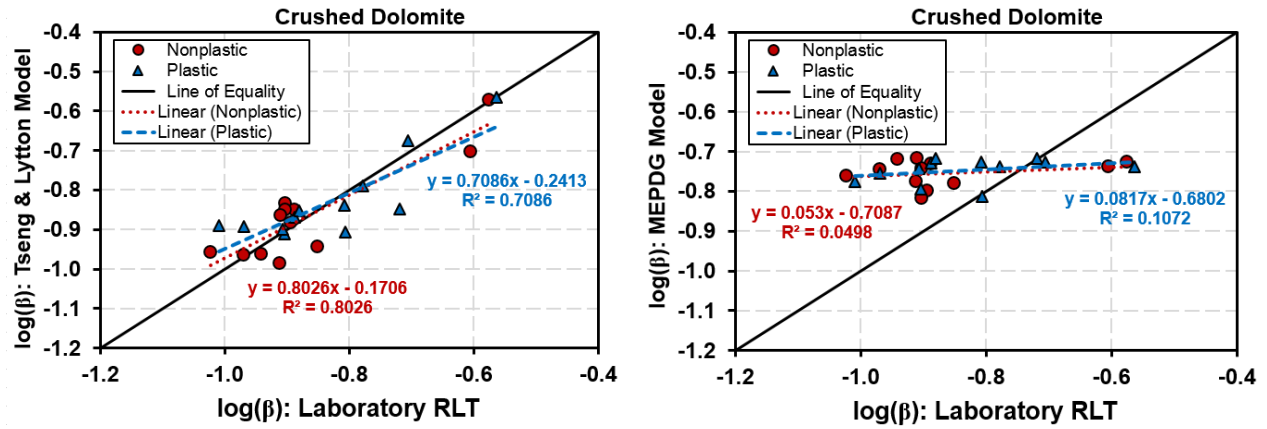
While the Tseng and Lytton's empirical relationships relatively outperform the MEPDG "universal" constants in predicting values of ϵ_0/ϵ_r , β , and ρ , much weaker agreement between laboratory measured and predicted values of ϵ_0/ϵ_r , β , and ρ by both models is observed in Figure 7.4 and Figure 7.5 for ICT crushed limestone and uncrushed gravel, respectively. This could be interpreted as the fact that material constants ϵ_0/ϵ_r , β , and ρ are not dependent only on moisture content, as contrary to the current MEPDG model; moreover, in addition to moisture content, resilient modulus, and bulk stress as adopted in the Tseng and Lytton's empirical relationships, there exists other fundamental or critical factors that significantly affect the permanent deformation behavior but remain uncaptured in both models.

Table 7.3 Permanent Strain Model Parameters for ICT Crushed Dolomite Materials of Different Physical Properties

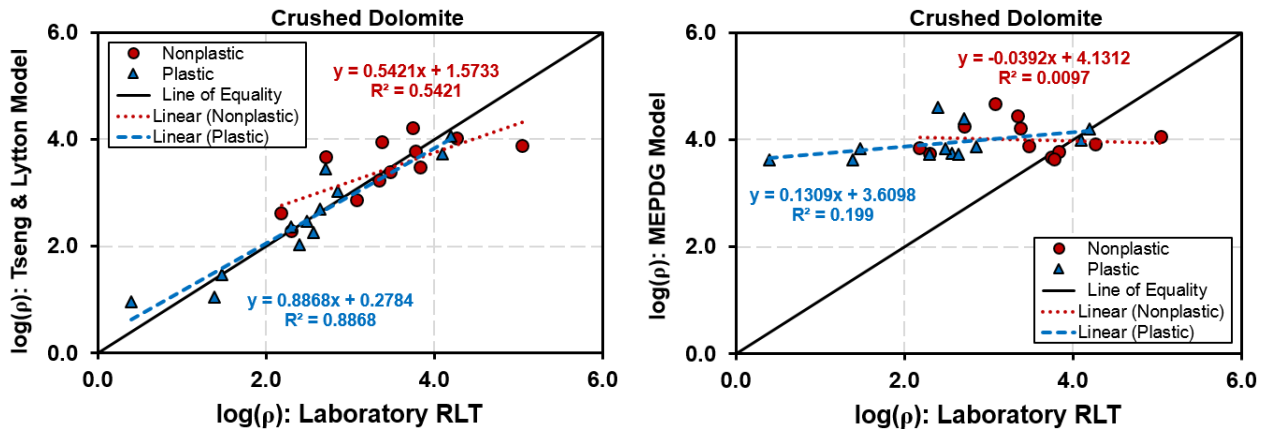
Material	Plasticity Index	Target Fines Content (%)	Moisture Condition	RLT Test Results		Model Parameters			
				ϵ_r (%)	M_R (ksi)	ϵ_0	ρ	β	R^2
ICT Crushed Dolomite	Non-plastic	0	Dry	0.06	24.64	0.63	518.66	0.14	0.999
			Optimum	0.06	23.89	0.68	2246.46	0.13	0.999
			Wet	0.07	23.36	0.61	1225.42	0.13	0.999
		4	Dry	0.06	24.06	0.84	18600.72	0.11	0.999
			Optimum	0.06	24.36	0.88	113920.09	0.09	0.999
			Wet	0.06	25.43	0.44	2409.96	0.12	0.998
		8	Dry	0.07	23.16	0.92	5666.45	0.11	0.999
			Optimum	0.07	21.07	1.45	7015.67	0.13	0.998
			Wet	0.07	21.42	1.06	3056.90	0.13	0.999
		12	Dry	0.07	20.80	1.46	6186.58	0.12	0.999
			Optimum	0.11	14.39	1.89	202.36	0.27	0.988
			Wet	0.08	18.00	1.16	152.93	0.25	0.994
	Plastic	0	Dry	0.07	22.65	1.13	15719.41	0.10	0.999
			Optimum	0.06	24.01	0.67	505.52	0.12	0.999
			Wet	0.06	23.62	0.49	250.26	0.16	0.997
		4	Dry	0.07	21.47	0.59	367.75	0.13	0.999
			Optimum	0.06	23.86	0.56	718.67	0.12	0.999
			Wet	0.07	23.10	0.90	12518.19	0.11	0.999
		8	Dry	0.08	19.96	0.62	24.55	0.19	0.998
			Optimum	0.08	19.15	0.85	200.47	0.16	0.998
			Wet	0.09	17.43	1.01	308.35	0.17	0.998
		12	Dry	0.07	20.56	0.50	2.49	0.13	0.998
			Optimum	0.19	7.87	2.46	438.56	0.20	0.999
			Wet	0.35	4.35	5.91	29.76	0.27	0.980



(a)



(b)

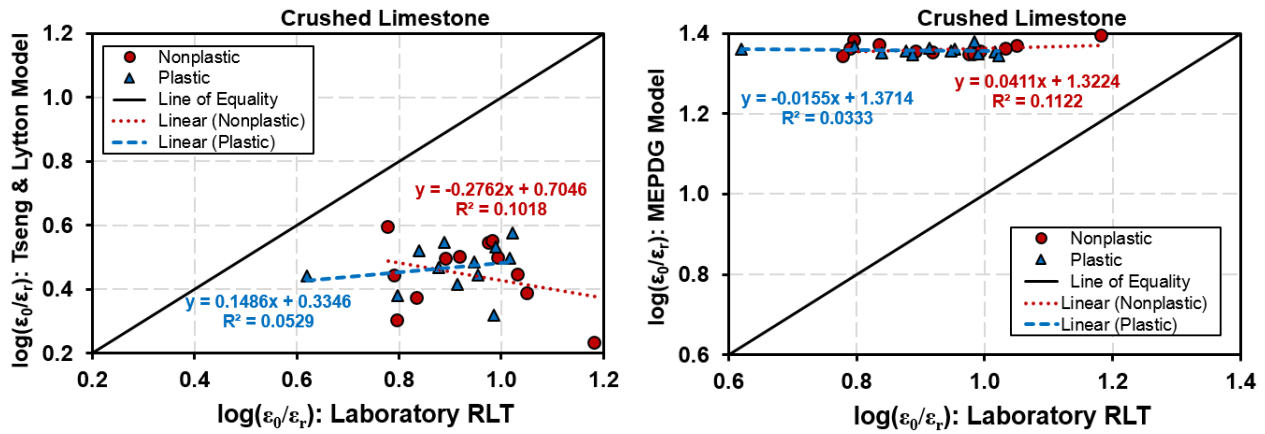


(c)

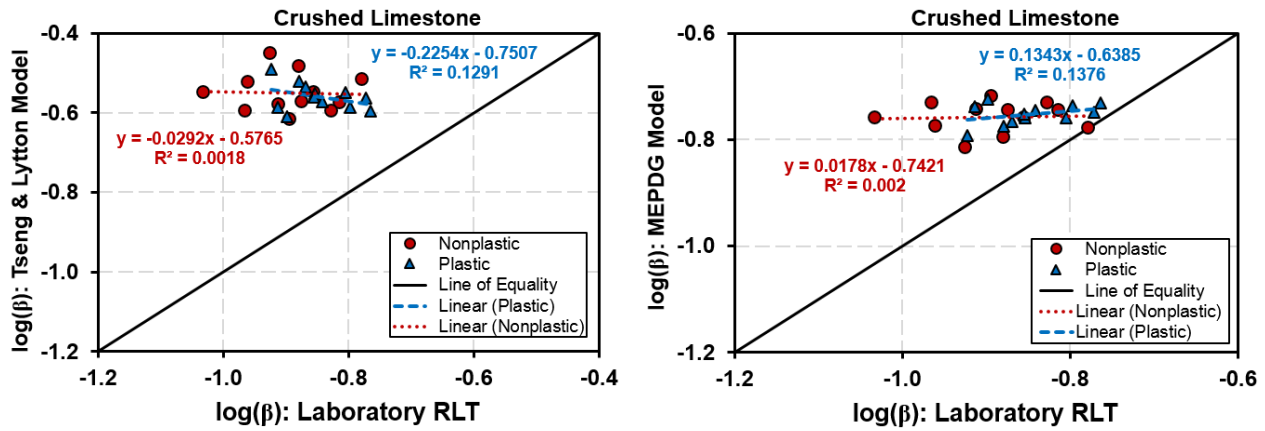
Figure 7.3 Relationship between Laboratory Measured and Predicted Values of (a) $\log(\epsilon_0/\epsilon_r)$, (b) $\log\beta$ and (c) $\log\rho$ by the Tseng & Lytton Model Form (Left) and by the MEPDG Model (Right) for Crushed Dolomite

Table 7.4 Permanent Strain Model Parameters for ICT Crushed Limestone Materials of Different Physical Properties

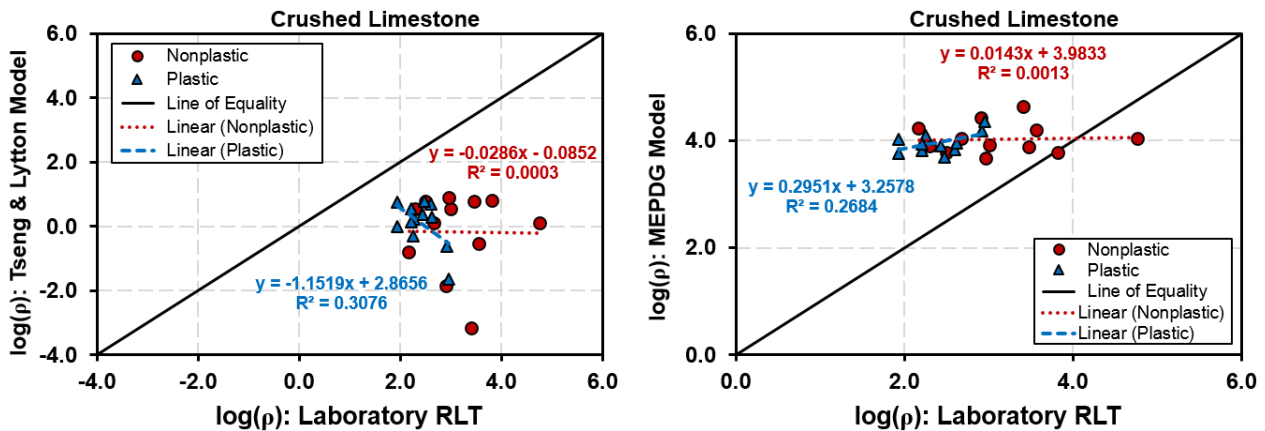
Material	Plasticity Index	Target Fines Content (%)	Moisture Condition	RLT Test Results		Model Parameters			
				ϵ_r (%)	M_R (ksi)	ϵ_0	ρ	β	R^2
ICT Crushed Limestone	Non-plastic	0	Dry	0.07	21.87	0.48	149.42	0.17	0.996
			Optimum	0.06	24.98	0.39	832.70	0.13	0.998
			Wet	0.07	22.56	1.04	2616.82	0.12	0.999
		4	Dry	0.07	21.76	0.70	202.77	0.15	1.000
			Optimum	0.06	23.91	0.40	486.86	0.14	0.999
			Wet	0.07	20.55	0.84	3770.17	0.11	0.999
		8	Dry	0.07	21.56	0.68	6818.01	0.11	0.999
			Optimum	0.07	23.57	0.51	1046.77	0.13	0.999
			Wet	0.07	20.97	0.79	59556.92	0.09	0.999
		12	Dry	0.07	21.76	0.42	955.05	0.13	0.998
			Optimum	0.07	22.91	0.65	319.69	0.15	0.999
			Wet	0.07	21.86	0.58	3051.97	0.12	0.999
	Plastic	0	Dry	0.07	22.80	0.28	189.80	0.14	0.997
			Optimum	0.06	24.98	0.39	832.70	0.13	0.998
			Wet	0.07	20.80	0.70	894.34	0.12	0.999
		4	Dry	0.07	20.45	0.51	396.56	0.12	0.999
			Optimum	0.06	23.66	0.48	415.55	0.14	0.999
			Wet	0.08	20.07	0.62	179.93	0.14	0.999
		8	Dry	0.07	21.58	0.54	85.88	0.17	0.999
			Optimum	0.07	20.51	0.76	273.22	0.14	0.999
			Wet	0.07	20.29	0.67	85.73	0.16	0.999
		12	Dry	0.08	18.54	0.86	302.29	0.13	1.000
			Optimum	0.07	20.39	0.73	161.76	0.16	0.999
			Wet	0.08	19.06	0.71	161.81	0.17	0.999



(a)



(b)

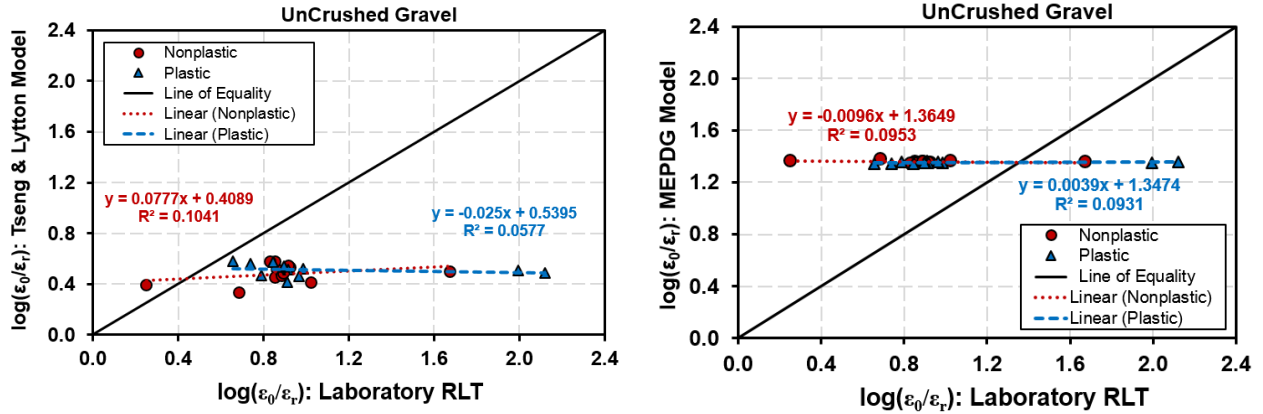


(c)

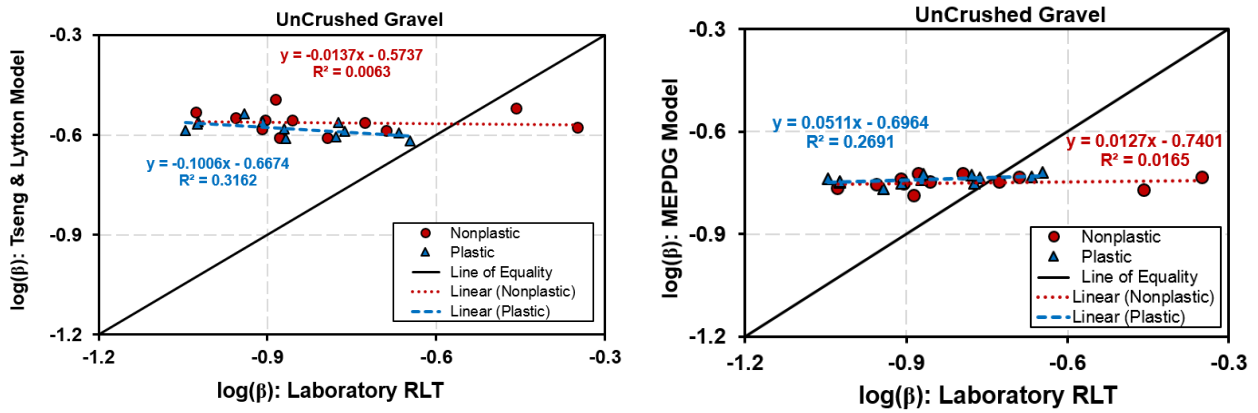
Figure 7.4 Relationship between Laboratory Measured and Predicted Values of (a) $\log(\epsilon_0/\epsilon_r)$, (b) $\log\beta$ and (c) $\log\rho$ by the Tseng & Lytton Model Form (Left) and by the MEPDG Model (Right) for Crushed Limestone

Table 7.5 Permanent Strain Model Parameters for ICT Uncrushed Gravel Materials of Different Physical Properties

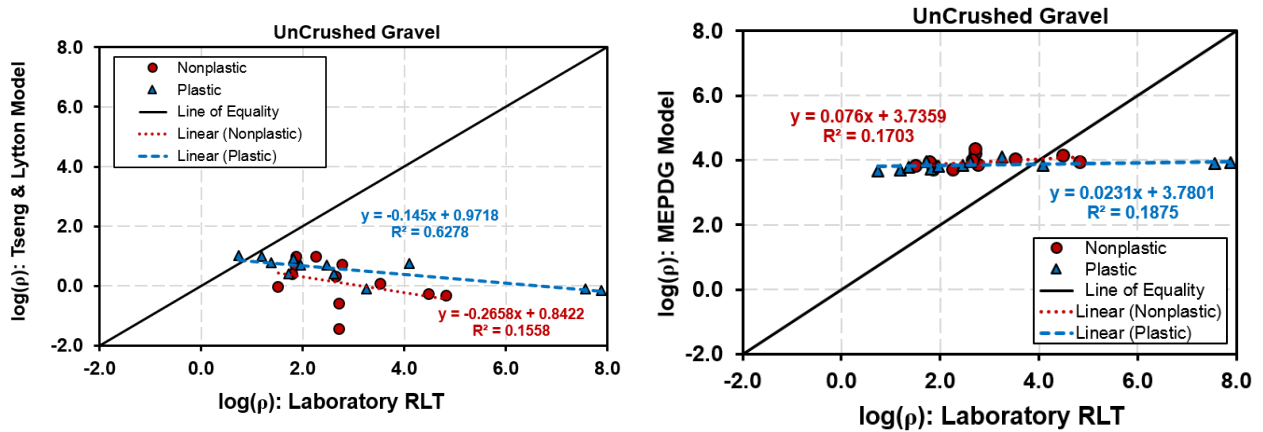
Material	Plasticity Index	Target Fines Content (%)	Moisture Condition	RLT Test Results		Model Parameters			
				ϵ_r (%)	M_R (ksi)	ϵ_0	ρ	β	R^2
ICT Uncrushed Gravel	Non-plastic	0	Dry	0.08	19.82	0.55	3.44E+03	0.11	0.999
			Optimum	0.08	20.04	0.14	519.96	0.35	0.998
			Wet	0.07	21.00	0.36	522.93	0.13	0.999
		4	Dry	0.08	18.92	0.59	609.83	0.12	0.998
			Optimum	0.08	18.10	0.65	460.80	0.13	0.999
			Wet	0.08	19.16	0.84	3.13E+04	0.09	0.999
		8	Dry	0.08	18.87	0.58	187.44	0.13	0.997
			Optimum	0.11	13.60	0.95	74.10	0.20	0.996
			Wet	0.09	16.30	0.73	64.05	0.19	0.998
		12	Dry	0.10	15.74	0.65	74.84	0.16	0.998
			Optimum	0.45	3.39	3.72	32.54	0.45	0.976
			Wet	0.26	5.83	12.25	6.90E+04	0.14	0.999
	Plastic	0	Dry	0.08	19.73	0.75	12406.25	0.09	0.999
			Optimum	0.08	19.76	0.47	52.24	0.17	0.998
			Wet	0.08	18.35	0.67	1793.45	0.11	0.999
		4	Dry	0.08	18.39	0.45	65.68	0.17	0.999
			Optimum	0.09	17.56	0.71	294.14	0.13	0.999
			Wet	0.08	18.85	0.74	411.70	0.12	0.999
		8	Dry	0.08	18.53	0.57	15.47	0.14	0.999
			Optimum	0.11	13.83	0.87	92.10	0.17	0.998
			Wet	0.31	4.87	41.57	7.49E+07	0.09	0.997
		12	Dry	0.08	17.82	0.38	5.44	0.23	0.999
			Optimum	0.12	13.08	0.91	23.58	0.22	0.998
			Wet	0.39	3.94	38.57	3.71E+07	0.09	0.999



(a)



(b)



(c)

Figure 7.5 Relationship between Laboratory Measured and Predicted Values of (a) $\log(\epsilon_0/\epsilon_r)$, (b) $\log\beta$ and (c) $\log\rho$ by the Tseng & Lytton Model Form (Left) and by the MEPDG Model (Right) for UnCrushed Gravel

7.1.3 Correlation between Resilient Modulus and Permanent Deformation for Unbound Aggregate under Repeated Loading

Under each application of continuous repeated loading caused by vehicular traffic, both resilient and plastic strains occur in unbound pavement layers. The magnitude of each of these strains and consequently the pavement performance are affected by many factors, including pavement structure, load level, and pavement material properties. To adequately design and analyze a pavement, both resilient modulus and plastic deformation need to be measured and assessed concurrently under loading and environmental conditions that those materials are expected to experience in the field.

Defined by the ratio of maximum deviator stress to resilient strain, resilient modulus is one of the most important material property input for structural analyses of conventional flexible pavements. Conversely, plastic deformation that accumulates in unbound pavement layers and subgrade soils is the primary failure criterion, as a large portion (over 40%) of the total pavement rutting observed at the pavement surface can be contributed by the plastic deformation in those layers, especially at high water content condition (Majidzadeh et al., 1978). As moisture content in those layers increases, the resilient modulus of unbound granular materials and subgrade soils decreases rapidly. This results in a common misunderstanding that low resilient modulus properties of unbound aggregates imply greater plastic deformation and vice versa, which is however not necessarily valid. Mohammad et al. (2006) reported that the plastic strain after 10,000 repetitions for untreated and treated pavement base materials was related to resilient modulus via the following regression equation, i.e., $M_R = 225 \cdot \varepsilon_p^{-0.25}$. This equation shows that the resilient modulus decreases with increasing plastic strain. However, according to field observations, it is not very uncommon to find some unbound granular materials that exhibit good

resilient modulus while still yielding significant rutting under service traffic loads (Puppala et al., 1999). Mohammad et al. (2006) also confirmed that the resilient modulus alone did not properly describe the performance of base materials.

As outlined above, there is still ambiguity when correlating resilient modulus and permanent deformation for unbound granular materials as well as subgrade soils. In this section, both the resilient and plastic responses of different aggregate materials to repeated loading under various dynamic stress states are analyzed concurrently from shakedown perspectives to study any correlations between plastic strain and resilient modulus. Specifically, both FAA P209 and P154 materials were subject to different combinations of dynamic stress states for 10,000 and 40,000 load repetitions (single stage), respectively; on the other hand, three different types of aggregates (crushed limestone, crushed dolomite, and uncrushed gravel) with varying combinations of aggregate physical properties were subject to the same stress state for up to 1,000 load repetitions unless failure occurs first. The shakedown concept reviewed in Chapter 2 is used to describe the accumulated plastic deformation and the strain-hardening and softening behavior.

7.1.3.1 Dynamic Stress States

According to the shakedown theory reviewed in Chapter 2, the behavior of unbound aggregates under repeated loading can be categorized as plastic shakedown, plastic creep, or incremental collapse. For an adequately designed pavement, incremental collapse should be avoided, yet unbound aggregates in the state of “plastic shakedown” or “plastic creep” could still result in rutting distress. Therefore, plastic shakedown is permitted only if sufficiently small plastic strain accumulates before developing fully resilient response, whereas plastic creep is acceptable only if the accumulated plastic strain does not lead to rutting distress. Note that in

order to differentiate the “plastic creep” state from the “incremental collapse” state, a considerable number of load applications are needed in the single-stage laboratory RLT tests; instead, multi-stage RLT tests have recently gained popularity due to reduced number of load applications. Due to the limited number of load applications to which FAA P209 and P154 materials were subject, only plastic shakedown and plastic creep behaviors were observed from the permanent deformation results with no incremental collapse behavior observed.

Figure 7.6 through Figure 7.8 plot the plastic strain and the resilient modulus against the number of load applications for P209 material at different CCP (stress slope $m=3$) and VCP ($m=1.5$ and 0) stress states. A general trend can be found from those figures. That is, the resilient modulus of unbound aggregates increases with increasing load cycles (i.e., strain-hardening) during the initial stage, followed by gradually reaching a constant level after a certain number of cycles; moreover, the strain-hardening phenomenon exhibited in the “plastic creep” state sustains longer than that exhibited in the “plastic shakedown” state. According to Khogali and Mohamed (2004), such strain-hardening behavior (or increase in resilient modulus) is attributed to microstructural changes related to aggregate particle rearrangement under the application of external loading, whereas reaching a relatively constant resilient modulus value afterwards indicates the establishment of a preferred particle orientation with no further microstructural changes (i.e., the steady state). The plastic strain, on the other hand, initially exhibits considerable increase with a much lesser rate of accumulation afterwards. This conforms to the shakedown behavior stated in Chapter 2, i.e., plastic deformation develops at an accelerated rate in the first few loading cycles due to changes in the microstructure while the material hardens. As this process continues, plastic deformation eventually either ceases to develop further or

accumulates at a relatively constant rate, which is also supported by the resilient modulus value reaching a constant level during the steady state.

Another interesting yet important observation from Figure 7.6 through Figure 7.8 is that the use of either resilient modulus or permanent deformation as a criterion for evaluating the impact of dynamic stress states could result in significantly different outcome. Specifically, in the cases where the impact of different dynamic stress states on resilient modulus is barely noticeable (e.g., Figure 7.6(d)), a substantial impact on the determined permanent deformation potential is detected as evident from different permanent deformation trends. This further confirms that relying on resilient modulus alone could result in inadequate characterization of unbound aggregates for use in pavement applications. Instead, resilient modulus and permanent deformation need to be examined concurrently.

Figure 7.9 through Figure 7.11 show the comparisons of resilient modulus and plastic strain for the FAA P154 material under different dynamic stress states. The previous observations are confirmed once again. In summary, the regions of material behavior described previously are found to be common to both P209 and P154 materials regardless of the dynamic stress state to which they were subjected. However, depending on whichever of the plastic shakedown and plastic creep states they were at, the duration of each of the deformation region is different.

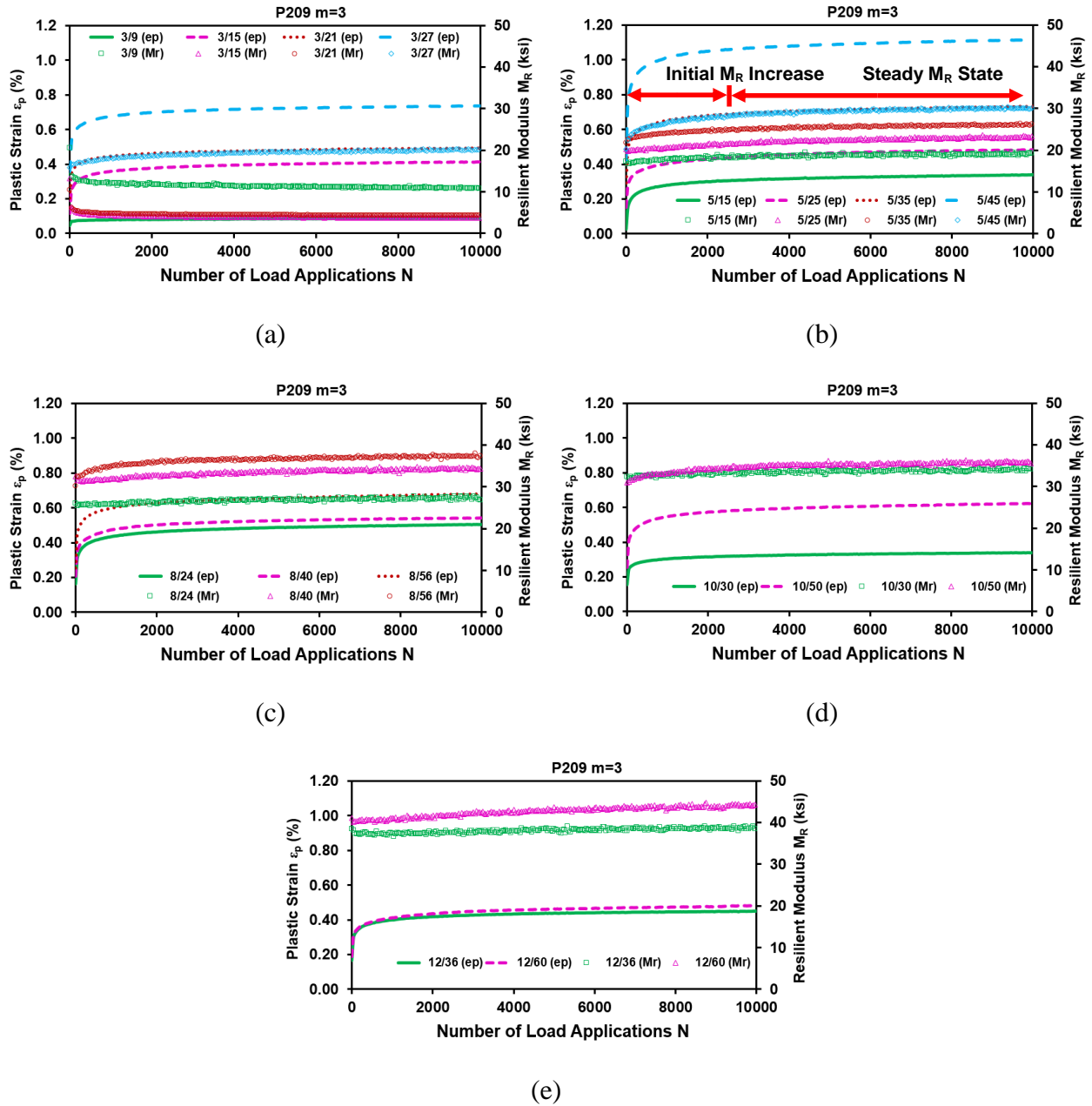


Figure 7.6 Relationship between Plastic Strain and Vertical Resilient Modulus for P209 Material Observed during CCP Test with Stress Slope $m=3$: (a) $\sigma_{3s}=3$ psi, (b) $\sigma_{3s}=5$ psi, (c) $\sigma_{3s}=8$ psi, and (d) $\sigma_{3s}=10$ psi

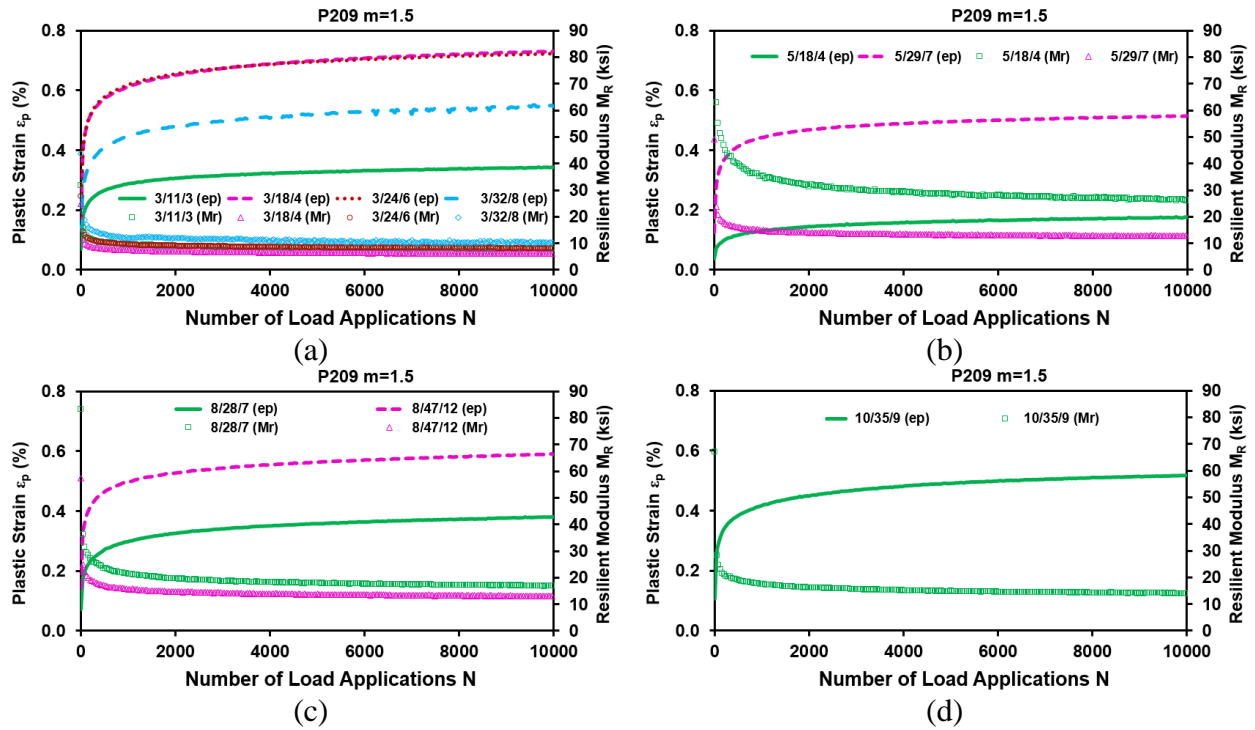


Figure 7.7 Relationship between Plastic Strain and Vertical Resilient Modulus for P209 Material Observed during VCP Test with Stress Slope $m=1.5$: (a) $\sigma_{3s}=3$ psi, (b) $\sigma_{3s}=5$ psi, (c) $\sigma_{3s}=8$ psi, and (d) $\sigma_{3s}=10$ psi

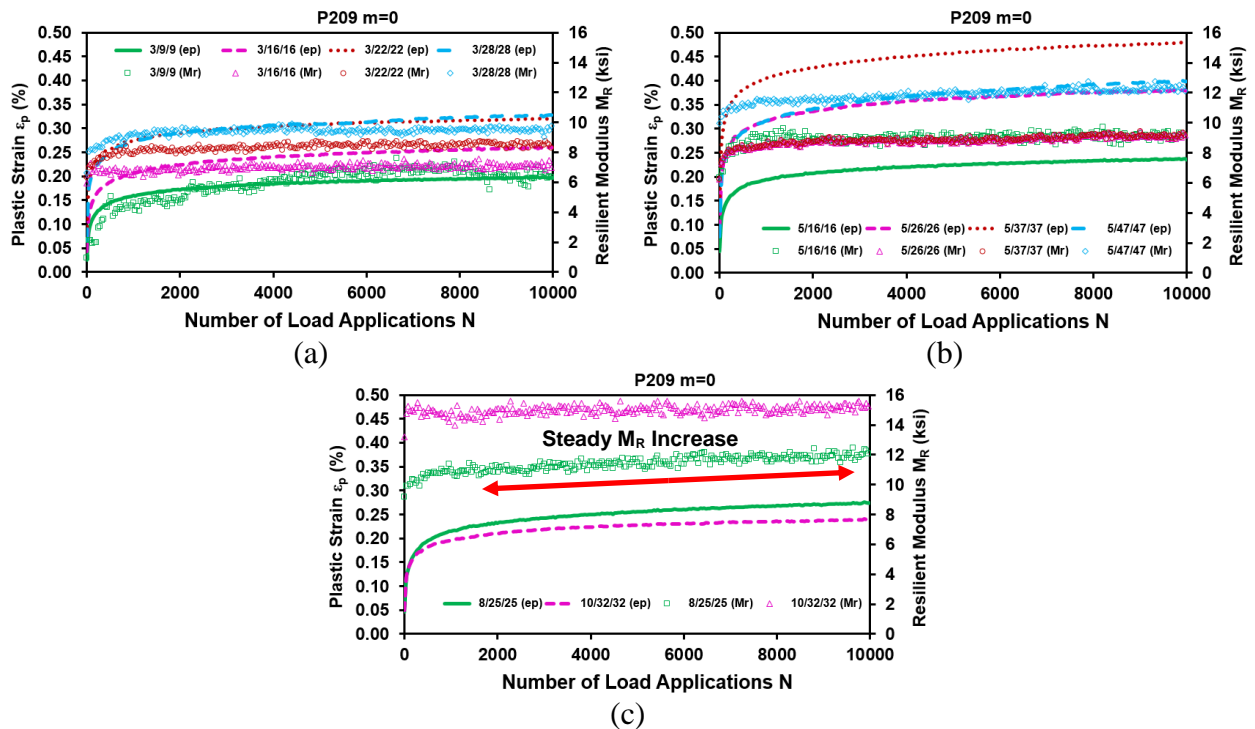


Figure 7.8 Relationship between Plastic Strain and Vertical Resilient Modulus for P209 Material Observed during VCP Test with Stress Slope $m=0$: (a) $\sigma_{3s}=3$ psi, (b) $\sigma_{3s}=5$ psi, and (c) $\sigma_{3s}=8$ psi

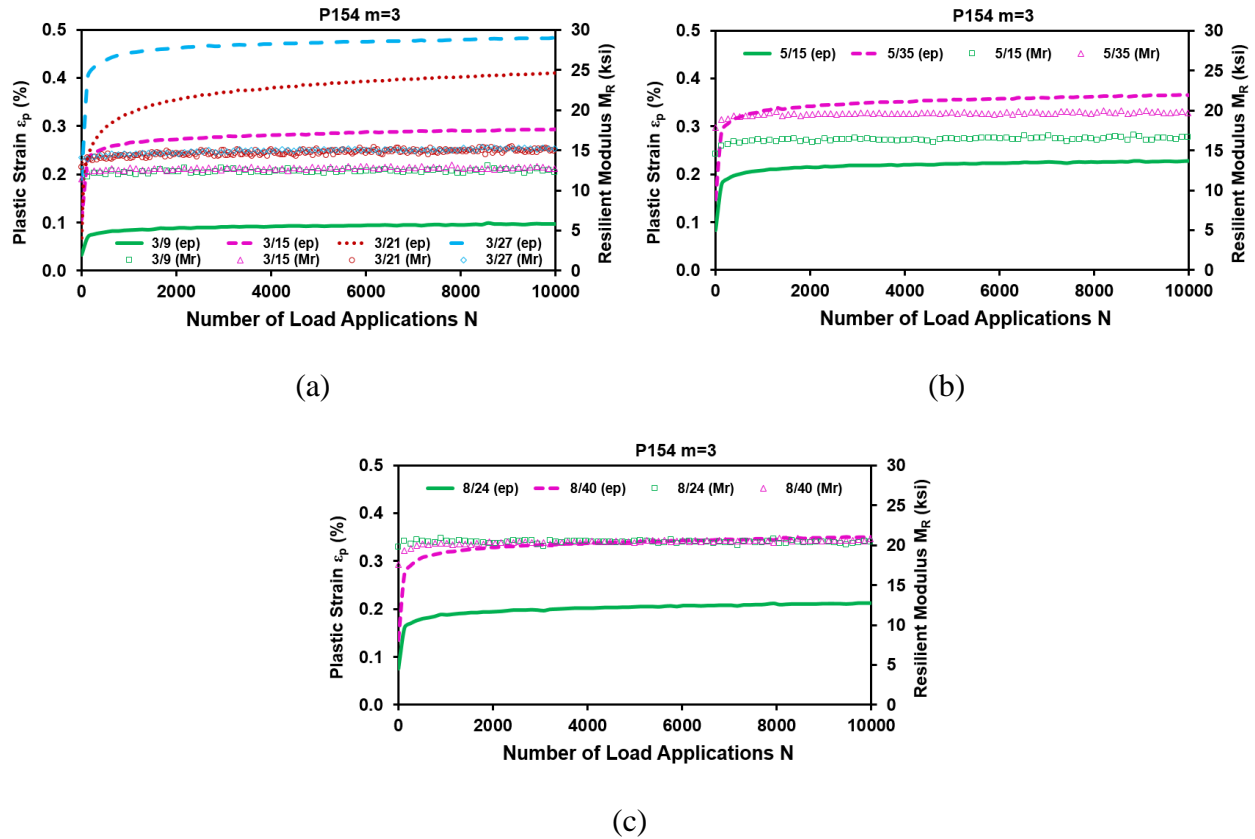


Figure 7.9 Relationship between Plastic Strain and Vertical Resilient Modulus for P154 Material Observed during CCP Test with Stress Slope $m=3$: (a) $\sigma_{3s}=3$ psi, (b) $\sigma_{3s}=5$ psi, and (c) $\sigma_{3s}=8$ psi

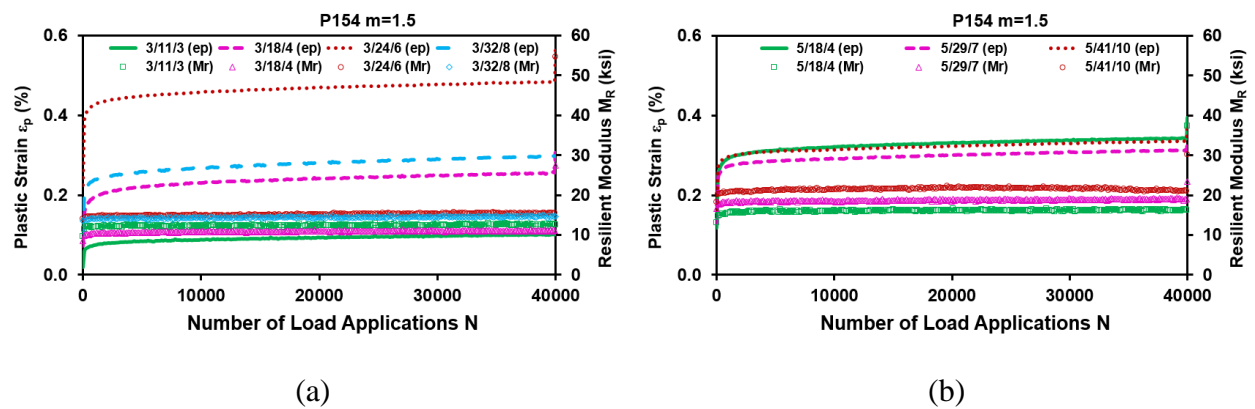


Figure 7.10 Relationship between Plastic Strain and Vertical Resilient Modulus for P154 Material Observed during VCP Test with Stress Slope $m=1.5$: (a) $\sigma_{3s}=3$ psi, (b) $\sigma_{3s}=5$ psi, (c) $\sigma_{3s}=8$ psi, and (d) $\sigma_{3s}=10$ psi

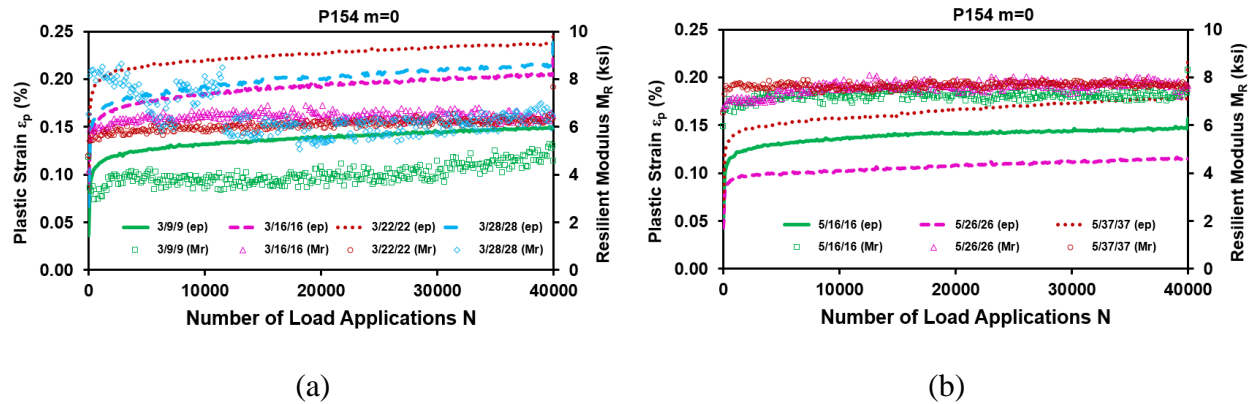


Figure 7.11 Relationship between Plastic Strain and Vertical Resilient Modulus for P154 Material Observed during VCP Test with Stress Slope $m=0$: (a) $\sigma_{3s}=3$ psi, (b) $\sigma_{3s}=5$ psi, and (c) $\sigma_{3s}=8$ psi

7.1.3.2 Different Aggregate Physical Properties

Three different types of aggregates were tested at varying combinations of aggregate physical properties under the same CCP stress state. This provides an opportunity to explore the potential use of the resilient modulus-permanent deformation relation in effectively discerning the material quality. The incremental collapse behavior that is absent from FAA P209 and P154 materials is observed for materials with high fines content on the wet side of the optimum moisture content. As indicated by Von Quintus and Killingsworth (1998) from field observations that the water content of cohesive subgrade soils in service were all on the wet side of optimum moisture content (OMC), the high moisture content that is 110% of the optimum one was also included in the laboratory test matrix.

Figure 7.12 through Figure 7.14 plot both the plastic strain and resilient modulus against the number of load applications for crushed dolomite, crushed limestone, and uncrushed gravel, respectively. Note that the target fines contents of 0%, 4%, 8%, and 12% (based on dry sieve analysis) correspond to the achieved fines contents of around 4%, 8%, 12%, and 16% (based on

wet sieve analysis) respectively, as explained previously. Despite the fact that no noticeable difference was found among resilient modulus values for each combination of aggregate physical conditions, significant differences among permanent deformation curves were observed. For crushed dolomite, the target fines content of 4% (i.e., 8.7% achieved fines content) results in the most negligible difference in permanent deformation among the various physical conditions studied (see Figure 7.12 (c) and (d)). Such an optimum fines content agrees well with the one proposed by Seyhan and Tutumluer (2002). Figure 7.12 (g) and (h) clearly illustrated the detrimental effect of high fines content (12% target and 16.6% achieved), as resilient modulus decreases and permanent deformation increases with increasing moisture content. This implies the development of an unstable aggregate matrix. Figure 7.14 (f), (g), and (h) show the incremental collapse behavior observed for uncrushed gravel materials with high fines content at the wet side of the optimum moisture content. The resilient modulus in the incremental collapse state is found to increase during the initial load cycles and then decrease with further load applications. This situation could be regarded as strain softening of the material under repeated loading. Meanwhile, excessive plastic strain accumulates rapidly, leading to an unstable state.

Based on the analysis results discussed above, the observed resilient modulus-permanent deformation relation for each of the three shakedown categories can be generalized as follows. During plastic shakedown, the stiffness of the material increases (due to strain-hardening) and the accumulated plastic strain stabilizes such that the material responds purely elastically to the applied load. As a result, both the plastic strain and the resilient modulus tend to reach a constant level, which signifies the occurrence of the steady state. At the state of plastic creep, more voids in the material are compacted due to the application of a higher stress level, thus strain hardening occurs and the plastic strain still accumulates with increasing number of load cycles. In other

words, the microstructure of the material is changing continuously. This can be confirmed by the fact that both the plastic strain and the resilient modulus increase at a specific rate. At a very high stress level, the material is in the incremental collapse state. The plastic strain accumulates rapidly, and strain softening of the material occurs. From the perspective of preventing rutting distress in the unbound pavement layers from occurring, it is important to accurately predict the allowable number of load cycles. In road pavements, plastic strain exceeding 4% would be deemed unacceptable (Muhanna, 1994).

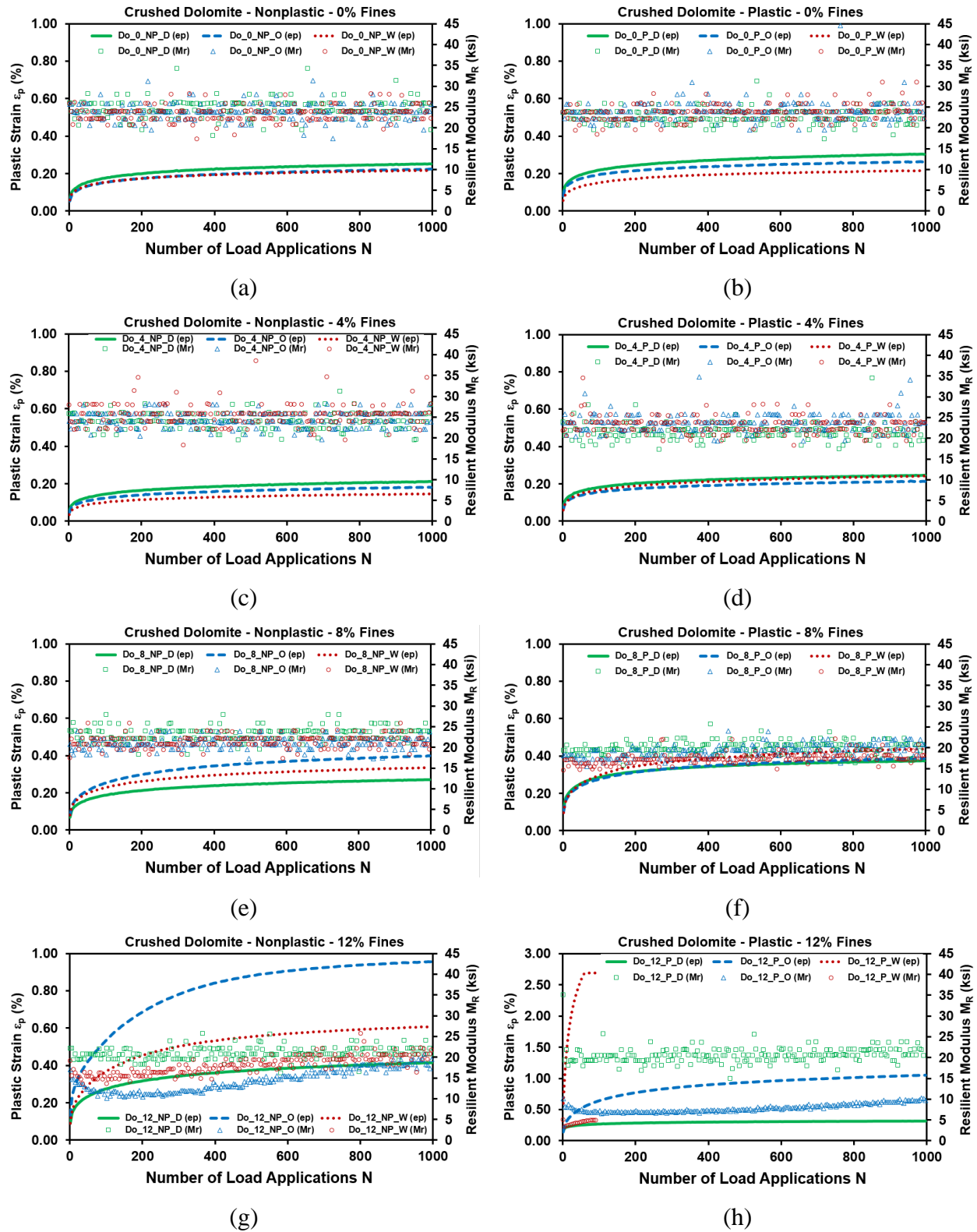


Figure 7.12 Relationship between Plastic Strain and Vertical Resilient Modulus for Crushed Dolomite with Varying Fines Content (Left: Non-plastic; Right: Plastic)

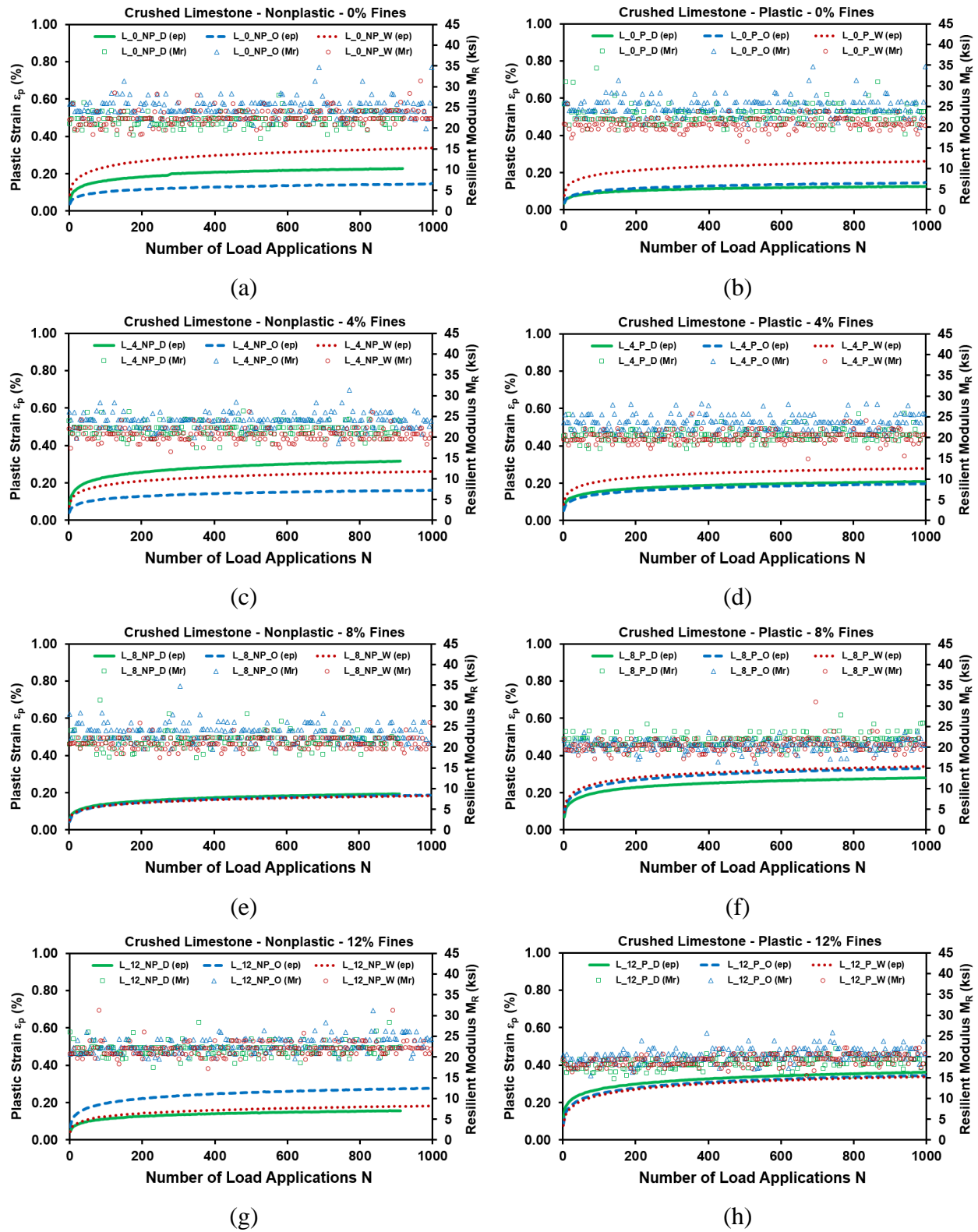


Figure 7.13 Relationship between Plastic Strain and Vertical Resilient Modulus for Crushed Limestone with Varying Fines Content (Left: Non-plastic; Right: Plastic)

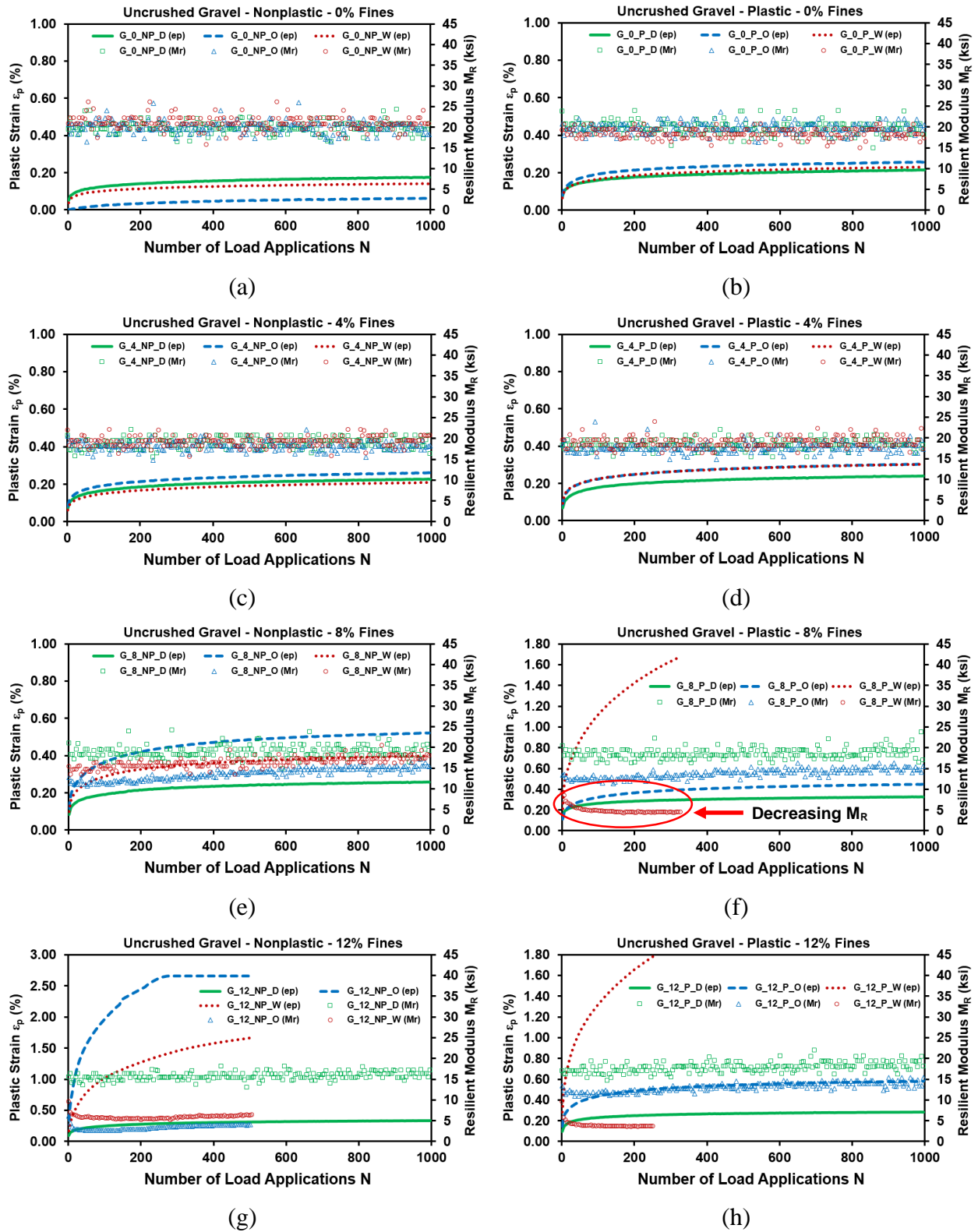


Figure 7.14 Relationship between Plastic Strain and Vertical Resilient Modulus for Uncrushed Gravel with Varying Fines Content (Left: Non-plastic; Right: Plastic)

7.1.4 Enhancement of the Current MEPDG Permanent Deformation Model for Unbound Materials

The original Tseng and Lytton model (1989) and the MEPDG rutting model, among many others, use resilient modulus or resilient strain as a variable to predict permanent strain of unbound granular materials. There is no doubt that ruts accumulate rapidly when the applied wheel load stress on the unbound layers exceeds a certain tolerable level based on its strength property. The NCHRP 4-23 study identified shear strength of unbound aggregates as one of the most significant mechanistic properties influencing pavement performance (Saeed et al., 2001). Moreover, shear strength rather than resilient modulus has been always shown to better correlate with unbound aggregate permanent deformation behavior for predicting field rutting performance (Thompson, 1998; Tao et al., 2010; Xiao and Tutumluer, 2012). From an extensive database of aggregate properties studied in Minnesota, Xiao and Tutumluer (2012) found no clear or significant modulus-strength relationships for unbound aggregates. In its current form, the Pavement ME Design software does not consider the effects of shear stress to strength ratio while predicting the performance of unbound aggregate base/subbase pavement layers under repeated traffic loading. This indicates that it still remains important for ME pavement design approaches to consider the effects of applied stress levels on aggregate layer rutting. However, from previous analyses of a series of laboratory triaxial test results, the inclusion of the resilient modulus as a predictive variable for estimating permanent deformation is at least not sufficient enough if not inaccurate. The fact that rutting in unbound pavement layers is actually a type of shear failure necessitates the inclusion of other predictive variables, such as the shear stress ratio (SSR), an important term identified by Seyhan and Tutumluer (2002), as well as the octahedral shear stress.

Based on the previous verification results of the original Tseng and Lytton model and the current MEPDG rutting model against laboratory RLT test results, the need for the further enhancement of both models becomes obvious. In this study, attention has been paid to develop an enhanced mechanistic rutting model for unbound materials based on the original Tseng and Lytton model as well as the MEPDG model. The proposed model was developed based on the two aforementioned databases.

7.1.4.1 Enhancement for Dynamic Stress States

To explore the relation between model parameters of the Tseng and Lytton rutting model and the shear stress ratio (SSR), bivariate plots are prepared. It is found that the correlation between the shear stress ratio and the model parameters of the Tseng and Lytton rutting model is statistically significant. Therefore, the enhancement proposed for the original Tseng and Lytton's empirical relationships (see Equation 7.1) includes the addition of the shear stress ratio and the octahedral shear stress terms as two new predictive variables, as shown in Equation 7.3. Note that only one extra regression coefficient is added in the enhanced model, as compared to the original empirical relationships that have five regression coefficients. The logarithmic transform of the shear stress ratio in Equation 7.3 was found necessary.

$$\begin{aligned} \epsilon_p(N) &= \epsilon_0 e^{-(\rho/N)^\beta} \\ \log\left(\frac{\epsilon_0}{\epsilon_r}\right) &= A_1 + A_2 \cdot \sigma_\theta + A_3 \cdot M_R + A_4 \cdot \log(\text{SSR}) + A_5 \cdot \tau_{oct} \\ \log \rho & \end{aligned} \quad (7.3)$$

where N=number of load applications; A₁ through A₆ are regression coefficients for log(ε₀/ε_r), logβ, and logρ models; SSR=shear stress to strength ratio, M_R=resilient modulus; σ_θ=bulk stress; and τ_{oct}=octahedral shear stress.

Table 7.6 and Table 7.7 list the model coefficients and R^2 values of the enhanced rutting model for both FAA P209 and P154 materials, respectively. As compared to the original Tseng and Lytton's empirical relationships, the enhanced model significantly improves the prediction accuracy as indicated by much higher R^2 values, especially for P154 material. This further supports the argument that plastic strain is more related to shear stress level than the resilient modulus itself.

Table 7.6 Enhanced Rutting Prediction Model for P209 Materials

Model Coefficients		m=3			m=1.5			m=0		
		$\log\left(\frac{\epsilon_0}{\epsilon_r}\right)$	$\log\beta$	$\log\rho$	$\log\left(\frac{\epsilon_0}{\epsilon_r}\right)$	$\log\beta$	$\log\rho$	$\log\left(\frac{\epsilon_0}{\epsilon_r}\right)$	$\log\beta$	$\log\rho$
A ₁		1.40	-1.74	-4.65	3.42	-3.86	20.96	-0.30	-0.78	-4.43
A ₂		0.01	-0.02	-0.02	0.017	-0.02	0.12	0.003	-0.001	-0.04
A ₃		-0.01	0.02	-0.05	0.015	-0.01	0.12	-0.005	0.01	0.06
A ₄		0.98	-1.94	-11.97	2.19	-2.50	15.36	-0.39	-0.06	-2.70
A ₅		-0.02	0.07	0.24	-0.19	0.21	-1.37	0.07	-0.05	2.76
R ²	New	0.40	0.46	0.35	0.97	0.95	0.98	0.44	0.75	0.44
	Original	0.21	0.26	0.32	0.88	0.77	0.90	0.12	0.71	0.23

Table 7.7 Enhanced Rutting Prediction Model for P154 Materials

Model		m=3			m=1.5			m=0		
		$\log\left(\frac{\epsilon_0}{\epsilon_r}\right)$	$\log\beta$	$\log\rho$	$\log\left(\frac{\epsilon_0}{\epsilon_r}\right)$	$\log\beta$	$\log\rho$	$\log\left(\frac{\epsilon_0}{\epsilon_r}\right)$	$\log\beta$	$\log\rho$
A ₁		-0.43	0.58	-16.36	2.63	2.29	-32.53	1.56	-1.55	8.18
A ₂		-0.03	-0.02	0.04	0.005	-0.02	0.24	0.005	-0.01	0.11
A ₃		0.07	0.04	-0.07	0.001	0.06	-0.54	-0.15	0.20	-2.76
A ₄		-0.57	1.56	-17.22	1.70	3.20	-34.36	0.08	0.08	-2.04
A ₅		0.05	-0.02	0.46	-0.11	-0.06	0.25	0.41	-0.60	7.41
R ²	New	0.83	0.58	0.80	0.79	0.99	0.97	0.93	0.69	0.78
	Original	0.78	0.02	0.39	0.27	0.49	0.79	0.27	0.31	0.54

7.1.4.2 Enhancement for Different Aggregate Physical Properties

Only moisture content is included as a predictive variable in the original Tseng and Lytton's empirical relationships (see Equation 7.1) as well as in the MEPDG rutting model (see Equation 7.2). This is obviously not sufficient enough to yield accurate prediction, as proved in the previous sections. In fact, fines content, plasticity nature of the fines, and their interactions with moisture content are also among the most important factors that affect both permanent deformation and resilient modulus behavior of unbound aggregates. In this section, the following enhancements were proposed and explored for their effectiveness: (i) replacing moisture content by percent saturation so that dry density information can be used as well; and (ii) the inclusion of weighted plasticity index (wPI) and shear stress ratio terms as new predictive variables. Previous studies have shown that the variable wPI can account for the effects of both plasticity index and

finer content (El-Badawy and Witczak, 2007). The final model form selected is shown as in Equation 7.4, in which the interaction term of wPI and SSR was found statistically significant.

$$\begin{aligned} \epsilon_p(N) &= \epsilon_0 e^{-(\rho/N)^\beta} \\ \log\left(\frac{\epsilon_0}{\epsilon_r}\right) & \\ \log\beta &= A_1 + A_2 \cdot S_r + A_3 \cdot \text{wPI} + A_4 \cdot \sigma_\theta + A_5 \cdot M_R + A_6 \cdot \text{SSR} + A_7 \cdot \text{wPI} \cdot \text{SSR} \\ \log\rho & \end{aligned} \quad (7.4)$$

where N=number of load applications; A₁ through A₆ are regression coefficients for log(ε₀/ε_r), logβ, and logρ models; SSR=shear stress to strength ratio, wPI=weighted plasticity index (=PI*%P200/100), PI=plasticity index (%), %P200=percent passing No. 200 sieve, and S_r=degree of saturation (in decimal); M_R=resilient modulus; and σ_θ=bulk stress.

Table 7.8 through Table 7.10 summarize the model coefficient and R² values obtained by the enhanced rutting prediction model for crushed dolomite, crushed limestone, and uncrushed gravel materials, respectively. It can be seen that the enhanced model yielded reasonably high R² values in predicting material constants ε₀/ε_r, β, and ρ of the original Tseng and Lytton model, considering that a variety of different aggregate physical conditions are involved. This indicates that the enhanced model can be more robustly applied to a wider range of material types and physical conditions, as contrary to the original empirical relationships. Both variables, i.e., percent saturation and weighted plasticity index, can be effectively used as essential variables to characterize physical conditions of unbound aggregate materials (i.e., fines content, plasticity index of fines, and moisture content).

Table 7.8 Enhanced Rutting Prediction Model for Crushed Dolomite Materials

Model Coefficients		Non-plastic			Plastic			Combined		
		$\log\left(\frac{\epsilon_0}{\epsilon_r}\right)$	$\log\beta$	$\log\rho$	$\log\left(\frac{\epsilon_0}{\epsilon_r}\right)$	$\log\beta$	$\log\rho$	$\log\left(\frac{\epsilon_0}{\epsilon_r}\right)$	$\log\beta$	$\log\rho$
A ₁		13.91	-4.09	-16.44	-2.33	2.56	-5.03	3.83	0.41	4.29
A ₂		-0.79	0.25	-2.91	-0.43	0.49	-4.30	-0.41	0.13	-0.57
A ₃		-31.87	56.10	-459.02	-1.77	1.78	-13.50	0.20	-0.08	0.31
A ₄		-0.18	0.05	0.40	0.09	-0.08	0.38	-0.03	-0.01	-0.03
A ₅		-0.04	-0.03	0.24	3.6E-04	-0.03	-0.03	-0.03	-0.02	0.01
A ₆		-1.88	3.46	-35.42	-5.79	6.27	-37.74	0.03	-0.64	5.32
A ₇		180.8	-305	2447.2	6.44	-7.24	43.54	-1.81	0.38	-7.10
R ²	New	0.79	0.95	0.76	0.66	0.82	0.60	0.60	0.68	0.45
	Original	0.69	0.80	0.54	0.44	0.71	0.89	0.14	0.64	0.38

Table 7.9 Enhanced Rutting Prediction Model for Crushed Limestone Materials

Model Coefficients		Non-plastic			Plastic			Combined		
		$\log\left(\frac{\epsilon_0}{\epsilon_r}\right)$	$\log\beta$	$\log\rho$	$\log\left(\frac{\epsilon_0}{\epsilon_r}\right)$	$\log\beta$	$\log\rho$	$\log\left(\frac{\epsilon_0}{\epsilon_r}\right)$	$\log\beta$	$\log\rho$
A ₁		-1.49	0.56	-21.20	20.56	-9.26	-26.63	-5.82	-2.94	-8.78
A ₂		0.92	-0.64	6.45	0.99	-0.10	-1.10	0.79	-0.19	2.42
A ₃		159.37	-1.66	-160.10	-1.81	0.64	-2.46	0.61	-0.25	2.75
A ₄		-0.002	-0.02	0.41	-0.28	0.11	0.54	0.10	0.03	0.14
A ₅		-0.02	0.02	-0.21	-2.3E-2	0.02	0.02	-0.02	0.01	-0.04
A ₆		9.92	0.35	-8.07	-14.67	5.11	-13.39	2.06	-0.23	10.77
A ₇		-707.1	-24.3	1029.2	10.44	-3.05	5.82	-3.04	1.37	-16.0
R ²	New	0.75	0.54	0.62	0.85	0.92	0.85	0.64	0.54	0.58
	Original	0.43	0.23	0.26	0.68	0.41	0.52	0.31	0.28	0.22

Table 7.10 Enhanced Rutting Prediction Model for Uncrushed Gravel Materials

Model Coefficients		Non-plastic			Plastic			Combined		
		$\log\left(\frac{\epsilon_0}{\epsilon_r}\right)$	$\log\beta$	$\log\rho$	$\log\left(\frac{\epsilon_0}{\epsilon_r}\right)$	$\log\beta$	$\log\rho$	$\log\left(\frac{\epsilon_0}{\epsilon_r}\right)$	$\log\beta$	$\log\rho$
A ₁		19.4	-11.2	9.5	-24.1	14.0	-145.7	-0.8	-0.6	-57.0
A ₂		-0.1	0.1	-2.5	1.3	-0.8	5.8	0.9	-0.4	6.1
A ₃		561.6	-406.4	238.5	-0.05	0.7	-5.0	0.7	-0.1	-0.8
A ₄		-0.4	0.2	-0.1	0.4	-0.2	2.4	0.02	0.01	0.8
A ₅		-0.002	-0.04	0.21	0.03	-0.06	0.28	-0.05	-0.01	0.11
A ₆		11.2	-8.9	-6.8	-1.44	2.57	-17.5	2.67	-1.06	8.24
A ₇		-1.6E3	1.2E3	-8.6E2	-0.02	-2.1	12.9	-1.59	-0.07	6.87
R ²	New	0.69	0.76	0.61	0.98	0.99	0.98	0.68	0.19	0.48
	Original	0.37	0.27	0.28	0.96	0.69	0.93	0.61	0.09	0.44

7.2 Modeling Degradation Stiffness for Permanent Deformation Prediction

As discussed in the previous sections, the resilient modulus (M_R) deals with the elastic response of the material and ignores the plastic component responsible for permanent deformation. However, the need for capturing permanent deformation, a more critical performance indicator, has been highlighted by results of field and laboratory investigations. Although many methods have been proposed for estimating permanent deformation of unbound materials under cyclic (or repeated) load, no generally accepted design procedure yet exists. In principle, the mechanical behavior of unbound materials under cyclic loads, including permanent deformation, can be simulated cycle by cycle using sophisticated material constitutive laws. However, it is almost impractical, if not impossible, for pavement designers to use such numerical models with implicit calculation concepts to estimate permanent displacement, mainly because the rate of permanent displacement accumulation is usually very small and a large

number of cycles are often required. On the other hand, the repeated applications of traffic loads (in the order of several millions throughout the service life) on the pavement structures make the empirical approach inevitable in relating responses to the deteriorations/distresses. With explicit methods, semi-empirical approaches are used to describe the permanent deformation response with respect to the number of load cycles. The development of cyclic deformations dependent on the number of cycles is directly described by empirical equations (as reviewed in Chapter 2). These methods are based on small-scale laboratory RLT test results or field accelerated pavement testing (APT) with a limited number of cycles, and their suitability for actual pavements subject to field conditions is not clear. Despite cyclic laboratory tests are suggested to assess the response of pavement foundation geo-materials under long-term cyclic loading, there is still no approved method for taking into account the results of such tests in the design of pavement layers for accumulated rutting.

The purpose of this section is to demonstrate how the results of laboratory repeated load triaxial tests on unbound aggregates can be applied in a numerical model to estimate the progressive deformation of unbound pavement layers under long-term cyclic load. To achieve this, the special numerical concept, namely the “degradation stiffness model”, is introduced in the following. The constitutive models for the degraded secant modulus are proposed based on the concept similar to that of the existing resilient modulus models, thus making them suitable for use with numerical tools such as the finite element simulation. By using the proposed models, the permanent deformation of unbound pavement layers under repetitive loading can be realistically predicted in a mechanistic manner, as contrary to the current empirical or semi-empirical methods.

7.2.1 Degradation Stiffness Model

The degradation stiffness model presented in this study was originally proposed by Achmus et al. (2009) for modeling the behavior of monopoles for offshore wind turbines. It is a method based on a combination of an evaluation of drained cyclic triaxial tests and a finite element (FE) simulation of the pavement structure. In cyclic triaxial tests, the plastic axial strain is observed to accumulate with the number of cycles under different loading conditions, whereas the material secant stiffness decreases. This is clearly shown in Figure 7.15(a), a schematic diagram of the typical stress–strain behavior of a soil sample under cyclic loading. The vertical and horizontal axes in Figure 7.15(a) represent the applied vertical cyclic stress and the resulting vertical strain, respectively. The accumulated total strain \mathcal{E}_t , contributed by all loading cycles, is represented by the peaks of the cyclic curve, whereas the accumulated permanent strain \mathcal{E}_p is represented by the line joining the ends of the load cycles. The magnitude of the resilient modulus is defined as the slope of the line joining the total and permanent strains for each cycle. Assessing the stress conditions in the distinct elements and introducing the stiffness degradation obtained by comparison with the cyclic test results in the finite element model yields the accumulated deformations of pavement layers. This is the basic concept of the degradation stiffness model.

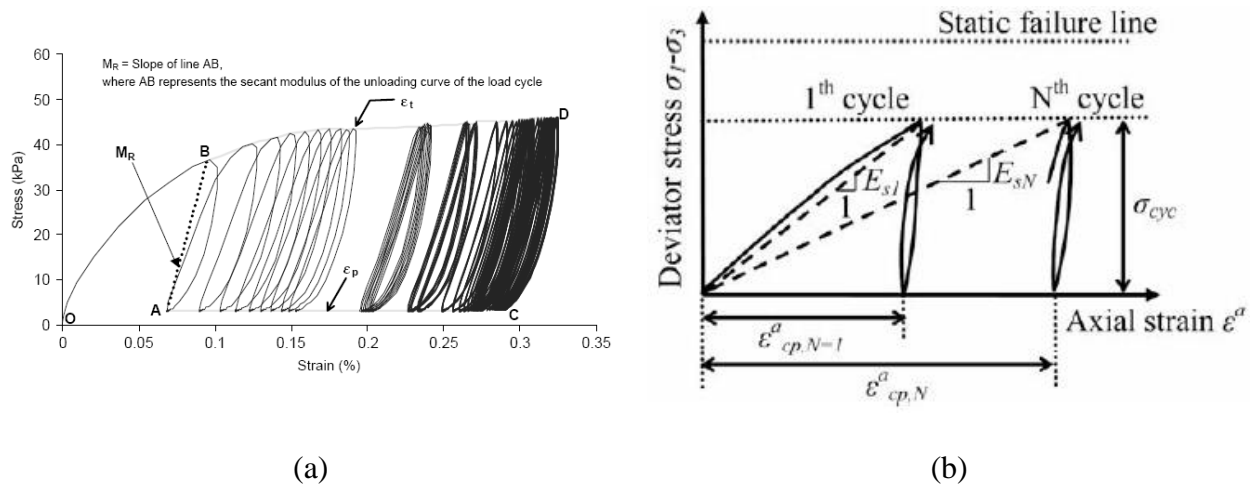


Figure 7.15 Characteristic Response of Unbound Material: (a) Stress-Strain Relationship (Khogali and Mohamed, 2004) and (b) the Concept of Degradation Stiffness (Achmus et al., 2009)

The degradation stiffness approach to account for cyclic loading effects is elucidated in Figure 7.15(b). The resilient and permanent strains developed in the first cycle are denoted by $\epsilon_{r,N=1}$ and $\epsilon_{p,N=1}$, respectively. The resilient and accumulated permanent strains after N cycles are denoted by $\epsilon_{r,N}$ and $\epsilon_{p,N}$, respectively. For adequately designed pavements, it is reasonable to consider that the magnitude of resilient strain converges after a specified number of load repetitions (NCHRP 2003; AASHTO 1999; LTPP 1996). Therefore, the degraded secant modulus, termed as the degradation stiffness by Achmus et al. (2009), is defined by the slope of the line that connects the peak of the curve at the N-th load cycle and the origin. Assuming the elastic strain to be negligible (as the material exhibits shakedown behavior), the degradation rate of secant stiffness after first cycle E_{s1} and N-th cycle E_{sN} can be presented by the plastic axial strains after first cycle $\epsilon_{p,1}^a$ and N-th cycle $\epsilon_{p,N}^a$ as in Equation 7.5.

$$E_{S1} = \frac{\sigma_{cyc}}{\varepsilon_{p,1} + \varepsilon_r}, \quad E_{SN} = \frac{\sigma_{cyc}}{\varepsilon_{p,N} + \varepsilon_r} \quad (7.5)$$

$$\frac{E_{SN}}{E_{S1}} = \frac{\varepsilon_{p,1}^a + \varepsilon_r}{\varepsilon_{p,N}^a + \varepsilon_r} \approx \frac{\varepsilon_{p,1}^a}{\varepsilon_{p,N}^a}$$

The accumulation of plastic strains in a cyclic triaxial test can be estimated from existing semi-empirical approaches. Here the classical power-law model ($\varepsilon_{p,N}^a = a \cdot N^b$) is considered for simplicity, and with it the degradation of stiffness can be described using one material parameters b as follows:

$$\frac{E_{SN}}{E_{S1}} \approx \frac{\varepsilon_{p,1}^a}{\varepsilon_{p,N}^a} = N^{-b} \quad (7.6)$$

7.2.2 Parameter Estimation for the Degradation Stiffness Model

After presenting the degradation stiffness model – a numerical concept which is able to account for cyclic loading in the determination of permanent deformations in a realistic manner, a series of laboratory triaxial tests is needed to assess the parameters describing cyclic behavior of the soil. By dividing the deviator (cyclic) stresses applied by the accumulated permanent strain, the degraded secant modulus was evaluated for each load repetition. As an example, Figure 7.16 shows the variation of the degraded secant modulus with the number of load cycles for FAA P154 material subject to different combinations of CCP type confining and deviator stresses ($m=3$). The decreasing trend of the degraded secant modulus is obvious. Also noticeable from Figure 7.16 is the stress dependency of the degraded secant modulus. Note that the initial degradation stiffness E_{s1} can be described by the current constitutive models for resilient modulus.

To express the dependency of the degraded secant modulus on the number of load cycles (N) and the stress states, the forms of the power-law permanent deformation models and resilient modulus models often used in pavement design were employed to construct the constitutive models of the degraded secant moduli as in Equation 7.7. This approach was also used by Ahn et al. (2013). It should be noted that using the exponential term of the bulk stress in Equation 7.7, instead of the power term in the current resilient modulus models, is to accommodate boundary value problems with zero or negative bulk stress, which may happen at the top and bottom surfaces of base layers due to wheel loading.

$$\begin{aligned}
 \text{Model I: } E_{SN} &= A \cdot p_a \cdot N^B \cdot e^{c \left(\frac{\theta}{p_a} \right)} \\
 \text{Model II: } E_{SN} &= A \cdot p_a \cdot N^B \cdot e^{c \left(\frac{\theta}{p_a} \right) \left(\frac{\tau_{oct}}{p_a} + 1 \right)^D}
 \end{aligned}
 \tag{7.7}$$

where E_{SN} =degraded secant modulus, p_a =atmosphere pressure (14.7 psi) to normalize the bulk and octahedral stress terms, N=the number of load applications, and A, B, C, and D=regression coefficients to be determined from laboratory triaxial tests.

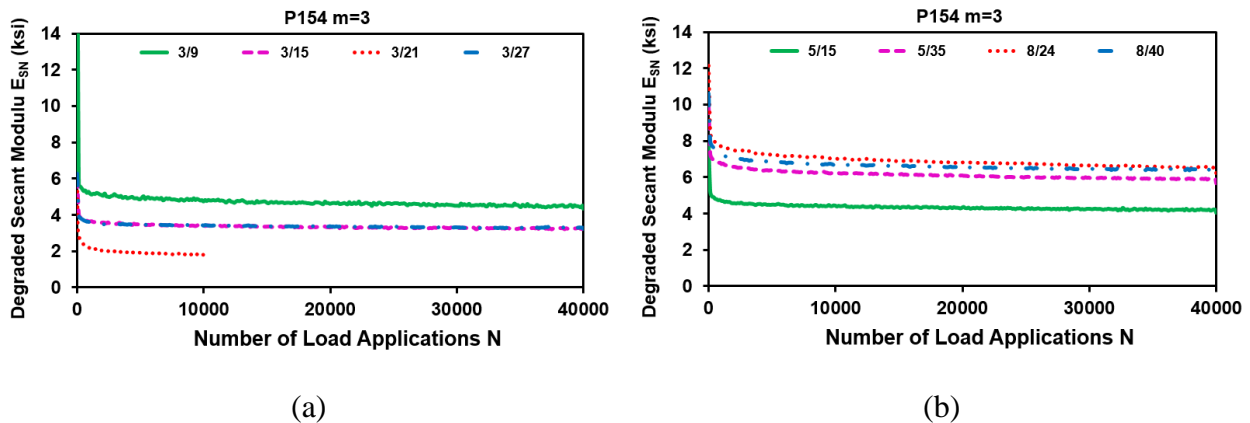


Figure 7.16 Variation of Degraded Secant Modulus with Load Cycles for FAA P154 Material during CCP Tests: (a) 3-psi Confining Stress and (b) 5-psi and 8-psi Confining Stresses

The model parameters A, B, C, and D in Equation 7.7 can be estimated by multiple linear regression of the experimental results after taking logarithmic forms of the equation. Test results under more stress combinations may be required for a reliable estimation of the parameters and therefore reliable estimation of permanent deformation. Table 7.11 summarizes the model parameters obtained for the Model II in Equation 7.7 at different stress states. A comparison of model results with existing test results for unbound materials indicate quite good agreement. The calibrations for degradation stiffness model with large-scale model tests can be planned in further research studies.

Table 7.11 Model Coefficients for Degraded Secant Modulus of FAA P154 Material (m=3)

Model Coefficients	Constant Confining Pressure (CCP) Type Stress State								
	03/09	03/15	03/21	03/27	05/15	05/35	08/24	08/40	All
A	258.6	49.74	102.08	314.18	89.86	2870.4	232.53	923.72	409.3
B	-0.04	-0.045	-0.103	-0.04	-0.04	-0.048	-0.05	-0.043	-0.06
C	-0.16	1.456	1.743	0.222	0.62	-0.132	0.61	0.053	0.47
D	3.90	-1.58	-5.21	-0.84	0.82	-1.369	-1.68	-0.724	-1.76
R ²	0.99	0.94	0.98	0.76	0.87	0.98	0.98	0.95	0.71
SEE	0.034	0.047	0.052	0.091	0.084	0.044	0.067	0.069	0.761

7.3 Shakedown based Interpretation of Permanent Deformation Test Results

As discussed previously, the permanent strain model parameters of both Tseng and Lytton model and the MEPDG model vary significantly with changing dynamic stress states (quantified by stress path slope and magnitude) and material physical conditions. By either considering only moisture content, bulk stress and resilient properties or using universal material constants, their prediction accuracy and potential usefulness for practical applications could be severely reduced. Therefore, it is highly desirable for a rational permanent deformation model to properly include the respective effect of these variables. It then becomes the major motivation of this section to analyze from laboratory permanent deformation database a viable criterion for ranking long-term rutting potential based on the shakedown theory.

The stress invariants will be used in this research to compare the stress paths applied by moving wheel loads and stress paths applied in laboratory tests. One of the ways to describe stress paths is to represent stress history on the deviatoric stress (q)-mean stress (p) space. For example, the second invariant of the deviatoric stress tensor S_{ij} (J_2), and the first invariant of the stress tensor σ_{ij} (I_1) can be used. The stress paths either induced by the moving wheel load in an unbound pavement layer or applied in laboratory tests can be plotted in p - q stress diagrams, and later compared with the shear stress failure of the material, by using a stress ratio analysis. The relative damage of the pavements was estimated by the stress ratio, which is the quotient between the actual stress applied and the stress at failure. If the stress ratio is low, the material will develop some plastic deformation for a finite number of load repetitions, but the response will remain essentially resilient after the initial loading. At higher stress ratios, the plastic deformation increases, up to a stress ratio limit, in which permanent deformation will accumulate rapidly. Therefore, the stress ratio has been considered as an approximate measure of the relative

damage that will result from repeated load applications at lower stress conditions than the peak stress triaxial monotonic conditions (Seyhan and Tutumluer, 2002).

7.3.1 Modeling the Primary and the Secondary Regions of Permanent Deformation Curves

A typical accumulated permanent strain curve of unbound granular base/subbase materials can be divided into three main regions, i.e., primary, secondary, and tertiary. Within the primary region, the permanent strain accumulates rapidly but with a decreasing rate until reaching a constant accumulation rate at the beginning of the secondary region. The secondary region is characterized by a constant (or stable) permanent strain accumulation rate, indicating the occurrence of the steady state. During the tertiary region, permanent strain accumulates rapidly with an increasing rate until rutting failure occurs. To assess the rutting potential of different unbound materials at different stress states and/ or physical conditions, it then becomes necessary to identify the locations of the boundary points connecting the primary to the secondary regions, and the secondary to the tertiary regions. However, there is currently no general acceptance regarding how to identify these two boundary points on the permanent deformation curves. Furthermore, the rate of the accumulated permanent strain depends on several parameters among which both the dynamic stress state and aggregate physical properties (e.g., moisture and density condition, fines content, and plasticity index) warrant further investigation.

Among the existing permanent deformation models, the semi-log model proposed by Barksdale (1972) and the power-law model developed by Monismith et al. (1975) can only represent the primary stage of the measured permanent deformation curve. The Tseng and Lytton's model, the precedent of the current MEPDG model, are also reported as incapable of characterizing either the secondary or tertiary stage (Zhou et al., 2004). One commonly used

method for identifying the boundary points on the permanent deformation curve is to use permanent strain per cycle $d\varepsilon_p/dN$ (Bayomy, 1982; Witczak et al., 2000; Kaloush and Witczak, 2002). However, this procedure was found to be quite misleading due to the infinitesimal $\Delta\varepsilon/\Delta N$. Zhou et al. (2004) proposed the three-stage permanent deformation model (as in Equation 7.8) based on the definition of each stage, as well as the algorithms to determine the transition points and parameters of the three-stage permanent deformation model. A logarithmic model by Kalyoncuoglu and Tigidemir (2010) is also reported to more accurately simulate the primary region of the permanent deformation curves than the Pow-law model by Monismith et al. (1975).

$$\begin{aligned}\varepsilon_p &= aN^b, \quad N \leq N_{PS} \\ \varepsilon_p &= \varepsilon_{PS} + c(N - N_{PS}), \quad N_{PS} \leq N \leq N_{ST} \quad \& \quad \varepsilon_{PS} = aN_{PS}^b \\ \varepsilon_p &= \varepsilon_{ST} + d(e^{f(N-N_{ST})} - 1), \quad N \geq N_{ST} \quad \& \quad \varepsilon_{ST} = \varepsilon_{PS} + c(N_{ST} - N_{PS})\end{aligned}\tag{7.8}$$

where ε_p =accumulated permanent strain, N=number of load applications, N_{PS} =number of load applications corresponding to the starting point of the secondary stage, N_{ST} =number of load applications corresponding to the starting point of the tertiary stage, ε_{PS} =plastic strain at the starting point of the secondary stage, ε_{ST} = plastic strain at the starting point of the tertiary stage, and a, b, c, d, f=regression coefficients.

According to Zhou et al. (2004), a power-law model is first fitted to each permanent deformation curve with the model coefficients determined using the statistical regression analysis. Afterwards, the accumulated permanent strain for each permanent deformation curve at the last loading cycle was calculated using the developed power-law model. The deviation error of the calculated accumulated permanent strains from the measured ones at the last loading cycle was determined for each permanent deformation curve using the following Equation:

$$D_e = \frac{|\varepsilon_{p(\text{Calculated})} - \varepsilon_{p(\text{Measured})}|}{\varepsilon_{p(\text{Measured})}} \quad (7.9)$$

where D_e =deviation error of calculated accumulated permanent strains from measured ones at a specific loading cycle; $\varepsilon_{p(\text{Calculated})}$ =calculated accumulated permanent strain at a specific loading cycle; and $\varepsilon_{p(\text{Measured})}$ = measured accumulated permanent strain at a specific loading cycle.

A threshold value of 3% was assigned to the deviation error by Zhou et al. (2004). If the deviation error of the power-law model from the measured accumulated permanent strain at the last loading cycle is less than 3%, the permanent deformation curve can be deemed to be still within the primary region at the last loading cycle. On the other hand, if the deviation error at the last loading cycle is larger than 3%, then the permanent deformation curve can be assumed to be within the secondary region at the last loading cycle. In the latter case, it is necessary to remove the last loading cycle and to repeat the aforementioned procedure until reaching a loading cycle with a deviation error of less than 3%. The resulted loading cycle is defined as the one at which the boundary point between the primary and secondary regions is located.

In this section, a stepwise method following the approach by Zhou et al. (2004) is employed to identify the location of the boundary point connecting the primary to the secondary region of the permanent deformation curves. The primary and the secondary regions of the permanent deformation curves, once separated using such a stepwise method, are fitted to the best possible model and analyzed subsequently for the effects of various dynamic stress states and aggregate physical properties on the permanent deformation behavior.

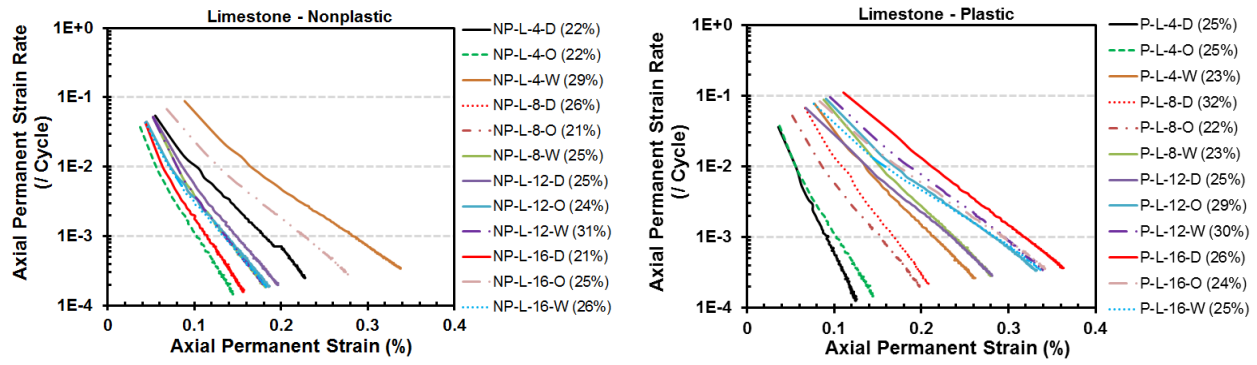
7.3.2 Effects of Aggregate Physical Properties

The unbound aggregate RLT test database collected from the ICT R27-1 Research Project is useful for assessing effects of individual material physical properties on permanent deformation behavior (Tutumluer et al., 2010; Mishra, 2012). It is worth noting that limited information regarding permanent deformation behavior is reflected in those data. This is because permanent deformation results were recorded from the pre-conditioning stage of the resilient modulus tests, and only one CCP type stress state of 103.42-kPa (15-psi) constant radial confining pressure (σ_3) and 206.84-kPa (30-psi) axial deviator stress (σ_d) was applied for up to 1,000 loading cycles (unless failure earlier) for each factorial combination of material physical properties. By applying the shakedown theory, Figure 7.17 illustrates the relationships between accumulated permanent axial strains and permanent axial strain rates (strain per load application) for each aggregate type (i.e., dolomite, limestone, and uncrushed gravel) at dry (D), optimum (O), and wet (W) moisture conditions, respectively. Note that the dolomite material (Do) with 12% plastic fines (P) at wet moisture condition (W), denoted by P-Do-12-W, was subject to only 91 load applications before the specimen collapsed, while 916 for NP-L-0-D, 501 for NP-G-12-O, 506 for NP-G-12-W, 326 for P-G-8-W, and 251 for P-G-12-W. With the shear strength parameters (c and ϕ) obtained from rapid shear strength tests, the shear stress ratio q_{ratio} ($q_{\text{failure}}/q_{\text{max}}$) was also calculated and included as a covariate (shown in the legends of Figure 7.17). It is worth mentioning that all the shear stress ratio values in this study were averaged from the actual stress magnitudes applied during RLT testing instead of the targeted stress values. The calculated shear stress ratio values are approximately within the range of 15% to 45%.

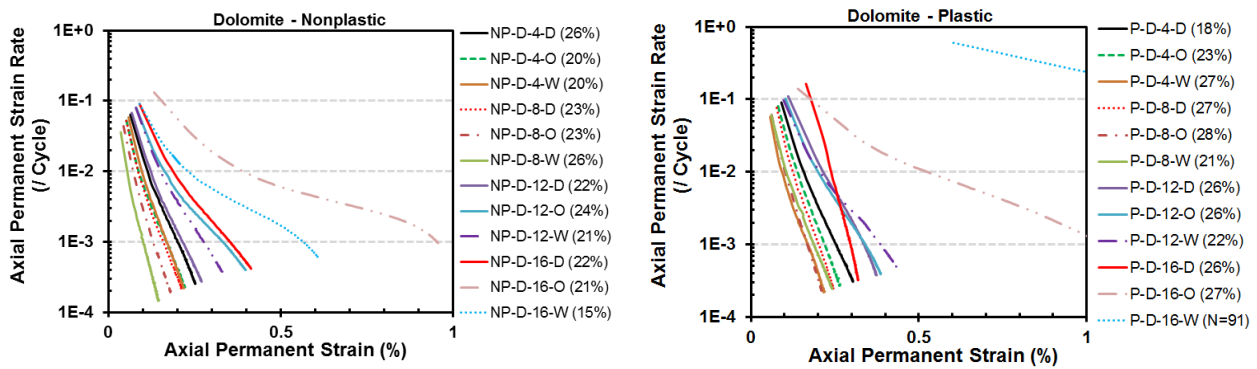
Figure 7.17 shows that larger cumulative permanent axial strain (ϵ_p) and greater permanent axial strain rate ($\dot{\epsilon}_p$) tend to be reached for materials of lower quality, as indicated by

curves shifting towards the upper right corner. For instance, the combination of the highest amount of fines (16%, either plastic or non-plastic) and wet moisture condition is consistently depicted among the worst scenarios for all three aggregate types. Overall, the shear stress ratio discerns fairly well different permanent deformation characteristics reflecting material quality aspects. The majority of these permanent deformation curves in Figure 7.17 exhibits steadily decreasing rate of cumulative permanent strain and thus can be categorized as plastic creep (Range B) behavior.

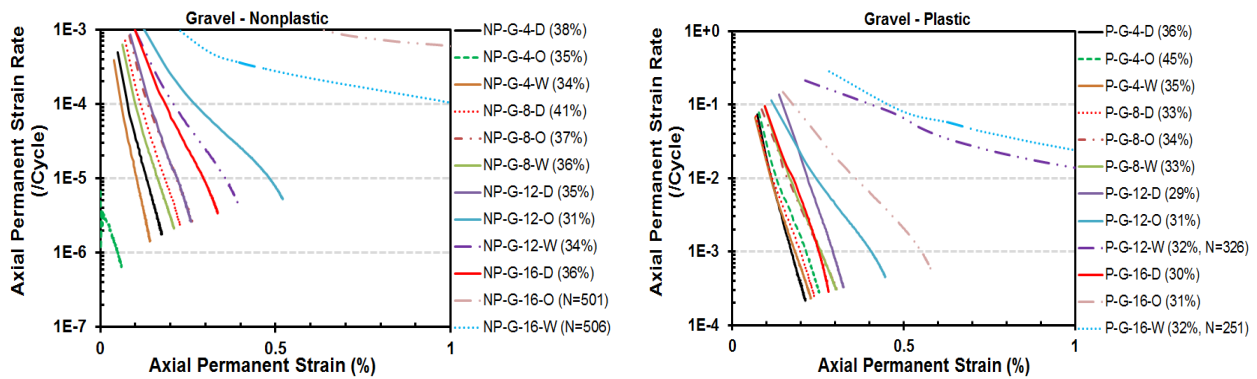
To obtain the stable permanent strain rate (i.e., linear slope of the secondary stage), permanent deformation test data (ϵ_p vs. N) were then fitted against models reviewed in Chapter 2. It turns out that the Theyse model (2001) and the Perez and Gallego model (2010) consistently outperform others in best fitting all test data at each factorial combination of material physical properties. Figure 7.18 shows relationships between such permanent strain rates (expressed as percentage of permanent strain accumulated per load application) and fines content for each aggregate type at each moisture condition. Note that the specimens collapsed prior to the completion of prescribed 1,000 load applications are excluded from the analysis for consistency purposes.



(a)

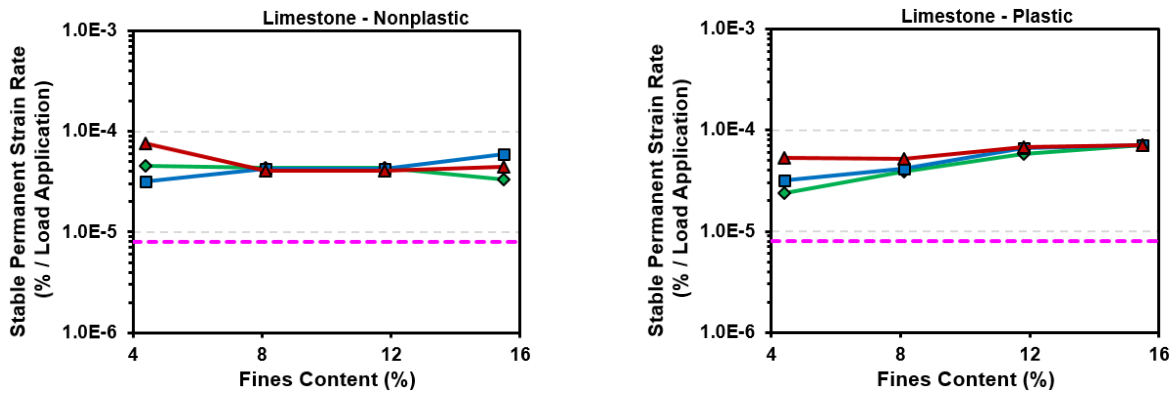


(b)

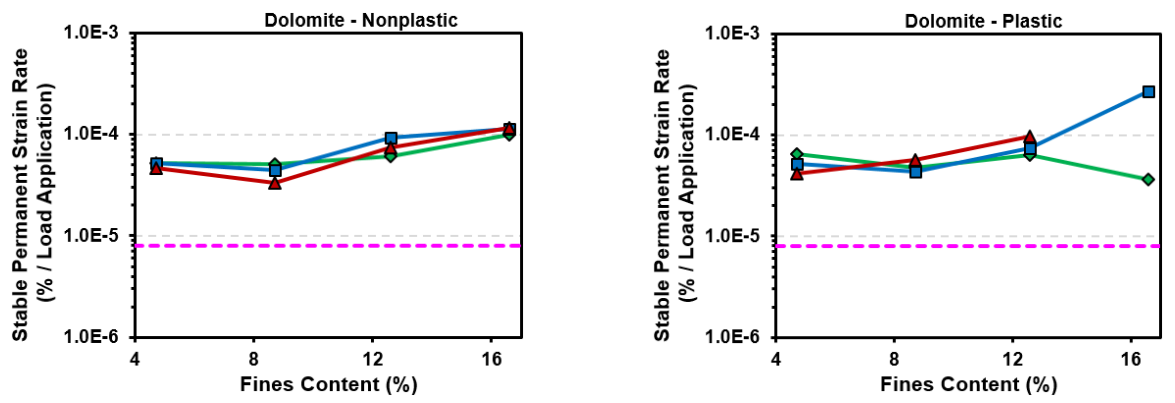


(c)

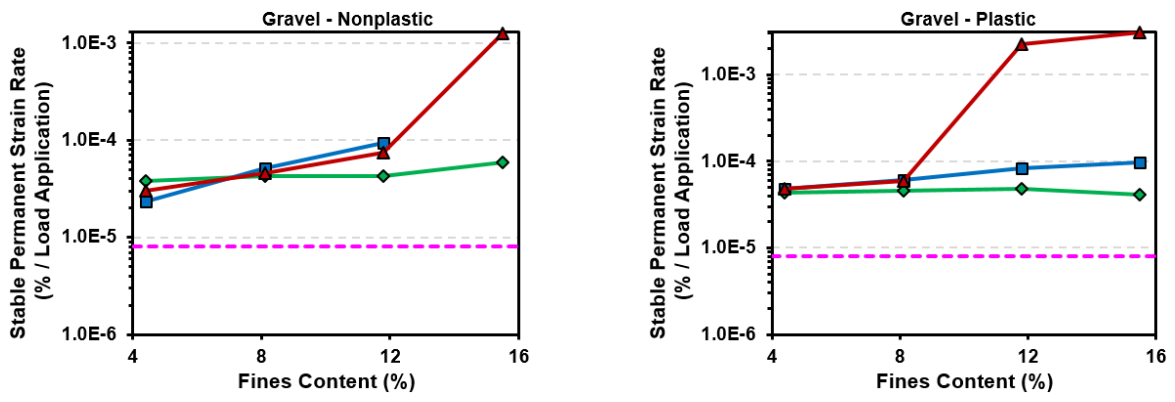
Figure 7.17 Cumulative Permanent Axial Strain ($\epsilon_p, N=1,000$) Varying with Permanent Axial Strain Rate for (a) Crushed Limestone, (b) Crushed Dolomite and (c) Uncrushed Gravel



(a)



(b)



(c)



Figure 7.18 Permanent Axial Strain Rate Varying with Fines Content for (a) Crushed Limestone, (b) Crushed Dolomite and (c) Uncrushed Gravel

For uncrushed gravel materials containing high amounts of plastic fines (exceeding 8.1%), a large increase in the permanent strain rate was observed in Figure 7.18(c) as moisture content increases beyond the optimum. On the contrary, nonplastic fines generally exhibit much less moisture susceptibility, especially for higher quality crushed aggregates (Dolomite and Limestone). Another noticeable observation is that eight percent seems to be the optimum fines content that overall leads to the least change in the permanent strain rate across all the test conditions. This remarkably matches previous findings reported by Tutumluer and Seyhan (2000). Using the directional dependency, anisotropy, of aggregate stiffness as the criterion, they determined an optimum fines content of 7%. The strain rate criteria proposed by Werkmeister (2003) to discern different shakedown ranges are also plotted as dotted lines in Figure 7.18, i.e., 10^{-8} and 8×10^{-8} per cycle for Range A-B boundary and Range B-C boundary, respectively. Note that the permanent deformations recorded for up to only 1,000 cycles may not reach the secondary stage yet, which explains that greater strain rate values than the threshold value defining Range B-C boundary were obtained, as shown in Figure 7.18.

7.3.3 Effects of Constant Confining Pressure (CCP) Stress States

Figure 7.19 illustrates the stress path loading scheme for both P209 and P154 aggregate materials, as well as the shakedown ranges (i.e., Range A, B, or C) identified for each CCP ($m=3$) stress state according to the criteria proposed by Werkmeister (2003). It can be seen that only Range A and Range B behavior were exhibited by both materials under such prescribed CCP stress states. Figure 7.20 shows permanent deformation characterization results of P209 and P154 aggregate materials under the applied CCP stress states. The legends in Figure 7.20 represent the CCP stress states applied, i.e., constant radial confining stress σ_3 (psi), pulsed axial deviator stress σ_d (psi), and the calculated shear stress ratio q_{ratio} . The total number of load

applications is 10,000 for P209 aggregate material and 40,000 for P154 aggregate material, respectively. Note that the P154 specimens subjected to the stress state of 3-psi constant confining pressure and 21-psi axial deviator stress (denoted as “3/21”) were excluded from the following analysis, as only 10,000 load applications were recorded from it.

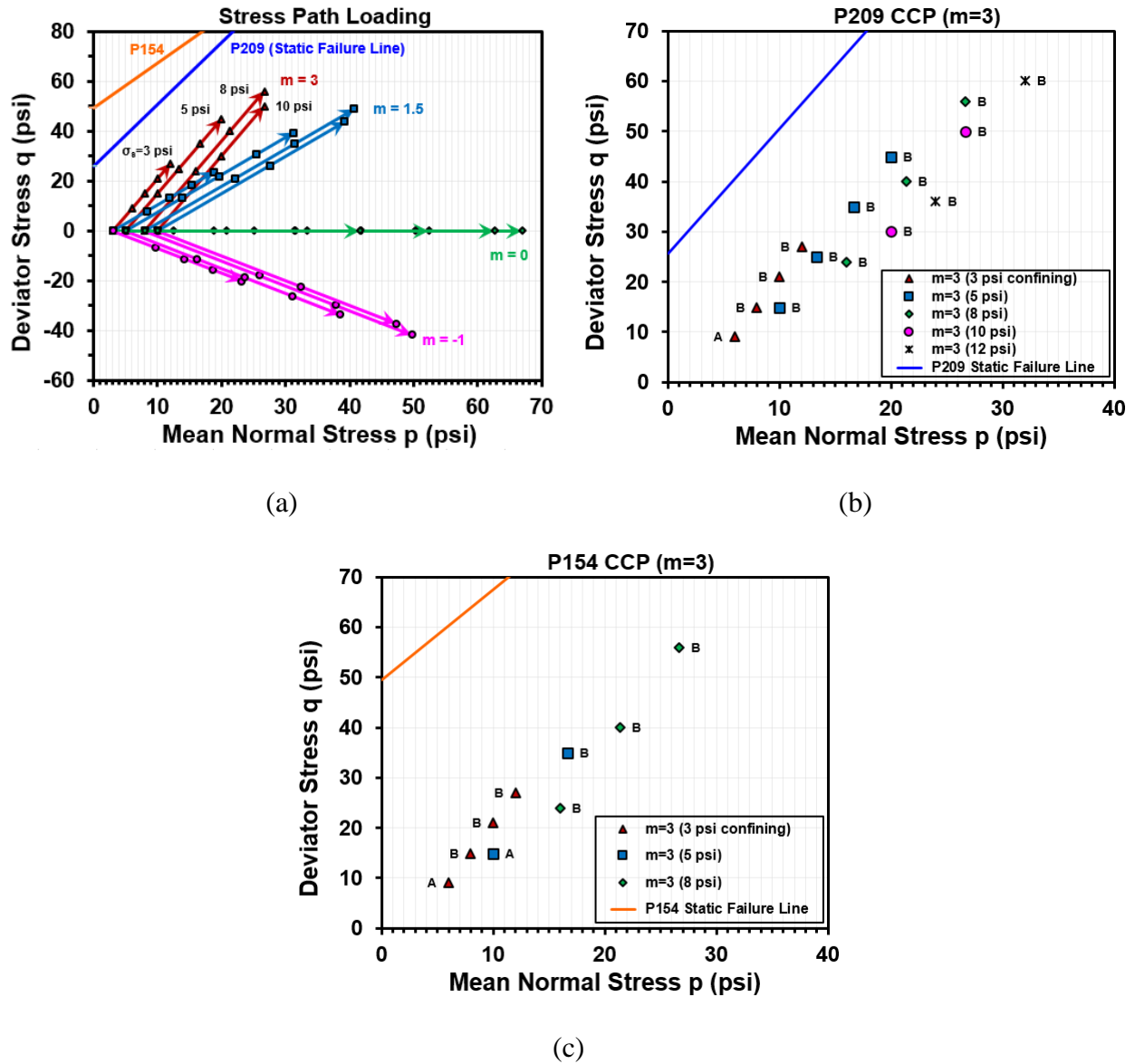
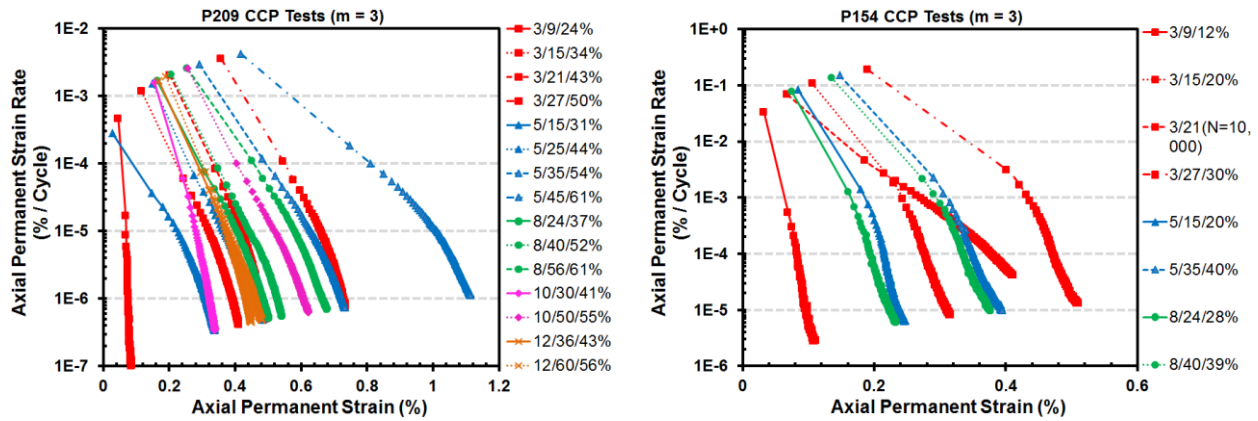


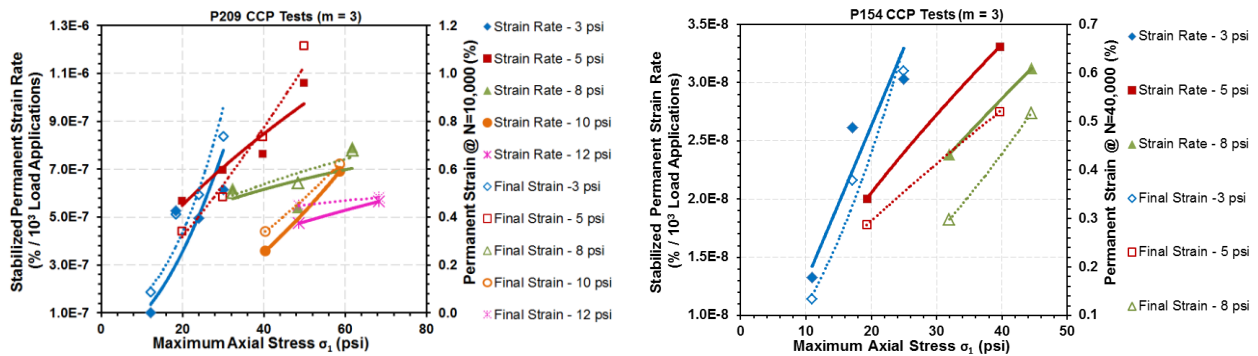
Figure 7.19 Laboratory Repeated Load Triaxial Permanent Deformation Tests for FAA NAPTF Aggregate Materials: (a) Stress Path Loading Scheme and Identified Shakedown Ranges for (b) P209 and (c) P154 Materials

As shown in Figure 7.20(a), for both materials, the permanent strain accumulation reaches a steady-state level at the end of the application of all stress states, as indicated by the decreasing or near constant cumulative permanent strain rate. This means that both materials exhibit plastic creep type permanent deformation behavior under such CCP stress states, which agrees with previous findings reported by Kim (2005). In particular, the P209 aggregate material is expected to undergo plastic shakedown under the stress state of 3-psi constant confining pressure and 9-psi axial deviator stress (“3/9/24%”), due to the radically decreasing cumulative permanent strain rate. The stress states resulting in higher shear stress ratio are seen to overall result in faster permanent strain rate during loading and greater final permanent strain. This may imply the capability of the shear stress ratio (SSR) as a variable to capture essential permanent deformation behavior. Detailed analyses of the role played by the shear stress ratio in controlling permanent deformation are discussed next in subsequent sections.

The aforementioned stable permanent strain rate values were obtained by fitting triaxial test data from each CCP stress state against the Theyse model (2001) for both materials, respectively. Such stable permanent strain rates are then plotted in Figure 7.20(b) against the maximum axial stress ($\sigma_1 = \sigma_3 + \sigma_d$) at each confinement level. It is interesting to note from Figure 7.20(b) that despite the limited number of CCP stress states investigated, a clear trend can still be observed. That is, the stable permanent strain rate for both materials consistently increases with increasing axial stress but decreases with increasing confinement level. The final accumulated permanent strain results also confirm such a consistent trend.



(a)



(b)

Figure 7.20 Permanent Deformation Characterization of P209 and P154 Aggregate Materials during CCP Tests: (a) Axial Permanent Strain Rate Vs. Axial Permanent Strain and (b) Stabilized Permanent Strain Rate Vs. Maximum Axial Stress

Figure 7.20(b) also highlights the differences among the permanent deformation trends of both aggregate materials investigated. The slopes of the stable permanent strain rate curves for the P209 change abruptly, while those for the P154 are aligned more parallel and closer to each other. This implies that for aggregate materials containing much less plastic fines such as the P209, the stable permanent strain rate increases much faster with decreasing confinement level (σ_3); on the contrary, relatively more cohesive materials such as the P154 rely less on the confinement due to more contribution of the shear cohesive strength component and thus are less

susceptible to the axial stress increase. Intuitively, with a lower increase rate, higher axial stress increase would be required in order to cause the same amount of increase in the stable permanent strain rate; hence, better capability of withstanding axial stress (i.e., hardening response) can be expected. In practice, this means that a suitable confinement is needed for frictional (non-cohesive) materials to avoid excessive permanent strain accumulation and offset the detrimental effect exerted by axial stress. This inference is indirectly supported by the GT-PAVE finite element analysis on the effect of compaction-induced residual stresses locked in granular bases (Tutumluer and Thompson, 1997). Conversely, cohesive materials may withstand higher permanent strains even in the absence of confinement by relying on the contribution of the shear cohesive strength component (e.g., pore water suction between interfaces of solid particles), which again confirms the importance of incorporating (unsaturated) shear strength behavior into permanent deformation prediction of unbound aggregate materials. Therefore, such stable permanent strain rate analysis is capable of discerning the changes in rutting behavior of materials dissimilar in nature.

7.3.4 Effects of Varying Confining Pressure (VCP) Stress States

As contrary to the aforementioned CCP type tests, deviator stresses in both vertical and horizontal directions are pulsed simultaneously during the varying confining pressure (VCP) type tests to simulate the moving wheel load effects. The stress path loading slopes (m) of VCP type tests represent the rotating principal stress directions caused by the moving wheel loads. This section examines the effects of VCP stress states on permanent deformation behavior of unbound aggregate materials from a different perspective, i.e., the stable permanent strain rate derived based on the shakedown theory.

Figure 7.21 shows the shakedown ranges (i.e., Range A, B, or C) identified for each VCP stress state according to the criteria proposed by Werkmeister (2003). It can be seen that only Range A and Range B behavior were exhibited by both materials under such prescribed CCP stress states.

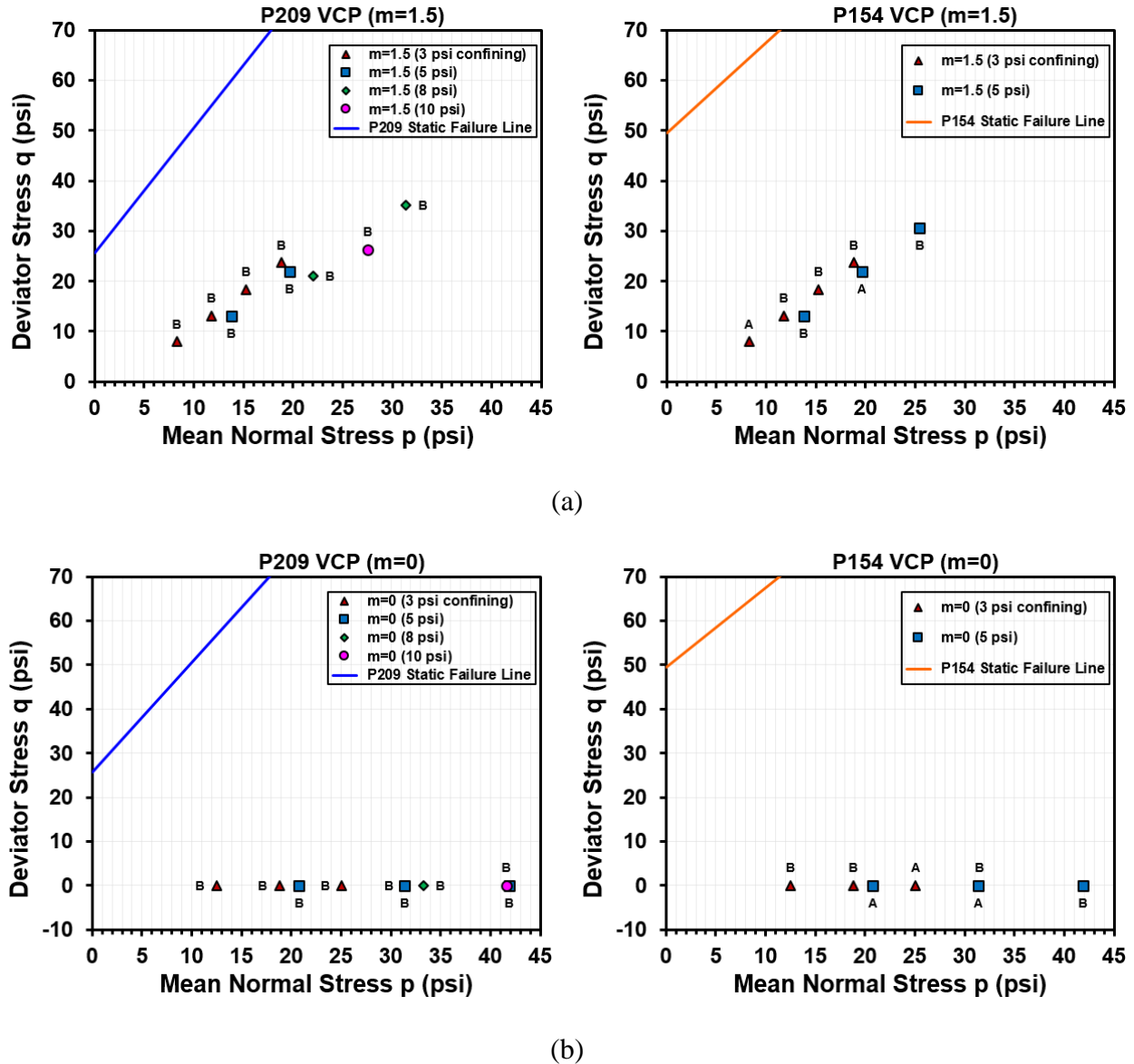


Figure 7.21 Shakedown Ranges Identified for P209 and P154 Materials under VCP Stress States: (a) Loading Slope $m=1.5$ and (b) $m=0$

Figure 7.22(a) plots the cumulative permanent axial strain against the permanent axial strain rate under different VCP stress states for both P209 and P154 materials, respectively. Note that the legends in Figure 7.22 sequentially represent the VCP stress states applied, i.e., constant hydrostatic confining stress σ_s (psi), vertical deviator stress σ_{1d} (psi), horizontal deviator stress σ_{3d} (psi), and the calculated maximum shear stress ratio q_{ratio} . Again, the total number of load applications is 10,000 for P209 material and 40,000 for P154 material, respectively. To be consistent, aggregate specimens that did not complete the entire prescribed load applications are excluded from the following analysis.

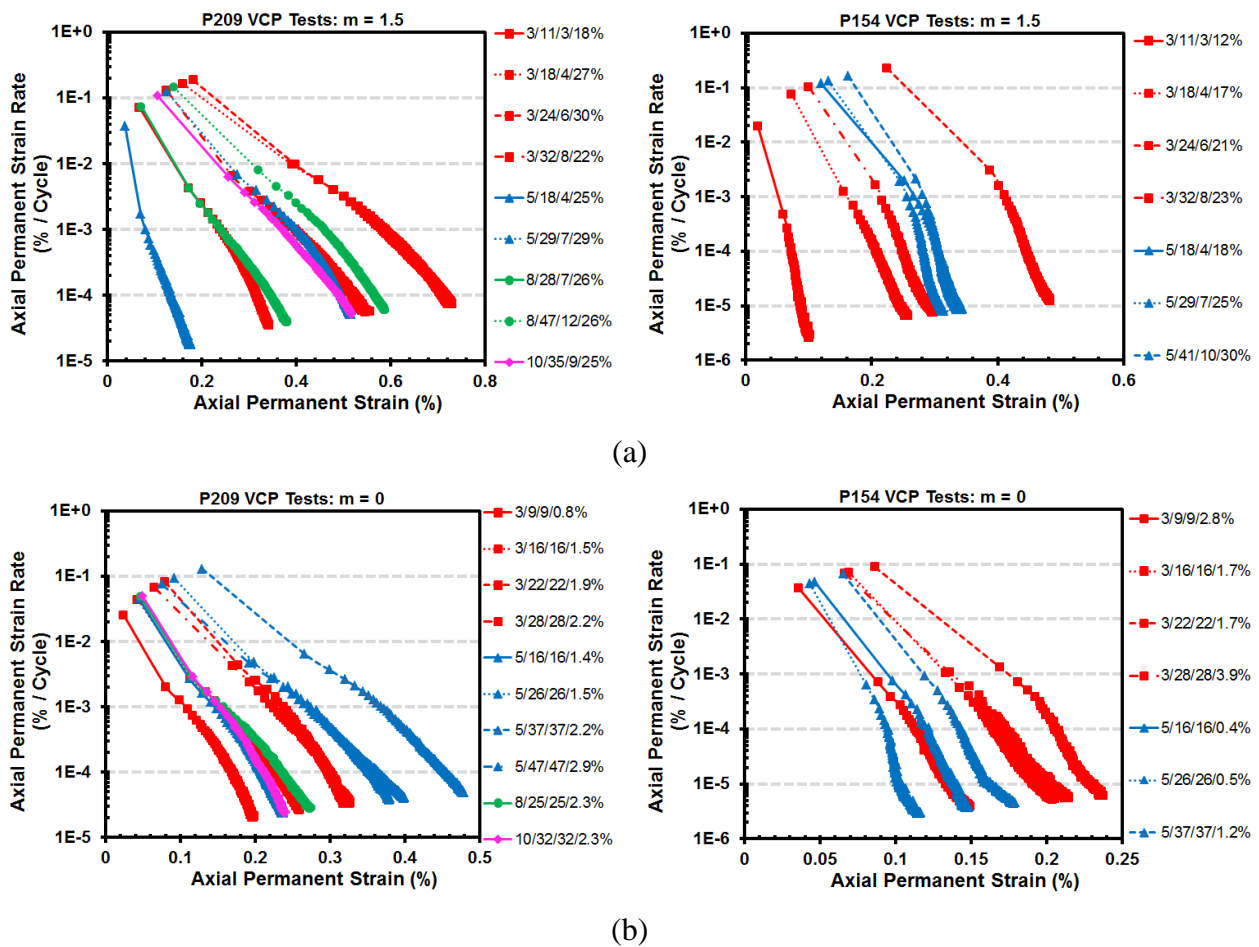


Figure 7.22 Permanent Axial Strain Rate versus Axial Stress at Different VCP Stress States for P209 and P154 Materials: (a) $m=1.5$ and (b) $m=0$

First of all, it can be clearly seen that VCP stress states generally increase the permanent strain rate due to the dynamic nature of the applied stress states, as compared to results shown in Figure 7.22. Increasing magnitudes of the axial deviator stress are consistently associated with greater permanent axial strain and larger permanent strain rate. As the stress path loading slope changes from $m=1.5$ to $m=0$, the permanent strain accumulates with a lower rate to a smaller value upon the end of load applications. The effect of increasing stress path length can also be visualized, as it is proportional to the magnitudes of both vertical and horizontal deviator stresses. A longer stress path length at constant stress path slope leads to an increase in permanent strain accumulation. However, the effect of stress path length becomes apparent only when one compares the permanent deformations accumulated under the same applied stress path slopes. Low stress path loading slopes may also increase volumetric strains and thus create ruts or heave (Kim, 2005).

Early research on permanent deformation has shown that permanent axial strains increase with increasing deviator stress q and decrease with increasing mean stress p . This has led to analytical relationships relating permanent axial strains (or shear strains) to p and q (Pappin, 1979). The repeated loading and unloading occur in the p - q space between the residual stress p_{\min} , q_{\min} , $p_{\min}+\Delta p$, $q_{\min}+\Delta q$ (see Figure 2.8). The stress state of p_{\min} and q_{\min} is resulted from the relatively small overburden and the compaction-generated “locked-in” (or residual) stresses. Two stress path loading related parameters, i.e., stress path length L and mean stress p , were screened by preliminary statistical analysis to affect the progressive increase of the permanent axial strain with the number of load applications. Figure 7.23 plots the stable permanent strain rates versus stress path loading parameters. Note that stress states causing Range A behavior (plastic shakedown) were excluded in Figure 7.23. Clearly shown is a statistically significant

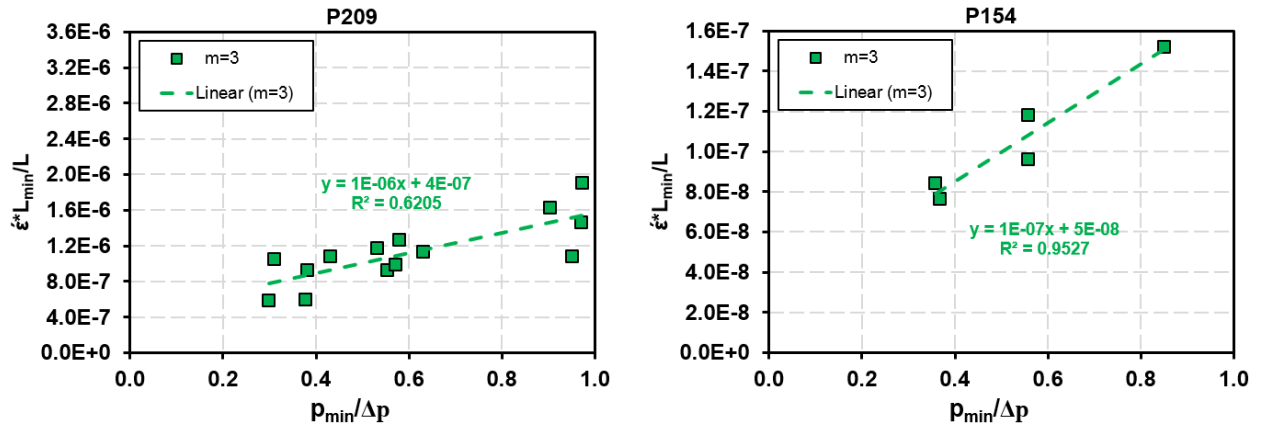
linear relationship ($R^2 > 0.62$) that relates the stable permanent strain rate with the stress path length (L), the applied stresses (Δp and Δq), and the initial stress state (L_{\min} and p_{\min}) of both P209 and P154 materials for each stress path loading slope ($m = \Delta q / \Delta p$). Note that the stress path loading with a slope of $m=3$ (i.e., CCP tests) can be regarded as a special type of VCP tests.

Equation 7.10 mathematically expresses the linear relationship identified in Figure 7.23. Interestingly, the intercept d in Equation 7.10 turns out to be constant among three different stress path loading slope (m) values for both P209 ($d = 4 \times 10^{-7}$) and P154 ($d = 5 \times 10^{-8}$) materials. Figure 7.24 shows that the slope c , on the other hand, can be statistically related to the stress path loading slope m in parabolic functions for both P209 and P154 materials, respectively. The different shape of those two parabolic functions could be possibly attributed to the differences among the permanent deformation trends of both aggregate materials investigated, as described previously for CCP stress states (see Figure 7.20).

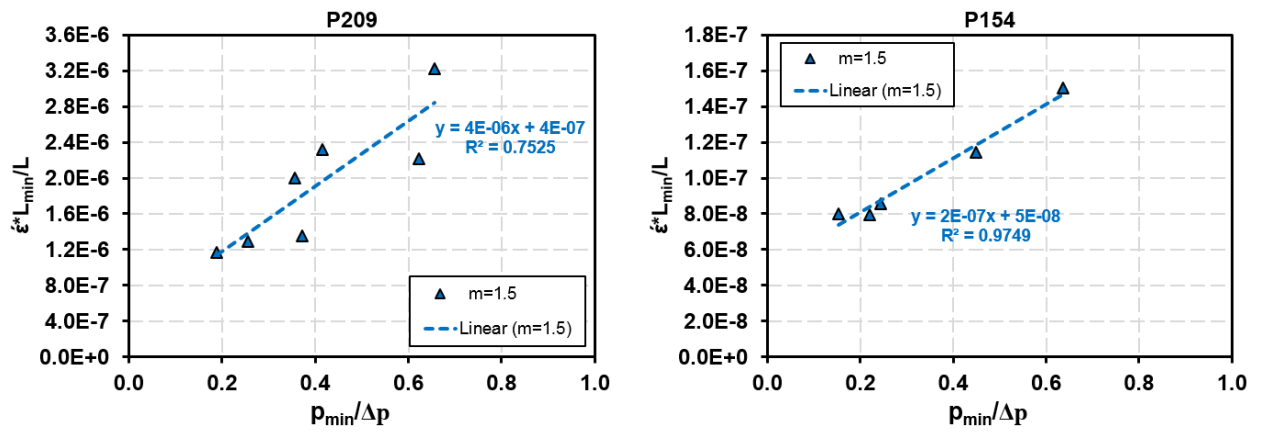
$$\dot{\epsilon}_p = \frac{L}{L_{\min}} \left(d + c \times \frac{p_{\min}}{\Delta p} \right) = \frac{\sqrt{\Delta p^2 + \Delta q^2}}{\sqrt{p_{\min}^2 + q_{\min}^2}} \left(d + c \times \frac{p_{\min}}{\Delta p} \right) \quad (7.10)$$

$$\Delta p = \frac{\sigma_{1d} + 2\sigma_{3d}}{3}; \quad \Delta q = \sigma_{1d} - \sigma_{3d}$$

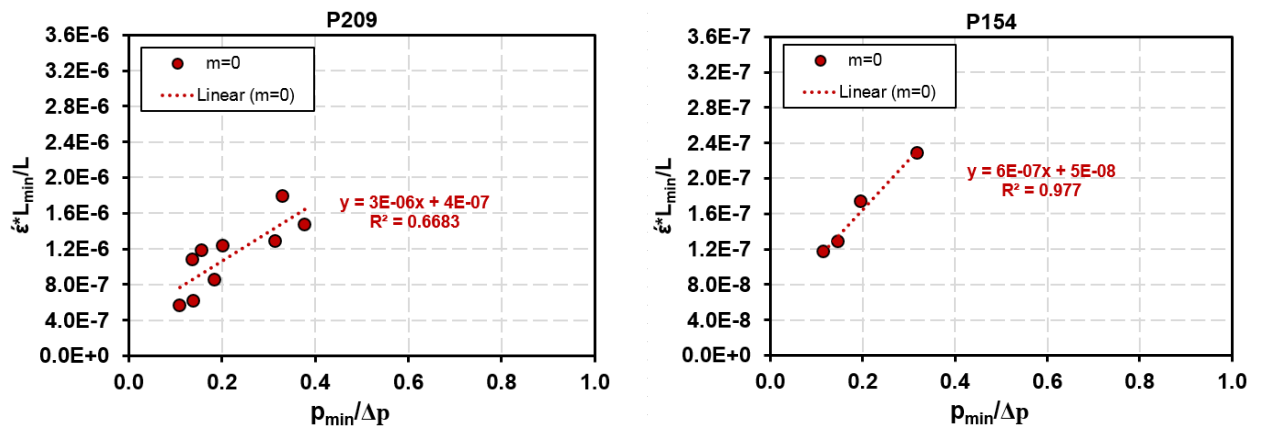
where $\dot{\epsilon}_p$ = stable permanent strain rate, Δp = mean stress increment ($p_{\max} - p_{\min}$), Δq = deviator stress increment ($q_{\max} - q_{\min}$), σ_{1d} = vertical deviator stress in triaxial stress space, σ_{3d} = horizontal deviator stress in triaxial stress space, and c and d are regression coefficients to be determined.



(a)



(b)



(c)

Figure 7.23 Relationship between Stable Permanent Axial Strain Rate ($\dot{\epsilon}$) and VCP Stress Path Loading Parameters for P209 and P154 Materials: (a) $m=3$, (b) $m=1.5$ and (c) $m=0$

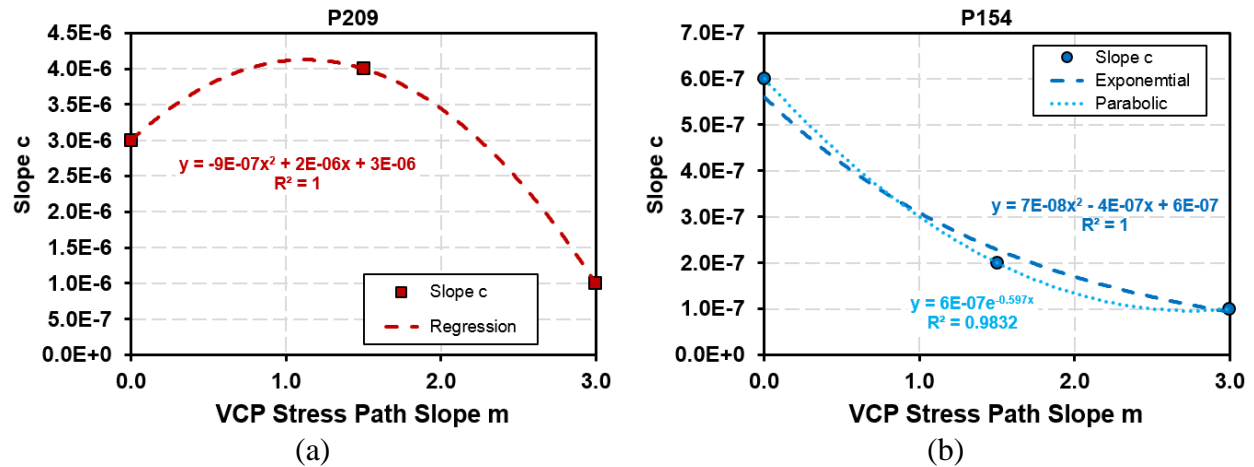


Figure 7.24 Regression Coefficient c in Equation 7.10 versus Loading Slope m for (a) P209 and (b) P154 Materials

7.4 Development of Phenominological Stable Permanent Strain Rate Model

7.4.1 Mohr-Coulomb Representation of Stable Permanent Strain Rate Envelope

After observing from Figure 7.20(b) the dependency of stable permanent strain rate on the maximum axial stress associated with certain confinement level, efforts were made accordingly to develop an analytical model for mathematically expressing such a dependency. As a result, a power law was found after several trials to well fit the experimental data. Equations 7.11 and 7.12 formulate the identified model forms. Both models are acceptable in terms of the reasonably high R^2 values and low standard error of estimates (SEE), both of which are frequently used measures of the differences between values predicted by a model and those actually observed. Note that the coefficient of σ_3 shown in the power term of σ_1 has different signs for both models (i.e., “-” sign for P209 and “+” sign for P154). This could be possibly due to the use of different sample sizes for regression-based model development, as well as due to varying dependence of shear strength development on confining pressure σ_3 . Figure 7.25 also

illustrates the predictive accuracy of each model by plotting measured stable permanent strain rate against its predicted values, respectively.

$$P209: \dot{\epsilon}_p = 1.9 \times 10^{-7} \sigma_3^{0.535} \sigma_1^{1.009 - 0.046\sigma_3} \quad (R^2 = 0.78, SEE = 9.78 \times 10^{-7}) \quad (7.11)$$

$$P154: \dot{\epsilon}_p = 2.65 \times 10^{-7} \sigma_3^{-0.855} \sigma_1^{0.808 + 0.012\sigma_3} \quad (R^2 = 0.92, SEE = 7.24 \times 10^{-8}) \quad (7.12)$$

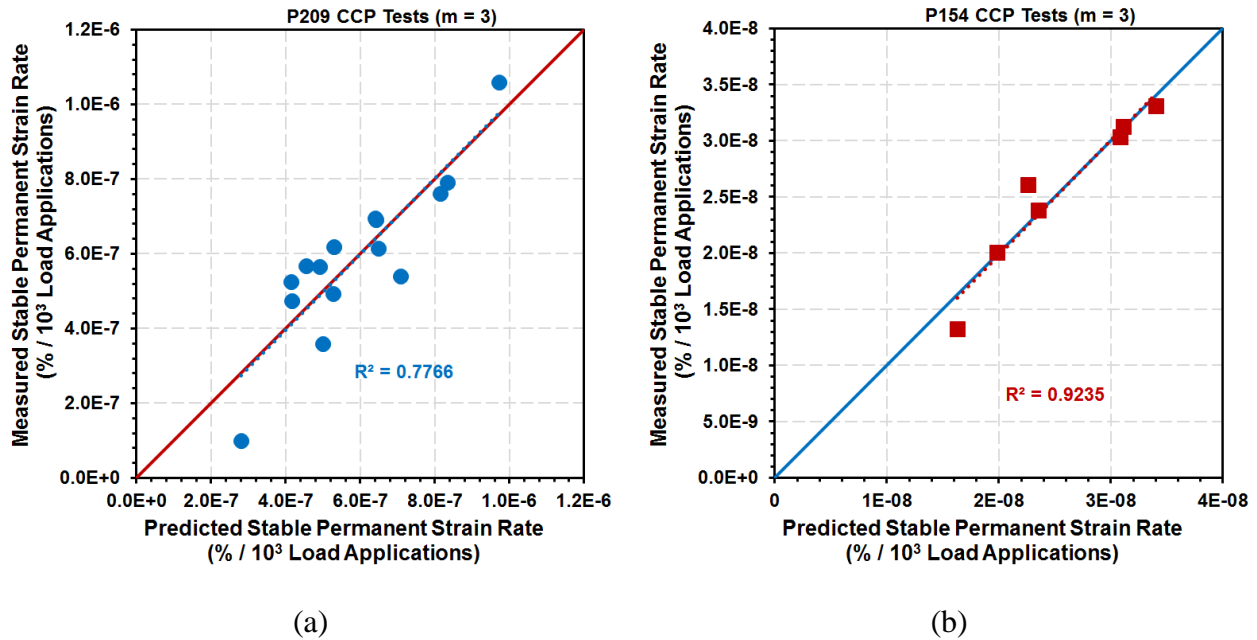


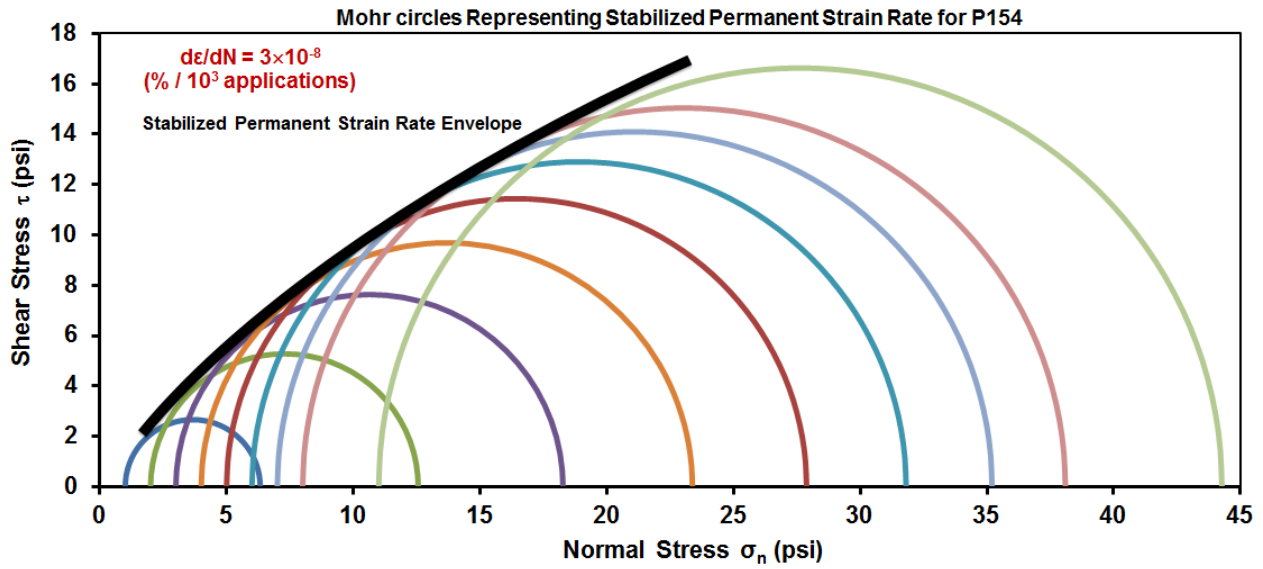
Figure 7.25 Predicted Vs. Observed Stable Permanent Strain Rate for (a) P209 and (b) P154

Note that the two simple but effective model forms above include the major and minor principal stresses (σ_1 and σ_3) as explanatory variables. To make them directly applicable to other multi-axial stress states, the proposed stable permanent strain rate models are then depicted on a Mohr-Coulomb diagram. By rearranging Equations 7.11 and 7.12, the major principal stresses σ_1 can be formulated below in Equations 7.13 and 7.14 as function of the minor principal stresses σ_3 and the stable permanent strain rate ($\dot{\epsilon}_p$).

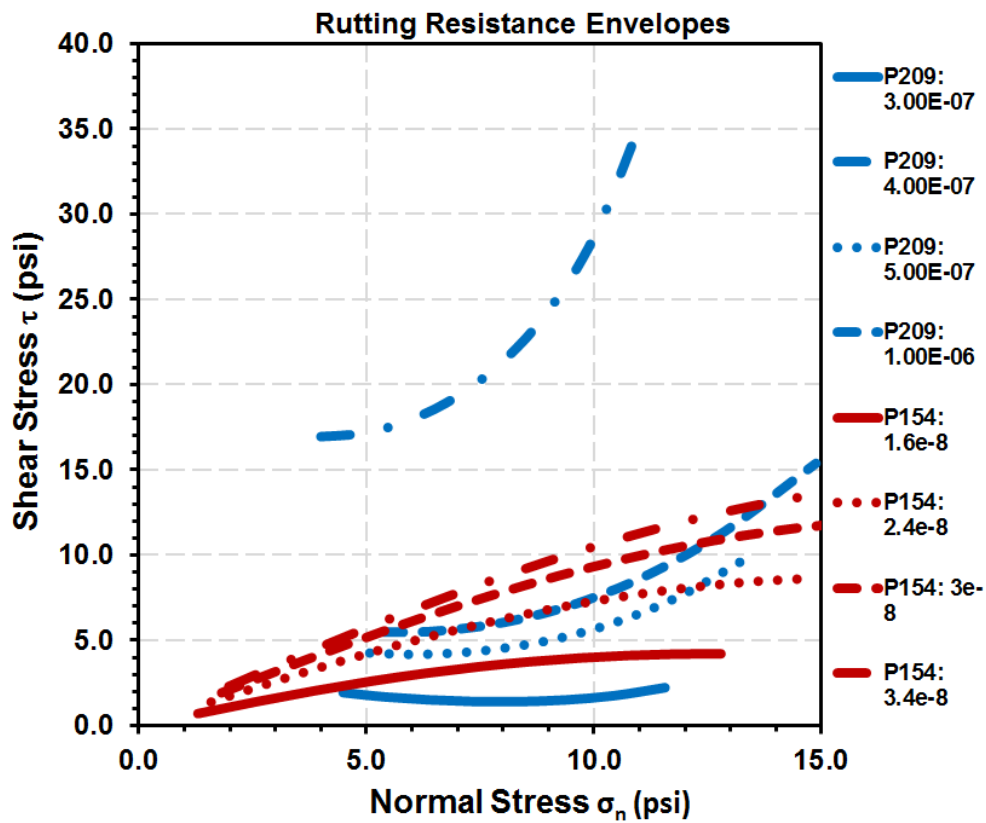
$$\text{P209 CCP: } \sigma_1 = \left(\frac{\dot{\epsilon}_p}{1.6 \times 10^{-8} \sigma_3^{0.560}} \right)^{\frac{1}{1.055 - 0.048 \sigma_3}} \quad (7.13)$$

$$\text{P154 CCP: } \sigma_1 = \left(\frac{\dot{\epsilon}_p}{6.61 \times 10^{-9} \sigma_3^{-0.855}} \right)^{\frac{1}{0.808 + 0.012 \sigma_3}} \quad (7.14)$$

Given a pre-specified permanent strain rate level, the major principal stress σ_1 (or axial stress in triaxial testing) in Equations 7.13 and 7.14 can be calculated for any paired minor principal stress σ_3 (or radial confining pressure in triaxial testing), both of which can be further used to construct the corresponding group of Mohr circles. Analogous to the concept of the Mohr-Coulomb failure envelope, the permanent deformation resistance envelopes can be defined by these Mohr circles representing all the possible stress states that cause the specified permanent strain rate condition. One prominent feature of such permanent deformation resistance envelopes is their potential usefulness in ranking and properly selecting different unbound pavement layer materials for use in specific traffic levels and site conditions, i.e., the rutting potential based on the shakedown theory is evaluated simultaneously in relation to the potential shear failure. Such a Mohr-Coulomb rutting resistance envelope representation also highlights the capacity of the proposed stable permanent strain rate model to distinguish the physical-mechanical properties of different unbound pavement materials effectively and reliably. Figure 7.26 shows as an example several envelopes representing different levels of the permanent deformation resistance for both P209 and P154 materials, respectively.



(a)



(b)

Figure 7.26 Mohr Circles (a) Representing Stable Permanent Strain Rate for P154 and (b) Rutting Resistance Envelopes for P209 and P154 Aggregate Materials

In many of the permanent deformation models reviewed in Chapter 2, the stress level and/or the shear stress to strength ratio are used to describe the permanent deformation behavior. Stresses above the shakedown threshold result in shearing; as a result, the permanent strain rate could either be stable or increase rapidly upon reaching failure, depending on how close to the strength the applied stress level is. A family of design curves can be developed using Equations 7.11 and 7.12, as represented in Figure 7.27. It should be noted that the combination of lower confinement level and higher shear stress ratio leads to much more rapid permanent strain accumulation. The vertical axis represents the permanent plastic strain rate obtained under a constant minor principal stress (σ_3) level with varying shear stress ratio. With the design traffic load and volume, the permanent plastic strain rate and thus the accumulated plastic strain in the unbound pavement layer can be predicted by the number of load cycles (N) and shear stress ratio corresponding to the design axle load. The adoption of this design chart in the pavement design process can avoid the development of excessive permanent deformation in the unbound pavement layers.

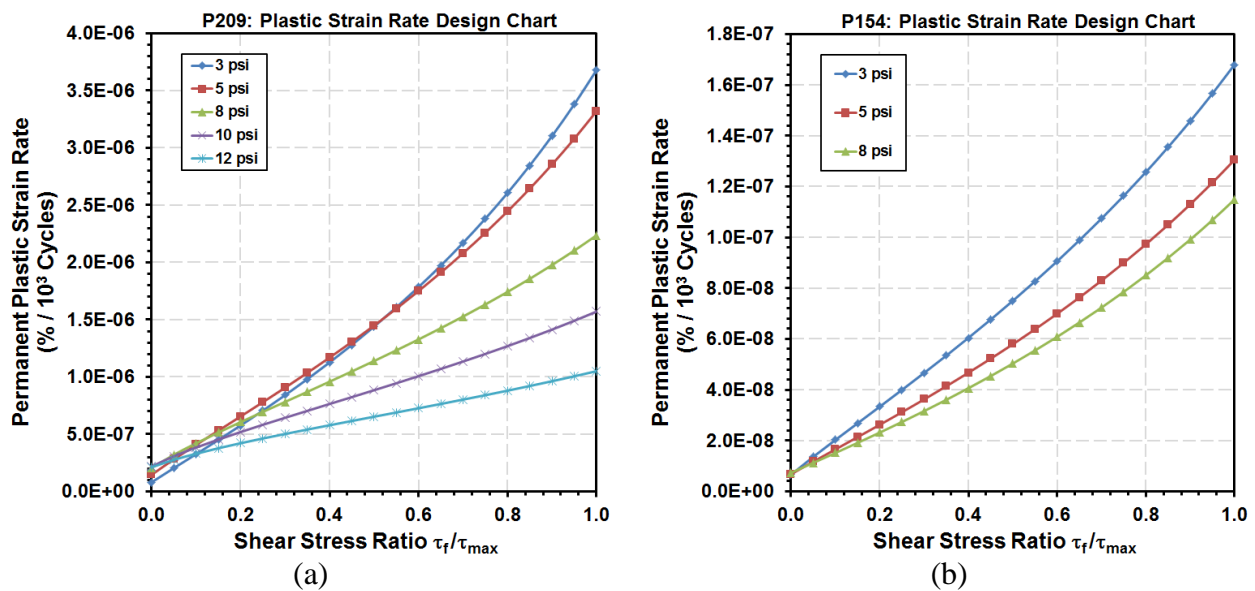


Figure 7.27 Stable Permanent Plastic Strain Rate Design Chart Using Shear Stress Ratio and Minor Principal Stress (σ_3) for (a) P209 and (b) P154 Aggregate Materials

7.4.2 p-q Diagram Representation of Stable Permanent Strain Rate Envelope

Previous research efforts have noted that the development of permanent deformation is directly related to the proximity of the applied stresses to the Mohr-Coulomb failure line expressed in q-p space (Barksdale, 1972). Huurmann (1997) showed that the closer the applied stress level is to the shear strength, the higher the permanent strain rate, which is logical due to the observations from laboratory permanent deformation test results.

According to Equation 7.10 and Figure 7.24, Equations 7.15 and 7.16 can be derived to formulate the stable permanent strain rate models obtained for P209 and P154 materials under VCP stress states, respectively. One prominent feature of those two models is that they can be readily implemented in finite element programs to predict axial permanent strain accumulation under any radial stress paths in the (p, q) plane (i.e., stress paths with constant slope m ranging from 0 to 3). It is worth noting that a CCP stress state (i.e., m=3) is a special type of VCP stress states; therefore, Equations 7.15 and 7.16 are more general than Equations 7.11 and 7.12.

$$P209 \text{ VCP: } \dot{\epsilon}_p = 10^{-7} \cdot \frac{\sqrt{\Delta p^2 + \Delta q^2}}{\sqrt{p_{\min}^2 + q_{\min}^2}} \cdot \left[3.74 + \frac{p_{\min}}{\Delta p} \cdot (-7m^2 + 14.2m + 33) \right] \quad (7.15)$$

$$(R^2 = 0.60, SEE = 1.31 \times 10^{-6}, n = 30)$$

$$P154 \text{ VCP: } \dot{\epsilon}_p = 10^{-8} \cdot \frac{\sqrt{\Delta p^2 + \Delta q^2}}{\sqrt{p_{\min}^2 + q_{\min}^2}} \cdot \left[2.43 + \frac{p_{\min}}{\Delta p} \cdot (38.35m^2 - 110.24m + 71.44) \right] \quad (7.16)$$

$$(R^2 = 0.93, SEE = 1.30 \times 10^{-7}, n = 15)$$

Figure 7.28 also illustrates the predictive accuracy of each model by plotting measured stable permanent strain rate against its predicted values, respectively. Both models yield reasonably good predictions of the stable permanent strain rate under different VCP stress states. As illustrated in Figure 7.29, the shear stress ratio for a stress path loading with a slope of m can be alternatively quantified in p-q diagram as the quotient between the actual stress applied and

the stress at failure. By employing Equations 7.15 and 7.16, it can be mathematically shown that the stable permanent strain rate under VCP states are in fact related to the shear stress ratio and the initial and current stress states (p_{min} , q_{min} , Δp , and Δq). Similar to the Mohr-Coulomb representation, the p - q diagram representation of the stable permanent strain rate can be established analogously.

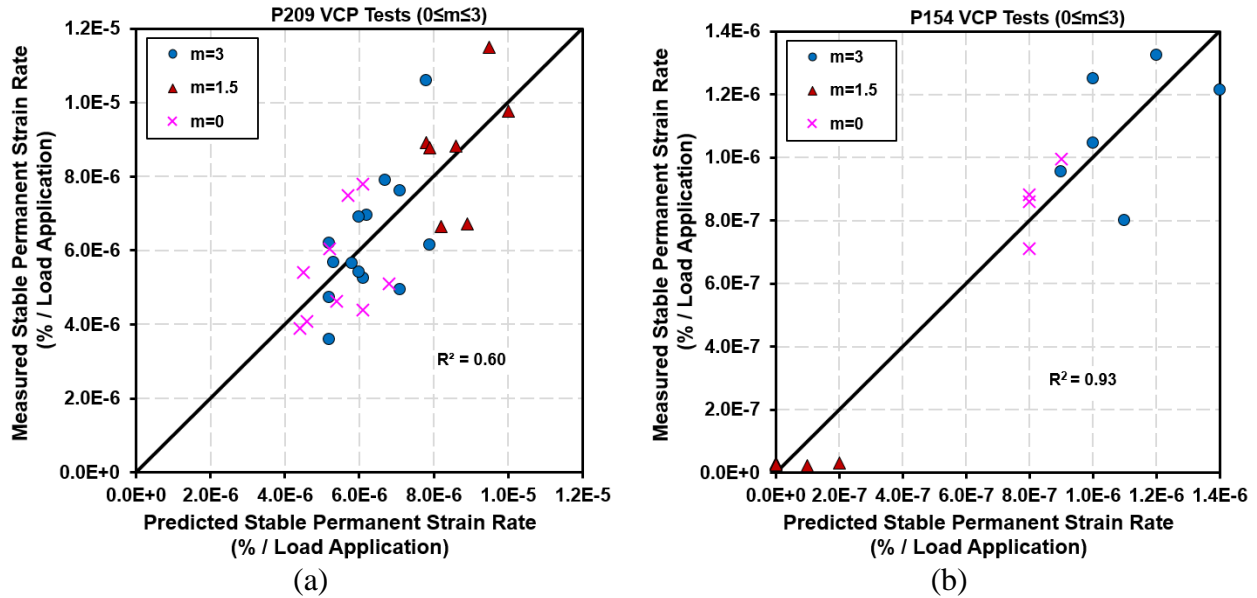


Figure 7.28 Predicted Vs. Observed Stable Permanent Strain Rate for (a) P209 and (b) P154 under VCP Stress States

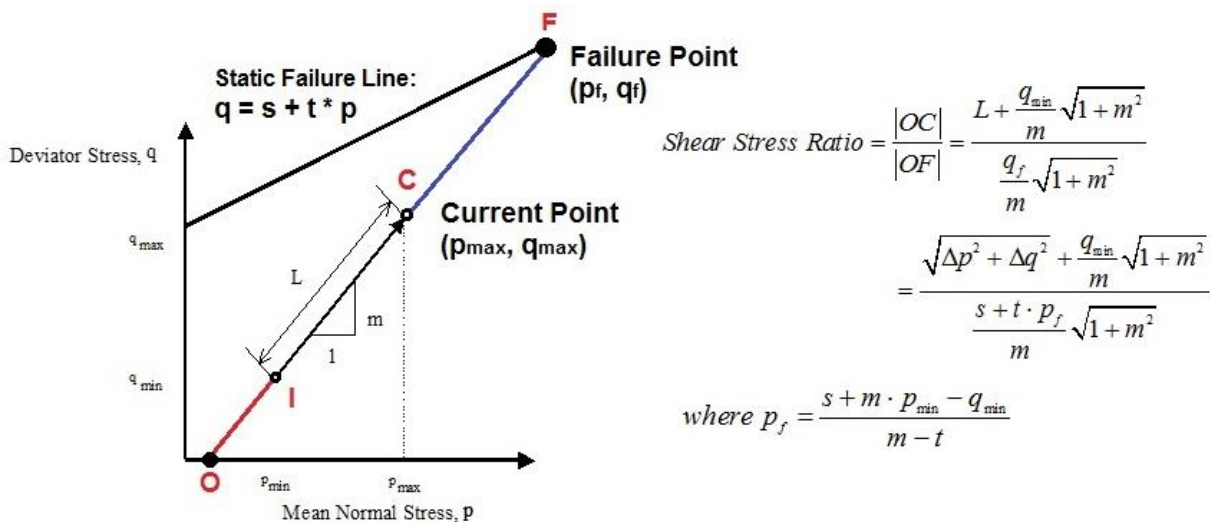


Figure 7.29 Schematic Representation of Shear Stress Ratio in p - q Diagram for Stress Path Loading Condition

7.5 Unified Rutting Prediction Model Development

The analysis results in previous sections clearly demonstrate that the permanent deformation accumulation of unbound aggregate layers is dictated by the shear stress ratio and the working stress states to which pavement layers are subjected. The progression of permanent deformation with the number of load applications, obtained either from laboratory RLT testing or from field rutting measurements, has been observed to include three distinct stages: Primary, Secondary, and Tertiary. The three-stage permanent deformation behavior can be regarded as the basic mechanical properties of unbound granular materials. A new three-stage model is proposed based on the shear strength properties to describe the primary, secondary, and tertiary stages. The stable permanent strain rate exhibited during the secondary stage is used as the rut indicator of unbound materials. Note that the majority of the permanent deformation results used in this study did not enter the tertiary stage but remain in the secondary region due to the limited number of load applications (up to 40,000). Therefore, identifying the transition point between the secondary and the tertiary stage and modeling the tertiary region are out of the scope of this thesis study. However, the framework developed in this study can be readily extended to incorporate the tertiary region, provided that the permanent deformation results up to the tertiary stage become available.

7.5.1 Model Development for Different Aggregate Physical Properties

The permanent deformation results from the ICT R27-1 research project were recorded from the conditioning stage of the resilient modulus tests with up to 1,000 load applications; therefore, the majority of the permanent deformation curves are for the primary stage only. The classical power-law model, proven to fit well the primary stage of the permanent deformation, is chosen as the basic model form to develop the unified rutting model for different aggregate

physical properties. It is expected that such unified rutting model could be applied with a high degree of confidence to a much wider range of materials by incorporating critical stress variables and essential material properties that govern rutting behavior.

It has been long realized that the variation in moisture is one of the environmentally driven variables that can affect permanent deformation behavior. At low moisture contents, the soil matric suction, as a fundamental stress state variable for unsaturated materials, contributed to the permanent strain responses of soils. To evaluate the impact of moisture variation, the moisture content is normalized corresponding to an optimum degree of saturation (S) and 100% compaction. For unbound materials, the influence of soil type (e.g., nonplastic and plastic) becomes more important as the moisture content goes beyond the vicinity of that under optimum conditions. An attempt to introduce the plasticity index (PI) as a predictive variable into the rutting model was made. It was decided to use the product of the decimal fraction of the material passing a No. 200 sieve (w) and PI (in percent) (wPI), because previous studies have shown that the variable wPI can account for the effects of both plasticity index and fines content (Zappata et al., 2013). It should be noted that this variable is also used in the MEPDG to estimate the soil water characteristic curve of the soil, which represents its moisture retention capability.

The NCHRP 1-26 (1990) study concluded that permanent strain accumulation prediction models should include a stress ratio factor. It was found in previous sections that the following enhancement to the original Tseng and Lytton's empirical relationships proved to be effective: (i) replacing moisture content by percent saturation; (ii) the inclusion of weighted plasticity index (wPI) and shear stress ratio terms as new predictive variables; and (iii) the inclusion of the statistically significant interaction term between wPI and shear stress ratio. As observed from Figure 7.27, the confinement level, in addition to the shear stress ratio, is also critical for

permanent strain accumulation of unbound granular materials. In this study, the bulk stress term that is responsible for the volume change behavior, is included to represent the confinement level.

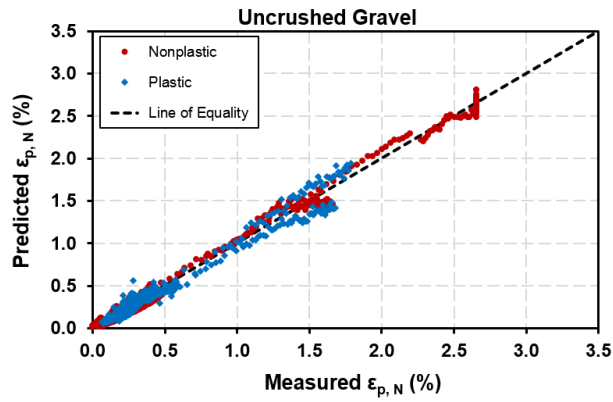
For the aggregate materials studied in ICT research studies, the proposed eight-parameter Power-law model to predict permanent axial strain is formulated as follows:

$$\varepsilon_p = a \left(\frac{\theta}{p_0} \right)^b \left(\frac{\tau_f}{\tau_{\max}} \right)^c N^d \cdot \text{EXP} \left[e \cdot (S - S_{opt}) + f \cdot wPI + g \cdot wPI \cdot \frac{\tau_f}{\tau_{\max}} + h \cdot (S - S_{opt}) \cdot \frac{\theta}{p_0} \right] \quad (7.17)$$

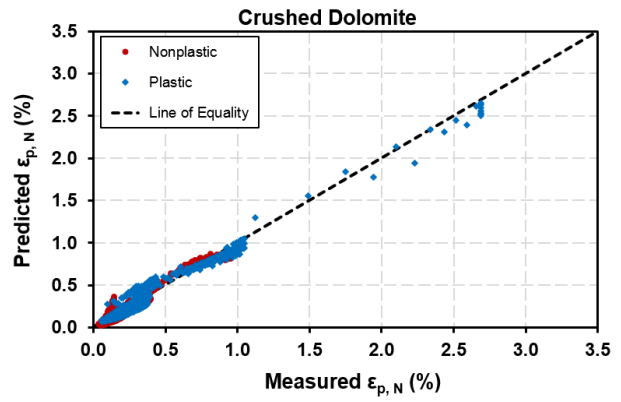
where ε_p = permanent axial strain (%), θ = bulk stress, $\frac{\tau_f}{\tau_{\max}}$ = shear stress to shear strength ratio,

p_0 = normalizing unit pressure (1 psi), N = the number of load applications, S = achieved saturation level in decimal, S_{opt} = optimum saturation level in decimal, wPI = weighted plasticity index, and a, b, c, d, e, f, g, and h = regression coefficients.

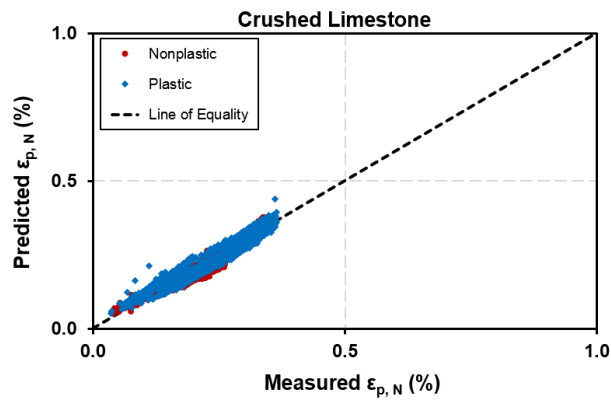
The proposed rutting model was then applied to the permanent deformation database of the ICT R27-1 Research Project. Figure 7.30 shows the model prediction results for those three different types of aggregates with varying quality aspects. As an example, the accuracy of the unified model in terms of R^2 values, as well as the model parameters, are shown in Table 7.12. Although many factors affecting permanent deformation behavior exist, the proposed model seems to be still able to predict reasonably well the permanent axial strain value accumulating with the number of loading cycles. Considering the fact that the stress state applied during the conditioning stage to obtain permanent deformation results is similar among different specimens, a simplified version of Equation 7.17 can be pursued by dropping the bulk stress term, thus making the shear stress ratio the only stress-related term.



(a)



(b)



(c)

Figure 7.30 Measured Cumulative Permanent Axial Strain vs. Predicted Cumulative Permanent Axial Strain for (a) Uncrushed Gravel, (b) Crushed Dolomite and (c) Crushed Limestone

Table 7.12 Summary of Permanent Strain Model Coefficients with Goodness of Fit for ICT Uncrushed Gravel Materials of Different Physical Properties

Material		a	b	c	d	e	f	g	h	R ²
Non-plastic	L_0_D	1.7E3	17	31	0.2	27.5	509	-29347	3.35	0.99
	L_0_O	0.82	-1.2	0.53	0.4	2.5	2.3	1.4	3.4	0.98
	L_0_W	62.4	21	23	0.15	-124	-4712	-22232	-4	0.99
	L_4_D	10.3	11.1	16.6	0.14	83.1	380.6	-6888	2.33	0.99
	L_4_O	3.42	-0.7	0.48	0.14	0.44	0.18	-0.005	0.46	0.99
	L_4_W	54.3	12.6	20.4	0.15	11.9	138	-10791	-2.64	0.99
	L_8_D	0.54	10.4	13.1	0.13	65.7	-89.8	-3495	2.15	0.99
	L_8_O	1.7	6.2	7	0.23	4.23	-916.5	-3192	0.024	0.99
	L_8_W	619	31.7	58.1	0.17	103	832.6	-18305	-5.44	0.99
	L_12_D	10713	13.3	28.4	0.14	-27	76.8	-5531	2.16	0.98
	L_12_O	1161	4.03	40.4	0.34	0	5832	-15356	0	0.99
	L_12_W	0.37	25.2	35.4	0.35	-44.4	-102	-8237.7	-3.9	0.99
All Non-plastic Data		3E-12	7	5.5	0.3	-33	818	-2084	0.6	0.99
Plastic	L_0_D	1.94	7.77	9.9	0.13	0.27	-8.8	-108.6	1.59	0.99
	L_0_O	1.39	0.64	398	0.14	1.5	2062	-2675	0	0.98
	L_0_W	19.54	42.5	62.6	0.15	17.1	-3.7	-582	-8.0	0.99
	L_4_D	2.76	15.6	21.2	0.14	97.1	0.14	-79.4	2.8	0.98
	L_4_O	9.26	1.73	323	0.15	0.59	803.7	-1201	4.87	0.99
	L_4_W	148.6	12.2	23.3	0.14	-48.3	8.13	-84.2	-2.2	0.99
	L_8_D	0.52	165	207	0.1	71.9	17.2	-743.7	32.4	0.99
	L_8_O	9E+5	3.8	135	0.18	1.37	195.5	-322	1.21	0.99
	L_8_W	3.3E+4	-34.3	-36.5	0.35	57.2	10.43	85.3	6.46	0.99
	L_12_D	1596	171	231	0.1	71.6	17.4	-542	35.6	0.97
	L_12_O	2.37	4.72	191	0.17	3.46	220.5	-352.7	0	0.99
	L_12_W	0.8	30.7	30.8	0.33	-337	-3.2	-52	-6	0.99
All Plastic Data		3E-59	32	0.4	0.2	95	1.1	-2.4	-1.5	0.96
Add Data Combined		4E-44	23	-1.4	0.4	-51	-1.1	4.7	0.85	0.91

The developed permanent strain models are so far applicable to a specific type of aggregates (i.e., crushed dolomite, crushed limestone, or uncrushed gravel) prepared at different fines contents and moisture contents. An attempt was also made to combine the permanent strain test results and to construct a unified model that are applicable to all three different types of aggregates. To achieve this goal, additional explanatory variables are needed to effectively distinguish the mineralogical difference among the three different types of aggregates. Particle shape, texture, and angularity characteristics of the three aggregate types were quantified in the laboratory using a validated image analysis system, the University of Illinois Aggregate Image Analyzer (UIAIA). Those imaging based aggregate morphological indices, as tabulated in Table 3.3, were previously identified to be closely related to mechanical performance indicators such as resilient modulus and permanent deformation (Tutumluer et al., 2009). Therefore, they are employed herein as explanatory variables to account for the difference among the three aggregate types. The final model form is mathematically expressed in Equation 7.18.

$$\varepsilon_p = a \left(\frac{\theta}{p_0} \right)^b \left(\frac{\tau_f}{\tau_{\max}} \right)^c N^d \cdot EXP[k \cdot FER + m \cdot AI + n \cdot ST] \cdot EXP \left[e \cdot (S - S_{opt}) + f \cdot wPI + g \cdot wPI \cdot \frac{\tau_f}{\tau_{\max}} + h \cdot (S - S_{opt}) \cdot \frac{\theta}{p_0} \right] \quad (7.18)$$

where FER, AI, and ST are imaging based aggregate morphological indices, i.e., Flat and Elongated Ratio, Angularity Index, and Surface Texture, respectively, and k, m, and n are additional regression coefficients corresponding to three aggregate morphological indices, respectively.

Table 7.13 lists the model coefficients of the unified permanent strain model. The reasonably high R^2 value (0.85) indicates that the unified model well fits all the test results. Figure 7.31 plots the measured permanent axial strain values against the predicted values by the

unified model. The data points are approximately scattered around the equality line. It should be noted that only the linear form of the predictive variables was explored in the developed unified model. Further refinement of the developed unified model by exploring other nonlinear forms may improve the prediction accuracy.

Table 7.13 Summary of Permanent Strain Model Coefficients with Goodness of Fit for All Three Different ICT Aggregate Materials of Varying Physical Properties

Model	a	b	c	d	e	f	g	h	k	m	n
Coefficients	0.44	24.4	-0.75	0.32	0.44	-1.26	5.21	-0.014	36.1	-1.02	165.2
R ²	0.85										
SEE	0.11										
Data Points	13,522										

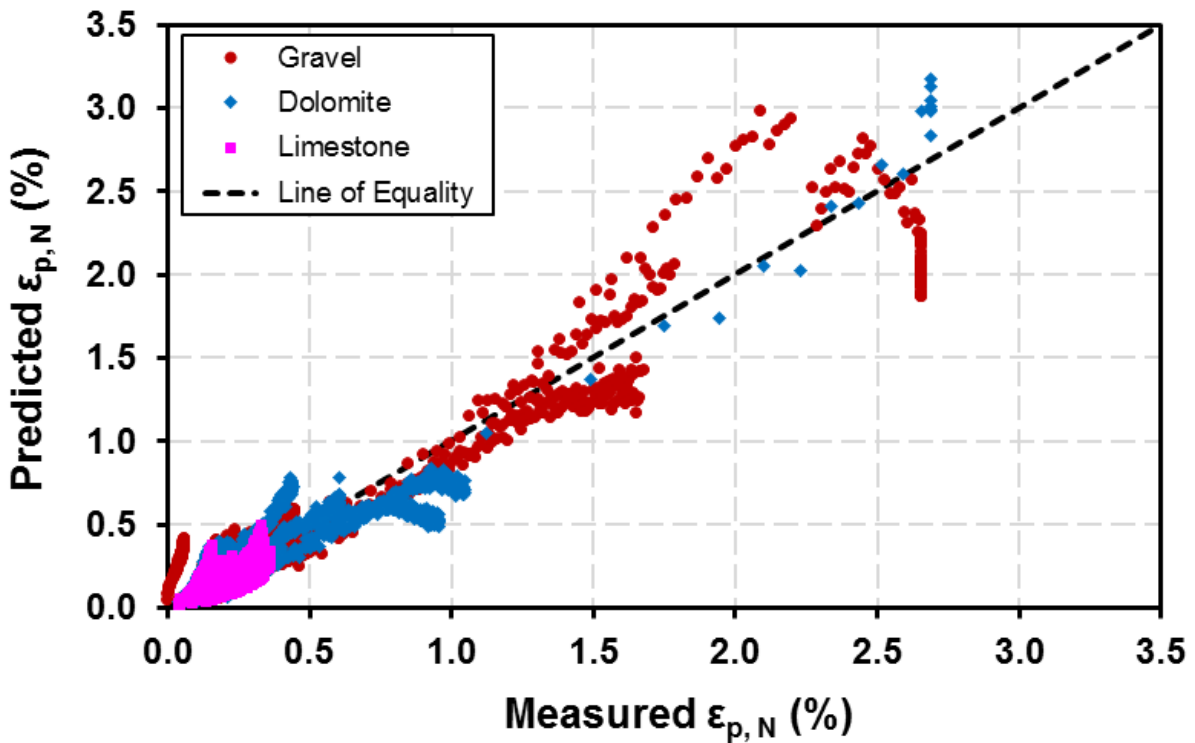


Figure 7.31 Measured Cumulative Permanent Axial Strain vs. Predicted Cumulative Permanent Axial Strain by the Unified Model

7.5.2 Model Development for Different Dynamic Stress States

7.5.2.1 Selection of Model Form

The major motivation of developing a unified rutting model is to predict permanent deformation accumulation with a high degree of confidence no matter what the applied stress states are in the granular layer and whether or not these stresses are due to stationary or moving wheel loads. The FAA database consists of permanent deformation results that were obtained at different dynamic stress states. The aim is to develop unified models that relate permanent strain to the number of cycles and the applied stresses, which have wider and more robust application than the models reviewed previously. The analysis is limited to permanent axial strain, as this is the most important for the estimation of rutting. Kim (2005) also developed CCP and VCP permanent deformation models using the same FAA database. According to Kim (2005), the R^2 values of the developed VCP models for $m=-1$ (triaxial extension) were in general the lowest possibly due to the high noise and fluctuations in the recorded triaxial data; therefore, permanent deformation test results for $m=-1$ is not analyzed in this study.

In addition to the model form presented previously for ICT aggregates, two commonly used rutting models incorporating stress terms were verified first for their general applicability to dynamic stress states. The first model verified was the one suggested by Gidel et al. (2001), as shown in Equation 7.19. It was developed using repeated multi-stage triaxial test apparatus and uses the maximum deviator (q_{\max}) and mean (p_{\max}) stresses to compute the permanent strain. This model explicitly combines the effects of stresses and number of cycles on the axial permanent strain.

$$\varepsilon_p(N) = \beta_1 \varepsilon_0 \left[1 - \left(\frac{N}{N_0} \right)^{-B} \right] \left(\frac{L_{\max}}{P_a} \right)^n \left(m + \frac{s}{P_{\max}} - \frac{q_{\max}}{P_{\max}} \right)^{-1} \quad (7.19)$$

where N_0 is the reference number of load applications (in this study=100),

$L_{\max} = \sqrt{p_{\max}^2 + q_{\max}^2}$, and n , B , m , s , and \mathcal{E}_0 are material constants.

The second model evaluated has a similar formulation as the first one and is proposed by Korkiala-Tanttu (2008). According to this model, the development of permanent deformation is directly related to the distance from the stress point to the Mohr-Coulomb failure line expressed in q-p space and it also relates the effect of stress on the permanent deformation through a hyperbolic function (see Equation 7.20). This model accounts for the effect of the number of cycles through the log-log approach suggested by Sweere (1990). This model is given by:

$$\varepsilon_p(N) = \beta_1 C N^b \frac{R}{A - R} \quad (7.20)$$

where C and b are material parameters, A is a parameter independent of the material ($A=1.05$)

and R is the deviatoric stress ratio given by $R = \frac{q_{\max}}{q_f} = \frac{q_{\max}}{s + m \cdot p_{\max}}$, $m = 6 \sin \phi / (3 - \sin \phi)$

and $s = 6c \cdot \cos \phi / (3 - \sin \phi)$, ϕ is the angle of internal friction, c is the cohesion of the material, and q_{\max} and p_{\max} are the maximum deviatoric and hydrostatic stresses of the load application, respectively.

As an example, permanent deformation results of FAA P154 material at different CCP and VCP stress states were used for comparison. Note that the s and m values required for calculating R value in Equation 8.18 are $s=19.46$ psi and $m=2.49$ for P209 material, and $s=54.36$ psi and $m=1.80$ for P154 material according to the shear strength test results, respectively. Figure 7.32 plots the measured permanent strain values again those predicted by each of the three models. The R^2 and SEE values for the model by Gidel et al. (2001) are 0.57 and 0.13, and 0.67 and 0.11 for the one by Korkiala-Tanttu (2008), respectively. Improved accuracy was obtained

by the model proposed in this study, as indicated by $R^2=0.90$ and $SEE=0.06$. It can also be observed from Figure 7.32 that the model proposed in this study yielded predictions that match the measured values more closely.

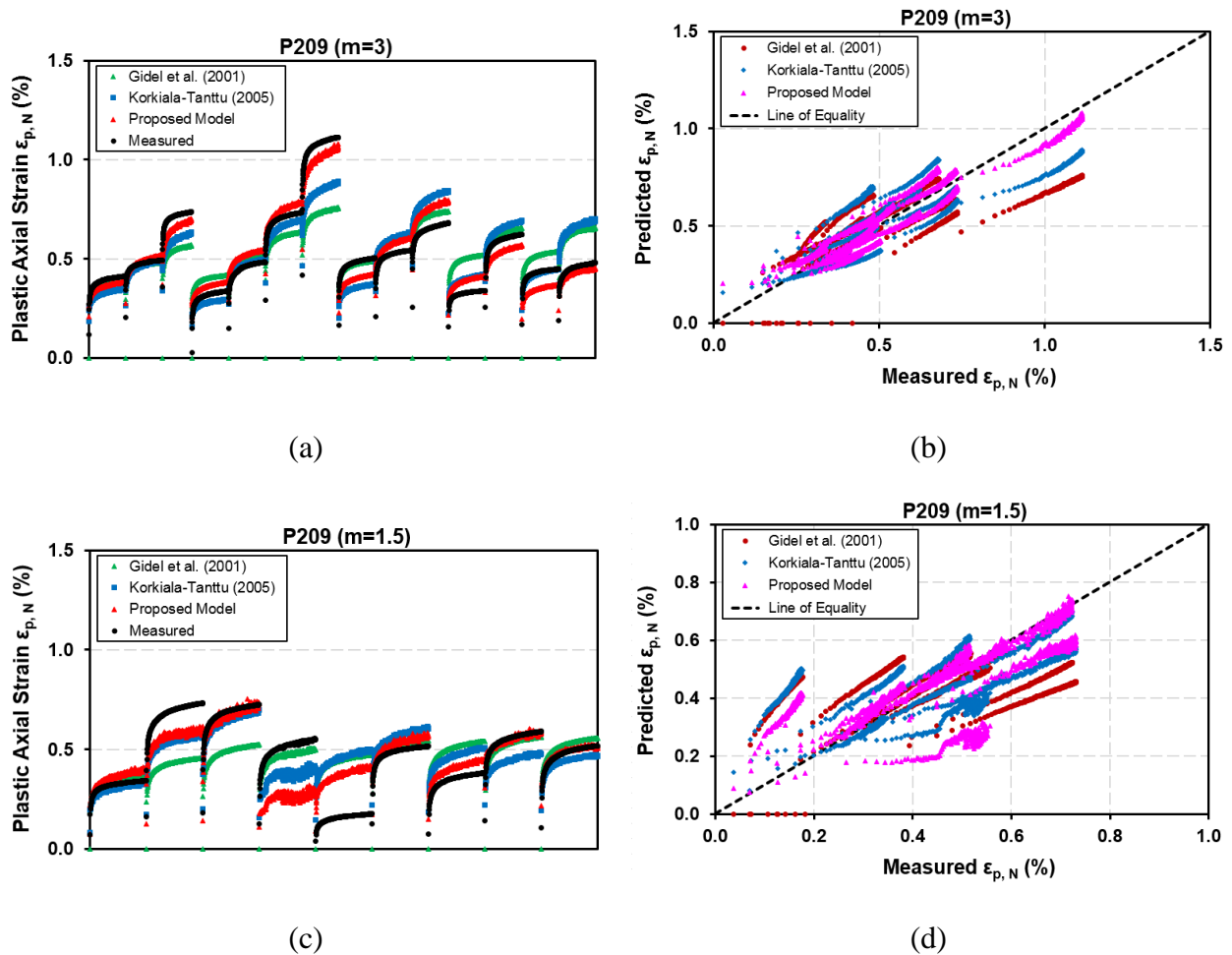


Figure 7.32 Measured Cumulative Permanent Axial Strain vs. Predicted Cumulative Permanent Axial Strain by Different Models for P209 Material at a Loading Slope of (a) $m=3$ and (b) $m=1.5$

7.5.2.2 Two-stage Model

Both primary stage and second stage exist in the permanent deformation curves recorded in the FAA database. Both the semi-log and power-law models were found to only represent the primary stage of the measured rutting curve, whereas the Tseng and Lytton's model cannot characterize either the secondary or tertiary stage (Zhou et al., 2004). In summary, these types of models appear to adequately characterize only the primary stage, and none of them can describe effectively the secondary and/or tertiary stages. Therefore, instead of using a single classical power-law formulation to describe the entire permanent deformation curve, Zhou et al. (2004) proposed the concept of the three-stage permanent deformation model to mathematically describe the whole permanent deformation curve. It has been reported as the most accurate model, among all the developed models in this field, to fit the permanent deformation curves and to identify the locations of the two boundary points on the permanent deformation curves.

Pérez and Gallego (2010) fitted several existing permanent deformation models to express the cumulative permanent strain as a function of the number of load cycles. They found that the sum of two well-known models offered excellent predictions, which in the long term did not tend to either underestimate or overestimate the measured values. The model has the following mathematical form as in Equation 7.21.

$$\varepsilon_{1,p} = AN^B + (m \cdot N + C)(1 - e^{-D \cdot N}) \quad (7.21)$$

As illustrated in Figure 7.33, the first term of this model produces a linear increase of permanent strain in relation to N on a log-log scale. It has a slope equal to infinity at N=0 and equal to the product of the two coefficients A and B at N=1. After a certain number of load cycles, the second summand reproduces a linear increase of permanent strain with N on a $\varepsilon_{1,p}$ -N scale. The model has a curvature determined by the value of coefficients B and D and an

eventual linear slope equal to coefficient m . The applicability of this model is limited to low-traffic roads whose structural response behavior, according to the shakedown concept, corresponds to “Range A” and “Range B”. It has been proven that this model offers an excellent description of the material behavior in “Ranges A and B” in a pavement section of low-traffic roads (Pérez and Gallego, 2010).

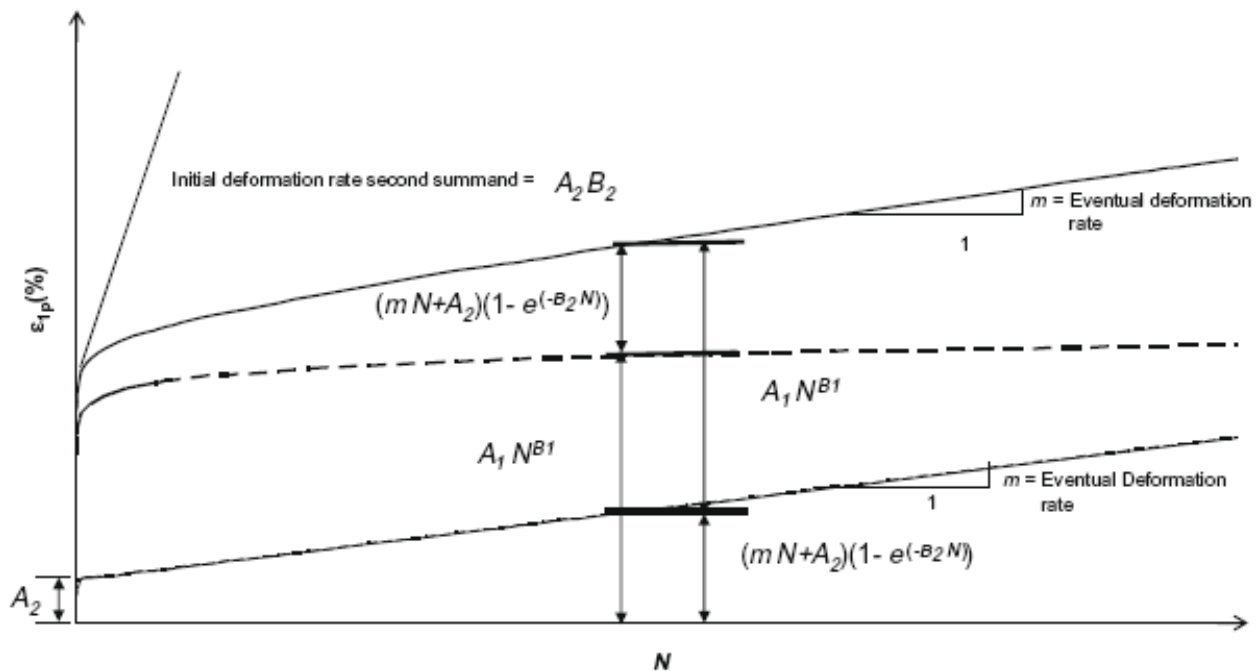


Figure 7.33 Schematic Representation of Model Parameters in Equation 8.19 (Pérez and Gallego, 2010)

In this study, the permanent deformation model form recommended by Pérez and Gallego (2010) is selected as the basic form for the unified rutting model to describe the plastic strain accumulation with the number of load applications. Note that such a basic form is conceptually similar to the three-stage model by Zhou et al. (2004). It is worth noting that the two-stage rutting model naturally combines the two unified models developed previously for modeling

primary and secondary stages, respectively. Therefore, it is capable of predicting the whole process of permanent deformation accumulation. The next step is to correlate the model parameters of the basic model form to a variety of stress variables so that it can accurately fit all the permanent deformation curves obtained at different stress states. To achieve this, the stress variables to be correlated with model parameters must be the fundamental ones that are sufficient to capture the stress sensitivity of the permanent strain accumulation. By combining the permanent deformation models developed by Kim (2005) primarily for describing the primary stage and the permanent strain rate model developed in this study for describing the secondary stage, the following model is proposed as in Equation 7.22 and then found to fit all the permanent deformation curves with good accuracy, as indicated by the high R^2 values and low SEE values, as shown in Figure 7.34 for P209 material.

$$\varepsilon_{1p} = AN^B + (\dot{\varepsilon}_{1p} \cdot N + C)(1 - e^{-D \cdot N})$$

where

$$A = \begin{cases} a \left(\frac{\theta}{p_0} \right)^b \left(\frac{\sigma_d}{p_0} \right)^c & \text{for CCP} \\ a \left(\frac{\sigma_s}{p_0} \right)^b \left(\frac{L}{p_0} \right)^c \left(1 + \frac{1}{10^{\Delta q / \Delta p}} \right)^d & \text{for VCP} \end{cases} \quad (7.22)$$

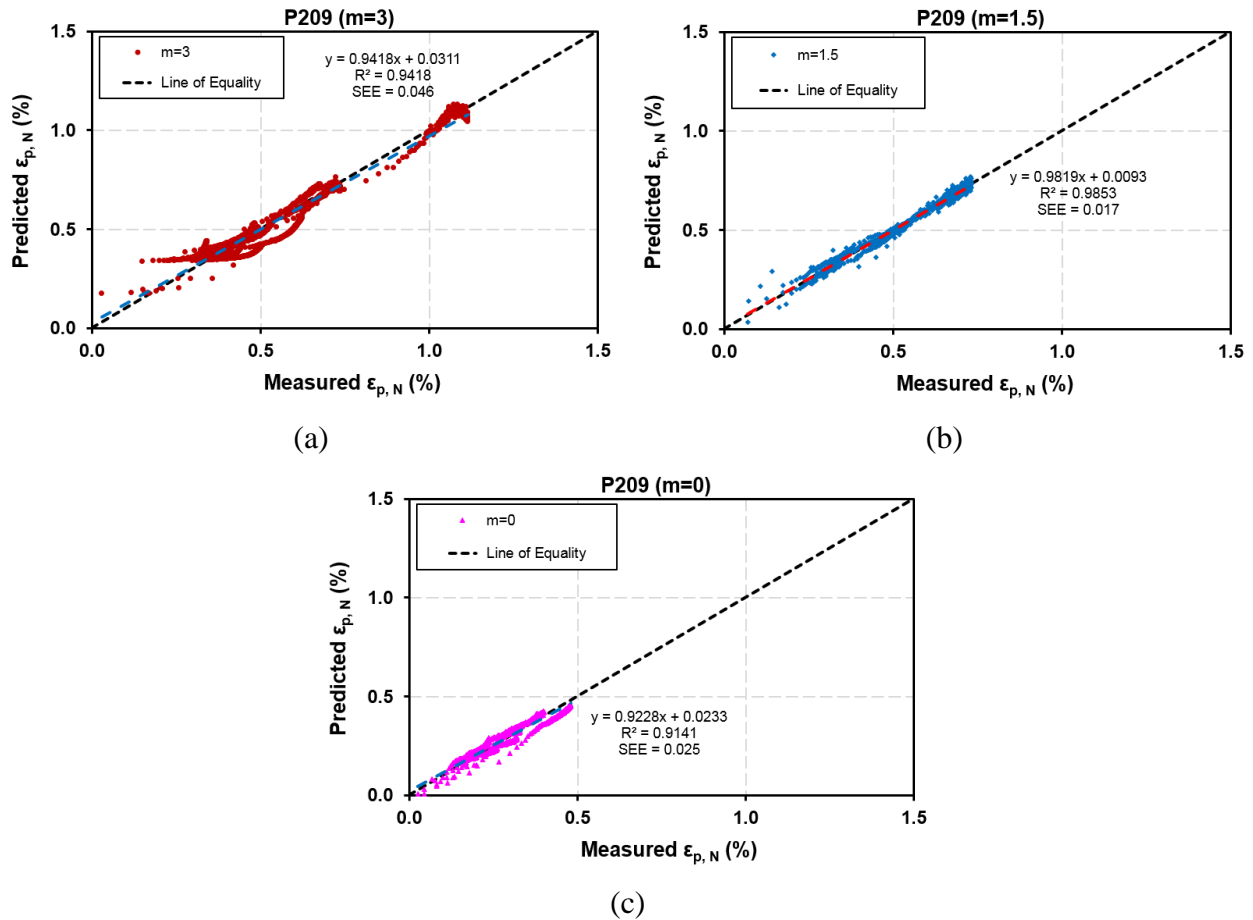


Figure 7.34 Measured Permanent Axial Strain Vs. Predicted Values by the Unified Model for FAA P209 and P154 Materials at Different Loading Slopes: (a) $m=3$, (b) $m=1.5$, and (c) $m=0$

It is worth noting that the unified rutting model and the stable permanent strain rate model developed in this study were based on two unique research project databases and were specific to unbound aggregate materials studied in those two databases, respectively. While the general forms of these two models could still be applicable to other changing materials and/or conditions, it is recommended that the model coefficients be calibrated using laboratory RLT permanent deformation test results prior to the use in actual predictions.

7.6 Summary

This chapter presented the development of viable criteria for ranking the long-term rutting potentials of unbound granular materials based on the shakedown theory and a unified approach for modeling permanent deformation behavior. A comprehensive aggregate mechanistic property database recently compiled at the University of Illinois from a number of research studies spanning almost two decades were re-examined from a fresh point of view, i.e., the shakedown theory for rutting behavior. Resilient modulus, shear strength, and permanent deformation test data for several base/subbase aggregate materials used in highway and airport pavement foundation layers were comprehensively documented in this database.

The adequacy of Pavement ME Design models to predict the influence of subgrade and unbound layer characteristics on the rutting performance of flexible pavements for a range of material, environment, and traffic conditions was first evaluated using this laboratory database. Based on the comparison results of the original Tseng and Lytton model and the current MEPDG rutting model against laboratory RLT test results, the need for further enhancement of both models becomes obvious. To improve the predictive ability of Pavement ME Design, rational modifications of the models contained in the Pavement ME Design were suggested, which will allow an improved analysis and design of flexible pavements against rutting distress. Both the resilient and plastic responses of different aggregate materials to repeated loading under various dynamic stress states and aggregate physical conditions were analyzed concurrently from shakedown perspectives to characterize the correlation between plastic strain and resilient modulus. This further confirms that relying on resilient modulus alone could lead to misleading characterization of unbound aggregates for use in pavement applications; instead, resilient modulus and permanent deformation need to be examined concurrently.

A special consideration of “degradation stiffness model” was introduced to demonstrate how the results of laboratory repeated load triaxial tests on unbound aggregates can be applied in a numerical model to estimate the progressive deformation of unbound pavement layers to the effects of long-term repeated loading. The constitutive models for the degraded secant modulus were proposed based on the concept similar to that of the existing resilient modulus models, thus making them suitable for use with numerical tools such as the finite element simulation. By using the proposed models, the permanent deformation of unbound pavement layers under repeated traffic loading can be realistically predicted using a mechanistic approach as opposed to the current empirical or semi-empirical methods.

A stable permanent strain rate dependency was observed for characterizing the dynamic stress states induced by moving wheel loads. Efforts were made accordingly to develop an analytical model for mathematically expressing such a dependency. Analogous to the concept of the Mohr-Coulomb failure envelope, permanent deformation resistance envelopes were defined by Mohr circles representing all the possible stress states that cause a specified permanent strain rate. One prominent feature of such permanent deformation resistance envelopes is their potential usefulness in ranking and properly selecting different unbound pavement layer materials for use in specific traffic levels and site conditions, i.e., the rutting potential based on the shakedown theory is evaluated simultaneously in relation to the potential shear failure.

A unified approach to rutting prediction was developed to predict permanent deformation accumulation with a high degree of confidence regardless of the applied stress states/material physical conditions in the granular layer and whether or not these stresses are due to stationary or moving wheel loads. This unified rutting modeling approach effectively takes into account various aggregate physical properties and field stress states induced by moving wheel loads and

thus can be applied with greater confidence to a wider range of conditions. This way, consequences of using different qualities of aggregates including local marginal and recycled materials can be effectively evaluated for a sustainable yet reliable utilization in pavement construction. Good agreement between model predictions and laboratory permanent deformation test results was achieved by using the developed unified models.

Chapter 8 Field Validation of Unified Rutting Prediction Model for Unbound Granular Materials Using Accelerated Pavement Tests

One of the reliable methods to quantify the effectiveness of the developed rutting prediction models is by testing full scale pavement sections and measuring the pavement rut depth accumulation with the applied load repetitions. Full-scale flexible pavement test sections, i.e., the NAPTF facility and the University of Illinois field test sections described in Chapter 3, are studied in this chapter for this purpose. The primary objective is to evaluate three permanent deformation models, i.e., the original Tseng and Lytton model, the current MEPDG rutting model, and the unified model developed in this thesis study, for unbound granular base/subbase materials using rutting measurements from full-scale accelerated pavement testing (APT). A method to determine the criterion of shear strength of unbound granular base/subbase materials is also established. By following this method, the expected pavement rutting during design service life should not exceed the maximum allowable one, provided that the shear strength of unbound base/subbase materials meet such established criteria.

8.1 Permanent Deformation Predictions of the NAPTF Test Sections

8.1.1 Modeling Responses of NAPTF Test Sections

To develop mechanistic based permanent deformation damage models for the unbound aggregate layers used in conventional flexible pavement sections, pavement stress and strain responses with depth are required. Using the NAPTF trafficking field data, individual rut accumulations in the granular layers had to be predicted accurately with the increasing number of load applications (or number of wheel passes) in order to validate the newly developed unified rutting models. This necessitated the estimation of the most accurate stress distributions in the

NAPTF P209/P154 granular layers to use as input in the permanent deformation models. Note that they can be calculated from the mechanistic response model. Accordingly, finite element (FE) models were created extensively in previous studies to simulate the accelerated pavement sections using axisymmetric programs (e.g., ILLI-PAVE and GT-PAVE) and 3D commercial software Abaqus® (Gopalakrishnan and Thompson, 2006; Kim, 2005; Kim and Tutumluer, 2009). Developing new pavement response models or assessing different existing pavement response models are out of the scope of this study; therefore, the relevant pavement responses were obtained from those previous studies to calculate the rut depth development with the number of passes. Detailed pavement analysis results can be found elsewhere (Gopalakrishnan and Thompson, 2003; Kim, 2005; Kim, 2007).

8.1.2 Permanent Deformation Predicted by the Unified Rutting Model

To validate the proposed stable permanent strain rate model, the permanent deformation data from the NAPTF Construction Cycle 1 (CC1) test sections, in which both P209 and P154 granular materials were extensively used in base/subbase layers, were selected. The rut depths were measured using Multi-Depth Deflectometers (MDDs) embedded. The displacements at specific depths were obtained by subtracting the specific depth displacement transducer (DT) response from the surface DT response. The cross sections of those pavement test sections are illustrated in Figure 3.2, whereas other details can be found elsewhere (Kim, 2005). The excessive shakedown and permanent deformations were reported to occur in the P209/P154 layers. The post-traffic trenching study on the MFC test section revealed that shear failure in the subgrade and P154 subbase contributed to the pavement structural failure (Hayhoe and Garg, 2002). The focus of this study is to predict the accumulation of rut depth with the number of load

repetitions for the P209 and P154 base/subbase layers, whereas permanent deformations of the asphalt surface layers and the subgrade soils are not the current focus.

Kim (2005) took two different approaches in utilizing the finite element predictions for the granular layer stress states as inputs to the permanent strain models. In the first approach, an average stress state was estimated at mid-depth of the granular layer and used as an input to the permanent strain models. The predicted permanent strain was then multiplied by the total thickness of the granular layer to compute the total layer permanent deformation. In the second approach, the granular layer was divided into several sublayers and the permanent strain in each sublayer was computed by the model individually using the average stress states predicted at mid-depth of that sublayer. The predicted permanent strain in each sublayer was then multiplied by the thickness of that sublayer. The total granular layer permanent deformation was finally obtained as the summation of all the sublayer deformations. According to Kim (2005), both the 1-layer and 10-layer (or 10-sublayer) results were somewhat close in predicting similar accumulations of permanent deformation with increasing number of Boeing 777 wheel passes showing only 0.02 in. (0.5 mm) difference in the results at 20,000 passes. For simplicity, only the permanent deformation predictions obtained following the first approach are presented and compared in this study with the measured rut values of NAPTF granular layers.

Equation 7.22 corresponding to CCP conditions was used, as shown in Equation 8.1. The model parameters were previously obtained from fitting laboratory permanent deformation test results in the FAA database. During the study conducted by Kim (2005) to validate the developed permanent deformation models against measured rut depths of the NAPTF test sections, he reported that the measured NAPTF P209/P154 layer rut accumulations have commonly much larger “B” values and smaller “A” values as in the power-law model

($\varepsilon_{1p} = A \cdot N^B$), due to the combined effects of load pulse duration and stress history. This could be interpreted as follows: (i) the magnitude of permanent deformation in the very first load cycles (or primary stage) observed in the field trafficking is less than that exhibited in the laboratory tests (NAPTF test sections were pre-loaded extensively); and (ii) the slope (rate) of permanent deformation accumulation line is greater than that observed in the laboratory tests (multiple dynamic wheel loads with wander patterns were applied in the field). Kim (2005) found that adjustment factors were necessary for the prediction models to more accurately predict the NAPTF measured granular layer ruts due to the NAPTF slow moving response tests conducted in the field prior to trafficking.

$$\varepsilon_{1p} = \beta_1 \cdot AN^{\beta_2 \cdot B} + \beta_3 \cdot (s \cdot N + C)(1 - e^{-D \cdot N})$$

where

$$A = a \left(\frac{\theta}{p_0} \right)^b \left(\frac{\sigma_d}{p_0} \right)^c \quad \text{for CCP} \quad (8.1)$$

$$s = p \cdot \sigma_3^q \cdot \sigma_1^{(r \cdot \sigma_3 + t)} \quad \text{for CCP}$$

where A, B, C, D, a, b, c, p, q, r, and t are regression parameters obtained from fitting laboratory permanent deformation test results; and β_1 , β_2 , and β_3 are calibration factor to represent the difference between laboratory testing and field trafficking conditions.

In this study, the model parameters of the unified model (Equation 8.1) were initially obtained from laboratory tests which were inconsistent with field conditions, as described previously. While not explicitly incorporated in the developed rutting models, the stress history effects are demonstrated as an important factor governing the field rutting accumulation. This is evidenced by the laboratory observed permanent deformation curve following the power-law relationship, as contrary to the field measured rutting depth increasing with an approximate linear trend. In the field, the FAA test sections were subjected to the initial application of

considerable cycles of aircraft gear loadings prior to the APT loading. To properly address such inconsistency between laboratory testing and field trafficking conditions, three calibration factors, i.e., β_1 , β_2 , and β_3 , were introduced into Equation 8.1. The use of those calibration factors is expected to properly predict the initial permanent deformation magnitude during the primary stage as well as the long-term permanent strain rate exhibited in the secondary stage. Note that this concept is in essence similar to the local and global calibration adopted by the current MEPDG, as well as to the adjustment factor approach used by Kim (2005). The values of those calibration factors were determined by a trial-and-error procedure until the P209/P154 layer rut depth predicted in the calibration section matched the accumulated permanent deformation data as well as the profile data measured after the moving-wheel test. The root mean squared error (RMSE) was set as the objective function to be minimized:

$$\Phi = \sqrt{\frac{\sum_{i=1}^N (\Delta_{mi} - \Delta_{ci})^2}{(N-1)}} \quad (8.2)$$

where N is the number of load repetitions; Δ_{mi} is the measured layer rut depth at the i -th load repetition; and Δ_{ci} is the calculated layer rut depth at the i -th load repetition.

Figure 8.1 and Figure 8.2 show the measured layer rut depths along with those predicted by the unified model for P209 and P154 layers, respectively. It can be seen that the model predicts the measured rut depth reasonably accurately. Note that the predicted curves in Figure 8.1 and Figure 8.2 were shifted using the shift factor parameter k to obtain a good agreement between the measured and the predicted permanent deformation. The shift factor parameter k is used to account for the differences in the actual field conditions among different NAPTF test sections. The shift factors used for P209 or P154 layers are approximately the same, further

indicating the capability of the proposed model to capture the stress sensitivity in predicting rut depth. As compared to the original prediction made by Kim (2005), the permanent deformation prediction generated by the proposed two-stage permanent strain model is much closer to the field measured values. Note that the Kim (2005) model employed to generate the corresponding permanent deformation curves shown in Figure 8.1 was not corrected for load pulse duration and stress history effects. Considering the rutting depth accumulated during the primary stage for the NAPTF test sections is relatively small as compared to long-term rutting depth accumulated during the secondary stage and up to failure, it seems reasonable to use the proposed stable permanent strain rate model for predicting rutting depth up to the initiation of the tertiary stage.

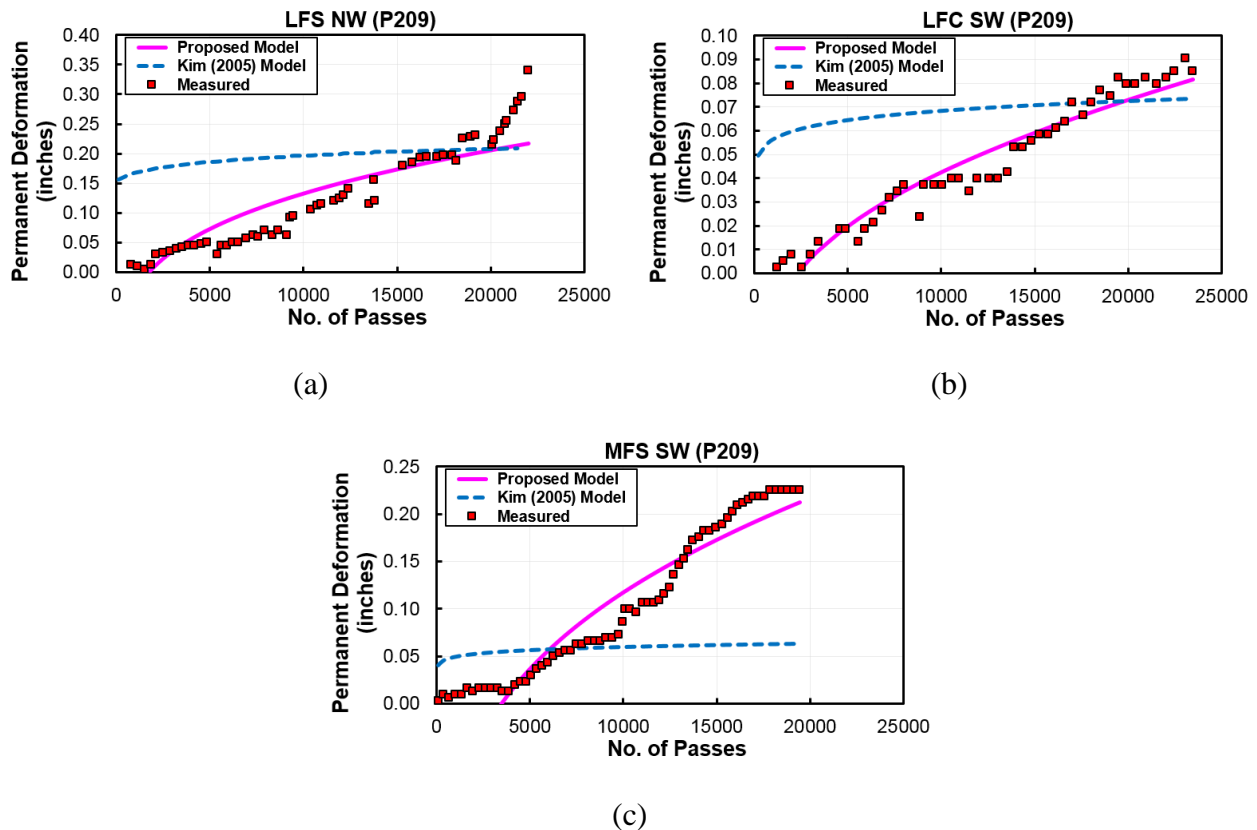


Figure 8.1 Comparison of Field-measured and Model-predicted Layer Rut Depth for P209 Layers

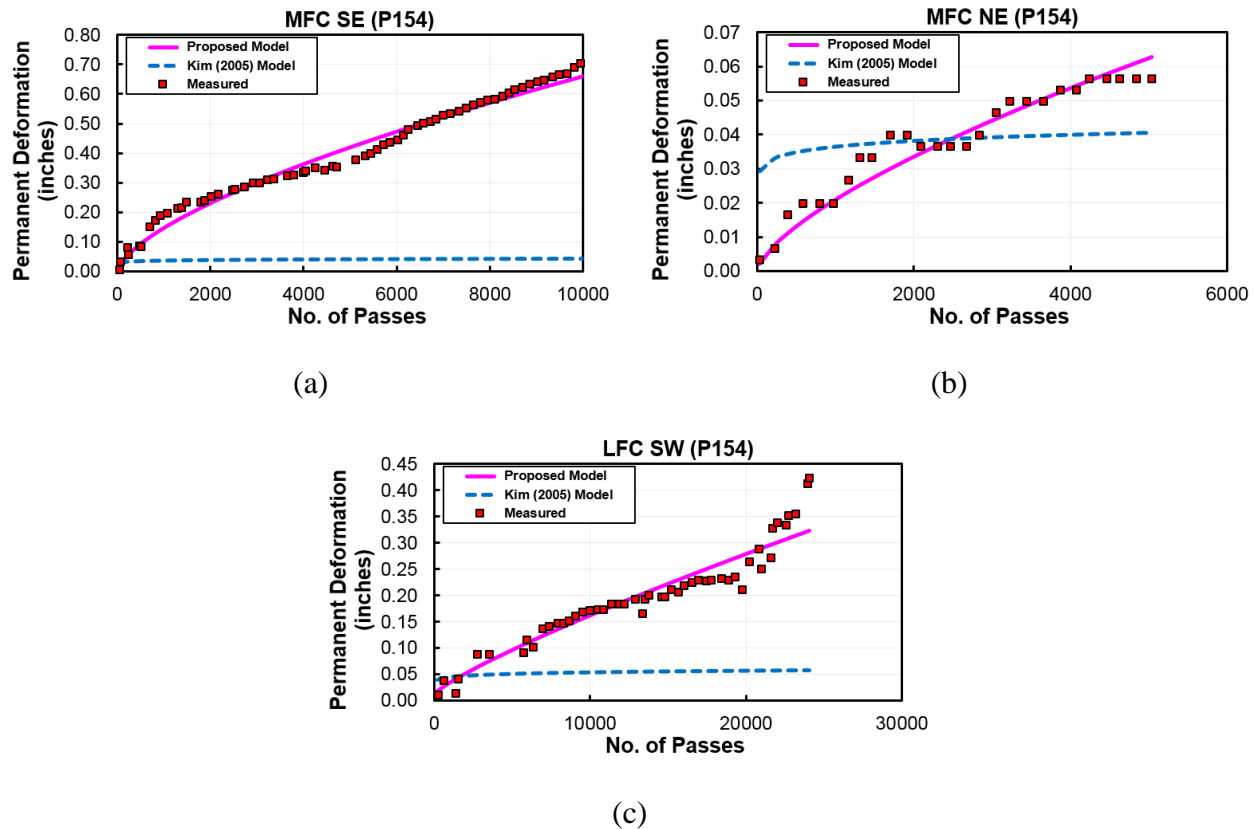


Figure 8.2 Comparison of Field-measured and Model-predicted Layer Rut Depth for P154 Layers

8.2 Permanent Deformation Predictions of ICT Full Scale Test Sections

8.2.1 Modeling Responses of ICT Full Scale Test Sections

Although it is ideal to use a 3D FE model to simulate the actual geometries of the pavement test sections, a 3D model demands much more computational resources due to the increased number of elements. The approximation of the ATLAS wheel load as uniformly-distributed circular load in this study led to axially symmetric loading conditions, which made it possible to employ the simplified axisymmetric models for the geometric model of the test sections. The axisymmetric models were expected to be more computationally inexpensive than 3D models. A moving wheel load applied on pavements may consist of a static load and a

continuously changing dynamic load. The component of the dynamic load is mainly due to the irregularity of the pavement surface. The dynamic component of the wheel load is not considered in the modeling. The cyclic moving load can be reasonably assumed to be a stationary static load, considering the pavement materials assumed in this study are independent of the loading frequency.

Numerical response models were first created with GT-PAVE, a nonlinear FE pavement analysis program, to simulate the result of the moving wheel test performed in this study. The vertical compressive strains along the center-line of the model were then extracted from the response model to calculate the rut depth development with the number of passes. Pavement response models serve two purposes in this study: (1) to provide forward modeling for comparison with instrumentation measurements; and (2) to predict pavement critical responses that were needed as the inputs in the mechanistic-empirical (ME) permanent deformation models based on field rutting measurements.

8.2.1.1 Geometry of Pavement Structures and FE Model

An 800-element, 2533-node axisymmetric finite element mesh was used to analyze the test sections as nonlinear elastic layered systems. The subgrade and the unbound aggregate layer were treated as nonlinear elastic materials, as deemed necessary by previous studies (Tutumluer et al., 2003; Kim and Tutumluer, 2009). As shown in Figure 8.3, the dimension of the response model should be large enough to minimize the boundary effect. Thus, the boundaries were set to be 135 inches in the radial direction and 420 inches in the vertical direction from the center of the load area. The as-constructed thickness and material of each layer were used in the response model for each test section. Tire pressure of 110 psi was applied to a circular contact area to simulate a 9-kips wheel load.

It is well known that compaction induces horizontal earth pressure increase within a certain influence depth. The increased horizontal stress, as realized by many researchers, can significantly increase the stiffness of the granular base layer. However, the compaction-induced horizontal stress has not been considered in the finite element response model in the current MEPDG (NCHRP, 2004). A constant compressive horizontal residual stress of 21 kPa (3 psi) was assumed to exist initially throughout the base and subbase courses before the wheel load was applied in order to consider the benefits of adequate compaction. The inclusion of residual stresses in the analysis was reported to improve the predictive ability of the anisotropic model by realistically assigning the moduli in a zone of little load influence (Tutumluer et al., 2003; Kim and Tutumluer, 2009).

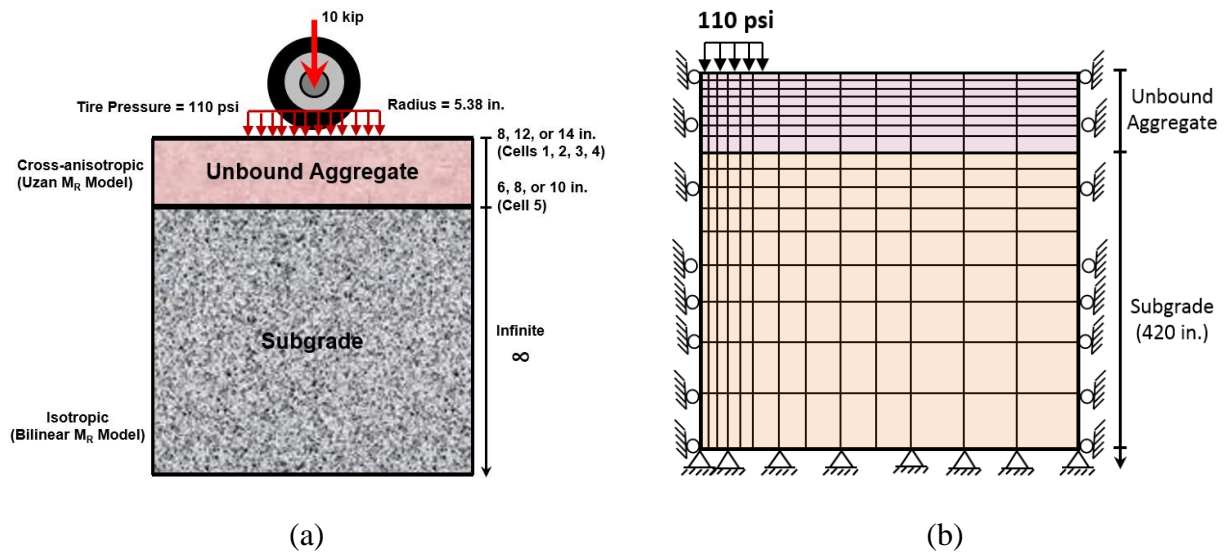


Figure 8.3 Pavement (a) Layer Thicknesses Considered and (b) the GT-PAVE FE Mesh

8.2.1.2 Material Properties

Material properties for the individual test cells were assigned based on previous laboratory test results for the aggregate subbase materials and the subgrade soil at the University of Illinois ATREL facility (Kwon, 2007; Mishra, 2012). The Uzan type stress-dependent modulus model (Uzan, 1995) was used to characterize cross-anisotropic resilient moduli of aggregate subbase materials, as shown in Equation 8.3. Table 8.1 lists the cross-anisotropic modulus model parameters determined accordingly. The constant Poisson's ratios used were $\nu_r=0.3$ and $\nu_z=0.1$. Tutumluer and Thompson (1997) considered a wide range and combination of values for Poisson's ratios and found negligible effect on the computed granular material stiffness.

$$\begin{aligned}M_R^H &= K_1 \left(\frac{\theta}{p_0} \right)^{K_2} \left(\frac{\sigma_d}{p_0} \right)^{K_3} \\M_R^V &= K_4 \left(\frac{\theta}{p_0} \right)^{K_5} \left(\frac{\sigma_d}{p_0} \right)^{K_6} \\G_R^V &= K_7 \left(\frac{\theta}{p_0} \right)^{K_8} \left(\frac{\sigma_d}{p_0} \right)^{K_9}\end{aligned}\tag{8.3}$$

where θ and σ_d are bulk stress ($\sigma_1 + 2\sigma_3$) and deviator stress ($\sigma_1 - \sigma_3$) in triaxial conditions, respectively; p_0 is normalizing unit pressure (1 psi); and K_i are regression constants from repeated load triaxial test data, respectively.

Table 8.1 Resilient Modulus Model Parameters for Aggregate Subbase Materials Used

Materials	Cell No.	E (Initial Guess, psi)	ν^h	ν^v	The Uzan Model Parameters		
					Horizontal Modulus M_R^H	Vertical Modulus M_R^V	Shear Modulus G_R^V
Nonplastic Uncrushed Gravel	1	8000	0.35	0.1	$K_1 = 221.7$ psi $K_2 = 3.36$ $K_3 = -2.63$	$K_4 = 1043.7$ psi $K_5 = 0.86$ $K_6 = -0.13$	$K_7 = 434.4$ psi $K_8 = 1.06$ $K_9 = -0.33$
Plastic Crushed Limestone	2/5	8000			$K_1 = 395.3$ psi $K_2 = 3.17$ $K_3 = -2.66$	$K_4 = 4066.1$ psi $K_5 = 0.67$ $K_6 = -0.16$	$K_7 = 1186.9$ psi $K_8 = 0.87$ $K_9 = -0.36$
Nonplastic Crushed Dolomite	3	8000			$K_1 = 359.7$ psi $K_2 = 3.14$ $K_3 = -2.65$	$K_4 = 3688.2$ psi $K_5 = 0.64$ $K_6 = -0.15$	$K_7 = 1077.8$ psi $K_8 = 0.84$ $K_9 = -0.35$
Nonplastic Crushed Limestone	4	8000			$K_1 = 394.7$ psi $K_2 = 3.16$ $K_3 = -2.65$	$K_4 = 4084.7$ psi $K_5 = 0.66$ $K_6 = -0.15$	$K_7 = 1189.8$ psi $K_8 = 0.86$ $K_9 = -0.35$

Note: 1 kPa = 0.145 psi.

The subgrade soil was in general reported to be classified as ML, CL, or a combination of ML and CL using the dual classification following the Unified Soil Classification System (with a specific gravity of 2.72 and an average plasticity index of 5). The average field moisture content of 18.75% for the silty clay subgrade soils was very high to be able to make test samples for repeated load triaxial testing. Therefore, the model parameters used in the bilinear models were

assumed from the previous study by Thompson and Elliot (1985). Thompson and Elliott (1985) presented ILLI-PAVE based design algorithms for flexible pavements including four fine-grained subgrade moisture conditions applicable to this study. Subgrade soil resilient modulus is characterized by the bilinear model in this study with model parameters tabulated in Table 8.2.

Table 8.2 Resilient Modulus Model Parameters for Subgrade Soils

Materials	CBR (%)	Cell No.	E (Initial Guess, psi)	v	Bilinear Model Parameters
Subgrade 1 (Top 12 in.)	3	1, 2, 3, 4	1450	0.45	$E_{RI}=1000$ psi $\sigma_{di}=6.2$ psi $K_3=1110$ $K_4=178$ $\sigma_{dII}=1$ psi $\sigma_{dUl}=21$ psi
Subgrade 2 (Top 12 in.)	6	5	2260		$E_{RI}=3020$ psi $\sigma_{di}=6.2$ psi $K_3=1110$ $K_4=178$ $\sigma_{dII}=1$ psi $\sigma_{dUl}=21$ psi
Natural Subgrade (Infinite)	-	1, 2, 3, 4, 5	4500		$E_{RI}=7680$ $\sigma_{di}=6.2$ psi $K_3=1110$ $K_4=178$ $\sigma_{dII}=1$ psi $\sigma_{dUl}=21$ psi

Note that subgrade was processed to a depth of 305 mm (12 in.) to achieve the desired subgrade CBR of 3% and 6% (Cell 5 only). Based on these algorithms and estimated CBR values, resilient modulus model parameters for the 305-mm prepared subgrade with CBR of 3% and 6% were assigned as very soft type soil and soft type soil, respectively. The rest of the underlying natural soils was assigned as medium soft type soil. This approach was also used by Kwon (2007) with reasonably good accuracy in his mechanistic modelling analysis of geogrid

reinforced test sections that were constructed at ATREL facility on top of the same type of subgrade soil.

8.2.1.3 Resilient Response

To first calibrate and validate the developed mechanistic model and its model parameters used in this study, the measured responses from the instrumented test sections were compared with those predicted by the developed mechanistic model. As described in Chapter 3, earth pressure cells were installed at the aggregate-subgrade interface along the North wheel path of individual test cells to monitor the subgrade vertical compressive stresses (Mishra, 2012). For illustration purpose, the field-measured subgrade vertical stress values for Section 2 and 3 (12-in. and 8-in. thick aggregate layers, respectively) in Cell 1, as previously reported by Mishra (2012), were plotted in Figure 8.4 along with the model-predicted values. It can be seen from Figure 8.4 that the cross-anisotropic aggregate layer characterization gave better predictions for subgrade vertical stresses than the isotropic aggregate layer characterization. In general, mechanistic model predictions match the field-measured values reasonably well, which would conclude the validity of the developed mechanistic model and its model parameters used. Note that both the cross-anisotropic and isotropic aggregate layer characterizations used the Uzan model (1985) for resilient modulus (M_R).

From the comparisons of subgrade vertical stress values, the differences found can be attributed to the dynamic nature of moving wheel loads. The developed mechanistic model performed a static analysis to approximate the wheel load as applied uniform circular pressure. Accordingly, important effects of the moving wheel loads, i.e., tire configuration, speed, interaction of tire and pavement, and non-uniform tire contact pressures on pavement responses were ignored. Even the low strength subgrade material can be more subjective to localized

effects due to moving wheel loads. Kwon et al. (2008) also reported that the cross-anisotropic base characterization gave much better predictions for the vertical LVDT displacements on top of subgrade and the radial LVDT displacements at the bottom of base course. Their goal was to predict the resilient responses of instrumented full-scale pavement test sections, both geogrid base reinforced and control sections, studied under single and dual wheel loadings at the University of Illinois. Therefore, the cross-anisotropic aggregate layer characterization was employed subsequently in this study to predict pavement responses of those field full-scale test sections.

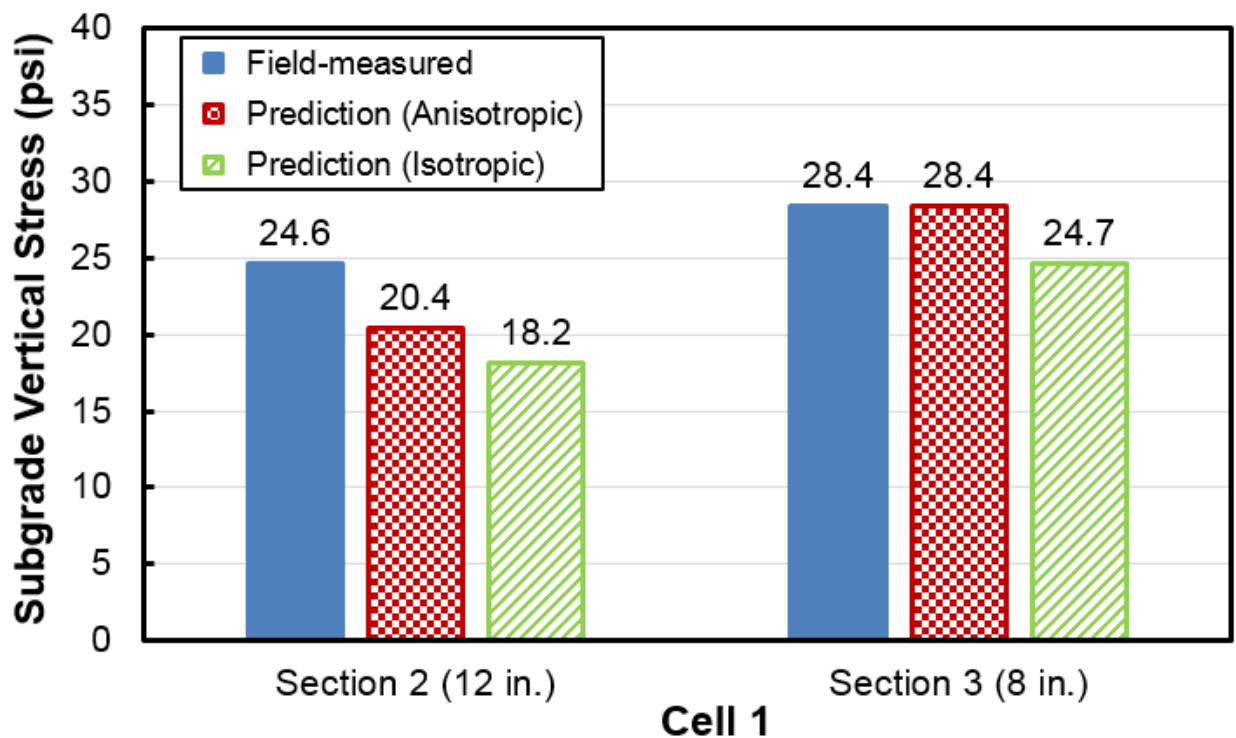


Figure 8.4 Comparisons of Measured and Predicted Subgrade Vertical Stress Values for Test Section 2 and 3 in Cell 1

Figure 8.5 shows the vertical resilient strains along the center line of the load. These resilient strain data can be input into the damage model to calculate the permanent deformation of the test sections. As it can be seen, the increase of aggregate layer thickness from 8 in. to 12 in. significantly reduces the vertical resilient strain values in aggregate layer as well as in the subgrade soil.

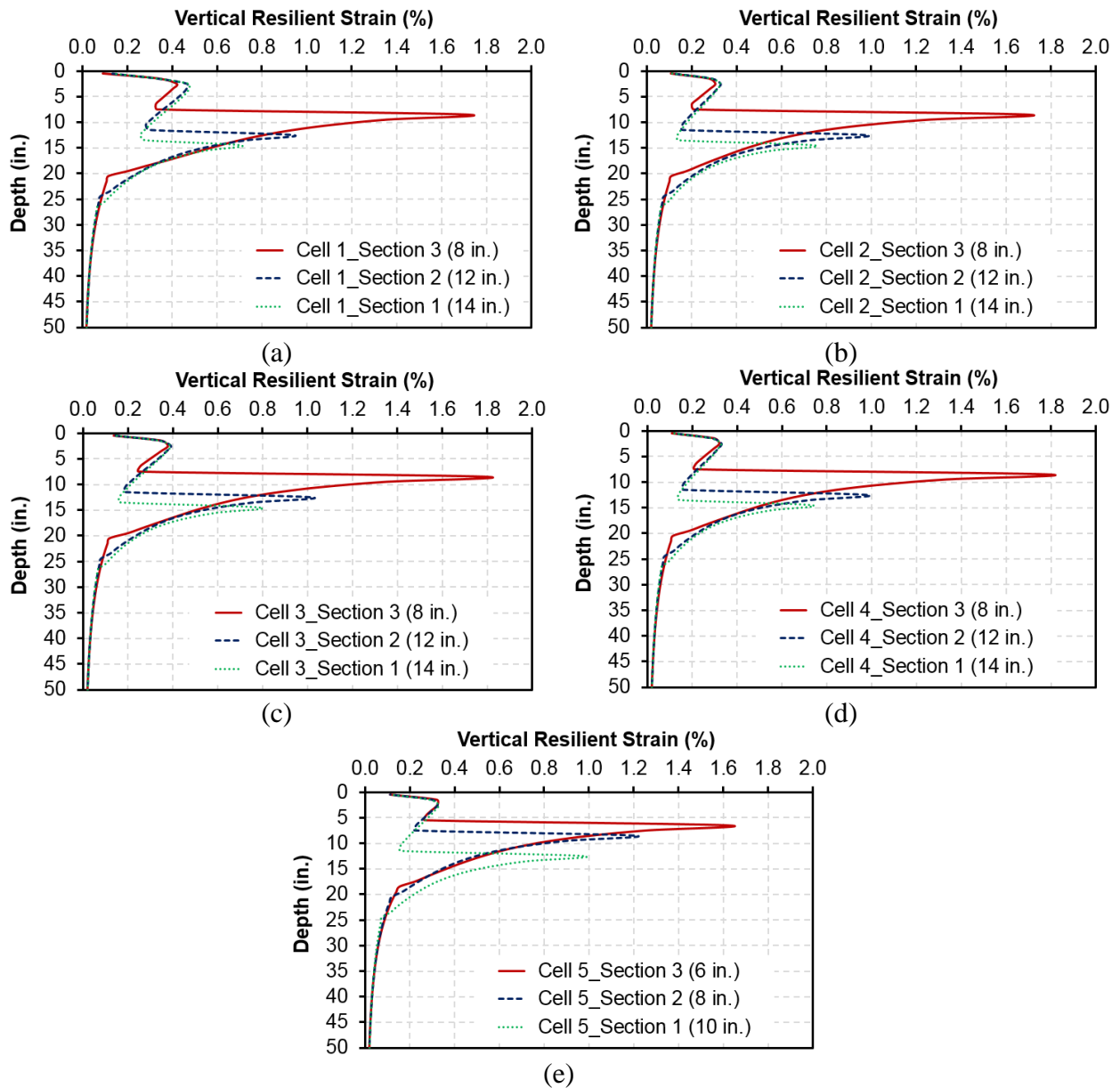


Figure 8.5 Vertical Resilient Strain Profile along the Center of the Wheel Load for: (a) Cell 1, (b) Cell 2, (c) Cell 3, (d) Cell 4, and (e) Cell 5

8.2.2 Permanent Deformation Predicted by the MEPDG Model

8.2.2.1 Calibration of the MEPDG Permanent Deformation Model

Note that the unified permanent deformation model developed in Chapter 7 for ICT aggregates with varying physical properties is limited to only one stress state that is commonly applied during the conditioning stage of the resilient modulus tests. Therefore, it would not be accurate enough, if not erroneous, to be extrapolated for use in much higher stress states experienced in the unsurfaced field full-scale test sections. Instead, the field validation is performed for the current MEPDG rutting model in this section. In this study, the total surface rutting was contributed by the aggregate layer and the underlying subgrade. No measurements were taken for deformation in each individual layer. The calibration of permanent deformation models was also limited by the number of tests, subgrade conditions, aggregate materials, and structural thickness.

From the vertical resilient strain data extracted from the response model, the average vertical resilient strain (ϵ_v) can be calculated for each layer of material in each section. Then, permanent strains accumulated in each layer can be calculated from the average resilient strain using the damage model. Since no external data is available for calibrating the factor k (in Equation 8.3) for each individual aggregate layer, one of the test sections of each cell was selected to determine the calibration factor. The permanent deformation parameters for subgrade soil also need to be calibrated since the repeated load triaxial test data for subgrade soil is also not available. Since Cell 3 survived the highest number of load repetitions as compared to other test cells, Section 1 of Cell 3 was selected for determining the permanent deformation parameters for subgrade soil (CBR=3%) as well as the calibration factor for aggregate material in Cell 3. The calibration was carried out by a trial-and-error procedure until the total surface permanent

deformation predicted in the calibration section matched the accumulated permanent deformation data as well as the profile data measured after the moving-wheel test. The root mean squared error (RMSE) as in Equation 8.3 was set as the objective function to be minimized. Note that the rutting damage model for subgrade soil in the MEPDG is modified by replacing the local and global calibration factors (see Equation 2.26) by a single calibration factor k (see Equation 8.3). The calibration factor k is used to account for the differences in the conditions between the soil sample under a cyclic triaxial test and the soil in the field under a moving-wheel load.

$$PD = k \varepsilon_v h_{soil} \left(\frac{\varepsilon_0}{\varepsilon_r} \right) e^{-\left(\frac{\rho}{N}\right)^\beta} \quad (8.3)$$

where PD is the permanent deformation in a particular layer, ε_v is the average vertical resilient strain along the center line of the model in this layer, h_{soil} is the thickness of this layer, and $\frac{\varepsilon_0}{\varepsilon_r}$, ρ , β are the material parameters obtained from the cyclic triaxial tests.

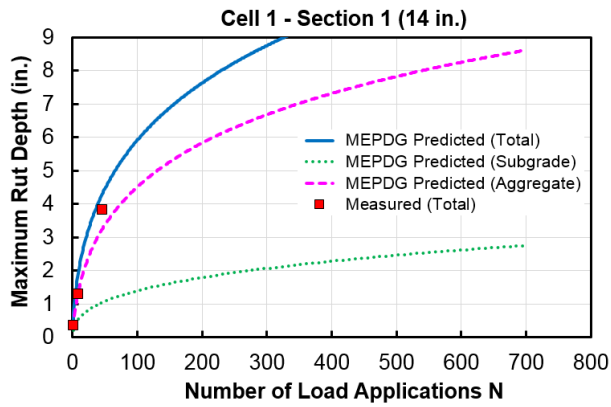
Table 8.3 lists the permanent deformation parameters calibrated for subgrade soils of CBR=3% in Cells 1 through 4 and of CBR=6% in Cell 5, respectively. Also listed are the calibration factor k values for individual aggregate materials in each of the five test cells. Section 1 (14 in. for Cells 1 through 4 and 10 in. for Cell 5) of each test cell was selected in this study for calibration purpose. The calibration factors for the aggregate layer as shown in Table 8.3 are considerably larger than 1. This is because the confining stress and cyclic stress applied to the sample in the repeated load triaxial test is not representative of the field stress level in an unsurfaced road subbase. For subgrade soil, k and $\left(\frac{\varepsilon_0}{\varepsilon_r} \right)$ was calibrated together. Tseng (1988) developed regression equations for estimating the model parameters for AC, granular materials, and subgrade soils and found that β was generally less than 0.2 while ρ ranged from 10^2 to 10^{26} .

Table 8.3 Calibrated Parameters for Rutting Prediction from Section 1 of Each Test Cell (based on Field Rutting Measurements)

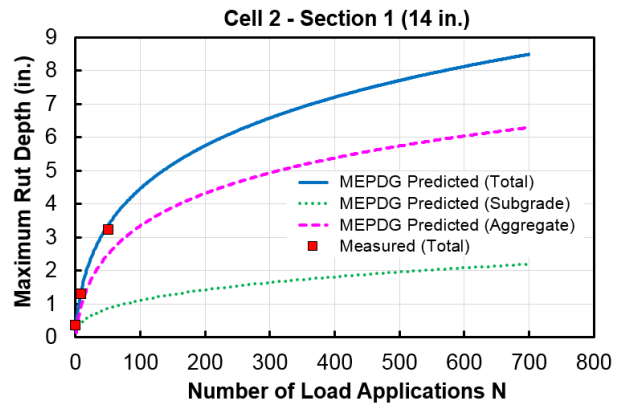
Subgrade Soil			Aggregate Subbase Layer (Section 1, 14 or 10 in.)				
Calibrated Parameters	Cell 1 ~ 4	Cell 5	Calibrated Parameters	Cell 1	Cell 2/5	Cell 3	Cell 4
$k \left(\frac{\epsilon_0}{\epsilon_r} \right)$	1.46E+5	4.27E+3	k	25.8	24.5	0.86	19.1
ρ	2.81E+22	5.07E+8					
β	0.045	0.103					

Figure 8.6 shows the calibration results in terms of predicted rut depth versus measured rut depth along the center line of the wheel load for each test section used for calibration. After well calibration, the trends shown in Figure 8.6 approximately agree with the key observations presented previously. That is, the total surface ruts in Cells 1 and 2 are contributed mainly by aggregate layers, whereas the crushed aggregate sections in Cells 3, 4, and 5 failed primarily due to subgrade rutting. Note that the calibration factor k is found to be zero for the aggregate layer in Cell 5, thus making the predicted total surface rut contributed only by subgrade deformation.

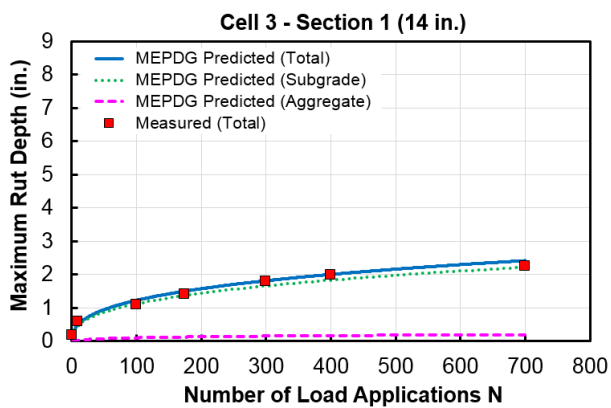
As an example, Figure 8.7 shows the transverse rut profile for Cell 3 which sustained the highest number of load repetitions. Note that the axisymmetric FE model used in this study can only predict symmetric transverse rut profile with respect to the center line of the wheel load, whereas the field measured transverse rut profile generally does not exhibit such symmetry.



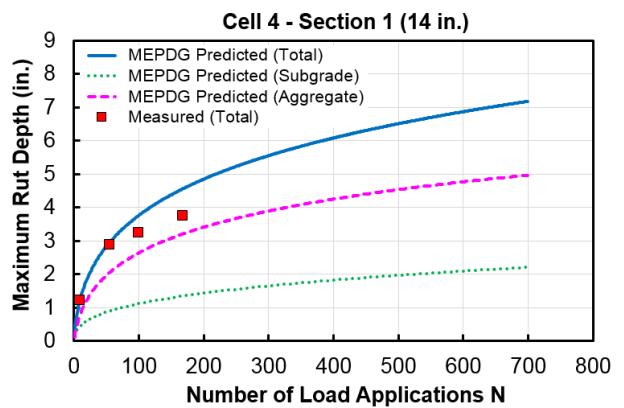
(a)



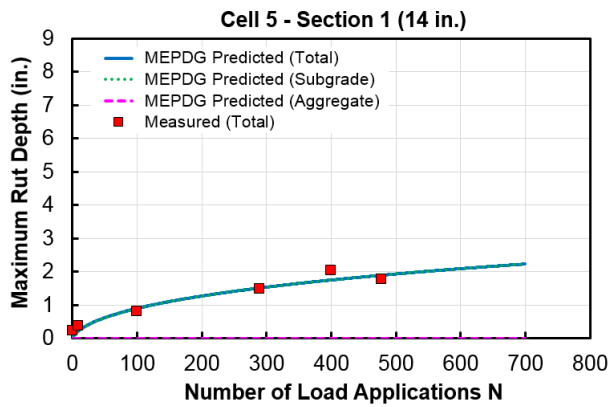
(b)



(c)

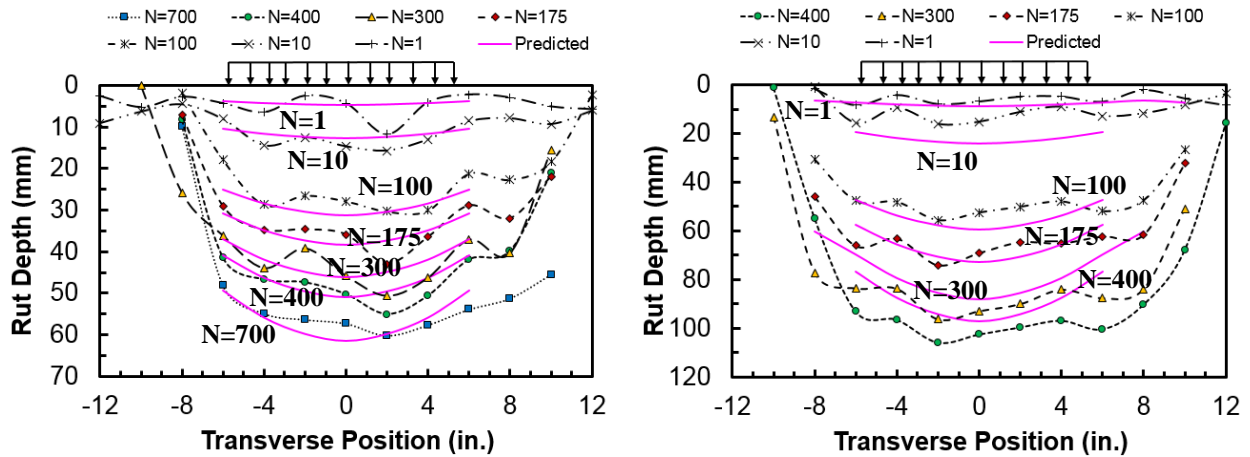


(d)



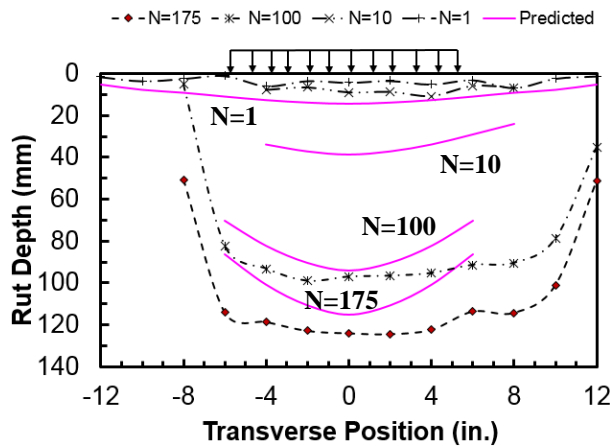
(e)

Figure 8.6 Measured Vs. Predicted Maximum Rut Depth for Test Sections Used for Calibration: (a) Cell 1, (b) Cell 2, (c) Cell 3, (d) Cell 4, and (e) Cell 5



(a)

(b)



(c)

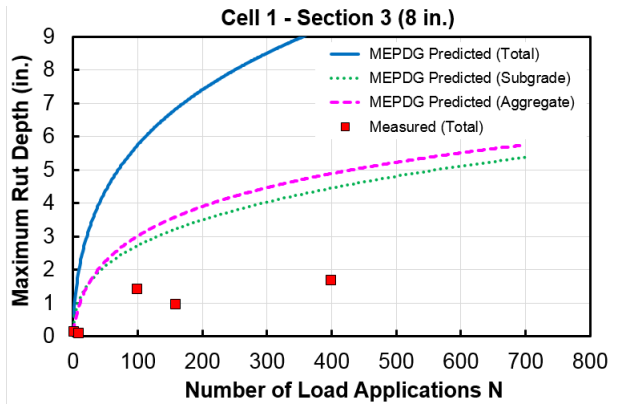
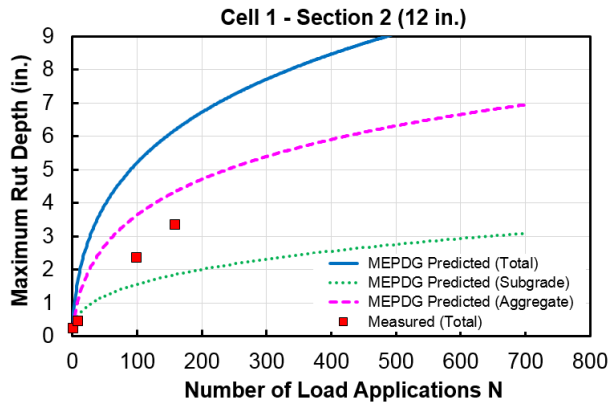
Figure 8.7 Transverse Rut Profile for Test Sections of Cell 3: (a) Section 1 (Used for Calibration), (b) Section 2, and (c) Section 3

8.2.2.2 Validation of the MEPDG Permanent Deformation Model

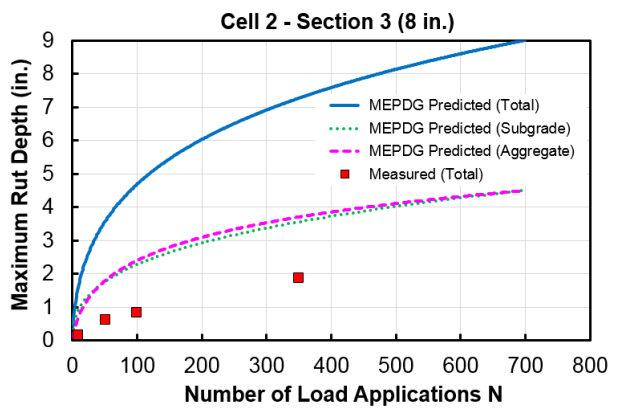
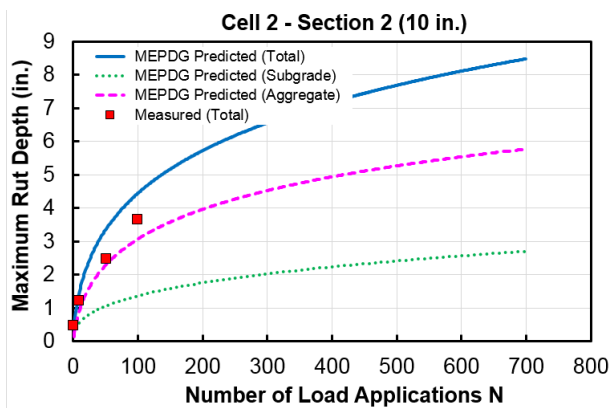
Following the same procedures described previously, the calibration factors listed in Table 8.3 were used to calculate the permanent deformation of other pavement sections in the APT that were not used for calibration purposes. Figure 8.8 and Figure 8.9 present the measured and predicted total surface permanent deformation along with the load repetitions. Overall, the

MEPDG rutting model overestimated the total surface permanent deformation for Cells 1 and 2, but underestimated the total surface permanent deformation for Cell 3. The prediction accuracy for Cells 4 and 5 was found to be reasonably good. However, it is worth mentioning that the shift factors used for matching predicted and measured rut depth values were found to vary significantly among different sections (even for the same aggregate subbase material type) within the same test cell. This further indicates the necessity to locally calibrate the MEPDG rutting model for specific field conditions.

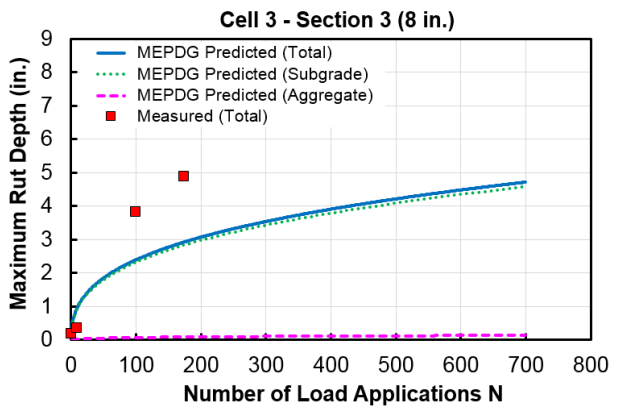
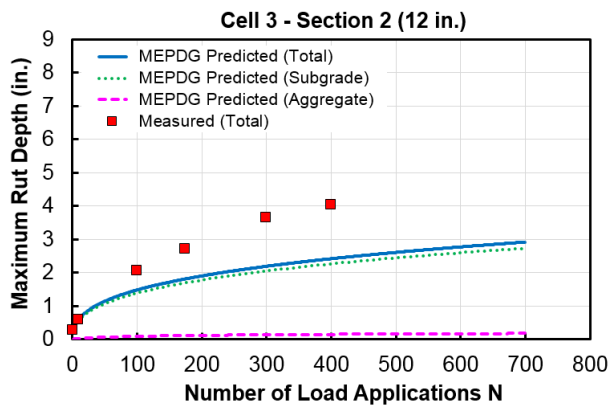
After careful calibration, the MEPDG rutting model appears to approximately distinguish the differences in rutting performance among the test sections, i.e., the predicted rank of the performance was consistent with the field observations made during APT trafficking. This could be most likely attributed to the fact that the effect of subgrade support was incorporated into the MEPDG model by means of vertical resilient strains which were extracted from the nonlinear finite element (FE) response model. In addition, the calibration factors even without physical meaning may also account for the subgrade support effects when they were calibrated to actual measurements. As contrary to traditional linear elastic programs (e.g., the MEPDG response module), the use of nonlinear FE response model with compaction-induced residual stress realistically considered in this study could be another contributing factor that results in better MEPDG rutting predictions. Without those efforts, the prediction accuracy of the MEPDG rutting model would be compromised due to its aforementioned deficiency.



(a)

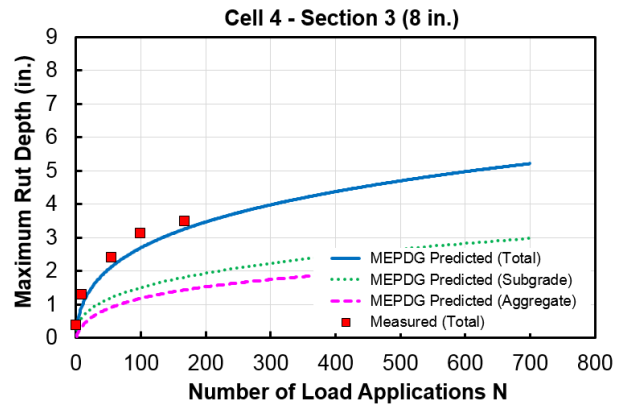
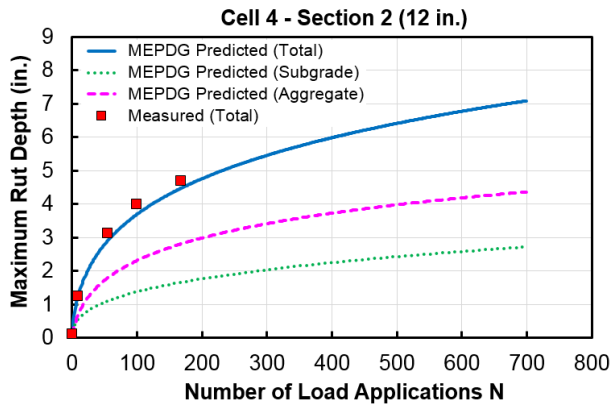


(b)

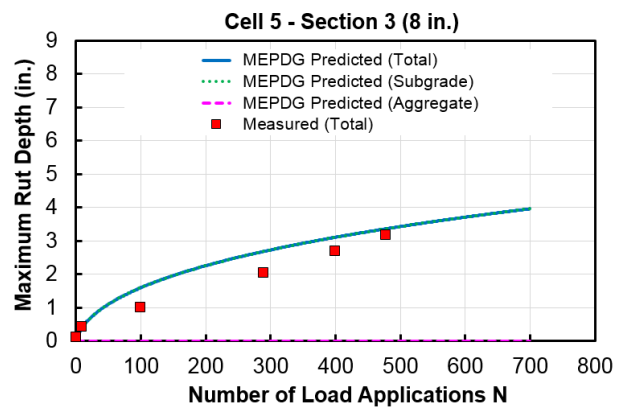
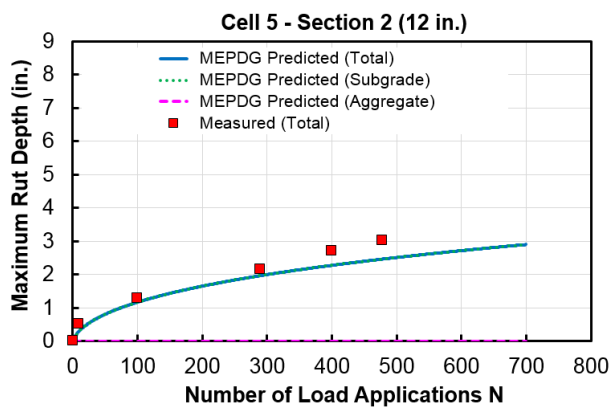


(c)

Figure 8.8 Measured Vs. Predicted Maximum Rut Depth for Test Sections Used in Validation: (a) Cell 1, (b) Cell 2, and (c) Cell 3



(a)



(b)

Figure 8.9 Measured Vs. Predicted Maximum Rut Depth for Test Sections Used in Validation: (a) Cell 4 and (b) Cell 5

8.3 Shear Stress Ratio Analysis for Interpreting Field Rutting Performance

The field-observed rutting performance of ICT full scale test sections that were constructed with different types of unbound aggregate subbase materials was interpreted and modeled using both laboratory and field data. The interpretation was conducted for different aggregate quality levels represented by resilient modulus and shear strength together. To be specific, the p-q stress diagrams were used to plot the stress paths induced by the moving wheel loads in field test sections, which were compared with the shear stress failure of aggregate subbase materials estimated from the laboratory testing. The fundamental shear properties (angle of internal friction and cohesion) of unbound aggregates were introduced using the Mohr-Coulomb failure criterion models reviewed in Chapter 2. The relative rutting damage of unbound aggregate subbase layers was estimated by the shear stress ratio (see Figure 7.29).

The four different types of aggregate subbase materials used to construct field test sections were tested in the laboratory for resilient modulus, shear strength, and permanent deformation behavior (Mishra, 2012). In the laboratory, the specimens were loaded either monotonically or cyclically with relatively simple triaxial compressive stress conditions, whereas more complex stress conditions with varying magnitudes of vertical, horizontal, and shear stresses are induced by the moving vehicle wheels. To better understand both laboratory and full-scale experimental results, a shear stress ratio analysis was performed. The stress paths induced by the moving wheel load in the aggregate subbase layer were plotted in p-q stress diagrams, and later compared with the static shear stress failure of aggregate subbase materials of different quality levels.

The shear stress ratio analysis consisted of the following steps: (i) calculation of principal stresses in the aggregate subbase layer at different depths (Z) and longitudinal (X) locations of

the pavement; (ii) calculation of stress invariants I_1 and J_2 (see Equation 8.4) for each of the previously mentioned pavement locations; (iii) plotting the stress state of the pavement in a I_1 - J_2 stress diagram; and (iv) calculation of the shear stress ratio by using the peak calculated stress condition of the pavement at different depths and the shear failure stress condition of the aggregate subbase. Each test section was modeled using as-constructed layer thicknesses in the GT-PAVE, a validated nonlinear finite element program (Tutumluer, 1995).

$$I_1 = \sigma_1 + \sigma_2 + \sigma_3$$

$$J_2 = \frac{1}{6} \left[(\sigma_1 - \sigma_2)^2 + (\sigma_2 - \sigma_3)^2 + (\sigma_1 - \sigma_3)^2 \right] \quad (8.4)$$

In the pavement model, the stresses were calculated at four different depths (z-axis) measured from the top of the aggregate subbase (i.e., 18.75%, 37.50%, 56.25%, and 75% of the total layer thickness, respectively), and at several longitudinal positions (x-axis), ranging from 0 mm (directly under the wheel), where the stress magnitude reaches a peak, to 40 in. (1000 mm) where the stress is approximately zero. The other longitudinal positions where the stresses were calculated were 2 in. (50 mm), 4 in. (100 mm), 6 in. (150 mm), 8 in. (200 mm), 10 in. (250 mm), 12 in. (300 mm), 16 in. (400 mm), and 20 in. (500 mm), as depicted in Figure 8.10. At each X-Z location, the six components of the stress tensor and the three principal stresses (σ_1 , σ_2 , and σ_3) were calculated and converted to I_1 and J_2 stress invariants of the stress tensor, using Equation 8.4. Note that the soil mechanics sign convention was adopted for the calculations, in which compressive stresses are positive and tensile stresses are negative. σ_1 , σ_2 , and σ_3 are the major, intermediate, and minor principal stresses, respectively.

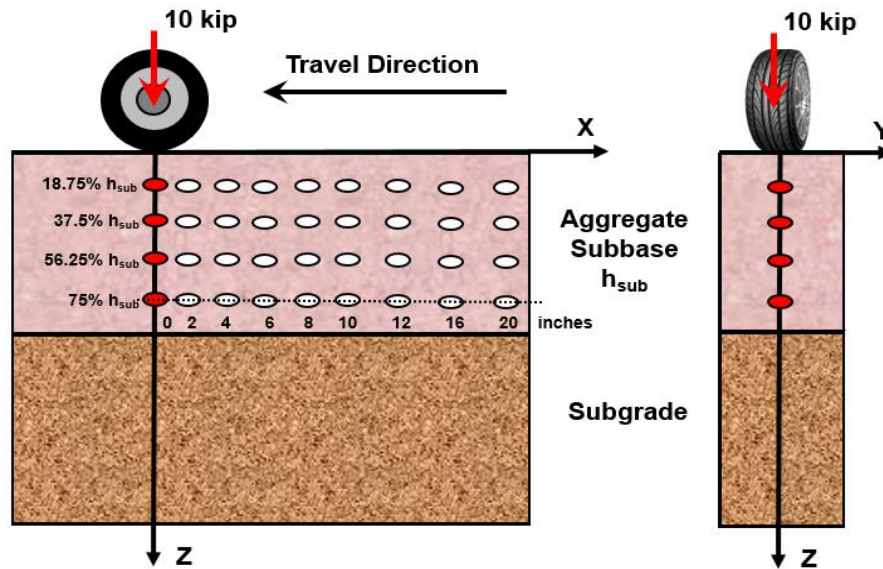


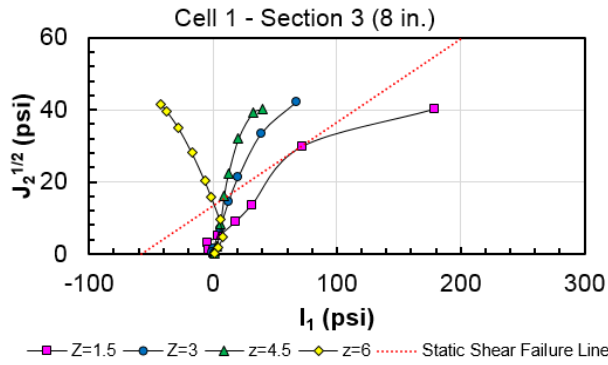
Figure 8.10 Schematic Illustrations of the Locations for Calculating Stress Path for Moving Wheel at Different Pavement Depths

For illustration purpose, Figure 8.11 depicts the calculated stress paths at the four different depths for Section 3 (8 in. thick aggregate subbase) of each test cell. The curves were plotted by connecting each of the points that represent the stress condition of the pavement at different longitudinal (X) distances. It can be clearly seen that unlike the simpler straight-line paths applied in the laboratory tests, those stress paths are curved, indicating the more complex stress conditions applied in the real pavements. It is worth noting that the stress paths calculated in this study did not consider other effects that could yield even more complex loading conditions, such as the non-uniform contact stress between tires and pavement surface and the dynamic load applied by the wheels. Note that negative tensile stresses were predicted near the bottom of aggregate subbase layer, as indicated by the stress paths curved towards the left half axis in Figure 8.11. This could possibly be due to the weak support of the underlying subgrade (CBR=3%). Further, nonlinear isotropic analyses alone, as adopted in this study, generally do not result in tensile stresses low enough to be considered admissible in the granular layer (Tutumluer,

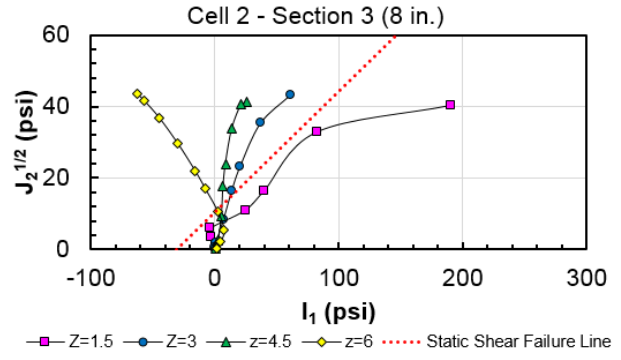
1995). To achieve drastic reductions in the predicted horizontal tension, nonlinear cross-anisotropy analyses need to be performed instead.

The static shear failure of those different aggregate materials, obtained from laboratory rapid shear strength (triaxial compression) tests, was indicated as red dashed lines in Figure 8.11 as well and compared with the stress state of the aggregate subbase layers. Note that it would not be appropriate to compare static shear failure against other stress paths than the one calculated at $x=0$. According to the findings made in Chapter 7, if the shear stress to strength ratio is low, the aggregate subbase will develop some plastic deformation for a finite number of load repetitions, but the response will remain essentially resilient after the initial loading. Conversely, if the stress ratio increases beyond a stress ratio limit, the plastic deformation will accumulate rapidly until rutting failure. Therefore, the shear stress ratio could be considered as an approximate measure of the relative damage that will result from repeated load applications.

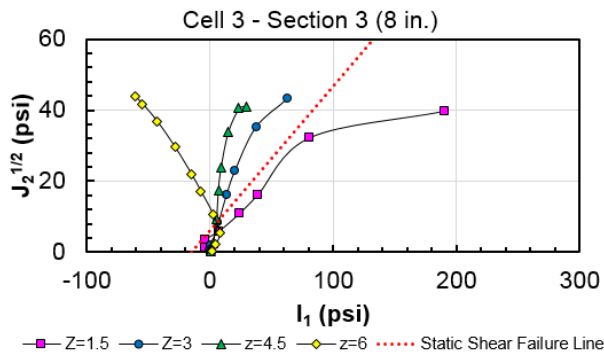
According to Figure 8.11, uncrushed aggregates in Cell 1 and crushed limestone with low fines content are expected to experience internal shear failure, as indicated by the high shear stress ratio approaching or greater than 1. This agrees well with field trenching observations as described in Chapter 3. Therefore, as compared to MEPDG rutting model predictions, the use of shear stress ratio can more realistically represent the shear failure-induced rutting development in unbound aggregates. The proper consideration of the applied stress state relative to the shear strength is critical in understanding and accurately predicting the rutting accumulation in unbound aggregate layers.



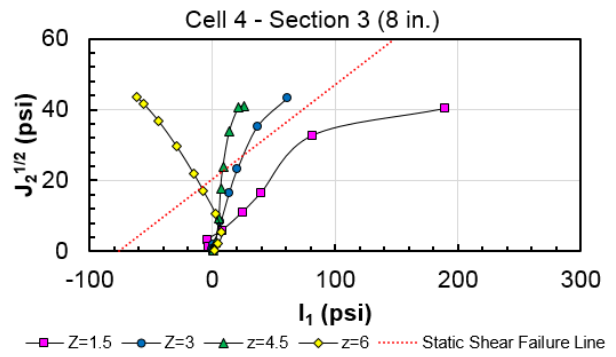
(a)



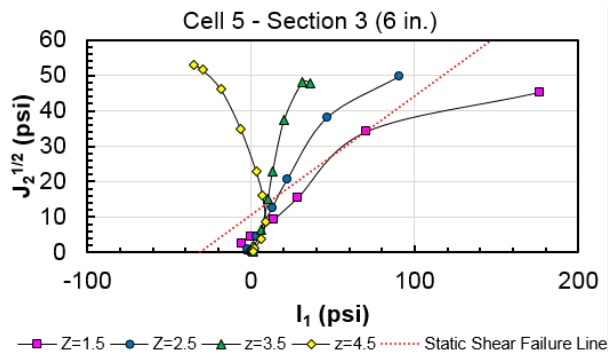
(b)



(c)



(d)



(e)

Figure 8.11 Stress Path Induced by Moving Wheel at Different Pavement Depths for ICT Full-scale Test Sections

8.4 Summary

This chapter presented the field validation of three permanent deformation models, i.e., the original Tseng and Lytton model, the current MEPDG rutting model, and the unified model developed in this thesis study, for unbound granular base/subbase materials by using rutting measurements from full-scale accelerated pavement testing (APT). A method to determine the criterion of shear strength of unbound granular base/subbase materials is also established. By following this method, the expected pavement rutting during design service life should not exceed the maximum allowable one, provided that the shear strength of unbound base/subbase materials meet such established criteria.

The accumulated rut depths from actual measurements at different combinations of layer material and thickness were compared with the predicted rut depths from different rutting models. Nonlinear FE models of the NAPTF test sections and the University of Illinois unsurfaced pavement test sections was developed and used to predict the stress and strain responses in the mid-depth of the unbound aggregate layers/sub-layers. The proposed unified model predicted the measured rut depth reasonably accurately. It was found that the shift factors used for P209 or P154 layers are approximately the same, further indicating the capability of the proposed to capture the stress sensitivity in predicting rut depth. As compared to the original prediction made by Kim (2005), the permanent deformation prediction generated by the proposed two-stage permanent strain model is much closer to the field measured values. Considering the rutting depth accumulated during the primary stage for the NAPTF test sections is relatively small as compared to long-term rutting depth accumulated during the secondary stage and up to failure, it is reasonable to use the proposed stable permanent strain rate model for predicting rutting depth up to the initiation of the tertiary stage.

The unified permanent deformation model developed for ICT aggregates with varying physical properties is limited to only one stress state that is commonly applied during the conditioning stage of the resilient modulus tests. Therefore, it would not be accurate enough, if not erroneous, to be extrapolated for use in much higher stress states experienced in the unsurfaced field full-scale test sections. Instead, the field validation is performed for the current MEPDG rutting model in this section. The shift factors used for matching predicted and measured rut depth values were found to be different among different sections. This further indicates the necessity to locally calibrate the MEPDG rutting model for specific field conditions. Nevertheless, the calibrated MEPDG model was able to approximately distinguish the difference in performance among the test sections, i.e., the predicted rank of the performance was consistent with the field observations made during APT trafficking. This could be possibly attributed to the inclusion of subgrade support effect, as well as to the use of nonlinear FE response model with compaction-induced residual stress realistically considered.

Chapter 9 Conclusions, Findings, and Recommendations

The research work described in this thesis focused on the effects of material properties affecting the mechanical behavior of unbound aggregate layers. The resilient modulus (M_R), shear strength, and permanent deformation resistance were evaluated as mechanistic response and performance indicators through experimental investigations and numerical simulations for the development/recommendation of performance-based unbound aggregate material specification guidelines. Three different methodologies were employed to achieve the study objective: (i) laboratory data analysis to link physical and mechanical properties of unbound aggregate materials to pavement response and performance; (ii) an image-aided discrete element method (DEM) modeling approach for engineering the aggregate shape and gradation properties for improved shear strength (or rutting resistance behavior); and (iii) a unified approach to permanent deformation (or rutting) prediction of unbound aggregate layers based on shear strength. Based on all these methodologies successfully employed, recommendations for improving material specifications for unbound aggregates used in conventional flexible pavements were presented. The conclusions of this study, detailed research findings and recommendations for future research are summarized next.

9.1 Conclusions

In accordance with the overall objective stated in Chapter 1, this dissertation study has reached the following conclusions. Aggregate shape properties properly quantified using imaging techniques need to be included in material property characterization in order to achieve more accurate mechanistic response and performance predictions of unbound aggregate layers. The use of imaging quantified aggregate shape indices significantly improved prediction

accuracy of both resilient modulus and shear strength models. Optimal aggregate packing configurations may exist to achieve desired shear strength properties when coarse aggregates form a strong skeleton to transmit external loads and fine aggregate materials fill the air voids in between coarse aggregate particles to achieve stability. The concept of the gravel-to-sand (G/S) ratio, identified from experimental observations and further verified by discrete element based packing simulation results, can be used as an effective means to evaluate and design such optimal aggregate packing configurations. The rutting accumulation is found to have a strong dependence on the applied stress level in relation to shear strength. The use of the shear stress to strength ratio term proves to be indispensable for accurately predicting unbound aggregate rutting depths.

9.2 Detailed Research Findings

The following detailed findings were obtained/reconfirmed from the research tasks described in this thesis:

- (1) A good correlation between aggregate shape properties and resilient modulus exists. Aggregates with high angularity index (AI) and surface texture (ST) index properties were found to have greater resilient moduli in comparison to aggregates with low AI and ST values (i.e., rounded particles with smooth surface texture). Interestingly, rounded aggregates exhibited a well-defined peak shear strength behavior, which could be influenced by their gradation properties and achieved specimen densities.
- (2) Unbound aggregate resilient modulus properties should not be used alone to predict aggregate base course performance, which is mainly governed by rutting potential in the field. Instead, laboratory permanent deformation tests should be conducted for evaluating rutting potentials of unbound base/subbase course materials.

- (3) Statistical analysis and reliability based sensitivity analysis were performed based on the developed model for estimating M_R . It was concluded that the complex maximum dry density (γ_{\max}^2 / P_{40}), coefficient of curvature (C_c), and relative moisture content ratio (ω / ω_{opt}) have the most important contributions to the resilient modulus behavior, and that the resilient modulus behavior is most sensitive to the variability in the distribution of coefficient of curvature (C_c) and relative moisture content ratio (ω / ω_{opt}). This revealed the significance of controlling gradation and moisture conditions to achieve proper resilient modulus behavior.
- (4) The effects of unbound aggregate quality on conventional flexible pavement performance were also investigated with a carefully designed comprehensive sensitivity analysis matrix of layer thicknesses and mechanistic design moduli. For low-volume roads in Minnesota, using locally available and somewhat marginal materials may be quite cost-effective provided that the 20-year design traffic level would not exceed 1.5 million ESALs. A high quality, stiff granular subbase was found to exhibit a bridging effect that better protected the subgrade and offset some detrimental effects of low aggregate base stiffness on rutting performance. As a result, the use of marginal quality locally available materials as aggregate base materials could be justified in some cases.
- (5) For the MnDOT database samples studied, the highest shear strength was reached around optimal gravel-to-sand (G/S) ratio of 1.6 where void spaces enclosed by the coarse aggregate fraction were probably filled completely by the sand size particles and fines.

- (6) There was inconclusive evidence of an apparent modulus-strength relationship which suggested incorporating a limiting working shear stress to strength ratio to avoid shear failure in base and especially subbase courses.
- (7) The DEM packing simulations using different gradations and particle shape were performed. Results of DEM simulations indicated that #4 sieve (or 4.75-mm sieve) could be regarded as the breaking sieve size that separated the coarse aggregate skeleton fraction and void-filling fine fraction for the MnDOT CL-6 gradation band. This further confirms that the concept of gravel-to-sand ratio, which uses the 4.75 mm sieve as the breaking sieve size, appears to be reasonable for typical Minnesota aggregate gradations studied.
- (8) Based on the DEM modeling approach, current unbound permeable aggregate base (PAB) material gradations were further engineered by optimizing the particle contact and packing characteristics. To maximize the coordination number, the optimal unbound PAB gradation should be close to the upper bound at the 19-mm sieve and be close to the mid-range at the 9.5-mm sieve. The optimal gradation predicted by the gravel-to-sand (G/S) ratio was found to agree more closely with the DEM simulation results that used realistic particle shapes, when compared to that predicted by the packing theory based analytical gradation framework using spherical particles only.
- (9) DEM simulations were performed on different gradations with varying G/S ratio values. The G/S ratio around 1.6 resulted in the highest coordination number due to the achieved densest packing (indicated by the lowest porosity). Therefore, the optimal G/S ratio of around 1.6 observed from experimental results agrees well with DEM simulation using 3D polyhedral particles with realistic aggregate shape.

- (10) Based on comparing results of both the original Tseng and Lytton model and the current MEPDG rutting model with the laboratory repeated load triaxial test results, the need for further enhancement of both models became obvious. Rational modifications of the models contained in the Pavement ME Design were developed.
- (11) Both the resilient and plastic responses of different aggregate materials to repeated loading under various dynamic stress states and aggregate physical conditions were analyzed concurrently from shakedown perspectives to investigate any correlation between plastic strain and resilient modulus. Established poor correlations confirmed resilient modulus alone could lead to misleading characterization of unbound aggregates for use in pavement applications; instead, resilient modulus and permanent deformation need to be examined together.
- (12) A new numerical perspective to degradation, namely the “degradation stiffness model”, was introduced to predict the progressive plastic deformation of unbound pavement layers under long-term repeated loading. By using the proposed models, the permanent deformation characteristics of unbound pavement layers under repetitive loading can be realistically predicted using a mechanistic framework, as contrary to the current empirical or semi-empirical methods.
- (13) A stable dependency of permanent strain rate on the variables characterizing the dynamic stress states induced by moving wheel loads was observed. An analytical model for mathematically expressing such a dependency was developed. Analogous to the concept of the Mohr-Coulomb failure envelope, the permanent deformation resistance envelopes were defined by these Mohr circles representing all the possible stress states that caused the specified permanent strain rate condition. They are

- potentially useful in ranking and properly selecting different unbound pavement layer materials for use in specific traffic levels and site conditions, i.e., the rutting potential based on the shakedown theory is evaluated simultaneously in relation to a potential shear failure.
- (14) A unified approach to rutting prediction was developed to predict permanent deformation accumulation with a high degree of confidence. This unified rutting model effectively takes into account various aggregate physical properties and field stress states induced by moving wheel loads and thus can be applied with greater confidence to a wider range of conditions. Good agreement between model predictions and laboratory permanent deformation test results was achieved by using the developed unified models.
- (15) The accumulated rut depths from actual measurements at different combinations of layer material and thickness were compared with the predicted rut depths from different rutting models. The proposed unified model predicted the measured rut depth reasonably accurately.
- (16) The field validation was performed for the current MEPDG rutting model. It shows the necessity to locally calibrate the MEPDG rutting model for specific field conditions. The importance of the inclusion of subgrade support effect, as well as the use of nonlinear FE response model with compaction-induced residual stress was highlighted.
- (17) The shear stress ratio concept was successfully applied to interpret field rut depth measurements on full-scale unsurfaced aggregate test sections.

9.3 Recommendations for Future Research

Based on utilizing the advanced statistical analysis and numerical modeling procedures and relying on laboratory repeated load triaxial test results, future research should further investigate the following areas:

- (1) The linkages between aggregate physical properties and mechanical properties can be further improved by resorting to advanced techniques such as Artificial Neural Network (ANN) and Gene Expressing Programming algorithms.
- (2) Other image-aided DEM simulations can be performed using different gradation design alternatives to study the gradation effects on shear strength behavior more thoroughly. DEM simulations of triaxial compression tests also incorporating dynamic compaction forces can be performed to investigate the shear strength behavior affected by packing and interlocking characteristics of aggregate skeleton. For example, geogrid-aggregate interlock can be studied this way for quantifying reinforcement benefits.
- (3) The methodologies presented in this dissertation can be further extended to establish aggregate gradation and shape property optimization framework for aggregate functional classification and improved material specification development.
- (4) While not explicitly incorporated into the developed rutting models, the stress history effects are demonstrated as an important factor governing the field rutting accumulation and need to be studied in the future. This is evidenced by the laboratory observed permanent deformation-load repetition trends following the power-law relationship, as contrary to the field measured rutting depth increasing with an approximate linear trend. This is because; the FAA field test sections were subjected

to the initial application of considerable cycles of aircraft gear loadings prior to the APT loading.

References

- AASHTO (1999). Standard Method of Test for Determining the Resilient Modulus of Soils and Aggregate Materials. Rep. No. AASHTO T 307, American Association of State Highway and Transportation Officials.
- AASHTO T307-99 (2002). “Determining the Resilient Modulus of Soils and Aggregate Materials.” Standard Specifications for Transportation Materials and Methods of Sampling and Testing, 20th Edition, AASHTO, Washington D.C.
- Achmus, M., Kuo, Y.-S., and Abdel-Rahman, K. (2009). Behaviour of Monopile Foundations under Cyclic Lateral Load. *Computer and Geotechnics*, 36(5), pp. 725–735.
- Agrawal, S. (2004). FAA’s Pavement Research Program. Presented at the 9th Plenary Meeting of U.S.- Japan Science & Technology Experts Meeting, May.
- Ahlvin, R.G., Ulery, H.H., Hutchinson, R.L., and Rice, J.L. (1971). Multiple-Wheel Heavy Gear Load Pavement Tests. Vol. 1: Basic Report, Technical Report No. AFWL-TR-70- 113, U.S. Army Engineer Waterways Experiment Station, Vicksburg, Mississippi.
- Ahn, J., Oh, J., and Shin, H. (2013). Analysis of Permanent Deformation under Repetitive Load Based on Degraded Secant Modulus. *Journal of the Korean Geotechnical Society*, Vol. 29, No. 2, pp. 15-21.
- Allen, J. (1973). The effect of non-constant lateral pressures of the resilient response of granular materials. PhD thesis, University of Illinois at Urbana-Champaign, Urbana, IL.
- Alsaleh, M. (2004). Numerical Modeling for Strain Localization in Granular Materials Using Cosserat Theory Enhanced with Microfabric Properties. Ph.D. Thesis, Louisiana State University, Baton Rouge, LA.

- Alsaleh, M., Voyiadjis, G., and Alshibli, K. (2006). Modeling Strain Localization in Granular Materials Using Micropolar Theory: Mathematical Formulations. *Int. J. Numer. Anal. Methods Geomech.*, 30 (15), pp. 1501–1524.
- Alsaleh, M.I., Alshibli, K.A., and Voyiadjis G.Z. (2004). On the Bridging of Length Scales and the Behavior of Granular Materials. *Proceedings of the GEO Jordan 2004, ASCE GPP.*
- Alshibli, K.A. and Alsaleh, M.I. (2004). Characterizing Surface Roughness and Shape of Sands Using Digital Microscopy. *ASCE Journal of Computing in Civil Engineering*, 18(1), pp. 36-45.
- Amer, A.M. and Awad, A.A. (1974). Permeability of Cohesionless Soils. *J. Geotech. Eng. Div., Am. Soc. Civ. Eng.*, 100(12), pp. 1309–1316.
- Antony, S.J. and Kruyt, N.P. (2009). Role of Interparticle Friction and Particle-Scale Elasticity on Shear Strength Mechanism in Three Dimensional Granular Media. *Physical Review E*, 79, 031308.
- Applied Research Associates (ARA), Inc. (2004). Development of the 2002 Guide for the Design of New and Rehabilitated Pavement Structures. Final Report and Software (Version 0.70) NCHRP Project 1-37A, Transportation Research Board, Washington D.C., April.
- Arika, C.N., Canelon, D.J., and Nieber, J.L. (2009). Subsurface Drainage Manual for Pavements in Minnesota. Final Report MN/RC 2009-17, Minnesota Department of Transportation, St. Paul, MN.
- Arnold, G.K., Dawson, A.R., Hughes, D., Werkmeister, S., and Robinson, D. (2002). Serviceability Design of Granular Pavement Materials. *Proc. 6th Int. Conf. Bearing Capacity of Roads, Railways and Airfields, Lisbon, Vol. 2*, pp. 957-966.

- ASTM Standard D2487-11 (2011). Standard Practice for Classification of Soils for Engineering Purpose (Unified Soil Classification System). ASTM International, West Conshohocken, PA, DOI: 10.1520/D2487-11, www.astm.org.
- Barksdale, R.D. (1971). Compressive Stress Pulse Times in Flexible Pavements for Use in Dynamic Testing. Highway Research Record No. 345, Highway Research Board.
- Barksdale, R.D. (1972). Laboratory Evaluation of Rutting in Base Course Materials. Proc., 3rd Int. Conf. on Struct. Des. of Asphalt Pavements, pp. 161–174.
- Barksdale, R.D., Brown, S.F., and Chan, F. (1989). Potential Benefits of Geosynthetics in Flexible Pavements. NCHRP Report 315, Transportation Research Council, Washington, D.C.
- Barksdale, R.D., Pollard C.O., Siegel, T., and Moeller, S. (1992). Evaluation of the Effect of Aggregate on Rutting and Fatigue of Asphalt. Technical Report FHWA-AG-92-8812, Georgia Department of Transportation, Atlanta, GA.
- Bayomy, F. (1982). Development and Analysis of a Cement Coating Technique: an Approach Towards Distress Minimization and Failure Delay in Flexible Pavements. PhD Dissertation, Ohio State Univ., Ohio.
- Bilodeau, J.-P., Dore, G., and Pierre, P. (2007). Erosion Susceptibility of Granular Pavement Materials. *International Journal of Pavement Engineering*, Vol. 8, No. 1, pp. 55-66.
- Bilodeau, J.-P., Dore, G., and Pierre, P. (2008). Gradation Influence on Frost Susceptibility of Base Granular Materials. *International Journal of Pavement Engineering*, Vol. 9, No. 6, pp. 397-411.
- Bilodeau, J.-P., Dore, G., and Pierre, P. (2009). Pavement Base Unbound Granular Materials Gradation Optimization. In *Proceedings of the 8th International Conference on the*

- Bearing Capacity of Roads, Railways and Airfields, Volume 1, Taylor & Francis Group, London, UK, pp. 145-154.
- Boyce, J.R. (1980). A Nonlinear Model for the Elastic Behavior of Granular Materials under Repeated Loading. International Symposium on Soils under Cyclic and Transient Loading, Swansea.
- Brown, S.F. and Brodrick, B.V. (1999). 25 years experience with the pilot-scale Nottingham Pavement Test Facility. Proc. Int. Conf. on Accelerated Pavement Testing. Reno, NV.
- Brown, S.F. and Chan F.W.K. (1996). Reduced Rutting in Unbound Granular Pavement Layers through Improved Grading Design. Proc. Inst. of Civil Engineers Transport, Vol. 117, pp. 40-49.
- Brown, S.F. and Hyde, A.F.L. (1975). Significance of Cyclic Confining Stress in Repeated-Load Triaxial Testing of Granular Material. Transportation Research Record No. 537, pp. 49–58.
- Buechler, S., Mustoe, G., Berger, J., and Mooney, M. (2012). Understanding the Soil Contact Problem for the LWD and Static Drum Roller by Using the DEM. Journal of Engineering Mechanics, 138(1), pp. 124-132.
- Bullen, F. (2003). Design and Construction of Low-Cost, Low-Volume Roads in Australia. Transportation Research Record No. 1819, pp. 173-179.
- California State Department of Transportation (1999). Standard Specifications. Sacramento, California.
- Cao, D. and Lin, H. (2010). Packing Model and Calculation Method of Aggregate in Asphalt Mixtures. Pavements and Materials: Characterization and Modeling Symposium at EMI Conference 2010, Los Angeles, California, United States, August 8-11, pp. 66-73.

- Carman, P.C. (1956). Flow of Gases through Porous Media. Butterworths Scientific Publications, London, UK.
- Ceylan, H. (2002). Analysis and Design of Concrete Pavement Systems Using Artificial Neural Networks. Ph.D. Dissertation, University of Illinois at Urbana-Champaign, Urbana, IL.
- Chan, F.W.K. (1990). Permanent deformation resistance of granular layers in pavements. PhD thesis, Dept. of Civ. Engrg., University of Nottingham, Nottingham, England.
- Chapuis R.P. (2004). Predicting the Saturated Hydraulic Conductivity of Sand and Gravel Using Effective Diameter and Void Ratio. *Can. Geotech. J.*, Vol. 41, pp. 787-795.
- Cheung, L.W. and Dawson A.R. (2002). Effects of Particle and Mix Characteristics on the Performance of some Granular Materials. *Transportation Research Record No. 1787*, pp. 90-98.
- Chen, Q., Abu-Farsakh, M., Voyiadjis, G., and Souci, G. (2013). Shakedown Analysis of Geogrid-Reinforced Granular Base Material. *ASCE Journal of Materials in Civil Engineering*, Vol. 25, No. 3, pp. 337-346.
- Chou, F.J. and Tutumluer, E. (2001). Stress Path Testing for A Proper Characterization of Unbound Aggregate Base Behavior. In CD-ROM Proceedings of the 80th Annual Meeting of the Transportation Research Board, Washington, D.C.
- Christopher, B.R., Schwartz, C., and Boudreau, R. (2006). Geotechnical Aspects of Pavements. Publication NHI-05-037, National Highway Institute, FHWA, U.S. Department of Transportation.
- Cook J.R. and Gourley, C.S. (2003). A Framework for the Appropriate Use of Marginal Materials. World Road Association-(PIARC), Technical Committee C12 Seminar, Mongolia.

- Crockford, W.W., Bendana, L.J., Yang, W.S., Rhee, S.K., and Senadheera, S.P. (1990). Modeling Stress and Strain States in Pavement Structures Incorporating Thick Granular Layers. Final Report, The Texas Transportation Institute, College Station, TX, pp. 57-71.
- CTL (1998). National Airport Pavement Test Machine – Instrumentation/Data Acquisition. A Report Prepared for US Army Corps of Engineers. Construction Technology Laboratories, Inc., Skokie, Illinois.
- Cunningham, C.N. (2009). Mechanical Response of Crushed Stone Mixtures. M.S. Thesis, Department of Civil Engineering, North Carolina State University, Raleigh, North Carolina.
- Dai, S., Boerner, D. and Isackson, C. (2007). Failure Analysis of Flexible Pavement Section on MnROAD. Transportation Research Board 86th Annual Meeting Compendium of Papers CD-ROM, Transportation Research Board, Washington D.C.
- Dai, S. and Zollars, J. (2002). Resilient Modulus of Minnesota Road Research Project Subgrade Soil. Transportation Research Record No. 1786, pp. 20-28.
- Dantu, P. (1957). Contribution a l'Etude Mechanique et Geometrique des Milieux Pulverulents. Proceedings of the 4th International Conference on Soil Mechanics, Vol. 1, London, UK.
- Dawson, A.R., Thom, N.H., and Paute, J.L. (1996). Mechanical Characteristics of Unbound Granular Materials as a Function of Condition. Flexible Pavements. Proc., Eur. Symp. Euroflex 1993, A. G. Correia, ed., Balkema, Rotterdam, The Netherlands, pp. 35–44.
- Djamarani, K.M. and Clark, I.M. (1997). Characterization of Particle Size Based on Fine and Coarse Fractions. Powder Technology, Vol. 93, Issue 2, pp. 101-108.

- Dobry, R., Ng, T.T., and Petrakis, E. (1989). Deformation Characteristics of Granular Soil in the Light of Particulate Mechanics. Proceedings of the 14th Conference on Geotechnics, Italian Geotechnical Association, Torino, Nov. 28-30.
- El abd, A., Hornyh, P., Breyse D., Denis, A., Chazallon, C. (2004). A Simplified Method of Prediction of Permanent Deformations of Unbound Pavement Layers. Proceedings of the 6th International Symposium on Pavements Unbound (UNBAR6), Nottingham, England.
- El-Badawy, S.M. and Witczak, M.W. (2007). Development of a Universal Permanent Strain Model for Subgrade Pavement Materials. In CD-ROM Proceedings of the 86th Annual Meeting of Transportation Research Board, Washington, D.C.
- Elliot, R.P. and Thornton, S.I. (1988). Resilient Modulus and AASHTO Pavement Design. Transportation Research Record No. 1196, pp. 116-124.
- El-Mitiny, M. R. (1980). Material Characterization for Studying Flexible Pavement Behavior in Fatigue and Permanent Deformation. Ph.D. Dissertation, Ohio State University, Columbus, OH.
- Erlingsson, S. (2012). Rutting Development in a Flexible Pavement Dstructure. Road Materials and Pavement Design, 13(2), pp. 218–234.
- Evans, T.M., Mojarrad, H., Cunningham, C., and Tayebali, A. (2009). Grain Size Distribution Effects in 2D Discrete Numerical Experiments. Proceedings of 2009 International Foundation Congress and Equipment Expo, pp. 58-65.
- Federal Aviation Administration (FAA) Advisory Circular AC 150/5370-10B, Standards for Specifying Construction of Airports. US Department of Transportation.

- Gabr, A.R. and Cameron, D.A. (2013). Permanent Strain Modeling of Recycled Concrete Aggregate for Unbound Pavement Construction. *ASCE Journal of Materials in Civil Engineering*, Vol. 25(10), pp. 1394-1402.
- Garg, N. (2003). Permanent Deformation Behavior of the Granular Layers Tested at the National Airport Pavement Test Facility. Presented at the 82nd Annual Transportation Research Board Meeting, Washington, D.C., January 14.
- Garg, N. and Thompson, M.R. (1997). Triaxial Characterization of Minnesota Road Research Project Granular Materials. *Transportation Research Record No. 1577*, pp. 27-36.
- Garg, N. and Thompson, M. (1998) Mechanistic-Empirical Evaluation of the Mn/Road Low Volume Road Test Sections Project IHR-535 Final Report, University of Illinois at Urbana-Champaign.
- Gervais, E.L., Hayhoe, G.F., and Garg, N. (2003). Towards a Permanent ACN Solution for 6-Wheel Landing Gear Aircraft. *Proceedings of the 2003 ASCE Airfield Pavement Specialty Conference*, Las Vegas, NV.
- Ghaboussi, J and Barbosa, R. (1990). Three-dimensional Discrete Element Method for Granular Materials. *International Journal for Numerical and Analytical Methods in Geomechanics*, Vol.14, pp. 451-72.
- Gidel, G., Breyse, D., Horny, P., Chauvin, J.J., and Denis, A. (2001). A New Approach for Investigating the Permanent Deformation Behavior of Unbound Granular Material Using the Repeated Load Triaxial Apparatus. *Bulletin des LCPC – 233 July – August*.
- Gomez-Ramirez, F. (2000) Characterizing Aircraft Multiple Wheel Load Interaction for Airport Flexible Pavement Design. Ph. D. Dissertation, University of Illinois, Urbana, IL.

- Gopalakrishnan, K. and Thompson, M.R. (2003). Rutting Study of NAPTf Flexible Pavement Test Sections. Presented at the 2003 ASCE Airfield Specialty Conference, ASCE, Sep. 21-24, Las Vegas, Nevada, USA.
- Gopalakrishnan, K. and Thompson, M.R. (2006). Assessing Damage to Airport Pavement Structure due to Complex Gear Loads. *Journal of Transportation Engineering*, 132(11), pp. 888-897.
- Gräbe, P.J. and Clayton, C.R.I. (2003). Permanent Deformation of Railway Foundations under Heavy Axle Loading. *Proceedings of the International Heavy Haul Association, Specialist Technical Session*, Dallas, Texas, USA.
- Gräbe, P.J. and Clayton, C.R.I. (2009). Effects of principal stress rotation on permanent deformation in rail track foundations. *ASCE Journal of Geotechnical and Geoenvironmental Engineering*, 135(4), pp. 555-565.
- Gräbe, P.J. and Clayton, C.R.I. (2014). Effects of Principal Stress Rotation on Resilient Behavior in Rail Track Foundations. *J. Geotech. Geoenviron. Eng.*, 140(2), 04013010.
- Gudehus, G. and Nübel, K. (2004). Evolution of Shear Bands in Sand. *Geotechnique*, 54(3), pp. 187–201.
- Gupta, S., Ranaivoson A., Edil T., Benson C., and Sawangsuriya A. (2007). Use of Taconite Aggregates in Pavement Applications. Final Report MN/RC-2007-11, Minnesota Department of Transportation, St. Paul, MN.
- Gupta, S., Singh, A., and Ranaivoson, A. (2005). Moisture Retention Characteristics of Base and Sub-base Materials. Technical Report MN/RC-2005-06, Minnesota Department of Transportation, Saint Paul, MN.

- Hashash, Y.M.A., Nezami, E., Zhao, D., and Ghaboussi, J. (2005). DBLOCK3D: A 3-D Discrete Element Analysis Code for Simulation of Granular Media and Soil-machine Interaction. NASA Workshop on Granular Materials in Lunar and Martian, Exploration, Kennedy Space Center, Florida.
- Hashem, B. and Zapata, C.E. (2013). Enhancement of the Permanent Deformation Model for Unbound Materials Used by Darwin-ME. In CD-ROM of the 92nd Annual Meeting of TRB, Washington, D.C.
- Hayhoe, G.F. and Garg, N. (2002). Subgrade strains measured in full-scale traffic tests with four- and six-wheel landing gears. Proc. FAA Airport Technology Transfer Conference, Atlantic City, NJ, USA, May 5-8.
- Haykin, S. (1999). Neural Networks: A Comprehensive Foundation. Prentice-Hall, Inc., New Jersey.
- Haynes, J.H. and Yoder, E.J. (1963). Effects of Repeated Loading on Gravel and Crushed Stone Base Material Used in the AASHTO Road Test. Highway Research Board Record No. 39, pp. 82–86.
- Hazen, A. (1930). Water Supply. American Civil Engineering Handbook, Wiley, New York, USA.
- Hecht-Nielsen, R. (1990). Neurocomputing. Addison-Wesley, New York.
- Hill, K., Yohannes, B., and Khazanovich, L. (2012). Unified Mechanistic Approach for Modeling Tests of Unbound Pavement Materials. Journal of Transportation Engineering, 138(9), pp. 1091-1098.
- Hornych, P., Kazai, A., and Quibel, A. (2000). Modeling A Full-Scale Experiment of Two Flexible Pavement Structures with Unbound Granular Bases. In Unbound Aggregates in

- Road Construction, Edited by A.R. Dawson, A.A. Balkema Publishers, Proceedings of the Unbound Aggregates in Roads (UNBAR5) Symposium, University of Nottingham, England, June 21-23, pp. 359-367.
- Huang, H. (2010). Discrete Element Modeling of Railroad Ballast Using Imaging Based Aggregate Morphology Characterization. Ph.D. Dissertation, University of Illinois at Urbana-Champaign, Urbana, IL.
- Huang, W., Nubel, K. and Bauer, E. (2002). Polar Extension of a Hypoplastic Model for Granular Materials with Shear Localization. *Mechanics of materials*, 34, pp. 563-576.
- Huang, Y. H. (1993). *Pavement Analysis and Design*, 1st edition, Prentice Hall, Englewood Cliffs, NJ, 805 pages.
- Huhtala, M. (2002). COST 337 – Unbound Granular Materials for Road Pavements, Proceedings of the 6th International Conference on the Bearing Capacity of Roads, Railways, and Airfields, Lisbon, Portugal.
- Huurman M. (1997). Permanent deformation in concrete block pavements, PhD Thesis, Delft University of Technology, pp. 119-125.
- Huurman, R. and Molenaar, A.A.A. (2006). Permanent Deformation in Flexible pavements with Unbound Base Course. *Transportation Research Record No. 1952*, pp. 31-38.
- Itani, S.Y. (1990). Behavior of Base Materials Containing Large-sized Particles. Ph.D. Thesis, Georgia Institute of Technology, School of Civil and Environmental Engineering.
- Johnston, I.W. (1985). The Strength of Intact Geomechanical Materials. *Journal of Geotechnical Engineering Division, ASCE*, Vol. 3(6), pp. 730-749.
- Jorenby, B.N. and Hicks, R.G. (1986). Base Course Contamination Limits. *Transportation Research Record No. 1095*, pp. 86-101.

- Kaloush, K. and Witczak, M.W. (2002). Tertiary Flow Characteristics of Asphalt Mixtures. *J. Asphalt Paving Technol.*, Vol. 71, pp. 248–280.
- Kalyoncuoglu, S.F. and Tigdemir, M. (2010). A Model for Dynamic Creep Evaluation of SBS Modified HMA Mixtures. *Journal of Construction and Building Materials*, 25(2), pp. 859-866.
- Kamal, M.A., Dawson, A.R., Farouki, O.T., Hughes, D.A.B., and Sha‘at, A.A. (1993). Field and Laboratory Evaluation of the Mechanical Behavior of Unbound Granular Materials in Pavements. *Transportation Research Record No. 1406*, pp. 88-97.
- Kasthurirangan G. (2004). Performance Analysis of Airport Flexible Pavements Subjected to New Generation Aircraft. Ph.D. Dissertation, University of Illinois at Urbana-Champaign, IL.
- Khedr, S. (1985). Deformation Characteristics of Granular Base Course in Flexible Pavement. *Transportation Research Record No. 1043*, pp. 131–138.
- Khogali, W.E. and Mohamed, E.H.H. (2004). Novel Approach for Characterization of Unbound Materials. *Transportation Research Record No. 1874*, pp. 38–46.
- Kim, I.T. (2005). Permanent Deformation Behavior of Airport Flexible Pavement Base and Subbase Courses. Ph.D. Dissertation, Department of Civil and Environmental Engineering, University of Illinois, Urbana, IL.
- Kim, W. and Labuz, J.F. (2007). Resilient Modulus and Strength of Base Course with Recycled Bituminous Material. Technical Report MN/RC-2007-05, Minnesota Department of Transportation, Saint Paul, MN.

- Kim, I.T. and Tutumluer, E. (2005). Unbound Aggregate Rutting Models for Stress Rotations and Effects of Moving Wheel Loads. Transportation Research Record No. 1913, pp. 41-49.
- Kim, I.T. and Tutumluer, E. (2006). Field Validation of Airport Pavement Granular Layer Rutting Predictions. Transportation Research Record No. 1952, pp. 48-57.
- Kim, M. (2007). Three-dimensional Finite Element Analysis of Flexible Pavements Considering Nonlinear Pavement Foundation Behavior. Ph.D. Dissertation, Department of Civil and Environmental Engineering, University of Illinois, Urbana, IL.
- Kim, M. and Tutumluer, E. (2009). Multiple Wheel-Load Interaction in Flexible Pavements. Transportation Research Record No. 2068, pp. 49-60.
- Kim, S.-H., Tutumluer, E., Little, N.L., and Kim, N. (2007). Effect of Gradation on Nonlinear Stress-Dependent Behavior of a Sandy Flexible Pavement Subgrade. Journal of Transportation Engineering, Vol. 133, No. 10, pp. 582-589.
- Knutson, R.M. and Thompson, M.R. (1977). Resilient Response of Railway Ballast. Transportation Research Record No. 651, pp. 31-39.
- Korkiala-Tanttu, L. (2008). Calculation Method for Permanent Deformation of Unbound Pavement Materials. VTT Publications 702, Espoo 2008.
- Kwon, J. (2007). Development of a Mechanistic Model for Geogrid Reinforced Flexible Pavements. Ph.D. Dissertation, Department of Civil and Environmental Engineering, University of Illinois, Urbana, IL.
- Lade, P.V. and Nelson, R.B. (1987). Modeling the Elastic Behavior of Granular Materials. International Journal for Numerical and Analytical Methods in Geomechanics, Vol. 11, pp. 521-542.

- Ledbetter, R.H. (1977). General Deformation (Elastic and Inelastic) and Stress Distribution Theory in Soils. Technical Report S-77-10, Soils and Pavements Laboratory, US Army Engineer Waterways Experiment Station, Vicksburg, Mississippi, 117 pages.
- Lee, S.J., Hashash, Y.M.A., and Nezami, E.G. (2012). Simulation of Triaxial Compression Test with Polyhedral Discrete Elements. *Computers and Geotechnics*, Vol. 43, pp. 92–100.
- Lekarp, F., and Dawson, A. (1998). Modeling Permanent Deformation Behavior of Unbound Granular Materials. *Constr. and Build. Mat.*, 12(1), pp. 9–18.
- Lekarp, F., Issacson, U., and Dawson, A. (2000a). State of the Art. I: Resilient Response of Unbound Aggregates. *Journal of Transportation Engineering*, 126(1), pp. 66-75.
- Lekarp, F., Issacson, U., and Dawson, A. (2000b). State of the Art. II: Permanent Strain Response of Unbound Aggregates. *Journal of Transportation Engineering*, 126(1), pp. 76-83.
- Liang, R.Y. (2007). Evaluation of Drainable Bases under Asphalt Pavements. Final Report FHWA/OH-2007/10, Ohio Department of Transportation, Columbus, OH.
- Lin, X. and Ng, T.T (1997). A Three-dimensional Discrete Element Model Using Arrays of Ellipsoids. *Géotechnique*, Vol. 47, No.2, pp. 319-329.
- Lindly, J., Townsend, J.T., and Elsayed, A. (1995). How Top-Size Affects the Resilient Modulus of Roadway Base Materials. *Engineering Journal of University of Qatar*, Vol. 8, pp. 127-138.
- Lira, B., Jelagin, D., and Birgisson, B. (2013). Gradation-based Framework for Asphalt Mixture. *Materials and Structures*, Vol. 46, pp. 1401-1414.

- Lourens, J.P. (1995). Towards Improved Understanding of Surfacing, Base, and Tyre Interaction for Low-Cost Pavement Design, South African Department of Transport, Chief Directorate Roads, Report No. RR 93/559, Pretoria, South Africa.
- LTPP (1996). Resilient Modulus of Unbound Granular Base/Subbase Materials and Subgrade Soils. Long-Term Pavement Performance P46.
- Lytton, R.L. (1995). Foundations and Pavements on Unsaturated Soils. First International Conference on Unsaturated Soils, Paris.
- Majidzadeh, K., Bayomy, F., and Khedr, S. (1978). Rutting Evaluation of Subgrade Soils in Ohio. Transportation Research Record No. 671.
- Maree, J.H. (1978). Design Parameters for Crushed Stone in Pavements. MS Thesis, University of Pretoria, South Africa.
- Masad, E., Al-Rousan, T., Button, J., Little, D.N., and Tutumluer, E. (2007). Test Methods for Characterizing Aggregate Shape, Texture, and Angularity. Final Report 555, Project 4-30A, National Cooperative Highway Research Program (NCHRP), Transportation Research Board, National Research Council, Washington, D.C.
- Meier, R. and Tutumluer, E. (1998). Uses of Artificial Neural Networks in the Mechanistic-Empirical Design of Flexible Pavements. Proc. Intl. Workshop on Artificial Intelligence and Mathematical Methods in Pavement and Geomechanical Engineering Systems. Florida International University, Florida, pp. 1-12.
- Mishra, D. (2012). Aggregate Characteristics Affecting Response and Performance of Unsurfaced Pavements on Weak Subgrades. Ph.D. Dissertation, Department of Civil and Environmental Engineering, University of Illinois, Urbana, IL.

- Mishra, D. and Tutumluer, E. (2012). Aggregate Physical Properties Affecting Modulus and Deformation Characteristics of Unsurfaced Pavements. *ASCE Journal of Materials in Civil Engineering*, 24(9), pp. 1144-1152.
- Mishra, D. and Tutumluer, E. (2013). Field Performance Evaluations of Illinois Aggregates for Subgrade Replacement and Subbase – Phase II. Final Report, Illinois Center for Transportation Project R27-81, University of Illinois at Urbana-Champaign, Urbana, IL.
- Moaveni, M., Wang, S., Hart, J.M., Tutumluer, E., and Ahuja, N. (2013). Evaluation of Aggregate Size and Shape by Means of Segmentation Techniques and Aggregate Image Processing Algorithms. *Transportation Research Record No. 2335*, pp. 50-59.
- Mohammad, L., Herath, A., Rasoulia, M., and Zhang, Z. (2006). Laboratory Evaluation of Untreated and Treated Pavement Base Materials from a Repeated Load Permanent Deformation Test. In CD-ROM of the 85th Transportation Research Board Annual Meeting, Washington, D.C.
- Molenaar, A.A.A. and Van Niekerk, A.A. (2002). Effects of Gradation, Composition, and Degree of Compaction on the Mechanical Characteristics of Recycled Unbound Materials. *Transportation Research Record No. 1787*, pp. 73-82.
- Monismith, C.L., Ogawa, N., Freeme, C.R. (1975). A Permanent Deformation Characteristics of Subgrade Soils due to Repeated Loading. *Transportation Research Record No. 537*, pp. 1-17.
- Morgan, J.R. (1966). The Response of Granular Materials to Repeated Loading. *Proceedings, Third Conference, Australian Road Research Board, Sydney*, pp. 1178-1192.

- Muhanna, A.S. (1994). A Testing Procedure and a Model for Resilient Modulus and Accumulated Plastic Strain of Cohesive Subgrade Soil. Ph.D. Dissertation, North Carolina State University, Raleigh, NC.
- Mulvaney, R. and Worel, B. (2002). MnROAD Cell 26 Forensic Investigation. Technical Report No. 2002-06, Minnesota Department of Transportation, Saint Paul, MN.
- Nezami, E.G., Zhao, D., Hashash, Y.M.A., and Ghaboussi, J. (2004). A Fast Contact Detection Algorithm for 3-D Discrete Element Method. *Computers and Geotechnics*, Vol. 31, pp. 575-587.
- NCHRP 1-26 (1990). Calibrated Mechanistic Structural Analysis Procedure for Pavements, NCHRP Project 1-26, Final Report, Phase I, TRB, National Research Council, Washington D.C.
- NCHRP (2003). Harmonized Test Methods for Laboratory Determination of Resilient Modulus for Flexible Pavement Design. Rep. No. NCHRP 1-28A, National Cooperative Highway Research Program, TRB, National Research Council, Washington D.C.
- NCHRP 01-53 (2014). Proposed Enhancements to Pavement ME Design: Improved Consideration of the Influence of Subgrade and Unbound Layers on Pavement Performance. Transportation Research Board, National Research Council, <http://apps.trb.org/cmsfeed/TRBNetProjectDisplay.asp?ProjectID=3625>, last accessed in Jan. 2014.
- NordFoU (2010). Pavement Performance Models. Part 2 Project Level.
- Oda, M. and Iwashita, K. (2000). Study on Couple Stresses and Shear Band Development in Granular Media based on Numerical Simulation Analyses. *International Journal of Engineering Science*, 38, pp. 1713–1740.

- Pan, T. (2006). Investigation of Coarse Aggregate Morphology Affecting Hot Mix Behavior Using Image Analysis. Ph.D. Dissertation, University of Illinois at Urbana-Champaign, Champaign, Illinois.
- Pan, T., Tutumluer, E., and Carpenter, S.H. (2005). Effect of Coarse Aggregate Morphology on Resilient Modulus of Hot Mix Asphalt. Transportation Research Record No. 1929.
- Pan, T., Tutumluer, E., and Anochie-Boateng, J. (2006). Aggregate Morphology Affecting Resilient Behavior of Unbound Granular Materials. Transportation Research Record No. 1952.
- Pappin, J.W. (1979). Characteristics of Granular Material for Pavement Analysis. PhD thesis, Dept. of Civ. Engrg., University of Nottingham, Nottingham, England.
- Parker, D.B. (1985). Learning Logic. Technical Report TR-47, Center for Computational Research in Economics and Management Science, Massachusetts Institute of Technology, Cambridge, MA.
- Paute, J.L., Hornych, P., Benaben, J.P. (1994). Comportement mécanique des graves non traitées. Bulletin de Liaison des Laboratoires des Ponts et Chaussées 190, pp. 27–38.
- Paute, J. L., Hornych, P., and Benaben, J. P. (1996). Repeated Load Triaxial Testing of Granular Materials in the French Network of Laboratoires des Ponts et Chaussées. Flexible Pavements, Proc., Eur. Symp. Euroflex 1993, A. G. Correia, ed., Balkema, Rotterdam, The Netherlands, pp. 53–64.
- Perez, I. and Gallego, J. (2010). Rutting Prediction of a Granular Material for Base Layers of Low-Traffic Roads. Construction and Building Materials, 24 (2010), pp. 340–345.

- Pezo, R.F. (1993). A General Method of Reporting Resilient Modulus Tests of Soils – A Pavement Engineer’s Point of View. In CD-ROM of the Transportation Research Board 72nd Annual Meeting, National Research Council, Washington D.C.
- Pumphrey, Jr., N. D., and Lentz, R. W. (1986). A Deformation Analysis of Florida Highway Subgrade Sand Subjected to Repeated Load Triaxial Tests. Transportation Research Record No. 1089, pp. 49-56.
- Puppala, A.J., Mohammad, L.N., and Allen, A. (1999). Permanent Deformation Characterization of Subgrade Soils from RLT Test. Journal of Materials in Civil Engineering, 11(4), pp. 274–282.
- Puppala, A.J., Chomtid, S., and Bhadriraju, V. (2005). Using Repeated-Load Triaxial Tests to Evaluate Plastic Strain Potentials in Subgrade Soils. Transportation Research Record No. 1913, pp. 86-98.
- Puppala, A.J. (2008). Estimating Stiffness of Subgrade and Unbound Materials for Pavement Design. NCHRP Synthesis 382, TRB, National Research Council, Washington, D.C.
- Qian, Y., Lee, S., Tutumluer, E., Hashash, Y.M.A., Mishra, D., and Ghaboussi, J. (2013). Discrete Element Method for Simulating Ballast Shear Strength from Large Triaxial Tests. Transportation Research Record No. 2374, pp. 126-135.
- Von Quintus, H. and Killingsworth, B. (1998). Analyses Relating to Pavement Material Characterizations and Their Effects on Pavement Performance. Federal Highway Administration Publication No. FHWA-RD-97-085, McLean, VA.
- Raad, L. and Figueroa, J.L. (1980). Load Response of Transportation Support Systems. Journal of Transportation Engineering Division, Vol. 106, No. TE1.

- Raad, L. and Minassian, G. (2005). The Influence of Granular Base Characteristics on Upper Bound Shakedown of Pavement Structures. *Road Mater Pavement*, 6, pp. 53-79.
- Rao, C. (2001). Development of 3-D Image Analysis Techniques to Determine Shape and Size Properties of Coarse Aggregate. Ph.D. Dissertation, University of Illinois at Urbana-Champaign. Champaign, Illinois.
- Rao, C, Tutumluer, E., and Kim, I.T. (2002). Quantification of Coarse Aggregate Angularity Based on Image Analysis. *Transportation Research Records No. 1787*, pp. 117-124.
- Rao, C., Pan, T., and Tutumluer, E. (2003). Determination of Coarse Aggregate Surface Texture Using Image Analysis. In *Proceedings of the Pavement Mechanics Symposium at the 16th ASCE Engineering Mechanics Division Conference (EM2003)*, Seattle, Washington.
- Rondón, H. A., Wichtmann, T., Triantafyllidis, T., and Lizcano, A. (2009). Comparison of Cyclic Triaxial Behavior of Unbound Granular Material under Constant and Variable Confining Pressure. *Journal of Transportation Engineering*, Vol. 135, No. 7, pp. 467-478.
- Rowshanzamir, M.A. (1995). Resilient Cross-Anisotropic Behavior of Granular Base Materials Under Repetitive Loading. Ph.D. Thesis, University of New South Wales, School of Civil Engineering, Australia.
- Rumelhart D.E., Hinton, G.E., and Williams, R.J. (1986). Learning Representations by Back-Propagating Errors. *Nature*, Vol. 323, pp. 533-536.
- Rushing, J.F. and Little, D.N. (2013). Static Creep and Repeated Load as Rutting Performance Tests for Airport HMA Mix Design. *ASCE Journal of Materials in Civil Engineering*, 04014055(8).

- Saeed, A., Hall J., and Barker W. (2001). Performance-related Tests of Aggregates for Use in Unbound Pavement Layers. NCHRP Report No.453, National Academy Press, Washington, D.C.
- Sánchez-Leal, F.J. (2007). Gradation Chart for Asphalt Mixes: Development. *Journal of Materials in Civil Engineering*, Vol. 19, No. 2, pp.185-197.
- Sayao, A.S.F. and Vaid, Y.P. (1989). Deformations Due to Principal Stress Rotation. *Proceedings of the 12th International Conference on Soil Mechanics and Foundation Engineering*, Vol. 1, Rio de Janeiro, Brazil, pp. 107-110.
- Shackel, B. (1973). Repeated Loading of Soils: A Review. *Aust. Road Research*. Vol. 5 No 3. Oct., pp. 22-49.
- Seed, H.B., Mitry, F.G., Monismith, C.L., and Chan, C.K. (1967). Factors Influencing the Resilient Deformations of Untreated Aggregate Base in Two Layer Pavements Subjected to Repeated Loading. *Highway Research Record No. 190*, pp. 19-55.
- Seyhan, U. (2002). Characterization of Anisotropic Granular Layer Behavior in Flexible Pavements. PhD dissertation, University of Illinois, Urbana, U.S.
- Seyhan, U. and Tutumluer, E. (2002). Anisotropic Modular Ratios as Unbound Aggregate Performance Indicators. *Journal of Materials in Civil Engineering*, 14(5), pp. 409-416.
- Shaw, P (1980). Stress-Strain Relationships for Granular Materials under Repeated Loading. PhD dissertation, University of Nottingham, Nottingham, U.K.
- Sharp, R.W. and Booker, J.R. (1984). Shakedown of Pavements under Moving Surface Loads. *Journal of Transportation Engineering*, Vol. 110, pp. 1-14.

- Shen, S. and Yu, H. (2011). Analysis of Aggregate Gradation and Packing for Easy Estimation of Hot-Mix-Asphalt Voids in Mineral Aggregate. *Journal of Material in Civil Engineering*, Vol. 23, No. 5, pp. 664-672.
- Sweere, G.T.H. (1990). Unbound Granular Bases for Roads. PhD Dissertation, University of Delft, Delft, The Netherlands.
- Talbot, A.N. and Richart, F.E. (1923). The Strength of Concrete and its Relation to the Cement, Aggregate, and Water. In *Bulletin No. 137*: pp. 1-116.
- Tang, X. (2011). A Study of Permanent Deformation Behavior of Geogrid-reinforced Flexible Pavements Using Small Scale Accelerated Pavement Testing. Ph.D. Dissertation, The Pennsylvania State University, State College, PA.
- Tao, M., Abu-Farsakh, M., and Zhang, Z. (2008). Optimize Drainable Unbound Aggregate Through Laboratory Tests. *Proceedings of GeoCongress 2008: Characterization, Monitoring, and Modeling of Geosystems*.
- Tao, M., Mohammad, L.N., Nazzal, M.D., Zhang, Z., and Wu, Z. (2010). Application of Shakedown Theory in Characterizing Traditional and Recycled Pavement Base Materials. *Journal of Transportation Engineering*, Vol. 136, No. 3, pp. 214-222.
- Theyse, H.L. (2001). The Development of Mechanistic-Empirical Permanent Subgrade Deformation Models from Heavy Vehicle Simulator Data. M. Eng. Thesis, Rand Afrikaans University, Johannesburg, South Africa.
- Theyse, H.L. (2002). Stiffness, Strength, and Performance of Unbound Aggregate Material: Application of South African HVS and Laboratory Results to California Flexible Pavements. Final Report, Institute of Transportation Studies, University of California, Berkeley.

- Theyse, H.L., De Beer, M., and Rust, F.C. (1996). Overview of South African Mechanistic Pavement Design Method. Transportation Research Record No. 1539, pp. 6-17.
- Thom, N.H. and Brown, S.F. (1987). Effect of Moisture on the Structural Performance of a Crushed-Limestone Road Base. Transportation Research Record No. 1121, pp. 50–56.
- Thom, N.H. and Brown, S.F. (1988). The Effect of Grading and Density on the Mechanical Properties of a Crushed Dolomitic Limestone. Proc., 14th ARRB Conf., pp. 94–100.
- Thompson, M.R. (1998). State-Of-The-Art: Unbound Base Performance. Proceedings of the 6th Annual Symposium of the International Center for Aggregates Research (ICAR).
- Thompson, M.R. and Elliot, R.P. (1985). ILLI-PAVE Based Response Algorithms for Design of Conventional Flexible Pavements. Transportation Research Record No. 437, pp. 50-57.
- Thompson, M.R. and Nauman, D. (1993). Rutting Rate Analyses of the AASHO Road Test Flexible Pavements. Transportation Research Record No. 1384, pp. 36–48.
- Thompson, M.R. and Smith, K.L. (1990). Repeated Triaxial Characterization of Granular Bases. Transportation Research Record No. 1278, pp. 7-17.
- Thompson, M.R. and LaGrow, T. (1988). A Proposed Conventional Flexible Pavement Thickness Design Procedure. Civil Engineering Studies, Transportation Engineering Series No. 55, University of Illinois at Urbana-Champaign.
- Thompson, M.R. and Robnett, Q.L. (1979). “Resilient Properties of Subgrade Soils,” Transportation Engineering Journal, ASCE, Vol. 105, NO. TE1.
- Tian, P., Zaman, M.M., and Laguros, J.G. (1998). Gradation and Moisture Effects on Resilient Moduli of Aggregate Bases. Transportation Research Record No. 1619, pp. 7-17.
- Tseng, K. (1988). A Finite Element Method for the Performance Analysis of Flexible Pavements. Ph.D. Dissertation, Texas A&M University, College Station, TX.

- Tseng, K., and Lytton, R. (1989). Prediction of permanent deformation in flexible pavement materials. STP1016-EB, ASTM International, West Conshohocken, PA, pp. 154–172.
- Tutumluer, E., (1995). Predicting Behavior of Flexible Pavements with Granular Bases, Ph.D. Dissertation, Georgia Institute of Technology, Atlanta, Georgia.
- Tutumluer, E. (2013). Practices for Unbound Aggregate Pavement Layers. NCHRP Synthesis 445, TRB, National Research Council, Washington, D.C.
- Tutumluer, E., Rao, C., and Stefanski, J.A. (2000). Video Image Analysis of Aggregates. Technical Report FHWA-IL-UI-278, Civil Engineering Studies UILU-ENG-2000-2015, University of Illinois at Urbana-Champaign, Urbana, Illinois.
- Tutumluer, E., Ceylan, H., and Seyhan, Ü., (2001). Advanced Characterization of Granular Material Behavior Using Artificial Neural Networks. XVth International Conference on Soil Mechanics and Geotechnical Engineering, Istanbul, Turkey, August 27-31.
- Tutumluer, E., Mishra, D., and Butt, A. (2009). Characterization of Illinois Aggregates for Subgrade Replacement and Subbase. Final Report, Illinois Center for Transportation (ICT) R27-1 Project, University of Illinois Urbana-Champaign, Urbana, IL.
- Tutumluer, E., Huang, H., Hashash, Y.M.A., and Ghaboussi, J. (2009). AREMA Gradations Affecting Ballast Performance Using Discrete Element Modeling (DEM) Approach. Proceedings of the AREMA 2009 Annual Conference, Chicago, Illinois, Sep. 20-23.
- Tutumluer, E., Little, D.N., and Kim, S.-H. (2003). Validated Model for Predicting Field Performance of Aggregate Base Courses. Transportation Research Record No. 1837, pp. 41-49.

- Tutumluer, E. and Pan, T. (2008). Aggregate Morphology Affecting Strength and Permanent Deformation Behavior of Unbound Aggregate Materials. *ASCE Journal of Materials in Civil Engineering*, Vol. 20, No. 9, pp. 1-11.
- Tutumluer, E. and Seyhan, U. (1998). Neural Network Modeling of Anisotropic Aggregate Behavior from Repeated Load Triaxial Tests. *Transportation Research Record No. 1615*, pp. 86-93.
- Tutumluer, E. and Seyhan, U. (1999). Stress Path Loading Effects on Granular Material Resilient Response. In *Unbound Granular Materials – Laboratory Testing, In-situ Testing and Modeling*, Edited by A. Gomes-Correia, A.A. Balkema Publishers, Proc. Workshop at the Instituto Superior Técnico – IST, Lisbon, Portugal, January 21-22, pp. 109-121.
- Tutumluer, E. and Seyhan, U. (2000). Effects of Fines Content on the Anisotropic Response and Characterization of Unbound Aggregate Bases. *Proceedings of the 5th International on Unbound Aggregates in Roads (UNBAR5)*, Unbound Aggregates in Road Construction, Edited by A.R. Dawson, A.A. Balkema, University of Nottingham, UK, pp. 153-161.
- Ullidtz, P. (1997). Modeling of Granular Materials Using the Discrete Element Method. *Proceedings of the 8th International Conference on Asphalt Pavements*, Seattle, WA, pp. 757-769.
- Uthus, L., Tutumluer, E., Horvli, I., and Hoff, I. (2007). Influence of Grain Shape and Surface Texture on the Deformation Properties of Unbound Aggregates in Pavements. *International Journal of Pavements*, Vol. 6, pp. 75-88.
- Uzan (1985). Characterization of Granular Materials. *Transportation Research Record No. 1022*.
- Vallejo, L.E. (2001). Interpretation of the Limits in Shear Strength in Binary Granular Mixtures. *Canadian Geotechnical Journal*, Vol. 38, pp. 1097-1104.

- Van Niekerk, A.A. (2002). Mechanical Behavior and Performance of Granular Bases and Sub-Bases in Pavements. Ph.D. Thesis, Technische Universiteit Delft, Delft, The Netherlands.
- Van Niekerk, A.A. and Huurman, M. (1995). Establishing Complex Behavior of Unbound Road Building Materials from Simple Material Testing. Technical Report No. 7-95-200-16, Delft University of Technology, Delft.
- Vardanega, P.J. and Waters, T.J. (2011). Analysis of Asphalt Concrete Permeability Data Using Representative Pore Size. *ASCE Journal of Materials in Civil Engineering*, 23(2), pp. 169-176.
- Vardoulakis, I. and Sulem, J. (1995). *Bifurcation Analysis in Geomechanics*. Blackie Academic and Professional, Glasgow.
- Vavrik, W.R., Pine, W.J., and Carpenter, S.H. (2002). Aggregate Blending for Asphalt Mix Design: Bailey Method. *Transportation Research Record No. 1789*, pp. 146-153.
- Wang, H. (2011). Analysis of Tire-Pavement Interaction and Pavement Responses Using a Decoupled Modeling Approach. Ph.D. Dissertation, University of Illinois at Urbana-Champaign, Urbana, Illinois.
- Werbos, P. (1974). *Beyond Regression: New Tools for Prediction and Analysis in the Behavioral Sciences*. Ph.D. Dissertation, Harvard University, MA.
- Werkmeister, S. (2003). Permanent Deformation Behavior of Unbound Granular Materials in Pavement Constructions. Ph.D. thesis, Technical Univ. of Dresden, Dresden, Germany.
- Werkmeister, S., Dawson, A.R., and Wellner, F. (2001). Permanent Deformation Behavior of Granular Materials and the Shakedown Theory. *Transportation Research Record No. 1757*, pp 75-81.

- Werkmeister, S., Numrich, S., Dawson, A.R., and Wellner, F. (2003). Design of Granular Pavement Layers Considering Climatic Conditions. Transportation Research Record No. 1837, pp. 61-70.
- Werkmeister, S., Dawson, A.R., and Wellner, F. (2004). Pavement Design Model for Unbound Granular Materials. ASCE Journal of Transportation Engineering, 130(5), pp. 665-674.
- Wichtmann, T. (2005). Explicit Accumulation Model for Non-Cohesive Soils under Cyclic Loading. Ph.D. thesis, Ruhr Universitat Bochum, Germany.
- Witczak, M.W., Bonaquist, B., Von Quintus, H., and Kaloush, K. (2000). Specimen Geometry and Aggregate Size Effects in Uniaxial Compression and Constant Height Shear Tests. J. Asphalt Paving Technol., Vol. 69, pp. 733–782.
- Witczak, M. and El-Basyouny, M.M. (2004). Calibration of Permanent Deformation Models for Flexible Pavements. In Guide for Mechanistic–Empirical Design of New and Rehabilitated Pavement Structures, ARA, Inc., ERES Division, Champaign, Ill., Appendix GG-1, p. GG-1.31.
- Witczak, M.W. and Uzan J. (1988). The Universal Airport Pavement Design System Report I of V: Granular Materials Characterization. University of Maryland, pp. 79.
- Wolff, H. (1992). The Elasto-Plastic Behavior of Granular Pavement Layers in South Africa. Ph.D. Dissertation, University of Pretoria.
- Wolff, H. and Visser, A.T. (1994). Incorporating Elasto-Plasticity in Granular Layer Pavement Design. Proc., Instn. of Civ. Engrs. Transp., Vol. 105, pp. 259–272.
- Wong, R.K.S. and Arthur, J.R.F. (1986). Sand Shear by Stresses with Cyclic Variations in Direction. Geotechnique, Vol. 36, No. 2, pp. 215-226.

- Wood, D.M. (1982). Laboratory Investigations of the Behavior of Soils under Cyclic Loading: A Review. *Soil Mechanics-Transient and Cycle Loads*, G. N. Pance and O. C. Zienkiewicz, eds., John Wiley and Sons Inc., New York, NY, pp. 513-582.
- Wu, Z., Chen, X., and Yang, X. (2011). Finite Element Simulation of Structural Performance on Flexible Pavements with Stabilized Base/Treated Subbase Materials under Accelerated Loading. Final Report FHWA/LA.10/452, Louisiana Transportation Research Center, Baton Rouge, LA.
- Xiao, Y., Tutumluer, E., and Siekmeier, J.A. (2011). Mechanistic-Empirical Evaluation of Aggregate Base/Granular Subbase Quality Affecting Flexible Pavement Performance in Minnesota. *Transportation Research Record No. 2227*, pp. 97-106.
- Xiao, Y. and Tutumluer, E. (2012). Best Value Granular Material for Road Foundations. Final Report MN/RC 2012-01, Minnesota Department of Transportation, St. Paul, MN.
- Xiao, Y., Tutumluer, E., Qian, Y., and Siekmeier, J. (2012). Gradation Effects Influencing Mechanical Properties of Aggregate Base and Granular Subbase Materials in Minnesota. *Transportation Research Record No. 2267*, Washington, D.C., pp. 14-26.
- Xu, M., Song, E., and Chen, J. (2012). A Large Triaxial Investigation of the Stress-Path-Dependent Behavior of Compacted Rockfill. *Acta Geotechnica*, Vol. 7, pp. 167-175.
- Yideti, T.F., Birgisson, B., and Jelagin, D. (2013). Influence of Aggregate Packing Structure on CBR Values of Unbound Granular Road Materials. In CD-ROM Proceedings of the Transportation Research Board 92nd Annual Meeting, TRB, Washington, D.C.
- Yideti, T.F., Birgisson B., Jelagin D., and Guarin, A. (2013). Packing-based Theory Framework to Evaluate Permanent Deformation of Unbound Granular Materials. *Int. J. of Pav. Eng.*, Vol. 14, No. 3, pp. 309-320.

- Yu, H.S. (2005). Three-dimensional Analytical Solutions for Shakedown of Cohesive-frictional Materials under Moving Surface Loads. *Proc. R. Soc. A* (2005) 461, pp. 1951–1964.
- Zhao, D., Nezami, E.G., Hashash, Y.M.A., and Ghaboussi, J. (2006). Three-dimensional Discrete Element Simulation for Granular Materials. *Engineering Computations*, 23(7), pp.749-770.
- Zhou, F., Scullion, T., and Sun, L. (2004). Verification and Modeling of Three-Stage Permanent Deformation Behavior of Asphalt Mixes. *Journal of Transportation Engineering*, 130(4), pp. 486-494.